JACOBS
UNIVERSITY

Sea-Ice Mass Balance Influenced by Ice Shelves

Mario Hoppmann

A Thesis submitted in partial fulfillment
of the requirement for the degree of

Doctor of Philosophy

in Geosciences

Approved Dissertation Committee

Prof. Dr. Rüdiger Gerdes

Prof. Dr. Vikram Unnithan

Dr. Marcel Nicolaus

Dr. Stefan Hendricks

Date of Defense: 24 March 2015

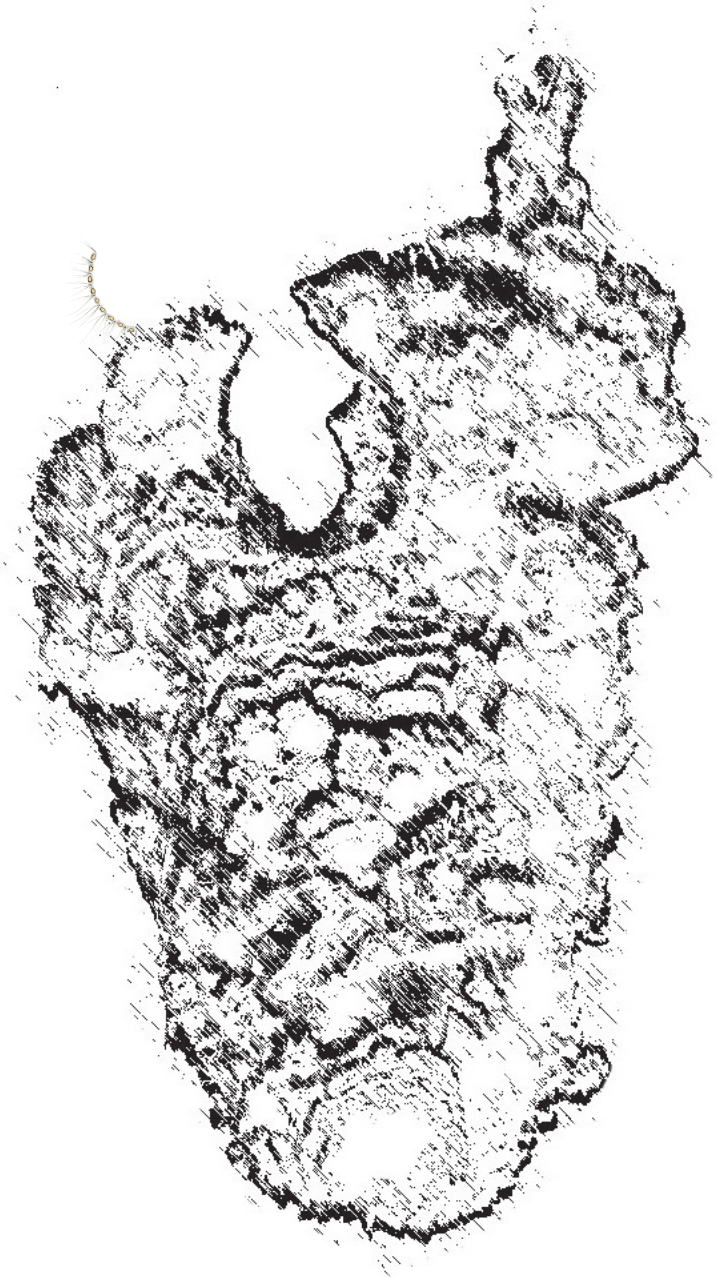

To my loved ones

"There is pleasure in the pathless woods,
there is rapture in the lonely shore,
there is society where none intrudes,
By the deep sea, and music in its roar;
I love not Man the less, but Nature more."

"Es wohnt Genuss im dunklen Waldesgrüne,
Entzücken weilt auf unbetretener Düne,
Gesellschaft ist, wo alles menschenleer,
Musik im Wellenschlag am ewigen Meer;
Die Menschen lieb ich, die Natur noch mehr."

- Lord George Gordon Noel Byron (1788 - 1824)

Table of Contents

Abstract

Floating ice shelves at the boundary between the Antarctic ice sheet and the Southern Ocean play a crucial role in Antarctica's mass balance through iceberg calving and basal melting. The latter has strong implications for coastal Antarctic sea-ice properties through the formation of a sub-ice platelet layer. This matrix of intertwined individual ice crystals influences sea-ice properties, mass- and energy balance, and represents an important habitat for a highly productive and uniquely adapted microbial community. Although its potential significance has been recognized already 100 years ago, a comprehensive understanding of this system and associated processes is still not well established due to logistical and methodological difficulties. At the same time, snow precipitation over the the coastal margin and its redistribution through seaward winds may increase the amount of snow deposited on coastal Antarctic sea ice. The presence of a thick, highly reflective and insulating snow cover has manifold consequences for sea-ice mass- and energy balance. However, in situ observations of snow on Antarctic sea ice are sparse, and remote-sensing techniques still lack the ability to infer accurate information about the snow pack.

The aim of this thesis was to overcome these limitations by the detailed investigation of a sea-ice regime heavily influenced by a nearby ice shelf. An ongoing monitoring program was developed and realized on the landfast sea ice of Atka Bay, a small embayment in front of the Ekström Ice Shelf in the eastern Weddell Sea, Antarctica. By combining measurements of sea ice, ocean and atmosphere over a period of five years, this work revealed important information about the seasonal cycle of the sea ice, its properties, and how it is influenced by the presence of thick snow on the surface and a several meter thick platelet layer underneath.

This study showed that ice platelets emerge from the ice-shelf cavity in episodic events, and interact with the fast ice as early as June. The average annual platelet-layer thickening was 4 m, and the additional buoyancy partly prevented surface flooding and snow-ice formation despite a high snow load. The highly reflective snow cover and the thick platelet layer shielded the solid sea ice from increased radiative and oceanic heat fluxes in summer, respectively. A combination of drillhole measurements, sea-ice temperature profiles and model studies was used to calculate the ice-volume fraction in the platelet layer, a parameter necessary to estimate the overall contribution of ice-shelf processes to sea-ice mass balance. Results yielded ice-volume fractions between 0.18 and 0.35, consistent with earlier studies in other regions of Antarctica. We found that the contribution of ocean/ice-shelf interaction dominated the total sea-ice production, effectively accounting for up to 70 % of annual sea-ice growth. The total annual ice-platelet volume underlying Atka Bay fast ice was equivalent to more than one fifth of the annual basal melt volume under the Ekström Ice Shelf.

In addition to the development of a sea-ice monitoring and the scientific outcomes outlined above, this work contributed to the advance of several innovative methodological approaches, which are expected to facilitate sea-ice research in the future: thermistor chains with active heating, multi-frequency electromagnetic induction sounding, and high-resolution X-band synthetic aperture radar (SAR) imagery from satellites.

First, this study applied a comprehensive analysis to sea-ice temperature- and heating profiles over a period of 15 months in order to infer the seasonal cycle of sea-ice and platelet-layer properties. By doing so, we were able to show that, in contrast to the established acoustic sounding approach, a thermistor chain with an active heating of embedded resistors is well suited to derive the fast-ice mass balance in regions influenced by ocean/ice-shelf interaction. Our results further indicate that the active heating technique is able to detect the platelet-layer bottom through the steep gradient in current speed, similar to a hot-wire anemometer.

Second, we used a ground-based, multi-frequency electromagnetic induction sounding device to quantify sub-ice platelet-layer properties. The combination of in situ data with theoretical responses yielded bulk platelet-layer conductivities of 1154 mS $m^{-1} \pm 271$ mS m^{-1}, corresponding to ice-volume fractions between 0.29 and 0.43. Detailed descriptions of calibration routines and measurement uncertainties were provided to facilitate future sea-ice studies with such an instrument. First results of platelet-layer thickness retrieval by geophysical inversion of our unique dataset suggest that this method is promising to efficiently map sub-ice platelet-layer thickness on a larger spatial scale than previously feasible.

Third, we linked the evolution of X-band synthetic aperture radar (SAR) backscatter during spring/summer transition to changes in the seasonal snow pack. Between 75 % and 93 % of the spatio-temporal variations of the recorded backscatter signal were explained by combination of up to four snow-pack parameters: especially after the onset of early-melt processes and freeze-thaw cycles, the majority of the backscatter variations were influenced by changes primarily in snow/ice-interface temperature, snow depth and grain size. This study implies a great potential to retrieve snow physical properties from X-Band SAR backscatter, albeit more research is necessary to achieve this aim.

Chapter 1

Motivation and Thesis Outline

1.1. Motivation

Sea ice is a crucial component in the global climate system. It governs the exchange processes between the ocean and atmosphere in the polar regions, and represents a sensible indicator of climate change. At the same time, polar marine ecosystems heavily depend on the properties of the sea-ice cover. While the Arctic Ocean showed a substantial decline in sea-ice thickness, -extent and -age in recent decades in response to global warming, the evolution of sea ice in the Southern Hemisphere has been different. Antarctic sea-ice extent and -area exhibit a positive trend, an observation which is counter-intuitive in a warming world and currently one of the major puzzles in sea-ice research. Although several hypotheses have been raised to address this issue, results remain inconclusive.

At the boundary between the continental ice sheet and the Southern Ocean with its vast sea-ice cover, Antarctic ice shelves have recently been proposed as a potential driver of the observed sea-ice expansion in the Southern Hemisphere, an issue which has since been controversially discussed. In order to better understand the complex interplay between ocean, atmosphere, ice sheets and sea ice (Fig. 1.1) on a larger scale, it is necessary to develop a more detailed process understanding than is currently available. Process studies based on in situ observations of sea-ice properties are necessary to obtain such knowledge, and are at the same time crucial for validation of numerical models. However, the remoteness and harsh environmental conditions of the Antarctic significantly complicate this undertaking. Only few wintering stations with permanent access to nearby sea ice exist along the Antarctic coastline, and urgently needed observational (long-term) datasets are sparse.

Although the investigation of interactions among different cryospheric elements (Fig. 1.1, black circle) is a relatively new research field, one mechanism by which ice shelves heavily affect coastal sea-ice properties is known since the 1970s: supercooled water originating from ice-shelf cavities may lead to the formation of ice crystals deep in the water column, which then rise to the surface and accumulate below nearby landfast sea ice (fast ice) and pack ice to form a several meter thick sub-ice platelet layer. The properties of such special sea-ice regimes are a direct reflection of ocean/ice-shelf interaction in the inaccessible cavities, which is in itself a critical aspect of current climate research, especially since the recent collapse of large ice shelves on the Antarctic Peninsula. Numerous observations of ice platelets originating from depth and their accumulation below solid sea ice have been reported from all around the continent, but year-round investigations of sub-ice platelet layers are currently limited to the Ross Sea. As a consequence, most aspects of their spatio-temporal variability remain elusive, and their overall role for sea ice in different regions of Antarctica is currently poorly understood.

The proximity of ice shelves may also lead to the deposition of a substantial amount of snow on coastal

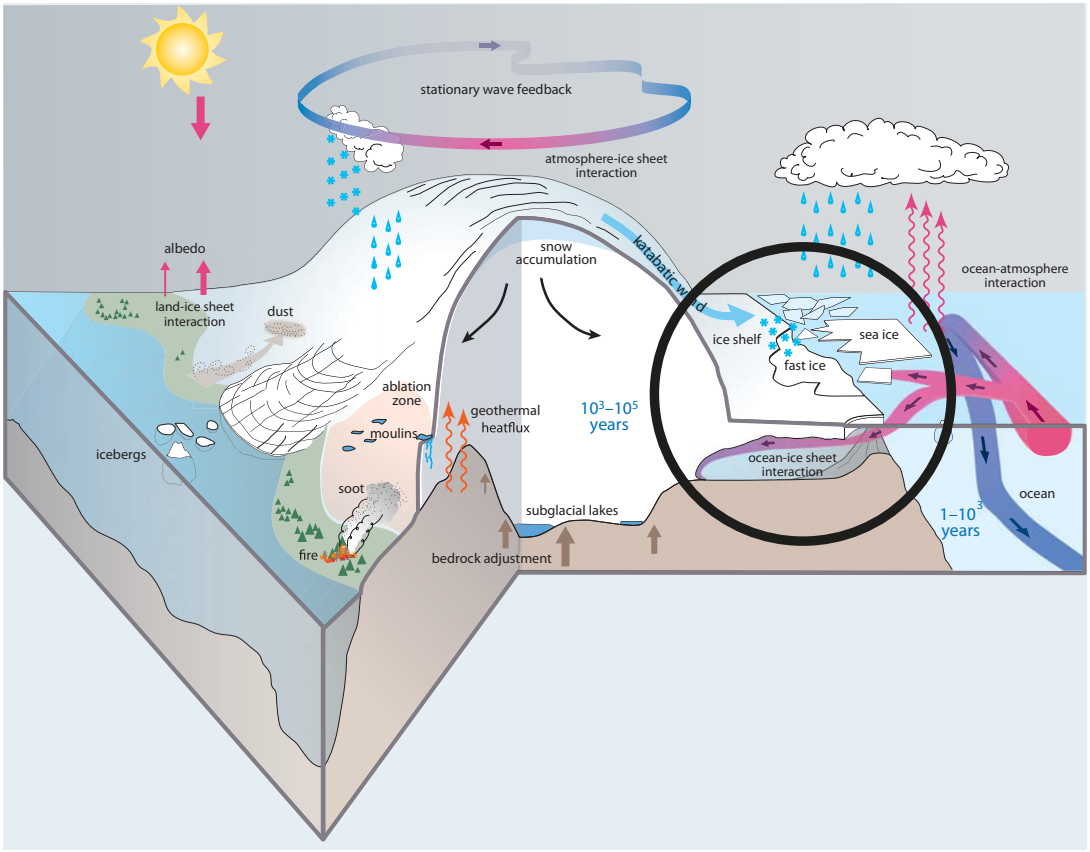

Figure 1.1: Schematic illustration of climate processes and interactions in the Southern Hemisphere (modified after IPCC, 2013, p. 403). The black circle highlights the elements and interactions under investigation in this thesis.

sea ice as a result of redistribution by winds. Such a thick snow cover influences sea-ice growth and surface energy balance by its low thermal conductivity and high albedo. In addition, snow directly contributes to sea-ice thickness by surface flooding and snow-ice formation, as well as refreezing of meltwater (superimposed ice). However, the large-scale determination of snow properties on sea ice remains a major challenge, especially in the Antarctic.

1.2. Aim

The main aim of this thesis is to overcome the described limitations by creating new knowledge on ice-shelf processes influencing sea ice in the eastern Weddell Sea, Antarctica (Fig. 1.2). Atka Bay, a 440 km^2 large embayment in the front of the Ekström Ice Shelf, is seasonally covered with fast ice and exhibits both, a substantial sub-ice platelet layer and a thick snow cover. Although the German wintering station Neumayer is just a few kilometers away from the fast ice, only two sea-ice studies were performed here since its establishment in 1980. An integral part of this thesis is to develop and maintain a continuous sea-ice monitoring program at Atka Bay, taking advantage of the infrastructure and wintering personnel present at Neumayer year-round. Although it was unclear at the beginning whether such a monitoring

program would be generally feasible at Atka Bay, let alone possible, this work aims to lay the foundation for its permanent establishment.

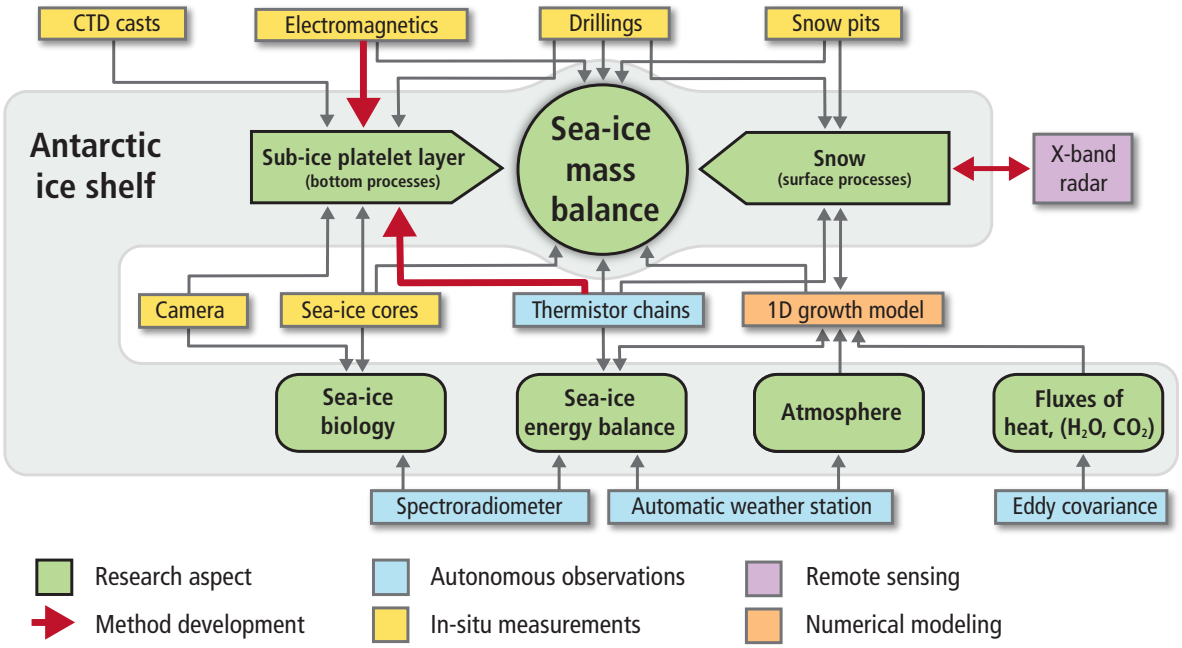

Figure 1.2: Schematic diagram linking the applied methods and techniques (non-green boxes) to different important aspects under investigation in this thesis (green boxes). Red arrows indicate the links that are developed/enhanced as part of this work.

The monitoring activities (Chapter 4) are designed to yield a better understanding of sea-ice properties at Atka Bay with a focus on the drivers governing its evolution. In addition, a dedicated field campaign to Atka Bayhad the additional aim to develop innovative approaches allowing a more efficient determination of sub-ice platelet layer and snow properties on larger spatio-temporal scales than previously feasible (Fig. 1.2, red arrows).
The following three key hypotheses define the outline of this thesis:

1. **Ocean/ice-shelf interaction dominates fast-ice properties, -mass and -energy balance in the eastern Weddell Sea** (Chapters 5 and 6). Sub-ice platelet layers are known to contribute substantially to coastal sea-ice mass balance for example in McMurdo Sound, Ross Sea. In contrast, few studies exist in the Weddell Sea, and knowledge about the overall role of ocean/ice-shelf interaction for sea-ice properties in this region is currently limited. In addition to the basal processes associated with sub-ice platelet layers, high snow accumulations in the Weddell Sea also impact fast-ice mass- and energy balance in ways that are only poorly understood. A variety of both traditional and innovative measurements related to atmosphere, ocean, sea ice and snow are applied over a study period of several years in order to determine the main factors governing sea-ice properties, -mass and energy balance at Atka Bay.

2. **Multi-frequency induction sounding and thermistor chains with active heating are promising**

tools to determine sub-ice platelet layer properties on larger spatio-temporal scales (Chapters 6 and 7). Electromagnetic (EM) induction sounding is an established method to derive regional sea-ice thickness distributions, bridging the gap between drillings and satellite remote sensing. Compared to the traditional, single-frequency approach, multi-frequency EM sounding provides additional information about a sea-ice cover. Although its full potential is unclear, we expect that this approach is generally suitable to detect sub-ice platelet-layer properties. If this expectation is confirmed, it would be possible to map platelet layer thickness without the need for time-consuming drillings, with huge implications for coastal Antarctic sea-ice research, oceanography, glaciology and biology. In addition, there is currently no single feasible method which is able to autonomously monitor platelet-layer evolution at a fixed site. Thermistor chains with active heating are in principle able to detect gradients in flow velocity of a liquid medium, a situation expected in the presence of a sub-ice platelet layer. This approach therefore bears the potential to complement EM measurements in the temporal dimension. However, there is currently no single study available which has investigated this issue.

3. **X-Band radar backscatter reveals detailed information about physical and stratigraphic snow properties** (Chapter 8). Interactions between snow on sea ice and microwave radiation emitted by a space-borne synthetic aperture radar hold the potential to estimate snow physical properties from space. Studies in the Antarctic are sparse, and the detailed interrelation between local processes in the snow and their microwave response yet needs to be identified. One aim of this study was to fill this gap and identify potential links between snow properties from direct measurements and high-resolution X-Band radar imagery.

1.3. Thesis outline

Section 2.1 gives a short introduction to sea ice and briefly summarizes its significance for the global climate and polar marine ecosystems. Typical sea-ice formation processes in the Southern Hemispheres are described in more detail in order to understand the peculiarities of ice-platelet formation at depth introduced later. Section 2.2 is dedicated to the puzzle of Southern Hemisphere sea-ice evolution under climate change, before Section 2.3 introduces fast ice as an important feature of the Antarctic coastline. Section 2.4 reviews aspects of the Antarctic ice sheet, and introduces ice shelves as an important boundary between the ice sheet and the Southern Ocean.

The core of this thesis is represented by 3 manuscripts/publications (Publication I to III), represented by Chapters 3, 5 and 6, respectively.

Chapter 3 (Publication I) presents a comprehensive overview of the current state of knowledge regarding sub-ice platelet layers around Antarctica. Since such an overview is entirely missing in the literature, albeit urgently needed, the intention is to publish the compiled information as a review paper after completion.

Chapter 4 summarizes the fast-ice monitoring between 2010 and 2014, along with field measurements from an additional expedition performed in the framework of this study. These served as the main data sources for all of the presented publications. A more detailed description is given in annual field reports

published in AWI's online repository EPIC.

Publications II and III, represented by Chapters 5 and 6, are the most important scientific outcomes of this research, and describe in detail the fast-ice properties, -mass and -energy balance in the eastern Weddell Sea, with special emphasis on ocean/ice-shelf interaction.

Publications IV to VI are summarized in Chapter 7. These were prepared in collaboration with another PhD student, Priska A. Hunkeler, and aim to lay the foundation for an alternative approach on sub-ice platelet layer detection with multi-frequency electromagnetic induction sounding. The publications are provided in the appendix.

Publications VII and VIII, summarized in Chapter 8, were prepared in collaboration with the Earth Observing Systems (EOS) group and the University of Trier. They highlight the potential of X-band radar for cryospheric research, and contribute to a better understanding of linkages between snow properties and X-Band radar backscatter in order to facilitate large-scale investigation of snow on sea ice. Both publications are provided in the appendix.

Finally, Chapter 9 summarizes the main outcomes of this thesis and provides an outlook on the potential for future research.

1.4. List of own publications and reports

Publication I:

Hoppmann, M., G. S. Dieckmann, I. J. Smith , P. J. Langhorne: "Sub-ice platelet layers and their role for sea-ice properties and -ecology: a review", manuscript in preparation (Chapter 3)

Publication II:

Hoppmann, M., M. Nicolaus, S. Paul, P. A. Hunkeler, G. Heinemann, S. Willmes, R. Timmermann, O. Boebel, T. Schmidt, M. Kühnel, G. König-Langlo and R. Gerdes: "Ice platelets below Weddell Sea landfast sea ice", Annals of Glaciology 56(69), 2015, http://dx.doi.org/10.3189/2015AoG69A678 (Chapter 5)

Publication III:

Hoppmann, M., M. Nicolaus, P. A. Hunkeler, P. Heil, L.-K. Behrens, G. König-Langlo and R. Gerdes: "Seasonal evolution of an ice-shelf influenced fast-ice regime, derived from an autonomous thermistor chain", Journal of Geophysical Research: Oceans 120(3), 2015, http://dx.doi.org/10.1002/2014JC010327 (Chapter 6)

Publication IV:

Hunkeler, P. A., S. Hendricks, **M. Hoppmann**, S. Paul and R. Gerdes: "Towards an estimation of sub sea-ice platelet-layer volume with multi-frequency electromagnetic induction sounding", Annals of Glaciology 56(69), 2015, http://dx.doi.org/10.3189/2015AoG69A705 (Appendix I)

Publication V:

Hunkeler, P. A., S. Hendricks, **M. Hoppmann**, C. Farquharson, T. Kalscheuer, M. Grab, Manuela S. Kaufmann L. Rabenstein and R. Gerdes. "Improved 1D inversions for sea ice thickness and conductivity from EM induction data: Inclusion of nonlinearities caused by passive bucking", accepted by Geophysics (Appendix II)

Publication VI:

Hunkeler, P. A., **M. Hoppmann**, S. Hendricks, T. Kalscheuer and R. Gerdes. "A glimpse beneath Antarctic sea ice: platelet-layer volume from multi-frequency electromagnetic induction sounding", submitted to Geophysical Research Letters (Appendix III)

Publication VII:

Dierking, W., S. Lienow, C. Wesche, W. Rack, **M. Hoppmann** and S. Willmes: "TSX-data for studies of snow on ice sheets and sea ice - preliminary results", 5. TerraSAR-X / 4. Tandem-X Science Team Meeting, 2013 (Appendix IV)

Publication VIII:

Paul, S., S. Willmes, **M. Hoppmann**, P. A. Hunkeler, G. Heinemann, M. Nicolaus and R. Timmermann. "The impact of early summer snow properties on landfast sea-ice X-band backscatter", Annals of Glaciology 56(69), 2015, http://dx.doi.org/10.3189/2015AoG69A715 (Appendix V)

Report I:

Hoppmann, M., M. Nicolaus and H. Schmithüsen. "Summary of AFIN measurements on Atka Bay landfast sea ice in 2010" (15 pages), 2011, `http://dx.doi.org/hdl:10013/epic.37766.d001` (not attached)

Report II:

Hoppmann, M., M. Nicolaus and J. Asseng. "Summary of AFIN measurements on Atka Bay landfast sea ice in 2011" (31 pages), 2012, `http://dx.doi.org/hdl:10013/epic.39903.d001` (not attached)

Report III:

Hoppmann, M., S. Paul, P. A. Hunkeler, U. Baltes, M. Kühnel, T. Schmidt, M. Nicolaus, G. Heinemann and S. Willmes. "Field work on Atka Bay land-fast sea ice in 2012/13" (120 pages), 2013, `http://dx.doi.org/hdl:10013/epic.42767.d001` (not attached)

Report IV:

Hoppmann, M., M. Nicolaus, L.-K. Behrens and J. Regnery. "Field work on Atka Bay landfast sea ice in 2013" (29 pages), 2014, `http://dx.doi.org/hdl:10013/epic.43850.d001` (not attached)

Chapter 2

Introduction

2.1. Sea ice - a general overview

2.1.1. What is sea ice?

Sea ice is a thin layer of frozen seawater, which floats atop the polar oceans due to its lower density. When sea ice starts to form as the temperature of the high-latitude surface oceans drops below the freezing point at approximately -1.8°C, a major part of the Arctic and Southern Oceans is covered under a vast white blanket. This blanket shrinks again in spring and summer, due to higher air and ocean temperatures as well as increased solar radiation. The seasonal cycle of sea-ice formation and decay in the polar oceans is thereby one of the most profound alterations of the earth's surface. Salt is rejected during growth, and becomes trapped in millimeter to centimeter scale enclosures and tubes between the crystals to form pockets of brine (Malmgren, 1927). These may connect to a complex net of channels, and provide a route for dense brine to leave the ice (e.g., Niedrauer and Martin, 1979). The small brine inclusions in sea ice determine many of its physical and mechanical properties (Pringle et al., 2007; Weeks, 2010), provide nutrients necessary for biological activity (Vancoppenolle et al., 2010; Arrigo, 2014), and give rise to a number of chemical and biogeochemical characteristics and processes fundamentally different from freshwater ice.

2.1.2. The significance of sea ice for the climate- and ecosystem

Sea ice, ocean and atmosphere form a complex and interactive system. Although only a few meters thick, sea ice provides a substantial "barrier" between the ocean and atmosphere, the two most essential elements of the global climate system. Sea ice significantly modifies the fluxes of heat, gases, moisture and momentum across the ocean/atmosphere interface. Due to its higher albedo, a sea-ice cover reflects far more sunlight relative to an uncovered ocean, thus affecting the planetary energy budget (Perovich, 1996). As salt is expelled during sea-ice growth and brine is released into the underlying ocean, salinity and density of the surface ocean are increased (Toggweiler and Samuels, 1995), driving production of dense shelf water. During sea-ice melt, freshwater is released with implications for ocean stratification and -circulation by forming a stable low-salinity ocean surface layer. In addition to its important physical role, sea ice governs the biogeochemical seasonal dynamics of the high-latitude oceans. Gases released during sea-ice growth affect the composition of the atmosphere and the deposition of chemical compounds such as mercury. Finally, sea ice has a crucial significance for biological productivity by influencing the light and nutrient regimes of the upper ocean, and impacts polar marine ecosystems by providing habitat, refuge, and a source of food or nutrients for many species (Thomas and Dieckmann, 2002; Dieckmann

and Hellmer, 2010; Arrigo, 2014)

The sea-ice cover is exceptionally vulnerable to small perturbations within the polar ocean and atmosphere, which in turn may significantly alter the areal extent and thickness. At the same time, sea-ice properties may also play a vital, albeit poorly-understood role in modulating climatic changes and variabilities.

It is because of these intertwined relations between key elements of the earth's climate system, that sea ice has become one, if not the most important, subject in the research of the past, present and future climate (Dieckmann and Hellmer, 2010). Although the efforts to study sea ice were intensified in recent decades, and many technological advances such as numerical modeling and remote sensing now facilitate the understanding of the climate system, the processes controlling the mass, properties, distribution and seasonality of sea ice still remain poorly understood.

This is especially owed to the fact that in-situ observations are very limited, particularly in winter, and key properties, such as sea-ice thickness, essentially remain unobserved.

2.1.3. Snow on sea ice

> *"A thick coating of snow has a most distinct effect in retarding the growth of sea ice in the early stages, for it acts as a blanket, and largely prevents the exchange of heat between the mass of the ice and the water beneath it and the air above."*
>
> Wright, C. and Priestley, R. (1922). *Glaciology - British (Terra Nova) Antarctic Expedition 1910-1913*, Harrison and Sons, London, UK (p. 333)

The impacts of sea ice on exchange processes between the ocean and atmosphere are further enhanced by the accumulation of snow on sea ice, which therefore also has a critical role in Earth's climate system. A thick snow cover, as often found on Antarctic sea ice, influences sea-ice growth and surface energy balance in various ways (Massom et al., 2001a). Through its low thermal conductivity, snow acts as a barrier for the heat transport from the sea ice to the atmosphere, effectively reducing ice growth at the bottom. On the other hand, snow contributes to sea-ice thickening at the surface through two distinct processes, snow-ice and superimposed-ice formation. High snow load leads to the depression of the sea-ice surface below the water surface (negative freeboard) and causes surface flooding of floes in large areas of the Southern Ocean. Refreezing of the snow/seawater mixture (slush) results in snow-ice formation, a layer of very saline ice on the surface of a floe. In addition, the formation of superimposed ice from snow melt water refreezing is a characteristic feature of Antarctic sea ice and adds to ice thickening from the top. These processes lead to a significant contribution of a snow cover to the total sea-ice mass balance in many regions around Antarctica (Lange et al., 1990; Eicken et al., 1994a; Eicken, 1998; Jeffries et al., 1994, 1997, 1998, 2001; Haas et al., 2001b; Kawamura et al., 2004; Nicolaus, 2006).

One of the most important feedback processes related to snow and sea ice results from the ability of these surfaces to reflect most short-wave irradiance back to the atmosphere (Perovich, 1996) and the relationship between this ability and temperature, also known as the ice-albedo feedback (Curry et al.,

1995; Morassutti, 1991). Furthermore, optical properties of snow and sea ice dominate the seasonal timing of biological processes and biogeochemical fluxes into and through sea ice, but their implications for these processes in sea-ice environments are much less known in the Antarctic compared to the Arctic. Hence, most biological studies and numerical models are based on rough estimates from few observations. In general, the number of direct observations and measurements of snow are very limited for both polar regions (e.g., Yackel and Barber, 2007; Massom et al., 2001a; Barber and Thomas, 1998)). At the same time, snow on sea ice accumulates and redistributes in different rates and snow properties are highly variable even on small spatial and temporal scales (Massom et al., 2001a).

Overcoming the difficulties to obtain reliable measurements of snow depth and physical snow properties by remote sensing techniques remains one of the big challenges of polar research. In addition, this research field is of ever-increasing importance since the impact of snow on sea-ice freeboard is the major source of uncertainty for sea-ice thickness retrieval from space (Ricker et al., 2014), especially in the Antarctic. Finally, the enhanced coverage and instrumentation of modern satellites bears great potential and is the only means to derive surface properties on an ocean-wide scale, especially in the polar regions. This study contributes to this important research field by identification of potential linkages between the physical properties of snow on Antarctic sea ice and the backscatter of X-band synthetic aperture radar, with a focus on the transition between spring and summer (Chapter 8).

2.1.4. Sea-ice formation in the Southern Ocean

The initial growth of sea ice starts with the formation of tiny ice crystals in the upper few millimeters of the ocean, so-called “frazil ice” (Weeks, 2010). If moderate wind and wave action leaves the ocean relatively undisturbed, a soupy layer of slush is created on the sea surface, also known as “grease ice” (WMO, 1970). When grease ice consolidates, flexible sheets of several centimeters in thickness are formed, commonly referred to as nilas (Petrich and Eicken, 2010).

Under the high turbulence levels of the Southern Ocean, the initial sea-ice formation process is slightly different. Persisting turbulent wind and wave motion results in the predominance of the so-called pancake cycle (Fig. 2.1; Doble et al., 2003), where aggregation of frazil crystals leads to the formation of centimeter-sized floes (“shuga”) in their earliest agglomerations, which later stick together to form decimeter-sized pans of ice (Fig. 2.1a, b,c).

Under the damped agitation of wind and ocean swell that penetrate from higher latitudes deep into the southern sea-ice zone, these pancakes collide and grind against one another. This process leads to a semi-consolidated cover composed of larger ice discs with raised edges, which eventually congeal into larger units reaching diameters of up to 5 m diameter (Figure 2.1d,e). When these larger pancakes subsequently freeze together, a continuous, solid sea-ice cover may form (“consolidated pancake ice”, Figure 2.1f). When snow finally accumulates on top, it is nearly impossible to visually distinguish it from other sea ice formed under quiet conditions. Only stratigraphic analysis of sea-ice cores reveals that the sea-ice cover is largely composed of individual pancakes stacked on top of each other, with the interstices consolidated through a combination of frazil and congelation ice. This process may account for rapid sea-ice thickening of up to 0.5 m in a matter of days (Wadhams et al., 1987; Worby et al., 1998), even in

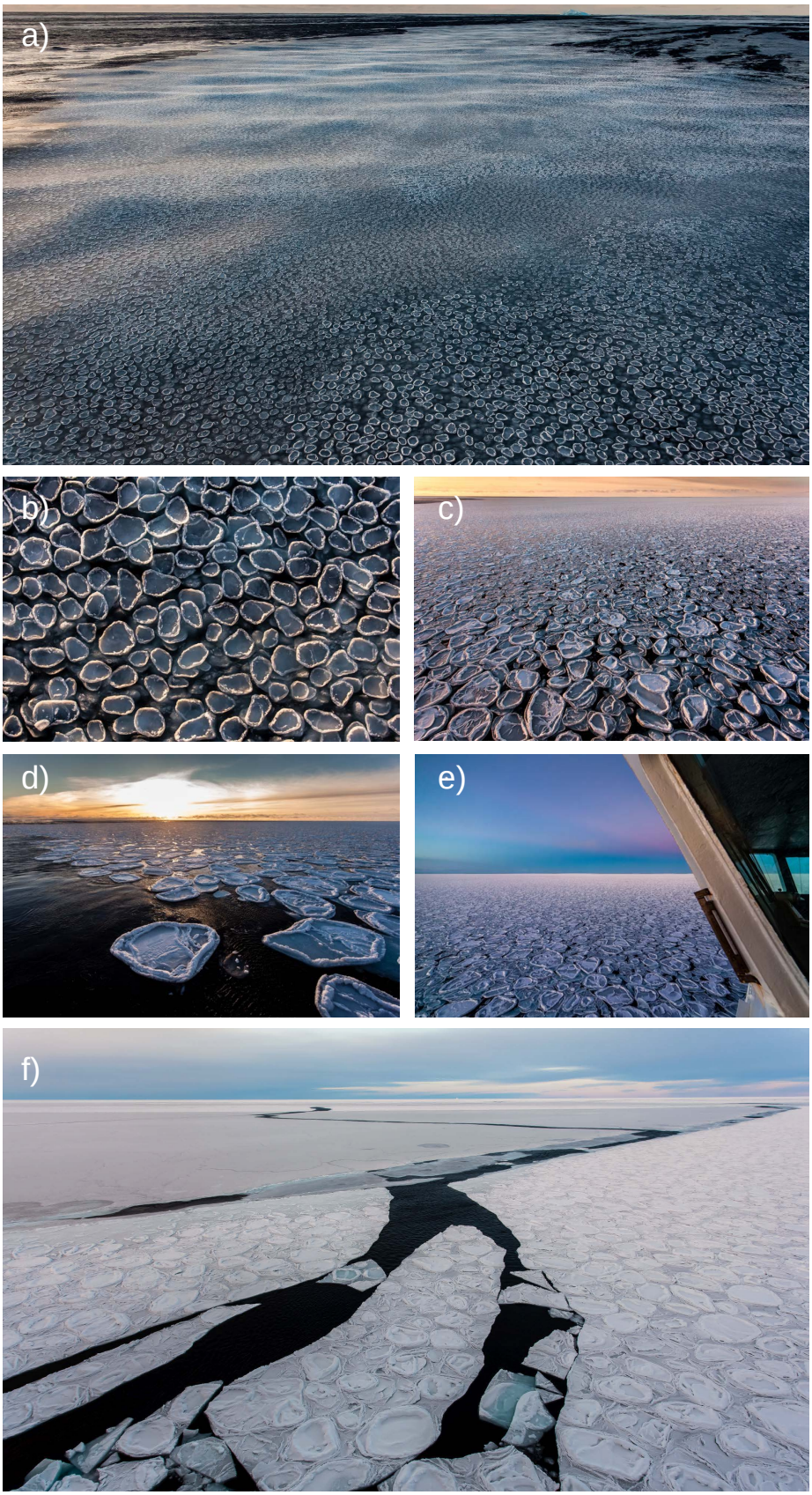

Figure 2.1: The Southern Ocean "pancake cycle". The photographs show different stages of initial sea-ice growth, as observed during the Polarstern expedition ANT-XXIX/6 to the Weddell Sea. The hand-size pancakes (a) consequently freeze together to form large discs of several meters in diameter (b-e), before they finally freeze together to form a closed sheet (f). After they are covered under snow, as is typical for Antarctic sea ice, this evolution is no longer apparent from visual inspection alone.

the presence of a high oceanic heat flux (Squire, 1998). In the Southern Ocean, the pancake cycle thereby has a significant influence on sea-ice mass balance (Weeks, 1998). Textural investigations of sea ice in the central Weddell Sea for example have shown that pancake ice growth is in fact the dominant mechanism for pack-ice formation in this area (Lange et al., 1989; Lange and Eicken, 1991; Clarke and Ackley, 1984; Gow et al., 1987), whereas the oceanic heat flux almost balances the heat loss by conduction upwards through the ice (Gordon and Huber, 1990).

2.2. Antarctic sea ice in the climate system

In recent years, an increasing number of headlines have highlighted dramatic changes in the high latitudes (e.g., Gille, 2002; Comiso, 2002; Scambos et al., 2003; Atkinson et al., 2004; Nicol et al., 2008; Stroeve et al., 2012; IPCC, 2013). The extraordinary retreat in northern annual sea-ice extent of 3.5 - 4.1 % per decade (95% confidence level) for the period 1979 - 2012 (IPCC, 2013) is probably the most dramatic example of climate change anywhere on Earth (Perovich, 2011). In 2012, the Arctic experienced a record minimum of summer sea-ice extent since the beginning of the satellite era in 1979 (Simmonds and Rudeva, 2012). But climate change is not only manifested in a declining sea-ice area and extent: the ongoing decrease of Northern Hemisphere sea-ice thickness (Haas et al., 2008a) and age (e.g., Kwok et al., 2009) additionally contributed to the strong focus of sea-ice research on the Arctic Ocean in the last decades.

The profoundly different distribution of land and ice masses of the Antarctic continent and the associated atmospheric and oceanographic conditions in the Southern Ocean lead to significant differences in northern and southern sea ice. For example, Antarctic sea ice has a more complex structure and growth history (Section 2.1.4), and many properties and key processes cannot be transferred directly from Arctic to Antarctic sea ice (e.g., Haas et al., 2001b; Willmes et al., 2006; Nicolaus et al., 2006). In addition, logistical challenges contribute to the fact that Antarctic sea ice is much less studied and understood than its northern counterpart.

2.2.1. Historical observations

The earliest observations of sea ice around Antarctica were documented in the logbooks of vessels as early as the 18th century. Parkinson (1990) used records from the expeditions of Cook, Bellingshausen, Wilkes, and Ross in the late 18th and early 19th centuries to compare them with the location of the 1973-1976 ice edge as determined from satellite data. Although the study revealed some differences between the datasets, no indications for the present-day ice edge being much different to that of 200 years ago were found. Mackintosh and Herdman (1940) and Mackintosh (1972) used data from several cruises to the Southern Ocean by the UK Discovery Committee to compile a circumpolar map of the monthly variation of the average position of the ice edge. Comparisons between these early ice-edge charts and satellite observations, as well as limited regional observations (Murphy et al., 1995), suggest that sea-ice extent in the 1970s was less than during the 1930s. However, due to the limited spatial and temporal scope of the early records, these observations have been regarded as inconclusive (Zwally et al., 1983). De la Mare (1997) used whalecatch data as a proxy for the ice-edge location, revealing a 25 % decline

in summer (January) Antarctic sea ice between the mid-1950s and early 1970s. Although these results are supported by ice core records of methanesulphonic acid (MSA) concentrations (Curran et al., 2003; Abram et al., 2010), they are contradictory to ship-based ice edges observed in the 1920s and 1930s when corrected for a typical offset of 1 and 2 degrees of latitude during the summer months (Ackley et al., 2003; Worby and Comiso, 2004). In contrast to the questionable results obtained when comparing the early ship observations to modern satellite measurements, the monitoring of the sea-ice extent over the last 40 years from satellite remote sensing alone is very reliable.

2.2.2. Sea-ice expansion in the Antarctic: The paradoxon

Although the oceanographic conditions around Antarctica have previously been found to isolate the continent (Kennett, 1977; Martinson, 2012), the ongoing changes particularly related to ice-shelf stability (Section 2.5) are an undeniable indication of climate change starting to affect the Southern Ocean. These changes were not foreseen only a few decades ago. But in contrast to the melting Antarctic glaciers, and the retreating sea ice in the Arctic, the Southern Hemisphere sea-ice cover responds differently to a changing climate.

Passive-microwave data revealed that the frozen ocean around Antarctica ranges in size from approximately 3 x 10^6 km^2 in February to about 19 x 10^6 km^2 in September (Gloersen et al., 1993; Parkinson and Cavalieri, 2012). The size of the Antarctic land mass is approximately 14 x 10^6 km^2 (Convey et al., 2009), so that the maximum extent of sea ice effectively more than doubles the size of the Antarctic continent. In the Arctic, the ocean is surrounded by land, and sea ice therefore does not exhibit such a large variation.

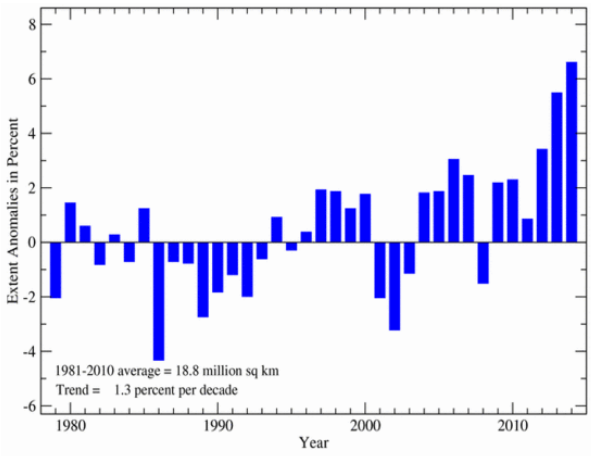

Figure 2.2: Southern Hemisphere sea-ice extent anomaly for September. Figure provided by the National Snow and Ice Data Center (NSIDC).

In recent decades (1979-2006/07), annual average Antarctic sea-ice area and extent showed a small, but statistically significant positive trend of around 1.2 $\pm$ 0.5 % and 1 $\pm$ 0.4 % per decade, respectively (Cavalieri and Parkinson, 2008; Turner et al., 2009). This trend even increased to around 1.8 $\pm$ 0.4 % and 1.5 $\pm$ 0.4 % respectively per decade when considering the period until 2010 (Parkinson and Cavalieri, 2012). Furthermore, the extent of Antarctic sea ice reached consecutive maxima over the 1979 to 2014

modern satellite record in 2012 (Turner et al., 2013b), 2013 (Reid et al., 2014) and again in 2014 (Figs. 2.2 and 2.3).

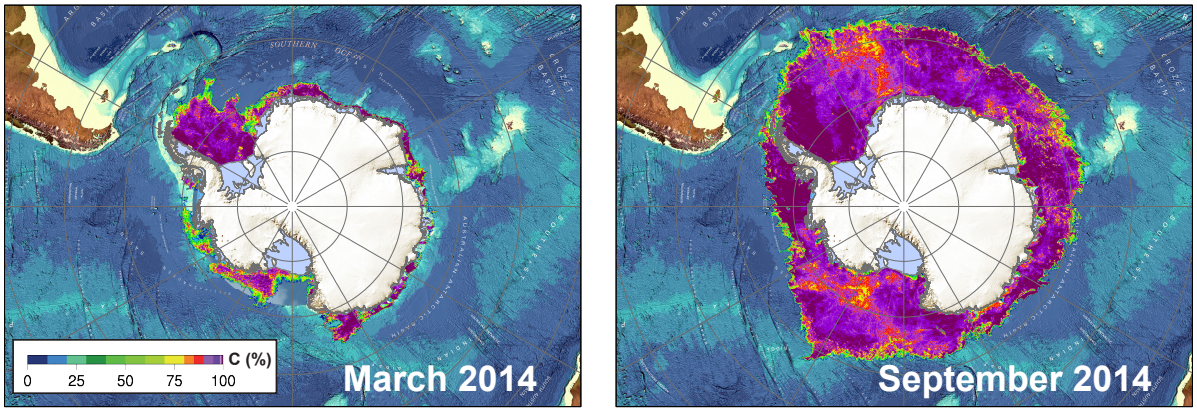

Figure 2.3: Southern Hemisphere sea-ice concentration in 2014. Data provided by University Bremen.

In addition, sea-ice extent in the Southern Ocean has also been highly variable. For example, austral summer minimum sea-ice extents have varied by as much as 25 % since 1979 (Parkinson and Cavalieri, 2012). This variability is further confirmed by a recent study of early satellite images (Nimbus program, late 1960s, Gallaher et al., 2014). Mapping of the September 1964 ice edge, typically the austral winter sea ice maximum, reveals that 1964 likely exceeded both the 2012 and 2013 record monthly-average maxima, followed in August 1966 by an extent considerably smaller than the record low August monthly extent set in 1986. It hence appears that Antarctica's sea ice variability may be greater than the 35-year modern satellite record would indicate, and that the current growth trend, while important, is not yet reaching unprecedented levels seen within the past century. Finally, model studies indicate that, by the end of the century, annual mean Antarctic sea ice extent and volume might reduce by 24% and 34%, respectively (Arzel et al., 2006). There is no question that such dramatic changes will have far-reaching effects on global climate and marine ecosystems.

2.2.3. Antarctic sea-ice thickness determination: the problem

In addition to sea-ice area and -extent, sea-ice thickness is another fundamental parameter in the Earth's climate system and needed to calculate total sea-ice volume as a measure of climate change (Kwok and Rothrock, 2009). Sea-ice thickness in Antarctica has been measured with a number of different field techniques including surface drilling (e.g., Wadhams et al., 1987; Jeffries et al., 1998; Perovich et al., 2004; Ozsoy-Cicek et al., 2013), ground-based and airborne electromagnetic induction soundings (Haas et al., 1997, 2009), airborne laser altimetry (e.g., Wang et al., 2013), and ship-based observations (Worby et al., 2008a; Ozsoy-Cicek et al., 2011). However, there is still no single measurement technique of Antarctic sea-ice thickness available, that provides global, daily coverage in a way comparable to passive microwave satellite imagery providing sea-ice area and extent. As a consequence, important changes in Antarctic sea-ice thickness and -volume may currently be going unnoticed.

More recently, satellite altimetry has been used to study Antarctic sea-ice thickness. Radar altimeters

have long been used to estimate sea-ice thickness in the Arctic. Antarctic sea ice, however, is often covered with thick snow, which significantly complicates the freeboard to thickness conversion (Giles et al., 2008; Willatt et al., 2010). Independent estimates of snow depth, as well as of snow and sea-ice density can be used for this conversion (Markus et al., 2011; Zwally et al., 2008), and recent studies even demonstrated that a reasonable level of accuracy is achieved using the assumption that the snow-ice interface is at sea level (Kurtz and Markus, 2012; Ozsoy-Cicek et al., 2013).

The available data are currently limited to the 5 year operational lifetime of the Ice, Cloud, and Land Elevation Satellite (ICESat) mission and airborne operations, such as NASA's Operation IceBridge, and is therefore not suited to provide reliable trends in sea-ice thickness. Zwally et al. (2008) and Yi et al. (2011) used a combination of satellite laser altimetry data from ICESat with snow depth retrievals from passive microwave data to estimate sea-ice thickness in the Weddell Sea, revealing a near-zero trend in sea-ice volume in that area. Kurtz and Markus (2012) used laser altimetry data from ICESat to investigate Antarctic-wide sea-ice thickness, covering from one to three 1-month-long periods per year for 2003-08. Their approach had a reasonable agreement with in-situ observations (Kurtz and Markus, 2012; Ozsoy-Cicek et al., 2013; Worby et al., 2008a), and revealed a very slight decrease in spring sea-ice thickness. However, these data are very limited in temporal coverage, and therefore unable to provide reliable trends in sea-ice thickness. Sea-ice thickness products, derived from satellites such as ESA's ongoing CryoSat-2 mission, are currently under development, with the ultimate aim to generate consistent time series similar to those of sea-ice extent. These are expected to provide a vital component for understanding long-term changes in Antarctic sea ice and its impact on the climate (McMillan et al., 2014).

2.2.4. West *versus* East: local variabilities and seasonality

Sea-ice variability around Antarctica is spatially heterogeneous, and only considering the overall sea-ice extent is misleading. The observed increase in overall Antarctic sea-ice cover masks pronounced, regionally-contrasting changes, occurring in both the extent and seasonality of sea ice, which almost compensate each other (Comiso et al., 2011; Stammerjohn et al., 2012; Parkinson and Cavalieri, 2012; Simpkins et al., 2013). The trend in sea-ice extent has been positive in all sectors except the Bellingshausen/Amundsen Seas, where a major decrease has occurred at a rate of -5.1 $\pm$ 1.6 % per decade (Parkinson and Cavalieri, 2012). In contrast, sea-ice extent in the Ross Sea has increased by 5.2 $\pm$ 1.4 % per decade (Parkinson and Cavalieri, 2012). Since trends in the remaining Antarctic sectors are comparable to the overall circumpolar situation, the observed increased Antarctic sea-ice extent is the sum of similar trends in East Antarctica and much larger and opposing trends in West Antarctica. Changes in the latter are of the same magnitude as those observed in the Arctic (Holland et al., 2014). However, the Arctic Ocean does not feature comparable regions of sea-ice expansion that offset the regions of loss, like it is the case in the Antarctic.

Another crucial parameter to potentially deduce ongoing climatic changes in a certain region is the duration of the sea-ice season (Massom and Stammerjohn, 2010; Maksym et al., 2012). The ice-free summer duration governs solar heat input and wind-mixing of the upper ocean layer (Perovich et al., 2008), which in turn affect sea surface temperatures (Meredith and King, 2005) and ocean upwelling

(Martinson, 2012). Since the life cycles of many polar marine organisms are adapted to specific seasonal rhythms, serious consequences may arise when these are altered too quickly. A specific sea-ice duration is usually determined from the timings of annual sea-ice advance and retreat. In the Antarctic, patterns of regional-scale change in sea-ice seasonality similar to the evolution of sea-ice extent are observed (Maksym et al., 2012). The most pronounced changes are occurring along the Antarctic Peninsula and in the Bellingshausen Sea, where the length of the sea-ice season has been shortening by more than three months in the period between 1979/80 and 2010/11 (Stammerjohn et al., 2012). This rate of change is even greater than that occurring in regions of greatest sea-ice loss in the Arctic (Stammerjohn et al., 2012), where most regions exhibit trends towards a shorter sea-ice season. This development is entirely opposed by the western Ross Sea, where the sea-ice season persists for two months longer.

Considering the rate of change in sea-ice extent, and in particular its seasonality, further complicates the matter. In this approach, the Ross, Weddell and Amundsen-Bellingshausen Sea trends show different patterns (Simpkins et al., 2013; Holland, 2014), and all regions seem to contribute equally to the overall trend at different times of the year (Holland, 2014).

The ultimate causes and processes underlying the regional patterns that add to an overall increase in sea-ice cover still remain elusive.

2.2.5. The explanations of southern sea-ice expanse

The response of Antarctic sea ice to climate change and -variability seems far from simple, and several hypotheses have been proposed to drive the observed evolution (Holland et al., 2014; Raphael and Hobbs, 2014): changes in atmospheric temperature and wind stress (Liu et al., 2004; Lefebvre and Goosse, 2005, 2008; Turner et al., 2009), increased precipitation leading to reduced upward ocean heat transport (Liu and Curry, 2010), increased ocean temperature in West Antarctica (Jacobs and Comiso, 1997; Meredith and King, 2005), atmosphere and ocean feedbacks (Zhang, 2007; Stammerjohn et al., 2012), changes in storminess and wave climate (Kohout et al., 2014), trends in ice drift caused by changes in near-surface winds (Holland and Kwok, 2012), and an increased freshwater flux through melting of the Antarctic Ice Sheet (Bintanja et al., 2013, 2014).

The most likely contributor to the observed changes in the sea-ice cover is the strengthening of the dominant circumpolar westerly wind belt over the Southern Ocean by 15-20 % (Korhonen et al., 2010; Turner, 2011), as well as its poleward shift by 1-2° of latitude since the late 1970s. These changes in large-scale atmospheric circulation patterns are related to changes in various climate modes, such as the the Southern Annular Mode (SAM) and the El Niño-Southern Oscillation (ENSO) (e.g., Renwick, 2002; Yuan and Li, 2008; Pezza et al., 2012; Simpkins et al., 2012). The atmospheric pressure gradient in the Southern Hemisphere has changed in such a way that pressure has increased at mid-latitudes and decreased around the Antarctic coast over the past 50 years in austral summer and autumn (Thompson et al., 2011, and references therein). This corresponds to a more positive phase of the SAM, which is a measure of this gradient and is the dominant mode of variability in atmospheric circulation at high southern latitudes (Simmonds, 2003; Lieser et al., 2013). This change is likely associated with ozone depletion (Gillett et al., 2009; Turner et al., 2009; Thompson et al., 2011) and increased greenhouse gas

concentrations in the atmosphere (Marshall et al., 2004), although other studies suggest that the loss of ozone would result in a decrease of sea ice extent (Sigmond and Fyfe, 2010).

Furthermore, the dramatic evolution of the West Antarctic sea-ice cover is very likely tied to a deepening of the Amundsen Sea Low (ASL), a recurrent low atmospheric pressure anomaly in the South Pacific (Turner et al., 2013c). This change in pressure is a direct cause of the increased intensity of westerly winds and the geographical configuration of the Antarctic continent (Turner et al., 2013a). It is probably part of a trend which started in the early 1900s (Abram et al., 2010), and has also been attributed to increasing greenhouse gas concentrations and stratospheric ozone depletion (Turner et al., 2014). Persistent southerly (colder) winds along the west of the low over the Ross Ice Shelf are thereby responsible for a more extensive and longer sea-ice cover in the Ross Sea, while northerly (warmer) winds brought south by the Amundsen Sea Low reduce the sea-ice cover in the Bellingshausen Sea and impede the advance of the sea ice to the west of the peninsula (Turner et al., 2014). In addition, recent studies on the record sea-ice extents of 2012 and 2013 (Turner et al., 2013a; Reid et al., 2014) revealed unusual short-term wind patterns that enhanced sea-ice growth and drift, which were related to the size and strength of the Amundsen Sea low pressure area late in the growth season. For a more detailed treatment of atmospheric circulations around Antarctica, refer to Turner et al. (2013c), Lieser et al. (2013), and Turner et al. (2014).

Since the rate of sea-ice formation and melt is sensitive to oceanic heat flux, and hence to the stratification of the upper ocean, there may also be an important link to the Antarctic ice sheet, which is however the subject of a lively debate. Bintanja et al. (2013) and Bintanja et al. (2014) suggested that enhanced input of melt water from basal melting of Antarctic ice shelves into the upper ocean leads to the formation of a relatively cool and fresh surface layer that shields the surface ocean from the warmer deeper waters. These surface layers can then freeze more easily, which could explain why observed overall Antarctic sea-ice extent trends peak in autumn and early winter. The extra ice-shelf melting potentially also results from the changing wind patterns, which act to draw deep warm ocean water towards the continent to replace surface water and sea ice that is pushed northward and eastward by the stronger westerlies. By thickening, spreading, and stabilizing the polar surface ocean layer (which is comprised of cool, near-freezing water) the increased melt from the ice sheet edges potentially helps sea ice grow around the Antarctic continent. This effect would be most pronounced in the western Pacific, because most of the increased freshwater discharge from the Antarctic Ice Sheet has entered the Amundsen Sea (Shepherd et al., 2012) and followed the coastal current westward into the Ross Sea, causing a significant freshening (Jacobs and Giulivi, 2010). However, other modeling studies suggested that an increased Antarctic Ice Sheet freshwater flux has no significant influence on the sea-ice cover (Swart and Fyfe, 2013).

As a summary, the reasons for the overall increase in Antarctic sea-ice extent over the last 30 years are still heavily debated and no comprehensive explanation has yet emerged. The changes in large-scale atmospheric circulations, especially the deepening of the Amundsen Sea Low and resulting changes in wind patterns around Antarctica, seem to be a widely accepted explanation at least for the opposing behavior in West Antarctica and the Ross Sea. In other regions, a variety of factors may influence the sea-ice cover to different degrees, and individual contributions may vary depending on the sea-ice season (Raphael and Hobbs, 2014). The influence of ice-sheet melt water is under debate, and more research into ice-shelf/sea-ice interactions, such as provided in this thesis, is urgently needed.

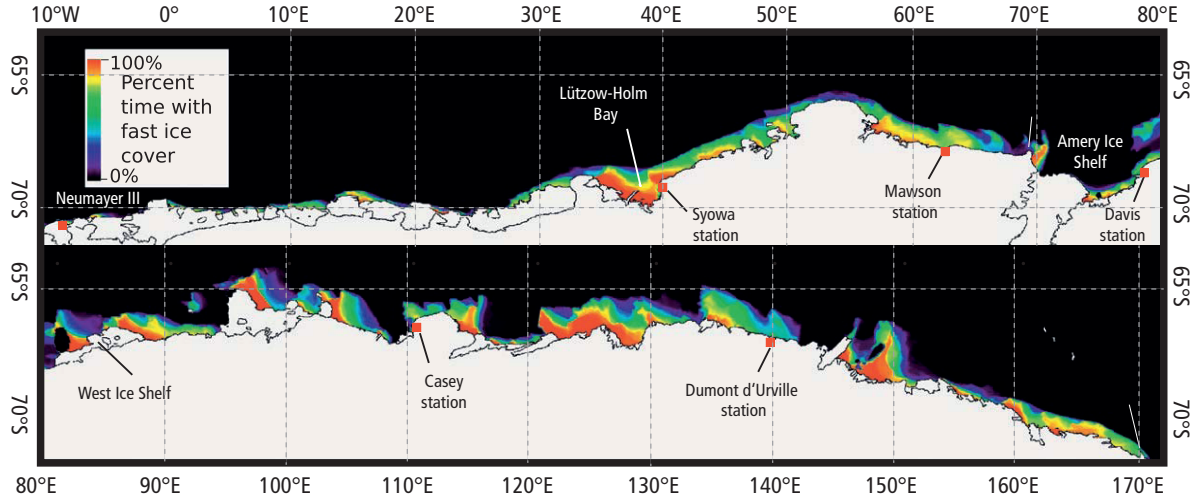

Figure 2.4: Average fast-ice coverage on the coast of East Antarctica from March 2000 to December 2008. A value of 100% corresponds to thick, persisting fast ice (modified after Fraser et al., 2012).

2.3. Land-fast sea ice

The highly dynamic aggregations of sea-ice floes floating in the oceans are referred to as pack ice. But not all sea ice is moving under the influence of winds and ocean currents. Around the coastal margin of Antarctica, a narrow band of sea ice rarely exceeding 150 km (for East Antarctica) is held in place by features like promontories, embayments and grounded icebergs (Giles et al., 2008; Fraser et al., 2012). Since it is fastened (attached) to coasts, ice bergs and ice shelves, it is known under the term "landfast sea ice", or just "fast ice".

According to the World Meteorological Organization WMO (1970), landfast sea ice is defined as

> *"Sea ice which forms and remains fast along the coast, where it is attached to the shore, to an ice wall, to an ice front, between shoals and grounded icebergs. Vertical fluctuations may be observed during changes of sea-level. Fast ice may be formed in situ from sea water or by freezing of pack ice of any age to the shore, and it may extend a few meters or several hundred kilometres from the coast."*

Again, there are strong contrasts in fast-ice extent and persistence in the Arctic and Antarctic. The lack of grounded icebergs in the Arctic often leads to fast ice grounding in shallow waters, with the seaward fast-ice edge usually located around the 20-30 m isobath (e.g., Mahoney et al., 2007). In the Antarctic, where icebergs ground in water depths of up to several hundred meters (Massom et al., 2001b), extensive fast-ice growth occurs over deeper water. The two main processes for fast-ice formation are either thermodynamic growth (Kawamura et al., 1997; Tison et al., 1998) or dynamic thickening and attachment of floes through winds and ocean currents (Massom et al., 2001b). Certain geographic locations, such as

embayments or the lee-side of coastal features, may be favorable for recurrent fast-ice formation (Giles et al., 2008).

Fast ice around Antarctica is usually seasonal and reaches thicknesses around 2 meters (Jeffries et al., 1998), although it may attain greater ages and thicknesses in some regions (Massom et al., 2010). Fast ice mostly forms and breaks out annually as a response to environmental conditions (Divine et al., 2003; Heil, 2006; Fraser et al., 2012). Although fast-ice area only varies between 5 % and 35 % of overall sea-ice area in winter and summer for East Antarctica respectively (Fig. 2.4), an improved understanding of its properties and interaction with the environment is of crucial importance for a number of reasons (modified after Fraser, 2011):

1. Fast ice may contribute significantly to the overall volume of Antarctic sea ice, especially in spring (Giles et al., 2008).

2. fast ice is an important boundary between the Antarctic ice sheet and the pack ice/ocean. In addition to potentially prolonging the residence times of icebergs (Massom et al., 2003), it mechanically stabilizes floating glacier tongues and ice shelves, delaying their calving and ultimately affecting ice-sheet mass balance (Massom et al., 2010).

3. Fast-ice features are often associated with coastal polynyas, regions of high sea-ice production (Massom et al., 2001b). It thereby has important implications for Antarctic Bottom Water formation (Rintoul, 1985; Tamura et al., 2008; Williams et al., 2008; Tamura et al., 2012).

4. Fast ice responds quickly to atmospheric and oceanic forcing (Heil, 2006; Mahoney et al., 2007) and is likely a sensitive indicator of climate change (Murphy et al., 1995; Divine et al., 2003; Mahoney et al., 2007a).

5. Fast ice provides a stable habitat for micro-organisms (McMinn et al., 2000; Arrigo et al., 1993b; Günther and Dieckmann, 2001), and serves as a breeding ground for larger animals such as Weddell seals (*Leptonychotes weddellii*) (Reijnders et al., 1990) and Emperor penguins (*Aptenodytes forsteri*) (Massom et al., 2009).

6. The thickness and extent of fast ice has significant consequences for polar marine navigation and logistics, as its presence can both impede and facilitate access to Antarctic bases.

7. Finally, fast ice is currently not represented in global climate models.

The main study area of this thesis is a fast-ice regime attached to the Ekström Ice Shelf in the eastern Weddell Sea (Fig. 2.4, top left). It is one of the very few sea-ice sites in the Southern Ocean which is accessible nearly year-round through the presence of the German wintering station Neumayer III. The field setting is described in detail in Section 4.2.

Especially near the Antarctic coastline, sea-ice formation and -properties are likely governed by nearby ice shelves. Current patterns in ice-shelf cavities may give rise to the formation of sea ice deep in the ocean, a process which is profoundly different from usual sea-ice formation at the ocean surface. The

following sections provide a brief overview about Antarctic ice shelves and serve as an introduction to Chapter 3, which reviews the current state of knowledge about the implications of ice shelves for sea ice.

2.4. The Antarctic ice sheet

2.4.1. Geography

Antarctica is a continent of superlatives: it is renowned as the highest, driest, windiest and coldest continent, with the lowest recorded temperature on Earth, -89.28°C, at Russia's Vostok Station on the Polar Plateau (Turner and Overland, 2009). The continent covers an area of approximately 14 x 10^6 km^2, which is about 10 % of the land surface of the Earth (Convey et al., 2009). It is dominated by the Antarctic Ice Sheet, a giant mass of glacial ice that rests on the bedrock and surrounding seas, which contains around 30 x 10^6 km^3 of ice or 70 % of the Earth's freshwater and covers over 99.6 % of the continent (Convey et al., 2009). The entire ice sheet (IS) corresponds to a sea level equivalent of 58 m (Fretwell et al., 2013), and consists of three distinct glaciological zones, the East Antarctic Ice Sheet (EAIS, covering an area of 10.35 x 10^6 km^2), the West Antarctic Ice Sheet (WAIS, 1.97 x 10^6 km^2) and the Antarctic Peninsula Ice Sheet (APIS, 0.52 x 10^6 km^2) (Convey et al., 2009). The EAIS, which includes the high Polar Plateau, and the WAIS are separated by the Transantarctic Mountains, which extend from Victoria Land to the Ronne Ice Shelf. The summits rise above the surrounding ice sheet to a maximum height of 4528 m. The Antarctic Peninsula, a narrow mountainous region with an average width of 70 km and a mean height of 1500 m, extends a significant way northwards from the main ice sheet. Since the northern tip of the Peninsula nearly reaches 63°S, it acts as a geographic barrier that exerts a major influence on the oceanic and atmospheric circulations of the high southern latitudes (Convey et al., 2009). While the WAIS (e.g., Pine Island and Thwaites glaciers) exhibits increasing volume loss in recent decades, a thickening occurs in regions of East Antarctica (Helm et al., 2014) mainly through distinct, large-scale accumulation events in 2009 and 2011 (Lenaerts et al., 2013).

2.4.2. Ice shelves

The mass balance of the Antarctic Ice Sheet is a complex combination of multiple interactions (Fig. 1.1). The Antarctic Ice Sheet slowly gains mass at its surface by deposition of snow and frost over the continent, especially around the Central Plateau. The weight of the overlying newer snow pack compresses the snow and leads to the formation of firn. When a density threshold of around 800 kg m^{-3} is reached, bubbles are formed and the firn is transformed into glacial ice, capturing a chemical record of past climates and environments. Under the influence of gravity the ice mass slowly moves down towards the coastline, being heavily deformed near the ice-bedrock interface. When passing the coastal mountain ranges, the ice parts into individual ice streams, eventually merging again further downstream. As soon as these individual streams reach the ocean, they start floating due to their lower density, and may spread over the ocean's surface due to the lack of friction. When some of those ice tongues later merge in the ocean, they form a floating ice shelf. The two largest ice shelves are the Filchner-Ronne Ice Shelf in the Weddell Sea and the Ross Ice Shelf in the Ross Sea (0.53 x 10^6 km^2 and 0.54 x 10^6 km^2, respectively; Convey et al., 2009).

More than 50 % of the continent's coastline is fringed with ice shelves and floating ice tongues (Le Brocq et al., 2010), which cover an area of >1.56 x 10^6 km^2, or 11% of the total area, comparable in size to the Greenland Ice Sheet (Barkov, 1985; Swithinbank, 1988). Ice shelves exert considerable control on glacier stability and Antarctic Ice Sheet mass balance (Jacobs et al., 1992; Hooke, 2005; Cuffey and Paterson, 2010) and play important roles in ocean stratification and bottom water formation (Hellmer, 2004).

The area where the ice flow ungrounds is referred to as grounding line. Topographical features such as islands or ice rises may exert back stresses on the ice flow, leading to a decrease in velocity due to frictional losses. However, when these back stresses are minimal, the ice shelves may expand even further. As a result, vertical fractures and larger rifts may form near the front, finally leading to the break up of icebergs. These usually drift into the open ocean with the currents, where they eventually melt in lower latitudes. This process of iceberg formation is generally referred to as calving, and is one of the main mechanisms which regulate the flow of continental ice towards the ocean. This process is a main factor governing the amount of freshwater added to the ocean, and indirectly contributes to global sea-level rise. An even more important mechanism of ice sheet mass loss is bottom melt at the base of an ice shelf due to the seawater temperature being above the in situ freezing point.

2.5. Ocean/ice-shelf interaction

The 19 x 10^6 km^2 large ocean beneath Antarctic sea ice, and especially below ice shelves (referred to as "ice-shelf cavity"), is probably the least well observed physical system on earth. This "black box" represents one of the major impediments to our understanding of Southern Hemisphere climate processes.

Since surface melt rates of the Antarctic ice sheet are considered low (Joughin et al., 2012), oceanic heat fluxes melting floating ice shelves from below (Robin, 1979) are the most critical aspect of Antarctica's mass balance. Increased basal melt, driven by transport of warm Circumpolar Deep Water onto the continental shelves, thereby results in a thinning (or more dramatically, a collapse) of Antarctic ice shelves. At the same time, increased calving rates also result in higher rates of ice loss (Rignot et al., 2011). Despite large uncertainties, basal melt has been identified as the largest contributor to mass loss of the Antarctic ice sheet (~55 %), with iceberg calving accounting for the remainder (Rignot et al., 2013; Depoorter et al., 2013, see also Fig. 3.6). Both processes lead to a reduction of the ice-shelves' buttressing effect (Dupont and Alley, 2005) and a subsequent acceleration of glacier flow. The more rapid discharge of ice from the continent contributes to an increase in sea level (De Angelis and Skvarca, 2003; Rignot et al., 2011; Pritchard et al., 2012; Joughin et al., 2014).

The main processes which are responsible for basal melt are:

1. Relatively warm Circumpolar Deep Water intrudes onto the continental shelf and into the cavity. This water is well above the local surface freezing point and is able to enhance basal melt rates by tens of meters per year or more (Joughin et al., 2012).

2. Tidal and wind mixing that moves warmer surface waters beneath the ice shelf (Hattermann et al., 2012).

3. The formation of dense High Salinity Shelf Water in polynyas close to the ice-shelf front.

Warming atmospheric temperatures and oceanographic change have already resulted in large scale ice-shelf collapse along the Antarctic Peninsula (Larsen A and B) (Scambos et al., 2003; Cook and Vaughan, 2010), leading to a reduced buttressing effect and enhanced glacier flow. The giant Ross, Filchner and Ronne IS only account for 15% of net melt, whereas ten southeast Pacific ice shelves and six East Antarctic ice shelves have high melt/area ratios, suggesting large oceanic heat fluxes at their grounding lines (Rignot et al., 2013). The collapse of the Thwaites and Pine Island glaciers (West Antarctica) through melt-induced thinning has already begun, whith strong implications for sea-level rise (Pritchard et al., 2012; Joughin et al., 2014; Rignot et al., 2014; Favier et al., 2014). For comparison, the entire marine-based West Antarctic Ice Sheet would correspond to a global sea-level rise of 3.3 m (Bamber et al., 2000). In addition, large parts of the East Antarctic ice sheet are marine-based, and hence are potentially subject to the marine ice shelf instability (Fretwell et al., 2013). The Totten Glacier for example has recently lost mass at a rate comparable to the Pine Island Glacier, which is likely linked to nearby polynya activity (Khazendar et al., 2013). Finally, a recent modeling study suggested that a thinning of sea ice in the Weddell Sea in the latter half of this century potentially enhances the surface stress on the underlying ocean and causes a re-routing of the warm coastal current into the Filchner-Ronne IS cavity (Hellmer et al., 2012). The resulting basal melt would increase by an order of magnitude, to values equivalent to 80 % of the current Antarctic surface mass balance.

Apparently, sea ice is a major factor in modulating ocean/ice-shelf interaction in the Southern Hemisphere. The other way around, ice shelves may strongly impact sea ice, especially if it is attached to their edges. One of the mechanisms relevant for this work is the so-called “ice pump” (Section 3.3), in which a particular circulation pattern beneath a floating ice shelf impacts nearby sea ice by the formation of a sub-ice platelet layer. The following chapter provides a review of sub-ice platelet layers in Antarctica and their role for sea-ice properties and -ecology. Chapter 4 then describes the measurements performed at our main study site in the eastern Weddell Sea, before Chapters 5 and 6 present the new knowledge gained on this phenomenon in the framework of this thesis.

Chapter 3

Publication I: Sub-ice platelet layers and their role for sea-ice properties and -ecology

By **Mario HOPPMANN**, Inga J. SMITH, Patricia J. LANGHORNE and Gerhard S. DIECKMANN

This chapter is an early version of a manuscript which is intended to be submitted to Progress in Oceanography in 2015. The aim of this manuscript is to give a comprehensive overview of the impacts of ice platelets on sea ice and the associated ecosystem. Such a review is currently missing from the literature. My contribution is that I completely rewrote and restructured an existing manuscript by G. S. Dieckmann, and included newer literature (2000-now). Please note that the order of authors, including the first author, is still subject to change depending on the individual contributions to the manuscript at submission stage.

3.1. Introduction

Basal melt of ice shelves has recently been identified as the major source of Antarctica's ice sheet mass loss (Section 2.5). Although this process has also been hypothesized to contribute to the recent sea-ice expanse in the Southern Ocean (Bintanja et al., 2013, 2014), its overall significance for sea-ice formation is not well understood.

In the presence of a heat sink deep in a water body, tiny ice crystals, similar to those formed at the ocean's surface during initial sea-ice growth, may form at depth. Ice shelves fringing around 50 % of the Antarctic coastline are such a heat sink. The frazil crystals nucleate on impurities in the water column when in situ supercooling from ice-shelf basal melt is relieved during adiabatic rise of a cold plume (Foldvik and Kvinge, 1974). During further growth, their buoyancy increases and these crystals may float upwards. When they accumulate below a solid sea-ice cover, a semi-consolidated layer is formed, which is consequently incorporated into the solid sea ice by the advancing freezing interface (Fig. 3.1).

Reports of such crystals grown at depth date back as far as the Discovery Expedition of 1901-1904 near Winter Quarters Bay, McMurdo Sound (Hodgson, 1907). They reported ice crystals forming on lines and nets used for the collection of biological samples. Probably the earliest references on the potential significance of this phenomenon in the coastal regions of Antarctica were made by Wright and Priestley (1922) during the Terra Nova Expedition 1910-1913. They observed similar growth on ropes (Fig. 3.2) and loose "frazil" below sea ice in McMurdo Sound. They reported that

> *"In the early part of the winter all additions to the thickness of the sea ice are due to conduction by the cold air above, but there is every reason to believe that later in the winter the sea ice grows to its great thickness of 8 and 9 feet largely by the deposition of frazil crystals from below."*

More recent studies confirmed that processes inside the inaccessible ice-shelf cavities may have a huge impact on coastal Antarctic sea-ice mass balance and -properties (Lange et al., 1989; Gough et al., 2012b). Being the most porous among all sea-ice habitats, these layers of loose ice crystals provide a large surface area and at the same time enable free nutrient exchange with the underlying seawater (Bunt, 1964a; Arrigo and Thomas, 2004). Although light availability is generally limited below (snow-covered) sea ice, this special habitat has been found to host some of the largest microbial accumulations among all sea-ice types (Arrigo et al., 1993b), forming the physical basis of an entirely own ecosystem (Günther and Dieckmann, 1999).

Owing to its significance throughout various disciplines, this special sea-ice type has been given many different names in the literature, mostly depending on the context of observation and field of research of the authors (Smith et al., 1999, 2001). There is for example inconsistency in the ways that the terms "frazil ice", "platelet ice", "anchor ice" and even "marine ice" are used, often interchangeably (Smith et al., 1999; Mager et al., 2013). As a result, the terminology for this special sea-ice type is confusing, and a comprehensive overview is still missing albeit urgently needed. The terminology used here is summarized in Table 3.1.

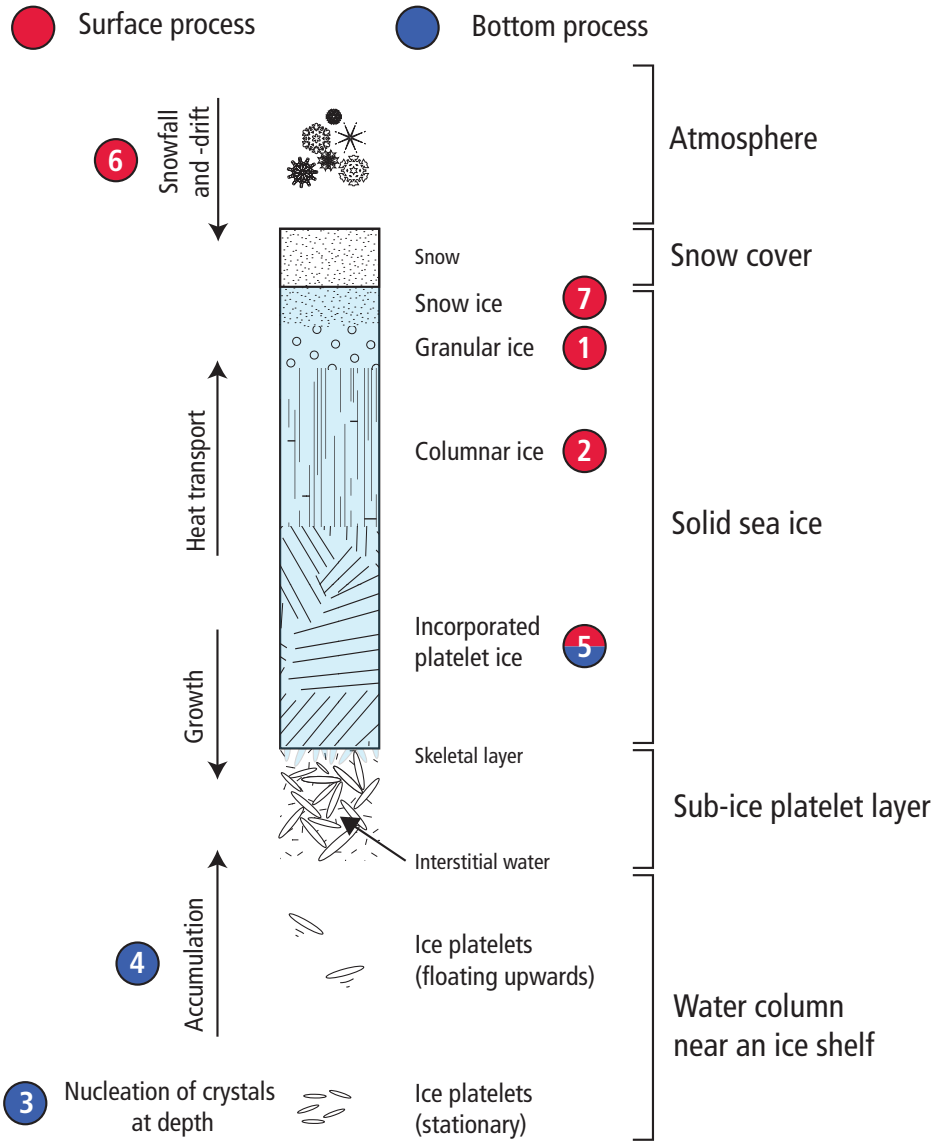

Figure 3.1: Schematic illustration of a typical Antarctic sea-ice cover in late winter, close to an ice shelf. Both, surface (atmospheric) and bottom (oceanic) processes, contribute to sea-ice growth. The consolidation of frazil crystals on the sea surface during freezing conditions leads to the formation of granular ice at the top of the sea-ice cover (1). Upward heat transport then results in the growth of columnar ice (2). In the course of winter, small ice platelets start to nucleate in the water column (3) and rise up to accumulate beneath the solid sea ice to form a sub-ice platelet layer (4). As the freezing interface advances into the porous matrix of disordered platelet crystals, platelet ice is formed (5). At the same time, snowfall and -drift above the sea ice result in a (partly thick) snow cover (6). Due to the heavy snow load, the sea ice surface is eventually flooded through cracks, and refreezing of slush results in snow-ice formation (7). Please note that dynamic sea-ice thickening, such as rafting or ridging, is not accounted for in this scheme.

Figure 3.2: Frazil crystals deposited on a rope (Wright and Priestley, 1922, Plate LXVIII). A person is standing in the background, holding a long rope with an agglomerate of ice crystals (white object in the front) attached to it. This photograph was taken during the Terra Nova Expedition 1910-1913 and is one of the earliest evidences of sea-ice growth deep in the water column.

Table 3.1: Definitions of different ice types associated with supercooled water (after Mager et al., 2013).

Ice type	Definition	References
Sea ice	Ice formed in or on the surface of the sea by seawater freezing	Weeks (2010)
Frazil (ice)	Fine spicules or plates of ice suspended in water	WMO (1970)
Ice platelets	Single, dendritic crystals suspended in the water column, larger than frazil	Moretskii (1965), Jeffries et al. (1993)
Sub-ice platelet layer	Layer of dendritic crystals accumulated beneath an overlying sea-ice cover	Gow et al. (1998)
Platelet ice	Structural component of a solid sea-ice cover modified by incorporation of ice platelets	Dempsey et al. (2010), Gough et al. (2012b)
Anchor ice	Ice that is attached to, or anchored to, a substrate, e.g. the bed of a river or sea floor	Modified from WMO (1970)
Marine ice	Layer of dendritic crystals accumulated beneath an ice shelf	Souchez et al. (1991), Tison et al. (1993)

3.2. Supercooling

Supercooled water is in the metastable state of exhibiting a temperature below its in situ freezing point. It is essential for the formation and growth of ice crystals at depth in the water column, a process which would otherwise not occur. In the polar oceans, frazil ice forms under several conditions where the ocean becomes supercooled (Martin, 1981; Daly, 1994; Mager et al., 2013): (i) in surface layers of leads and polynyas; (ii) at the interface between two fluid layers, each at their freezing point and with different salinities and (iii) in the water column adjacent to ice shelves.

(i) **Surface cooling:** Low atmospheric temperatures above regions of open seawater result in massive heat transport from the ocean into the atmosphere. Seawater density increases as a result of cooling and salt rejection, and convection within the mixed layer kicks in. Strong winds generate turbulence in the mixed layer, bringing cold, relatively dense water back to the surface where it can lose even more heat. Under persisting stormy conditions, the entire mixed layer may become supercooled.

(ii) **Interface of two fluid layers:** Fluid bodies of different salinities and temperatures in close proximity to each other may be generated by a number of mechanisms. Although these processes may be spatially isolated or episodic in nature, they are all based on the different diffusivities of heat and salt (Mager et al., 2013).

For example, where rivers flow into the ocean, fresh melt water at 0°C may be situated above seawater at -1.8°C. Since heat transfer from the upper freshwater layer to the colder seawater occurs about 100 times faster than the mass transfer of salts in the other direction (Martin, 1981), the upper layer becomes supercooled because it is cooled faster than its freezing point temperature is depressed by the introduction of salts.

As another example, the brine rejected episodically during sea-ice growth has a higher density and lower freezing point than the surrounding water. It sinks and mixes with less saline water, resulting in supercooling of the water parcel. As much as 50 % of the sea ice formed from the cold brine flow develops into frazil crystals (Dayton and Martin, 1971). Under calm conditions, the supercooled brine may form pipes of ice protruding from the sea-ice bottom, a phenomenon termed “brine icicle”, “brinicle” or “ice stalactite” (Fig. 3.3, Dayton and Martin, 1971; Martin, 1974, 1981).

Finally, when fresh ground- or meltwater is periodically discharged to the near-shore zone below sea level, or when freshwater is ejected from the base of ice streams through sub-glacial drainage channels (e.g. Horgan et al., 2012), the latent heat released by the freezing freshwater is absorbed by the colder seawater, allowing frazil crystals to grow.

(iii) **Adjacent to ice shelves:** Water at its in situ freezing point at depth will become supercooled if raised adiabatically, because the freezing point decreases with depth. This physical law has important implications for the formation of supercooled water near ice shelves, and is described in detail in Section 3.3. Although this process my also apply to water adjacent to large icebergs, we do not consider this case here.

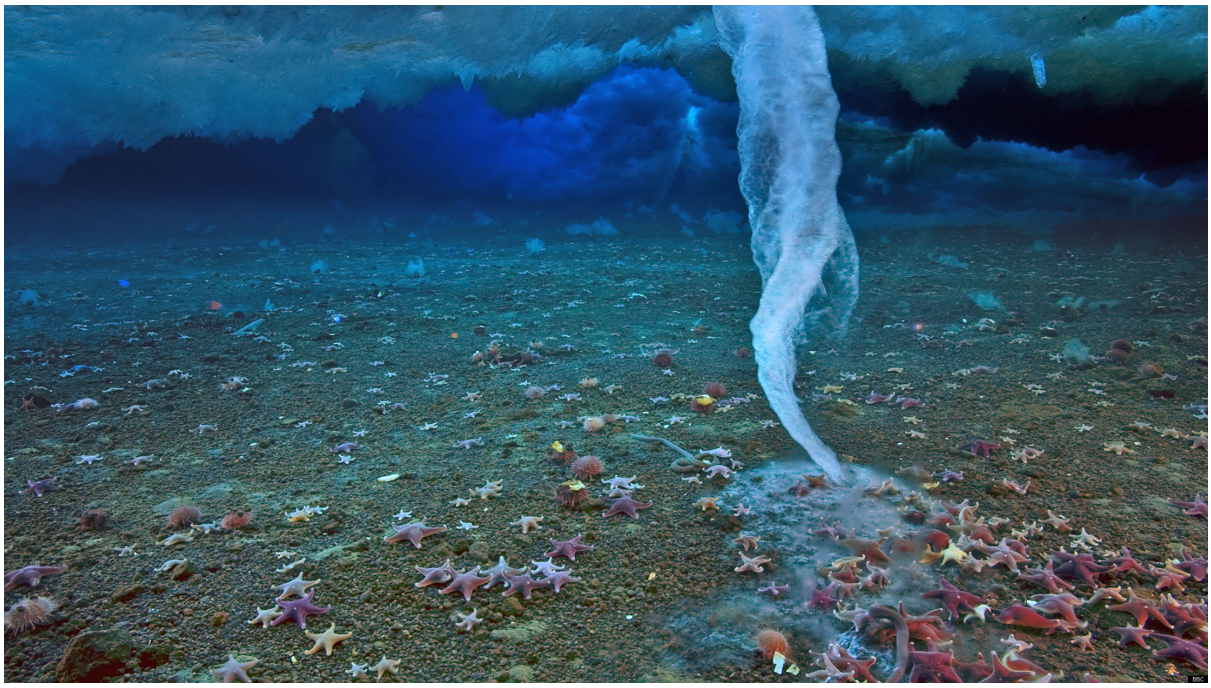

Figure 3.3: Brinicle, as shown in the BBC series "*Frozen Planet*" in 2011

3.3. The ice pump

The main mechanism for ice crystal formation at depth in Antarctica is a special case of thermohaline convection below and in front of an ice shelf (Foldvik and Kvinge, 1977), mainly driven by the pressure dependence of seawater's freezing point temperature (Foldvik and Kvinge, 1974). This process was first utilized by Robin (1979) to explain the deposition of marine ice at the base of the Amery Ice Shelf. Lewis and Perkin (1986) later coined the term "ice pump", which is essentially a heat engine melting ice at depth in the ocean and depositing it at a shallower location (Fig. 3.4).

Growing sea ice in front of an ice shelf produces cold and saline surface water due to salt rejection when changing into the solid phase. This process is further enhanced by seaward katabatic winds continuously driving the new sea ice offshore, leading to the formation of coastal polynyas. These areas of rapid sea-ice growth are major sources of High Salinity Shelf Water, dense water which sinks down and either flows towards the continental shelf slope, or inland into the ice-shelf cavities where the continental shelf deepens. It may penetrate as far as the grounding line, several hundred meters below the surface. Since this transfer is mainly adiabatic (without heat exchange), the temperature of that water mass is still close to the freezing point at surface pressure. Due to the 7.5 x 10^{-4}°C dbar^{-1} decrease in seawater freezing temperature with increasing depth, the water temperature may be lower than the in-situ melting point by as much as 1°C (Jacobs et al., 1992). This extra latent heat is used up to melt the meteoric (glacial) ice at depth. The melting leads to a cooling and freshening of the ambient water, producing a less dense Ice Shelf Water plume with temperatures below the sea-surface freezing point, that rises at the slope of the ice shelf towards its front.

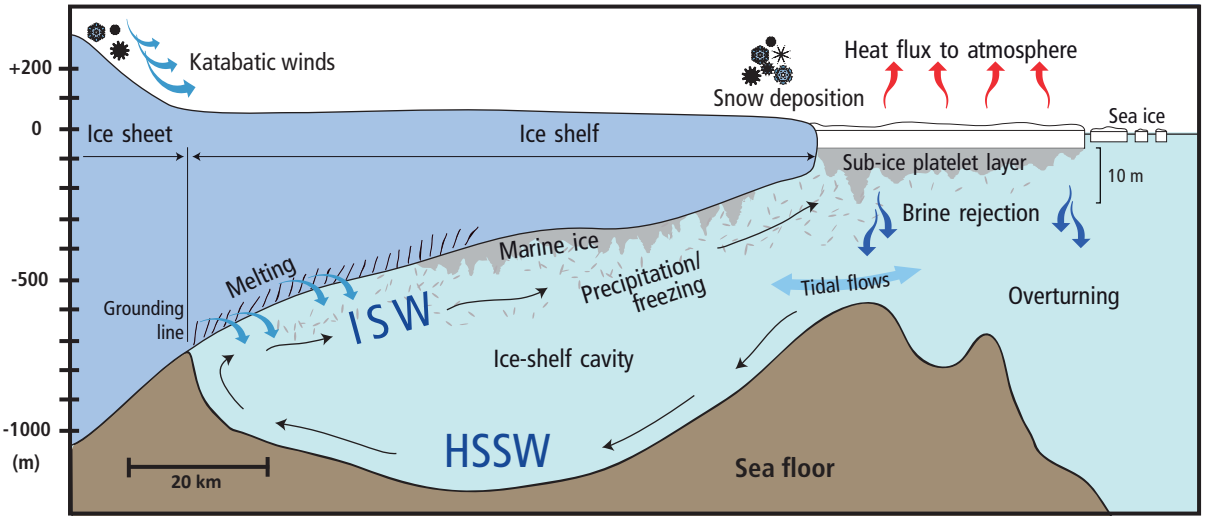

Figure 3.4: Schematic illustration of ice pump process in an ice-shelf cavity. High Salinity Shelf Water (HSSW) enters the cavity and melts the base of the ice shelf. Basal melting leads to the formation of very cold, less saline Ice Shelf Water (ISW). The ISW rises and the plume becomes supercooled since the freezing point depends on pressure. Supercooling is relieved through formation of ice platelets. The crystals float upwards, eventually grow further, and accumulate below the ice shelf as marine ice, or beneath coastal sea ice, where they are later incorporated into the fabric to form platelet ice (modified after Hughes, 2013). See text for further details. Sea-ice and platelet-layer thickness are not to scale.

During adiabatic rise-up, the water eventually reaches a critical (shallower) depth where the temperature of the plume is lower than its in-situ freezing point. That water is then supercooled, and thermodynamic re-adjustment takes place through the release of latent heat by generation of individual ice crystals in the water column. This is only possible in the presence of suspended condensation nuclei, such as biogenic and sediment particles. These small frazil crystals may further grow during suspension, rise up due to their buoyancy, and eventually accumulate in depressions of the basal ice-shelf topography. These marine ice layers have been observed to exceed 100 m thickness in certain locations (Section 3.6, Craven et al., 2009).

Depending on oceanographic conditions, especially the local density contrasts, it is possible that Ice Shelf Water emerges from the ice-shelf cavity (Robinson et al., 2014). It may even be transported some distance away into the open ocean, eventually leading to the formation of stationary clouds of ice crystals at depth (Dieckmann et al., 1986b). Early models of this type of thermohaline circulation and associated frazil ice production (Hellmer and Olbers, 1989, 1991; Jenkins and Doake, 1991) are constantly in the process of refinement (Determan and Gerdes, 1994; Jenkins and Bombosch, 1995; Bombosch and Jenkins, 1995; Williams et al., 1998; Smedsrud and Jenkins, 2004; Hattermann et al., 2014; Hughes et al., in press, and references therein). Measurements and models further suggest that, if ISW continues beyond the ice shelf edge, it can substantially enhance sea-ice growth (Hellmer, 2004; Purdie et al., 2006; Gough et al., 2012b).

According to Jacobs et al. (1992) there are two other modes of melting beneath ice shelves. The second mode is linked to intermediate depth inflow of warm Circumpolar Deep Water into the cavity. The warm

water either fills most of the ice-shelf cavity, resulting in greater melting (Potter and Paren, 1985), or the inflows are restricted to shallower depths and have much of their heat re-circulated to the ocean. The third mode is characterized by high basal loss rates within 100 km of the ice fronts, where melting is high due to tidal pumping and the seasonally warmer surface waters of the coastal currents. While the first circulation mode dominates the basal melt of the larger Filchner-Ronne and Ross Ice Shelves, smaller ice shelves (e.g. Amery and George IV Ice Shelves) rather exhibit other circulation types.

The buoyant uprise of Ice Shelf Water and suspended ice crystals ultimately leads to an accumulation of larger ice platelets below a closed fast-ice cover, where platelets may attach and grow further at the sea-ice underside (Smith et al., 2001; Dempsey et al., 2010). This phenomenon has been reported from various locations around Antarctica.

3.4. Characteristics and occurrence of ice platelets

Ice platelets are large, plate-like dendritic single crystals without inclusions (Moretskii, 1965; Jeffries et al., 1993). They are larger than frazil crystals, may grow up to 200 mm in diameter, and are up to about 3 mm thick (Fig. 3.5; McGuinness et al., 2009). An accumulation of such platelets fused together in a porous matrix below sea ice is referred to as a sub-ice platelet layer. The water filling the interstices between the platelets is referred to as interstitial water (Fig. 3.1). This additional sea-ice mass is highly variable in time and space, and difficult to sample due to its residence below a several meter thick, solid sea-ice cover.

This porous layer is essentially similar to the layers of marine ice observed below ice shelves (Section 3.6; Craven et al., 2009). However, the physical conditions below a relatively thin sea-ice cover and a deep ice shelf are substantially different, resulting in different consolidation mechanisms and different ice fabrics (Tison et al., 1998). A crucial parameter to assess the contribution of ocean/ice-shelf interaction to total sea-ice mass balance is the solid- or ice-volume fraction (IVF, β) in the platelet layer. Since it is nearly impossible to directly measure this property, a variety of methods have been used to give an estimate. The determination of this crucial parameter was one of the key outcomes of this study, and is covered in more detail in Chapters 5 and 6.

The presence of a sub-ice platelet layer under a growing sea-ice cover leaves a signature in the overlying sea ice (Gough et al., 2012b; Hoppmann et al., 2015a). When heat is transferred from the ocean upwards through the sea ice during regular congelation growth, the upper part of the sub-ice platelet layer slowly consolidates. While the interstitial water freezes, ice platelets are subsequently incorporated into the sea-ice fabric. Through this process, the lower part of sea-ice cores taken in areas of ocean/ice-shelf interaction displays a characteristic texture, with blade-shaped crystals of a range of sizes and random orientations of their c-axes. This part of a core is referred to as platelet ice (Fig. 3.1). The additional thickness provided by the platelets modifies the overall sea-ice properties, energy- and mass balance. Chapters 5 and 6 provide a case study of these processes in the Eastern Weddell Sea.

Manifestations of ocean/ice-shelf interaction and associated phenomena have been observed in many locations around Antarctica (Fig. 3.6). Sub-ice platelet layers and associated platelet ice in sea-ice cores have been observed by Eicken and Lange (1989) and Lange et al. (1989) 35 km off the southeastern

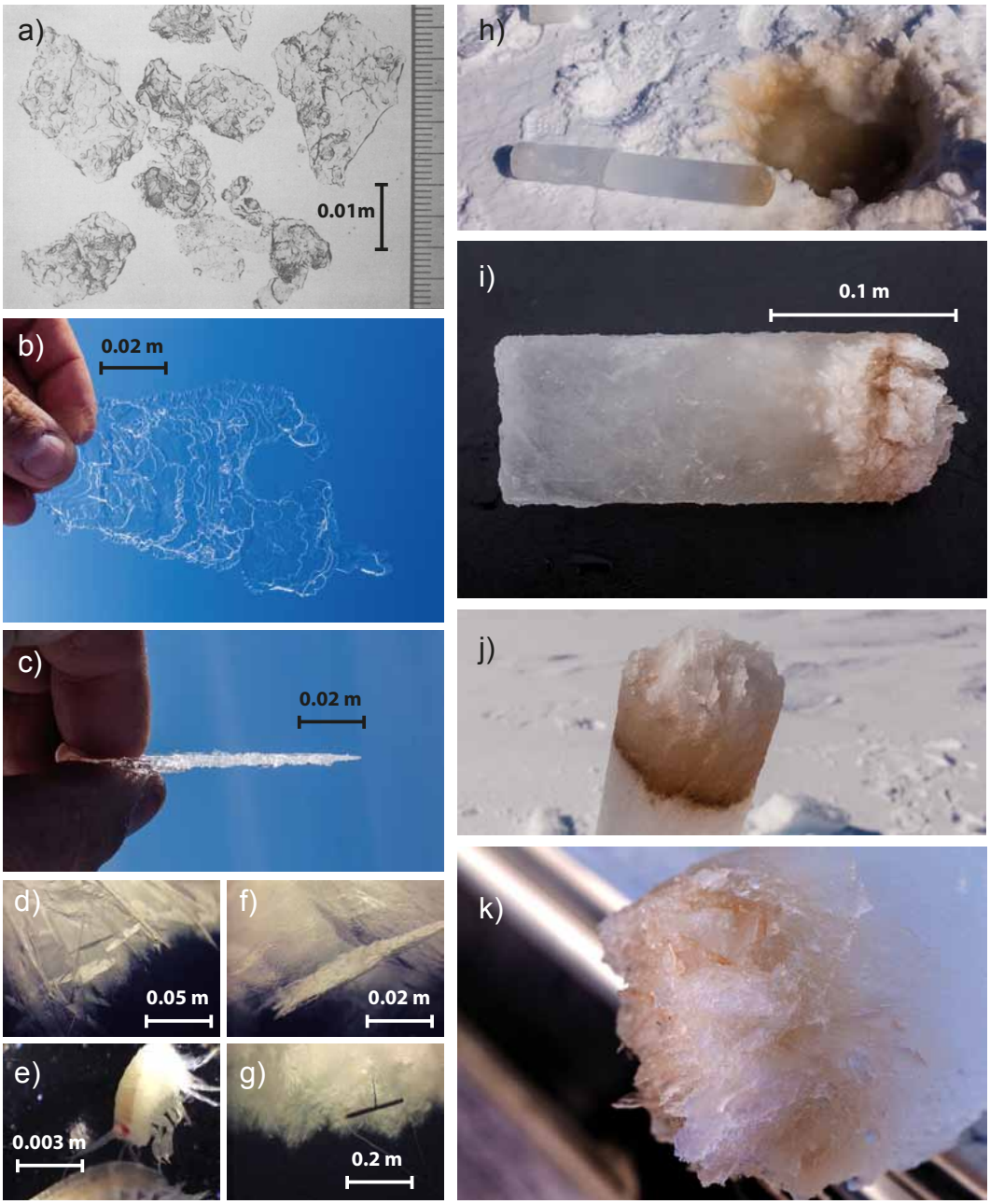

Figure 3.5: Photos of ice platelets in its various forms. a) Small ice platelets recovered from 250 m water depth (Dieckmann et al., 1986b); b,c) larger ice platelet recovered from a sea-ice corehole at Atka Bay in 2012; d-g) screenshots of the sub-ice platelet layer recorded from an under-ice camera in 2012; h) brown-colored seawater emerging from a corehole at Atka Bay in 2012; i-k) sea-ice core retrieved at Atka Bay in 2012, showing consolidated platelet ice and the skeletal layer. The brown color originates from a sea-ice algae bloom in November/December

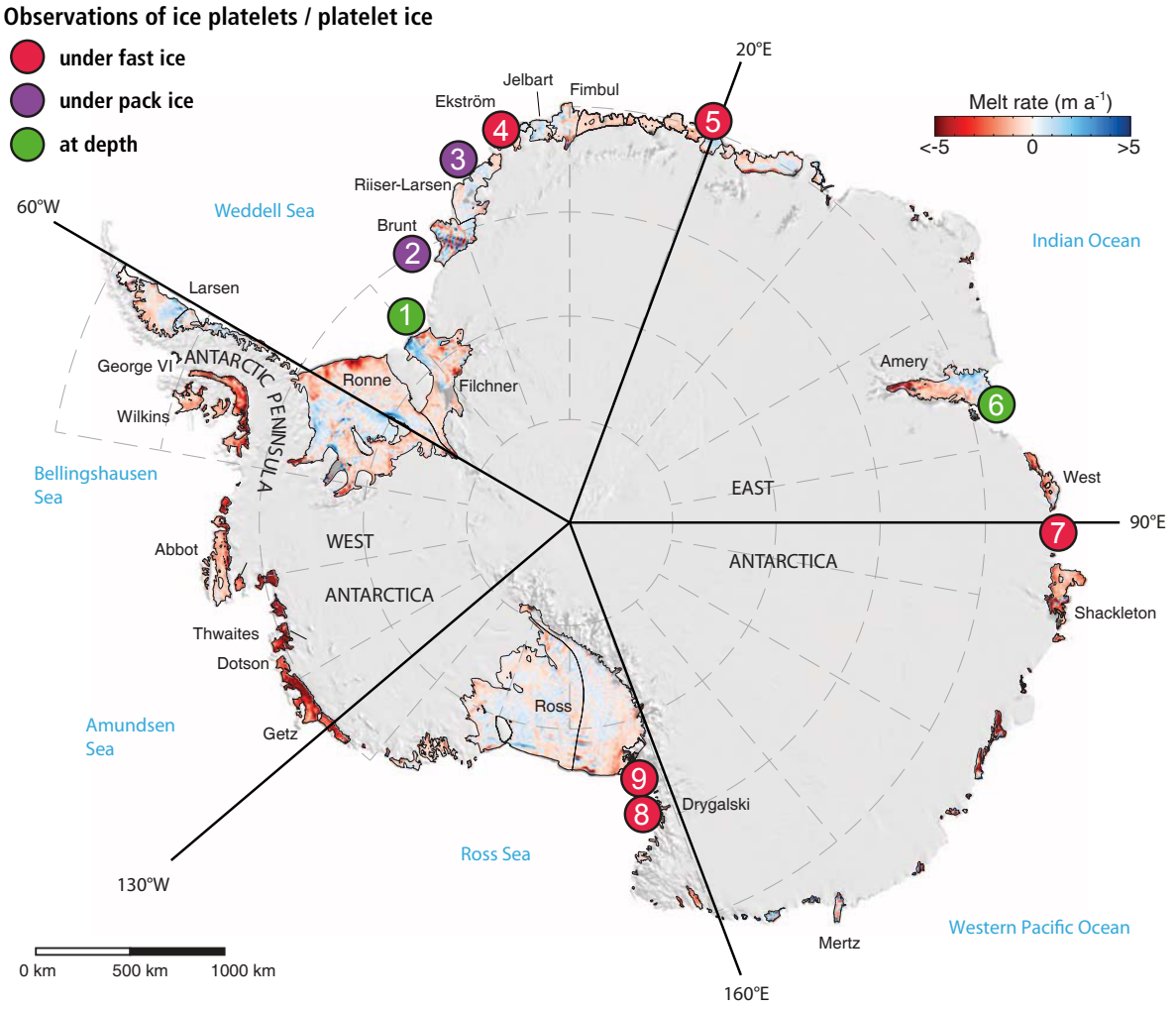

1. Dieckmann et al. (1986b)
2. Smetacek et al. (1992), Grossmann et al. (1996)
3. Eicken and Lange (1989), Lange et al. (1989)
4. Kipfstuhl (1991), Günther and Dieckmann (1999), Günther et al. (1999), Günther and Dieckmann (2001), Hoppmann et al. (2015)
5. J.-L. Tison (2014), personal communication
6. Penrose et al. (1994)
7. Serikov (1963), Moretskii (1965), Buynitskiy (1967), Baranov et al. (1969)
8. Vacchi et al. (2004), Regoli et al. (2005), Lazzara et al. (2007), Mangoni et al. (2009)
9. Wright and Priestley (1922), Bunt (1963), Littlepage (1965), Paige (1966), Bunt and Lee (1970), Dayton et al. (1969), McGrath Grossi et al. (1987), Sullivan et al. (1987), Jeffries et al. (1993), Arrigo et al. (1993b), Gow et al. (1998), Smith et al. (2001), Jones and Hill (2001), Leonard et al. (2006), Purdie et al. (2006), Dempsey et al. (2010), Mahoney et al. (2011), Gough et al. (2012a), Smith et al. (2012), Price et al. (2014)

Figure 3.6: Map of Antarctica including ice shelves and their basal melt rate, color coded from $<$ -5 m a^{-1} (freezing) to $>$ +5 m a^{-1} (melting), and overlaid on a 2009 Moderate Resolution Imaging Spectroradiometer (MODIS) mosaic of Antarctica (modified after Rignot et al., 2013). Observations of ice platelets and platelet ice are indicated by colored circles.

Table 3.2: Observations of ice-platelet/sea-ice interactions and a list of associated studies. The numbering corresponds to the respective location on the map (Fig. 3.6). Abbreviations: WS: Weddell Sea; EWIS: Eastern Weddell Ice Shelves; IS: Ice Shelf; IT: Ice Tongue.

Location	Study
1. Southern WS	Dieckmann et al. (1986b) (at depth)
2. Eastern WS	Smetacek et al. (1992), Grossmann et al. (1996) (underneath pack ice)
3. Northeastern WS	Eicken and Lange (1989), Lange et al. (1989) (underneath pack ice)
4. Northeastern WS	Kipfstuhl (1991), Günther and Dieckmann (1999), Günther et al. (1999), Günther and Dieckmann (2001), Hoppmann et al. (2015b) (underneath fast ice)
5. Northeastern WS	J.-L. Tison (2014), personal communication (underneath fast ice)
6. Prydz Bay	Penrose et al. (1994) (at depth)
7. Davis Sea	Serikov (1963), Moretskii (1965), Buynitskiy (1967), Baranov et al. (1969) (underneath fast ice)
8. Terra Nova Bay	Vacchi et al. (2004), Regoli et al. (2005), Lazzara et al. (2007), Mangoni et al. (2009) (underneath fast ice)
9. McMurdo Sound	Wright and Priestley (1922), Bunt (1963), Littlepage (1965), Paige (1966), Bunt and Lee (1970), Dayton et al. (1969), McGrath Grossi et al. (1987), Sullivan et al. (1987), Jeffries et al. (1993), Arrigo et al. (1993b), Gow et al. (1998), Smith et al. (2001), Jones and Hill (2001), Leonard et al. (2006), Purdie et al. (2006), Dempsey et al. (2010), Mahoney et al. (2011), Gough et al. (2012a), Smith et al. (2012), Price et al. (2014) (underneath fast ice)

shelf ice edge of the Weddell Sea. Smetacek et al. (1992) observed platelets underneath drifting pack ice bordering the coastal Weddell Sea polynyas. Serikov (1963) and Moretskii (1965) discovered ice platelets up to 40 km off the coast of russian Antarctic station Mirny. More recent studies of platelet ice formation and related processes were performed in the Ross Sea, benefiting from the presence of the US and New Zealand stations at McMurdo. These studies focused on the deposition of platelet ice under sea ice and the influence of brine rejection from the freezing process (McGuinness et al., 2009), the spatial variability based on ice-core analyses (Smith et al., 2001), and the development of a numerical description of small-scale ice-platelet processes (Dempsey et al., 2010; Dempsey and Langhorne, 2012; Wongpan et al., 2015). Jeffries et al. (1993) and Smith et al. (2001) showed that platelet ice can add up to more than 40 % of the total sea-ice mass.

Another phenomenon, which is closely related to the formation of individual ice crystals in the water column, is the growth of ice crystals on suspended ropes and instruments (Section 3.6, Wright and Priestley, 1922; Leonard et al., 2006; Mahoney et al., 2011), as already shown above. These must originate

from relief of supercooling in the water column, since no other heat sinks exist. Finally, ice crystals with diameters between 10 and 25 mm have been captured by trawl nets at depths of 125 and 250 m in front of the Amery and Filchner IS (Penrose et al., 1994; Dieckmann et al., 1986b). While aspects of these interactions have been investigated in detail at McMurdo Sound, Ross Sea, for more than a decade, little is known about the role of ice platelets for coastal sea ice in all the other regions of coastal Antarctica.

3.5. Significance of ice platelets for sea-ice ecology

The first extensive description and study of biology associated with sub-ice platelet layers dates back to the 1960s in McMurdo Sound (Bunt, 1963; Bunt and Wood, 1963; Bunt and Lee, 1970). It became apparent that this special habitat constitutes a favorable environment for the development of various sea-ice biota and supports extremely dense microbial assemblages (e.g. Palmisano et al., 1985; Dieckmann et al., 1992; Arrigo et al., 1993b; Ackley and Sullivan, 1994; Arrigo and Thomas, 2004). The high concentration of biological matter in platelet layers is usually immediately evident by the reddish-brown color of the water (Fig. 3.5h).

The colonization of the platelet layer by microalgae and other small planktonic organisms probably commences concurrently to its formation (Günther and Dieckmann, 1999). Whether the ice platelets themselves are instrumental in scavenging the organisms from the water column is still not clear, albeit very likely (Garrison et al., 1983; Dieckmann et al., 1986b; Garrison et al., 1988; Walker and Marchant, 1989). However, other evidence of particle inclusions is known from marine ice (Kipfstuhl et al., 1992; Warren et al., 1993; Goodwin, 1993; Eicken et al., 1994b; Craven et al., 2009), where resuspended sediment particles may be incorporated in a similar manner.

The timing of a phytoplankton bloom is strongly affected by light conditions, primarily controlled by the properties of the overlying snow cover (McGrath Grossi et al., 1987; Palmisano et al., 1987). The spectral irradiance regime is generally the main limitation for growth of bottom-ice and under-ice microalgae (Palmisano et al., 1985, 1987; Cota and Smith, 1991), and light levels in the platelet layer are lower than in the congelation ice above (Bunt, 1964b). The role of light in controlling algal growth and production in platelet layers has been studied intensively, and there is evidence of extreme shade adaptation in platelet-layer associated algae (Palmisano and Sullivan, 1985; Palmisano et al., 1987; Lizotte and Sullivan, 1991; Arrigo et al., 1991, 1993b; Guglielmo et al., 2000; Lazzara et al., 2007; Mangoni et al., 2009). However, other factors seem to compensate the light limitation, strongly favoring algal growth in this habitat: stable temperatures near the freezing point of sea water, stable salinity, a continuous supply of nutrients, ample opportunity for colonization as well as protection from large grazers such as krill. The organisms either dwell while suspended within the interstitial water between the platelets, or grow attached to ice platelets themselves (Smetacek et al., 1992). Grossmann et al. (1996) showed that substantial heterotrophic potential can be established within this special habitat. Nutrient profiles and small-scale distribution of algal and bacterial cells suggest close couplings between these two groups of organisms, thus implying the establishment of community structure. Late summer sub-ice platelet layers seem to constitute a protected refugium for ice-associated algae and bacteria during a phase of intense pack-ice melting. Under reduced grazing pressure, considerable algal and bacterial biomass may accumulate

within this environment. This unique combination leads to productivity and biomass accumulation often exceeding values observed in the skeletal layer and brine channels of congelation ice (Bunt and Lee, 1970; McGrath Grossi et al., 1987; Sullivan et al., 1987; Smetacek et al., 1992; Arrigo et al., 1993a; Lazzara et al., 2007; McGrath Grossi et al., 1987; Arrigo et al., 1993b, 1995; Günther and Dieckmann, 1999) Seasonal peaks in Chl-*a* concentrations in Antarctic and Arctic sea-ice types are up to 5400 mg Chl-*a* m^{-3} and 800 mg Chl-*a* m^{-3}, respectively (Arrigo et al., 2010). Reported peak accumulation in sub-ice platelet layer habitats are >6000 mg Chl-*a* m^{-3}, higher than any other sea-ice habitat either in the Arctic or the Antarctic (Arrigo et al., 2010). Therefore, sub-ice platelet layers are the most productive sea-ice habitat anywhere in the world, and their uniqueness to Antarctic coastal regions is one of the main reasons why sea ice in the Southern Ocean is on average more productive than its northern counterpart (Arrigo and van Dijken, 2003).

As with the bottom sea-ice community, the platelet layer communities provide an important nutritional resource for invertebrates such as juvenile krill (Marschall, 1988; Frazer, 1996; Quetin et al., 2013), amphipods (Rakusa-Suszczewski, 1972) and other zooplankton. Much of their production is exported to deeper layers by means of rapidly sinking faecal pellets of copepods and krill (Gonzales, 1992; Daly, 2013; Schnack-Schiel et al., 2013).

The notothenioid Antarctic silverfish (*Pleuragramma antarcticum*) has a pivotal importance in Southern Ocean ecosystems. In the adult stage, this fish is widely distributed and abundant in shelf waters around the continent, and represents a major contribution to the diet of most Antarctic vertebrates such as whales, seals, penguins, flying birds and benthic fish especially in the Ross Sea (La Mesa et al., 2004). They also constitute the major link between lower (invertebrates) and higher (birds and mammals) levels of the food web. The sub-ice platelet layer has been found to play a crucial role in the early stages of the life cycle of this species (Vacchi et al., 2004), providing an important food source, but also a favourable environment, protected from predation (Gutt, 2002). These fish use antioxidants as adaptive responses to extreme environmental conditions and to the rapid changes of pro-oxidant pressure associated to the sub-ice platelet layer (Regoli et al., 2005).

The role of sub-ice platelet layers for marine mammals is currently unknown. It is however likely that the additional thickness provided by incorporated ice platelets further stabilizes coastal fast-ice regimes, favoring for example the breeding of Emperor penguins at those sites. It is further unclear in which way benthic organisms are affected by sedimentation of the high biomass after melting of sub-ice platelet layers in summer.

3.6. Other sea-ice types formed at depth

Anchor Ice

In the polar marine context, the term “anchor ice” is used to describe frazil ice crystals formed in a supercooled water column that adhere to the seabed (Mager et al., 2013). The continued presence of supercooled water allows these initial ice crystals to grow rapidly (Osterkamp and Gosink, 1984) and form delicate leaf-like ice structures that clump together (Fig. 3.7a, Kempema et al., 1993). This results

in a patchy covering of ice that provides a lair for benthic species and is a potentially fatal environment for shallow water benthic communities (Denny et al., 2011). These ice clusters can grow large enough to become buoyant and detach from the sea floor, lifting any adhered sediment, flora or fauna into the overlying ice (Dayton et al., 1969).

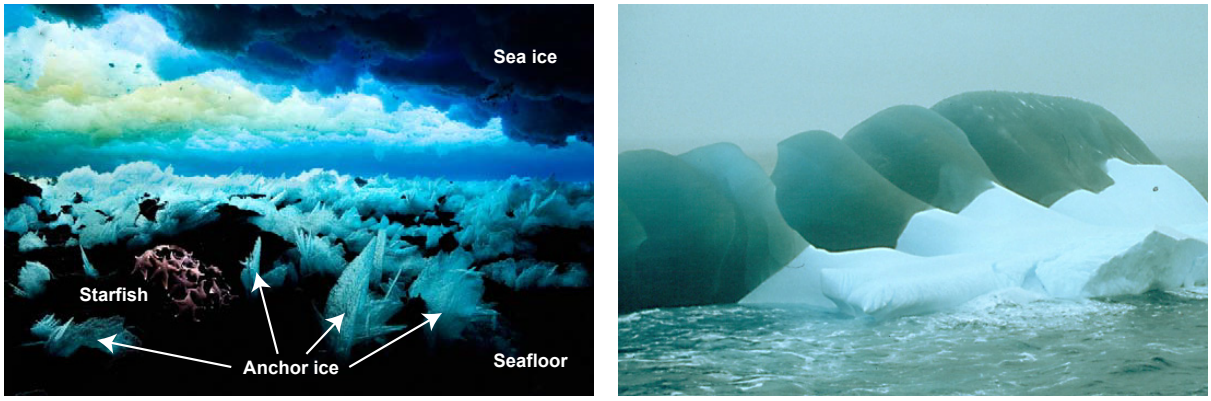

(a) Anchor ice attached to the seafloor in McMurdo Sound (Mager et al., 2013)

(b) Green iceberg (Southern Ocean, photo: Sellmann, kindly provided by G. Dieckmann)

Figure 3.7: Other ice types associated with sea-ice growth at depth

Marine Ice

Ice shelves are essential to the stability of ice sheets (e.g. Kulessa et al., 2014). A major factor in this regard is the process of ice-shelf thickening through marine ice accretion from below (Tison et al., 1998), essentially counteracting calving events and basal melting. However, the basal mass balance of ice shelves is a variable still difficult to assess. As summarized by Bombosch and Jenkins (1995), most of the ice shelves protruding from Antarctica are composed of meteoric ice which originates either from fast flowing ice streams, which drain the inland ice sheet, or from snow that falls on the surface of the ice shelf. As an ice column is advected toward the ice front, its content of inland ice is gradually reduced due to basal melting and surface accumulation. In places, a third substratum appears at the base of the ice shelf, which is clearly distinguished from the upper two strata. The fundamental differences in origin between meteoric ice and marine ice are reflected in their physical and physico-chemical properties such as in isotopic composition, electrical conductivity, crystal structure as well as gas bubbles and particle inclusions (Tison, 2002).

It was in the early 1970s that the first glaciological Antarctic field investigations unveiled the potential significance of ice-ocean interactions in the mass-balance and stability of ice shelves. Gow and Epstein (1972) first demonstrated the existence of refrozen seawater at the base of the Koettlitz Ice Tongue, Antarctica. The same year, Morgan (1972) found evidence for ice of seawater origin located below 270 meters of ice of meteoric origin in the 350-m long G1 ice core drilled at the surface of the Amery Ice Shelf. A few years later, Zotikov et al. (1980) reported 6 meters of refrozen seawater at the bottom of a 416-m ice core recovered from the Ross Ice Shelf. Two cores drilled through the Filchner-Ronne Ice

Shelf in the late 1980s and early 1990s also supplied evidence for substantial marine ice accretion (Oerter et al., 1992; Eicken et al., 1994b). Oerter et al. (1992) were the first to introduce the term "marine ice" to characterize these bodies of sea ice in a glaciological context, a terminology that has since established. The list of further observational evidence of ice-platelet accretions under ice shelves ice can be continued (e.g. Doake, 1976; Engelhardt and Determann, 1987; Tison et al., 1998) and is further supported by modeling results (Bombosch and Jenkins, 1995; Jenkins and Bombosch, 1995; Smedsrud and Jenkins, 2004). Since heat conduction through the thick ice sheet is limited and only leads to a thickening of a few centimeters per year (Robin, 1979; Zotikov et al., 1980) it cannot account for the hundreds of meter thick layers of marine ice (Kipfstuhl et al., 1992). Mass balance calculations yielded basal accumulation rates under the Amery and Ronne ice shelves of up to 1 and 2 m solid ice per year (Budd et al., 1982; Determann, 1991), giving further evidence for an ice pump process. Finally, substantial evidence has been found that compacted marine ice is the source of occasionally observed green icebergs around Antarctica (Dieckmann et al., 1986a; Kipfstuhl et al., 1992). Their green color (Fig. 3.7b) is attributed to marine-derived organic matter included in the ice, which has also been detected in basal ice of the Amery Ice Shelf and in nearby seawater. These constituents absorb blue photons and shifts the icebergs color to green (Warren et al., 1993).

Chapter 4

Development and realization of a sea-ice monitoring program

The development, realization and supervision of a continuous monitoring program on the fast ice of Atka Bay was a substantial part of this work. A scheme of the different methods and approaches, as well as their purpose, was already presented earlier (Fig. 1.2). Those methods, along with preliminary results, are described in more detail in annual field reports published in the AWI online repository EPIC (Hoppmann et al., 2011, 2012, 2013, 2014). Part of the data are the basis of Publications II and III (Chapters 5 and 6), and the other data present valuable additions to the Antarctic Fast Ice Network (Section 4.1). The major part of the data is archived in the online database PANGAEA. This chapter describes the field setting at Atka Bay, and gives a brief summary of the measurements performed annually between 2010 and 2014, with a focus on the evolution and continuous improvement of the monitoring program. In order to account for the timing of sea-ice formation and breakup at Atka Bay, a monitoring season is not given as a calendar year, but rather considered as the period between April of one year until April the next year. A time line of the various data obtained in the framework of the monitoring program is provided at the end of the respective section (Figs. 4.6, 4.10, 4.15, 4.19 and 4.20). A colored bar indicates that at least one measurement was made during the corresponding month. All measurements were performed by the Neumayer III overwintering meteorologist with the help of other overwinterers. They also deployed and recovered the autonomous stations and buoys. In addition to the regular monitoring activities, a dedicated field campaign to Atka Bay (Section 4.6) contributed to all publications in this thesis.

4.1. The Antarctic Fast Ice Network (AFIN)

Studies of fast ice have been conducted around the Antarctic coastline for several years. They were mostly limited to a few different locations where Antarctic stations facilitate the logistics, most notably at Prydz Bay (Heil et al., 1996; Heil, 2006; Tang et al., 2007; Lei et al., 2010), Lützow Holm Bay (Kawamura et al., 1997; Uto et al., 2006; Kawamura et al., 2006) and McMurdo Sound (Trodahl et al., 2000; Smith et al., 2001; Pringle et al., 2006; Leonard et al., 2006; McGuinness et al., 2009; Dempsey et al., 2010; Leonard et al., 2011). During International Polar Year 2007/08, the Antarctic Fast Ice Network (AFIN) was established with the aim to coordinate and facilitate fast-ice research at Antarctic stations (Heil et al., 2011). By now a number of international partners have joined this network, and many have already set up fast-ice monitoring programs near their Antarctic bases (Fig. 4.1).

The main data collected under AFIN include sea-ice thickness and snow depth, freeboard, as well as dates of fast-ice formation and - breakup. Auxiliary data include meteorological and oceanic parameters,

such as air and water temperatures, air pressure and seawater salinity. The data are available to members within the AFIN network and to the wider scientific community under the Antarctic Sea Ice Processes and Climate (ASPeCt) data library (Heil et al., 2011). Germany joined AFIN with monitoring activities on Atka Bay fast ice in 2010, filling the knowledge gap of fast-ice properties and processes in the Weddell Sea sector of Antarctica.

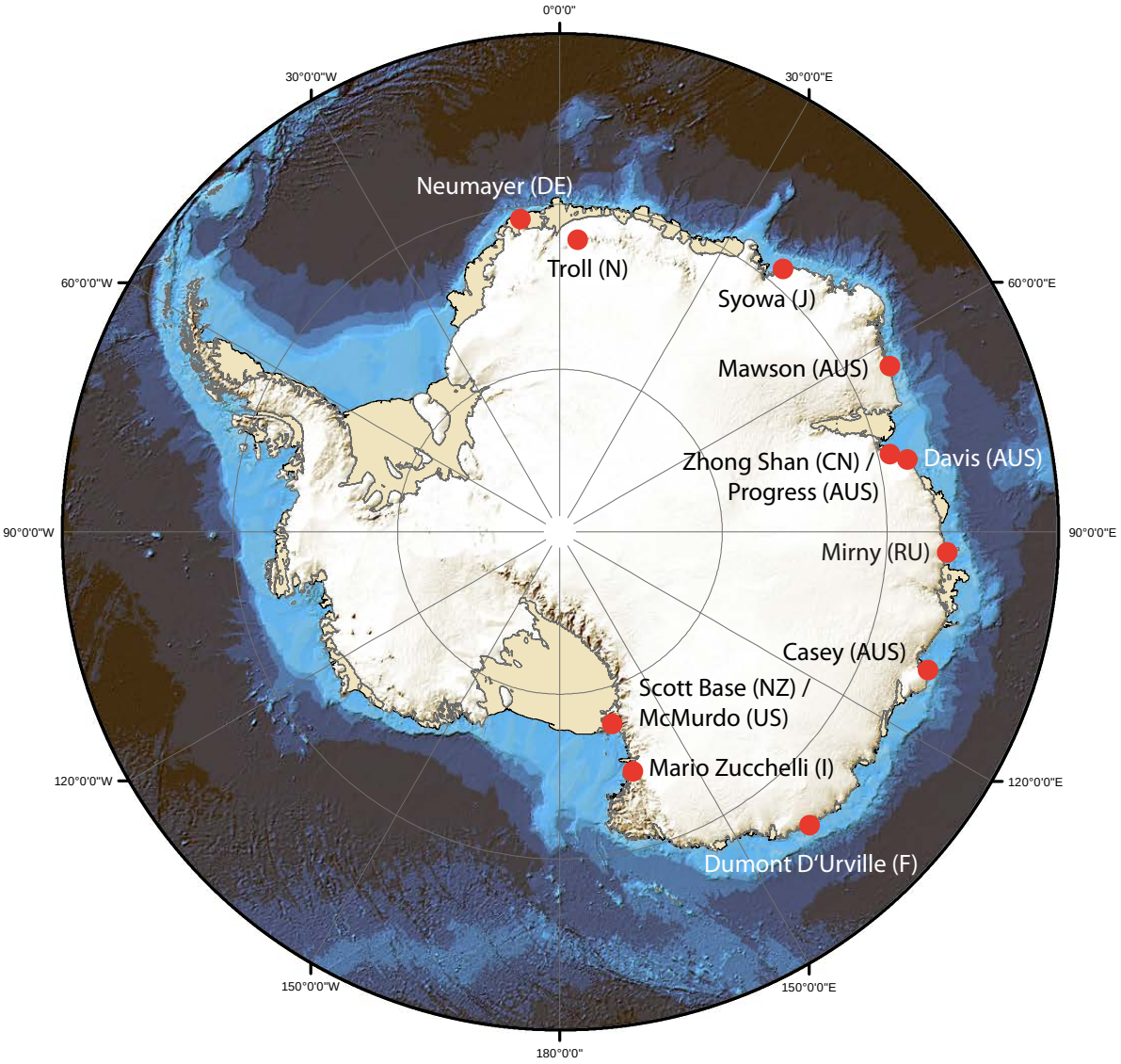

Figure 4.1: Stations currently contributing to the Antarctic Fast Ice Network. The map incorporates data from the SCAR Antarctic Digital Database 6.0, Bedmap-2 (Fretwell et al., 2013) and the International Bathymetric Chart of the Southern Ocean (IBCSO) (Arndt et al., 2013)

4.2. Description of main study area

Historical Overview

The main study area of this thesis is Atka Bay (also known as Atka Iceport, 70°35'S. 7°51'W), a 440 km^2 large embayment in the front of Ekström Ice Shelf (EIS). It is located on the coast of Dronning Maud Land in the eastern Weddell Sea (Fig. 4.2). The area was surveyed by aero-photogrammetry during the German Schwabenland Expedition in 1939, and mapped in great detail afterwards by Norwegian cartographers from surveys and aerial photographs taken during the the Norwegian-British-Swedish Antarctic Expedition (NBSX or NBSAE) in 1949-1952, led by the Norwegian scientist John Schjelderup Giæver (Giæver, 1954). The Ekström Ice Shelf (or Ekströmisen) was named after an expedition member tragically lost on the expedition. Atka Bay itself was named by personnel of the U.S. ship "USS Atka (AGB-3)" (named after the small Aleutian island of Atka), which moored at the site in February 1955 while investigating possible base sites for International Geophysical Year operations. Parts of the descriptions in this section were adapted from Hoppmann et al. (2015b) and Bunge and Roß-Reginek (2005).

Geography

The Ekström Ice Shelf is part of the Eastern Weddell Ice Shelves (EWIS), a group of ice shelves which are small when compared with the major ice shelves Ross and Filchner/Ronne in the south (Fig. 4.2a). It is separated into a western and eastern part (Fig. 4.2b), which cover areas of 6800 and 1900 km^2, respectively (Bindschadler et al., 2011). It has been under study since the 1980s when the first German year-round station was established there.

The general ice-flow direction near the coast is northwards, with a geographically stable breaking edge. Several undulations of the sea floor rise higher than the underside of the northern ice shelf. When the ice is pushed over these obstacles by the flow, ice rises or ice rumples are formed with heavily crevassed surfaces (Fig. 4.2c). Since icebergs cannot break off from the ice shelf before the risings have been passed over, ice is steadily breaking away behind the risings because of the fissured state of the ice. At the western side of Atka Bay, deep and narrow inlets in the ice front are formed when the northward flowing ice is forced to round the western end of the rise. Atka Bay is generally flanked by floating or grounded ice shelf with up to 20 m high, cliff-like edges. Investigations of currents, ice thickness, bedrock topography and basal melting in this region were performed for example by Nicolaus and Grosfeld (2004), Sandhäger and Blindow (2000), Kipfstuhl (1991) and more recently by Neckel et al. (2012). Information about cavity geometry is available from Kobarg (1988). The continental shelf here is only about 5 km in width, and water depths range between 100 and 500 m. Beyond, water depths rapidly increase to 1000 m. In the central part of Atka Bay, submarine contours are characterized by a steep canyon of 275 m depth. The sea bottom is mainly covered with glacial mud, and extends to unknown distances under the floating ice shelf. No typical coastal conditions with shallow water zones, sandy gravel beaches or rocky cliffs exist in the region. In the west, the Weddell Sea extends south to 78 °S. Along the eastern coast, the narrow continental shelf has a maximum width of about 90 km. Typical water depths range between 200 and 500 m. Shallower areas are mostly covered by grounded ice with high ice cliffs forming the coast-line of

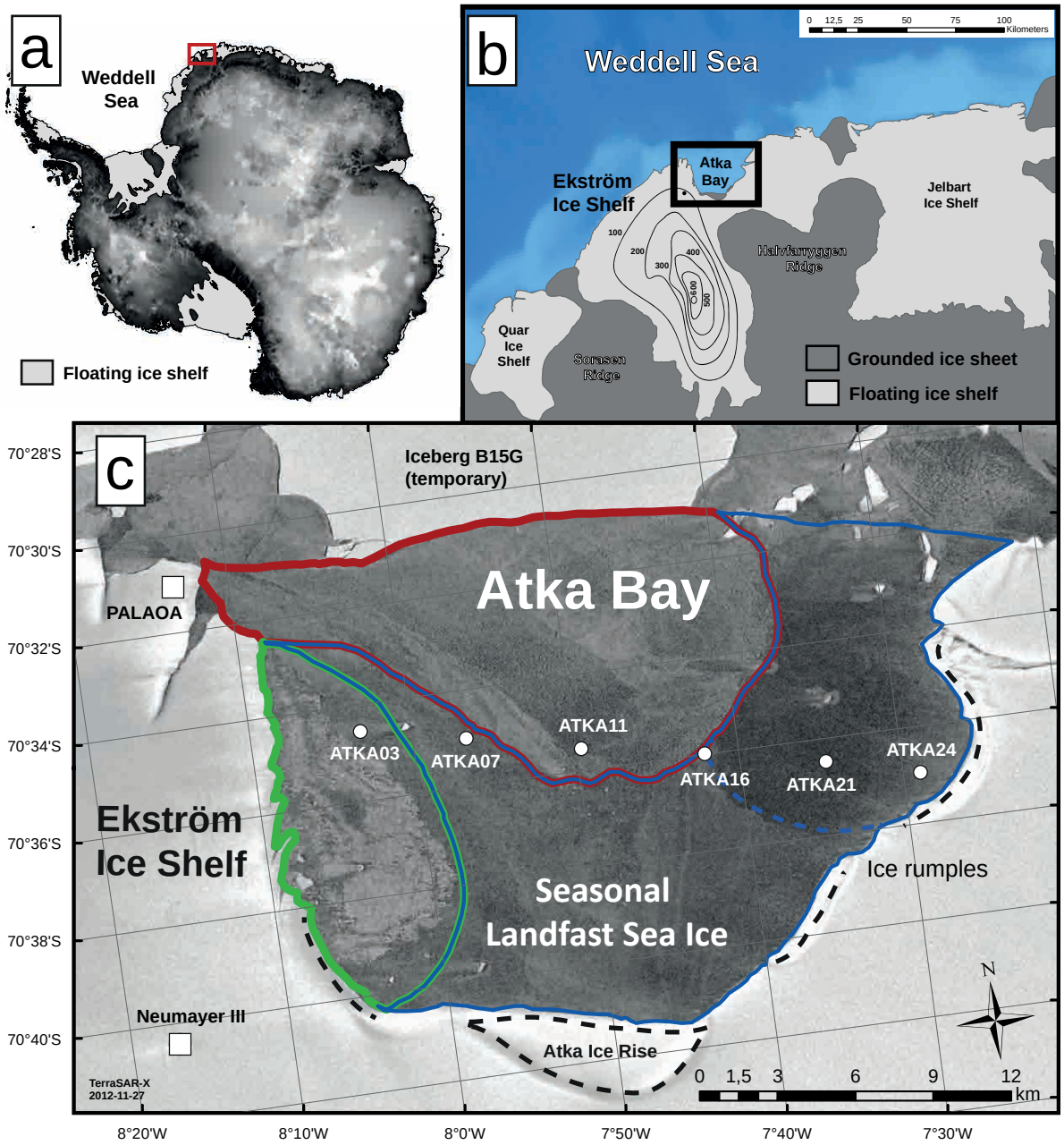

Figure 4.2: Location of study sites at Atka Bay. a) The Ekström Ice Shelf is located in the eastern Weddell Sea (highlighted as red box). b) Enlargement of a). The contour lines show the depth in metres of the water column below the ice shelf following Kobarg (1988). Bathymetry and coastline data were taken from BEDMAP-2 (Fretwell et al., 2013) and from SCAR Antarctic Digital Database 6.0. c) Enlargement of b). Sampling sites are indicated by white circles. The TerraSAR-X image provided by the German Aerospace Center (DLR) reveals the different sea-ice regimes in 2012: second-year/first-year sea ice (green), first-year sea ice (blue) and new sea ice grown in October (red). The dotted black lines indicate the locations of ice rises and rumples. The figure and description are taken from Publication II (Hoppmann et al., 2015b).

the eastern and southern part of the Weddell Sea. The shelf edge exhibits water depths between 500 and 800 m. A strong southward current flows along the eastern coast, which is part of the clockwise rotating Weddell Gyre. The ice cliffs along the coast provide anchor points for fast ice, which extends westwards to the pack-ice region of the central Weddell Sea between March and December.

Meteorology

Meteorological data are readily available from the nearby Neumayer III station, where atmospheric conditions have been recorded since 1981 (König-Langlo and Loose, 2007). An overview for the period between 1991 and 1995 is discussed in König-Langlo et al. (1998), the period between 1982 and 2011 in Rimbu et al. (2014). Winds from the north are rare, while weak southward winds derived from local downslope currents of cold air near the ground sometimes occur under stable weather conditions. The weather at the location of Neumayer is strongly influenced by cyclone activities (König-Langlo et al., 1998). Eastward moving cyclones north of the station are responsible for frequent blizzards from easterly directions, contributing to a general predominance of strong, easterly winds. Blowing snow commonly occurs at wind velocities around 5 m/s, and becomes drifting snow at 10 m/s. The variability of snow accumulation rate is high even over short periods, and amounts to 0.7 m to 0.8 m of snow or 320 kg/m^2 per year at undisturbed areas near Neumayer Stations (Schlosser, 1999).

Sea ice

Information about general sea-ice conditions is usually obtained from satellite images, recorded for example by Synthetic Aperture Radar onboard Envisat, Radarsat and TerraSAR-X, the Moderate Resolution Imaging Spectroradiometer onboard Aqua and Terra, the Enhanced Thematic Mapper onboard Landsat or the Advanced Very High Resolution Radiometer onboard the Polar Orbiting Environmental Satellites. Satellite imagery is especially needed to fill the gap between late summer and early winter, when direct sea-ice observations are not available and dates of initial formation and breakup need to be determined. Atka Bay is seasonally covered with fast ice attached to ice-shelf edges bordering in the west, south and east. Due to the protection from offshore winds and currents, sea ice typically forms earlier (around March) and breaks up later (January/February) than sea ice in adjacent waters. Fast-ice thickness typically reaches about 2 m by late winter. The extent mainly depends on the strength of winds and ocean currents offshore from Atka Bay, and also on the interaction with passing icebergs. The fast ice does not melt in situ during summer, but breaks up once it is destabilized enough. Although no studies exist to date which have closer investigated the responsible physical factors, contributions of increased water and air temperatures as well as of solar radiation, tidal motion, wind forcing, and a combination thereof, are most likely. The interaction with stationary and passing icebergs also plays a role. The breakup usually happens after the retreat of the pack ice in front of the fast ice, and normally begins in the eastern part of the bay (generally in December or January). In the southwestern part, sea ice may stay as long as March, but in most years Atka Bay is completely ice free at the end of March. Persistent strong easterly winds during initial formation lead to an increased dynamic growth towards the western ice shelf edge. Once a solid sea-ice cover is established in the major part of Atka Bay (usually in April/May), further growth proceeds thermodynamically. Icebergs

often ground in the bay, with some of them remaining for years before breaking up again and drifting westwards with the coastal current. Drifting snow is building natural though steep ramps from sea ice to ice shelf surfaces at many places when it is deposited in the calm zones of the ice edge. A polynya is formed in front of Atka Bay and the northern ice shelf front at irregular intervals of a few days under the action of intermittent katabatic winds. Another polynya of different extent (about 300 nautical miles across) and cause (upwelling water), named Weddell Polynya, is more or less regularly appearing in the sea or pack ice about 500 nautical miles northeast of Atka Bay, allowing easier navigation than elsewhere around. There is a distinct semi-diurnal tide at the ice coast with an average range of 1.2 m, being followed by the ice shelf where not resting on sea-bottom risings. Tidal currents accordingly reach far under the ice shelf and have been directly measured at Neumayer through holes in the ice. At the station the elevation above mean sea level is around 25 m, and the thickness of the ice shelf is 230 m. The ice flows at a rate of 150 to 200 m/year towards north in the area of the station.

Fauna

The wind-sheltered fast ice at the foot of the ice cliffs provides ideal breeding sites for Emperor penguins and Weddell seals. Even under conditions of maximum sea-ice cover during winter, the animals have easy access to the open sea at the wide mouth of Atka Bay due to the presence of a pronounced polynya along the coast. A large colony of Emperor penguins (several thousand breeding pairs, Woehler, 1993, Fig. 4.3) is located at the south-western corner of Atka Bay, which is sheltered by high ice cliffs in the west and grounded icebergs in the east.

Figure 4.3: Colony of Emperor penguins on Atka Bay fast ice

Adults gather at the traditional breeding site for courtship and pairing throughout April and May. Eggs are laid in late May and early June, and the males breed alone for about 9 weeks throughout the winter months June and July. Chicks are hatched in late July and early August, and after a 5-month rearing period they are ready to leave the colony site with the break-up of the fast sea ice at the end of the year. At this time, large parts of the bay become ice-free within a few days, and most of the adult and juvenile penguins have left, except for several hundred adults associated with groups of still moulting chicks which

are hatched outside the optimal period. These animals gather on the remaining fast ice in the innermost parts of the south-west inlets. The penguins have also been observed to use the natural snow ramps to climb up to the ice shelf (Zitterbart et al., 2014). Weddell seals are also common at Atka Bay, returning to their traditional pupping sites close to the ice cliffs during spring. Perennial cracks associated with grounded icebergs and tidal motion of the fast ice provide permanent access to the water. The whelping season lasts from late September to early November, and the pups are weaned at the age of 6 weeks. In the summer months, Adélie penguins, crabeater seals, southern giant petrels (*Macronectes giganteus*), skuas (*Catharacta spp.*), Antarctic petrels (*Thalassoica antarctica*), and snow petrels (*Pagodroma nivea*) can also be observed, albeit in smaller numbers.

4.3. Sea-ice monitoring 2010/11: the first steps

The first sea-ice monitoring activities in the framework of AFIN took place on eight occasions between June and December 2010. We chose six sampling locations distributed evenly over a transect across Atka Bay (Fig. 4.4), where we measured sea-ice thickness, snow depth and freeboard by repeated drill-hole measurements (Fig. 4.5).

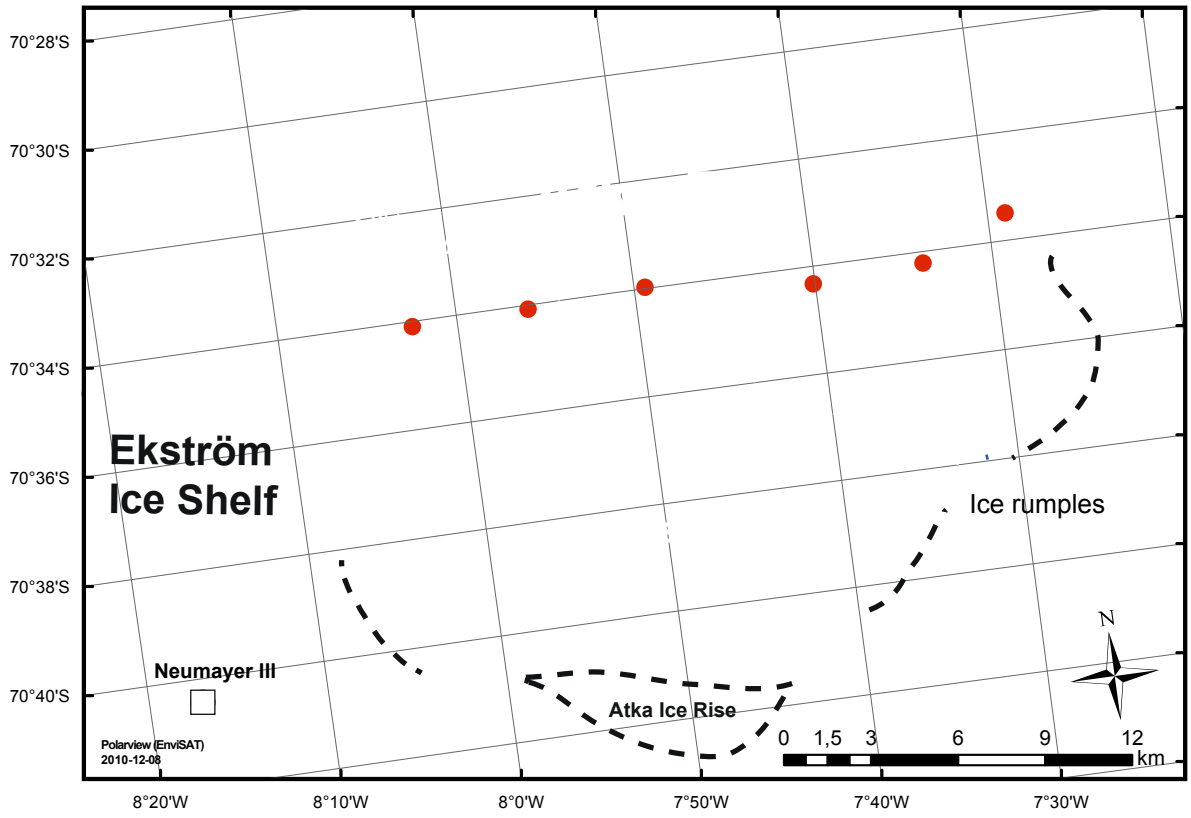

Figure 4.4: Radar image of the study area in November 2010. Sampling sites are indicated by red circles. The xx in ATKAxx refers to the distance to the western ice-shelf edge. The background radar image was provided by Polarview.

At each measurement location, 5 holes were drilled through the sea ice in order to account for small-scale variabilities: one in the center and one in a distance of five meters in each direction. Snow depth and freeboard were measured with a ruler stick, and sea-ice thickness was determined with a regular thickness tape. Auxiliary parameters, such as temperatures of air (2 m), snow surface, snow, snow/sea-ice interface and water were measured by a hand held thermometer. In addition, photos of sea-ice conditions in each direction were taken, and seawater conductivity was measured. Several efforts were undertaken to determine the thickness of the sub-ice platelet layer, but were not successful.

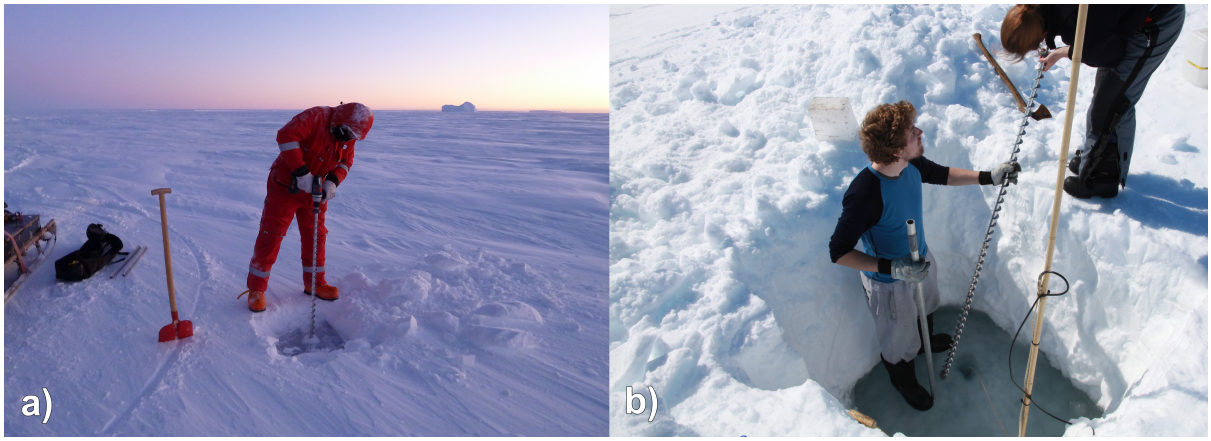

Figure 4.5: Drilling work in a) thin snow, b) thick snow conditions (photos by Jölund Asseng)..

Sea-ice thickness was on average 0.4 m in June, and grew to 1.5 m in December. The three western sites were about 0.5 m thinner than the three eastern stations in December. Snow depth was on average around 0.6 m in December, causing negative freeboard at the three eastern sites as early as August. The highest snow accumulation of 0.5 m was observed in September and October (Hoppmann et al., 2011). A large part of the fast ice broke up in the northeastern part of Atka Bay in mid-December (Fig. 4.4). The measurements were immediately discontinued due to security reasons. The time line of measurements is given in Figure 4.6.

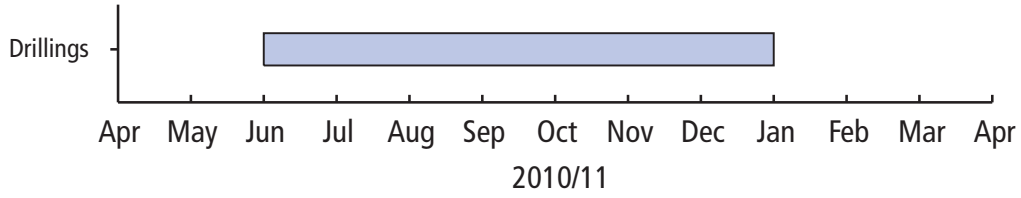

Figure 4.6: Time line of data obtained during sea-ice monitoring in 2010/11. A month is highlighted by a colored bar if at least one measurement was performed in the corresponding month.

4.4. Sea-ice monitoring 2011/12: autonomous measurements

Drillings

We repeated the drillhole measurements of 2010 on 11 occasions between 06 June 2011 and 17 January 2012. In response to the fast-ice breakup in December 2010 (Fig. 4.4), we relocated the eastern sampling sites further south in order to be able to obtain likely a longer time series (Fig. 4.2). A measurement of platelet-layer thickness was again not achieved, but the presence of ice platelets in the drillholes was documented starting in August.

At the beginning of our field work, sea-ice thickness was >0.8 m at ATKA03, and >0.5 m at ATKA24. It increased to an approximate thickness of 1.3 to 1.5 m in September, when growth rates started to decline. The thickest sea ice and highest small-scale spatial variability was regularly found at ATKA07. The maximum overall thickness of 2.42 m was found on 11 December 2011 at ATKA07. Snow cover increased steadily at all sites. Most of the snow was accumulated between June and October, but was redistributed westwards due to persisting easterly winds. From November, snow depths declined at all stations. Freeboard was highly variable during the season. At ATKA03, the heavy snow cover depressed the sea-ice surface under water level from July, whereas freeboard at ATKA07 stayed positive all the season due to the very thick ice. At ATKA11, ATKA16 and ATKA21, freeboard was constantly negative from September, whereas it stayed positive at ATKA24 from August due to the thin snow cover. Ice platelets appeared in some boreholes from August, but were never observed at ATKA07, where sea-ice was thickest. Platelets were found in nearly every hole drilled on 29 December 2011 and 17 January 2012 (except at ATKA07). At ATKA24, brown colored water was observed in boreholes between end of October and January, being an indication of a local diatom bloom (such as in Fig. 3.5h). Finally, two sets of full-length sea-ice cores were obtained in December 2011 and January 2012. Due to a transport delay of more than year, the cores have not been processed (yet).

Sea-ice thickness from electromagnetic induction sounding

Starting in November 2011, total (sea ice + snow) thickness profiles were obtained by electromagnetic (EM) induction sounding using an EM31 (Geonics Ltd.) mounted in a kayak and pulled behind a snowmobile (Fig. 4.7).

The EM31 is a frequency-domain induction sounder, which uses the emission and reception of electromagnetic fields to determine the distribution of conductive layers. A time-harmonic (primary) EM-field is generated by a transmitter coil, which induces currents in every nearby conductive medium and results in a secondary field. The sum of both primary and secondary field is subsequently detected at the receiver coil of the instrument. When operated on sea ice, the conductivities of the sea ice itself and the overlying snow are neglected, with the additional assumption that all media can be described by flat layers ("1D Approximation"). The distance between the instrument and the conductive seawater is inferred from the complex ratio of secondary to primary field. It has to be noted that the instrument is not able to distinguish between sea ice and snow, and therefore we are only able to calculate the total thickness.

A 114 km long EM31 transect at the end of November 2011 shown here as an example (Fig. 4.8)

Figure 4.7: Kayak with EM31 pulled behind a snowmobile (photo by Jölund Asseng).

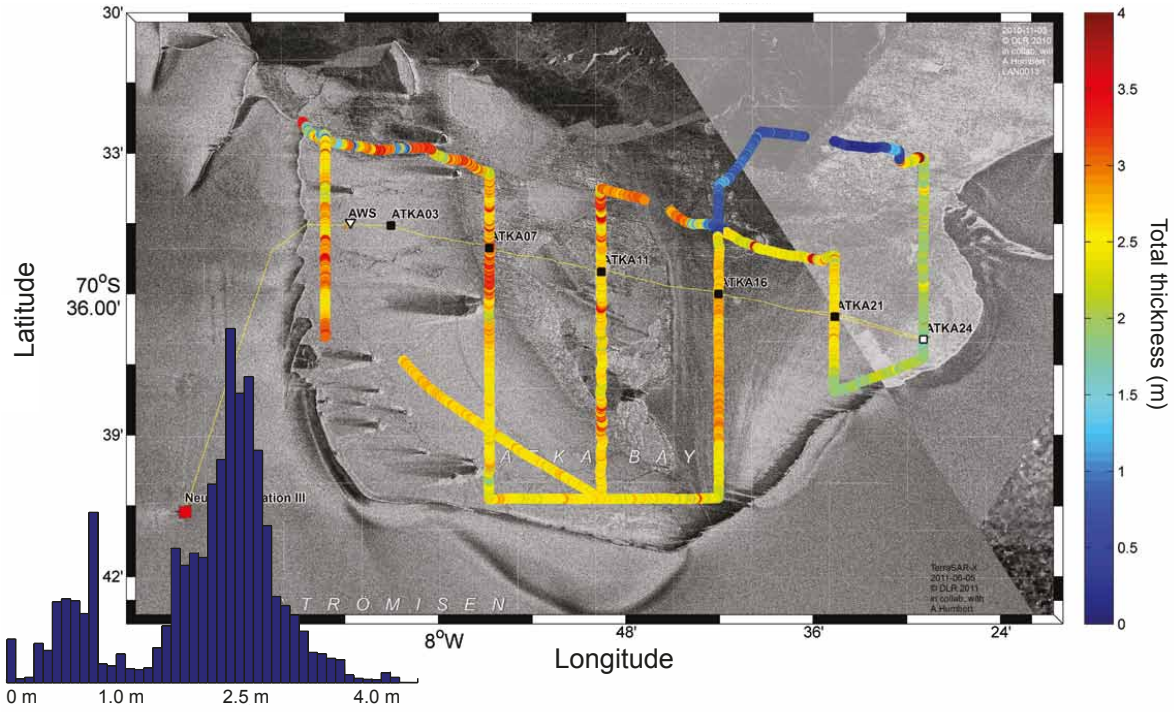

Figure 4.8: Total thickness measurements at Atka Bay on 29 November 2011, calculated from EM31 soundings. The histogram in the lower left shows the corresponding frequency distribution. Please note that sea-ice thicknesses $<$1 m are likely an underestimation due to the mode of operation of the instrument.

yielded two total thickness modes, at 0.9 m and around 2.5 m. Simultaneously measured snow depths yielded modes at 0.1 m and 0.9 m. The data showed high variability in the western and central parts of Atka Bay, and rather uniform thicknesses in the south and east. The lack of snow in the far eastern part lead to a lower total thickness, while sea ice in the northeastern part was generally very thin.

Autonomous measurements

On 6 July 2011, an Automatic Weather Station (AWS) was deployed 1.6 km from the ice shelf edge. The AWS measured temperature (2 m), relative humidity, barometric pressure, wind velocity, wind speed as well as downward and upward radiation and snow depth in 1-minute intervals (Fig. 4.9, Tab. 4.1).

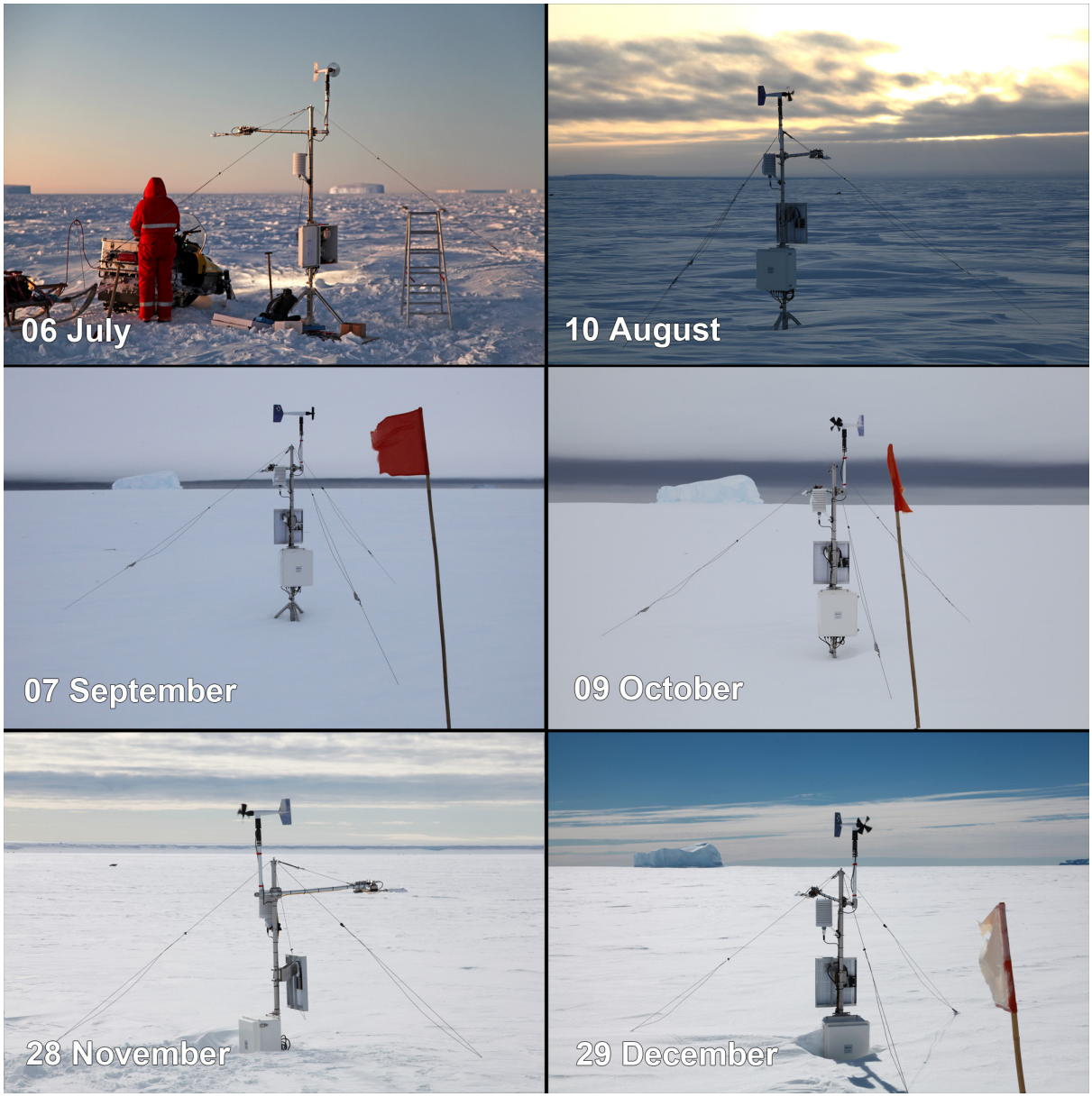

Figure 4.9: Photos of automatic weather station in 2011

Table 4.1: Instrumentation and measured parameters of the automatic weather station

Instrument	Measured parameter
Temperature and Humidity Probe (shielded HMP155A, Vaisala)	Air temperature, relative humidity
Barometric Pressure Sensor (61302V, RM Young Company)	Barometric pressure
Marine Wind Monitor (05106-5, RM Young Company)	Wind direction, wind speed
Net Radiometer (CNR4, Kipp & Zonen)	Bulk long- and short-wavelength radiation
Sonic Ranging Sensor (SR50A, Campbell Scientific)	Snow height

The temperature minimum of -42°C occurred on 21 September, the maximum of +4.8°C on 18 December. The mean temperature between 10 August and 29 December was -16.5°C. Atmospheric pressure was highest on 21 July with 1014.5 hPa, and lowest on 09 December with 953.5 hPa. Relative humidity was highly variable and ranged from 44.8 % on 06 November to 97.6 % on 18 December. Humidity may be strongly influenced by dry katabatic winds and moist oceanic air masses. The wind showed two preferred directions, about 90° (easterly winds) and about 250° from north (southwesterly winds). The wind speed was highly variable, but the winds from the east were strongest. The maximum of 29 m s^{-1} was measured on 01 November, the mean wind speed was 7.33 m s^{-1}. Between August and October, daily mean albedo varied between 0.54 and 0.98. Between October and January, the variation beca less, and the minimum value did not fall below 0.78.

On 10 August 2011, a thermistor chain sea-ice mass-balance buoy (SAMS/SRSL, Oban, Scotland) was deployed at the AWS site to measure sea-ice thickness and snow depth in high resolution and to derive the heat flux through sea ice and snow. Because of an instrument malfunction, data was only available between August 10th and September 15th (with a data gap from 5 to 8 September), and between 18 and 28 November. The instrument was recovered on 29 December 2011. The time line of measurements is given in Figure 4.10.

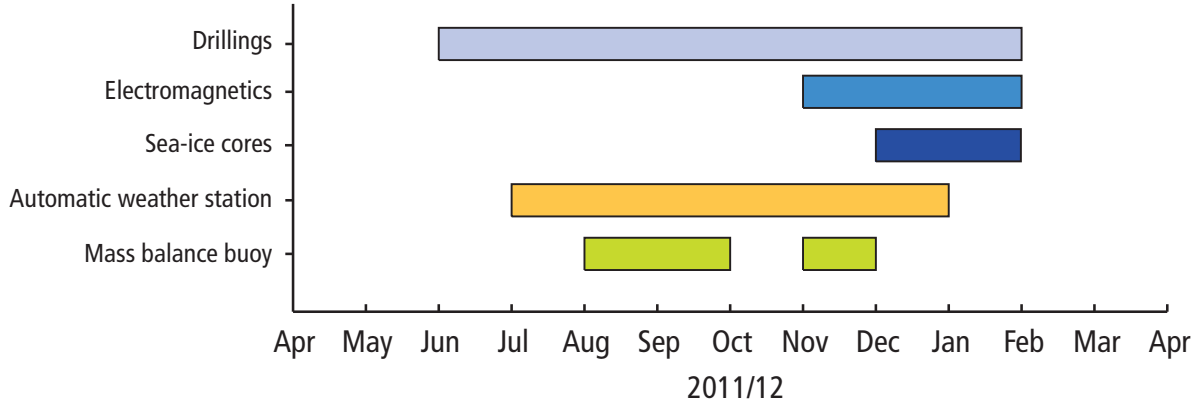

Figure 4.10: Time line of data obtained during sea-ice monitoring in 2011/12

4.5. Sea-ice monitoring 2012/13: enhanced autonomous measurements and cores

General conditions

Publications II (Chapter 5) and III (Chapter 6) are largely based on measurements performed in 2012/13. A more detailed description about sea-ice conditions in this period is therefore given there. During a storm in August 2012, a rare breakup event occurred where about 144 km^2 of sea ice in the central Bay drifted away, following the Antarctic Coastal Current in westward direction towards the central Weddell Gyre. We can only speculate about the causes of this event: a mixture of strong winds, tidal motion and probably icebergs touching the fast-ice edge could be responsible. Unfortunately, a number of instruments was installed in this area shortly before the event, and these were lost during the break-up (Section 4.5).

New sea ice started to form in the breakup area, but was pushed out of the Bay regularly by coastal winds. It was not until the grounding of the large iceberg B15G in late September 2012, that a stable cover of newly formed sea ice was established (Fig. 4.11). General sea-ice conditions were stable until the end of January. We were able to perform the last series of drillings for this season at ATKA03 and ATKA07 on 30 January 2013.

Drillings

We repeated the measurements of 2011 at the same locations on 10 occasions between 14 June 2012 and 30 January 2013. On the advice of our colleagues from New Zealand, we used a thickness tape weighted with a metal bar to estimate the thickness of the sub-ice platelet layer (Fig. 4.12). We often experienced difficulties in penetrating the clogged boreholes or recovering the metal bar. Although being time-consuming and often frustrating, this is currently the only simple approach to determine sub-ice platelet-layer thickness. A more detailed description and interpretation of the data is given in Chapter 5. Alternative methods of platelet-layer thickness determination are the subject of Chapters 6 and 7.

Electromagnetic sea-ice thickness surveys were repeated on 7 occasions between 14 June 2012 and 30

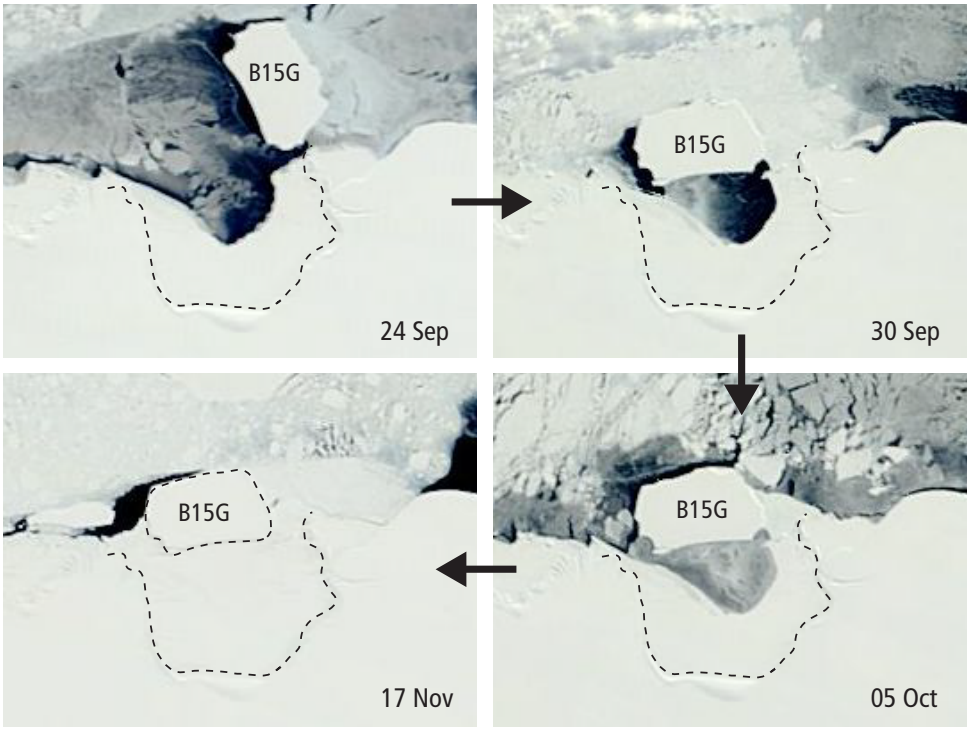

Figure 4.11: MODIS satellite images from September to November 2012, showing the grounding of iceberg B15G in front of Atka Bay.

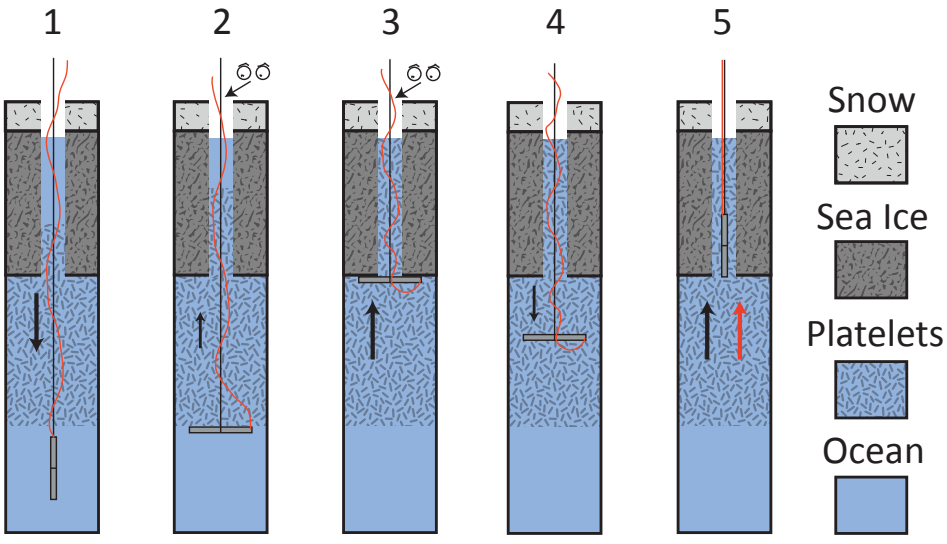

Figure 4.12: Measuring platelet-layer thickness with a modified thickness tape. 1) A thickness tape is weighted with a solid metal bar in order to penetrate the dense platelet layer. 2) The bar is pulled up gently until a slight resistance is felt. This is defined as the bottom of the sub-ice platelet layer. 3) The bar is pulled through the platelets until it reaches the sea-ice bottom. 4) The pressure is released and the bar sinks down. 5) The cord fastened at one end of the bar is pulled to recover the "instrument".

January 2013. Snow depths were manually measured in parallel. Sea-ice thickness maps and probability density functions are given in Hoppmann et al. (2013).

Autonomous measurements

In July and August 2012, an automatic weather station, a spectral radiation station (Nicolaus et al., 2010a) and a sea-ice mass balance buoy were installed at 70.586°S 7.913°W, about 8 km from the western ice-shelf edge along the usual transect. The instruments were lost during the fast-ice breakup on 17 August 2012. However, the thermistor-chain mass balance buoy continued to send GPS positions via Iridium satellite for an entire year (Fig. 4.13), before data transmission ceased on 26 August 2013.

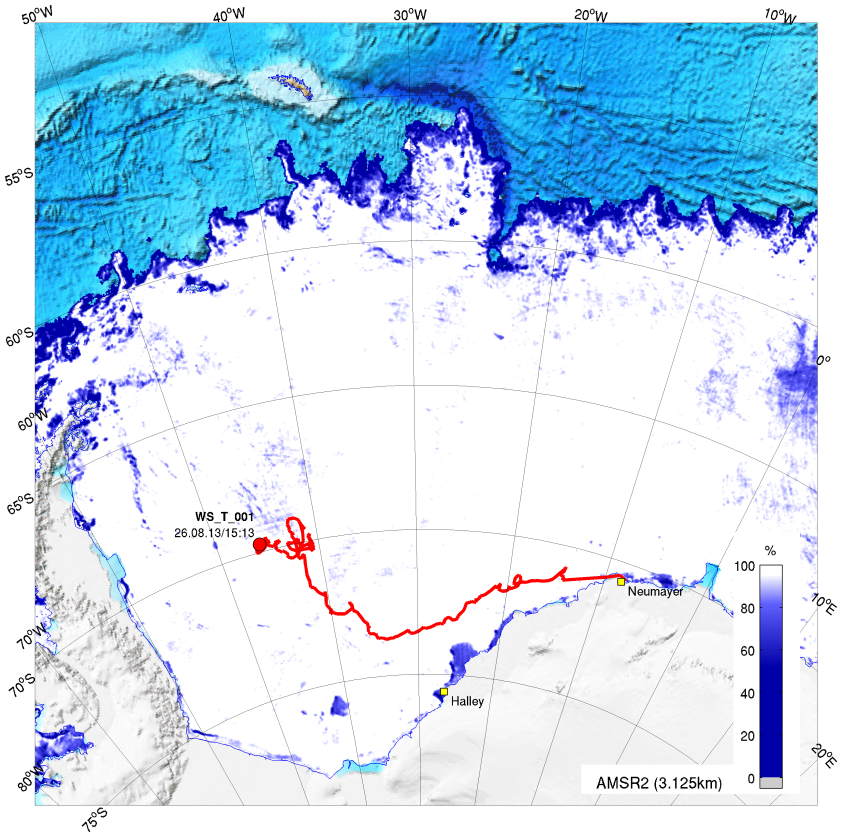

Figure 4.13: Drift track of autonomous instruments lost during fast-ice breakup. The drift started on 17 August 2012, and data transmission ceased a year later, on 26 August 2013. Figure prepared by Jölund Asseng for www.meereisportal.de, using sea-ice concentration data provided by University Bremen.

Following the loss of these instruments, backup setups of AWS and radiation station with similar configuration were deployed at ATKA03 in October 2012, and retrieved in January 2013. In addition, a sea-ice mass balance buoy was frozen into the sea ice at ATKA03 on 21 November 2012 (Fig. 4.14).

Temperature and heating profiles measured by the sea-ice mass balance buoy laid the foundation for Paper III. The AWS data was used in Paper II to create a consistent forcing for a thermodynamic sea-ice growth model. Time-series of spectral irradiance measured by the radiation station (incoming, reflected

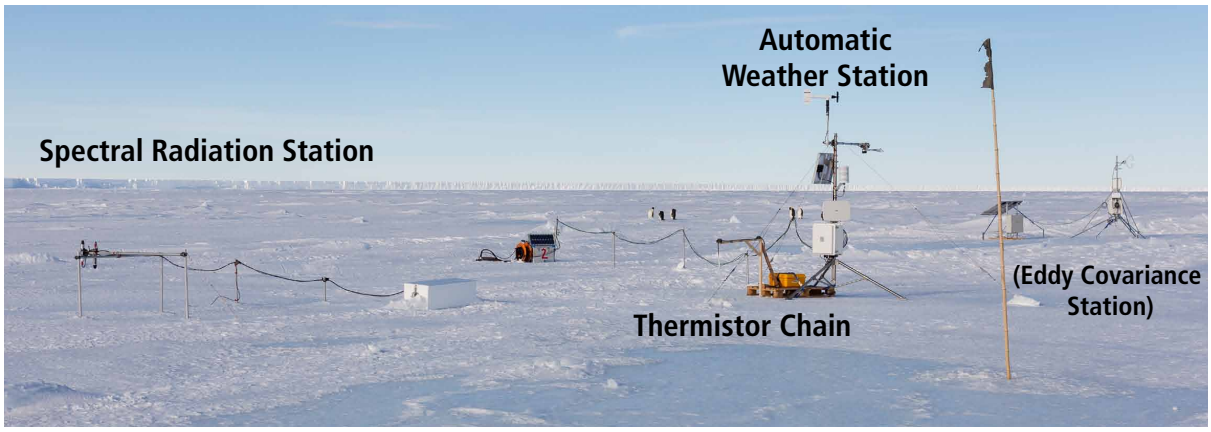

Figure 4.14: Typical instrument setup for autonomous measurements, photographed in November 2012. The eddy covariance measurements were part of two-month long field campaign (Section 4.6).

and transmitted irradiance as well as albedo and transmittance) are presented in Hoppmann et al. (2013). The time line of measurements is given in Figure 4.15.

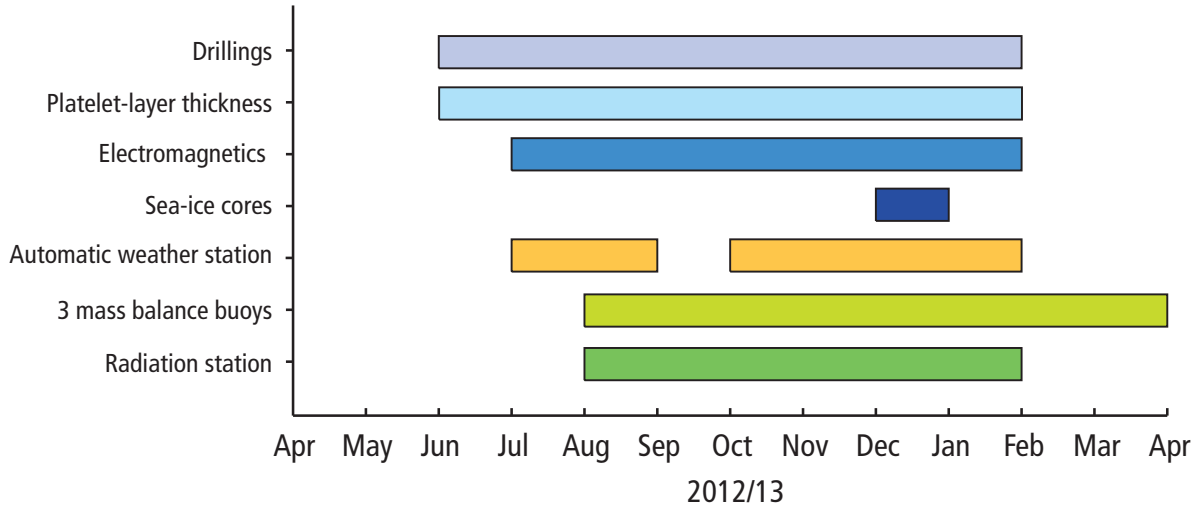

Figure 4.15: Time line of data obtained during sea-ice monitoring in 2012/13

4.6. Atka Bay field campaign, Nov 2012 - Jan 2013

During a field campaign between 17 November 2012 and 08 January 2013, we extended the regular drillings and EM surveys by a variety of other measurements (Hoppmann et al., 2013). These included CTD casts (used in Publications II, III and IV), snow transects and -physical properties (used in Publications VII and VIII), sea-ice coring (Section 4.6, used in Publications II and III), albedo transects, under-ice spectral irradiance measurements and aerial photography. We obtained more than 100 km of multi-frequency electromagnetic induction soundings (GEM-2, Geophex Ltd.) over the entire Atka Bay. These data were

crucial to Publications IV and VI. Finally, we deployed an eddy covariance station to obtain sensible and latent heat fluxes, as well as turbulent fluxes of H_2O and CO_2. Part of these data were used in Publication II.

Sea-ice cores and texture analysis

A set of full-length sea-ice cores were retrieved with a Kovacs Mark II coring system (9 cm diameter) at six stations on 19 December 2012. We recorded temperature, salinity, density and Chlorophyll-*a* profiles of each core with a 0.1 m spacing. Vertical thin sections of four cores were prepared along the entire core length using a Leica Microtome. Horizontal thin sections were produced at a regular spacing of about 0.1 m. All thin sections were photographed between crossed polarizers to highlight the crystal structure. Results of two sea-ice cores are published (Chapters 5 and 6), while two other cores are included here for completion (Figs. 4.16 and 4.17).

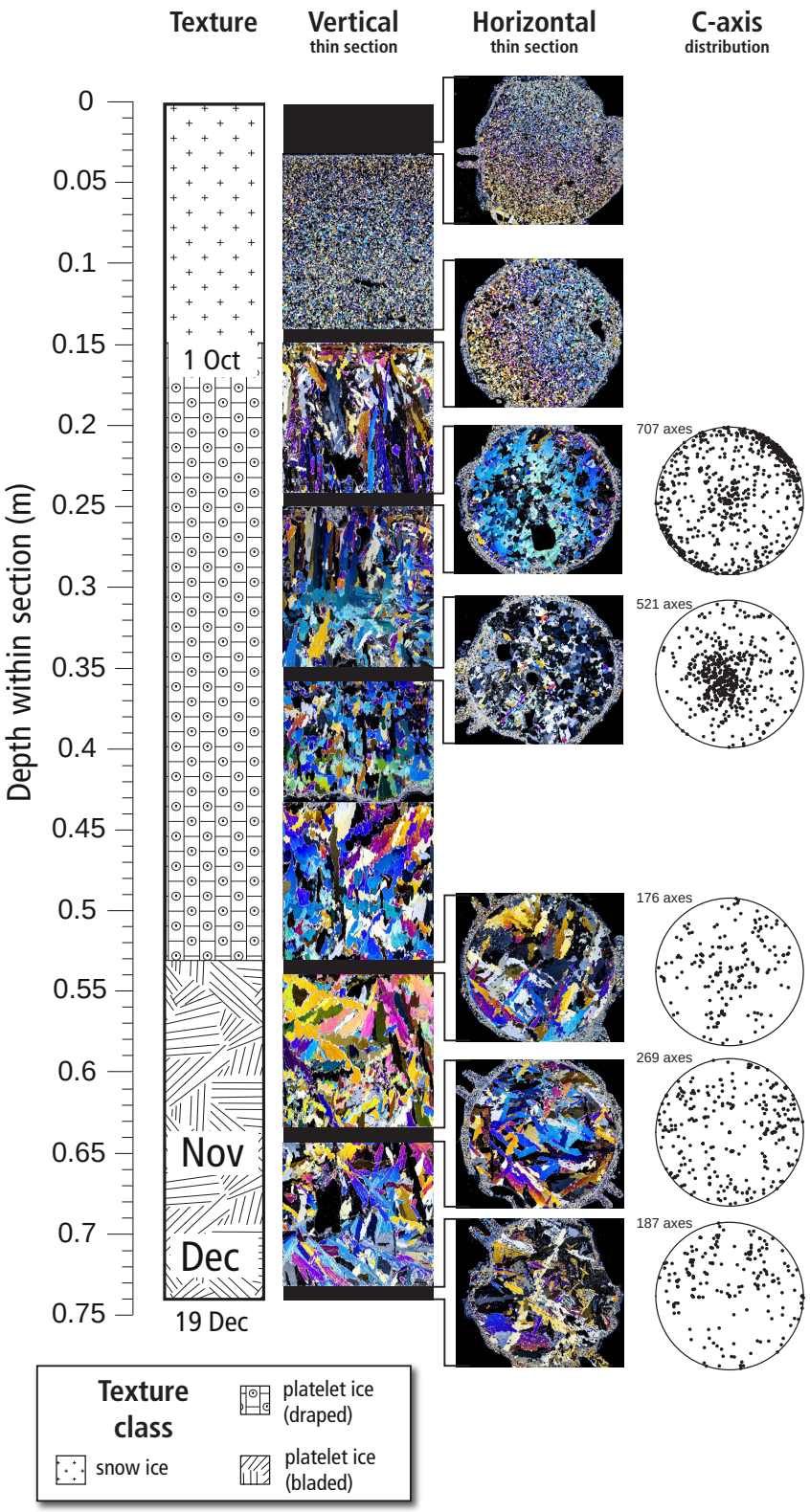

Figure 4.16: Crystal structure of sea-ice core retrieved at ATKA11 in 2012.

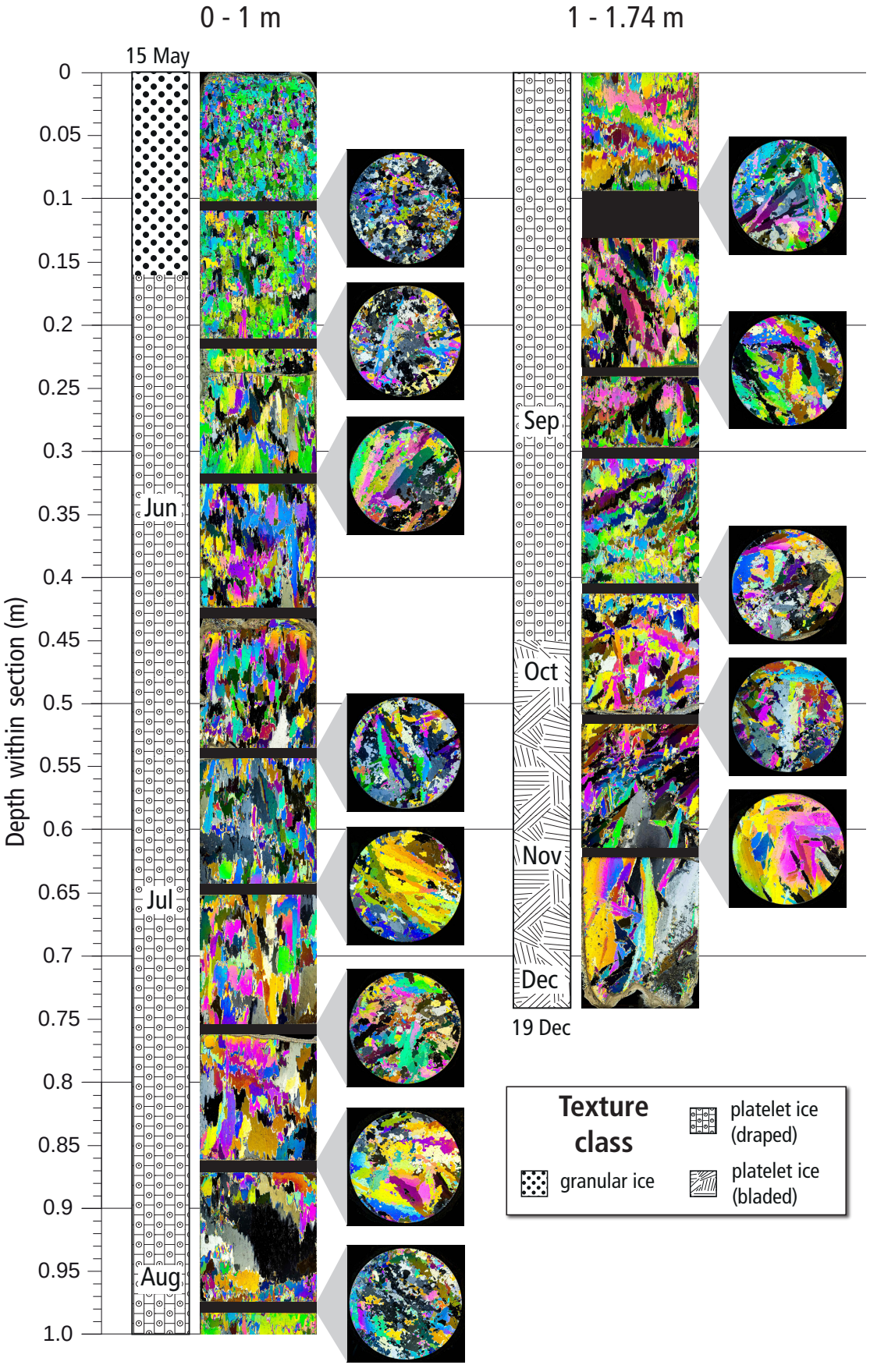

Figure 4.17: Crystal structure of sea-ice core retrieved at ATKA21 in 2012.

4.7. Sea-ice monitoring 2013/14: increased reliability

General conditions

In 2013, the fast-ice cover of Atka Bay consisted exclusively of thick multi-year sea ice, a situation rarely observed at Atka Bay. The large iceberg B15G, which grounded in front of Atka Bay in September 2012, prevented fast-ice destabilization and subsequent breakup at the beginning of 2013. These conditions were in strong contrast to recent years, when initial breakups occurred as early as December. These atypical conditions presented a unique opportunity to start our measurements earlier in the year.

Iceberg B15G detached between 10 and 12 August 2013. It left behind several smaller grounded segments in the northwest. Unfortunately, no satellite imagery is available of this event. On 23 August 2013, it had traveled almost 200 km to the west. The fast-ice conditions at Atka Bay were generally unaffected by this event. The fast ice started to break up at the beginning of February 2014. The sea ice disintegrated evenly from north, mostly into floes smaller than 200 m. Sea ice covering about 1/3 of the total Atka Bay area remained in the south (Chapter 6).

Drillings

Sea-ice measurements were repeated between 28 April 2013 and 17 January 2014. The locations of these measurements were the same as in 2011 and 2012 for consistency. Sub-ice platelet-layer thickness was again obtained by the metal-bar method. Sea-ice thickness was high at all sites, because of its age and the absence of bottom melt during summer 2012/13. The sea-ice age also had an impact on the snow cover, which was substantial also due to the minor occurrence of surface melt during summer 2012/13. For these reasons, only one drilling was conducted per visit and site. Sometimes, an accurate freeboard measurement was not possible due to the high snow load and platelets additionally obstructing the measurement. Quick refreezing of the drill-hole was also an issue.

Sea-ice thickness was >2 m at nearly all sites already in April 2013. Only ATKA11 had a lower thickness because of the intermediate breakup in August 2012. At the end of the growth season, sea-ice thickness ranged from 2.5 (ATKA21) to 4 m (ATKA03). Due to the low number of measurements at each site, a high local variability was not accounted for. Snow cover steadily increased between January and November 2013, when a slight overall decline set in. This was likely due to enhanced melt during summer 2013/14, leading to a very wet and partly ponded surface. Snow cover was again lowest at ATKA03, where the iceberg heavily influenced the snow drift and deposition. At ATKA24, the influence of the nearby ice-shelf edge again prevented stronger snow deposition. The other sites exhibited a very thick snow cover, with extrema of nearly 2 m in November, also partly leading to negative freeboard despite the thick sea ice. The evolution of the sub-ice platelet layer is described in detail in Chapter 5.

We performed 8 electromagnetic induction sounding thickness surveys between 28 April 2013 and 17 January 2014. Generally, an expected increase in total thickness was evident. Between April 2013 and January 2014, the total thickness gain was on the order of 2 m. According to sea-ice thickness data from drillings and a mass balance buoy (see below), the average sea-ice growth was on the order of 1 m in 2013. Snow precipitation and drift would then also amount for about 1 m. In November and December 2013,

thicknesses below 2 m rarely occurred.

Autonomous measurements

The automatic weather station was operated at ATKA03 between 30 May 2013 and 03 January 2014. A WLAN antenna was used to transfer the data directly to Neumayer III. The data was again used to generate a consistent forcing for a thermodynamic sea-ice growth model (Chapter 6).

A spectral radiation station was deployed at ATKA03 on 06 September 2013, consisting of three RAMSES spectral radiometers measuring incoming, reflected and transmitted irradiance through snow. On 11 September, the instruments failed (most likely due to electrostatic discharge problems) and were recovered a few days later. On 29 September 2013, a backup system of similar configuration was deployed at the same spot, and retrieved on 03 January 2014. The data are shown in Figure 4.18. The maximum incoming irradiance was recorded throughout December, as expected. At the end of December 2013, the transmitted irradiance (and also the transmittance) start to increase continuously until the end of the measurements on 03 January 2014. As the snow depth above this sensor only decreased slightly, metamorphism processes and an increase in grain size are the most likely explanations. This is also in accordance with the decrease of surface albedo, although this evolution seems to set in a few days earlier. From the broadband albedo and transmittance it is evident that the changes occur at the same time, but the increase in transmittance is divided into two distinct periods: first, a period of about 5 days where it increases very slowly, and afterwards a period in which it increases drastically. The “spikes” in the data cannot be explained currently, but it is unlikely that these were measurement errors. Although these data have not been used in this work, they are expected to make a valuable contribution to studies of snow melt-onset on Antarctic sea ice.

Due to the continuous operation of the thermistor chain deployed in November 2012, no additional instrument was deployed in 2013. Instead, the unit’s batteries were changed in January 2014 in preparation for a potentially long drift into the central Weddell Sea (such as in Fig. 4.13). Unfortunately, the buoy did not last until after the breakup in early February, ceasing operation on 09 February 2014.

Finally, two newly developed snow depth buoys, with four sonic ranging sensors each, were deployed near the Neumayer Station for a first-time long-term test in the Antarctic. It turned out that these prototypes suffered from electrostatic discharge problems, which were fixed by a redesign of the electronics. This test was important in increasing the reliability and lifetime of these buoys, which will be deployed on the fast ice in the coming years. The time line of measurements is given in Figure 4.19.

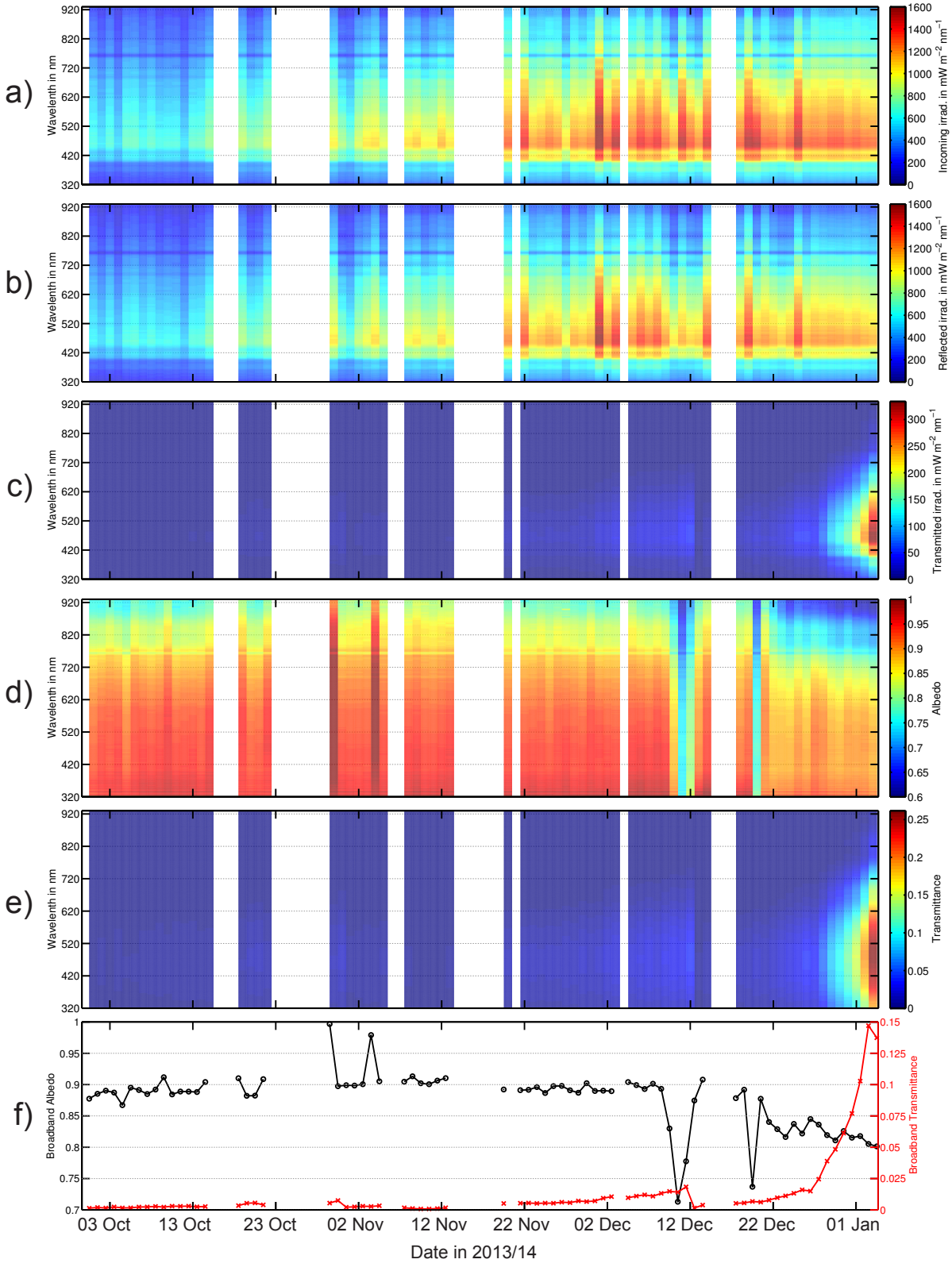

Figure 4.18: Spectral irradiance measurements in 2013/14. a) Incoming irradiance; b) reflected irradiance; c) transmitted irradiance through snow; d) spectral albedo; e) spectral transmittance though snow; f) broadband albedo (black) and -transmittance (red).

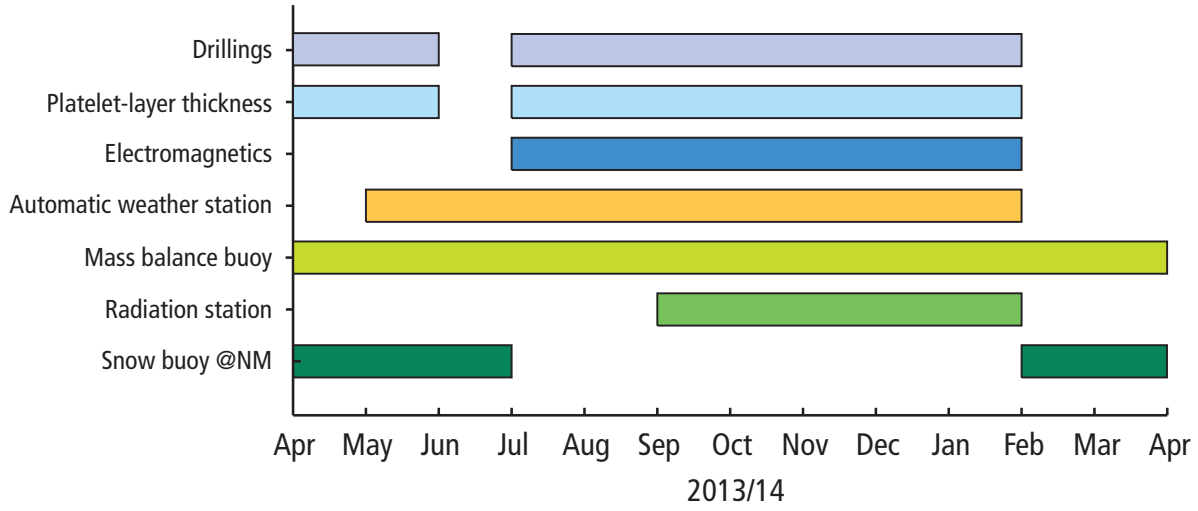

Figure 4.19: Time line of data obtained during sea-ice monitoring in 2013/14

4.8. Sea-ice monitoring 2014/15: bad weather!

The monitoring activities 2014/15 are still in progress, and have not yet been compiled. A combination of bad weather periods and frequent instrument failures prevented an early start into the measurement season. The time line of measurements in 2014/15 is given in Figure 4.20. A comprehensive summary of the monitoring activities is given in Chapter 9.

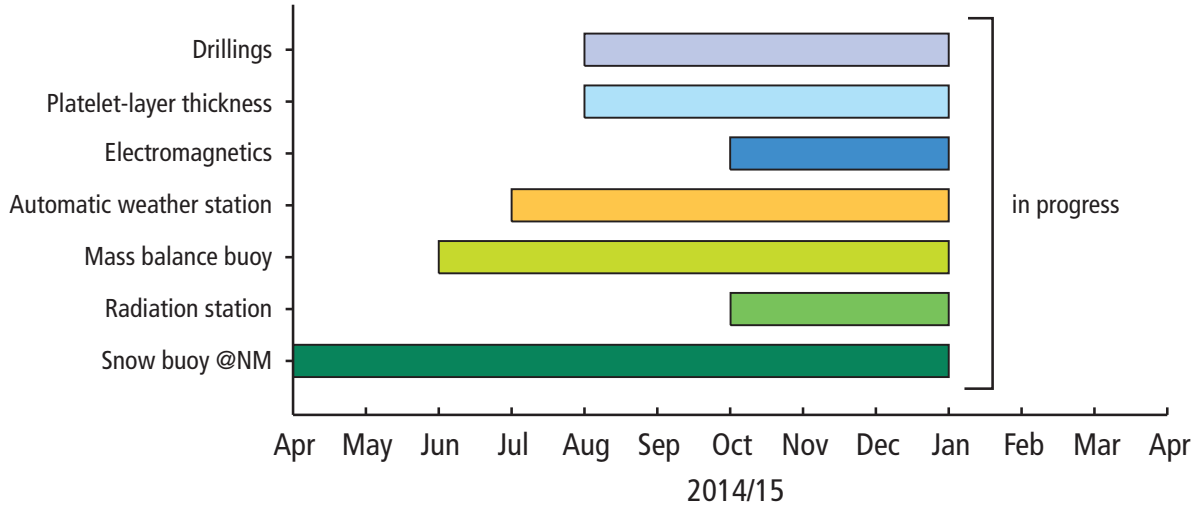

Figure 4.20: Time line of data obtained during sea-ice monitoring in 2014/15

The following Chapters merge the multitude of data introduced here into a comprehensive picture of fast-ice evolution and underlying processes at Atka Bay. Chapters 5 and 6 represent the main scientific outcomes of this thesis under the author's sole responsibility, while Chapters 7 and 8 benefited from

the cooperation with other PhD students and should be mainly regarded as their work. The author's contribution is always stated on the respective Chapter's first page.

Chapter 5

Publication II: Ice platelets below Weddell Sea landfast sea ice

By **Mario HOPPMANN**, Marcel NICOLAUS, Stephan PAUL,
Priska A. HUNKELER, Günther HEINEMANN, Sascha WILLMES,
Ralph TIMMERMANN, Olaf BOEBEL, Thomas SCHMIDT,
Meike KÜHNEL, Gert KÖNIG-LANGLO and Rüdiger GERDES.

This paper is reprinted from the Annals of Glaciology with permission of the International Glaciological Society (Hoppmann et al., 2015b). My contribution to this paper is that I coordinated and co-performed the field work, did all model experiments and lab work, analyzed and interpreted the data, created all figures and tables and did the main writing.

Annals of Glaciology 56(69) 2015 doi: 10.3189/2015AoG69A678 175

Ice platelets below Weddell Sea landfast sea ice

Mario HOPPMANN,[1] Marcel NICOLAUS,[1] Stephan PAUL,[2] Priska A. HUNKELER,[1] Günther HEINEMANN,[2] Sascha WILLMES,[2] Ralph TIMMERMANN,[1] Olaf BOEBEL,[1] Thomas SCHMIDT,[1] Meike KÜHNEL,[1] Gert KÖNIG-LANGLO,[1] Rüdiger GERDES[1]

[1]*Alfred-Wegener-Institut Helmholtz-Zentrum für Polar- und Meeresforschung, Bremerhaven, Germany*
E-mail: Mario.Hoppmann@awi.de
[2]*Environmental Meteorology, University of Trier, Trier, Germany*

ABSTRACT. Basal melt of ice shelves may lead to an accumulation of disc-shaped ice platelets underneath nearby sea ice, to form a sub-ice platelet layer. Here we present the seasonal cycle of sea ice attached to the Ekström Ice Shelf, Antarctica, and the underlying platelet layer in 2012. Ice platelets emerged from the cavity and interacted with the fast-ice cover of Atka Bay as early as June. Episodic accumulations throughout winter and spring led to an average platelet-layer thickness of 4 m by December 2012, with local maxima of up to 10 m. The additional buoyancy partly prevented surface flooding and snow-ice formation, despite a thick snow cover. Subsequent thinning of the platelet layer from December onwards was associated with an inflow of warm surface water. The combination of model studies with observed fast-ice thickness revealed an average ice-volume fraction in the platelet layer of 0.25 ± 0.1. We found that nearly half of the combined solid sea-ice and ice-platelet volume in this area is generated by heat transfer to the ocean rather than to the atmosphere. The total ice-platelet volume underlying Atka Bay fast ice was equivalent to more than one-fifth of the annual basal melt volume under the Ekström Ice Shelf.

KEYWORDS: basal melt, ice/ocean interactions, sea ice, sea-ice growth and decay, sea-ice/ice-shelf interactions

INTRODUCTION

The expanse of Antarctic sea ice is currently one of the major puzzles in sea-ice research (Maksym and others, 2012). Recent observations of increasing Antarctic sea-ice extent (e.g. Parkinson and Cavalieri, 2012) are contradictory to an expected decline in a warming environment, as observed in the Arctic (Comiso and Hall, 2014). The failure of global climate models to reproduce this behavior is an indication that key processes are missing in the implementation of the models (Turner and others, 2013). One important piece of the puzzle might be the interactions and feedback processes between the sea-ice cover and the Antarctic ice shelves, which link the grounded ice sheet to the Southern Ocean (Bintanja and others, 2013). One aspect of these interactions is the accumulation of ice platelets, inclusion-free single crystals up to 0.2 m in diameter and <0.003 m in thickness, beneath a nearby sea-ice cover (Eicken and Lange, 1989). These form a dense layer of intertwined individual crystals, herein referred to as a sub-ice platelet layer, following the terminology of Gow and others (1998). The suspended crystals may attach to the sea-ice bottom and become incorporated into the sea-ice fabric through consequent freezing of interstitial water. This sea-ice type is then referred to as (consolidated) platelet ice, which has a distinct crystal structure and a *c*-axis distribution different from other sea ice (e.g. Jeffries and others, 1993; Tison and others, 1998). The ice platelets form and grow in supercooled water, which results from basal melting in the cavities below the floating ice shelves. Lewis and Perkin (1986) termed this process an 'ice pump'. This also means that ice-platelet formation and accumulation below a sea-ice cover may be an indirect indicator of basal melt.

However, continuous studies of ice platelets and associated processes are impossible in the mobile pack ice around the Antarctic continent, because they have only been observed up to 35 km from the coast (Eicken and Lange, 1989). In contrast to that, areas of immobile landfast sea ice (fast ice) are comparatively easy to access from nearby coastal stations, making them an ideal platform to study Antarctic sea-ice properties and associated processes (Heil and others, 2011). At the same time, fast ice may act as an early indicator of climate change affecting the polar system, through its link with atmospheric forcing (Heil, 2006).

Ice-platelet accumulations have been observed in several locations around Antarctica (e.g. Serikov, 1963; Moretskiy, 1965; Veazey and others, 1994). By far the most studies have been performed in the Ross Sea, benefiting from the presence of the US and New Zealand stations at McMurdo. Recent investigations of ice platelets near the McMurdo Ice Shelf, for example, focused on frazil deposition (Dempsey and others, 2010; Dempsey and Langhorne, 2012) and the links between supercooling of the ocean and platelet-ice formation (e.g. Mahoney and others, 2011; Gough and others, 2012).

In the eastern Weddell Sea, a number of smaller ice shelves fringe the coastline of Dronning Maud Land. This region is characterized by a narrow and steep continental shelf margin. Although deep or bottom water formation does not occur there (Fahrbach and others, 1994), this region is of critical importance to water-mass preconditioning and formation in the Weddell Sea (Thoma and others, 2006). At the same time, the geographic setting promotes the penetration of modified Warm Deep Water into the ice-shelf cavities (Nøst and others, 2011), which results in high basal melt rates and modifications of the coastal current (Hellmer,

2004). This also means that this region is particularly susceptible to changing climate conditions (Holland and others, 2008). According to previous studies by Lange and others (1989), a substantial fraction of the near-coastal sea-ice cover of Dronning Maud Land originates from incorporation of underlying ice platelets. However, most aspects of the mechanisms of platelet accumulation and their link to oceanographic conditions remain unclear, especially in this region. Wherever a sub-ice platelet layer is present, the solid sea ice grows thicker than can be accounted for by a conductive flux alone. This is due to the incorporation of ice mass formed by heat loss to the ocean, rather than to the atmosphere. It is therefore necessary to determine how much of the solid fast ice in this region results from ocean/ice-shelf interactions. To answer this question, an accurate estimate of the ice-volume fraction of the platelet layer is needed. As the platelet layer modifies the electrical conductivity below the solid sea ice (Hunkeler and others, 2015) and contributes to its freeboard, this parameter is also crucial to accurately determine near-coastal Antarctic sea-ice thickness based on electromagnetic induction sounding (Rack and others, 2013) or altimetry methods (Price and others, 2013). Finally, it is desirable to link the properties of the platelet layer to basal melt processes of nearby ice shelves, as these are particularly susceptible to future environmental changes (Hellmer and others, 2012).

In this paper, we aim to improve our understanding of how ice shelves influence nearby sea ice in Antarctic coastal waters. We present the seasonal cycle of sea ice attached to the Ekström Ice Shelf in the eastern Weddell Sea, a region that is currently under-represented in investigations of ice-shelf/sea-ice interactions. We continue the work of Kipfstuhl (1991) and Günther and Dieckmann (1999), who studied ice platelets underlying the solid fast ice of Atka Bay in the 1980s–90s. Through a combination of field observations and model studies, we derive the ice-volume fraction of the platelet layer at six sites on Atka Bay fast ice. Together with observations of platelet-layer thickness evolution, we estimate how much sea ice at Atka Bay is formed by heat transfer to the ocean rather than to the atmosphere. We relate this result to Ekström Ice Shelf basal melt and discuss several implications of the platelet layer for fast-ice properties in this region.

STUDY SITE AND METHODS

Study site

Atka Bay is a 440 km^2 large embayment in front of the Ekström Ice Shelf, which is part of a group of small ice shelves located on the coast of Dronning Maud Land, eastern Weddell Sea (Fig. 1). This relatively small ice shelf covers an area of 6800 km^2 (Bindschadler and others, 2011) and has been studied since the 1980s, when the first German year-round station was established there. Investigations of ice thickness, bedrock topography and basal melting in this region have been undertaken by, for example, Kipfstuhl (1991), Sandhäger and Blindow (2000) and Neckel and others (2012). Information about cavity geometry is available from Kobarg (1988).

Atka Bay is seasonally covered with fast ice attached to ice-shelf edges bordering to the west, south and east. Knowledge of the sea-ice conditions in this region is crucial to providing logistical support of the German and South African Antarctic stations. Information about general sea-ice conditions is obtained from satellite images, recorded by, for example, synthetic aperture radar on board Envisat, RADARSAT and TerraSAR-X, the Moderate Resolution Imaging Spectroradiometer on board Aqua and Terra, the Enhanced Thematic Mapper on board Landsat or the Advanced Very High Resolution Radiometer on board the Polar Orbiting Environmental Satellites. Satellite imagery is especially needed to fill the gap between late summer and early winter, when direct sea-ice observations are not available and dates of initial formation and break-up need to be determined.

Visual inspection of satellite imagery in previous years reveals that the seasonal fast-ice cover of Atka Bay usually starts to form during March–April. The extent mainly depends on the strength of winds and ocean currents offshore of Atka Bay, and also on the interaction with often passing icebergs. The fast ice does not melt in situ during summer, but breaks out once it is sufficiently destabilized. Although no studies exist to date which have investigated the responsible physical factors more closely, contributions from increased water and air temperatures, as well as from solar radiation, tidal motion, wind forcing and a combination thereof, are most likely. The interaction with stationary and passing icebergs also plays a role. The break-up usually happens after the retreat of the pack ice in front of the fast ice, and normally begins in the eastern part of the bay (generally in December or January). In the southwestern part, sea ice may persist until March, but in most years Atka Bay is completely ice-free at the end of March. Persistent strong easterly winds during initial formation lead to an increased dynamic growth towards the western ice-shelf edge. Once a solid sea-ice cover is established over the major part of Atka Bay (usually in April/May), further growth proceeds thermodynamically.

Meteorological data are readily available from the nearby Neumayer III station, where atmospheric conditions have been recorded since 1981 (König-Langlo and Loose, 2007). An overview for the period 1991–95 is given by König-Langlo and others (1998) and for the period 1982–2011 by Rimbu and others (2014). Generally, the region is characterized by low temperatures, extreme temperature fluctuations during winter and persistent easterly winds. The winds lead to frequent drifting and blowing snow.

Field measurements

We set up six study sites along a 25 km long west–east profile to monitor fast-ice thickness, snow depth, freeboard and platelet-layer thickness (Hoppmann and others, 2013a). These sites are referred to in this paper as ATKAxx, where xx represents their distance in kilometers to the western ice-shelf edge (Fig. 1; Table 2). Our measurements started in June 2012, as soon as enough snow had accumulated at the ice-shelf edge to access the sea ice several meters below with snowmobiles. We measured sea-ice thickness and freeboard through 0.05 m auger holes using regular (before August) and modified thickness tapes, while snow depth was measured using ruler sticks. Freeboard, the distance from the water surface to the sea-ice surface, is negative when the sea-ice surface is depressed below the water surface. Each time a study site was visited, up to five measurements were performed in an undisturbed area, one in the center and one at a distance of 5 m in each direction.

During the course of austral winter, the platelet accumulations started to complicate the measurements. In order to penetrate the platelet layer, it became necessary to weigh

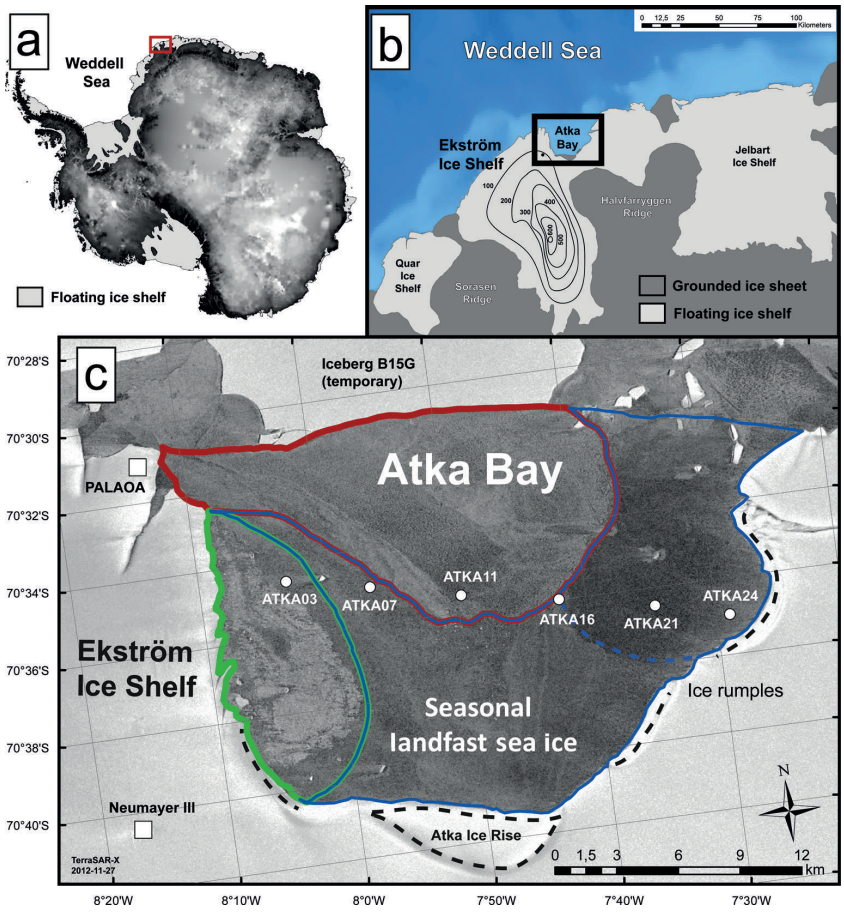

Fig. 1. Location of the study site. (a) The Ekström Ice Shelf is located in the eastern Weddell Sea (highlighted as red box). (b) Enlargement of (a). The contours show the depth of the water column below the ice shelf following Kobarg (1988). Bathymetry and coastline data were taken from Bedmap2 (Fretwell and others, 2013) and from SCAR (Scientific Committee on Antarctic Research) Antarctic Digital Database 6.0. (c) Enlargement of (b). Sampling sites are indicated by white circles. The TerraSAR-X image provided by the German Aerospace Center (DLR) reveals the different sea-ice regimes in 2012: second-year/first-year sea ice (green), first-year sea ice (blue) and new sea ice grown in October (red). The dotted black curves indicate the locations of ice rises and rumples.

down the tape using a metal bar (as described by Crocker, 1988; Gough and others, 2012). We located the bottom of this layer by gently pulling the tape upwards, trying to feel the first resistance to the metal bar. But during most of our measurements, the bottom of the platelet layer was not well defined: the interface was often mushy rather than consolidated. We also used an under-ice camera (CAM1) fitting through a regular borehole to obtain visual impressions of the platelet layer in real time. In doing so, it became apparent that using the 'metal-bar' method we frequently underestimated the 'true' platelet-layer thickness by up to 0.3 m. However, we then defined the thickness as the point where a first resistance was felt against a slight pressure, rather than the scratching of single crystals on the metal. The number of measurements at each study site varied, depending on the difficulties the platelet layer imposed on our sampling. The presence of consolidated parts within the otherwise mushy platelet layer sometimes prevented the metal bar from penetrating through the entire thickness. In addition, the bar got stuck several times and we were not able to retrieve it.

Several in situ observations of platelets suspended in the water column were made by colleagues, who installed an under-ice camera (CAM2) in a crack near the western ice-shelf edge (70°37.3′ S, 8°05.5′ W) between 22 and 30 November 2012, to observe the behavior of Weddell seals (personal communication from I. van Opzeeland, 2012).

In order to link our platelet-layer observations to the prevailing oceanographic conditions, we used conductivity–temperature–depth (CTD) data recorded by the Perennial Acoustic Observatory in the Antarctic Ocean (PALAOA; Boebel and others, 2006). PALAOA was constructed on the Ekström Ice Shelf in 2005/06, 1.53 km from the ice-shelf edge (70°31′ S, 8°13′ W). The instrument itself was lowered through a hot-water drillhole, and was installed in the water column at ∼155 m depth, 70 m below the ice-shelf bottom and 90 m above the seafloor. Relevant oceanographic parameters were calculated using the Gibbs Seawater (GSW) Oceanographic Toolbox (McDougall and Barker, 2011).

We operated two automatic weather stations (AWS) on the fast ice in 2012, recording air temperature and relative humidity (shielded HMP155A, Vaisala; height ∼2 m),

Table 1. Corrections applied to meteorological data measured at Neumayer III

Parameter	Correction
Air temperature (2 m)	+1.05°C
Relative humidity (2 m)	−3.6%
Barometric pressure (2 m)	+5.6 hPa
Upward longwave radiation	+8 W m^{-2}

barometric pressure (61302V, RM Young Company; height ~1 m), wind speed and direction (Marine Wind Monitor 05106-5, RM Young Company; height ~3 m), as well as downward and upward long- and shortwave radiation (CNR4, Kipp & Zonen; height ~2.4 m) at 1 min intervals (Hoppmann and others, 2013b,c). AWS1 was deployed at a site (70°35.135′ S, 7°54.802′ W) between ATKA07 and ATKA11 from 6 July to 17 August. AWS2 was deployed at ATKA03 from 2 October to 27 December 2012. We also deployed an eddy covariance (EC) station at ATKA03 between 21 November and 30 December 2012. The EC station was equipped with a three-dimensional sonic anemometer (CSAT3, Campbell Scientific Inc.; height 2.55 m) and a CO_2/H_2O analyzer (LI-7500, LI-COR Environmental; height 2.35 m). Turbulent fluxes of sensible and latent heat were calculated using a modified version of ECPACK (Van Dijk and others, 2004; Mauder and others, 2013).

Finally, we retrieved a set of full-length sea-ice cores (one at each study site) on 19 December 2012 to investigate the impact of ice platelets on the fast-ice crystal structure. All cores were drilled using a 0.09 m diameter titanium corer. The cores were transported to Bremerhaven, and a detailed texture analysis is currently in progress. In this study, we show one exemplary sea-ice core retrieved at ATKA24. We used a microtome to prepare horizontal and vertical thin sections ($\leq 5 \times 10^{-4}$ m) along the entire core length. All thin sections were photographed between crossed polarizing filters. Crystal *c*-axis orientation measurements were made on selected thin sections using a G50 Automated Fabric Analyzer (Wilson and others, 2003) and the Investigator software (Russell-Head Instruments). The data were plotted onto Schmidt equal-area nets, following Langway (1958), utilizing a uniform grid of 500 points covering the sample area.

Model simulations

We applied a one-dimensional thermodynamic model (Bitz and Lipscomb, 1999) to simulate sea-ice growth at Atka Bay with local atmospheric forcing. We used data recorded at the meteorological observatory of Neumayer III to generate a continuous time series of atmospheric conditions throughout the growth season (König-Langlo, 2013a,b). To account for the differences on the ice shelf and directly on the sea ice, we applied corrections to air temperature, barometric pressure, relative humidity and upward longwave radiation (Table 1). These corrections were based on comparison with the data recorded by the two weather stations (Hoppmann and others, 2013b,c). The corrected data are presented in Figure 2a–d.

We used these data to calculate sensible and latent heat fluxes by a bulk method (Andreas and others, 2010), and compared the results with the EC-based flux data. The two datasets are in good agreement (Fig. 2e and f). We used short- and longwave radiation, as well as sensible and latent heat fluxes, for model forcing. In addition, several other parameters were initialized in the model. We used a sea-ice density, ρ_{si}, of 925 kg m^{-3} (near the top of the range reviewed by Timco and Frederking, 1996), a snow density, ρ_s, of 330 kg m^{-3} (slightly higher than reviewed by Massom and others, 2001, for the Weddell Sea) and introduced a C-shaped salinity profile, typical of the southeastern Weddell Sea in winter (Eicken, 1992). Since the snow cover is a crucial factor in sea-ice growth, we included a step function based on the observed snow-depth evolution. Finally, we adjusted the bulk albedo to 0.9, which is in the upper range of our preliminary results of albedo measurements in November (0.8–0.9). This was necessary to avoid extensive surface melt in the model, which was not observed during summer. At sites where dynamic growth was not observed and the dates of initial sea-ice formation were accurately known from satellite imagery, the model was initialized with a minimal sea-ice thickness and the known date of initial formation. Otherwise we initialized the model with results from measurements of our first visit. Assuming that the platelet layer buffers the solid sea ice to potential positive oceanic heat fluxes throughout the growth season (May–December), we set the oceanic heat flux to 0 W m^{-2}. However, in our model runs an oceanic heat flux of +3 W m^{-2} starting in mid-December 2012 was necessary to prohibit further growth. Since the freezing interface grows into a water body with only a fraction of interstitial water available for freezing, we modified the sea-ice growth rate, GR, in the model by

$$\mathrm{GR}(\beta) = \frac{1}{1-\beta}\,\mathrm{GR}, \qquad (1)$$

where β is the ice-volume fraction in the platelet layer.

This is reasonable, since only the latent heat to freeze a water fraction of $1-\beta$ of a given volume is transported towards the colder atmosphere during sea-ice growth. If $\beta = 0$, ice crystals in the water near the freezing interface are absent, and growth progresses as usual. According to our field observations (see below), the platelet layer was not established before June in 2012, and we set $\beta = 0$ in the model accordingly. From the beginning of June 2012, ice platelets were present below the fast ice and the modified growth rate was used in the model. For the purposes of our simulations, the platelet layer is assumed to be infinite in extent and thickness with regard to the freezing interface.

RESULTS

Observed fast-ice thickness and snow cover

During our study in 2012, the recorded air temperatures ranged from –46.1°C (25 July) to +2.2°C (17 December). The average air temperature was –16.2°C, while the lowest and highest monthly averages of –29.5 and –3.4°C were measured in July and December, respectively. The average 2 m wind speed measured was 7.5 m s^{-1}, peaking at 34 m s^{-1} on 6 August. Easterlies dominated, with ~30% of the winds arriving in the range 80–100° from the north. Sea-ice thickness, snow depth and freeboard obtained at the various sites occupied during 2012/13 exhibited considerable spatial variability (Fig. 3, Table 2).

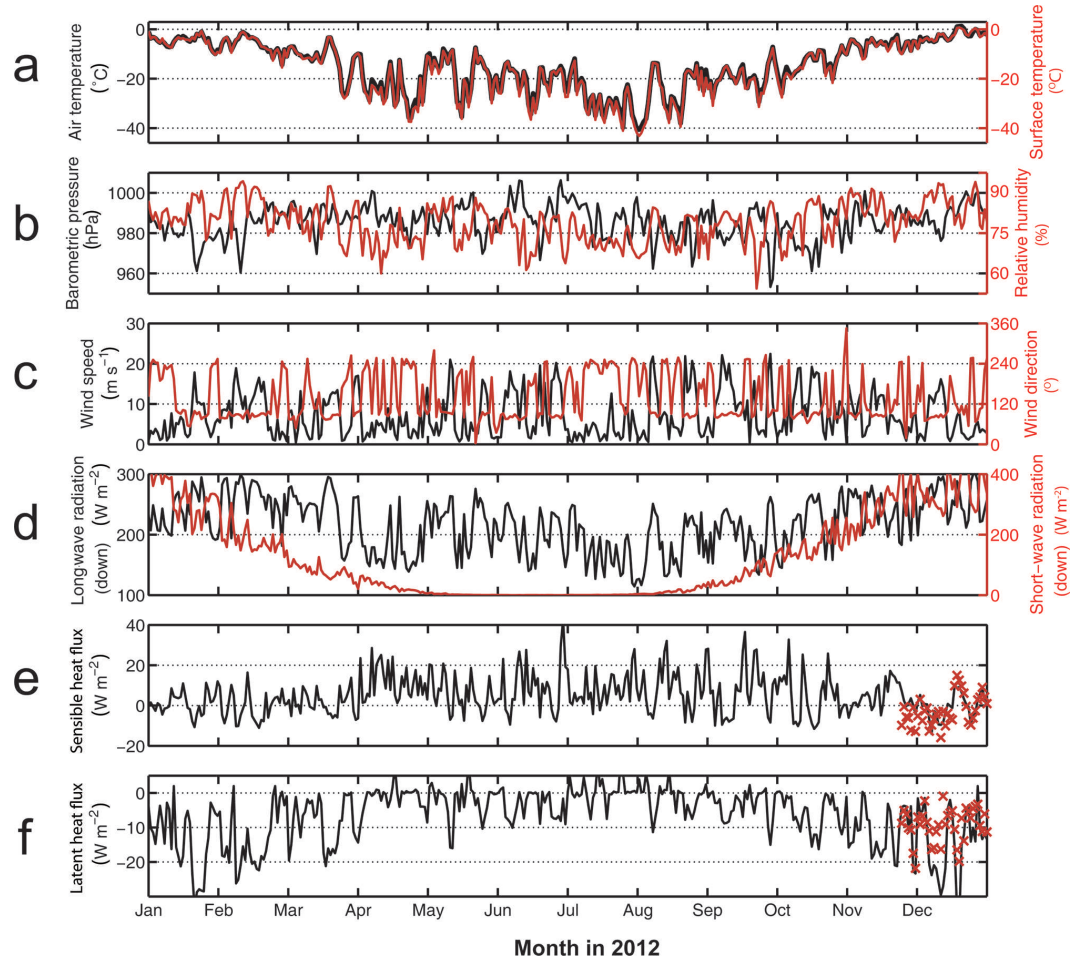

Fig. 2. Daily averages of modified atmospheric parameters recorded at the Neumayer III meteorological observatory in 2012. (a) Air (black) and surface (red) temperatures. (b) Barometric pressure (black) and relative humidity (red). (c) Wind speed (black) and wind direction (red). (d) Downward longwave (black) and shortwave (red) radiation. (e) Sensible heat flux calculated by the bulk method (black) and the eddy covariance method (red). (f) Latent heat flux determined by the bulk method (black) and the EC method (red). Fluxes are considered negative (positive) if directed towards the atmosphere (sea ice).

Sea-ice thickness and its spatial variability were generally higher at the westernmost sites, where persistent easterly winds (Fig. 2c) pushed the sea ice towards the ice-shelf edge. While sea-ice thicknesses greater than 2 m were measured at ATKA03 and ATKA07 as early as August/September 2012 (and later also at ATKA16), sea ice at the eastern sites was thinner. Sites with lower sea-ice thicknesses generally exhibited lower horizontal variability

Table 2. Study sites in 2012. Abbreviations: D: deformed ice; L: level ice; d_w: water depth determined by CTD casts in November and December 2012; T_{form}: formation of continuous sea-ice cover; max(z_{si}): maximum sea-ice thickness (December); $\overline{z_s}$: mean snow depth; $\overline{z_f}$: mean freeboard; β: ice-volume fraction in the platelet layer

Study site*	Latitude (S)	Longitude (W)	Ice type	d_w	T_{form}	max(z_{si})	$\overline{z_s}$	$\overline{z_f}$	β
				m		m	m	m	
ATKA03	70°34.513′	8°02.961′	D	140	March	2.56	0.02	0.29	0.18
ATKA07	70°34.995′	7°56.732′	D	175	March	2.62	0.41	0.26	0.35
ATKA11	70°35.530′	7°49.485′	D/L	>250	March/October	0.73	0.17	–0.02	0.31
ATKA16	70°35.988′	7°42.095′	D	175	April	2.01	0.70	–0.06	0.3
ATKA21	70°36.471′	7°34.610′	L	135	May	1.71	0.27	0.1	0.28
ATKA24	70°36.955′	7°28.965′	L	135	May	1.83	0.08	0.14	0.22

*The number indicates the distance to the western ice-shelf edge.

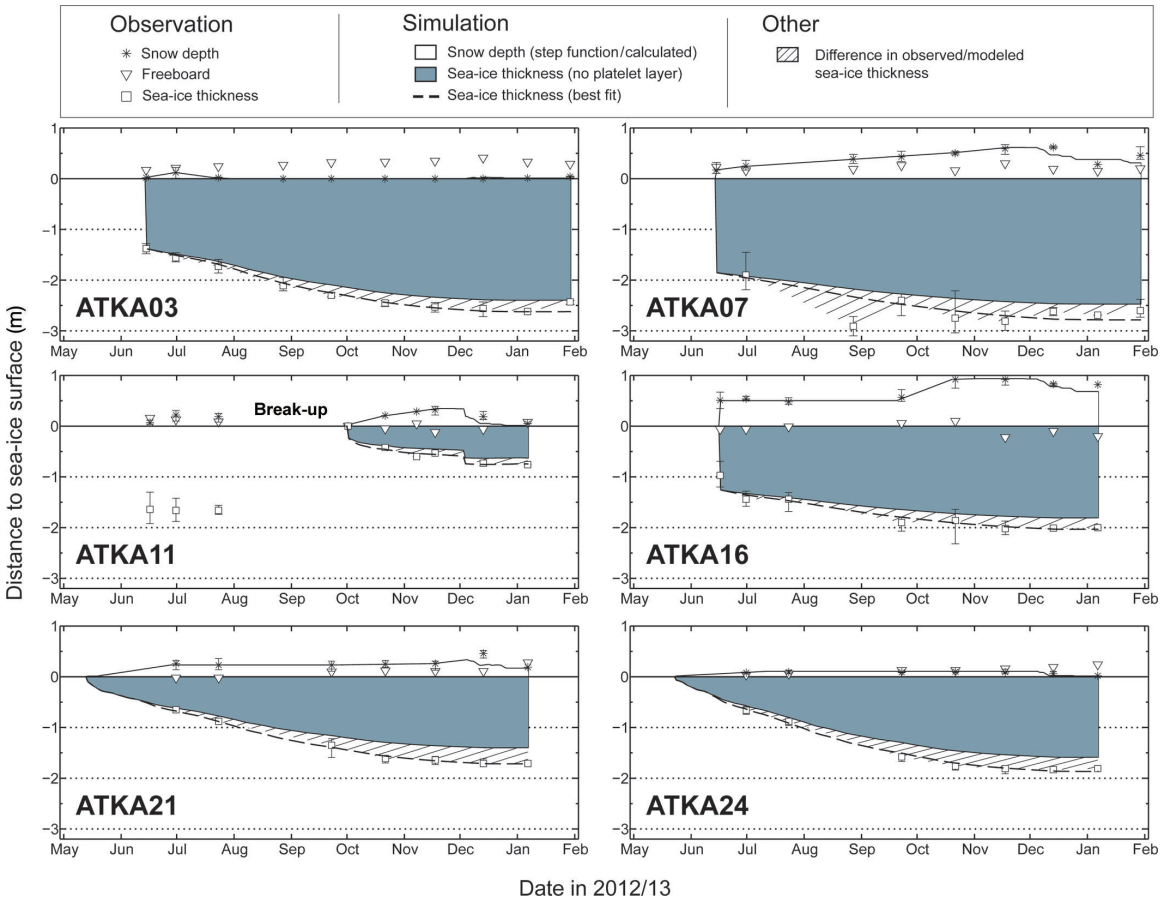

Fig. 3. Fast-ice and snow conditions at the six sampling sites on Atka Bay fast ice in 2012/13. Observed parameters and their variability ranges are indicated, along with results from simulated sea-ice growth.

(ATKA11 (late), ATKA21, ATKA24). Due to a partial break-up of fast ice in the central Atka Bay during a storm in late August 2012, sea ice at ATKA11 only grew to a maximum thickness of 0.73 m after its new formation. Although there had been early sea-ice break-up events in previous years, this is not generally representative.

The snow depth generally increased towards the center of Atka Bay, with highest snow depths (>0.5 m) at ATKA07 and ATKA16 in October 2012. Due to the fast-ice break-up, snow at ATKA11 was first exported with the sea ice and then blown into the ocean. As soon as a continuous sea-ice cover established again at ATKA11, in October 2012, snow accumulation followed the same pattern as at other sites. Low snow accumulations (<0.1 m) were observed at ATKA03, due to the influence of a nearby iceberg, and at ATKA24, due to the proximity of the ice-shelf edge. Intermediate accumulations were recorded at ATKA11 and ATKA21 (0.1–0.5 m). Wherever a snow cover was present, it was highly variable. Snow sastrugi up to 2 m long and 0.5 m wide were frequently observed, adding to local variability. The overall seasonal cycle of snow depth was generally characterized by an increase from initial sea-ice formation to November 2012, but no significant surface melt was observed until the end of our study in January 2013.

While freeboard was positive at most sites throughout the study, the snow load at ATKA11, and to a smaller extent at ATKA16, caused surface flooding in November. The subsequent snow-ice formation at ATKA11 led to a near-instant increase in sea-ice thickness of ~0.15 m. As the model does not account for snow-ice formation, this additional sea-ice growth was manually added in the simulation.

Simulated fast-ice growth

Due to substantial differences in initial formation dates, dynamic growth and snow cover among the study sites, we simulated local sea-ice growth for each site separately. Despite the high albedo of 0.9, the model results indicate that snow ablation would have taken place in summer when forced by the observed downwelling radiation. The control simulations without any ice platelets in the water column below the fast ice ($\beta = 0$) are depicted as gray areas in Figure 3, with the differences between them and the observed thickness hatched. In order to match the measured temporal evolution of the sea-ice thickness, the simulations were repeated, varying β between 0 and 0.5 in steps of 0.01. After each run, the difference from the measured sea-ice thickness was determined (Fig. 4). By minimizing this discrepancy, we were able to identify a best-fit β for each

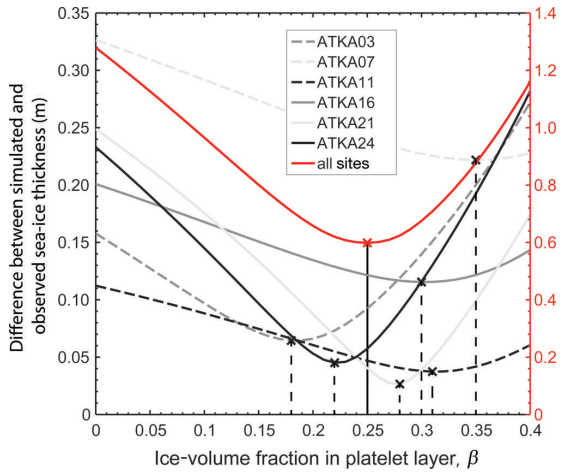

Fig. 4. The difference between simulated and observed sea-ice thicknesses with variable ice-volume fractions in the platelet layer.

site. The computed best-fit values of β ranged from 0.18 (ATKA03) to 0.35 (ATKA07), while intermediate values were 0.22 (ATKA24), 0.28 (ATKA21), 0.30 (ATKA16) and 0.31 (ATKA11). The simulated sea-ice thickness at each site with its best-fit β is also shown in Figure 3 (dashed curve). In order to calculate an average ice-volume fraction, we determined the combined difference between simulations and observations at all sites and samplings. By addition of all curves and subsequent determination of an overall minimum, we obtained an average β of 0.25 (Fig. 4, red curve). In contrast to a calculation of the arithmetic mean, in this approach the sampling sites with less-consistent measurements, resulting in a flatter curve (e.g. ATKA07), were weighted lower.

Sub-ice platelet-layer thickness

Figure 5 shows the evolution of the platelet-layer average thickness, z_p, at the six sites, along with a location map of the area and selected oceanographic data, as recorded by the CTD below the northern part of the ice shelf. The ice shelf is grounded in the south and east of Atka Bay (Fig. 5), resulting in ice rises (dark gray) and ice rumples (dashed curves), where no water exchange with the cavity is possible. The direction and magnitude of the Antarctic Coastal Current (ACoC) are mostly governed by wind patterns and tides, leading to small-scale fluctuations (even reversals) and high seasonal variability (Fahrbach and others, 1992).

The seasonal cycle of z_p (Fig. 5b) showed a nearly linear increase at all sites between June and December 2012. Due to equipment failure and the break-up in August 2012, the time series at ATKA16 only started in October 2012. z_p reached its maximum in December 2012 at five sites. The maximum at ATKA16 occurred in January 2013. This was most likely due to an underestimation of z_p in December 2012, which is an average of only two measurements. z_p was generally highest at the two westernmost sites ($z_p > 4$ m in December 2012), compared with the other sites ($z_p < 4$ m). The spatial distribution of z_p revealed a general increase towards the center of Atka Bay, with local maxima at ATKA07 and ATKA16. Of our sites, ATKA07 obtained the maximum observed platelet-layer thickness (5.65 m, December 2012), while ATKA11 recorded the lowest maximum platelet-layer thickness (1.32 m, December 2012). We attribute this to an export of platelets into the open ocean during the August 2012 break-up. The amount is unknown

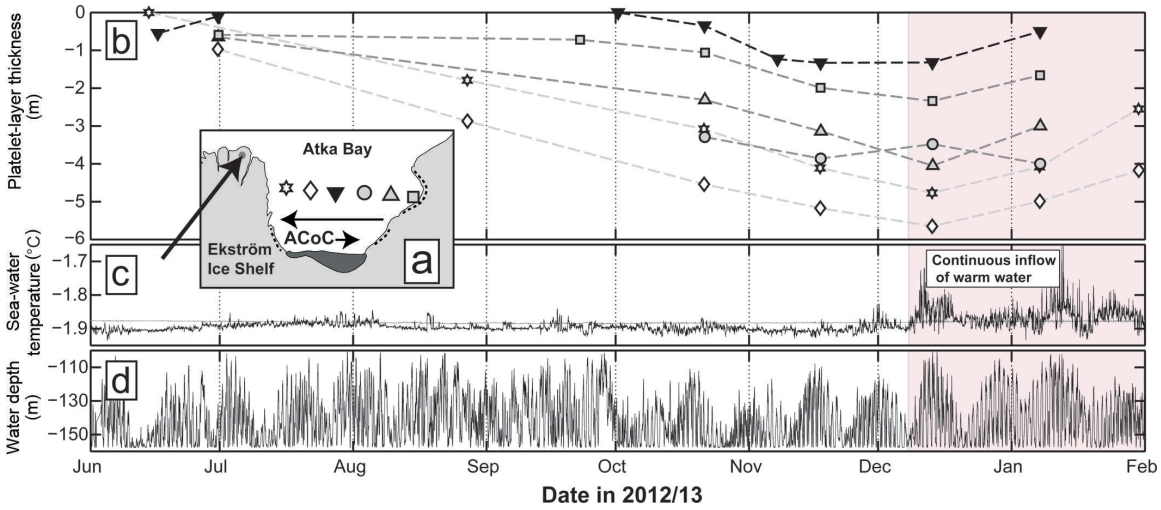

Fig. 5. Platelet-layer thickness at the six sampling sites on Atka Bay fast ice in 2012/13, along with oceanographic conditions recorded at a measurement site below the Ekström Ice Shelf. (a) Location map of the study area. Sampling sites are indicated by symbols (ATKA03: star; ATKA07: diamond; ATKA11: inverted black triangle; ATKA16: gray circle; ATKA21: gray triangle; ATKA24: gray square) and grouped into western, central and eastern sites. The location of the oceanographic measurements in (c) is indicated by the dot and the arrow. The two other arrows depict the two extremes of the strength and direction of the Antarctic Coastal Current in this area. (b) Sub-ice platelet-layer thickness evolution at the different sites, with symbols corresponding to their location according to (a). (c) In situ temperature (black) and corresponding surface freezing point (gray) of the water at a location below the northern Ekström Ice Shelf in 2012/13. When the temperature is below the surface freezing point, the water is potentially supercooled. The shaded area indicates the continuous inflow of warm water masses. (d) Water depth of the corresponding temperature record.

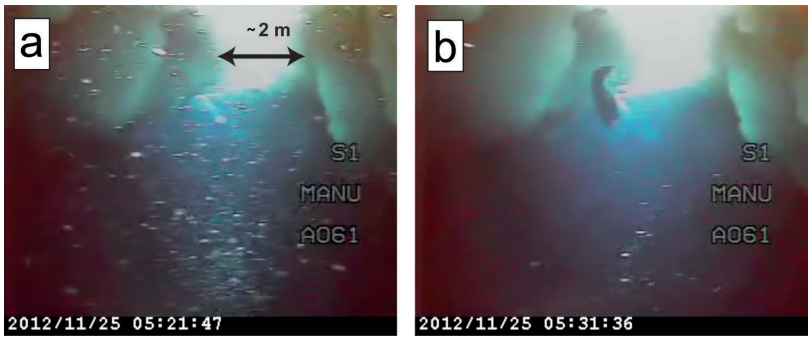

Fig. 6. Video still images from under-ice video recordings. (a) Masses of ice platelets float upwards during a high-flux event. (b) 'Normal' conditions at the end of November 2012.

and it cannot be assessed whether an absolute maximum in the center of Atka Bay would be observed under normal conditions. However, the small amount of platelets at the beginning of the measurements in June 2012 and the low accumulation rate after October 2012 suggest that a local minimum was to be expected in this area. Since sporadic measurements at other sites in southern central Atka Bay yielded thicknesses of up to 10 m, and assuming that z_p is generally lower in the northern part of Atka Bay, we estimate a bay-wide average of 4 m in December.

Figure 5c and d show the time series of sub-ice-shelf water temperature, the corresponding surface freezing point and the depth of the instrument during the temperature measurement. The depth variations revealed a 14 day cycle overlying the 12 hourly tidal cycle. The depth varied between 100 and 155 m, reflecting the strength and direction of the tidal- and wind-induced ACoC. The maximum depth of 155 m was limited by the length of the cable, while the ACoC was strong enough to lift the instrument to depths as shallow as 100 m. In this sense, the instrument became a vertical profiler of the water column between 100 and 155 m. The water temperatures ranged from –1.94 to –1.6°C. It is apparent that the in situ temperature of the water column was mostly below the surface freezing point between June and December 2012. At the beginning of December 2012, the water temperatures of nearly the entire water column rose above the surface freezing point. The high temperature variability indicated that the water column was also very inhomogeneous between December 2012 and February 2013. At the same time, the highest temperatures were measured at shallower water depths.

The video recordings of CAM2 indicated that platelet accumulation was not the result of a uniform flux of platelets. Instead, a small continuous upward flux was overlaid by periods of very high fluxes with a time span usually $\ll$1 hour (Fig. 6). Speed and direction of the ice platelets were highly variable, and most likely depended on their volume and the influence of tidal currents and local turbulences.

Upon arrival at the sea-ice/platelet-layer bottom, crystals of different sizes and shapes integrated into a porous layer in random orientations (Fig. 7). The individual platelets in the bottom part were not firmly fixed in the lattice, but were still prone to resuspension by turbulence and strong currents. Small filaments of phytoplankton growing at the platelet edges were frequently observed. These provide a rich food source for amphipods grazing the platelet layer, which were observed in great numbers on several occasions in November and December 2012 (Fig. 7d).

Sea-ice texture and growth history

As seen from the texture analysis of a 1.94 m long sea-ice core obtained at ATKA24 in mid-December 2012 (Fig. 8), the level sea ice in this area grew predominantly thermodynamically, with no indications of ridging or rafting. Satellite imagery revealed the establishment of a closed sea-ice cover at this site around 25 May 2012. This core is therefore representative of thermodynamically grown fast ice, but with a comparatively late formation date. Each core depth was assigned an approximate date of formation by comparison with the sea-ice thickness evolution at that site (Fig. 3).

Horizontal and vertical thin sections (Fig. 8) revealed a typical granular texture in the early period of formation (25 May to early June 2012). This is an indication of typical wind- and wave-induced growth, especially since snow ice did not contribute to sea-ice growth at this location. This granular ice contributed ~0.12 m (6%) of the total sea-ice thickness. The texture in the following 1.5 m (77%) mostly resembles that termed draped platelet ice by Jeffries and others (1993, their fig. 10b and c), Tison and others (1998, their fig. 1a) and Dempsey and others (2010, their figs 4 and 5). According to Jeffries and others (1993), those crystals are less angular, more equidimensional and have wavy, uneven edges. The lower 0.32 m (17%) of our core consisted of blade-like crystals, partially also with wavy edges. These resemble the bladed platelet ice shown by Jeffries and others (1993, their fig. 11), Eicken and Lange (1989, their fig. 5) and Dempsey and others (2010, their figs 4 and 5). The individual crystals in this part have various sizes, with crystal lengths of 0.01–0.1 m, even in the same thin section. As apparent from the Schmidt net plots (Fig. 8, right-hand side), the crystal *c*-axis orientations showed a random distribution for all the analyzed samples. This distribution is typical for platelet ice (Dempsey and Langhorne, 2012).

DISCUSSION

Seasonal cycle of fast-ice thickness and snow cover

We have performed regular year-round measurements of fast-ice properties at Atka Bay since 2010. Although differences in dynamic-growth contribution, dates of

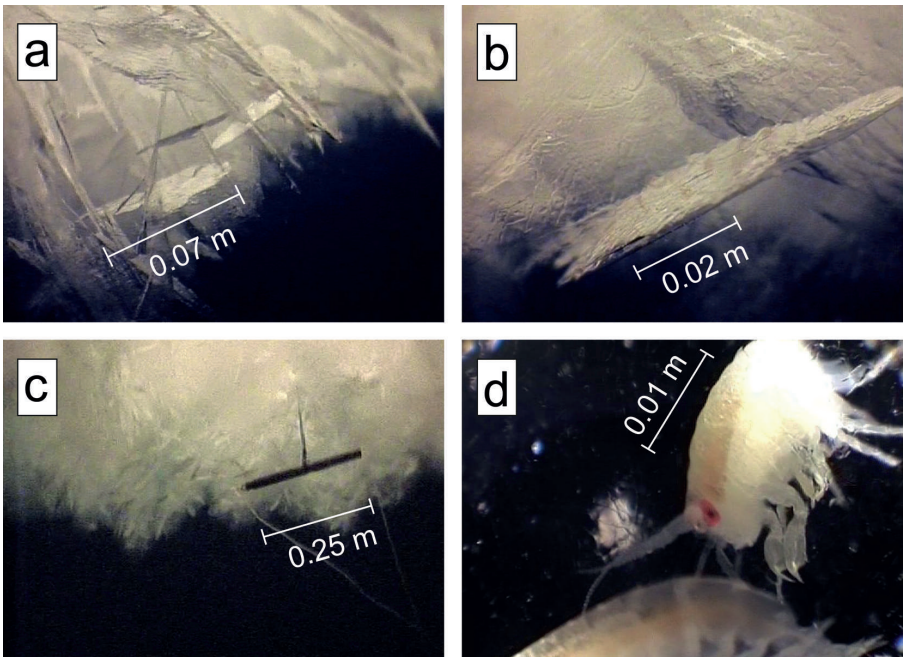

Fig. 7. Video still images of the platelet layer. (a) Single ice platelets several centimeters wide and <0.001 m thick stick together to form a porous layer. (b) Close-up of an ice platelet. (c) Measuring the platelet-layer thickness with a metal bar (0.25 m). (d) Amphipods (<0.02 m) grazing the platelets for phytoplankton growing at the platelet edges.

formation and snow cover determine the sea-ice evolution at Atka Bay each year, the results of our fast-ice observations in 2012 are generally in accordance with field measurements performed in previous years. The seasonal fast-ice cover of 2011 started to break up in late February 2012. Satellite observations revealed that several smaller sea-ice floes remained in the embayment, reattached to the ice-shelf edge in the southwestern part and became second-year sea ice. In the second half of March 2012, initial sea-ice growth started, while easterly winds constantly pushed the thin ice towards the ice-shelf edge. Visual observations confirmed a closed fast-ice sheet in the western part of Atka Bay at the end of April 2012, while the rough surface indicated the large contribution of dynamic processes to sea-ice growth. This area of mixed first/second-year sea ice is also characterized by a high radar backscatter (Fig. 1; bright color, marked in green). (A more detailed description of fast-ice surface properties at Atka Bay and their influence on TerraSAR-X radar backscatter is presented by Paul and others, 2015.) Strong winds constantly cleared away thin sea ice in the eastern part, where a closed fast-ice sheet was finally established 1 month later, at the end of May 2012. Dynamic growth again led to a greater thickness at ATKA16 than at the easternmost sites. A GPS buoy on one of the floes broken up in August 2012 revealed that it had drifted into the central Weddell Sea by the time data transmission finally stopped due to a power failure (69°43.8′ S, 45° 49.9′ W on 26 August 2013). New sea ice immediately started to grow in the break-up area, but was cleared out of the embayment by persistent winds. At the beginning of October 2012, a closed fast-ice cover was again formed in the break-up area (Fig. 1; marked in red) after the grounding of the large iceberg B15G in front of Atka Bay.

The great thicknesses and local variability (Fig. 3) confirm that dynamic growth contributed to sea-ice formation at ATKA03, ATKA07, ATKA11 (early) and ATKA16. No dynamic growth was observed at ATKA21 and ATKA24, where initial formation was delayed until May 2012. Kipfstuhl (1991) and Günther and Dieckmann (1999) found maximum sea-ice thicknesses of 2.19 and 2.17 m, and snow depths up to 0.62 m, at their study site ~3 km southwest of ATKA03 (70°35.05′ S, 8°8.41′ W) in 1982 and 1995, respectively. Our results showed a higher maximum thickness of 2.56 m at ATKA03, which may be attributed to higher growth rates due to increased upward conductive heat flux, owing to the lack of snow. While the small snow depths at ATKA24 were associated with topographic/local-wind patterns in close proximity to the ice shelf (~1 km away), the lack of snow at ATKA03 is explained by the presence of a small, grounded iceberg ~2 km to the east. In 2010 and 2011, we observed much higher snow depths (~0.8 m in December) in the western part of Atka Bay. While an east–west gradient in snow depth is expected, due to the prevailing wind conditions and consequent snow redistribution, local topographic features (e.g. icebergs and pressure ridges) alter snow accumulation locally (e.g. at ATKA03 and ATKA16). This gradient generally introduces additional variabilities in sea-ice growth rates, and at the same time opposes the gradient in dynamic growth. For example, the large contribution of dynamic thickening in the west of Atka Bay is partly compensated for by a lower thermodynamic growth, due to the greater snow depth.

Snow-ice formation is a major contributor to pack ice in the Southern Ocean (Eicken and others, 1995; Jeffries and others, 2001). Günther and Dieckmann (1999) observed no negative freeboard at Atka Bay during their study. Our

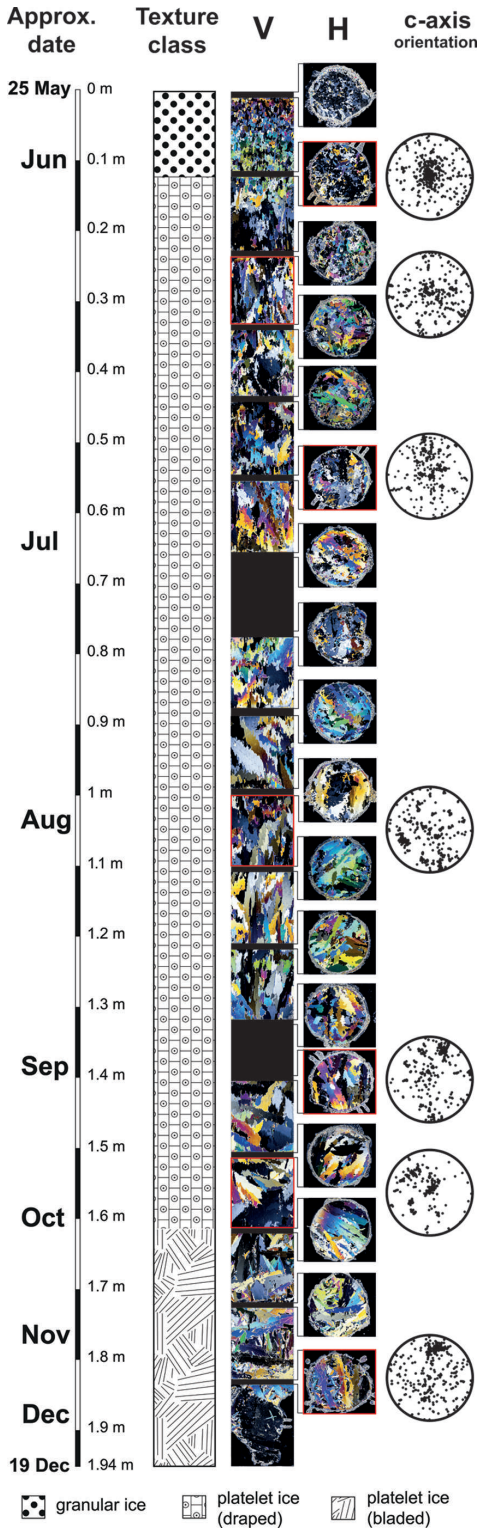

Fig. 8. Crystal structure of horizontal (H) and vertical (V) thin sections of a sea-ice core retrieved at ATKA24. The black areas represent segments where no data are available. The Schmidt equal-area net diagrams (right) depict the *c*-axis orientations of samples indicated by a red border.

results agree with the findings of Kipfstuhl (1991), who found flooding in areas with snow depths greater than 1 m. However, the relative number of negative freeboard observations was very low. An exception was the area of new ice with a negative freeboard in November 2012. The sea ice there became permeable at the beginning of December 2012, when subsequent surface flooding and refreezing of slush resulted in a 0.15 m thick, fine-grained layer of snow ice. But, since such a late formation and the resulting low thickness is usually not observed, we consider the contribution of snow-ice formation to total sea-ice mass at Atka Bay to be very low, despite the thick snow cover. This finding is directly linked to the presence of ice platelets below the fast ice. Through its buoyancy, the platelet layer effectively increases the freeboard and simultaneously reduces the occurrence of surface flooding and subsequent snow-ice formation, which would otherwise be more frequent. The strength of this effect depends on the thickness and ice-volume fraction of the platelet layer.

Seasonal cycle of the platelet layer

Günther and Dieckmann (1999) took advantage of the buoyancy effect and used Archimedes' law to calculate the platelet-layer thickness during their study. They obtained a platelet-layer thickness of ~1.2 m in December 1995. Kipfstuhl (1991) used a sinking weight of 1 kg to determine the depth at which it sank freely. By doing so, he was able to provide an estimate of a 4 m thick platelet layer in November 1982. Neither study provided an uncertainty estimate. While our results obtained with the 'metal-bar' method yield good agreement with the 'sinking-weight' method of Kipfstuhl (1991), the results of Günther and Dieckmann (1999) suggest that either the uncertainty in their method is very large or the platelet accumulations were profoundly different between the years. We consider the 'metal-bar' method as the most robust and exact of the three procedures. Finally, our result of platelet-layer thicknesses of several meters is also in accordance with Eicken and Lange (1989), who found platelet layers of >5 m below fast ice at Drescher Inlet.

We observed ice-platelet accumulations under the fast ice as early as June (Fig. 5). This is in accordance with Günther and Dieckmann (1999), while Kipfstuhl (1991) noticed ice platelets in boreholes as early as the end of April. The onset of ice-platelet accumulation below the fast ice of McMurdo Sound was also found to be variable. Gough and others (2012) recorded ice-platelet growth on suspended 'hot wires' in mid-July and a thin platelet layer of 0.02 m in early August, while Leonard and others (2006) identified a modified sea-ice texture in first-year sea-ice cores as early as April. Like similar structured studies involving the evolution of platelet-layer thickness, we observed a steady increase throughout the winter and spring. However, results obtained from CAM2 near the western ice-shelf edge in November 2012 suggest that the ice-platelet accumulation is mainly a result of episodic events of high flux overlying a very low continuous flux. This episodic flux was also observed in McMurdo Sound, where Leonard and others (2006) interpreted episodically present acoustic scatterers in the water column as a flux of buoyant platelet crystals.

Below McMurdo Sound fast ice, ice platelets have also been observed growing while already attached to the fast ice above, rather than being advected from depth (Smith and others, 2001). Smith and others (2012) found that single ice platelets attached to the fast-ice bottom grow in

discontinuous, episodic bursts, mainly depending on the influence of variable currents during periods of continuous supercooling directly below the fast ice. While the potential supercooling observed under the front of the Ekström Ice Shelf throughout the winter (Fig. 5c) is indicative of ice-platelet formation at depth, we currently have no indication of in situ supercooling directly below the fast ice. As the rising ice platelets observed in the videos were also already large in diameter, we hypothesize that the main mechanism for the establishment of the Atka Bay platelet layer is crystal growth at depth, while growth at the ice/water interface is of minor (if any) importance. This is in accordance with the conclusions of Eicken and Lange (1989), who suggested that the platelets in the southeastern Weddell Sea (pack ice) most likely form at greater depth.

Very little is known about the currents in the Ekström Ice Shelf cavity. Nicolaus and Grosfeld (2004) using model studies found that the circulation is dominated by a strong cyclonic gyre, taking half a year between eastern inflow and western outflow. Like Neckel and others (2012), they did not find any evidence for marine-ice accretion under the ice shelf itself. The presence of ice rises and rumples east of Atka Bay (Fig. 1) and the spatial distribution of ice platelets suggest that they are mainly advected from the area north of Neumayer III. As revealed by fluctuations of CTD recorded pressure (Fig. 5d), the magnitude of the ACoC is highly variable in the region (Fahrbach and others, 1992). Quantification of the current velocity derived from the pressure data is generally possible and currently under investigation. Tidal- and wind-induced currents may cause turbulence in the cavity when the predominantly westward ACoC weakens or even reverses in direction. The resulting turbulent flow is likely to provide transport for the platelet crystals (Fig. 5a). If this is true, a significant amount of supercooled water would be transported into the open ocean along the main current direction. Currently, we have no direct evidence for this hypothesis, but studies in the southwestern Weddell Sea (e.g. Eicken and Lange, 1989) found accumulations of ice platelets far from the coast, which agrees with our hypothesis.

As apparent from the evolution of water temperatures, the declining thickness of the platelet layer in December 2012 at nearly all study sites (Fig. 5b) is linked to the inflow of warm water masses and subsequent melt of ice platelets. Additional under-ice CTD casts in December 2012 revealed that warm surface water penetrates into Atka Bay from the east. At the same time, the buoyant ascent of ice platelets visible in the recordings ceased completely. Apart from the shrinking platelet layer, only a very slight bottom melt is apparent from the thickness data in Figure 3. Preliminary results (not shown) from high-resolution temperature profile data suggest that at ATKA03 no bottom melt occurred whatsoever. In addition, sea-ice cores taken in December 2012 showed a slight increase in sea-ice porosity from interior melt. Although we do not quantify the process here, the platelet layer acts as an efficient buffer between the fast ice and the incoming warm water in summer (Eicken and Lange, 1989). Usually the increased instability of the fast-ice cover through interior melt combined with tides and strong winds, as well as a pack-ice-free zone in front of the Ekström Ice Shelf, would lead to fast-ice break-up early in the following year. The flocking effect of iceberg B15G in front of Atka Bay (Fig. 1) held the 2012 fast ice in the bay, so 2013 saw second-year fast ice in the region. The iceberg itself detached and drifted westwards in August 2013. It is unclear whether the iceberg also modified the properties of the platelet layer in 2012 compared with other years.

Table 3. Selected estimates for the ice-volume fraction of the platelet layer, modified after Gough and others (2012)

Location	Ice fraction	Method	Source
Atka Bay	0.25	Modeled heat flux forced by atmosphere	This study
	0.29–0.43	Multi-frequency electromagnetic induction sounding	Hunkeler and others (2015)
	0.46	Archimedes' law	Günther and Dieckmann (1999)
	0.2	Modeled heat flux forced by atmosphere	Kipfstuhl (1991)
McMurdo Sound	0.16	Archimedes' law	Price and others (2014)
	0.25	Measured heat flux from sea-ice temperature profiles	Gough and others (2012)
	0.35	Measured heat flux from sea-ice temperature profiles	Purdie and others (2006)
	~0.33	Estimate from sea-ice temperature profiles	Trodahl and others (2000)
	>0.50	Estimate from horizontal thin sections	Jeffries and others (1993)
	0.50	Estimate from core holes	Crocker and Wadhams (1989)
	0.20	Estimate from core holes	Bunt and Lee (1970)
Model domain	0.06	Three-dimensional geometric model	Dempsey and others (2010)

Ice-volume fraction in the platelet layer

While ice platelets accumulate episodically below the fast ice during winter, the advancing freezing interface incorporates the upper portion of the underlying platelet layer into the sea-ice fabric by freezing of the interstitial water. As a result, part of the solid fast ice originates from heat loss to the ocean. This is in contrast to the usual process of heat conduction to the atmosphere, which gives rise to congelation growth. In this sense, the energy- and mass balance of the fast ice is altered and must be accounted for. To quantify this impact, it becomes necessary to determine the ice-volume fraction, β, in the platelet layer. The model results (Fig. 4) suggest a bay-wide average β of 0.25, with individual results 0.18–0.35.

Ice-volume fractions in the platelet layer have been estimated in a number of previous investigations (Table 3). Our average β of 0.25 agrees well with the findings of Kipfstuhl (1991), who derived a β of 0.2 from their comparison between a thermodynamic model and sea-ice thickness observations at their study site 3 km southwest of ATKA03. In addition, our result is in good agreement with a recent study at McMurdo Sound by Gough and others (2012), who calculated an ice-volume fraction of 0.25 from measured ice-temperature profiles and claim their 'result being the most precise to date'. This suggests that our growth model results are reasonably good. Three studies (Crocker and Wadhams, 1989; Jeffries and others, 1993; Günther and Dieckmann, 1999; Table 3) obtained significantly higher results ($\beta > 0.46$), which we attribute either to profoundly different conditions or unsuitable methods. Dempsey and

others (2010) attribute their low result ($\beta = 0.06$) to in situ platelet growth and secondary platelet movement, which were not accounted for in their model.

Possible uncertainties in our calculation arise from the fact that some physical processes are not implemented in the model (e.g. gravity drainage) and from constant parameters (e.g. albedo, salinity profile and sea-ice and snow densities). However, the forcings of downward radiant heat fluxes are expected to be very reliable, as they were derived using data from a World Meteorological Organization standard meteorological observatory. Some uncertainty is introduced through the sensible and latent heat fluxes derived from the bulk method. Further potential uncertainties arise from the limited information about snow depths, individual dates of freeze onset, the uncertainty of sea-ice thickness measurements and the date of first platelet accumulation at each site. Furthermore, our approach of introducing a simple growth-rate modification does not reflect the true physics involved in this process. One example is the possible supercooling directly below the fast ice (Smith and others, 2012), though this might not be as important as it is below McMurdo Sound fast ice. At the same time, our metal-bar measurements revealed that the resistance of the platelet layer, and consequently the ice-volume fraction, is very variable, temporally as well as spatially (even during a single measurement). In addition, our method is, in principle, only suitable for determining the ice-volume fraction of the part which is already incorporated into the solid sea ice, not taking into account the lower platelet layer. This leads to additional uncertainties, particularly under the assumption that the upper part is likely compressed by the buoyancy pressure of the underlying ice platelets.

Since these uncertainties are so manifold, we performed sensitivity studies to identify the parameters and constants with the biggest impact on β. Simulations were set up to yield $\beta = 0.25$ as a control, then relevant input parameters and constants were varied by up to $\pm 5\%$, one at a time. In the following, the absolute minimum and maximum variations corresponding to the 5% are indicated in parentheses. The results show that the model is comparatively insensitive to changes in downward shortwave radiation (0–24 W m^{-2}), wind speed (0.01–1.1 m s^{-1}), relative humidity (2.6–4.6%) and constants such as sea-ice density (46 kg m^{-3}), snow density (16 kg m^{-3}) and surface albedo (0.05). In contrast, the outcomes for β vary strongly with varying sea-ice thickness (0.02–0.14 m), oceanic heat flux (+2 W m^{-2}), air temperature (0.066–2°C), as well as downward longwave radiation (5.7–15.1 W m^{-2}). The sea-ice thickness measurements are considered reliable, since the measurement itself has a very low uncertainty (± 0.01 m) and most data points are an average of up to five spot measurements. A positive oceanic heat flux is very unlikely to be present during sea-ice growth, due to the presence of the platelet layer. Air temperature and downward longwave radiation are measured directly at Neumayer III with high accuracy. By far the largest influence is exerted by the variation of the upward longwave radiation (7.9–16 W m^{-2}), which is used to compute the surface temperature and to calculate the turbulent heat fluxes used as a model input. This significantly modifies the surface energy balance and heavily influences sea-ice thickness evolution and, consequently, β. Upward longwave radiation is, in principle, available from Neumayer III with the limitation that the surface temperature of the ice shelf naturally differs from that of the sea ice (as measured by the AWS). For this reason we applied a correction of +8 W m^{-2} to upward longwave radiation after careful analysis of both datasets, finally yielding the best match to the EC flux data. Our study also revealed that, with larger variations of upward longwave radiation, more surface melt occurs and a strong deviation from the sensible and latent heat fluxes measured by the EC method is evident. These effects become even more apparent when increasing the variation above 5%. We therefore consider a corresponding uncertainty of ± 0.05 as an upper limit. Since, according to our sensitivity study, the effect of a change in upward longwave radiation is as strong as that of all the other parameters combined, we estimate that their contributions sum to an additional uncertainty of ± 0.05. We therefore estimate the overall uncertainty at 0.1, yielding $\beta = 0.25 \pm 0.1$.

The impact of ice platelets on fast-ice crystal structure

The complete absence of columnar growth in a core representative of thermodynamical growth is atypical in most sea-ice covered areas. However, in our study region this seems to be the norm, due to the sustained contribution of ice platelets. Our texture analysis provides evidence that the ice platelets disrupted the potential columnar growth as early as June 2012, leading to a mix of incorporated ice platelets and interstitial congelation ice (Jeffries and others, 1993) in 94% of the core. However, the resulting texture is not always unambiguous. Sea-ice crystal structure is very variable and classification is not straightforward. Different analysts may describe the same texture entirely differently. This becomes especially evident when platelet ice is involved. Here *c*-axis measurements using the fabric analyzer provide independent confirmation, in agreement with our visually obtained texture classification. Although we currently have only a small number of analyzed samples, our data support the findings of earlier studies (Dempsey and others, 2010) that there is no apparent distinction in the *c*-axis distribution between draped and bladed platelet ice, which are both characterized by a Schmidt net with randomly distributed points.

Until now it has not been clear which processes govern the shapes and sizes of the crystals, of which there is a large spectrum visible in our core. Jeffries and others (1993) and Tison and others (1998) suggest that this fabric may be related to a variable amount of supercooling in the ice-shelf water from which the ice platelets form. In this study we were unable to address this question. The transition from draped to bladed platelet ice is striking in our vertical thin sections, and analysis of the other cores needs to be completed to gain additional insights.

It should be noted that our results based on one core may present a significant overestimation when compared with the entire Atka Bay. The governing factor is the present sea-ice thickness (and to a lesser degree the snow depth) at a sampling site when a platelet layer starts to form. The greater this thickness, the lower is the remaining growth of solid sea ice during winter and, at the same time, the relative contribution of platelet ice. For our sampling sites in 2012 (Fig. 3), we would expect the least contribution of platelet ice at ATKA07, as this site had a very high initial thickness ($\sim$2 m) and only grew $\sim$1 m during winter. Estimating the fraction of platelet ice there as $\sim$30%, an appropriate estimate of the average bay-wide platelet-ice fraction would be $\sim$60%. Note

that these numbers do not represent the contribution of ice platelets to the total sea-ice mass (next subsection), but rather the fraction of platelet-influenced crystal structure.

Contribution of ice platelets to total fast-ice mass and freeboard

In order to assess the contribution of ice platelets to the total sea-ice mass and the influence on freeboard, it is necessary to separate the part of sea ice grown by heat conduction to the atmosphere on the one hand, and the ice-platelet formation by relieved supercooling in the water column on the other. Based on our field observations and model results, we assume $\beta = 0.25$, initial sea-ice formation in April and the accumulation of a moderate snow cover from June onwards. A sea-ice growth simulation with the model then yields a December maximum thickness of solid fast ice of 2 m. This is a reasonable estimate for the conditions of 2012, since the quick build-up of thickness in the west by wind stress is at least partly compensated by a delayed freeze onset in the east. Under these conditions, and taking into account that ice-platelet accumulation starts in June, our growth model suggests that the lower 1.2 m of solid sea ice contains incorporated ice platelets. This estimate is also supported by the sea-ice texture. Their total mass then amounts to an effective thickness of ~0.3 m, or 15% of the solid sea ice. This thickness gain is on the same order of magnitude as that found in the theoretical study of Hellmer (2004). He calculated that the ice-shelf/ocean interaction may contribute up to 0.2 m of the sea-ice thickness over significant areas of fast and pack ice in the Southern Ocean. However, his approach did not explicitly take into account the contribution of ice platelets. Subtracting this contribution of incorporated ice platelets, the remaining sea-ice thickness becomes 1.7 m, or 85%, as a result of growth by heat conduction from the ocean to the atmosphere. Multiplication of the average $z_p = 4$ m with $\beta = 0.25 \pm 0.1$, and addition of the contribution of incorporated ice platelets, yields an effective sea-ice thickness equivalent to ~1.3 $\pm$ 0.52 m as a result of heat loss to the ocean during ice-platelet formation at depth. This corresponds to 43 $\pm$ 12% of solid and loose sea ice altogether.

Because the thickness of the platelet layer changes with time, its contribution to freeboard is also variable. Here we perform a sample calculation of how the additional buoyancy of the ice platelets influences freeboard under the assumption of hydrostatic equilibrium, using Archimedes' law:

$$z_f = \frac{z_p \cdot (\rho_p - \rho_w) + z_s \cdot \rho_s + z_{si} \cdot (\rho_{si} - \rho_w)}{\rho_w}, \qquad (2)$$

where the subscript 'f' refers to freeboard, 's' to snow, 'si' to sea-ice, 'p' to platelet layer and 'w' to water; z is the thickness and ρ is the density of the respective medium. Again considering the conditions in December, we assume an average sea-ice thickness of 2 m, a platelet-layer thickness of 4 m and $\beta = 0.25 \pm 0.1$. Using typical densities (ρ_w= 1032.3 kg m^{-3}, ρ_{si} = 925 kg m^{-3} and ρ_s = 330 kg m^{-3}), the resulting freeboard is ~0.11 $\pm$ 0.05 m higher than the situation where underlying platelets are not present, independent of the snow cover.

Basalt melt of the Ekström Ice Shelf

Kipfstuhl (1991) calculated that the volume of ice platelets accumulated under Atka Bay landfast sea ice accounts for 12% of the basal melt volume observed under the Ekström Ice Shelf (for $\beta = 0.2$). Multiplication of the average effective thickness equivalent of ice platelets found in this study (1.3 m) by the fast-ice area (~440 km^2) yields a total annual platelet volume of $V_p = 0.57$ km^3 underlying the fast ice of Atka Bay. Table 4 shows average basal melt rates of the (main) western part of the Ekström Ice Shelf from selected studies, along with total basal melt volume calculated for an area of 6000 km^2. Based on our V_p and recent results of Neckel and others (2012) for basal melt from mass-flux divergence, we find that more than one-fifth of the basal melt volume of the Ekström Ice Shelf is refrozen as loose and incorporated platelets.

Table 4. Ekström Ice Shelf basal melt from previous studies and contribution of ice platelets to total melt volume. $\dot{a}_b$: mean basal melt rate; V_b: volume of basal melt for an area of 6000 km^2; $V_p\,V_b^{-1}$: fraction of ice-platelet volume from basal melt volume

Source	$\dot{a}_b$	Method	V_b	$V_p\,V_b^{-1}$
	m a^{-1}		km^3	
Neckel and others (2012)	0.44	Mass balance	2.64	0.22
Nicolaus and Grosfeld (2004)	0.98	Ocean-circulation model	5.88	0.1
Sandhäger and Blindow (2000)	0.53	Ice-shelf flow model	3.18	0.18
Kipfstuhl (1991)	0.73	Mass balance	4.38	0.13

SUMMARY AND CONCLUSION

We have investigated the seasonal evolution of landfast sea ice and the underlying platelet layer at Atka Bay, eastern Weddell Sea, during 2012/13. Sea-ice formation started in March, and variable sea-ice conditions were observed across Atka Bay, with different dates of initial formation, contribution of dynamic growth processes and snow accumulation. Sea-ice thickness was ~2 m at the end of the growth season, while dynamic growth and snow depths of up to 1 m introduced large spatial variability. A thick platelet layer was observed underlying the entire solid fast-ice sheet, with first observations of platelets in boreholes and sea-ice cores in June. Potentially supercooled water was present under the ice shelf during the entire winter. Under-ice video recordings revealed episodic events of high upward fluxes of ice platelets, overlying a very low continuous flux. The platelet-layer thickness increased until December, with a bay-wide average of 4 m and a local maximum of 10 m. When warm surface water intruded into Atka Bay at the beginning of December, ice-platelet accumulation ceased and the platelet layer thinned, shielding the solid ice above from significant bottom melt. Through the additional buoyancy, surface flooding and snow-ice formation were rarely observed, despite the thick snow cover. Using a one-dimensional thermodynamic sea-ice model, we found a best-fit ice-volume fraction of $\beta = 0.25 \pm 0.1$ in the platelet layer. This corresponds to an effective sea-ice thickness equivalent of 1.3 m as a result of heat loss to the ocean, which is nearly half the combined mass of solid sea ice and the underlying platelet layer. In relation to Ekström Ice Shelf basal melt, we found that >20% of the basal melt volume is refrozen as ice platelets trapped

under Atka Bay fast ice. It is likely that the oceanographic conditions in this area promote the transport of potentially supercooled water out of the cavity, possibly leading to further ice-platelet formation away from the coast.

In conclusion, this study highlights the dependence of coastal sea-ice regimes on local ocean/ice-shelf interactions. Basal processes mostly dominate sea-ice properties, with platelet accumulations below the solid sea ice directly impacting sea-ice energy and mass balance. As a consequence, uncertainties are introduced into numerical models which do not account for heat loss to the ocean. Furthermore, the additional buoyancy complicates sea-ice thickness retrieval by altimetry techniques, an effect which adds to other difficulties of remote-sensing techniques in coastal areas (e.g. complex coastlines and snow cover). Since this study was limited to Atka Bay and the Ekström Ice Shelf, it is necessary to gain more insight into the temporal and spatial variability of ice-platelet accumulations over larger areas under Antarctic sea ice.

Although no obvious changes in sea-ice and oceanographic conditions were found in this study compared with investigations 30 years ago, this will not necessarily be the case in the future. Hellmer and others (2012), Pritchard and others (2012) and Depoorter and others (2013) have previously highlighted that the complex interactions between the Southern Ocean, the Antarctic ice shelves and the sea-ice cover have significant global implications, and they concluded that much more process understanding related to ice-shelf cavities is needed. But since sub-ice-shelf processes are particularly difficult to investigate in situ, alternative approaches are needed to detect eventual changes in this complex system. Studies of fast-ice properties are comparatively easy to conduct, and we emphasize that fast-ice characteristics, especially near ice shelves, may provide a very sensitive, and yet practical, indicator of the conditions and possible changes in the Antarctic. Hence there exists an urgent need to perform these studies on a more regular and circum-Antarctic basis, for example by extending and intensifying the work in the Antarctic Fast Ice Network (Heil and others, 2011).

ACKNOWLEDGEMENTS

We thank the Neumayer III overwintering teams 2010–13 for their dedicated fieldwork. We thank the German Aerospace Center (DLR) for the TerraSAR-X image, and Christine Wesche for post-processing and calibrating the satellite data. We are grateful to Holger Schmithüsen and Clemens Drüe for help with the meteorological and flux data. We also appreciate the helpful suggestions of Christof Lüpkes, Wolfgang Dierking and Martin Losch, and the technical support of Bernd Loose and Uwe Baltes. We thank Lars Kindermann for the CTD data and Ilse van Opzeeland for inspiring us with the platelet video recordings. We also thank Sepp Kipfstuhl and Ilka Weikusat for help with *c*-axis determination. Our research at Neumayer III would not have been possible without the support of the AWI logistics. This work was supported by the German Research Council (DFG) in the framework of the priority programme 'Antarctic Research with comparative investigations in Arctic ice areas' grants SPP1158, NI 1092/2 and HE2740/12, and the Alfred-Wegener-Institut Helmholtz Zentrum für Polar- und Meeresforschung. Supplementary data to this paper are available at http://dx.doi.org/10.1594/PANGAEA.824434. Finally, we thank two anonymous reviewers whose comments significantly improved the manuscript.

REFERENCES

Andreas EL and 6 others (2010) Parameterizing turbulent exchange over sea ice in winter. *J. Hydromet.*, **11**(1), 87–104 (doi: 10.1175/2009JHM1102.1)

Bindschadler R and 17 others (2011) Getting around Antarctica: new high-resolution mappings of the grounded and freely-floating boundaries of the Antarctic ice sheet created for the International Polar Year. *Cryosphere*, **5**(3), 569–588 (doi: 10.5194/tc-5-569-2011)

Bintanja R, Van Oldenborgh GJ, Drijfhout SS, Wouters B and Katsman CA (2013) Important role for ocean warming and increased ice-shelf melt in Antarctic sea-ice expansion. *Nature Geosci.*, **6**(5), 376–379 (doi: 10.1038/ngeo1767)

Bitz CM and Lipscomb WH (1999) An energy-conserving thermodynamic model of sea ice. *J. Geophys. Res.*, **104**(C7), 15 669–15 677 (doi: 10.1029/1999JC900100)

Boebel O and 7 others (2006) Real-time underwater sounds from the Southern Ocean. *Eos*, **87**(36), 361 (doi: 10.1029/2006EO360002)

Bunt JS and Lee CC (1970) Seasonal primary production in Antarctic sea ice at McMurdo Sound in 1967. *J. Mar. Res.*, **28**(3), 304–320

Comiso JC and Hall DK (2014) Climate trends in the Arctic as observed from space. *WIREs Climate Change*, **5**(3), 389–409 (doi: 10.1002/wcc.277)

Crocker GB (1988) Physical processes in Antarctic landfast sea ice. (PhD thesis, Cambridge University)

Crocker GB and Wadhams P (1989) Modelling Antarctic fast-ice growth. *J. Glaciol.*, **35**(119), 3–8 (doi: 10.3189/002214389793701590)

Dempsey DE and Langhorne PJ (2012) Geometric properties of platelet ice crystals. *Cold Reg. Sci. Technol.*, **78**, 1–13 (doi: 10.1016/j.coldregions.2012.03.002)

Dempsey DE, Langhorne PJ, Robinson NJ, Williams MJM, Haskell TG and Frew RD (2010) Observation and modeling of platelet ice fabric in McMurdo Sound, Antarctica. *J. Geophys. Res.*, **115**(C1), C01007 (doi: 10.1029/2008JC005264)

Depoorter MA and 6 others (2013) Calving fluxes and basal melt rates of Antarctic ice shelves. *Nature*, **502**(7469), 89–92 (doi: 10.1038/nature12567)

Eicken H (1992) Salinity profiles of Antarctic sea ice: field data and model results. *J. Geophys. Res.*, **97**(C10), 15 545–15 557 (doi: 10.1029/92JC01588)

Eicken H and Lange MA (1989) Development and properties of sea ice in the coastal regime of the southeastern Weddell Sea. *J. Geophys. Res.*, **94**(C6), 8193–8206 (doi: 10.1029/JC094iC06p08193)

Eicken H, Fischer H and Lemke P (1995) Effects of the snow cover on Antarctic sea ice and potential modulation of its response to climate change. *Ann. Glaciol.*, **21**, 369–376

Fahrbach E, Rohardt G and Krause G (1992) The Antarctic coastal current in the southeastern Weddell Sea. *Polar Biol.*, **12**(2), 171–182 (doi: 10.1007/BF00238257)

Fahrbach E, Peterson RG, Rohardt G, Schlosser P and Bayer R (1994) Suppression of bottom water formation in the southeastern Weddell sea. *Deep-Sea Res. I*, **41**(2), 389–411 (doi: 10.1016/0967-0637(94)90010-8)

Fretwell P and 59 others (2013) Bedmap2: improved ice bed, surface and thickness datasets for Antarctica. *Cryosphere*, **7**(1), 375–393 (doi: 10.5194/tc-7-375-2013)

Gough AJ, Mahoney AR, Langhorne PJ, Williams MJM, Robinson NJ and Haskell TG (2012) Signatures of supercooling: McMurdo Sound platelet ice. *J. Glaciol.*, **58**(207), 38–50 (doi: 10.3189/2012JoG10J218)

Gow AJ, Ackley SF, Govoni JW and Weeks WF (1998) Physical and structural properties of land-fast sea ice in McMurdo Sound,

Antarctica. In Jeffries MO ed. *Antarctic sea ice: physical processes, interactions and variability*. (Antarctic Research Series 74) American Geophysical Union, Washington, DC, 355–374

Günther S and Dieckmann G (1999) Seasonal development of high algal biomass in snow-covered fast ice and the underlying platelet layer in Atka Bay, Antarctica. *Antarct. Sci.*, **11**(3), 305–315 (doi: 10.1017/S0954102099000395)

Heil P (2006) Atmospheric conditions and fast ice at Davis, East Antarctica: a case study. *J. Geophys. Res.*, **111**(C5), C05009 (doi: 10.1029/2005JC002904)

Heil P, Gerland S and Granskog MA (2011) An Antarctic monitoring initiative for fast ice and comparison with the Arctic. *Cryos. Discuss.*, **5**(5), 2437–2463 (doi: 10.5194/tcd-5-2437-2011)

Hellmer HH (2004) Impact of Antarctic ice shelf basal melting on sea ice and deep ocean properties. *Geophys. Res. Lett.*, **31**(10), L10307 (doi: 10.1029/2004GL019506)

Hellmer H, Kauker F, Timmermann R, Determann J and Rae J (2012) Twenty-first-century warming of a large Antarctic ice-shelf cavity by a redirected coastal current. *Nature*, **485**(7397), 225–228 (doi: 10.1038/nature11064)

Holland PR, Jenkins A and Holland DM (2008) The response of ice shelf basal melting to variations in ocean temperature. *J. Climate*, **21**(11), 2558–2572 (doi: 10.1175/2007JCLI1909.1)

Hoppmann M, Nicolaus M, Paul S, Hunkeler PA, Schmidt T and Kühnel M (2013a) *Field measurements of sea-ice thickness, snow depth, freeboard and sub-ice platelet-layer thickness on the land-fast ice of Atka Bay in 2012* (doi: 10.1594/PANGAEA.824434)

Hoppmann M, Nicolaus M, Schmidt T and Kühnel M (2013b) *Meteorological observations by an automated weather station on Atka Bay land-fast sea ice, 2012-10-02 to 2012-12-27* (doi: 10.1594/PANGAEA.824527)

Hoppmann M, Nicolaus M, Schmidt T and Kühnel M (2013c) *Meteorological observations by an automated weather station on Atka Bay land-fast sea ice, 2012-07-06 to 2012-08-17* (doi: 10.1594/PANGAEA.824526)

Hunkeler P, Hendricks S, Hoppmann M, Paul S and Gerdes R (2015) Towards an estimation of sub-sea-ice platelet-layer volume with multi-frequency electromagnetic induction sounding. *Ann. Glaciol.*, **56**(69), (doi: 10.3189/2015AoG69A705) (see paper in this issue)

Jeffries MO, Weeks WF, Shaw R and Morris K (1993) Structural characteristics of congelation and platelet ice and their role in the development of Antarctic land-fast sea ice. *J. Glaciol.*, **39**(132), 223–238

Jeffries MO, Krouse HR, Hurst-Cushing B and Maksym T (2001) Snow-ice accretion and snow-cover depletion on Antarctic first-year sea-ice floes. *Ann. Glaciol.*, **33**, 51–60 (doi: 10.3189/172756401781818266)

Kipfstuhl J (1991) Zur Entstehung von Unterwassereis und das Wachstum und die Energiebilanz des Meereises in der Atka Bucht, Antarktis. *Ber. Polarforsch/Rep. Pol. Res.* 85

Kobarg W (1988) Die gezeitenbedingte Dynamik des Ekström-Schelfeises, Antarktis. *Ber. Polarforsch/Rep. Pol. Res.* 50

König-Langlo G (2013a) *Basic and other measurements of radiation at Neumayer Station in 2012, links to datasets*. Alfred Wegener Institute, Helmholtz Center for Polar and Marine Research, Bremerhaven (doi: 10.1594/PANGAEA.793020)

König-Langlo G (2013b) *Continuous meteorological observations at Neumayer station in 2012, links to datasets*. Alfred Wegener Institute, Helmholtz Center for Polar and Marine Research, Bremerhaven (doi: 10.1594/PANGAEA.792931)

König-Langlo G and Loose B (2007) The meteorological observatory at Neumayer Stations (GvN and NM-II) Antarctica. *Ber. Polar-Meeresforsch./Rep. Pol. Mar. Res.*, **76**(1–2), 25–38

König-Langlo G, King JC and Pettré P (1998) Climatology of the three coastal Antarctic stations Dumont d'Urville, Neumayer and Halley. *J. Geophys. Res.*, **103**(D9), 10 935–10 946 (doi: 10.1029/97JD00527)

Lange MA, Ackley SF, Wadhams P, Dieckmann GS and Eicken H (1989) Development of sea ice in the Weddell Sea. *Ann. Glaciol.*, **12**, 92–96

Langway CC Jr (1958) Ice fabrics and the universal stage. *SIPRE Tech. Rep.* 62

Leonard GH, Purdie CR, Langhorne PJ, Haskell TG, Williams MJM and Frew RD (2006) Observations of platelet ice growth and oceanographic conditions during the winter of 2003 in McMurdo Sound, Antarctica. *J. Geophys. Res.*, **111**(C4), C04012 (doi: 10.1029/2005JC002952)

Lewis EL and Perkin RG (1986) Ice pumps and their rates. *J. Geophys. Res.*, **91**(C10), 11 756–11 762 (doi: 10.1029/JC091iC10p11756)

Mahoney AR and 6 others (2011) The seasonal appearance of ice shelf water in coastal Antarctica and its effect on sea ice growth. *J. Geophys. Res.*, **116**(C11), C11032 (doi: 10.1029/2011JC007060)

Maksym T, Stammerjohn SE, Ackley S and Massom R (2012) Antarctic sea ice – a polar opposite? *Oceanography*, **25**(3), 140–151 (doi: 10.5670/oceanog.2012.88)

Massom RA and 12 others (2001) Snow on Antarctic sea ice. *Rev. Geophys.*, **39**(3), 413–445 (doi: 10.1029/2000RG000085)

Mauder M and 7 others (2013) A strategy for quality and uncertainty assessment of long-term eddy-covariance measurements. *Agric. Forest Meteorol.*, **169**, 122–135 (doi: 10.1016/j.agrformet.2012.09.006)

McDougall TJ and Barker PM (2011) Getting started with TEOS-10 and the Gibbs Seawater (GSW) Oceanographic Toolbox. (Tech. Rep.) SCOR/IAPSO, WG27 http://www.teos-10.org/software.htm

Moretskii VN (1965) Morskoy vnutrivodnyy led [Underwater sea ice]. *Probl. Arkt. Antarkt.*, **19**, 32–38 [in Russian] Translation by E.R. Hope, DRB Canada Report T-497-R, 1968

Neckel N, Drews R, Rack W and Steinhage D (2012) Basal melting at the Ekström Ice Shelf, Antarctica, estimated from mass flux divergence. *Ann. Glaciol.*, **53**(60 Pt 2), 294–302 (doi: 10.3189/2012AoG60A167)

Nicolaus M and Grosfeld K (2004) Ice–ocean interactions underneath the Antarctic Ice Shelf Ekströmisen. *Polarforschung*, **72**(1), 17–29

Nøst OA and 7 others (2011) Eddy overturning of the Antarctic Slope Front controls glacial melting in the Eastern Weddell Sea. *J. Geophys. Res.*, **116**(C11), C11014 (doi: 10.1029/2011JC006965)

Parkinson CL and Cavalieri DJ (2012) Antarctic sea ice variability and trends, 1979–2010. *Cryosphere*, **6**(4), 871–880 (doi: 10.5194/tc-6-871-2012)

Paul S and 6 others (2015) The impact of early-summer snow properties on landfast sea-ice x-band backscatter. *Ann. Glaciol.*, **56**(69) (doi: 10.3189/2015AoG69A715) (see paper in this issue)

Price D, Rack W, Haas C, Langhorne PJ and Marsh O (2013) Sea ice freeboard in McMurdo Sound, Antarctica, derived by surface-validated ICESat laser altimeter data. *J. Geophys. Res.*, **118**(7), 3634–3650 (doi: 10.1002/jgrc.20266)

Price D, Rack W, Langhorne PJ, Haas C, Leonard G and Barnsdale K (2014) The sub-ice platelet layer and its influence on freeboard to thickness conversion of Antarctic sea ice. *Cryosphere*, **8**(3), 1031–1039 (doi: 10.5194/tc-8-1031-2014)

Pritchard HD, Ligtenberg SRM, Fricker HA, Vaughan DG, Van den Broeke MR and Padman L (2012) Antarctic ice-sheet loss driven by basal melting of ice shelves. *Nature*, **484**(7395), 502–505 (doi: 10.1038/nature10968)

Purdie CR, Langhorne PJ, Leonard GH and Haskell TG (2006) Growth of first-year landfast Antarctic sea ice determined from winter temperature measurements. *Ann. Glaciol.*, **44**, 170–176 (doi: 10.3189/172756406781811853)

Rack W, Haas C and Langhorne PJ (2013) Airborne thickness and freeboard measurements over the McMurdo Ice Shelf, Antarctica, and implications for ice density. *J. Geophys. Res.*, **118**(C11), 5899–5907 (doi: 10.1002/2013JC009084)

Rimbu N, Lohmann G, König-Langlo G, Necula C and Ionita M (2014) Daily to intraseasonal oscillations at Antarctic research station Neumayer. *Antarct. Sci.*, **26**(2), 193–204 (doi: 10.1017/S0954102013000540)

Sandhäger H and Blindow N (2000) Surface elevation, ice thickness, and subglacial-bedrock topography of Ekström Ice Shelf (Antarctica) and its catchment area. *Ann. Glaciol.*, **30**, 61–68 (doi: 10.3189/172756400781820723)

Serikov MI (1963) Struktura morskogo antarkticheskogo l'da [Structure of Antarctic sea ice]. *Sov. Antarct. Exped. Inf. Bull.*, **39**, 13–14 [in Russian]

Smith IJ, Langhorne PJ, Haskell TG, Trodahl HJ, Frew R and Vennell MR (2001) Platelet ice and the land-fast sea ice of McMurdo Sound, Antarctica. *Ann. Glaciol.*, **33**, 21–27 (doi: 10.3189/172756401781818365)

Smith IJ, Langhorne PJ, Frew RD, Vennell R and Haskell TG (2012) Sea ice growth rates near ice shelves. *Cold Reg. Sci. Technol.*, **83–84**, 57–70 (doi: 10.1016/j.coldregions.2012.06.005)

Thoma M, Grosfeld K and Lange MA (2006) Impact of the Eastern Weddell Ice Shelves on water masses in the eastern Weddell Sea. *J. Geophys. Res.*, **111**(C12), C12010 (doi: 10.1029/2005JC003212)

Timco GW and Frederking RMW (1996) A review of sea ice density. *Cold Reg. Sci. Technol.*, **24**(1), 1–6 (doi: 10.1016/0165-232X(95)00007-X)

Tison J-L, Lorrain RD, Bouzette A, Dini M, Bondesan A and Stiévenard M (1998) Linking landfast sea ice variability to marine ice accretion at Hells Gate Ice Shelf, Ross Sea. In Jeffries MO ed. *Antarctic sea ice: physical processes, interactions and variability*. (Antarctic Research Series 74) American Geophysical Union, Washington, DC, 375–407 (doi: 10.1029/AR074p0375)

Trodahl HJ and 6 others (2000) Heat transport in McMurdo Sound first-year fast ice. *J. Geophys. Res.*, **105**(C5), 11 347–11 358 (doi: 10.1029/1999JC000003)

Turner J, Bracegirdle TJ, Phillips T, Marshall GJ and Hosking JS (2013) An initial assessment of Antarctic sea ice extent in the CMIP5 models. *J. Climate*, **26**(5), 1473–1484 (doi: 10.1175/JCLI-D-12-00068.1)

Van Dijk A, Moene AF and De Bruin HAR (2004) The principles of surface flux physics: theory, practice and description of the ECPACK library. (Internal Rep. 2004/1) Meteorology and Air Quality Group, Wageningen University, Wageningen

Veazey AL, Jeffries MO and Morris K (1994) Small-scale variability of physical properties and structural characteristics of Antarctic fast ice. *Ann. Glaciol.*, **20**, 61–66 (doi: 10.3189/172756494794586925)

Wilson CJL, Russell-Head DS and Sim HM (2003) The application of an automated fabric analyzer system to the textural evolution of folded ice layers in shear zones. *Ann. Glaciol.*, **37**, 7–17 (doi: 10.3189/172756403781815401)

Chapter 6

Publication III: Seasonal evolution of an ice-shelf influenced fast-ice regime, derived from an autonomous thermistor chain

By **Mario HOPPMANN**, Marcel NICOLAUS, Priska A. HUNKELER,
Petra HEIL, Lisa-Katharina BEHRENS, Gert KÖNIG-LANGLO
and Rüdiger GERDES

This paper is reprinted from the Journal of Geophysical Research: Oceans, with permission of the American Geophysical Union (Hoppmann et al., 2015a). My contribution to this paper is that I had the idea, coordinated and co-performed the field work, did all model experiments and lab work, analyzed and interpreted all data and did the main writing.

AGU PUBLICATIONS

JGR

Journal of Geophysical Research: Oceans

RESEARCH ARTICLE
10.1002/2014JC010327

Seasonal evolution of an ice-shelf influenced fast-ice regime, derived from an autonomous thermistor chain

M. Hoppmann[1], M. Nicolaus[1], P. A. Hunkeler[1], P. Heil[2,3], L.-K. Behrens[1], G. König-Langlo[1], and R. Gerdes[1]

[1]Alfred-Wegener-Institut Helmholtz-Zentrum für Polar-und Meeresforschung, Bremerhaven, Germany, [2]Australian Antarctic Division, Department of the Environment, Kingston, Tasmania, Australia, [3]Antarctic Climate and Ecosystems Cooperative Research Centre, University of Tasmania, Hobart, Tasmania, Australia

Key Points:
- Ocean/ice-shelf interaction dominates coastal sea-ice mass balance
- Basal energy balance reveals platelet layer ice-volume fraction of a fifth
- Thermistor chain heating is a suitable tool to study platelet-layer evolution

Correspondence to:
M. Hoppmann,
Mario.Hoppmann@awi.de

Citation:
Hoppmann, M., M. Nicolaus, P. A. Hunkeler, P. Heil, L.-K. Behrens, G. König-Langlo, and R. Gerdes (2015), Seasonal evolution of an ice-shelf influenced fast-ice regime, derived from an autonomous thermistor chain, *J. Geophys. Res. Oceans*, *120*, 1703–1724, doi:10.1002/2014JC010327.

Received 18 JUL 2014
Accepted 30 JAN 2015
Accepted article online 6 FEB 2015
Published online 19 MAR 2015

Abstract Ice shelves strongly interact with coastal Antarctic sea ice and the associated ecosystem by creating conditions favorable to the formation of a sub-ice platelet layer. The close investigation of this phenomenon and its seasonal evolution remains a challenge due to logistical constraints and a lack of suitable methodology. In this study, we characterize the seasonal cycle of Antarctic fast ice adjacent to the Ekström Ice Shelf in the eastern Weddell Sea. We used a thermistor chain with the additional ability to record the temperature response induced by cyclic heating of resistors embedded in the chain. Vertical sea-ice temperature and heating profiles obtained daily between November 2012 and February 2014 were analyzed to determine sea-ice and snow evolution, and to calculate the basal energy budget. The residual heat flux translated into an ice-volume fraction in the platelet layer of 0.18 $\pm$ 0.09, which we reproduced by a independent model simulation and agrees with earlier results. Manual drillings revealed an average annual platelet-layer thickness increase of at least 4 m, and an annual maximum thickness of 10 m beneath second-year sea ice. The oceanic contribution dominated the total sea-ice production during the study, effectively accounting for up to 70% of second-year sea-ice growth. In summer, an oceanic heat flux of 21 W m^{-2} led to a partial thinning of the platelet layer. Our results further show that the active heating method, in contrast to the acoustic sounding approach, is well suited to derive the fast-ice mass balance in regions influenced by ocean/ice-shelf interaction, as it allows subdiurnal monitoring of the platelet-layer thickness.

1. Introduction

Sea ice is a critical component in the global climate system, and an important marine habitat. Its influence ranges from the formation of polar deep water masses involved in the global thermohaline circulation [*Fahrbach et al.*, 2001], over the global radiation budget via albedo effects on the lower atmosphere [*Perovich et al.*, 2007] to the heat and light distribution in the water column [*Nicolaus et al.*, 2012]. In the Southern Ocean, sea ice spreads over millions of square kilometers at all times of the year. The Antarctic sea-ice cover has, on average, expanded since the late 1970s [*Parkinson and Cavalieri*, 2012], an evolution which is the sum of large regional differences whose drivers are currently only poorly understood. Proposed explanations include teleconnections of atmospheric circulation systems and changes in wind forcing [*Liu et al.*, 2004; *Lefebvre and Goosse*, 2008; *Simpkins et al.*, 2012; *Holland and Kwok*, 2012; *Li et al.*, 2014], increased precipitation [*Fichefet and Maqueda*, 1999; *Liu and Curry*, 2010], as well as atmosphere and ocean feedbacks [*Zhang*, 2007; *Stammerjohn et al.*, 2008]. Several other studies investigated the influence of an increased freshwater flux by enhanced melting of Antarctic ice shelves on sea-ice formation, but results remain inconclusive [*Swingedouw et al.*, 2008; *Bintanja et al.*, 2013, 2015; *Swart and Fyfe*, 2013]. In order to understand the complex interactions, much more insight into the relevant processes is needed.

The changing large-scale wind patterns almost exclusively affect the drifting pack ice, while sea ice attached to coastal features is often strongly influenced by nearby ice shelves [e.g., *Mahoney et al.*, 2011; *Smith et al.*, 2012]. This land-fast sea ice (fast ice) is an important interface between the Antarctic ice sheet and the pack ice or the ocean [*Massom et al.*, 2001] and constitutes between 5% and 35% of total sea-ice area during months of maximum and minimum total sea-ice area in East Antarctica [*Fraser et al.*, 2012], respectively. It is ideal to study in detail the processes which modify Antarctic sea-ice properties in general [*Heil et al.*, 2011].

AGU Journal of Geophysical Research: Oceans 10.1002/2014JC010327

Research on the physical properties of fast ice has largely been focusing on areas close to Antarctic bases, for example, at Lützow Holm Bay [*Kawamura et al*., 1997; *Ohshima et al*., 2000; *Uto et al*., 2006], Prydz Bay [*Heil*, 2006; *Tang et al*., 2007; *Lei et al*., 2010], and McMurdo Sound [*Jeffries et al*., 1993; *Purdie et al*., 2006; *Gough et al*., 2012].

Some of these locations exhibit characteristics that reflect a strong ocean/ice-shelf interaction, manifested through the presence of a sub-ice platelet layer. This special sea-ice type not only modifies the properties, mass and energy balance of an overlying solid sea-ice cover [*Hoppmann et al*., 2015], it also acts as a habitat for a substantial amount of algal biomass [*Arrigo et al*., 1993; *Günther and Dieckmann*, 1999, 2001], provides a protective environment for coastal fish species [*Vacchi et al*., 2000], and might also allow conclusions about processes in the ice-shelf cavity. While the formation mechanisms of ice crystals in supercooled waters are in principle understood [*Mager et al*., 2013], little is known about the spatiotemporal variability of sub-ice platelet layers in Antarctica. Despite their importance for the climate and ecosystem, a means to effectively monitor Antarctic platelet layers remains a challenge due to the lack of suitable methodology. A promising approach to determine its spatial variability is the application of (ground-based) multi-frequency EM induction sounding [*Hunkeler et al*., 2015]. However, no method is currently available to provide information about its temporal evolution without the need for extensive logistics.

Providing a relatively inexpensive alternative to field campaigns, autonomous Ice Mass Balance Buoys (IMBs) have been widely used in recent years to monitor the sea-ice mass balance at a fixed study site [*Perovich and Elder*, 2001]. Typical IMBs are equipped with a thermistor chain extending through the snow and sea-ice cover into the upper ocean, as well as with acoustic sensors monitoring the position of the ice/water and air/snow (air/ice) interfaces [*Richter-Menge et al*., 2006]. They usually also record GPS position, sea level pressure and 2 m air temperature. If combined, these data not only reveal changes in the sea-ice mass balance due to ice growth, surface melt, and bottom ablation, they also provide valuable information about the snow cover. In a next step, the observed changes can be correlated with variables associated with the external drivers, such as the beginning and duration of the summer melt season, the length of the growth season, and the oceanic heat flux. By doing so, one is not only able to obtain information about the state of the sea-ice cover, but also to gain important insight into the driving forces behind the ongoing changes. However, these instruments are usually expensive and take a substantial effort to deploy.

Recently, a promising new type of thermistor chain IMB has been developed [*Jackson et al*., 2013], which is significantly lower in cost than comparable instruments and very easy to deploy. A special feature of this design is the ability to actively heat embedded resistors near the temperature sensors, which is described in more detail below. Despite the growing demand and application of this buoy type, no consistent data set has been published to date and the instrument's full potential is still to be determined.

In this study, we analyzed data from such a thermistor chain, in order to determine the physical properties of an ice-shelf influenced sea-ice cover and its seasonal evolution. The instrument was operated on the fast ice of Atka Bay, eastern Weddell Sea, between November 2012 and February 2014. These measurements were combined with continuous meteorological and oceanographic data, as well as manual thickness measurements and model simulations, in order to quantify the processes governing sea-ice mass balance, and to characterize their seasonality. At the same time, we assessed the potential of this relatively new instrument design on the basis of this unique data set, highlighting its advantages and pointing out its caveats to assist the interpretation of such data sets in future studies.

2. Methods

2.1. Field Setting

This study was conducted on the generally first-year fast ice of Atka Bay, a sheltered embayment adjacent to the Ekström Ice Shelf (Figure 1). The geographic setting is described in more detail in *Hoppmann et al*. [2015] and references therein. A large iceberg (B15G) grounded in front of Atka Bay in September 2012 (Figure 1b, dashed red curve), which sheltered the fast ice and prevented a breakup in early 2013. The fast ice survived the summer and became thick second-year sea ice in 2013. The iceberg dislodged itself in August 2013 and drifted away westward with the coastal current. Between 9 and 16 February 2014, approximately two-thirds of the fast-ice area finally disintegrated into small floes, marking the end of our study (Figure 1c).

AGU Journal of Geophysical Research: Oceans 10.1002/2014JC010327

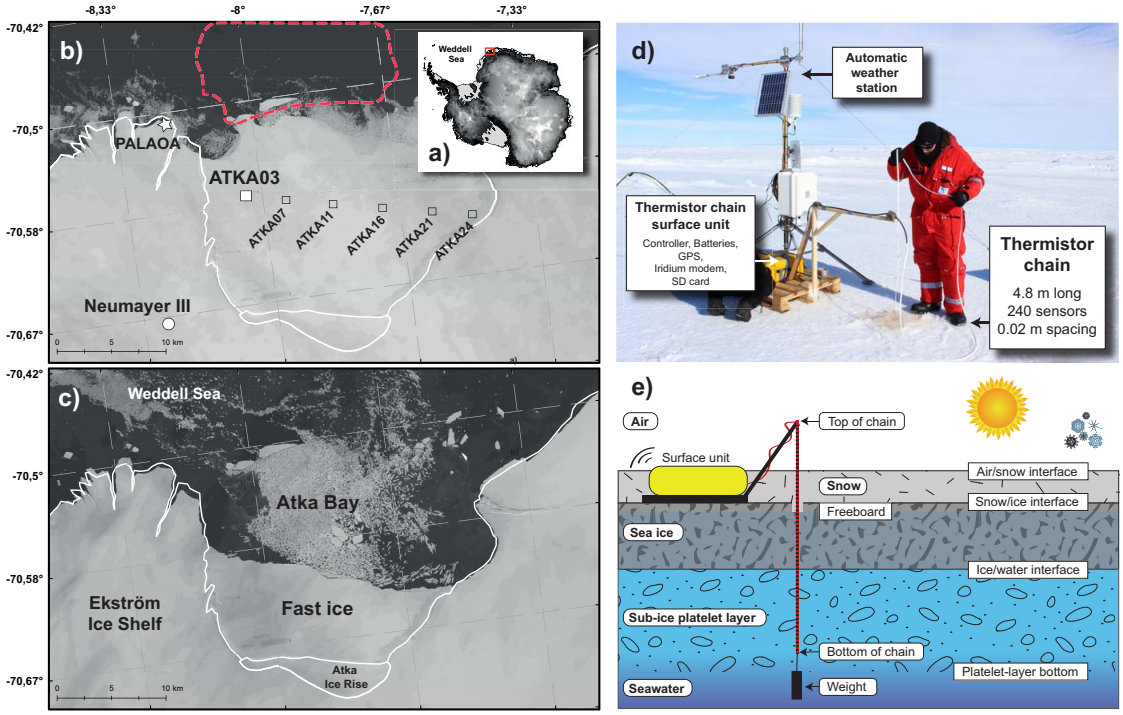

Figure 1. Study area and thermistor chain deployment. (a) Location of this study on a map of Antarctica. (b) Landsat image of Atka Bay at the beginning of the fast-ice breakup (9 February 2014). The main sampling site was located 3 km east of the western ice-shelf edge (ATKA03, white square). Auxiliary study sites are also indicated (squares), along with the former position of grounded iceberg B15G (dashed red curve). (c) Landsat image from 16 February 2014, when 2/3 of the sea ice has broken up. Landsat imagery courtesy of NASA Goddard Space Flight Center and U.S. Geological Survey, coastline data from Antarctic Digital Database 6.0. (d) Photo of thermistor chain deployment (21 November 2012). (e) Schematic diagram of thermistor chain extending through air, snow, sea ice, and the sub-ice platelet layer.

2.2. Thermistor Chains

On 21 November 2012, we deployed a thermistor chain (Scottish Association for Marine Science, Oban, Scotland) approximately 3 km from the Ekström Ice Shelf (Figure 1b). This location is a regular site of an ongoing sea-ice monitoring program, mainly chosen for logistical reasons. It was within an area of moderately deformed sea ice, which initially formed in March/April 2012. For consistency with other studies [*Hoppmann et al.*, 2015; *Paul et al.*, 2015; *Hunkeler et al.*, 2015], we refer to this site as ATKA03.

The vertical thermistor chain (TC) was installed on level sea ice, through a 0.05 m diameter borehole (Figure 1d). It consisted of 240 thermistors at a spacing of 0.02 m, with a total length of 4.8 m. To prevent the chain from floating upward in the platelet layer, we attached a weight of 3 kg to the end of the chain. The hole did not refreeze all the way up to the original snow/ice interface due to the large positive freeboard, so it was filled up with snow after deployment. For our analysis we neglect this effect, and define the original snow/ice interface as our reference snow/ice interface.

The surface unit was placed onto a wooden rack for stability, with a side arm to guide the chain (Figure 1e). The temperature sensors (Maxim DS28EA00) have a resolution of 0.0625°C, and a worst-case accuracy of ±2°C [*Jackson et al.*, 2013]. We did not calibrate the chain, as the temperature sensors are offset-corrected by the manufacturer in a precision temperature-controlled water bath at 1°C. Sensor drift is considered low. The unique feature of this design is the operation similar to a combination of constant-current hot-wire anemometer and needle-probe thermal conductivity mode: after each regular temperature reading, embedded resistors (1 kΩ) near the temperature sensors are heated to above ambient temperature with an excitation voltage of 8 V, generating 63 mW of thermal energy. Heat is conducted away from the thermistors at a rate dependent on the

AGU Journal of Geophysical Research: Oceans 10.1002/2014JC010327

temperature gradient, the thermal conductivity of the surrounding medium and its flow rate, if liquid. Needle-probe thermal conductivity measurements were previously in snow research [*Sturm and Johnson*, 1992; *Riche and Schneebeli*, 2013], while hot-wire anemometry is a standard technique of experimental fluid dynamics and has been described, for example, by *La Barbara and Vogel* [1976] and *Perry* [1982]. Generally, a greater temperature rise is expected in air and snow than in water and ice due to their lower thermal conductivities. Since ice and water thermal conductivities lie very close together, the additional cooling introduced by a nonzero flow velocity in water may counteract the seawater's slightly lower thermal conductivity, potentially leading to difficulties in the determination of an ice/water interface. A quantitative relationship between the temperature response of this instrument and the thermal conductivity or flow speed of a medium has not been found yet, mostly due to the complex geometry, and this is also beyond the scope of this study. However, we will investigate in detail how well the instrument is suited to accurately determine the location of the interfaces between air, snow, ice, and water under field conditions. A full description of the TC and the "heating mode" is available in *Jackson et al.* [2013].

In our study, the heating duration and duty cycle were 120 s and 100% (of 63 mW), respectively, while the temperature rise was recorded after 30 s and 120 s. This configuration represents the default setting, recommended by *Jackson et al.* [2013] to provide a clear separation between the different media without reaching saturation. The temperature difference after 30 s of heating is referred to as "30 s heating" or δT_{30} throughout this paper. The temperature difference after 120 s of heating is referred to as "120 s heating" or δT_{120}, accordingly.

Upon deployment, snow depth, freeboard, and sea-ice thickness at ATKA03 were 0.01 m, 0.40 $\pm$ 0.05 m, and 2.45 $\pm$ 0.05 m, respectively. Determination of freeboard was difficult due to ice platelets clogging the borehole. The high initial thickness was the result of early formation and additional thickening due to floe-rafting. Sub-ice platelet-layer thickness was 4 m, with several interfaces of varying mechanical resistance within the layer. Due to its deployment late in the growth season, the chain did not extend below the platelet layer. In the first 3 weeks, the TC was configured to record the data every 6 h. It was reconfigured to hourly measurements on 11 December 2012. During February 2013, the sea ice became nearly isothermal. To save energy, the measurement interval was set to twice a day from February 2013. The batteries were changed on 28 April 2013 and again on 5 January 2014, to prepare for a potential sea-ice breakup and subsequent drift into the central Weddell Sea. However, the instrument ceased operation during sea-ice disintegration on 9 February 2014 (Figure 1b).

Due to the variable measurement intervals, the data were interpolated to a daily grid. The thermistor numbers were converted to depth, with the original snow/ice interface as the zero reference. Data from one broken sensor were removed. Erroneous thermistor readings, appearing as spikes in the temperature profiles, occurred sporadically (about 200 instances), and were removed manually. Spikes in the heating data were removed automatically, and the missing data points were linearly interpolated. Air/snow/ice interfaces were extracted automatically from temperature and heating profiles. The algorithms are not supplied because they were specifically tuned to this data set. The ice/water interface was determined by visual inspection to ensure the highest possible quality.

The temperature profiles and the interfaces extracted from heating profiles were used to calculate the sea-ice basal energy balance. Sea-ice growth, which is essentially a phase change at the ice bottom (latent heat flux, F_l), is a function of the conductive heat transfer through the sea ice to the air (F_c), the specific heat flux due to internal warming or cooling (F_s), and the oceanic heat flux (F_w). Following the approach of *Gough et al.* [2012], we calculated the oceanic heat flux F_w by a residual method [*McPhee and Untersteiner*, 1982; *Purdie et al.*, 2006] as

$$F_w = F_c + F_l + F_s. \tag{1}$$

We calculated the conductive, latent, and sensible heat fluxes after *Semtner* [1976]:

$$F_c = k_{si} \cdot \frac{\partial T}{\partial z}, \tag{2}$$

$$F_l = \rho_{si} \cdot L_f \cdot \frac{\partial H}{\partial t}, \tag{3}$$

AGU Journal of Geophysical Research: Oceans 10.1002/2014JC010327

$$F_s = -\rho_{si} \cdot c_{si} \cdot \frac{\partial T}{\partial t} \cdot \Delta H, \quad (4)$$

where the thermal conductivity k_{si} (ρ, S, T) is given by *Pringle et al*. [2007], $\frac{\partial T}{\partial z}$ is the sea-ice temperature gradient, z is the vertical coordinate, ρ_{si} is sea-ice density, L_f (S, T) is the sea-ice latent heat of fusion given by *Yen* [1981] with a typographical error corrected as described by *Pringle et al*. [2007], $\frac{\partial H}{\partial t}$ is the sea-ice growth rate, c_{si} (S, T) is the specific heat capacity [*Yen*, 1981], $\frac{\partial T}{\partial t}$ is the temporal gradient in sea-ice temperature, and H is the position of the ice/water interface. The latent heat L_f (S, T) and the specific heat of sea ice c_{si} (S, T) are functions of its temperature and salinity according to *Untersteiner* [1961] and *Yen et al*. [1991]. Upward heat fluxes, warming and melting have positive sign, and z decreases from zero at the sea-ice surface. The energy balance has to be solved for a near-bottom reference level z_r, through which heat transport by brine convection is unlikely to contribute significantly [*Gough et al*., 2012]. A stable bulk salinity may provide the necessary indication for this [*Petrich et al*., 2006]. The selection of the reference level is critical for the calculation of F_c due to the nonlinearity of the vertical sea-ice temperature profile. A variety of reference levels have been used in the literature, most recently summarized by *Lei et al*. [2014]. *Gough et al*. [2012] defined the reference layer at 0.15 m above the ice/water interface, in a study comparable to ours. Based on the latter study and in agreement with our salinity measurements from the sea-ice core near ATKA03 (Figure 3), we used a reference level of 0.16 m from the ice/water interface for which we calculated the energy balance. The position of the ice/water interface H and also its change with time $\frac{\partial H}{\partial t}$ were derived from the heating profiles with an uncertainty of $\pm$0.02 m. The reference level always followed the ice/water interface by $z_r = H + 0.16$ m. The temperature gradient $\frac{dT}{dz}$ across the reference level is obtained by a linear fit to all thermistors within $\pm$0.14 m of z_r. $\frac{dT}{dt}$ is determined from the temperature T at the same level in neighboring time steps. Salinity is taken near z_r from the interpolated profile in Figure 3. We assumed ρ_{si} is 910 kg m^{-3} throughout, which is near the top of the range for multiyear sea ice reviewed by *Timco and Frederking* [1996]. This is slightly higher than the density measured from a sea-ice core in December 2012, where brine loss occurred during the measurement. The sea-ice growth rate was calculated as the temporal change in the evolution of the ice/water interface, derived from the δT_{120} data. The interface had previously been smoothed to remove the discrete steps originating from the thermistor spacing.

In order to assess the instrument's ability to detect the presence of a sub-ice platelet layer, we compared our main data set to a similar one obtained by a thermistor chain of the same type, deployed in the Weddell Sea during Polarstern cruise ANT-XXIX/9. This IMB was installed on a platelet-free floe at 74°23.340′S, 33°24.012′W on 5 February 2014.

2.3. Automatic Weather Station

We twice deployed an automatic weather station (AWS) at ATKA03. First, it was operated from 2 October to 27 December 2012, but only data since the deployment of the TC (21 November 2012) are shown here. The AWS was recovered to avoid instrument loss due to a weakening of the fast-ice cover in late summer. Second, we deployed the same setup again a few meters from the thermistor chain on 31 May 2013. Measurements comprised air temperature and relative humidity (shielded HMP155A, Vaisala), barometric pressure (61302V, RM Young Company), wind speed and direction (Marine Wind Monitor 05106-5, RM Young Company) as well as downward and upward longwave and shortwave radiation (CNR4, Kipp and Zonen) in 2 m height at 1 min intervals. We also recorded snow height using an acoustic sounder (SR50A, Campbell Scientific) as an independent measurement to compare to snow depth derived from TC temperature and heating profiles. Finally, the AWS data were combined with data obtained at the meteorological observatory of Neumayer III [*König-Langlo and Loose*, 2007] to generate a consistent forcing for a thermodynamic sea-ice growth model [*Bitz and Lipscomb*, 1999; *Hoppmann et al*., 2015].

2.4. Oceanographic Data

We used oceanographic data from the Perennial Acoustic Observatory in the Antarctic Ocean (PALAOA) [*Boebel et al*., 2006]. An unpumped Sea-Bird Electronics (SBE) 37 MicroCAT was installed in the water column at a depth of about 155 m, 70 m below the ice shelf bottom and 90 m above the sea floor, in 2006. Since then, PALAOA was gradually transported closer to the ice-shelf edge due to the flowing glacier, and an end of its operation is expected in 2015. The instrument continuously records conductivity, temperature, and pressure at 30 min intervals, with an accuracy of $\pm$0.0003 S m^{-1}, $\pm$0.002°C, and $\pm$0.5 m, respectively.

AGU Journal of Geophysical Research: Oceans 10.1002/2014JC010327

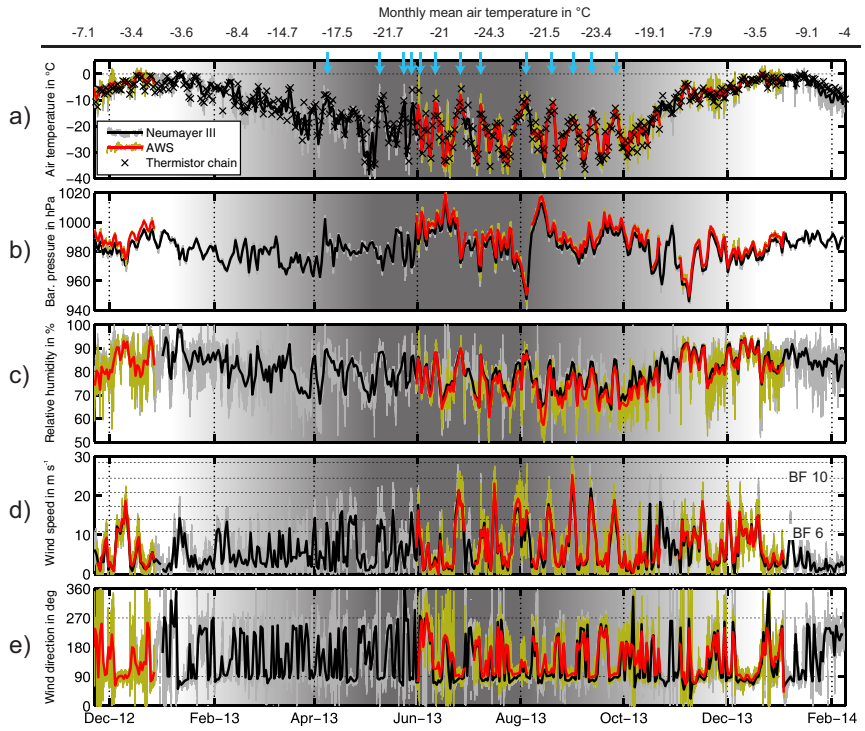

Figure 2. Meteorological conditions during the study period, as measured by the automatic weather station (red/green) and at Neumayer III (black/gray). Thin curves represent the measurements every minute, thick curves are daily averages. (a) Air temperature (2 m); (b) barometric pressure; (c) relative humidity; (d) wind speed (BF: Beaufort) and (e) wind direction. The blue arrows indicate the passage of synoptic systems in winter, associated with an advection of warm air, lower barometric pressure, high relative humidity, and strong easterly winds. The shaded area illustrates the annual cycle of polar day and night.

The distance to ATKA03 was ∼10 km in 2012/2013 (Figure 1b). The data set was checked for consistency and it can safely be assumed that the recordings were not affected by ice accretion on the instrument due to the presence of supercooled water. From the measurements, we calculated absolute salinity, potential temperature, and the surface freezing point using the Gibbs Seawater (GSW) Oceanographic Toolbox [*McDougall and Barker*, 2011].

2.5. Sea-Ice Cores

Two full-thickness, 0.09 m diameter cores to determine sea-ice physical properties were retrieved at ATKA03 on 19 and 27 December 2013. We measured in situ temperatures in the core from 19 December in 0.1 m intervals, using a hand-held thermometer inserted into 2 mm holes drilled to the center of the core. The core was packed in a styrofoam box, temporarily stored at Neumayer III, and later transported to Bremerhaven at −20°C in order to perform a texture analysis. We drilled another core on 27 December, which was segmented into 0.1 m pieces on a bench immediately after being brought to the surface. The porosity of the segments was high and brine drainage could not be prevented. The segments were sealed in plastic boxes and transported to the laboratory. The density of each segment was calculated using a mass/volume approach [*Timco and Frederking*, 1996]. The segments were melted at a temperature of 4°C to minimize cell damage to algae present in the sea ice. Salinity was determined using a calibrated conductivity meter (WTW Cond3110). The samples were filtered and Chlorophyll-a was measured by a fluorometric method [*Welschmeyer*, 1994]. We used the sea-ice temperature, salinity, and density profiles to calculate brine and gas volume fractions according to *Leppäranta and Manninen* [1988]. Horizontal and vertical thin sections of the archived core were prepared and photographed between crossed polarizers.

AGU Journal of Geophysical Research: Oceans 10.1002/2014JC010327

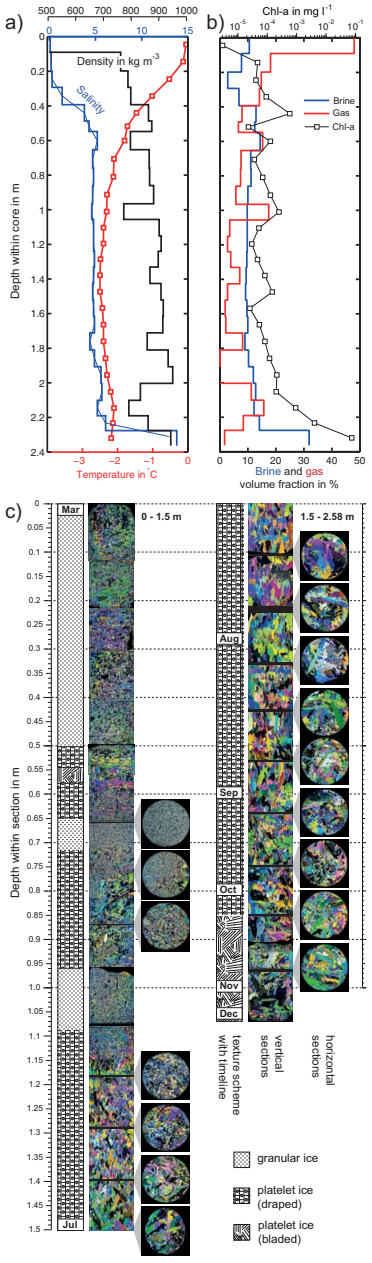

Figure 3. Sea-ice properties from cores retrieved at ATKA03 in December 2012. (a) Temperature (red), salinity (blue), and density profiles (black). The thin blue curve represents an interpolated salinity profile. (b) Brine (blue) and gas volume fractions (red), and Chlorophyll-a content (black). (c) Horizontal and vertical thin sections, photographed between crossed polarizers. The texture scheme to the left of the respective vertical thin sections was derived by visual inspection. The formation time in 2012 was determined by comparison to sea-ice thickness measurements (see text).

2.6. Drillings

Since the 4.8 m long thermistor chain did not extend through the entire platelet layer, the temperature and heating data shown here do not allow unambiguous conclusions about the evolution of its thickness. In order to reveal the platelet-layer's spatiotemporal evolution across the entire Atka Bay, we provide additional platelet-layer thickness data obtained by manual drillings at different sites throughout the study. One measurement was performed per site and visit. We thereby expand the study of *Hoppmann et al.* [2015], who described the platelet-layer evolution under first-year fast ice, to second-year fast ice.

2.7. Sea-Ice Growth Simulation

We simulated fast-ice growth by a one-dimensional, thermodynamic model [*Bitz and Lipscomb*, 1999] forced with local atmospheric data, and with snow depth derived from TC temperature profiles. We modified the original sea-ice growth rate $\frac{\partial H}{\partial t}$ in the model by

$$\frac{\partial H}{\partial t}(\beta) = \frac{1}{1-\beta} \cdot \frac{\partial H}{\partial t}, \tag{5}$$

where β is the fraction of solid ice mass in a defined volume in the platelet layer (ice-volume fraction).

The initial setup and preparation of the forcing data were performed as described by *Hoppmann et al.* [2015], with corrections applied to air temperature (+0.5°C), relative humidity (−2%), barometric pressure (+4.1 hPa), and upward longwave radiation (+6.5 W m^{-2}) to account for the different meteorological conditions on the sea ice compared to Neumayer III on the ice shelf (see Figure 2).

3. Results

This section is structured as follows: first, we highlight the environmental conditions during the study period, then we present results from our sea-ice core analysis. We investigate our main data set, thermistor chain temperature and heating profiles, and use these to calculate the basal energy balance. We then determine sea-ice growth from conductive heat flux alone and compare our observations to simulated fast-ice growth. Finally, we complement the results of our main data set with results of manual sub-ice platelet-layer thickness measurements and oceanographic conditions.

AGU Journal of Geophysical Research: Oceans 10.1002/2014JC010327

3.1. Environmental Conditions

Between TC deployment and mid-December 2012, the 2 m air temperature remained below the freezing point (Figure 2a). On 17 December, daily average temperatures rose above the freezing point for four consecutive days, before steadily decreasing until April 2013. During late autumn and winter, the air temperature fluctuated widely. Sudden changes in daily average air temperatures in excess of 20 K were recorded over 2 or 3 days. The overall minimum daily mean temperature of -38.5°C was measured on 3 May 2013. Temperatures stabilized in early spring, and increased again from October 2013.

Storm activities, accompanied by increased wind speed and warm air advection, occurred about twice a month during the entire study, and about once per week during winter (Figure 2d). Those events were always associated with easterly winds (Figure 2e). These observations are in accordance with the general climatology of Neumayer III [*König-Langlo et al.*, 1998].

3.2. Sea-Ice Cores

The sea-ice core recovered at ATKA03 on 19 December 2012 was 2.58 m long. There was no snow, freeboard was about 0.4 m, and the platelet-layer thickness was about 4 m. The core obtained on 27 December 2012 was 2.4 m long, without any snow on top. The platelet-layer thickness was 4.2 m, and freeboard was not recorded.

Temperatures were near-isothermal below 0.65 m, and above -2.5°C throughout the entire sea-ice core (Figure 3a). Salinity ranged from 0 at the surface to 13.8 in the skeletal layer at the bottom, with an overall average of 4.54. Sea-ice density was on average 850 kg m^{-3}, with a minimum of 490 kg m^{-3} near the top. This measurement underestimated the real density by up to 10% due to imprecise sawing, missing ice pieces, and especially brine loss at these high temperatures. For our calculation of air-volume fraction, we therefore used a sea-ice density of 910 kg m^{-3}. Air volume fraction was on average 9%, and highest at the top of the core ($>$40%), which is explained by surface melt and brine drainage. The brine volume fraction was on average 11%, with the usually observed maximum in the skeletal layer of 35%.

The crystal structure (Figure 3c) was classified by visual inspection of thin sections from the sea-ice core, acknowledging that this interpretation may be subjective. Fine-grained crystals and air inclusions were evident in the upper 0.5 m of the core. While crystal edges in the upper layer had largely eroded, these crystals mostly resembled typical granular new ice formed under turbulent conditions. In the next 0.15 m, the texture showed distinct, albeit randomly oriented frazil crystals. We refer to this texture as platelet ice [*Eicken and Lange*, 1989; *Jeffries et al.*, 1993; *Tison et al.*, 2013; *Dempsey et al.*, 2010], with a crystal structure unlike that of granular or columnar ice [*Dempsey et al.*, 2010]. Multiple rafting was indicated by fine-grained crystals, typical of snow ice (0.66–0.71 m), followed by platelet ice, and again by granular ice near 1 m. Below 1.15 m, larger crystals of draped platelet ice [*Tison et al.*, 2013; *Dempsey et al.*, 2010], also sometimes referred to as mixed columnar/platelet ice [*Mahoney et al.*, 2011] were apparent throughout a large part of the core length. Below 2.35 m, the shape of the platelets became blade-like [*Eicken and Lange*, 1989; *Tison et al.*, 2013; *Dempsey et al.*, 2010]. The growth history of the sea ice was determined by comparison to thickness measurements made at ATKA03 throughout 2012 [*Hoppmann et al.*, 2015]. These measurements started in mid-June, when the sea ice was already about 1.4 m thick. Rafting seemed to have occurred until May. Continuous thermodynamic growth set in afterward (at approximately 1.15 m), and was immediately disrupted by the presence of platelets. In summary, about 25% of the core consisted of granular ice (and eventually snow ice), the other 75% of platelet ice. A pure columnar texture was not observed.

3.3. Temperature and Heating Profiles

Figure 4 presents the main data set of this study, comprising (a) temperature, (b) δT_{30}, and (c) δT_{120} measurements obtained by the TC between 21 November 2012 and 9 February 2014, interpolated to daily profiles. The prominent vertical structures in Figures 4b and 4c were a result of a drop in voltage applied to the resistors during heating.

In the following, we will try to uncover the variety of information hidden in these data: the temporal evolution of (1) the snow cover, (2) the snow/ice interface (including surface melt); (3) the ice/water interface (sea-ice growth); (4) the presence of internal melt and refreezing; (5) sub-ice platelet-layer thickness; (6) conductive heat flux; and finally (7) the basal energy balance including the calculation of a residual (oceanic) heat flux. The effect of solar radiation penetrating into the snow and potentially leading to a warming of the upper thermistors is neglected throughout this paper.

AGU Journal of Geophysical Research: Oceans 10.1002/2014JC010327

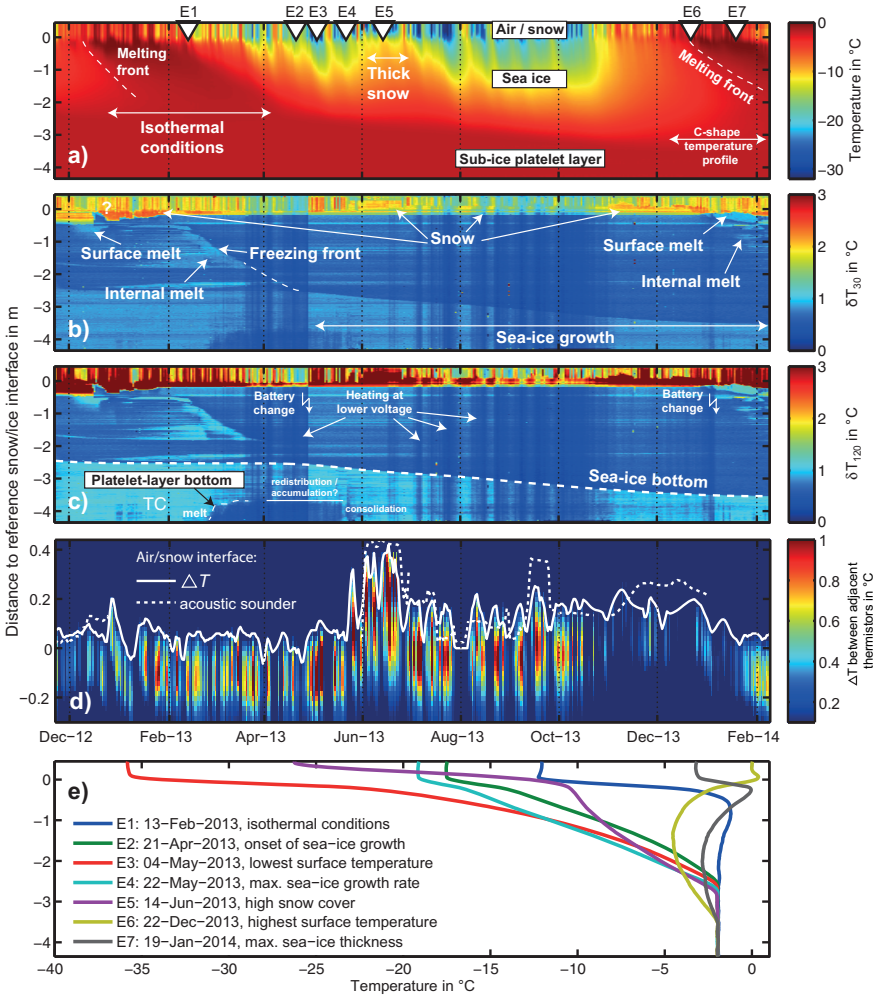

Figure 4. Data measured by the thermistor chain during the study period. (a) Daily temperature profiles; (b) temperature rise after 30 s heating (δT_{30}); (c) temperature rise after 120 s heating (δT_{120}); (d) snow surface retrieved from temperature difference between adjacent upper thermistors (ΔT, solid curve) and acoustic sounding (dashed curve); (e) selected temperature profiles under different environmental conditions at times indicated in (a).

3.4. Snow Depth

Comparison of snow depths derived from temperature differences between adjacent thermistors (ΔT) in the upper part of the chain with those determined from the AWS acoustic sounder revealed generally similar patterns and features, despite the high snow-depth variability (Figure 4d). The large temperature differences in the top 0.2–0.3 m of the sea ice originated from the lack of refreezing in the part of the deployment hole above the sea surface. Snow depth was on average 0.14 ± 0.09 m throughout the study. June exhibited by far the thickest snow cover, 0.31 ± 0.11 m, with a maximum of 0.42 m. Snow depth before June was 0.08 ± 0.05 m and 0.16 ± 0.06 m afterward.

3.5. Snow/Ice Interface

The evolution of the snow/ice interface was best identified from the δT_{30} and δT_{120} profiles (Figures 4b and 4c). It was characterized by a high temperature difference of up to 2°C between adjacent thermistors in the

AGU Journal of Geophysical Research: Oceans 10.1002/2014JC010327

Table 1. Monthly Average Residual Heat Flux (F_w) in W m^{-2} and Sea-Ice Thickness Increased (Δz_{si}) in mm During the Study

	2012		2013												2014		
Monthly average	Nov	Dec	Jan	Feb	Mar	Apr	May	Jun	Jul	Aug	Sep	Oct	Nov	Dec	Jan	Feb	Σ
Mean	−2.26	−0.74	0.63	−0.01	−0.40	−0.28	−2.31	−1.81	−1.61	−2.01	−1.02	−0.68	−1.13	−2.04	−0.60	0.97	
Std	0.44	1.45	0.30	0.13	0.07	0.32	1.11	0.64	0.45	0.68	0.57	0.84	0.83	0.48	0.81	0.09	
Δz_{si} in mm	20	46	5	1.2	4.4	49	147	113	101	140	132	123	95	74	32	0.01	1080
% due to F_w	36	21				7	21	20	21	19	10	7	15	36	24		18

δT_{120} data. This originated from the difference in thermal conductivity between snow and sea ice, which was about one order of magnitude. This interface was variable in height, differing by up to 0.3 m throughout the study. This was most likely again a consequence of the limited refreezing of the deployment hole, and does not reflect natural processes. However, the δT_{30} and δT_{120} profiles exhibited some interesting features near the snow/ice interface. During summer 2012/2013 and more pronounced in 2013/2014, areas with thermal characteristics that resemble the lower thermistors were apparent. It is likely that these were manifestations of meltwater formation and refreezing at the surface. Please note that the changing snow/ice interface described here is different from the reference snow/ice interface, which was assumed as constant for the calculation of snow depth and sea-ice thickness in this paper.

3.6. Ice/Water Interface

Isothermal conditions in the sea ice and the sub-ice platelet layer dominated the temperature profiles from January to May 2013, more than 1/3 of the year (Figure 4a). Under these circumstances, a determination of the ice/water interface from temperature measurements alone was impossible. However, the evolution of the ice/water interface was most pronounced in the δT_{120} profiles (Figure 4c, dashed white curve). For all further calculations in this study, we used an ice/water interface manually derived from the δT_{120} profiles. The resulting interface was additionally smoothed by a 10 day running mean to overcome the discrete distance between adjacent thermistors. During the study, the sea-ice thickness increased by 1.1 m, from 2.44 to 3.54 m. 0.1 m of this growth occurred between mid-November and mid-December 2012, when growth ceased for approximately 4 months. The remaining 1 m of growth occurred between mid-April 2013 and early January 2014. The average growth rate was 0.0024 ± 0.0017 m d^{-1} over the entire study, and 0.0033 ± 0.0011 m d^{-1} over the growth season only. The monthly sea-ice thickness increase is shown in Table 1.

3.7. Internal Melt and Refreezing

Several areas are present within the sea ice that exhibited a slightly higher δT_{30} and δT_{120} than the surrounding sea ice (Figures 4b and 4c, lighter blue). Due to the limited precision of the thermistors, these are difficult to identify. They are most likely indications of a phase transition from solid sea ice into the liquid phase, indicating internal melt. These structures were then altered by the advancing freezing front, which subsequently increased the solid fraction in the interior. This transition started approximately 0.5 m below the zero reference in February 2013. Shortly before April 2013, it was masked by the sea ice below, probably due to decreased melt in lower layers, leading to a reduction in the contrast. However, an artificial freezing front can be set to the bottom of the sea ice, marking the onset of active basal growth at the end of April 2013 (Figure 4b, dashed curve). Minor instances of different thermal characteristics inside the upper sea-ice layer were also apparent from January 2014, marking again the beginning of internal melt. Note that the freezing front (in contrast to the ice/water interface) may also be inferred from the temperature profiles (Figure 4a), by below-freezing temperatures which advanced through the sea-ice cover between February and April 2013.

3.8. Sub-ice Platelet Layer

TC-derived temperatures of the sub-ice platelet layer remained slightly below the freezing point throughout the study. Compared to simultaneous temperature measurements taken with a CTD75M (Sea and Sun Technology) in or near the platelet layer, thermistor temperatures were always lower. This is due to the thermistor's limited resolution causing a low signal-noise ratio given the very small temperature differences found in the seawater/platelet mixture. In order to interpret the heating data in the sub-ice platelet layer of Atka Bay (AB), it is useful to compare our results to measurements by an identical instrument in a sea-ice regime

AGU Journal of Geophysical Research: Oceans 10.1002/2014JC010327

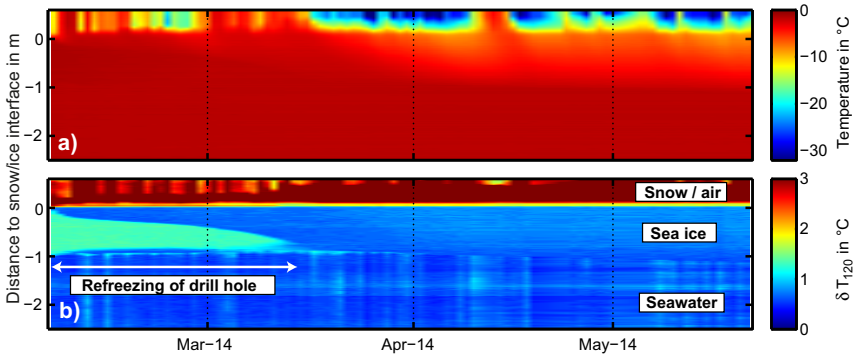

Figure 5. (a) Temperature and (b) δT_{120} profiles from a drifting thermistor chain in the central Weddell Sea.

without a platelet layer. Therefore, we chose to include a data set recorded in the central Weddell Sea (WS) in 2014 (Figure 5). It is immediately evident that the δT_{120} of sub-sea-ice thermistors at AB was ~0.5°C higher than in the WS, which is nearly 10 times the stated precision. Between February and May 2013, this difference partly vanished in the lowermost thermistors. This could be an indication of either the presence of flowing seawater, or sea ice temporarily attaching itself to the chain. We will discuss this in greater detail later.

When closely investigated, the WS data set exhibits another striking feature. When a thermistor chain is installed, it usually takes a while for the hole to refreeze entirely, especially under warmer conditions. Such a refreezing front is clearly visible in the heating data depicted in Figure 5b. At the same time, the thermistors located in the deployment hole obviously detected different thermal characteristics than those in the ocean below, again reflecting the sensitivity of this approach to the flow velocity of a medium.

3.9. Conductive Heat Flux

Bulk conductive heat flux F_c was estimated for layers of 0.2 m thickness through the entire sea-ice cover according to equation (2). For the calculation of k_{si} (ρ, S, T), we used a smoothed salinity profile based on Figure 3 and a sea-ice density of 910 kg m^{-3}. The average conductive heat flux was calculated between the actual snow/ice interface and the ice/water interface (Figure 6a).

The conductive heat flux near the snow/ice interface showed typical short-term fluctuations as a response to the rapid changes in the synoptic-scale atmospheric forcing, particularly air temperature. The absolute magnitude of F_c as well as the gradient generally decreased between upper and lower layers. The bottom layer lagged the induced variations in the upper sea-ice layer, which is most pronounced (up to 2 months) in autumn and spring. Apart from the expectedly low conductive heat flux in summer, several local minima also occurred during winter. These were especially apparent between August and October 2014, and are linked to relatively warm surface air advected to the site by passing synoptic systems (Figure 2). Another local minimum was observed during June 2013, lasting for more than 1 month. This was associated with a local maximum of snow cover (up to 0.4 m) described above. In contrast to the passage of the synoptic systems, this change of snow conditions also strongly affected the lower sea-ice layers.

Average F_c was low at the beginning of the study. Between December 2012 and February 2013, the temporal lag of warming in the sea-ice interior resulted in vertical temperature inversions and a subsequent negative F_c. This is a reflection of thermal energy transported into the sea-ice interior, downward at the top and upward at the base, leading to internal sea-ice warming and eventually also melt as described by *Lei et al.* [2014]. This condition was also observed between late December 2013 and February 2014. Typical vertical temperature inversion profiles are shown in Figure 4e (E1, E6, and E7). The average F_c increased gradually during atmospheric cooling in the transition from summer to winter (Figure 6b), reaching its absolute

AGU Journal of Geophysical Research: Oceans 10.1002/2014JC010327

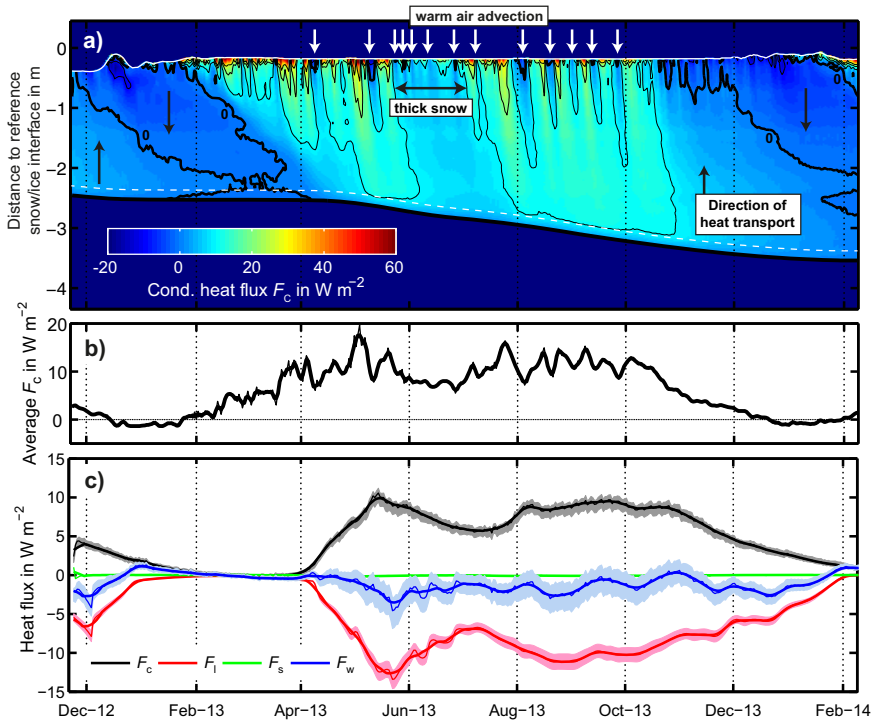

Figure 6. (a) Conductive heat flux through sea ice with contours at −20, −10, 0 (thick black curve), 10 and 20 W m^{-2}. Due to snow in the drill hole, the part between the reference snow/ice interface (zero) and the true snow/ice interface (solid white curve) was omitted. The white arrows correspond to the synoptic systems shown in Figure 2. (b) Average vertical conductive heat flux between the snow/ice interface and the ice/water interface. (c) Daily heat fluxes (thin curves) through a reference layer near the sea-ice base (dashed white curve in Figure 6a). The thick curves represent the 5 day running mean. F_c is the heat conducted upward through the reference layer, F_l is the latent heat required to form the thickness of sea ice added, F_s is the sensible heat flux which accounts for a temperature change in the reference layer, and F_w is the residual heat flux. The shaded areas represent the cumulative individual measurement uncertainties. Upward heat fluxes, warming and melting have a positive sign.

maximum of approximately 20 W m^{-2} in early May 2013. It then fluctuated around 10 W m^{-2}, until atmospheric warming from October 2013 as well as the increased sea-ice thickness again led to a gradual decrease.

3.10. Basal Energy Balance

In the basal energy balance (Figure 6c), upward heat fluxes, warming and melting have a positive sign, and shaded areas represent the overall uncertainties described below. The conductive heat flux through the reference layer (F_c, black) showed a similar pattern, although smoothed, to the vertically averaged conductive heat flux described above. The temperature change in the reference layer (F_s, green) was negligible. The (latent) heat removed to grow sea ice (F_l, red) roughly followed, but at the same time, exceeded the amount of heat conducted upward to the atmosphere and thus allowed for sea-ice thermodynamic growth. This resulted in a negative residual heat flux (F_w, blue) between −5 and 0 W m^{-2} throughout the growth periods (November 2012 to January 2013, April 2013 to January 2014). The monthly averages of F_w are given in Table 1. On average, 18% of the sea-ice thickness gain during the study period was not accounted for by upward heat conduction (thermodynamic growth).

The overall uncertainties were estimated by cumulative variation of individual uncertainties in the measurements. Those were ±1 for salinity, ±0.0625°C for thermistor readings and ±25 kg m^{-3} for the sea-ice density. Although the principal uncertainty in the retrieval of the ice/water interface is ±0.02 m, the uncertainty in the running mean, which is used for the growth-rate calculation, is considered to be very small. Note that

AGU Journal of Geophysical Research: Oceans 10.1002/2014JC010327

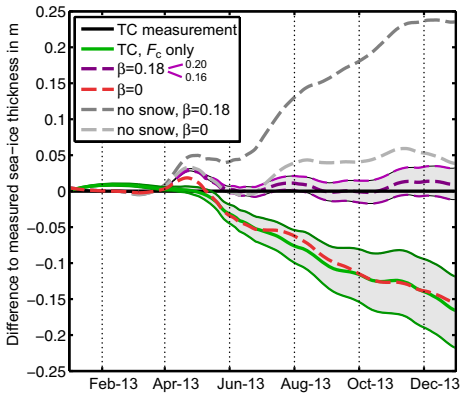

Figure 7. Comparison of sea-ice growth in 2013, derived from thermistor chain (TC) measurements and calculated from conductive heat flux alone (solid curves), along with results of different model simulations (dashed curves). The actual TC measurement (black line) is used as a zero reference. The upper half of the graph indicates thicker sea ice than this reference, the lower half indicates thinner sea ice. Filled areas represent a variation of ice-volume fraction β of ± 0.02 in the model (dashed violet curves), and the variation of the reference layer of ± 0.02 m for the calculation of the conductive heat flux (solid green curves).

these considerations do not account for a variation of the reference layer and the range of thermistors used for calculation of the temperature gradient, both of which move the curves upward and downward, and therefore have substantial influence on the residual flux.

3.11. Model Results and Ice-Volume Fraction

The results of different model runs (dashed curves) are shown in Figure 7, where the actual sea-ice thickness as determined from TC heating profiles is used as a zero reference. A positive sea-ice thickness difference (upper part of the graph) means thicker sea ice than observed, and vice versa.

Simulated sea-ice thickness with an unmodified growth rate and TC snow depth ($\beta = 0$, dashed red curve) differed from the observed sea-ice thickness by about 0.15 m at the end of growth. We performed additional model simulations with measured snow depth and modified growth rates according to equation (5), and show here only the results for $\beta = 0.16$, 0.18, and 0.20 (violet curves, bottom to top). The best fit between simulated and observed thickness was achieved for $\beta = 0.18$. Uncertainties of β were discussed in detail in *Hoppmann et al.* [2015], and are estimated as approximately 0.10 mainly due to uncertainties in upward longwave radiation. Further model experiments without a snow cover and $\beta = 0.18$ yielded a sea-ice thickness gain of 0.23 m (dashed, dark gray curve), while the combined absence of snow and platelets resulted in a net gain of 0.025 m (dashed, light gray curve).

Also shown is the adjusted growth rate $\left(\frac{\partial H}{\partial t}\right)_{adj}$, which was calculated from the basal energy balance only accounting for the conductive heat flux ($F_w = 0$, solid green curve):

$$\left(\frac{\partial H}{\partial t}\right)_{adj} = \frac{F_c + F_s}{\rho_{si} \cdot L_f}. \tag{6}$$

This generally represents a platelet-free scenario, and agrees well with the model result for $\beta = 0$. The uncertainties caused by a slight shift of the reference layer (± 0.02 m, shaded area between green curves) are also given for illustration.

3.12. Sub-ice Platelet Layer Thickness

Part of the platelet-layer thickness data (Figure 8; November 2012 to February 2013) were already described in detail in *Hoppmann et al.* [2015] and are included here due to the overlapping study interval. The initial platelet-layer thickness was on average about 4 m at the beginning of this study, decreasing to 3 m in January and toward 2 m in February. This thinning was associated with the inflow of warm water. Although not many data points are available between February and April 2013 due to safety concerns, it is likely that a platelet layer of 1–2 m thickness survived the summer. The first measurements at the end of April revealed an average thickness of about 4 m (with a high variability), steadily increasing at all sites between June and December 2013. The average platelet accumulation at all sites between April and December was approximately 4 m, leading to a mean overall thickness of about 8 m. The highest annual thickness gain of 6 m was observed at ATKA11 (Figure 8b, black triangle), the highest absolute thickness of 10 m was measured at ATKA07 (white diamond) in October 2013. The seawater temperature below the northern ice shelf (Figure 8c) was below the surface freezing point between April and November 2013, with a minimum in late May. With the continuous inflow of relatively warm water at the end of November 2013, as determined from CTD

AGU Journal of Geophysical Research: Oceans 10.1002/2014JC010327

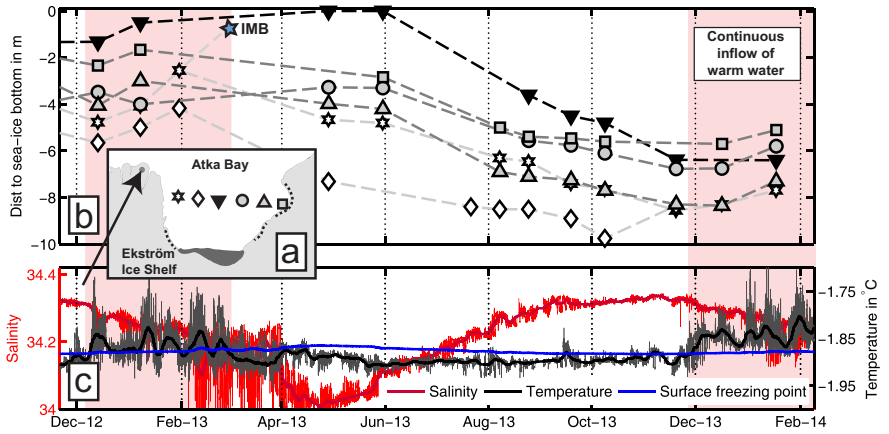

Figure 8. Platelet-layer thickness at the six sites between 2012 and 2014, along with oceanographic conditions recorded at a measurement site below the Ekström Ice Shelf. (a) Coarse map of the study area. The dark gray and dashed curves represent ice rises and rumples, respectively. (b) Sub-ice platelet-layer thickness evolution at different study sites, with symbols corresponding to their location according to Figure 8a. The blue star indicates the likely platelet-layer thickness determined by the IMB. (c) Seawater salinity (red) and temperature (black) measured by the MicroCAT at a depth of 155 m, at full resolution (thin curves) and 7 day running mean (thick curves). The corresponding surface freezing point is given in blue. The shaded area indicates the continuous inflow of relatively warm water.

measurements under the sea ice, the platelet-layer thickness again started to decrease. The time series stops shortly before the fast-ice breakup on 9 February 2014.

4. Discussion

In the first part of the discussion, we focus on the following factors that influenced the properties of the fast-ice cover and its basal energy balance in our study: (1) the general atmospheric conditions and the passage of synoptic systems, (2) the snow cover, (3) near-surface seawater temperatures, and (4) the properties of the sub-ice platelet layer. Combining all our results, we finally provide a schematic diagram depicting the seasonal evolution of fast ice in Atka Bay (2012–2014) near the Ekström Ice Shelf. In the second part, we discuss the potential of the instrument on the basis of this unique data set, and point out several limitations.

4.1. Seasonal Cycle of Fast Ice near an Ice Shelf

Since the sea-ice bottom was always near or at the freezing point (Figure 4a), near-surface air temperatures and snow depth governed the overall sea-ice temperature gradient, and with it the conductive heat flux. While the recurrent passage of relatively warm synoptic systems (Figure 2) strongly modified the temperature gradient in the upper part of the sea ice, these relatively rapid changes barely influenced the sea-ice bottom (Figure 6a). This is mainly due to the large thickness of the second-year sea ice and therefore these conditions did not influence the conductive heat flux through the near-bottom reference layer (Figure 6c). In contrast, the atmospheric conditions determined the presence of precipitation and snow drift, which play a crucial role in the evolution of a sea-ice cover through the low thermal conductivity of the snow. The strong insulating effect was particularly apparent in June and July 2013, when snow depth was at its maximum of up to 0.4 m (Figure 4e). With a delay of several weeks, this effect led to a drastic reduction of the temperature gradient, and consequently the sea-ice growth rate. As also shown in our model simulations, snow depth had a substantial influence on overall sea-ice growth. When comparing model runs with the measured snow depth throughout 2013 to a snow-free scenario, the sea-ice thickness at the end of the growth season was reduced by 23% (Figure 7). Unfortunately, ATKA03 was in the lee of an iceberg 2 km to the east (Figure 1), leading to a strong modification of snow deposition. The evolution of the snow cover shown here, with an average of 0.14 m, is therefore not representative for Atka Bay in general, which exhibited a significantly higher overall snow depth. A more realistic snow cover, derived from snow measurements on transects across Atka Bay at 1 km intervals, yielded bay-wide averages of 0.3 m in April, to 1.3 m in December 2013 (not shown). A corresponding model simulation with a linearly increasing snow cover revealed a sea-ice thickness increase of only 0.58 m (not shown), including a contribution from ice platelets. The observed

AGU Journal of Geophysical Research: Oceans 10.1002/2014JC010327

sea-ice growth of 1.1 m over this study (corresponding to 1 m in 2013) is therefore considered significantly above-average.

The presence of in situ supercooling in and in front of the ice-shelf cavity, also referred to as (supercooled) Ice Shelf Water plumes, [*Robinson et al.*, 2014], determines the formation of ice platelets [*Lewis and Perkin*, 1986]. As we do not have near-surface ocean data available at depths where in situ supercooling is most likely to occur [*Smith et al.*, 2001], we consider the presence of potentially supercooled water as an indicator for potential ice-platelet formation. Since the sub-ice shelf seawater temperature was consistently below the surface freezing point between late April and December 2013, and with higher variability even earlier (Figure 8b), platelet formation is possible throughout. *Hoppmann et al.* [2015] showed that in Atka Bay a sub-ice platelet layer starts to form during June. In contrast, results from our sea-ice texture analysis suggest that small platelets already modified the sea-ice texture up to two months earlier, although we cannot identify the exact timing from our measurements (Figure 3c). This is explained by the fact that the freezing interface in the early stage of formation may outgrow the comparably slow platelet accumulation [*Dempsey et al.*, 2010]. This hypothesis is also confirmed by the pattern of platelet-layer thickness evolution in 2013, which showed already a net increase between February and May (Figure 8). It is unclear if this is the results of new accumulation or just redistribution from sites closer to the ice shelf with higher platelet-layer thickness. However, our results confirm the pattern of seasonal platelet-layer thickness evolution as found in *Hoppmann et al.* [2015], although a higher rate of thickness increase suggests the presence of strong platelet redistribution by currents directly under the sea ice. This has to be taken into account when interpreting platelet-layer thickness data in years where the fast ice did not break out completely during the previous summer. As soon as warm Antarctic Surface Water reaches the ice-shelf front in November/December [*Hattermann et al.*, 2012], the platelet layer thinned at a rate of approximately 1 m month^{-1} (Figure 8b). Using an ice-volume fraction of 0.18, as found in the present study, this roughly corresponds to an oceanic heat flux of $+21$ W m^{-2}, in accordance with observations on fast ice in other regions [*Heil et al.*, 1996; *Lei et al.*, 2010]. At the same time, melting of the solid sea ice only occurred to a minor degree at the surface and in the ice interior (Figure 4). Despite the relatively high summer temperatures (Figure 2a), the increased radiative heating and the high oceanic heat flux, thermodynamic sea-ice growth even continued until the end of the study, albeit slowly (Figures 4b and 4c). This is due to the platelet layer shielding the sea ice from below and the slow temporal progression of the 0 W m^{-2} contour in the conductive heat flux (Figure 6a) due to the large sea-ice thickness.

According to the basal energy balance, about 18% (0.2 m) of the overall sea-ice growth (1.1 m) originated from a residual heat flux. The selection of the reference level and the number of thermistors for the linear fit of the temperature gradient may alter this result significantly. However, if the reference level is shifted, results for which this residual heat flux becomes positive, especially during the growth season, are implausible. It can therefore be safely assumed that the residual heat flux should be <0 W m^{-2} until at least mid-November. The negative residual heat flux can be interpreted as a representation of the ice crystals just below the advancing freezing interface [*Gough et al.*, 2012]. These reduce the amount of heat that needs to be transported upward in order to grow a certain sea-ice thickness. In this interpretation, our results translate into an ice-volume fraction β, of 0.18. In order to provide an uncertainty estimate, β can also be calculated inserting equation (6) into equation (5) as a platelet-free growth rate:

$$\beta = 1 - \frac{F_c + F_s}{F_l}. \tag{7}$$

Averaging over the active sea-ice growth (May–January) results in $F_c = 7.06 \pm 2.08$ W m^{-2}, $F_l = -8.5 \pm 2.24$ W m^{-2}, and $F_s = -0.06 \pm 0.05$ W m^{-2}. According to equation (7), and using Gaussian error propagation, this corresponds to $\beta = 0.18 \pm 0.09$.

In an independent approach, our model simulations with local atmospheric forcing and a variable growth rate reproduced the observed sea-ice thickness evolution best with a $\beta = 0.18$ (Figure 7). In addition to the good agreement of this independent approach to our residual flux calculation, this result also agrees well with the findings of *Kipfstuhl* [1991] and especially *Hoppmann et al.* [2015], who simulated sea-ice growth at several study sites with the same model setup, but with forcing data and independent observations (drillings) for the year 2012. Their result for ATKA03, the site of the present study, agrees within error, giving further confidence in our results, the performance of the model and the quality of the forcing data. Using a similar approach, *Gough et al.* [2012] found in their study an ice-volume fraction of 0.25 $\pm$ 0.06. The

AGU Journal of Geophysical Research: Oceans 10.1002/2014JC010327

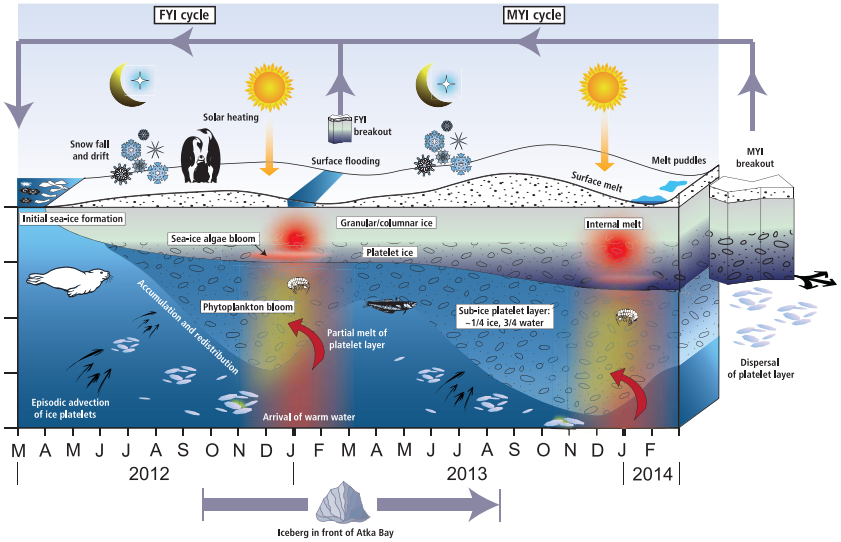

Figure 9. Schematic diagram of the seasonal cycle of Atka Bay fast ice and the sub-ice platelet layer, based on results of *Hoppmann et al.* [2015] for 2012 and this study for 2013/2014.

difference could be a reflection of the different TC setup, or more likely, the spatiotemporal variability in the platelet layer itself. It is for example currently unclear how the crystal-size distribution depends on the geographical setting and the time of the year, and how this potentially modifies the ice-volume fraction.

According to *Hoppmann et al.* [2015], accumulation and incorporation of platelets lead to an overall contribution to first-year sea-ice mass of about 50% in Atka Bay. Here we extend this result to multiyear sea ice: the platelet-layer thickness at ATKA03 increased by about 7 m, from approximately 1.5 m in February to 8.5 m in December. With $\beta = 0.18$, this corresponds to an effective sea-ice thickness of 1.26 m, or 60% of the combined solid and "loose" sea ice in 2013 (2.1 m). Including the amount that is already frozen into the sea ice (0.2 m), the overall oceanic contribution at the study site is 1.46 m, or 70% of the overall sea-ice thickness. This is considered an upper limit since it is unknown how much platelets were actually just redistributed from other locations.

It may also be useful to recalculate these results for the estimated bay-wide averages. The effective sea-ice thickness increase represented by the platelet layer is 4 m $\times$ 0.18 = 0.72 m. An estimation for the average sea-ice growth with incorporated platelets was already calculated earlier from a model simulation using bay-wide measurements of snow cover (0.58 m). Multiplication with β yields an effective sea-ice thickness from incorporated platelets of 0.10 m, with a thermodynamic growth of 0.48 m. Using these numbers, the contribution of ice platelets to the annual sea-ice thickness increase becomes 63%, or nearly 2/3. Taking into account a specific area and a defined sea-ice density, this result may be directly translated into sea-ice mass or volume. This result thereby shows that in areas where sea ice grows slowly, such as multiyear sea ice or where a thick snow cover is present, much of the sea-ice volume gained is a direct result of ocean/ice-shelf interaction in nearby cavities.

Finally, we present a schematic diagram (Figure 9) mainly incorporating findings from the present study and from *Hoppmann et al.* [2015], to summarize the seasonal evolution of the fast-ice regime of Atka Bay.

Although our study provided a further piece in the puzzle of how the physical environment of a fast-ice regime affected by platelet accumulations behaves and evolves over time, the major challenge is now to unravel its implications for the associated ecosystem and to identify the linkages between different trophic levels, such as micro algae [*Dieckmann et al.*, 1986; *Günther and Dieckmann*, 1999], invertebrates [*Günther et al.*, 1999], notothenioid fish [*La Mesa et al.*, 2004; *Vacchi et al.*, 2004], seals [*Davis et al.*, 1999], and penguins [*Zitterbart et al.*, 2014].

AGU Journal of Geophysical Research: Oceans 10.1002/2014JC010327

4.2. Assessment of the Instrument's Potential

Sea-ice mass balance buoys have been an important tool in sea-ice research in the recent past, and they remain crucial to monitor changes in the polar oceans. However, commonly used IMBs are too expensive to be deployed in large numbers, which would be needed to assess the large-scale changes and to identify responsible processes. The main difference between the TC used here and other, well established IMBs [*Richter-Menge et al*., 2006], is the lack of acoustic sounders above the snow surface and below the sea-ice bottom. The simpler construction allows for easy deployment, taking one person about 30 min. At the same time, it is however difficult to infer the interfaces between air, snow, sea ice and seawater from temperature profiles alone. Based on our data, the main questions we try to address are: (1) How well is the heating mode able to compensate the loss of information due to the lack of acoustic sounders? (2) Which additional information about a sea-ice cover can be inferred from the heating data?

Due to the large air temperature fluctuations typically observed in polar regions, the temperature gradient near the upper snow surface is substantial. In contrast, thermistors in the air usually measure the same temperature (within their accuracy). Consequently, the air/snow interface, and hence the snow depth, may be inferred from temperature differences between adjacent thermistors. Although the heating profiles generally indicated a similar snow-depth evolution, the highest difference in temperature response between adjacent thermistors was generally located a few centimeters below the air/snow interface determined from temperature profiles. We explain this by the fact that the wind moves the upper part of the chain, creating an air gap around the upper few thermistors. Due to the lack of contact area, these thermistors then record the same characteristics as those in the air above. This effect did not influence the temperature measurements to a comparable degree. As a result, the temperature measurements provide a better indication of snow depth than the heating profiles, which reproduce the general pattern but underestimate snow depth by up to 0.1 m. In summer, the retrieval of the air/snow interface is additionally influenced by radiative warming of the chain, an effect which we have neglected here.

As stated earlier, the temperature response to a defined heat input is generally proportional to the thermal conductivity and specific heat capacity of a medium. The difference between δT_{120} and δT_{30} was close to zero for sea ice, around 0.1 K for the platelet/water mixture and some regions in the sea-ice interior, and up to 4 K for snow and air (not shown). For sea ice it was therefore not possible to derive a plausible thermal conductivity from these data, mainly because the measurements at 30 and 120 s were not in the linear part of the temperature rise curve. Although a calculation should in principal be possible for snow, the complex geometry of the sensors modifies the typical equations used for needle-probe measurements, and a detailed investigation was beyond of the scope of this paper.

Through the 10-fold difference in thermal conductivity of sea ice and snow, the snow/ice interface is sharply pronounced in the heating profiles and easily extracted. This is also true for the air/ice interface in the absence of snow. However, the evolution of the sea-ice surface is admittedly more interesting in the presence of surface melt, which is more pronounced in the Arctic compared to the Antarctic. To our knowledge, no study has yet been published using the heating mode of the TC to infer the evolution of surface melt and the formation of a melt pond. However, it has been shown above that determining a (nonflowing) ice/water interface is very promising with this method, provided only diffusive heat transfer is likely to take place. This should be the case for surface meltwater. Since it is expected that the location of an air/water interface is also easily determined, this approach is promising to monitor melt-pond depth evolution, and even refreezing (under the assumption that the instrument stays in place).

When calculating a sea-ice mass budget, internal melt processes are usually neglected due to the lack of a suitable methodology. As described above, several areas in the heating data sets can be interpreted as internal melt or even the formation of gap layers. These mainly occurred in summer, most prominently between February and April 2013. Although we do not study these in detail here, this potentially provides additional insight into melt processes.

In our case, the heating data effectively provided 3 months of additional information about the evolution the ice/water interface, mainly for isothermal conditions in summer 2013. However, such a clear identification was only possible due to a presence of a sub-ice platelet layer. Sea ice and flowing water exhibit a similar thermal response to an applied heating. Under flowing conditions, the ice/water interface may still be inferred from the variations of flow speed of the underlying water, which results in slightly variable

AGU Journal of Geophysical Research: Oceans 10.1002/2014JC010327

temperature differences. This behavior was also described in *Jackson et al.* [2013], and is indicated in the Weddell Sea data set as different shades of blue (Figure 5b). However, this effect significantly complicates the implementation of general algorithms to automatically retrieve the ice/water interface. In addition, a longer time series is needed to accurately interpret the subtle differences not visible from few measurements alone, noting a higher measurement frequency might also assist. Furthermore, Figure 5b demonstrates that the thermal characteristic of refreezing in the upper borehole differ from those of the surrounding medium. According to the scenario described above, this is most likely explained by a near-zero flow rate in the drill hole, in contrast to the ocean below.

This effect leads to an interesting application of this instrument in sea-ice regimes with a sub-ice platelet layer: dealing with supercooled seawater and associated processes, temperature differences in the order of several mK need to be resolved. This prerequisite is not met by the thermistors embedded in the chain. However, although the platelet layer is highly porous, it is safe to assume that the geometric properties of the platelet matrix impede the oceanic currents enough to significantly reduce the flow. Comparison of the Atka Bay (Figure 4c) and the Weddell Sea data sets (Figure 5b) suggest that it is therefore in principle possible to distinguish a sub-ice platelet layer from an unimpeded seawater flow. If this hypothesis holds, we are now able to interpret the darker blue areas below the sea-ice base from February to June 2013 (Figures 4b and 4c) as a temperature response associated with thinning and reconsolidation processes in the platelet layer. The thinning, or more specifically, the presence of ice-free, flowing seawater surrounding the lowermost thermistors in March is consistent with results from manual platelet-layer thickness measurements at ATKA03 (Figure 8b, star symbols), because further bottom melt is expected as long as relatively warm water is present until the beginning of March (Figure 8c). Between March and the beginning of May 2013, the data quality is too low due to artifacts caused by power issues. In mid-May, the lowermost thermistors exhibit a sudden increase in their temperature response, showing a signature similar to that before platelet-layer melt (especially visible in Figure 4c). This is again consistent with Figure 8b, in that our drillings showed the platelet-layer thickness had already increased to more than 4 m in April. This was seemingly not reproduced by the IMB data. However, a closer investigation of Figures 4b and 4c reveals that the temperature response of the lower thermistors in the first half of May was slightly different from that observed in March. We interpret this as a signature of the early phase of platelet-layer establishment, where the connectivity in the interstitial water is still high enough to allow for a detectable flow rate. The rapid transition in mid-May would then correspond to an enhanced consolidation, reduced connectivity and consequently, reduced flow rates. These results suggest that the heating mode is able to detect the platelet-layer bottom, although the possibility of the lower thermistors simply being encased in platelet ice cannot be ruled out entirely.

The most important constraint to this application, as also shown in our study, is the chain length. Although a typical thermistor chain length of 4.8 m seems long enough for a deployment in typical sea ice, it is too short to also monitor the evolution of a platelet layer over the course of winter, which can well reach up to 10 m. In our case, a length of about 10 m (with a wider thermistor spacing in the lower 5 m) would be needed to cover the entire seasonal cycle. But as the shear stresses on such a long chain increase dramatically due to the strong under-ice currents, the risk of a failure is high. Further testing is necessary to assess if such a long chain is practical. In addition, an IMB equipped with an acoustic sounder below the sea ice is generally not suited to be operated in areas where a sub-ice platelet layer is present or expected. Objects or instruments hanging below the sea ice serve as an ideal body for large amounts of ice crystals to grow on, a phenomenon for example photographed by *Mahoney et al.* [2011]. Even if the sensor would remain ice-free, a detection of the sea-ice/platelet layer interface would rely on temperature measurements alone, leading to higher uncertainties.

As usual, there are also several difficulties and problems associated with the operation of such an instrument. Here we identify some issues we experienced which the user needs to be aware of. The obvious is that predeployment calibration and testing is crucial to characterize the instrument.

The prominent vertical structures in Figures 4b and 4c are a result of a drop in voltage applied to the resistors during heating, which is usually 8 V. This effect leads to less pronounced contrasts between different media and occurred whenever the general battery voltage dropped below 10 V. It affected roughly 1/3 of the heating profiles. However, the other measurements were still sufficient for an accurate determination of interfaces between different media. The temperature profiles, and therefore all energy balance calculations,

AGU Journal of Geophysical Research: Oceans 10.1002/2014JC010327

are not impacted at all by this effect. For a calculation of thermal properties (not shown here), this effect has to be taken into account. The heating voltage is usually also recorded, and is included in the status message when operated via Iridium.

In order to obtain a continuous time series of snow depth throughout a certain study, a part of the thermistor chain has to remain above the snow surface (Figure 4b). The chosen length of this segment depends on the expected snow accumulation in a study region, and the construction of a suitable rack. In our study, 0.5 m above the snow surface was just enough to keep track of the snow-depth evolution. Under conditions of $>$0.5 m snow accumulation, continuous snow-depth retrieval is therefore difficult. In addition, the surface unit is quickly buried under the thick snow, and data transmission is potentially hampered when the snow becomes too thick or wet.

Our data processing, the development of algorithms and the setting of thresholds was tuned to fit the presented data set. Since the heating profiles strongly depend on a combination of the thermal characteristics of a medium and its flow speed, the presentation of a generally applicable procedure to infer the different interfaces for other sea-ice data sets is difficult and beyond the scope of this paper. However, with a quickly increasing number of such data sets, we identify the need for a set of generally applicable algorithms to facilitate speedy and unified data processing and interpretation.

5. Summary and Conclusion

Measurements of the atmosphere, sea ice, ocean, and sub-ice platelet layer have been made on Antarctic first/second-year fast ice over 15 month. The grounding of a large iceberg in front of Atka Bay, which prevented a usual sea-ice breakup in 2013, presented a unique opportunity to perform a continuous and detailed study of the sea-ice processes, and especially the sub-ice platelet-layer evolution, over such a long period. The main data set presented here is a consistent time series of air, snow, sea-ice, and ocean/platelet-layer temperature profiles recorded by a thermistor chain which is also able to actively heat resistor components mounted near the temperature sensors. This data set is one of the longest of its kind recorded to date, and highlights various features in the seasonal sea-ice evolution.

It is supplemented by simultaneous, consistent time series of sub-ice-shelf temperatures and salinities, and high quality meteorological data partly obtained directly next to the thermistor chain. The total solid sea-ice thickness gain during 2013 was about 1 m, due to the high initial thickness of 2.5 m and the snow cover that was thick for some of the time. In total, 18% of the ice grown between April and December 2013 was not accounted for by heat conduction to the atmosphere. The translation of this result to a platelet-layer ice-volume fraction of 0.18 ± 0.09 was also confirmed by independent sea-ice growth simulations, which yielded an ice-volume fraction of 0.18 ± 0.10. The platelet-layer thickness near ATKA03 increased by about 7 m (from 1.5 to 8.5 m) in 2013, with a bay-wide average of about 4 m. Overall, oceanic contribution to sea-ice thickness accounted for up to 70% of the total thickness. We showed that an approximate oceanic heat flux of 21 W m^{-2} during summer months is not sufficient to melt the entire platelet layer. Therefore, our study directly supplies evidence that in areas where sea ice grows slowly, such as thick multiyear sea ice or in the presence of a thick snow cover, most of the ice volume is contributed by ocean/ice-shelf interaction.

We also showed that, by the distinction of media through their thermal properties and flow speed, the heating mode is able to compensate the lack of acoustic sounders present on standard IMBs. This makes this buoy far easier to deploy and more reliable. By careful extraction of the interfaces from both measurement modes, it is possible to accurately determine the basal energy budget. In addition, the instrument is able to resolve internal structures such as gap layers and their refreezing. Although it is generally possible to derive the thermal conductivity and specific heat capacity of sea ice and snow with this approach, their quantification was beyond the scope of this work.

Finally, our study supplied evidence that a thermistor chain with active heating is capable of detecting the sub-ice platelet layer thickness through the lower current speed compared to the underlying ocean. Thereby it is currently the only automated method to continuously monitor the formation of a sub-ice platelet layer. This makes it the ideal tool to study sea-ice regimes influenced by ocean/ice-shelf interaction continuously over an extended time.

AGU Journal of Geophysical Research: Oceans 10.1002/2014JC010327

Acknowledgments
The authors are most grateful to the Neumayer III overwintering teams in 2012 and 2013 for their support in the field. We acknowledge Lars Kindermann and Olaf Boebel for the CTD data, and Sandra Schwegmann for the buoy deployment. Our research at Neumayer III and onboard RV Polarstern ANT-XXIX/9 would not have been possible without the help of the crew and the AWI logistics. This work was supported by the German Research Council (DFG) in the framework of the priority programme "Antarctic Research with comparative investigations in Arctic ice areas" by grants to SPP1158, NI 1092/2 and HE2740/12, and the Alfred-Wegener-Institut Helmholtz-Zentrum für Polar- und Meeresforschung. The data used here are publicly available at http://doi.org/10.1594/PANGAEA.833978. PH was supported under AAS grant #4301 and by the Australian Government's Cooperative Research Centre's Program through the Antarctic Climate and Ecosystems Cooperative Research Centre. Finally, the authors are grateful to two anonymous reviewers whose constructive comments significantly improved this manuscript.

References

Arrigo, K. R., D. H. Robinson, and C. W. Sullivan (1993), A high-resolution study of the platelet ice ecosystem in McMurdo Sound, Antarctica: Photosynthetic and bio-optical characteristics of a dense microalgal bloom, *Mar. Ecol. Prog. Ser.*, *98*(1–2), 173–185, doi:10.3354/meps098173.

Bintanja, R., G. J. van Oldenborgh, S. S. Drijfhout, B. Wouters, and C. A. Katsman (2013), Important role for ocean warming and increased ice-shelf melt in Antarctic sea-ice expansion, *Nat. Geosci.*, *6*, 376–379, doi:10.1038/ngeo1767.

Bintanja, R., G. J. van Oldenborgh, and C. A. Katsman (2015), The effect of increased fresh water from Antarctic ice shelves on future trends in Antarctic sea ice, *Ann. Glaciol.*, *56*(69), 120–126.

Bitz, C. M., and W. H. Lipscomb (1999), An energy-conserving thermodynamic model of sea ice, *J. Geophys. Res.*, *104*(C7), 15,669–15,677, doi:10.1029/1999JC900100.

Boebel, O., L. Kindermann, H. Klinck, H. Bornemann, J. Plötz, D. Steinhage, S. Riedel, and E. Burkhardt (2006), Real-time underwater sounds from the Southern Ocean, *Eos Trans. AGU*, *87*(36), 361, doi:10.1029/2006EO360002.

Davis, R. W., L. A. Fuiman, T. M. Williams, S. O. Collier, W. P. Hagey, S. B. Kanatous, S. Kohin, and M. Horning (1999), Hunting behavior of a marine mammal beneath the Antarctic fast ice, *Science*, *283*(5404), 993–996, doi:10.1126/science.283.5404.993.

Dempsey, D. E., P. J. Langhorne, N. J. Robinson, M. J. M. Williams, T. G. Haskell, and R. D. Frew (2010), Observation and modeling of platelet ice fabric in McMurdo Sound, Antarctica, *J. Geophys. Res.*, *115*, C01007, doi:10.1029/2008JC005264.

Dieckmann, G., G. Rohardt, H. Hellmer, and J. Kipfstuhl (1986), The occurrence of ice platelets at 250 m depths near the Filchner Ice Shelf and its significance for sea ice biology, *Deep Sea Res., Part A*, *33*(2), 141–148, doi:10.1016/0198-0149(86)90114-7.

Eicken, H., and M. A. Lange (1989), Development and properties of sea ice in the coastal regime of the southeastern Weddell Sea, *J. Geophys. Res.*, *94*(C6), 8193–8206, doi:10.1029/JC094iC06p08193.

Fahrbach, E., S. Harms, G. Rohardt, M. Schröder, and R. A. Woodgate (2001), Flow of bottom water in the northwestern Weddell Sea, *J. Geophys. Res.*, *106*(C2), 2761–2778, doi:10.1029/2000JC900142.

Fichefet, T., and M. A. M. Maqueda (1999), Modelling the influence of snow accumulation and snow-ice formation on the seasonal cycle of the Antarctic sea-ice cover, *Clim. Dyn.*, *15*(4), 251–268, doi:10.1007/s003820050280.

Fraser, A. D., R. A. Massom, K. J. Michael, B. K. Galton-Fenzi, and J. L. Lieser (2012), East Antarctic landfast sea ice distribution and variability, 2000–08, *J. Clim.*, *25*(4), 1137–1156, doi:10.1175/JCLI-D-10-05032.1.

Gough, A. J., A. R. Mahoney, P. J. Langhorne, M. J. M. Williams, N. J. Robinson, and T. G. Haskell (2012), Signatures of supercooling: McMurdo Sound platelet ice, *J. Glaciol.*, *58*(207), 38–50, doi:10.3189/2012JoG10J218.

Günther, S., and G. S. Dieckmann (1999), Seasonal development of algal biomass in snow-covered fast ice and the underlying platelet layer in the Weddell Sea, Antarctica, *Antarct. Sci.*, *11*(3), 305–315, doi:10.1017/S0954102099000395.

Günther, S., and G. S. Dieckmann (2001), Vertical zonation and community transition of sea-ice diatoms in fast ice and platelet layer, Weddell Sea, Antarctica, *Ann. Glaciol.*, *33*(1), 287–296, doi:10.3189/172756401781818590.

Günther, S., M. Gleitz, and G. S. Dieckmann (1999), Biogeochemistry of Antarctic sea ice: A case study on platelet ice layers at Drescher Inlet, Weddell Sea, *Mar. Ecol. Prog. Ser.*, *177*, 1–13.

Hattermann, T., O. A. Nøst, J. M. Lilly, and L. H. Smedsrud (2012), Two years of oceanic observations below the Fimbul Ice Shelf, Antarctica, *Geophys. Res. Lett.*, *39*, L12605, doi:10.1029/2012GL051012.

Heil, P. (2006), Atmospheric conditions and fast ice at Davis, East Antarctica: A case study, *J. Geophys. Res.*, *111*, C05009, doi:10.1029/2005JC002904.

Heil, P., I. Allison, and V. I. Lytle (1996), Seasonal and interannual variations of the oceanic heat flux under a landfast Antarctic sea ice cover, *J. Geophys. Res.*, *101*(C11), 25,741–25,752, doi:10.1029/96JC01921.

Heil, P., S. Gerland, and M. A. Granskog (2011), An Antarctic monitoring initiative for fast ice and comparison with the Arctic, *Cryosphere Discuss.*, *5*(5), 2437–2463, doi:10.5194/tcd-5-2437-2011.

Holland, P. R., and R. Kwok (2012), Wind-driven trends in Antarctic sea-ice drift, *Nat. Geosci.*, *5*, 872–875, doi:10.1038/ngeo1627.

Hoppmann, M., et al. (2015), Ice platelets below Weddell Sea land fast sea ice, *Ann. Glaciol.*, *56*(69), 175–190, doi:10.3189/2015AoG69A678, in press.

Hunkeler, P., S. Hendricks, M. Hoppmann, S. Paul, and R. Gerdes (2015), Towards an estimation of sub-sea-ice platelet-layer volume with multi-frequency electromagnetic induction sounding, *Ann. Glaciol.*, *56*(69), 137–146, doi:10.3189/2015AoG69A705.

Jackson, K., J. Wilkinson, T. Maksym, J. Beckers, C. Haas, D. Meldrum, and D. Mackenzie (2013), A novel and low cost sea ice mass balance buoy, *J. Atmos. Oceanic Technol.*, *30*, 2676–2688, doi:10.1175/JTECH-D-13-00058.1.

Jeffries, M. O., W. F. Weeks, R. Shaw, and K. Morris (1993), Structural characteristics of congelation and platelet ice and their role in the development of Antarctic land-fast sea-ice, *J. Glaciol.*, *39*(132), 223–238.

Kawamura, T., K. I. Ohshima, T. Takizawa, and S. Ushio (1997), Physical, structural and isotopic characteristics and growth processes of fast sea ice in Lützow-Holm Bay, Antarctica, *J. Geophys. Res.*, *102*(C2), 3345–3355, doi:10.1029/96JC03206.

Kipfstuhl, J. (1991), Zur Entstehung von Unterwassereis und das Wachstum und die Energiebilanz des Meereises in der Atka Bucht, Antarktis, *Ber. Polarforsch.*, *85*, 88 pp., doi:10013/epic.10085.d001.

König-Langlo, G., and B. Loose (2007), The meteorological observatory at Neumayer Station (GvN and NM-II) Antarctica, *Polarforschung*, *76*, 25–38.

König-Langlo, G., J. C. King, and P. Pettré (1998), Climatology of the three coastal Antarctic stations Dumont d'Urville, Neumayer, and Halley, *J. Geophys. Res.*, *103*(D9), 10,935–10,946, doi:10.1029/97JD00527.

La Barbara, M., and S. Vogel (1976), An inexpensive thermistor flowmeter for aquatic biology, *Limnol. Oceanogr.*, *21*, 750–756.

La Mesa, M., J. T. Eastman, and M. Vacchi (2004), The role of notothenioid fish in the food web of the ross sea shelf waters: A review, *Polar Biol.*, *27*(6), 321–338, doi:10.1007/s00300-004-0599-z.

Lefebvre, W., and H. Goosse (2008), An analysis of the atmospheric processes driving the large-scale winter sea ice variability in the Southern Ocean, *J. Geophys. Res.*, *113*, C02004, doi:10.1029/2006JC004032.

Lei, R., Z. Li, B. Cheng, Z. Zhang, and P. Heil (2010), Annual cycle of landfast sea ice in Prydz Bay, East Antarctica, *J. Geophys. Res.*, *115*, C02006, doi:10.1029/2008JC005223.

Lei, R., N. Li, P. Heil, B. Cheng, Z. Zhang, and B. Sun (2014), Multiyear sea ice thermal regimes and oceanic heat flux derived from an ice mass balance buoy in the Arctic Ocean, *J. Geophys. Res. Oceans*, *119*, 537–547, doi:10.1002/2012JC008731.

Leppäranta, M., and T. Manninen (1988), The brine and gas content of sea ice with attention to low salinities and high temperatures, technical report 1988-2, *Finn. Inst. of Mar. Res.*, Helsinki, Finland.

Lewis, E. L., and R. G. Perkin (1986), Ice pumps and their rates, *J. Geophys. Res.*, *91*(C10), 11,756–11,762, doi:10.1029/JC091iC10p11756.

AGU Journal of Geophysical Research: Oceans 10.1002/2014JC010327

Li, X., D. M. Holland, E. P. Gerber, and C. Yoo (2014), Impacts of the north and tropical Atlantic Ocean on the Antarctic Peninsula and sea ice, *Nature*, *505*(7484), 538–542, doi:10.1038/nature12945.

Liu, J. P., and J. A. Curry (2010), Accelerated warming of the Southern Ocean and its impacts on the hydrological cycle and sea ice, *Proc. Natl. Acad. Sci. U. S. A.*, *107*(34), 14,987–14,992, doi:10.1073/pnas.1003336107.

Liu, J. P., J. A. Curry, and D. G. Martinson (2004), Interpretation of recent Antarctic sea ice variability, *Geophys. Res. Lett.*, *31*, L02205, doi:10.1029/2003GL018732.

Mager, S. M., I. J. Smith, E. W. Kempema, B. J. Thomson, and G. H. Leonard (2013), Anchor ice in polar oceans, *Prog. Phys. Geogr.*, *37*(4), 468–483, doi:10.1177/0309133313479815.

Mahoney, A. R., A. J. Gough, P. J. Langhorne, N. J. Robinson, C. L. Stevens, M. M. J. Williams, and T. G. Haskell (2011), The seasonal appearance of ice shelf water in coastal Antarctica and its effect on sea ice growth, *J. Geophys. Res.*, *116*, C11032, doi:10.1029/2011JC007060.

Massom, R. A., K. L. Hill, V. I. Lytle, A. P. Worby, M. Paget, and I. Allison (2001), Effects of regional fast-ice and iceberg distributions on the behaviour of the Mertz Glacier polynya, East Antarctica, *Ann. Glaciol.*, *33*, 391–398, doi:10.3189/172756401781818518.

McDougall, T., and P. Barker (2011), Getting started with TEOS-10 and the Gibbs Seawater (GSW) Oceanographic Toolbox, 28 pp., SCOR/IAPSO WG127.

McPhee, M., and N. Untersteiner (1982), Using sea ice to measure vertical heat flux in the ocean, *J. Geophys. Res.*, *87*(C3), 2071–2074, doi:10.1029/JC087iC03p02071.

Nicolaus, M., C. Katlein, J. Maslanik, and S. Hendricks (2012), Changes in Arctic sea ice result in increasing light transmittance and absorption, *Geophys. Res. Lett.*, *39*, L24501, doi:10.1029/2012GL053738.

Ohshima, K. I., T. Kawamura, T. Takizawa, S. Ushio, and T. Miyakawa (2000), Current variability under landfast sea ice in Lützow-Holm Bay, Antarctica, *J. Geophys. Res*, *105*(C7), 17,121–17,132, doi:10.1029/2000JC900080.

Parkinson, C. L., and D. J. Cavalieri (2012), Antarctic sea ice variability and trends, 1979–2010, *Cryosphere*, *6*, 871–880, doi:10.5194/tc-6-871-2012.

Paul, S., S. Willmes, M. Hoppmann, P. A. Hunkeler, G. Heinemann, M. Nicolaus, and R. Timmermann (2015), The impact of early summer snow properties on land-fast sea-ice X-band backscatter, *Ann. Glaciol.*, *56*(69), 263–273, doi:10.3189/2015AoG69A715, in press.

Perovich, D. K., and B. C. Elder (2001), Temporal evolution of Arctic sea-ice temperature, *Ann. Glaciol.*, *33*(1), 207–211.

Perovich, D. K., S. V. Nghiem, T. Markus, and A. Schweiger (2007), Seasonal evolution and interannual variability of the local solar energy absorbed by the Arctic sea icеocean system, *J. Geophys. Res.*, *112*, C03005, doi:10.1029/2006JC003558.

Perry, A. (1982), *Hot-Wire Anemometry*, Clarendon, Oxford, U. K.

Petrich, C., P. Langhorne, and Z. Sun (2006), Modelling the interrelationships between permeability, effective porosity and total porosity in sea ice, *Cold Reg. Sci. Technol.*, *44*(2), 131–144, doi:10.1016/j.coldregions.2005.10.001.

Pringle, D. J., H. Eicken, H. J. Trodahl, and L. G. E. Backstrom (2007), Thermal conductivity of landfast Antarctic and Arctic sea ice, *J. Geophys. Res.*, *112*, C04017, doi:10.1029/2006JC003641.

Purdie, C., P. J. Langhorne, G. Leonard, and T. Haskell (2006), Growth of first-year landfast Antarctic sea ice determined from winter temperature measurements, *Ann. Glaciol.*, *44*(1), 170–176, doi:10.3189/172756406781811853.

Riche, F., and M. Schneebeli (2013), Thermal conductivity of snow measured by three independent methods and anisotropy considerations, *Cryosphere*, *7*(1), 217–227, doi:10.5194/tc-7-217-2013.

Richter-Menge, J., D. K. Perovich, B. C. Elder, K. Claffey, I. Rigor, and M. Ortmeyer (2006), Ice mass-balance buoys: A tool for measuring and attributing changes in the thickness of the Arctic sea-ice cover, *Ann. Glaciol.*, *44*, 205–210, doi:10.3189/172756406781811727.

Robinson, N. J., M. J. M. Williams, C. L. Stevens, P. J. Langhorne, and T. G. Haskell (2014), Evolution of a supercooled Ice Shelf Water plume with an actively growing sub-ice platelet matrix, *J. Geophys. Res. Oceans*, *119*, 3425–3446, doi:10.1002/2013JC009399.

Semtner, A. J. (1976), A model for the thermodynamic growth of sea ice in numerical investigations of climate, *J. Phys. Oceanogr.*, *6*(3), 379–389, doi:10.1175/1520-0485(1976)006<0379:AMFTTG>2.0.CO;2.

Simpkins, G. R., L. M. Ciasto, D. W. J. Thompson, and M. H. England (2012), Seasonal relationships between large-scale climate variability and Antarctic sea ice concentration, *J. Clim.*, *25*(16), 5451–5469, doi:10.1175/JCLI-D-11-00367.1.

Smith, I. J., P. J. Langhorne, T. G. Haskell, H. J. Trodahl, R. Frew, and M. R. Vennell (2001), Platelet ice and the land-fast sea ice of McMurdo Sound, Antarctica, *Ann. Glaciol.*, *33*(1), 21–27, doi:10.3189/172756401781818365.

Smith, I. J., P. J. Langhorne, R. D. Frew, R. Vennell, and T. G. Haskell (2012), Sea ice growth rates near ice shelves, *Cold Reg. Sci. Technol.*, *8384*, 57–70, doi:10.1016/j.coldregions.2012.06.005.

Stammerjohn, S. E., D. G. Martinson, R. C. Smith, X. Yuan, and D. Rind (2008), Trends in Antarctic annual sea ice retreat and advance and their relation to El Niño Southern Oscillation and Southern Annular Mode variability, *J. Geophys. Res.*, *113*, C03S90, doi:10.1029/2007JC004269.

Sturm, M., and J. B. Johnson (1992), Thermal-conductivity measurements of depth hoar, *J. Geophys. Res.*, *97*(B2), 2129–2139, doi:10.1029/91JB02685.

Swart, N. C., and J. C. Fyfe (2013), The influence of recent Antarctic ice sheet retreat on simulated sea ice area trends, *Geophys. Res. Lett.*, *40*, 4328–4332, doi:10.1002/grl.50820.

Swingedouw, D., T. Fichefet, P. Huybrechts, H. Goosse, E. Driesschaert, and M. F. Loutre (2008), Antarctic ice-sheet melting provides negative feedbacks on future climate warming, *Geophys. Res. Lett.*, *35*, L17705, doi:10.1029/2008GL034410.

Tang, S. L., D. H. Qin, J. W. Ren, J. C. Kang, and Z. J. Li (2007), Structure, salinity and isotopic composition of multi-year landfast sea ice in Nella Fjord, Antarctica, *Cold Reg. Sci. Technol.*, *49*(2), 170–177, doi:10.1016/j.coldregions.2007.03.005.

Timco, G. W., and R. M. W. Frederking (1996), A review of sea ice density, *Cold Reg. Sci. Technol.*, *24*(1), 1–6, doi:10.1016/0165-232X(95)00007-X.

Tison, J. L., R. D. Lorrain, A. Bouzette, M. Dini, A. Bondesan, and M. StiéVenard (2013), Linking landfast sea ice variability to marine ice accretion at Hells Gate Ice Shelf, Ross Sea, in *Antarctic Sea Ice: Physical Processes, Interactions and Variability*, edited by M. O. Jeffries, AGU, Washington, D. C., doi:10.1029/AR074p0375.

Untersteiner, N. (1961), On the mass and heat budget of Arctic sea ice, *Arch. Meteorol. Geophys. Bioklimatol., Ser. A*, *12*(2), 151–182, doi:10.1007/BF02247491.

Uto, S., H. Shimoda, and S. Ushio (2006), Characteristics of sea-ice thickness and snow-depth distributions of the summer landfast ice in Lützow-Holm Bay, East Antarctica, *Ann. Glaciol.*, *44*(1), 281–287, doi:10.3189/172756406781811240.

Vacchi, M., M. Mesa, and S. Greco (2000), The Coastal Fish Fauna of Terra Nova Bay, Ross Sea, Antarctica, in *Ross Sea Ecology*, edited by F. M. Faranda, L. Guglielmo, and A. Ianora, chap. 32, pp. 457–468, Springer, Berlin, doi:10.1007/978-3-642-59607-0_32.

Vacchi, M., M. La Mesa, M. Dalu, and J. Macdonald (2004), Early life stages in the life cycle of Antarctic silverfish, *Pleuragramma antarcticum* in Terra Nova Bay, Ross Sea, *Antarct. Sci.*, *16*(3), 299–305, doi:10.1017/S0954102004002135.

AGU Journal of Geophysical Research: Oceans 10.1002/2014JC010327

Welschmeyer, N. A. (1994), Fluorometric analysis of chlorophyll-a in the presence of chlorophyll-b and pheopigments, *Limnol. Oceanogr.*, *39*(8), 1985–1992, doi:10.4319/lo.1994.39.8.1985.

Yen, Y.-C. (1981), Review of thermal properties of snow, ice and sea ice, technical report, U.S. Army Cold Reg. Res. and Eng. Lab., *81*(10), CRREL Report, 35 pp., Hanover, N. H.

Yen, Y.-C., K. C. Chen, and S. Fukusako (1991), Review of intrinsic thermophysical properties of snow, ice, sea ice, and frost, in *Proceedings of 3rd International Symposium on Cold Regions Heat Transfer, Fairbanks, AK.*, June 11–14, edited by J. P. Zarling and S. L. Fausett, pp. 187–218, Univ. of Alaska, Fairbanks.

Zhang, J. (2007), Increasing Antarctic sea ice under warming atmospheric and oceanic conditions, *J. Clim.*, *20*(11), 2515–2529, doi:10.1175/JCLI4136.1.

Zitterbart, D. P., et al. (2014), Are environmental factors responsible for changed breeding behaviour in emperor penguins?, *Antarct. Sci., FirstView*, *26*(5), 563–564, doi:10.1017/S0954102014000285.

Chapter 7

Publications IV to VI: Sub-ice platelet layer properties from multi-frequency electromagnetic induction sounding

This chapter summarizes the following publications and manuscripts, which are based on work mainly done by Priska A. Hunkeler:

> Hunkeler, P. A., S. Hendricks, **M. Hoppmann**, S. Paul and R. Gerdes. "Towards an estimation of sub sea-ice platelet-layer volume with multi-frequency electromagnetic induction sounding" (Appendix I, Hunkeler et al. (2015))

This paper is published in Annals of Glaciology **56**(69), **2015**, submitted in February 2014 and accepted in September 2014. My contribution to this paper is that I co-performed the sea-ice field work, calculated sea-ice parameters, and co-wrote the paper.

◇

> Hunkeler, P. A., S. Hendricks, **M. Hoppmann**, C. Farquharson, T. Kalscheuer, M. Grab, Manuela S. Kaufmann L. Rabenstein and R. Gerdes. "Improved 1D inversions for sea ice thickness and conductivity from EM induction data: Inclusion of nonlinearities caused by passive bucking" (Appendix II, Hunkeler et al. (accepted))

The manuscript was accepted by Geophysics in June 2015. My contribution to this paper is that I co-wrote the paper.

◇

> Hunkeler, P. A., **M. Hoppmann**, S. Hendricks, T. Kalscheuer and R. Gerdes. "A glimpse beneath Antarctic sea ice: platelet-layer volume from multi-frequency electromagnetic induction sounding" (Appendix III)

This manuscript was submitted to Geophysical Research Letters in June 2015. My contribution to this paper is that I co-performed the sea-ice field work, co-processed the raw data, co-produced the figures and co-wrote the paper.

Electromagnetic induction sounding on sea ice

This introduction is based on "Improved 1D inversions for sea ice thickness and conductivity from EM induction data: Inclusion of nonlinearities caused by passive bucking" (Appendix I).

An accurate characterization of the state of the sea-ice cover in the polar oceans is of great importance (Section 2.1.2), but at the same time a huge logistical challenge. Sea-ice research was significantly facilitated by the use of satellites in the last decades, and the retrieval of sea-ice extent from satellite remote sensing is nowadays considered reliable. However, the accurate determination of sea-ice thickness and -volume still remain a challenge (Section 2.2.3). In addition to the limited knowledge of radar penetration depth and the snow cover itself, the main problem is the lack of comprehensive observational datasets to validate the algorithms (Ricker et al., 2014).

At the same time, the traditional method of sea-ice thickness determination by drilling is spatially very limited and not feasible on larger scales due to the necessary logistics. The gap between large-scale satellite observations and these small-scale thickness measurements is nowadays filled by ground-based and airborne electromagnetic (EM) induction sounding. In this approach, a single frequency in the range of 3 kHz to 10 kHz is used to estimate the distance of the sensor to the ice-water interface, based on the contrasting electrical conductivities of sea ice (typically <100 mS/m, Reid et al., 2003) and seawater (e.g. 2690 mS/m in the central Weddell Sea in winter).

Sea-ice thickness distributions on smaller scales are frequently acquired using a lightweight electromagnetic instrument (EM-31, Geonics, 9.8 kHz), operated on sea ice by either pulling it by hand or snowmobile across a floe while mounted on a sledge or in a kayak (Haas, 2004). Sea-ice thickness is calculated from the corresponding sounding using a exponential fit from a careful calibration. Alternatively, the EM31 is mounted at the front of an ice-breaking research vessel (Reid et al., 2003), in which case additional laser distance measurements are necessary to account for the elevation of the instrument. Airborne electromagnetic induction soundings on sea ice were first acquired by Kovacs et al. (1987) using a geophysical mineral deposits exploration device. By combination of the EM response providing the distance to the sea-ice/seawater interface, and a laser providing the distance to the sea-ice surface, the corresponding sea ice thickness is calculated. Results were promising and lead to the development of a sea ice dedicated device (Kovacs and Holladay, 1990; Holladay et al., 1990). Since 2001, airborne EM instruments have been under development for operational use on sea ice, and are now frequently used (Haas et al., 2008b, 2009, 2010). These instruments utilize frequencies of 3.68 and 112 kHz, but only the inphase component of the lower frequency is currently used for sea-ice thickness retrieval. In addition to a thickness determination with high spatial resolution and accuracy, this approach is also in principle suitable to investigate macroscopic sea-ice features, such as pressure ridges, as well as microscopic features, such as sea-ice porosity and electrical conductivity.

The presence of a porous platelet layer alters the conductivity of the seawater, and leads to either an overestimation of the solid sea-ice thickness (Rack et al., 2013), or an underestimation of total (solid ice + platelet layer) thickness with no possibility to resolve both. While single-frequency systems are sensitive to the thickness and the electrical bulk conductivity of the platelet layer, they do not provide

enough observational constraints for an unambiguous resolution of layer thicknesses and conductivities. Therefore, those systems are not able to resolve multiple sea-ice layers with different electrical parameters.

The importance of sub-ice platelet layers and the difficulty in the determination of its properties has been highlighted extensively throughout this thesis. One aim of this work was to contribute to the development of an innovative, EM-based approach for a feasible, large-scale platelet-layer volume estimation, without the need for time consuming sea-ice drilling experiments. The increased spatial coverage of platelet-layer thickness with EM methods would be ideal to complement the temporal evolution monitored by thermistor chains. The combination of both methods could potentially represent a breakthrough in coastal Antarctic sea-ice research.

Methods

In this study, we used a commercial, compact-sized electromagnetic induction sensor (GEM-2, Geophex Ltd) for soundings on sea ice with an underlying platelet layer. In contrast to the single-frequency EM31, the GEM-2 is able to operate at five frequencies in a range from 330 Hz to 96 kHz simultaneously. It is expected that, by combining the EM response at multiple frequencies, additional information about the sea-ice cover may be gained. Such an instrument was only sporadically used on sea ice to date, and its potential has not been assessed yet.

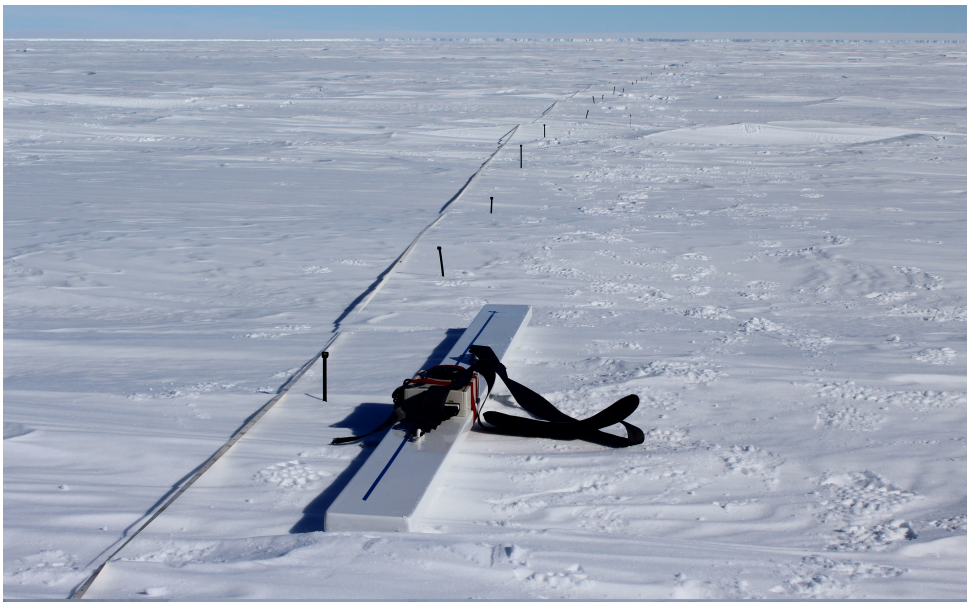

Figure 7.1: Measurement of sea-ice and platelet-layer thickness with the GEM-2 (Geophex Ltd.), a multi-frequency electromagnetic induction sounding instrument. Photo by Priska Hunkeler.

In order to obtain accurate sea-ice thickness data from the soundings, it was first necessary to determine calibration coefficients and measurement uncertainties. We therefore performed GEM-2 calibration measurements over seawater and "regular" sea ice in the central Weddell Sea (without a sub-ice platelet layer). We compared the field data to numerical forward models (Anderson, 1979), with the frequency,

the coil spacing and orientation, as well as the thickness and conductivity of multiple layers, as model parameters. We found a significant bias between the actual GEM-2 response and the forward models at all sites and all frequencies. It finally turned out that a third coil, the so-called bucking coil, caused this mismatch. We implemented the bucking coil in our forward models as a second receiver and subtracted the result from the receiver response. We achieved a good agreement between data and forward models with realistic calibration coefficients. In order to identify the influence of a sub-ice platelet layer on the soundings at different frequencies, we repeated the same calibration routine on the sea ice of Atka Bay.

In a second step, the GEM-2 was mounted in a kayak and pulled over the sea ice a few meters behind a snowmobile. More than 100 km of multi-frequency EM soundings were acquired at Atka Bay, with a sampling rate of 10 Hz (Fig. 7.2). In order to facilitate data processing, and accounting for the footprint of the instrument, the dataset was filtered to obtain a spacing of 4 m between soundings.

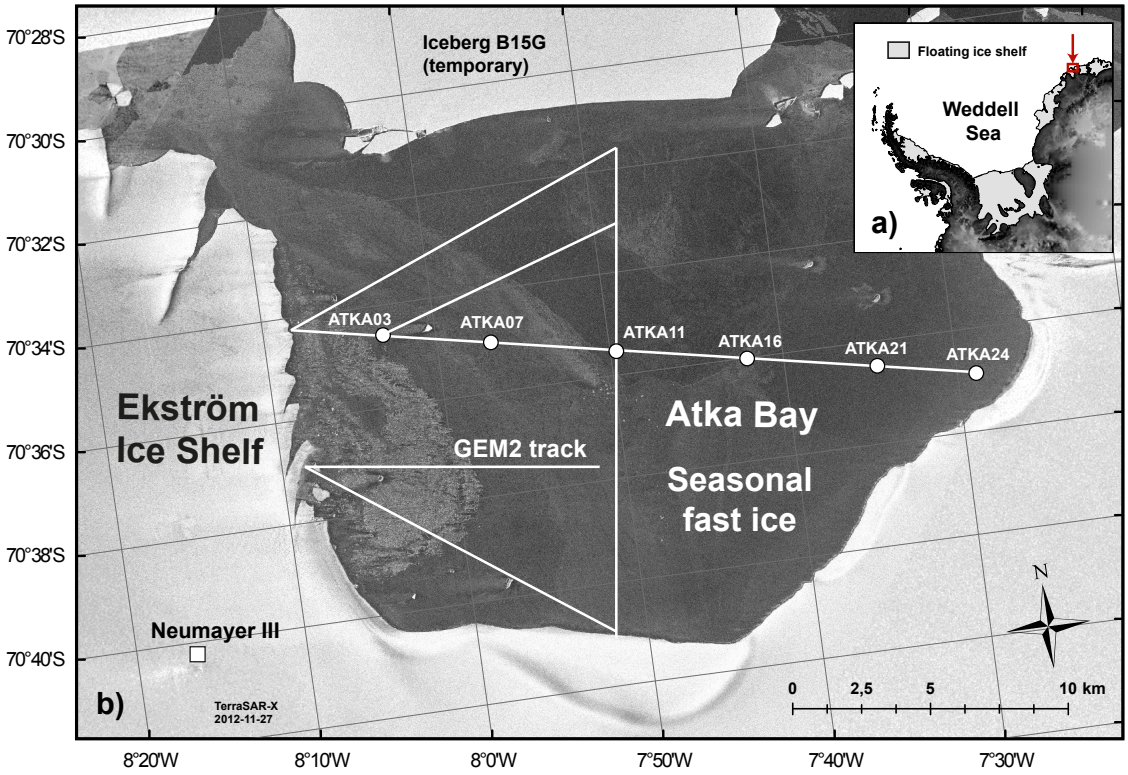

Figure 7.2: Detailed map of study site. a) Location of Atka Bay in the eastern Weddell Sea. b) Enlargement of a), indicating sites of drillings (circles) and GEM-2 transects (white lines). Background: TerraSAR-X image from 27 November 2012, kindly provided by the German Aerospace Agency (DLR).

Sub-ice platelet-layer conductivity and ice-volume fraction

These results are taken from "Towards an estimation of sub sea-ice platelet-layer volume with multi-frequency electromagnetic induction sounding" (Appendix II).

We applied the results from our calibrations on sea ice without a sub-ice platelet layer to selected

soundings at sites of known sea-ice and platelet-layer thickness at Atka Bay. Comparing the results to two-layered forward models, we obtained an average bulk platelet-layer conductivity of 1154 mS/m $\pm$ 271 mS/m (Fig. 7.3).

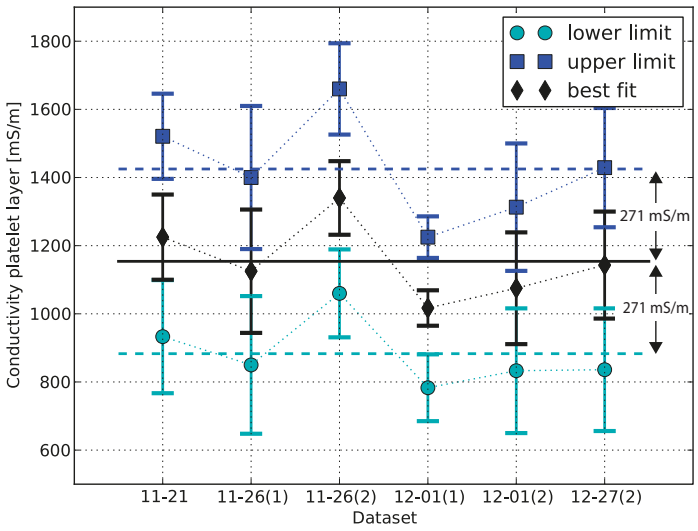

Figure 7.3: Bulk platelet-layer conductivities. Results obtained by different frequencies are averaged and shown for the individual sites. The conductivities and the corresponding standard deviations are shown for the best fit, the lower and upper limit of uncertainties (from Hunkeler et al., 2015).

We then used this result to estimate the platelet-layer ice volume fraction using Archie's Law

$$\sigma = \sigma_b(\Phi)^m \tag{7.1}$$

with the electrical conductivity σ of a porous layer, its porosity Φ, the brine conductivity σ_b and a cementation factor m (Archie, 1942). Assuming a range of plausible cementation factors for the platelet layer, we obtained ice-volume fractions between 0.29 and 0.43.

Sub-ice platelet-layer thickness

This section is based on a very early version of the manuscript "A glimpse beneath Antarctic sea ice: platelet-layer volume from multi-frequency electromagnetic induction sounding" (Appendix III)

In order to derive the sub-ice platelet layer thickness from the multi-frequency EM soundings, we applied a laterally constraint (LCI, Auken and Christiansen, 2004; Christiansen and Auken, 2004; Auken et al., 2005), singular value decomposition (SVD) based Marquardt-Levenberg inversion (Lines and Treitel, 1984). While the number of layers (sea ice, sub-ice platelet layer, seawater) was fixed during an inversion, the thickness and conductivities of the grid cells were variable. All inversions shown here were calculated using a modified version of the Electro-Magnetic Inversion with Least Intricate Algorithms

(EMILIA, Kalscheuer, 2014). The algorithm is based on the work of Siripunvaraporn and Egbert (2000), and was for example used for the delineation of quick clay layers (Kalscheuer et al., 2013). All data were corrected using instrument-specific calibration coefficients, as calculated by Hunkeler et al. (2015).

The performance of the LCI algorithm was tested using a set of synthetic data for our standard frequency setup, calculated from forward models (Anderson, 1979). We used combinations of sea-ice (0.4 - 4 m) and sub-ice platelet layer thicknesses (0.5 - 10 m) with increments of 0.5 m. Sea ice-thickness and -conductivity calculated from the inversion generally agreed well with the true value, with thin sea ice (0.5 m, 1 m) and a thin platelet layer (0.5 m) being the exceptions. Since we seldom observed sea-ice thicknesses $<$0.5 m and platelet-layer thicknesses $>$7 m in the field, we consider the performance of the inversion algorithm to be very reliable for our purposes.

Inversion of the $>$20000 multi-frequency soundings takes a lot of computational resources. Processing of the data was performed on computers clusters at the ETH Zürich, Switzerland, and the University of Uppsala, Sweden. We show here only the results of a selected sub-dataset obtained between ATKA11 and ATKA16 (Fig. 7.4).

The range of calculated conductivities for sea ice ($<$0.4 S/m, yellow tones) was generally in accordance with our expectations based on earlier results. The higher range of sea-ice conductivities was most likely a reflection of surface flooding through cracks in the ice, which increased the apparent conductivity. Visual observations during the EM transects confirmed that surface flooding was very common in the area of the August sea-ice breakup around ATKA11, because the thickness of the new sea ice was small compared to the high snow load. Surface flooding was not observed on thick ice. The EM results are therefore likely an indication of the instruments ability to detect surface flooding and the presence of slush on the sea-ice surface, but a detailed investigation is beyond the scope of the current work. The range and evolution of total (sea ice + snow) thickness along the transect is also in very good agreement with observations from manual drillings, where a total thickness of $<$1 m was measured for the area of the August sea-ice breakup, and around 3 m in the close vicinity of ATKA16. Inspecting the sub-ice platelet layer properties is however where the results become really interesting. The conductivity of the sub-ice platelet layer was variable, but still in the range determined from calibration experiments (1154 mS/m $\pm$ 271 mS/m). It is unclear yet if the drop in platelet-layer conductivity below thick sea ice was due to an inaccurate inversion, or reflecting actual reality. It has been observed during earlier EM31 measurements (not shown), that there is a significant mismatch between drillhole thickness measurements and the EM thickness in the eastern part of Atka Bay. This could potentially be explained by a different conductivity of the sub-ice platelet layer, but further investigations are necessary to resolve this issue. The sub-ice platelet layer thickness was generally $<$2 m for the area of the August sea-ice breakup, and around 5 m near ATKA16. These results are also in very good agreement with measurements from drillings, especially when taking into account the local variability even over very short distances.

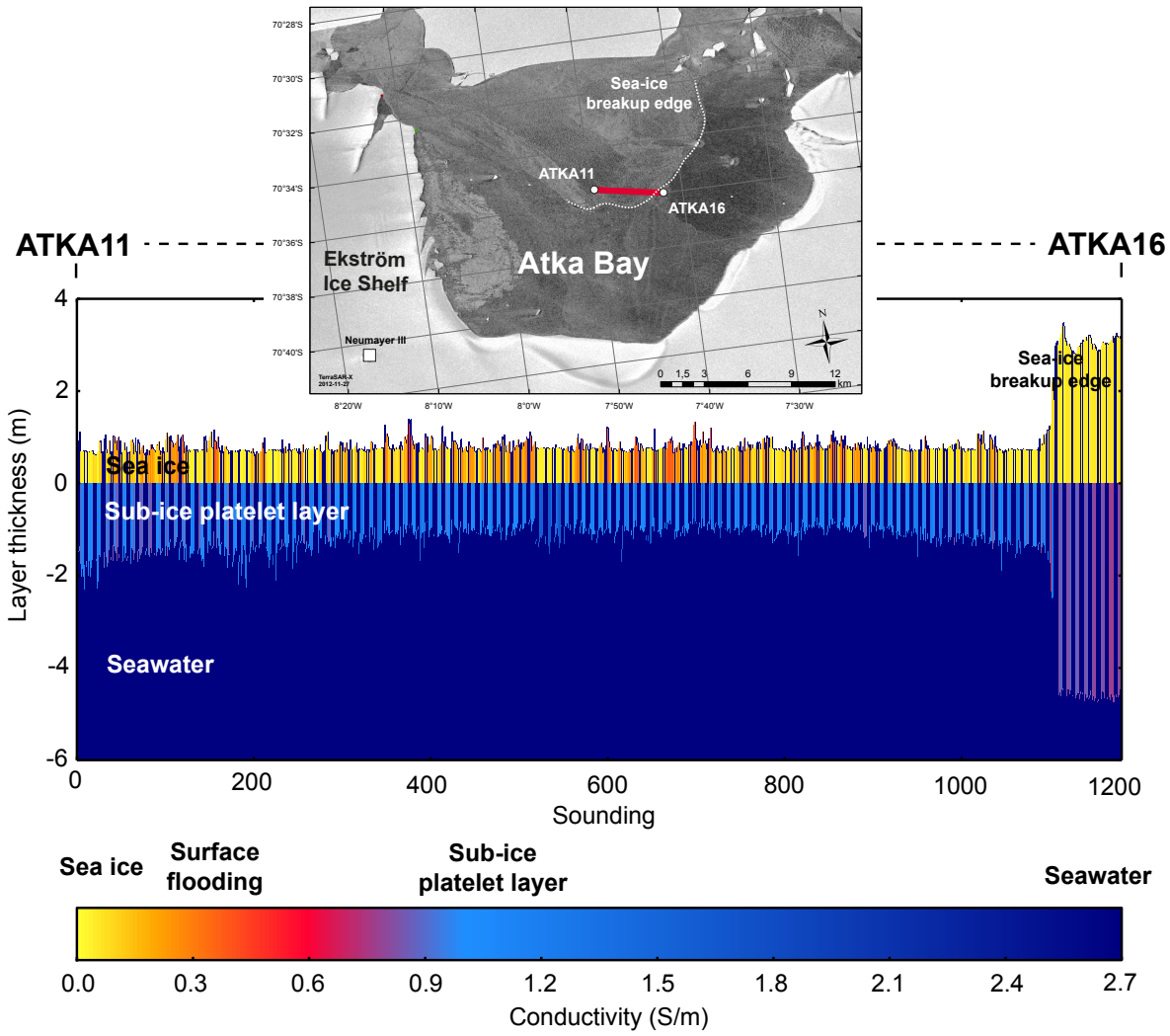

Figure 7.4: Sea-ice and sub-ice platelet layer thickness between sites ATKA11 and ATKA16, derived from geophysical inversion of GEM-2 electromagnetic induction soundings.

Conclusion

As a summary, these preliminary results suggest that electromagnetic induction sounding is a suitable tool to survey ice-platelet volume below the Antarctic near-coastal sea ice on a much larger scale than previously possible by drillhole measurements. Once all transects are processed, we look forward to present the first-ever sub-ice platelet-layer thickness distribution under Antarctic sea ice. Our findings will have critical implications for research of coastal Antarctic sea ice and ocean/ice-shelf interactions, opening the door to a feasible platelet-layer monitoring also at other Antarctic stations. We provide evidence that multi-frequency soundings are superior over single-frequency soundings and may also improve sea-ice thickness retrieval over deformed and porous sea-ice that has similar macro-scale properties to the platelet layer in Antarctica. Ultimately, this approach can potentially also be applied to airborne multi-frequency sensors (Pfaffhuber et al., 2012), allowing for an even larger coverage.

Chapter 8

Publications VII and VIII: Remote sensing of snow on Antarctic sea ice

This chapter summarizes the following publications, which are based on work mainly done by Wolfgang Dierking and Stephan Paul:

> W. Dierking, S. Lienow, C. Wesche, W. Rack, **M. Hoppmann** and S. Willmes. TSX-data for studies of snow on ice sheets and sea ice - preliminary results, 5. TerraSAR-X / 4. Tandem-X Science Team Meeting, **2013**

This paper is published in Proceedings of the 5. TerraSAR-X / 4. Tandem-X Science Team Meeting. My contribution to this publication is that I co-performed the field work.

◇

> S. Paul, S. Willmes, **M. Hoppmann**, P. A. Hunkeler, G. Heinemann, M. Nicolaus and R. Timmermann. The impact of early summer snow properties on land-fast sea-ice X-band backscatter (Appendix IV, Paul et al. (2015)).

This paper is published in Annals of Glaciology **56**(69), **2015**, submitted in January 2014 and accepted November 2014. My contribution to this publication is that I co-performed the field work and co-wrote the paper.

Snow from space - an overview

The importance of snow on sea ice (Section 2.1.3) raises the need for a detailed understanding of associated surface processes in the polar oceans. The analysis and interpretation of satellite data is essential to gain information on those processes, which take place on the large geographic scales that are covered by Antarctic sea ice. Moreover, satellite data provide a crucial link between local measurements, regional forcing and hemispheric peculiarities. In addition to the long-term investigation of general sea-ice conditions and extent in the Antarctic (Zwally et al., 2002), sea-ice surface and snow processes have been under investigation over the entire hemispheric sea-ice region by means of long-term microwave satellite data (Markus and Cavalieri, 2006; Haas, 2001a; Drinkwater and Liu, 2000). The effect of diurnal and daily changes in snow properties on the long-term evolution of the surface microwave emissivity and scattering were presented in Willmes et al. (2006) and Willmes et al. (2010), respectively. However, the detailed interrelation between local processes in the snow cover and their microwave response yet needs to be identified. Because of this, a link between limited point measurements and high-resolution spaceborne monitoring systems is desirable (Yackel and Barber, 2007).

Interactions between the sea-ice snow cover and microwave radiation, emitted e.g. by a spaceborne synthetic aperture radar (SAR) system, hold the potential to develop algorithms to estimate snow volume, as well as snow physical properties over sea ice on a global scale (Barber and Thomas, 1998). Snow affects the microwave interactions through direct scattering based on snow-physical properties (e.g. density, salinity, grain size and shape) and through thermodynamically controlled effects on the dielectric properties of the snow (e.g. its brine volume). Already a very shallow dry snow cover increases the backscatter from sea ice. However, additional dry snow does not further alter the received backscatter signal significantly (e.g., Barber and Thomas, 1998; Kim et al., 1984). This effect is linked to a higher ice-surface roughness and an increase in the dielectric contrast, which again is caused by brine wicking into the snow layer from the upper most sea-ice layer (Kim et al., 1984).

The backscatter signal of sea ice is generally affected by a two-way loss through the snow cover. If liquid water is present in the snow pack, both the real and the imaginary part of the dielectric constant increase, resulting in a higher signal loss. This makes the measured backscatter signal less sensitive to the underlying sea ice and boosts the surface and volume scattering contribution of the snow-pack to the total signal (Yackel et al., 2007; Barber and Thomas, 1998; Kim et al., 1984).

Recent space-borne SAR systems operate in different bands, at swath widths between 30 and 500 km and at different spatial resolutions, typically between 1 and 1000 m (Dierking, 2013). These systems are widely used for sea-ice monitoring and ice-type classification (e.g. Dierking, 2013, 2010; Eriksson et al., 2010), but the number of investigations on snow cover on Antarctic sea ice, and its interrelation with microwave radiation data, is still small compared when to the Arctic. In the Antarctic, several studies investigated the influence of the snow cover on SAR backscatter and its potential to retrieve snow properties over ice sheets (e.g., Kendra et al., 1998; Zahnen et al., 2002; Nagler and Rott, 2004; Dierking et al., 2012). Other studies examined the relationship between C-Band SAR / Ku-Band scatterometer data and snow properties on sea ice in different regions of Antarctica (Willmes et al., 2011; Kern et al., 2011; Ozsoy-Cicek et al., 2011; Worby et al., 2008b)), but the lack of spatio-temporal, high-resolution

measurements of snow properties remains a key problem for the validation of satellite data.

Methods and Results

In this study, we provide new knowledge on the relationship between snow physical properties on sea ice and the backscatter of space-borne SAR systems, by linking the spatio-temporal evolution of X-band SAR backscatter (σ^0) during spring/summer transition to simultaneously measured snow properties at Atka Bay. Due to its higher frequency, X-Band SAR is more sensitive to the snow cover, the upper sub-surface ice layer, as well as to the onset of melt and freeze-thaw processes, than C-Band SAR (Eriksson et al., 2010).

We obtained snow physical properties from a total of 41 snow pits on Atka Bay fast ice between November 2012 and January 2013. Each snow pit (Fig. 8.1) comprised measurements of snow temperature and -density gradients, as well as snow stratigraphy (i.e. grain-size distribution, snow-pack layering, qualitative estimates of snow liquid-water content, hardness and crystal type) following Fierz et al. (2009). Our measurements focused on the regular sampling sites (Fig. 4.2), while additional snow data were recorded sporadically at other locations.

Figure 8.1: Measurement of snow physical properties on sea ice in a snow pit

In addition, we acquired a total number of 13 TerraSAR-X (TSX) swaths shortly prior to and during the study. TerraSAR-X is a spaceborne X-band SAR instrument operated by the German Aerospace Center (DLR). The satellite is operational since June 2007 in a 514 km orbit, and is able to operate in four different imaging modes. Relevant to this study are the ScanSAR mode (SC) in single polarization, and the StripMap mode (SM) in single horizontal (HH), vertical (VV) and dual polarization. The swath width depends on the mode and polarization. In ScanSAR mode, a swath covers a 150 $\times$ 100 km^2 ground area. In StripMap mode, the coverage changes to 50 $\times$ 30 km^2 (50 $\times$ 15 km^2) in single (dual) polarization mode (Eineder et al., 2008).

In order to account for the wide range of local incidence angles (LIA) covered by the TSX swaths,

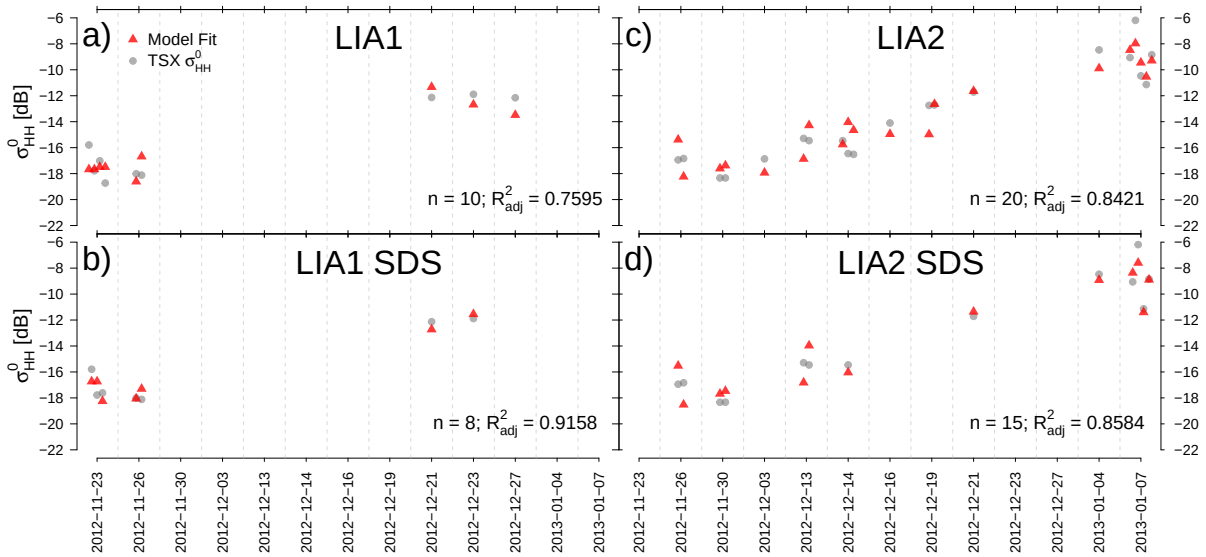

Figure 8.2: Multiple linear model fits (red triangles) and extracted σ^0_{HH} values from all available snow-pit measurements in a $\pm$ 5 day range (gray dots) for different Local Incidence Angles (LIA) and datasets. a) is based on all available snow-pit measurements for Local Incidence Angle class 1. b) is limited to snow-pit measurements with snow depth (z_{snow}) $<$ 60 cm for LIA class 1. In c) and d), the same setup is presented for LIA class 2. All model fits are significant (α<0.001) and explain between 75 % and 91 % (R^2_{adj}) of the total variance of σ^0_{HH}.

we divided our dataset into three different LIA classes (LIA1: LIA>36°, LIA2: 36° $\geq$ LIA $>$ 27° and LIA3: LIA $<$ 27°). Multiple linear models were applied to the TSX backscatter and the measured snow physical properties. Every model was initialized with all measured snow-pack parameters. Using step-wise regression modeling, the parameter with the least significant contribution to the overall explained variance was removed from the model in each iteration. After several iterations, a significant model fit was achieved. Four representative model fits are shown in Figure 8.2, where gray dots indicate the measured TSX σ^0_{HH} values and the red triangles correspond to the modeled backscatter. Figure 8.2a and c show the model fit of the complete data set for LIA1 and LIA2 classes respectively. Figure 8.2b and d refer to measurement sites with $z_{snow} < 0.6$ m (SDS). Model fit LIA1 (10 value pairs) explains 75% of the σ^0_{HH} variance (Fig. 8.2a), based on the predictors z_{snow} (snow depth), and SWE (snow-water equivalent). The model fit LIA2 (20 value pairs) explains 84% of the σ^0_{HH} variance (Fig. 8.2c), based on the predictors z_{snow}, T_i (snow/ice interface temperature) and E_{top} (top-layer grain size).

Also taking into account further model fits not explicitly shown here, our results indicate that between 75 % and 93 % of the observed TSX HH-polarized backscatter are explained by snow depth, snow-water equivalent, snow/ice interface temperature and grain size.

Discussion and Conclusion

The different quality of the model fits, i.e. their potential to explain a maximum percentage of the observed TerraSAR-X HH-polarized backscatter variance, results from different subsets and limitations to the data set such as excluding measurements in a dry snow environment. The correlation between the TerraSAR-X

HH-polarized backscatter and the snow depth also increases when reducing the dataset to measurements in areas with a snow depth $<$0.6 m. These relationships, as well as the potential to explain the variations in single polarization HH X-Band SAR backscatter with a few snow physical properties, has not yet been presented in comparable detail under non-laboratory conditions. The possibility to fit a simple multiple linear model based on up to four snow-pack parameters to simultaneously acquired TerraSAR-X HH-polarized backscatter data suggests great potential to derive snow-physical properties from X-Band backscatter in an inverse approach. However, the data presented here are not sufficient to achieve this aim due to the limitation to HH like-polarization data and the lack of snow-salinity and -liquid-water-content measurements, a limitation future studies should seek to overcome.

Chapter 9

Key findings and Outlook

Sea-ice monitoring at Atka Bay

Continuous monitoring of sea-ice properties is crucial to detect changes in the processes governing its evolution. The possibilities of such monitoring activities on sea ice are generally very limited in the high latitudes, particularly in the Southern Hemisphere. This is mainly due to environmental challenges, logistical constraints and the huge financial effort. The fast ice of Atka Bay in the eastern Weddell Sea is one of the few locations in Antarctica where continuous measurements are at all possible, due to the presence of the German wintering station Neumayer III and the associated excellent logistics and infrastructure. However, dedicated fast-ice studies were limited to two overwinterings in 1982 and 1995. This study laid the foundation for a multi-faceted, long-term fast-ice monitoring program at Atka Bay, filling a significant observational gap in one of the most important regions of the Southern Ocean. In contrast to the Ross and Davis Seas, where fast ice has been monitored for decades, the Weddell Sea sector remained underrepresented for a long time. Starting in 2010 only with manual measurements of sea-ice thickness and snow depth, we were able to expand the program despite the limited time the Neumayer III personnel can devote to the additional work (Fig. 9.1).

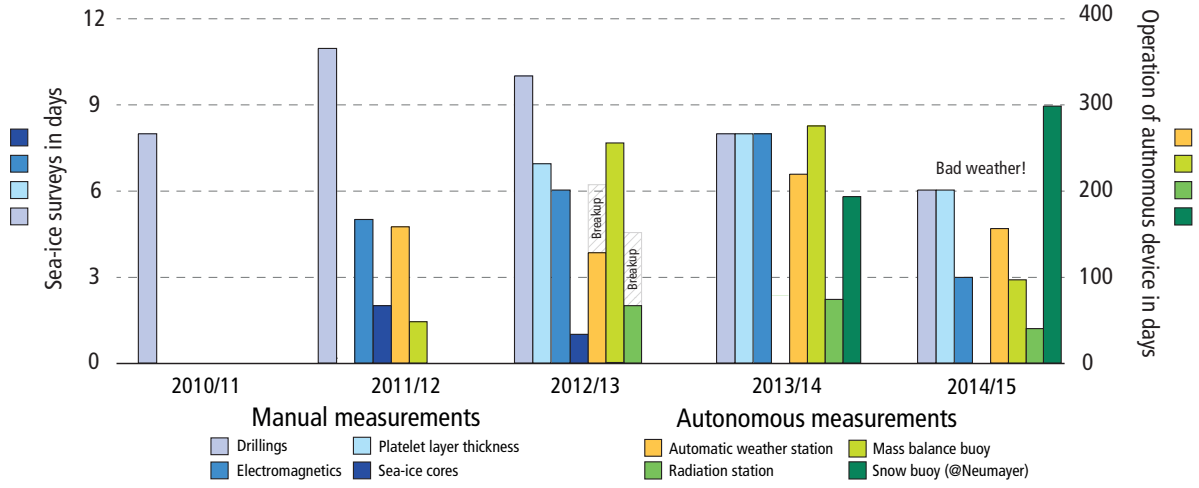

Figure 9.1: Development of sea-ice monitoring 2010-2014

In addition to the challenging sub-ice platelet-layer thickness measurements, we regularly recorded total thickness distributions by electromagnetic induction sounding. Furthermore, we established a suite of regular autonomous measurements directly on the fast ice, including sea-ice mass balance buoys,

meteorological observations and high-resolution spectral radiation measurements. Our data and experience have been proven to be a valuable addition to the Antarctic Fast Ice Network (AFIN), where other project partners are already benefiting from our work. Once the AFIN concept and database are finally established in the coming years, we expect our observatory to form one of the backbones of this international network.

Fast-ice and sub-ice platelet layer properties

This study contributed new knowledge on the seasonal evolution of fast ice and an underlying platelet layer at Atka Bay, eastern Weddell Sea, and highlighted the dependence of coastal Antarctic sea-ice regimes on local ocean-ice shelf interactions. Typical sea-ice thickness at Atka Bay was around 2 m at the end of the growth season, while dynamic thickening, such as ridging and rafting, and snow depths more than 1 m, introduced large spatial variability. A thick platelet layer was observed below the entire fast-ice cover, with first observations of platelets in drillholes and sea-ice cores as early as early as May/June (for first-year ice). Potentially supercooled water was regularly present under the ice shelf during winter. Under-ice video recordings revealed that the accumulation of ice platelets proceeds mainly through distinct episodic events of high upward fluxes, overlying a very low continuous flux. The platelet-layer thickness steadily increased until December, with a bay-wide average annual thickening of 4 m, and local maxima of 10 m. When warm surface water intruded into Atka Bay at the beginning of December, ice-platelet accumulation ceased and the platelet layer thinned, shielding the above solid ice from melting. Through the additional buoyancy, surface flooding and snow-ice formation were rarely observed, despite the thick snow cover. Comparison of drillhole measurements with a one-dimensional, thermodynamic sea-ice growth model yielded an ice-volume fraction, β, in the platelet layer of 0.18 - 0.35 $\pm$ 0.1. 43 % (70 %) of the combined mass of first-year (multi-year) sea ice and its underlying platelet layer originated from ocean/ice-shelf interaction. In relation to Ekström Ice Shelf basal melt, we found that more than 20 % of the annual basal melt volume is refrozen as ice platelets trapped under Atka Bay fast ice. It is very likely that the oceanographic conditions in this area promote the transport of potentially supercooled water out of the cavity, leading to further ice-platelet formation away from the coast.

New process understanding, such as provided in this study, is crucial to establish missing linkages between the ice sheet, ocean and sea ice. Figure 9.2 summarizes the seasonal evolution of the Atka Bay fast-ice regime, based on findings from Publications II and III.

Thermistor chains as a tool for research into ice-shelf/sea-ice interaction

One of the highlights of this study is a consistent time series of air, snow, sea-ice and ocean/platelet-layer temperature profiles recorded by a thermistor chain with the additional ability of cyclic heating embedded resistors (“heating mode”). This dataset is one of the longest of its kind recorded to date, and reveals various features in the seasonal sea-ice evolution which have not been analyzed in comparable detail. By calculating the basal energy balance of the sea ice, we were able to determine an annual average residual heat flux of -1 W m^{-2}. In total, 18 $\pm$ 9% of the ice grown between April and December 2013 was not accounted for by heat conduction to the atmosphere. The translation of this result to a platelet-layer ice-volume fraction of 0.18 $\pm$ 0.09 was also confirmed by independent sea-ice growth simulations. An

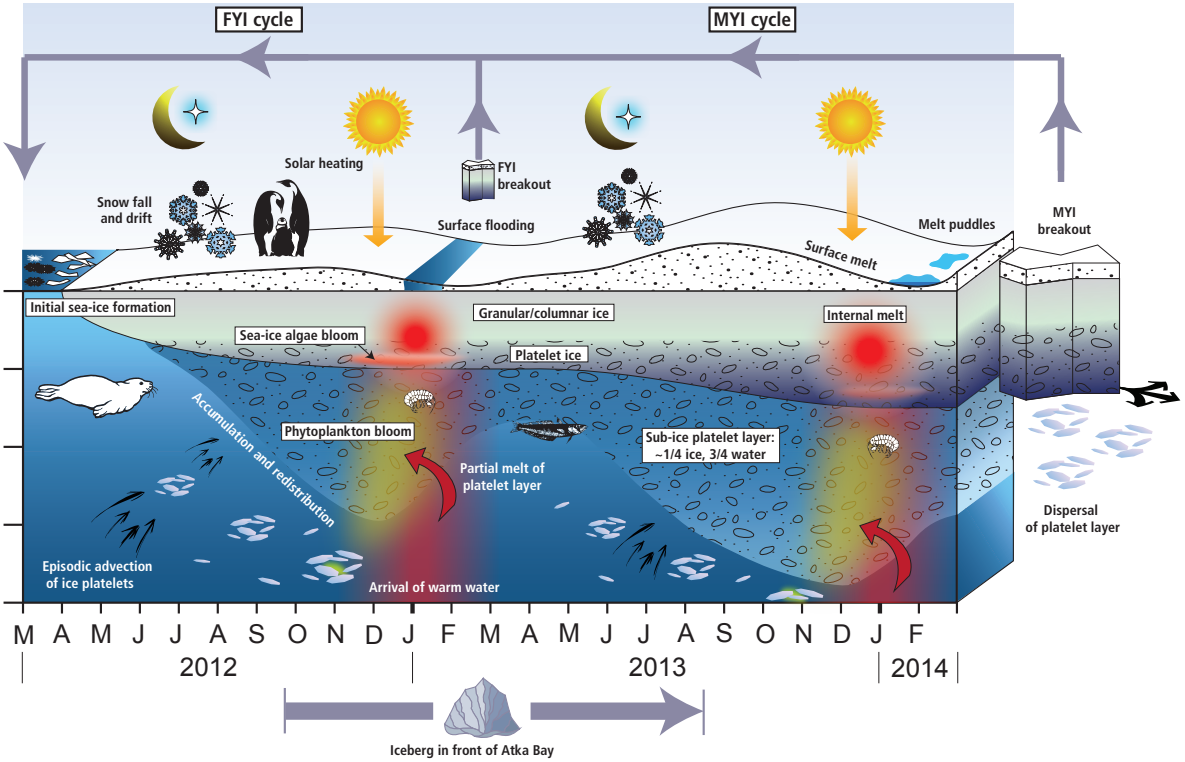

Figure 9.2: Schematic diagram of the seasonal cycle of Atka Bay fast ice and the sub-ice platelet layer (taken from Publication III).

approximate ocanic heat flux of 21 W m^{-2} during summer months was not sufficient to melt the entire platelet layer. This study directly supplied evidence that in areas where sea ice grows slowly, such as thick multi-year sea ice or in the presence of a thick snow cover, most of the sea-ice volume is contributed by ocean/ice-shelf interaction.

We also showed that, by the distinction of media through their thermal properties, the heating mode is able to compensate the lack of acoustic sounders present on standard mass balance buoys, making this buoy far easier to deploy and more reliable. By careful extraction of the interfaces from both measurement modes, it is possible to accurately determine the basal energy budget. In addition, the instrument is able to resolve internal structures such as gap layers and their refreezing. Although it should generally be possible to quantify the thermal conductivity and specific heat capacity of sea-ice and snow, our study could not provide the necessary methodology.

Finally, our study has proven that a thermistor chain with active heating is capable of detecting the sub-ice platelet layer thickness through the lower current speed compared to the underlying ocean. This instrument is thereby currently the only automated method to continuously monitor the formation and decay of a sub-ice platelet layer. This makes it the ideal tool to study sea-ice regimes influenced by ocean/ice-shelf interaction at a fixed site continuously over an extended time. We are confident that these instruments will provide valuable insight into ocean/ice-shelf/sea-ice interactions and the associate processes. While the interpretation of the temperature and especially the heating data may be challenging,

we hope that this study facilitates this process in the future and encourages other sea-ice studies to make use of this instruments design.

Thermodynamic model of fast-ice growth

An established one-dimensional, thermodynamic sea-ice growth model was modified by introduction of an enhanced growth rate accounting for the ice-volume fraction in the platelet layer. When initialized with parameters based on observations and forced with local atmospheric data as well as realistic snow depth, the model yielded an ice-volume fraction consistent with that calculated from other methods and studies. These results thereby suggest that the modified model is generally well suited to accurately reproduce fast-ice growth near ice shelves.

Sub-ice platelet-layer properties from multi-frequency EM

Multi-frequency electromagnetic induction sounding has recently been introduced into sea-ice research, with the aim to improve sea-ice thickness retrieval especially over deformed and porous sea-ice. In this study, we provided the first comprehensive treatment on the operation of a promising (ground-based) multi-frequency EM instrument (GEM-2, Geophex Ltd.) on sea ice, including calibration routines and uncertainty estimates. In a first step, we compared a multi-frequency dataset obtained at Atka Bay with a two-layer forward model, yielding a first-time average platelet-layer conductivity of 1154 mS $m^{-1} \pm$ 271 mS m^{-1}. This result is important in that it provides elemental physical constraints for the layer conductivities in geophysical inversions. In a second step, we implemented the instrument-specific bucking coil into a two-dimensional inversion code and successfully reproduced synthetic thickness data. Finally, we performed the first calculations of sub-ice platelet-layer thickness below near-coastal Antarctic sea ice. Our first results suggest that this approach allows a determination of sub-ice platelet-layer volume on a much larger scale than previously feasible by drillhole experiments.

Remote sensing of snow properties from X-band satellite imagery

Snow on sea ice is an important regulator of surface properties. While sea-ice extent has been effectively monitored from space using satellite imagery, sea-ice thickness retrieval from space is still a challenge due to the snow cover. In our study, we compared the spatio-temporal evolution of TerraSAR-X backscatter to in situ physical properties of snow on sea ice. We found that the changes in the seasonal snow cover are reflected in the evolution of TerraSAR-X backscatter, with between 75 % and 93 % of the spatio-temporal variability of the TerraSAR-X backscatter signal related to changes in snow/ice-interface temperature, snow depth and top- layer grain size. This further implies the potential to retrieve snow physical properties from X-band SAR backscatter in an inverse approach, which is work currently in progress.

Key elements for future research

As is common in scientific research, the findings presented in this work have generated new questions that may help to define pathways for future exploration.

Although no obvious changes of sea-ice and oceanographic conditions were found in this study compared to investigations 30 years ago, this will not necessarily be the case in the future. Hellmer et al. (2012), Pritchard et al. (2012) and Depoorter et al. (2013) previously highlighted that the complex interactions between the Southern Ocean, the Antarctic ice shelves, and the sea-ice cover have significant global implications, and they concluded that much more process understanding related to ice-shelf cavities is needed.

Fast-ice characteristics especially near ice shelves may provide a very sensitive, and yet practical, indicator of the conditions and possible changes in the Antarctic. At the same time, studies of fast-ice properties near coastal Antarctic stations are comparatively easy to conduct. Hence there exists an urgent need to perform these studies on a more regular and circum-Antarctic basis, e.g. through extending and intensifying the work in the Antarctic Fast Ice Network.

It is particularly necessary to extend the measurements and techniques introduced here to other areas where sea ice is affected by nearby ice shelves in order to gain more insight into the temporal and spatial variability of ocean/ice-shelf interaction around Antarctica. The question is: How much fast ice around Antarctica is actually impacted by ocean/ice-shelf interaction? Considering that nearly half of the entire Antarctic coastline is fringed by ice shelves, and that the fast-ice belt around the coast may reach widths of hundreds of kilometers, it is likely that platelet layers are prevalent over a substantial area around the continent. Our results suggest that there seems to be great potential to apply geophysical inversions similar to those shown here to airborne multi-frequency EM instruments. If this can be achieved, circum-Antarctic detection of ocean/ice-shelf interaction from air seems almost within reach. When combined, the two methods introduced here (thermistor chains with heating and multi-frequency EM induction sounding) complement each other in the sense that they allow for an investigation of ocean/ice-shelf interaction and its impact on sea ice on a larger spatial (EM) and temporal (TC) scale than ever possible before, with relatively limited effort. This would seemingly be a breakthrough for coastal Antarctic sea-ice research, oceanography, glaciology and probably even biology/ecology.

Probably the most challenging research aspect is the implementation of the various ice-ocean interaction processes into coupled climate models simulating the response of the Antarctic system to the ongoing global warming. Although a suite of tools was introduced here to study platelet accumulations under sea ice, we still lack the knowledge about the factors controlling basal melt and the formation of ice crystals at depth. Coastal polynyas are of particular interest as the main driver for the production of dense High Salinity Shelf Water. However, measurements of the ocean beneath Antarctic (sea) ice are sparse because traditional oceanographic tools are not suitable for sustained measurements in ice-covered seas. The use of recent technological advances, such as ice-capable profiling floats, oceanographic sensors deployed on seals, ice-tethered profilers, gliders and submersibles, ship-based hydrography, and moorings now allows to make sustained observations of the ocean beneath sea ice and ice shelves, and their coordinated use is a necessity to determine the driving factors.

Although aspects of the significance of sub-ice platelet layers for sea-ice ecosystems are at least partly understood, several important questions in this regard still remain unanswered. For example, how do sub-ice platelet layer properties govern primary production and community structure, and how is the potential increase in sedimentation of marine debris impacting the benthos? In addition, how do sub-ice

platelet layers affect marine mammals? Since the breeding cycle of penguins and seals is generally closely tied to the seasonal cycle of the sea ice, there might be an important link between the properties of fast ice near ice shelves and their breeding behavior. These are questions which can only be tackled in a multi-disciplinary approach, which directly link the physical environment to the associated ecosystem. Building up on the work presented here, we strongly suggest to realize an urgently needed integrated observatory at Atka Bay, combining sea-ice and oceanographic measurements with mammal observations (already performed by the ocean acoustics group) and regular biological sampling of the sub-ice platelet layer (as performed by Günther, 1999). This could even be enhanced by deploying sediment traps below sea ice (as already done in 1995) to establish the link to the benthos.

Chapter 10

Reference List

Abram, N. J., E. R. Thomas, J. R. McConnell, R. Mulvaney, T. J. Bracegirdle, L. C. Sime, and A. J. Aristarain. Ice core evidence for a 20th century decline of sea ice in the Bellingshausen Sea, Antarctica. *Journal of Geophysical Research: Atmospheres*, 115(D23101), 2010. http://dx.doi.org/10.1029/2010JD014644. (Cited on pages 13 and 17.)

Ackley, S. F. and C. W. Sullivan. Physical controls on the development and characteristics of Antarctic sea ice biological communities - a review and synthesis. *Deep Sea Research Part I: Oceanographic Research Papers*, 41(10):1583–1604, 1994. http://dx.doi.org/10.1016/0967-0637(94)90062-0. (Cited on page 34.)

Ackley, S., P. Wadhams, J. C. Comiso, and A. P. Worby. Decadal decrease of Antarctic sea ice extent inferred from whaling records revisited on the basis of historical and modern sea ice records. *Polar Research*, 22(1):19–25, 2003. (Cited on page 13.)

Anderson, W. L. Numerical integration of related hankel transforms of orders 0 and 1 by adaptive digital filtering. *Geophysics*, 44(7):1287–1305, 1979. http://dx.doi.org/10.1190/1.1441007. (Cited on pages 104 and 107.)

Archie, G. E. The Electrical Resistivity Log as an Aid in Determining Some Reservoir Characteristics. *Transactions of the AIME*, 146, 1942. http://dx.doi.org/http://dx.doi.org/10.2118/942054-G. (Cited on page 106.)

Arndt, J. E., H. W. Schenke, M. Jakobsson, F. O. Nitsche, G. Buys, B. Goleby, M. Rebesco, F. Bohoyo, J. Hong, J. Black, R. Greku, G. Udintsev, F. Barrios, W. Reynoso-Peralta, M. Taisei, and R. Wigley. The International Bathymetric Chart of the Southern Ocean (IBCSO) Version 1.0 - A new bathymetric compilation covering circum-Antarctic waters. *Geophysical Research Letters*, 40(12):3111–3117, 2013. http://dx.doi.org/10.1002/grl.50413. (Cited on page 39.)

Arrigo, K. R. Sea ice ecosystems. *Annual Review of Marine Science*, 6(1):439–467, 2014. http://dx.doi.org/10.1146/annurev-marine-010213-135103. (Cited on pages 8 and 9.)

Arrigo, K. R. and D. N. Thomas. Large scale importance of sea ice biology in the Southern Ocean. *Antarctic Science*, 16(4):471–486, 2004. http://dx.doi.org/10.1017/S0954102004002263. (Cited on pages 24 and 34.)

Arrigo, K. R. and G. L. van Dijken. Phytoplankton dynamics within 37 Antarctic coastal polynya systems. *Journal of Geophysical Research: Oceans*, 108(C8):3271, 2003. http://dx.doi.org/10.1029/2002JC001739. (Cited on page 35.)

Arrigo, K. R., C. W. Sullivan, and J. K. Kremer. A bio-optical model of Antarctic sea ice. *Journal of Geophysical Research*, 96(C6):10581–10592, 1991. (Cited on page 34.)

Arrigo, K. R., J. K. Kremer, and C. W. Sullivan. A simulated Antarctic fast ice ecosystem. *Journal of Geophysical Research*, 98(C4):6929–6946, 1993a. http://dx.doi.org/10.1029/93JC00141. (Cited on page 35.)

Arrigo, K. R., D. H. Robinson, and C. W. Sullivan. A high-resolution study of the platelet ice ecosystem In McMurdo Sound, Antarctica - photosynthetic and biooptical characteristics of a dense microalgal bloom. *Marine Ecology Progress Series*, 98(1-2):173–185, 1993b. http://dx.doi.org/10.3354/meps127255. (Cited on pages 19, 24, 33, 34 and 35.)

Arrigo, K. R., G. Dieckmann, M. Gosselin, D. H. Robinson, C. H. Fritsen, and C. W. Sullivan. High-resolution study of the platelet ice ecosystem in McMurdo Sound, Antarctica - biomass, nutrient, and production profiles within a dense microalgal bloom. *Marine Ecology-Progress Series*, 127(1-3): 255–268, 1995. http://dx.doi.org/10.3354/meps127255. (Cited on page 35.)

Arrigo, K. R., T. Mock, and M. P. Lizotte. *Primary Producers and Sea Ice*, pages 283–325. Wiley-Blackwell, 2010. (Cited on page 35.)

Arzel, O., T. Fichefet, and H. Goosse. Sea ice evolution over the 20th and 21st centuries as simulated by current AOGCMs. *Ocean Modelling*, 12(3-4):401–415, 2006. http://dx.doi.org/10.1016/j.ocemod.2005.08.002. (Cited on page 14.)

Atkinson, A., V. Siegel, E. Pakhomov, and P. Rothery. Long-term decline in krill stock and increase in salps within the Southern Ocean. *Nature*, 432(7013):100–103, 2004. http://dx.doi.org/10.1038/nature02996. (Cited on page 12.)

Auken, E. and A. V. Christiansen. Layered and laterally constrained 2d inversion of resistivity data. *Geophysics*, 69(3):752–761, 2004. http://dx.doi.org/10.1190/1.1759461. (Cited on page 106.)

Auken, E., A. V. Christiansen, B. H. Jacobsen, N. Foged, and K. I. Sørensen. Piecewise 1d laterally constrained inversion of resistivity data. *Geophysical Prospecting*, 53(4):497–506, 2005. http://dx.doi.org/10.1111/j.1365-2478.2005.00486.x. (Cited on page 106.)

Bamber, J. L., D. G. Vaughan, and I. Joughin. Widespread complex flow in the interior of the Antarctic ice sheet. *Science*, 287(5456):1248–1250, 2000. http://dx.doi.org/10.1126/science.287.5456.1248. (Cited on page 22.)

Baranov, G., Y. L. Nazintsev, and N. V. Cherepanov. Formation conditions and certain properties of Antarctic sea ice (according to observations of 1963). In *Collected Papers of Soviet Antarctic Expeditions*, volume 38, pages translated from Russian by Israel Program for Scientific Translations, Jerusalem. 1969. (Cited on page 33.)

Barber, D. and A. Thomas. The influence of cloud cover on the radiation budget, physical properties, and microwave scattering coefficient (σ^0) of first-year and multiyear sea ice. *IEEE Transactions on Geoscience and Remote Sensing*, 36(1):38–50, 1998. http://dx.doi.org/10.1109/36.655316. (Cited on pages 10 and 110.)

Barkov, N. I. *Ice Shelves of Antarctica*. Amerind Publishing Company, New Delhi, NY, 1985. (Cited on page 21.)

Bindschadler, R., H. Choi, A. Wichlacz, R. Bingham, J. Bohlander, K. Brunt, H. Corr, R. Drews, H. Fricker, M. Hall, R. Hindmarsh, J. Kohler, L. Padman, W. Rack, G. Rotschky, S. Urbini, P. Vornberger, and N. Young. Getting around Antarctica: new high-resolution mappings of the grounded and freely-floating boundaries of the Antarctic ice sheet created for the International Polar Year. *The Cryosphere*, 5(3): 569–588, 2011. http://dx.doi.org/10.5194/tc-5-569-2011. (Cited on page 40.)

Bintanja, R., G. J. van Oldenborgh, S. S. Drijfhout, B. Wouters, and C. A. Katsman. Important role for ocean warming and increased ice-shelf melt in Antarctic sea-ice expansion. *Nature Geoscience*, 6(5): 376–379, 2013. http://dx.doi.org/10.1038/ngeo1767. (Cited on pages 16, 17 and 24.)

Bintanja, R., G. J. van Oldenborgh, and C. A. Katsman. The effect of increased fresh water from Antarctic ice shelves on future trends in Antarctic sea ice. *Annals of Glaciology*, 56(69):120–126, 2014. http://dx.doi.org/10.3189/2015AoG69A001. (Cited on pages 16, 17 and 24.)

Bombosch, A. and A. Jenkins. Modeling the formation and deposition of frazil ice beneath Filchner-Ronne Ice Shelf. *Journal of Geophysical Research: Oceans*, 100(C4):6983–6992, 1995. http://dx.doi.org/10.1029/94JC03224. (Cited on pages 29, 36 and 37.)

Budd, W. F., M. J. Corry, and T. H. Jacka. Results from the Amery Ice Shelf project. *Annals of Glaciology*, 3:36–41, 1982. (Cited on page 37.)

Bunge, T. and E. Roß-Reginek. Final Comprehensive Environmental Evaluation of the Proposed Activities: Construction of the Neumayer III Station, Operation of the Neumayer III Station, Dismantling of the Existing Neumayer II Station, 2005. http://www.umweltbundesamt.de/sites/default/files/medien/pdfs/NMIII-Final-Comprehensive.pdf. Last checked: 11.12.2014. (Cited on page 40.)

Bunt, J. S. Microbiology of Antarctic sea ice: diatoms of Antarctic sea ice as agents of primary production. *Nature*, 199(4900):1255–1257, 1963. http://dx.doi.org/10.1038/1991255a0. (Cited on pages 33 and 34.)

Bunt, J. S. Primary Productivity Under Sea Ice in Antarctic Waters: 1.Concentrations and Photosynthetic Activities of Microalgae in the Waters of McMurdo Sound, Antarctica. In Lee, M. O., editor, *Biology of the Antarctic Seas*, pages 13–26. American Geophysical Union, Washington D.C., 1964a. http://dx.doi.org/10.1029/AR001p0013. (Cited on page 24.)

Bunt, J. S. Primary Productivity Under Sea Ice in Antarctic Waters: 2.Influence of Light and Other Factors on Photosynthetic Activities of Antarctic Marine Microalgae. In Lee, M. O., editor, *Biology of the Antarctic Seas*, pages 27–31. American Geophysical Union, Washington D.C., 1964b. http://dx.doi.org/10.1029/AR001p0027. (Cited on page 34.)

Bunt, J. S. and C. C. Lee. Seasonal primary production in Antarctic sea ice at McMurdo Sound in 1967. *Journal of Marine Research*, 28(3), 1970. (Cited on pages 33, 34 and 35.)

Bunt, J. S. and E. J. F. Wood. Microalgae and Antarctic sea. *Nature*, 199:1254–1257, 1963. (Cited on page 34.)

Buynitskiy, V. K. Structure, principal properties and strength of Antarctic sea ice. *Sov. Ant. Exp. Inf. Bull., Engl. Transl.*, 65:504–510, 1967. (Cited on page 33.)

Cavalieri, D. J. and C. L. Parkinson. Antarctic sea ice variability and trends, 1979-2006. *Journal of Geophysical Research: Oceans*, 113(C7):C07004, 2008. http://dx.doi.org/10.1029/2007JC004564. (Cited on page 13.)

Christiansen, A. V. and E. Auken. Optimizing a layered and laterally constrained 2d inversion of resistivity data using broyden's update and 1d derivatives. *Journal of Applied Geophysics*, 56(4):247–261, 2004. http://dx.doi.org/10.1016/j.jappgeo.2004.07.004. (Cited on page 106.)

Clarke, D. B. and S. F. Ackley. Sea ice structure and biological activity in the Antarctic marginal ice zone. *Journal of Geophysical Research: Oceans*, 89(Nc2):2087–2095, 1984. http://dx.doi.org/10.1029/JC089iC02p02087. (Cited on page 12.)

Comiso, J. C. A rapidly declining perennial sea ice cover in the Arctic. *Geophysical Research Letters*, 29 (20), 2002. http://dx.doi.org/10.1029/2002GL015650. (Cited on page 12.)

Comiso, J. C., R. Kwok, S. Martin, and A. L. Gordon. Variability and trends in sea ice extent and ice production in the Ross Sea. *Journal of Geophysical Research: Oceans*, 116(C04021), 2011. http://dx.doi.org/10.1029/2010JC006391. (Cited on page 15.)

Convey, P., R. Bindschadler, G. di Prisco, E. Fahrbach, J. Gutt, D. A. Hodgson, P. A. Mayewski, C. P. Summerhayes, J. Turner, and A. Consortium. Antarctic climate change and the environment. *Antarctic Science*, 21(6):541–563, 2009. http://dx.doi.org/10.1017/S0032247413000296. (Cited on pages 13 and 20.)

Cook, A. J. and D. G. Vaughan. Overview of areal changes of the ice shelves on the Antarctic Peninsula over the past 50 years. *The Cryosphere*, 4(1):77–98, 2010. http://dx.doi.org/10.5194/tc-4-77-2010. (Cited on page 22.)

Cota, G. F. and R. E. H. Smith. Ecology of bottom ice algae: III. Comparative physiology. *Journal of Marine Systems*, 2(3-4):297–315, 1991. http://dx.doi.org/10.1016/0924-7963(91)90038-V. (Cited on page 34.)

Craven, M., I. Allison, H. A. Fricker, and R. Warner. Properties of a marine ice layer under the Amery Ice Shelf, East Antarctica. *Journal of Glaciology*, 55(192):717–728, 2009. http://dx.doi.org/10.3189/002214309789470941. (Cited on pages 29, 30 and 34.)

Cuffey, K. M. and W. S. B. Paterson. *The Physics of Glaciers*. Elsevier, Burlington, MA, 4. edition, 2010. (Cited on page 21.)

Curran, M. A. J., T. D. van Ommen, V. I. Morgan, K. L. Phillips, and A. S. Palmer. Ice core evidence for Antarctic sea ice decline since the 1950s. *Science*, 302(5648):1203–1206, 2003. http://dx.doi.org/10.1126/science.1087888. (Cited on page 13.)

Curry, J. A., J. L. Schramm, and E. E. Ebert. Sea ice-albedo climate feedback mechanism. *Journal of Climate*, 8(2):240–247, 1995. http://dx.doi.org/10.1175/1520-0442(1995)008<0240:SIACFM>2.0.CO;2. (Cited on page 9.)

Daly, K. L. Physioecology of Juvenile Antarctic Krill (Euphausia Superba) During Spring in Ice-Covered Seas. In *Antarctic Sea Ice: Biological Processes, Interactions and Variability*, pages 183–198. American Geophysical Union, Washington, D. C., 2013. http://dx.doi.org/10.1029/AR073p0183. (Cited on page 35.)

Daly, S. *International Association for Hydraulic Research Working Group on Thermal Regimes: Report on frazil ice.* US Army Cold Regions Research and Research Laboratory, Virginia, 1994. (Cited on page 27.)

Dayton, P. K. and S. Martin. Observations of ice stalactites in McMurdo Sound, Antarctica. *Journal of Geophysical Research*, 76(6):1595–1599, 1971. (Cited on page 27.)

Dayton, P. K., G. A. Robilliard, and A. L. Devries. Anchor ice formation in McMurdo Sound, Antarctica, and its biological effects. *Science*, 163(3864):273–274, 1969. (Cited on pages 33 and 36.)

De Angelis, H. and P. Skvarca. Glacier surge after ice shelf collapse. *Science*, 299(5612):1560–1562, 2003. http://dx.doi.org/10.1126/science.1077987. (Cited on page 21.)

De la Mare, W. K. Abrupt mid-twentieth-century decline in Antarctic sea-ice extent from whaling records. *Nature*, 389(6646):57–60, 1997. http://dx.doi.org/10.1038/37956. (Cited on page 12.)

Dempsey, D. E. and P. J. Langhorne. Geometric properties of platelet ice crystals. *Cold Regions Science and Technology*, 78(0):1–13, 2012. http://dx.doi.org/10.1016/j.coldregions.2012.03.002. (Cited on page 33.)

Dempsey, D. E., P. J. Langhorne, N. J. Robinson, M. J. M. Williams, T. G. Haskell, and R. D. Frew. Observation and modeling of platelet ice fabric in McMurdo Sound, Antarctica. *Journal of Geophysical Research: Oceans*, 115, 2010. http://dx.doi.org/10.1029/2008JC005264. (Cited on pages 26, 30, 33 and 38.)

Denny, M., K. M. Dorgan, D. Evangelista, A. Hettinger, J. Leichter, W. C. Ruder, and I. Tuval. Anchor ice and benthic disturbance in shallow Antarctic waters: interspecific variation in initiation and propagation of ice crystals. *The Biological Bulletin*, 221(2):155–163, 2011. http://dx.doi.org/10.2307/23046964. (Cited on page 36.)

Depoorter, M. A., J. L. Bamber, J. A. Griggs, J. T. M. Lenaerts, S. R. M. Ligtenberg, M. R. van den Broeke, and G. Moholdt. Calving fluxes and basal melt rates of Antarctic ice shelves. *Nature*, 502(7469):89–92, 2013. http://dx.doi.org/10.1038/nature12567. (Cited on pages 21 and 118.)

Determan, J. and R. Gerdes. Melting and freezing beneath ice shelves: implications from a three-dimensional ocean-circulation model. *Annals of Glaciology*, 20(1):413–419, 1994. (Cited on page 29.)

Determann, J. Numerical modelling of ice shelf dynamics. *Antarctic Science*, 3(2):187–195, 1991. (Cited on page 37.)

Dieckmann, G., C. Hemleben, and M. Spindler. Biogenic and mineral inclusions in a green iceberg from the Weddell Sea, Antarctica. *Polar Biology*, 7(1):31–33, 1986a. http://dx.doi.org/10.1007/BF00286821. (Cited on page 37.)

Dieckmann, G. S., G. Rohardt, H. Hellmer, and J. Kipfstuhl. The occurrence of ice platelets at 250m depths near the Filchner Ice Shelf and its significance for sea ice biology. *Deep-Sea Research Part a-Oceanographic Research Papers*, 33(2):141–148, 1986b. http://dx.doi.org/10.1016/0198-0149(86)90114-7. (Cited on pages 29, 31, 33 and 34.)

Dieckmann, G. S., K. Arrigo, and C. W. Sullivan. A high-resolution sampler for nutrient and chlorophyll-a profiles of the sea ice platelet layer and underlying water column below fast ice in polar oceans - preliminary results. *Marine Ecology-Progress Series*, 80(2-3):291–300, 1992. (Cited on page 34.)

Dieckmann, G. S. and H. H. Hellmer. The Importance of Sea Ice: An Overview. In *Sea Ice*, pages 1–22. Wiley-Blackwell, 2010. (Cited on pages 8 and 9.)

Dierking, W. Mapping of Different Sea Ice Regimes Using Images From Sentinel-1 and ALOS Synthetic Aperture Radar. *IEEE Transactions on Geoscience and Remote Sensing,*, 48(3):1045–1058, 2010. (Cited on page 110.)

Dierking, W. Sea ice monitoring by synthetic aperture radar. *Oceanography*, 26:100–111, 2013. (Cited on page 110.)

Dierking, W., S. Linow, and W. Rack. Toward a robust retrieval of snow accumulation over the Antarctic ice sheet using satellite radar. *Journal of Geophysical Research: Oceans*, 117(D09110), 2012. http://dx.doi.org/10.1029/2011JD017227. (Cited on page 110.)

Divine, D., R. Korsnes, and A. Makshtas. Variability and climate sensitivity of fast ice extent in the north-eastern Kara Sea. *Polar Research*, 22(1):27–34, 2003. http://dx.doi.org/10.1111/j.1751-8369.2003.tb00092.x. (Cited on page 19.)

Doake, C. S. M. Thermodynamics of the interaction between ice shelves and the sea. *Polar Record*, 18(112):37–41, 1976. http://dx.doi.org/10.1017/S0032247400028692. (Cited on page 37.)

Doble, M. J., M. D. Coon, and P. Wadhams. Pancake ice formation in the Weddell Sea. *Journal of Geophysical Research: Oceans*, 108(C7), 2003. http://dx.doi.org/10.1029/2002JC001373. (Cited on page 10.)

Drinkwater, M. R. and X. Liu. Seasonal to interannual variability in Antarctic sea-ice surface melt. *IEEE Transactions on Geoscience and Remote Sensing*, 38(4):1827–1842, 2000. (Cited on page 110.)

Dupont, T. K. and R. B. Alley. Assessment of the importance of ice-shelf buttressing to ice-sheet flow. *Geophysical Research Letters*, 32(4):L04503, 2005. http://dx.doi.org/10.1029/2004GL022024. (Cited on page 21.)

Eicken, H. Deriving modes and rates of ice growth in the Weddell Sea from microstructural, salinity and stable-isotope data. In Jeffries, M. O., editor, *Antarctic Sea ice: Physical processes, interactions and variability*, volume 74, pages 89–122. American Geophysical Union, 1998. (Cited on page 9.)

Eicken, H. and M. A. Lange. Development and properties of sea ice in the coastal regime of the Southeastern Weddell Sea. *Journal of Geophysical Research: Oceans*, 94(C6):8193–8206, 1989. http://dx.doi.org/10.1029/JC094iC06p08193. (Cited on pages 30 and 33.)

Eicken, H., M. A. Lange, H. W. Hubberten, and P. Wadhams. Characteristics and distribution patterns of snow and meteoric ice in the Weddell Sea and their contribution to the mass balance of sea ice. *Annales Geophysicae*, 12:80–93, 1994a. http://dx.doi.org/10.1007/s00585-994-0080-x. (Cited on page 9.)

Eicken, H., H. Oerter, H. Miller, W. Graf, and J. Kipfstuhl. Textural characteristics and impurity content of meteoric and marine ice in the Ronne Ice Shelf, Antarctica. *Journal of Glaciology*, 40(135):386–398, 1994b. (Cited on pages 34 and 37.)

Eineder, M., T. Fritz, J. Mittermayer, A. Roth, E. Boerner, and H. Breit. Terrasar-x ground segment, basic product specification document. Technical report, 2008. (Cited on page 111.)

Engelhardt, H. and J. Determann. Borehole evidence for a thick layer of basal ice in the central Ronne Ice Shelf. *Nature*, 327(6120):318–319, 1987. http://dx.doi.org/10.1038/327318a0. (Cited on page 37.)

Eriksson, L. E. B., K. Borenäs, W. Dierking, A. Berg, M. Santoro, P. Pemberton, H. Lindh, and B. Karlson. Evaluation of new spaceborne SAR sensors for sea-ice monitoring in the Baltic Sea. *Canadian Journal of Remote Sensing*, 36(S1):S56–S73, 2010. http://dx.doi.org/10.5589/m10-020. (Cited on pages 110 and 111.)

Favier, L., G. Durand, S. L. Cornford, G. H. Gudmundsson, O. Gagliardini, F. Gillet-Chaulet, T. Zwinger, A. J. Payne, and A. M. Le Brocq. Retreat of Pine Island Glacier controlled by marine ice-sheet instability. *Nature Clim. Change*, 4(2):117–121, 2014. http://dx.doi.org/10.1038/nclimate2094. (Cited on page 22.)

Fierz, C., R. L. Armstrong, Y. Durand, P. Etchevers, E. Greene, D. M. McClung, K. Nishimura, P. K. Satyawali, and S. A. Sokratov. *The international classification for seasonal snow on the ground*. UNESCO/IHP, 2009. (Cited on page 111.)

Foldvik, A. and T. Kvinge. Conditional instability of seawater at the freezing point. *Deep-Sea Research*, 21(3):169–174, 1974. http://dx.doi.org/10.1016/0011-7471(74)90056-4. (Cited on pages 24 and 28.)

Foldvik, A. and T. Kvinge. Thermohaline convection in the vicinity of an ice shelf. In Dunbar, M., editor, *Polar oceans, Proceedings of the Polar Oceans Conference held at McGill University, Montreal, May, 1974*, pages 247–255. Arctic Institute of North America, Calgary, Alberta, 1977. (Cited on page 28.)

Fraser, A. D. *East Antarctic Landfast Sea Ice Distribution and Variability*. PhD thesis, Institute for Marine and Antarctic Studies, University of Tasmania, 2011. (Cited on page 19.)

Fraser, A. D., R. A. Massom, K. J. Michael, B. K. Galton-Fenzi, and J. L. Lieser. East Antarctic land-fast sea ice distribution and variability, 2000-08. *Journal of Climate*, 25(4):1137–1156, 2012. http://dx.doi.org/10.1175/JCLI-D-10-05032.1. (Cited on pages 18 and 19.)

Frazer, T. K. Stable isotope composition (d13C and d15N) of larval krill, Euphausia superba, and two of its potential food sources in winter. *Journal of Plankton Research*, 18(8):1413–1426, 1996. (Cited on page 35.)

Fretwell, P., H. D. Pritchard, D. G. Vaughan, J. L. Bamber, N. E. Barrand, R. Bell, C. Bianchi, R. G. Bingham, D. D. Blankenship, G. Casassa, G. Catania, D. Callens, H. Conway, A. J. Cook, H. F. J. Corr, D. Damaske, V. Damm, F. Ferraccioli, R. Forsberg, S. Fujita, Y. Gim, P. Gogineni, J. A. Griggs, R. C. A. Hindmarsh, P. Holmlund, J. W. Holt, R. W. Jacobel, A. Jenkins, W. Jokat, T. Jordan, E. C. King, J. Kohler, W. Krabill, M. Riger-Kusk, K. A. Langley, G. Leitchenkov, C. Leuschen, B. P. Luyendyk, K. Matsuoka, J. Mouginot, F. O. Nitsche, Y. Nogi, O. A. Nost, S. V. Popov, E. Rignot, D. M. Rippin, A. Rivera, J. Roberts, N. Ross, M. J. Siegert, A. M. Smith, D. Steinhage, M. Studinger, B. Sun, B. K. Tinto, B. C. Welch, D. Wilson, D. A. Young, C. Xiangbin, and A. Zirizzotti. Bedmap2: improved ice bed, surface and thickness datasets for Antarctica. *The Cryosphere*, 7(1):375–393, 2013. http://dx.doi.org/10.5194/tc-7-375-2013. (Cited on pages 20, 22, 39 and 41.)

Gallaher, D. W., G. G. Campbell, and W. N. Meier. Anomalous variability in Antarctic sea ice extents during the 1960s with the use of Nimbus data. *Selected Topics in Applied Earth Observations and Remote Sensing, IEEE Journal of*, 7(3):881–887, 2014. http://dx.doi.org/10.1109/JSTARS.2013.2264391. (Cited on page 14.)

Garrison, D. L., A. R. Close, and E. Reimnitz. Algae concentrated by frazil ice - evidence from laboratory experiments and field-measurements. *Antarctic Science*, 1(4):313–316, 1988. http://dx.doi.org/10.1017/S0954102089000477. (Cited on page 34.)

Garrison, D. L., S. F. Ackley, and K. R. Buck. A physical mechanism for establishing algal populations in frazil ice. *Nature*, 306(5941):363–365, 1983. (Cited on page 34.)

Giles, A. B., R. A. Massom, and V. I. Lytle. Fast-ice distribution in East Antarctica during 1997 and 1999 determined using RADARSAT data. *Journal of Geophysical Research: Oceans*, 113(C2):C02S14, 2008. http://dx.doi.org/10.1029/2007JC004139. (Cited on pages 15, 18 and 19.)

Gille, S. T. Warming of the Southern Ocean since the 1950s. *Science*, 295(5558):1275–1277, 2002. http://dx.doi.org/10.1126/science.1065863. (Cited on page 12.)

Gillett, N. P., J. F. Scinocca, D. A. Plummer, and M. C. Reader. Sensitivity of climate to dynamically-consistent zonal asymmetries in ozone. *Geophysical Research Letters*, 36, 2009. http://dx.doi.org/10.1029/2009GL037246. (Cited on page 16.)

Giæver, J. *The White Desert*. Dutton & Co., New York, 1954. http://www.spri.cam.ac.uk/resources/expeditions/nbsx/. (Cited on page 40.)

Gloersen, P., W. J. Campbell, D. J. Cavalieri, J. C. Comiso, and J. H. Parkinson, Claire L. Zwally. Satellite passive microwave observations and analysis of Arctic and Antarctic sea ice, 1978-1987. *Annals of Glaciology*, 17:149–154, 1993. (Cited on page 13.)

Gonzales, H. Distribution and abundance of minipellets around the Antarctic Peninsula. Implications for protistan feeding behaviour. *Marine Ecology - Progress Series*, 90:223–236, 1992. http://dx.doi.org/10.3354/meps090223. (Cited on page 35.)

Goodwin, I. D. Basal ice accretion and debris entrainment within the coastal ice margin, Law Dome, Antarctica. *Journal of Glaciology*, 39(131):157–166, 1993. (Cited on page 34.)

Gordon, A. L. and B. A. Huber. Southern Ocean winter mixed layer. *Journal of Geophysical Research: Oceans*, 95(C7):11655–11672, 1990. http://dx.doi.org/10.1029/JC095iC07p11655. (Cited on page 12.)

Gough, A. J., A. R. Mahoney, P. J. Langhorne, M. J. M. Williams, and T. G. Haskell. Sea ice salinity and structure: A winter time series of salinity and its distribution. *Journal of Geophysical Research: Oceans*, 117(C3):C03008, 2012a. http://dx.doi.org/10.1029/2011JC007527. (Cited on page 33.)

Gough, A. J., A. R. Mahoney, P. J. Langhorne, M. J. M. Williams, N. J. Robinson, and T. G. Haskell. Signatures of supercooling: McMurdo Sound platelet ice. *Journal of Glaciology*, 58(207):38–50, 2012b. http://dx.doi.org/10.3189/2012JoG10J218. (Cited on pages 24, 26, 29 and 30.)

Gow, A. J., S. F. Ackley, and K. R. Buck. Physical and structural characteristics of Weddell Sea pack ice . *Cold Regions Research and Engineering Laboratory (CRREL) Report*, 14:1–70, 1987. (Cited on page 12.)

Gow, A. J., S. F. Ackley, J. W. Govoni, and W. F. Weeks. Physical and Structural Properties of Land-Fast Sea Ice in McMurdo Sound, Antarctica. In Jeffries, M. O., editor, *Antarctic Sea Ice: Physical Processes, Interactions and Variability*, pages 355–374. American Geophysical Union, Washington D.C., 1998. http://dx.doi.org/10.1029/AR074p0355. (Cited on pages 26 and 33.)

Gow, A. and S. Epstein. On the use of stable isotopes to trace theorigins of ice in a floating ice tongue. *Journal of Geophysical Research*, 88(33):6552–6557, 1972. (Cited on page 36.)

Grossmann, S., K. Lochte, and R. Scharek. Algal and bacterial processes in platelet ice during late austral summer. *Polar Biology*, 16(8):623–633, 1996. http://dx.doi.org/10.1007/BF02329060. (Cited on pages 33 and 34.)

Guglielmo, L., G. C. Carrada, G. Catalano, A. Dell'Anno, M. Fabiano, L. Lazzara, O. Mangoni, A. Pusceddu, and V. Saggiomo. Structural and functional properties of sympagic communities in the annual sea ice at Terra Nova Bay (Ross Sea, Antarctica. *Polar Biology*, 23(2):137–146, 2000. http://dx.doi.org/10.1007/s003000050019. (Cited on page 34.)

Günther, S. *Jahreszeitliche Entwicklung von Festeis-Lebensgemeinschaften und ihrer Umwelt*. PhD thesis, Universität Bremen, 1999. (Cited on page 119.)

Günther, S. and G. S. Dieckmann. Seasonal development of algal biomass in snow-covered fast ice and the underlying platelet layer in the Weddell Sea, Antarctica. *Antarctic Science*, 11(3):305–315, 1999. http://dx.doi.org/10.1017/S0954102099000395. (Cited on pages 24, 33, 34 and 35.)

Günther, S. and G. S. Dieckmann. Vertical zonation and community transition of sea-ice diatoms in fast ice and platelet layer, Weddell Sea, Antarctica. *Annals of Glaciology*, 33:287–296, 2001. http://dx.doi.org/10.3189/172756401781818590. (Cited on pages 19 and 33.)

Günther, S., M. Gleitz, and G. S. Dieckmann. Biogeochemistry of Antarctic sea ice: a case study on platelet ice layers at Drescher Inlet, Weddell Sea. *Marine Ecology-Progress Series*, 177:1–13, 1999. (Cited on page 33.)

Gutt, J. The Antarctic ice shelf: an extreme habitat for notothenioid fish. *Polar Biology*, 25(4):320–322, 2002. http://dx.doi.org/10.1007/s00300-001-0352-9. (Cited on page 35.)

Haas, C. The seasonal cycle of ERS scatterometer signatures over perennial Antarctic sea ice and associated surface ice properties and processes. *Annals of Glaciology*, 33:69–73, 2001a. http://dx.doi.org/hdl:10013/epic.15008.d001. (Cited on page 110.)

Haas, C. Late-summer sea ice thickness variability in the Arctic Transpolar Drift 1991-2001 derived from ground-based electromagnetic sounding. *Geophysical Research Letters*, 31(9), 2004. http://dx.doi.org/10.1029/2003GL019394. (Cited on page 103.)

Haas, C., S. Gerland, H. Eicken, and H. Miller. Comparison of sea-ice thickness measurements under summer and winter conditions in the Arctic using a small electromagnetic induction device. *Geophysics*, 62(3):749–757, 1997. (Cited on page 14.)

Haas, C., D. N. Thomas, and J. Bareiss. Surface properties and processes of perennial Antarctic sea ice in summer. *Journal of Glaciology*, 47:613–625, 2001b. http://dx.doi.org/hdl:10013/epic.15007.d001. (Cited on pages 9 and 12.)

Haas, C., M. Nicolaus, S. Willmes, A. Worby, and D. Flinspach. Sea ice and snow thickness and physical properties of an ice floe in the western Weddell Sea and their changes during spring warming. *Deep-Sea Research II*, 55:963–974, 2008a. http://dx.doi.org/10.1016/j.dsr2.2007.12.020. (Cited on page 12.)

Haas, C., A. Pfaffling, S. Hendricks, L. Rabenstein, J.-L. Etienne, and I. Rigor. Reduced ice thickness in Arctic Transpolar Drift favors rapid ice retreat. *Geophysical Research Letters*, 35(L17501), 2008b. http://dx.doi.org/10.1029/2008GL034457. (Cited on page 103.)

Haas, C., J. Lobach, S. Hendricks, L. Rabenstein, and A. Pfaffling. Helicopter-borne measurements of sea ice thickness, using a small and lightweight, digital EM system. *Journal of Applied Geophysics*, 67:234–241, 2009. http://dx.doi.org/10.1016/j.jappgeo.2008.05.005. (Cited on pages 14 and 103.)

Haas, C., S. Hendricks, H. Eicken, and A. Herber. Synoptic airborne thickness surveys reveal state of arctic sea ice cover. *Geophysical Research Letters*, 37, 2010. http://dx.doi.org/10.1029/2010GL042652. (Cited on page 103.)

Hattermann, T., L. H. Smedsrud, O. A. Nøst, J. M. Lilly, and B. K. Galton-Fenzi. Eddy-resolving simulations of the Fimbul Ice Shelf cavity circulation: Basal melting and exchange with open ocean. *Ocean Modelling*, 82(0):28–44, 2014. http://dx.doi.org/10.1016/j.ocemod.2014.07.004. (Cited on page 29.)

Hattermann, T., O. A. Nøst, J. M. Lilly, and L. H. Smedsrud. Two years of oceanic observations below the Fimbul Ice Shelf, Antarctica. *Geophysical Research Letters*, 39:L12605, 2012. http://dx.doi.org/10.1029/2012GL051012. (Cited on page 21.)

Heil, P. Atmospheric conditions and fast ice at Davis, East Antarctica: A case study. *Journal of Geophysical Research: Oceans*, 111(C5), 2006. http://dx.doi.org/10.1029/2005JC002904. (Cited on pages 19 and 38.)

Heil, P., I. Allison, and V. I. Lytle. Seasonal and interannual variations of the oceanic heat flux under a landfast Antarctic sea ice cover. *Journal of Geophysical Research: Oceans*, 101(C11):25741–25752, 1996. http://dx.doi.org/10.1029/96JC01921. (Cited on page 38.)

Heil, P., S. Gerland, and M. A. Granskog. An Antarctic monitoring initiative for fast ice and comparison with the Arctic. *The Cryosphere Discuss.*, 5(5):2437–2463, 2011. http://dx.doi.org/10.5194/tcd-5-2437-2011. (Cited on pages 38 and 39.)

Hellmer, H. H. Impact of Antarctic ice shelf basal melting on sea ice and deep ocean properties. *Geophysical Research Letters*, 31(L10307), 2004. http://dx.doi.org/10.1029/2004GL019506. (Cited on pages 21 and 29.)

Hellmer, H. H., F. Kauker, R. Timmermann, J. Determann, and J. Rae. Twenty-first-century warming of a large Antarctic ice-shelf cavity by a redirected coastal current. *Nature*, 485(7397):225–228, 2012. http://dx.doi.org/10.1038/nature11064. (Cited on pages 22 and 118.)

Hellmer, H. and D. Olbers. A two-dimensional model for the thermohaline circulation under an ice shelf. *Antarctic Science*, 1(04):325–336, 1989. (Cited on page 29.)

Hellmer, H. and D. Olbers. On the thermohaline circulation beneath the Filchner-Ronne Ice Shelves. *Antarctic Science*, 3(04):433–442, 1991. (Cited on page 29.)

Helm, V., A. Humbert, and H. Miller. Elevation and elevation change of Greenland and Antarctica derived from CryoSat-2. *The Cryosphere*, 8(4):1539–1559, 2014. http://dx.doi.org/10.5194/tcd-8-1673-2014. (Cited on page 20.)

Hodgson, T. On collecting in Antarctic seas, British National Antarctic Expedition, 1901-1904, Vol. 3. Trustees of the British Museum, London, UK, pp. 1-10 (Volume III is entitled Zoology and Botany), 1907. (Cited on page 24.)

Holladay, J., J. Rossiter, and A. Kovacs. Airborne measurement of sea ice thickness using electromagnetic induction sounding. *Proceedings of the Ninth International Conference of Offshore Mechanics and Arctic Engineering Fracture Mechanics*, pages 309–315, 1990. (Cited on page 103.)

Holland, P. R. The seasonality of Antarctic sea ice trends. *Geophysical Research Letters*, 41(12):4230–4237, 2014. (Cited on page 16.)

Holland, P. R. and R. Kwok. Wind-driven trends in Antarctic sea-ice drift. *Nature Geoscience*, 5(12): 872–875, 2012. http://dx.doi.org/10.1038/ngeo1627. (Cited on page 16.)

Holland, P. R., N. Bruneau, C. Enright, M. Losch, N. T. Kurtz, and R. Kwok. Modeled Trends in Antarctic Sea Ice Thickness. *Journal of Climate*, 27(10):3784–3801, 2014. http://dx.doi.org/10.1175/JCLI-D-13-00301.1. (Cited on pages 15 and 16.)

Hooke, R. L. *Principles of Glacier Mechanics*. Cambridge University Press, Cambridge, 2005. (Cited on page 21.)

Hoppmann, M., M. Nicolaus, and H. Schmithüsen. Summary of AFIN measurements on Atka Bay landfast sea ice in 2010, 2011. http://dx.doi.org/hdl:10013/epic.37766.d001. (Cited on pages 38 and 45.)

Hoppmann, M., M. Nicolaus, and J. Asseng. Summary of AFIN measurements on Atka Bay landfast sea ice in 2011, 2012. http://dx.doi.org/hdl:10013/epic.39903.d001. (Cited on page 38.)

Hoppmann, M., S. Paul, P. A. Hunkeler, U. Baltes, M. Kühnel, T. Schmidt, M. Nicolaus, G. Heinemann, and S. Willmes. Field work on Atka Bay land-fast sea ice in 2012/13, 2013. http://dx.doi.org/hdl:10013/epic.42767.d001. (Cited on pages 38, 52 and 53.)

Hoppmann, M., M. Nicolaus, L.-K. Behrens, and J. Regnery. Field work on Atka Bay land-fast sea ice in 2013, 2014. http://dx.doi.org/hdl:10013/epic.43850.d001. (Cited on page 38.)

Hoppmann, M., M. Nicolaus, S. Paul, P. A. Hunkeler, P. Heil, L.-K. Behrens, G. König-Langlo, and R. Gerdes. Seasonal evolution of an ice-shelf influenced fast-ice regime, derived from an autonomous thermistor chain. *Journal of Geophysical Research: Oceans*, 120:1703–1724, 2015a. http://dx.doi.org/10.1002/2014JC010327. (Cited on pages 30 and 79.)

Hoppmann, M., M. Nicolaus, S. Paul, P. A. Hunkeler, G. Heinemann, S. Willmes, R. Timmermann, O. Boebel, S. T., M. Kühnel, K. König-Langlo, and R. Gerdes. Ice platelets below Weddell Sea land-fast sea ice. *Annals of Glaciology*, 56(69):175–190, 2015b. http://dx.doi.org/10.3189/2015AoG69A678. (Cited on pages 33, 40, 41 and 62.)

Horgan, H. J., S. Anandakrishnan, R. W. Jacobel, K. Christianson, R. B. Alley, D. S. Heeszel, S. Picotti, and J. I. Walter. Subglacial Lake Whillans - Seismic observations of a shallow active reservoir beneath a West Antarctic ice stream. *Earth and Planetary Science Letters*, 331:201–209, 2012. http://dx.doi.org/10.1016/j.epsl.2012.02.023. (Cited on page 27.)

Hughes, K. G., P. J. Langhorne, G. H. Leonard, and C. L. Stevens. Extension of an Ice Shelf Water plume model beneath sea ice with application in McMurdo Sound, Antarctica. *Journal of Geophysical Research: Oceans*, in press. http://dx.doi.org/10.1002/2013JC009411. (Cited on page 29.)

Hughes, K. *Propagation of an Ice Shelf Water Plume beneath Sea Ice in McMurdo Sound, Antarctica*. Master thesis, University of Otago, 2013. (Cited on page 29.)

Hunkeler, P. A., S. Hendricks, M. Hoppmann, S. Paul, and R. Gerdes. Towards an estimation of sub-sea-ice platelet-layer volume with multi-frequency electromagnetic induction sounding. *Annals of Glaciology*, 56(69):137–146, 2015. http://dx.doi.org/10.3189/2015AoG69A705. (Cited on pages 102, 106, 107 and 154.)

Hunkeler, P. A., S. Hendricks, M. Hoppmann, C. G. Farquharson, T. Kalscheuer, M. Grab, M. S. Kaufmann, L. Rabenstein, and R. Gerdes. Improved 1d inversions for sea ice thickness and conductivity from em induction data: Inclusion of nonlinearities caused by passive bucking. *Geophysics*, accepted. (Cited on page 102.)

IPCC. Climate Change 2013: The Physical Science Basis. Contribution of Working Group I to the Fifth Assessment Report of the Intergovernmental Panel on Climate Change. In Stocker, T., D. Qin, G.-K. Plattner, M. Tignor, S. Allen, J. Boschung, A. Nauels, Y. Xia, V. Bex, and P. Midgley, editors, *IPCC AR5*, page 1535 pp. Cambridge University Press, Cambridge, United Kingdom and New York, NY, USA, 2013. http://www.climatechange2013.org/report. (Cited on pages 2 and 12.)

Jacobs, S. S. and J. C. Comiso. Climate variability in the Amundsen and Bellingshausen Seas. *Journal of Climate*, 10(4):697–709, 1997. http://dx.doi.org/http://dx.doi.org/10.1175/1520-0442(1997)010<0697:CVITAA>2.0.CO;2. (Cited on page 16.)

Jacobs, S. S., H. Hellmer, C. S. M. Doake, A. Jenkins, and R. Frolich. Melting of ice shelves and the mass balance of Antarctica. *Journal of Glaciology*, 38(130):375–387, 1992. (Cited on pages 21, 28 and 29.)

Jacobs, S. S. and C. F. Giulivi. Large multidecadal salinity trends near the Pacific-Antarctic continental margin. *Journal of Climate*, 23(17):4508–4524, 2010. http://dx.doi.org/10.1175/2010JCLI3284.1. (Cited on page 17.)

Jeffries, M. O., W. F. Weeks, R. Shaw, and K. Morris. Structural characteristics of congelation and platelet ice and their role in the development of Antarctic land-fast sea-ice. *Journal of Glaciology*, 39(132): 223–238, 1993. (Cited on pages 26, 30 and 33.)

Jeffries, M. O., R. A. Shaw, K. Morris, A. L. Veazey, and H. R. Krouse. Crystal structure, stable isotopes (δ^{18}O), and development of sea ice in the Ross, Amundsen, and Bellingshausen seas, Antarctica. *Journal of Geophysical Research: Oceans*, 99(C1):985–995, 1994. http://dx.doi.org/10.1029/93JC02057. (Cited on page 9.)

Jeffries, M. O., A. P. Worby, K. Morris, and W. F. Weeks. Seasonal variations in the properties and structural composition of sea ice and snow cover in the Bellinghausen and Amundsen Sea, Antarctica. *Journal of Glaciology*, 43(143):138–151, 1997. (Cited on page 9.)

Jeffries, M. O., S. Li, R. A. Jaña, H. R. Krouse, and B. Hurst-Cushing. Late winter first-year ice floe thickness variability, seawater flooding and snow ice formation in the Amundsen and Ross Seas. In *Antarctic Sea Ice: Physical Processes, Interactions and Variability*, volume 74 of *Antarct. Res. Ser.*, pages 69–87. AGU, Washington, DC, 1998. http://dx.doi.org/10.1029/AR074p0069. (Cited on pages 9, 14 and 19.)

Jeffries, M. O., H. R. Krouse, B. Hurst-Cushing, and T. Maksym. Snow-ice accretion and snow-cover depletion on Antarctic first-year sea-ice floes. *Annals of Glaciology*, 33:51–60, 2001. http://dx.doi.org/10.3189/172756401781818266. (Cited on page 9.)

Jenkins, A. and A. Bombosch. Modeling the effects of frazil ice crystals on the dynamics and thermodynamics of ice shelf water plumes. *Journal of Geophysical Research: Oceans*, 100(C4):6967–6981, 1995. http://dx.doi.org/10.1029/91JC01842. (Cited on pages 29 and 37.)

Jenkins, A. and C. S. M. Doake. Ice-ocean interaction on Ronne Ice Shelf, Antarctica. *Journal of Geophysical Research: Oceans*, 96(C1):791–813, 1991. http://dx.doi.org/10.1029/90JC01952. (Cited on page 29.)

Jones, S. J. and B. T. Hill. Structure of sea ice in McMurdo Sound, Antarctica. *Annals of Glaciology*, 33(1): 5–12, 2001. http://dx.doi.org/10.3189/172756401781818347. (Cited on page 33.)

Joughin, I., R. B. Alley, and D. M. Holland. Ice-sheet response to oceanic forcing. *Science*, 338(6111): 1172–1176, 2012. http://dx.doi.org/10.1126/science.1226481. (Cited on page 21.)

Joughin, I., B. E. Smith, and B. Medley. Marine ice sheet collapse potentially under way for the Thwaites Glacier Basin, West Antarctica. *Science*, 344(6185):735–738, 2014. http://dx.doi.org/10.1126/science.1249055. (Cited on pages 21 and 22.)

Kalscheuer, T. EMILIA - ElectroMagnetic Inversion with Least Intricate Algorithms User manual. Technical report, Uppsala University, Department of Earth Sciences, 2014. (Cited on page 107.)

Kalscheuer, T., M. Bastani, S. Donohue, L. Persson, A. Pfaffhuber, F. Reiser, and Z. Ren. Delineation of a quick clay zone at Smørgrav, Norway, with electromagnetic methods under geotechnical constraints. *Journal of Applied Geophysics*, 92:121–136, 2013. http://dx.doi.org/10.1016/j.jappgeo.2013.02.006. (Cited on page 107.)

Kawamura, T., K. I. Ohshima, T. Takizawa, and S. Ushio. Physical, structural and isotopic characteristics and growth processes of fast sea ice in Lützow-Holm Bay, Antarctica. *Journal of Geophysical Research*, 102(C2):3345–3355, 1997. http://dx.doi.org/10.1029/96JC03206. (Cited on pages 18 and 38.)

Kawamura, T., M. O. Jeffries, J. L. Tison, and H. R. Krouse. Superimposed ice formation in summer on Ross Sea pack ice floes. *Annals of Glaciology*, 39:563–568, 2004. http://dx.doi.org/10.3189/172756404781814168. (Cited on page 9.)

Kawamura, T., H. Wakabayashi, and S. Ushio. Growth, properties and relation to radar backscatter coefficient of sea ice in Lützow-Holm Bay, Antarctica. *Annals of Glaciology*, 44:163–169, 2006. http://dx.doi.org/10.3189/172756406781811655. (Cited on page 38.)

Kempema, E. W., E. Reimnitz, J. R. Clayton, and J. R. Payne. Interactions of frazil and anchor ice with sedimentary particles in a flume. *Cold Regions Science and Technology*, 21(2):137–149, 1993. http://dx.doi.org/10.1016/0165-232X(93)90003-Q. (Cited on page 35.)

Kendra, J. R., K. Sarabandi, and F. T. Ulaby. Radar measurements of snow: experiment and analysis. *IEEE Transactions on Geoscience and Remote Sensing*, 36(3):864–879, 1998. http://dx.doi.org/10.1109/36.673679. (Cited on page 110.)

Kennett, J. P. Cenozoic evolution of Antarctic glaciation, the circum-Antarctic ocean, and their impact on global paleoceanography. *Journal of Geophysical Research*, 82(27):3843–3860, 1977. http://dx.doi.org/10.1029/JC082i027p03843. (Cited on page 13.)

Kern, S., B. Ozsoy-Cicek, S. Willmes, M. Nicolaus, C. Haas, and S. Ackley. An intercomparison between AMSR-E snow-depth and satellite C-and Ku-band radar backscatter data for Antarctic sea ice. *Annals of Glaciology*, 52(57):279–290, 2011. http://dx.doi.org/10.3189/172756411795931750. (Cited on page 110.)

Khazendar, A., M. P. Schodlok, I. Fenty, S. R. M. Ligtenberg, E. Rignot, and M. R. van den Broeke. Observed thinning of Totten Glacier is linked to coastal polynya variability. *Nature Communications*, 4, 2013. http://dx.doi.org/10.1038/ncomms3857. (Cited on page 22.)

Kim, Y.-S., R. Onstott, and R. Moore. Effect of a snow cover on microwave backscatter from sea ice. *IEEE Journal of Oceanic Engineering*, 9(5):383–388, 1984. http://dx.doi.org/10.1109/JOE.1984.1145649. (Cited on page 110.)

Kipfstuhl, J. On the formation of underwater ice and the growth and energy budget of the sea ice in Atka Bay, Antarctica (Zur Entstehung von Unterwassereis und das Wachstum und die Energiebilanz des Meereises in der Atka Bucht, Antarktis, mostly in German). *Reports on Polar and Marine Research (Berichte zur Polarforschung)*, 85:88p, 1991. http://dx.doi.org/hdl:10013/epic.10085.d001. (Cited on pages 33 and 40.)

Kipfstuhl, J., G. S. Dieckmann, H. Oerter, H. Hellmer, and W. Graf. The origin of green icebergs in Antarctica. *Journal of Geophysical Research: Oceans*, 97(C12):20319–20324, 1992. http://dx.doi.org/10.1029/92JC01754. (Cited on pages 34 and 37.)

Kobarg, W. The tide-dependent dynamics of the Ekström Ice Shelf, Antarctica. *Berichte zur Polarforschung*, 50, 1988. (Cited on pages 40 and 41.)

Kohout, A. L., M. J. M. Williams, S. M. Dean, and M. H. Meylan. Storm-induced sea-ice breakup and the implications for ice extent. *Nature*, 509(7502):604–607, 2014. http://dx.doi.org/10.1038/nature13262. (Cited on page 16.)

König-Langlo, G. and B. Loose. The meteorological observatory at Neumayer Station (GvN and NM-II) Antarctica. *Polarforschung*, 76:25–38, 2007. (Cited on page 42.)

König-Langlo, G., J. C. King, and P. Pettré. Climatology of the three coastal Antarctic stations Dumont d'Urville, Neumayer, and Halley. *Journal of Geophysical Research: Atmospheres*, 103(D9):10935–10946, 1998. http://dx.doi.org/10.1029/97JD00527. (Cited on page 42.)

Korhonen, H., K. S. Carslaw, P. M. Forster, S. Mikkonen, N. D. Gordon, and H. Kokkola. Aerosol climate feedback due to decadal increases in Southern Hemisphere wind speeds. *Geophysical Research Letters*, 37, 2010. http://dx.doi.org/10.1029/2009GL041320. (Cited on page 16.)

Kovacs, A. and J. Holladay. Sea-ice thickness measurement using a small airborne electromagnetic sounding system. *Geophysics*, 55(10):1327–1337, 1990. http://dx.doi.org/10.1190/1.1442780. (Cited on page 103.)

Kovacs, A., N. C. Valleau, and J. S. Holladay. Airborne electromagnetic sounding of sea ice thickness and sub-ice bathymetry. *Cold Regions Science and Technology*, 14(3):289–311, 1987. http://dx.doi.org/10.1016/0165-232X(87)90021-8. (Cited on page 103.)

Kulessa, B., D. Jansen, A. J. Luckman, E. C. King, and P. R. Sammonds. Marine ice regulates the future stability of a large Antarctic ice shelf. *Nature Communications*, 5, 2014. http://dx.doi.org/10.1038/ncomms4707. (Cited on page 36.)

Kurtz, N. T. and T. Markus. Satellite observations of Antarctic sea ice thickness and volume. *Journal of Geophysical Research: Oceans*, 117(C8):C08025, 2012. http://dx.doi.org/10.1029/2012JC008141. (Cited on page 15.)

Kwok, R. and D. A. Rothrock. Decline in Arctic sea ice thickness from submarine and ICESat records: 1958-2008. *Geophysical Research Letters*, 36, 2009. http://dx.doi.org/10.1029/2009GL039035. (Cited on page 14.)

Kwok, R., G. F. Cunningham, M. Wensnahan, I. Rigor, H. J. Zwally, and D. Yi. Thinning and volume loss of the Arctic Ocean sea ice cover: 2003-2008. *Journal of Geophysical Research: Oceans*, 114(C7): C07005, 2009. http://dx.doi.org/10.1029/2009JC005312. (Cited on page 12.)

La Mesa, M., J. T. Eastman, and M. Vacchi. The role of notothenioid fish in the food web of the Ross Sea shelf waters: a review. *Polar Biology*, 27(6):321–338, 2004. http://dx.doi.org/10.1007/s00300-004-0599-z. (Cited on page 35.)

Lange, M. A. and H. Eicken. The sea ice thickness distribution in the northwestern weddell sea. *Journal of Geophysical Research: Oceans*, 96(C3):4821–4837, 1991. http://dx.doi.org/10.1029/90JC02441. (Cited on page 12.)

Lange, M. A., S. F. Ackley, P. Wadhams, G. S. Dieckmann, and H. Eicken. Development of sea ice in the Weddell Sea. *Annals of Glaciology*, 12:92–96, 1989. (Cited on pages 12, 24, 30 and 33.)

Lange, M. A., P. Schlosser, S. F. Ackley, P. Wadhams, and G. S. Dieckmann. $d^{18}O$ concentrations in sea ice of the Weddell Sea, Antarctica. *Journal of Glaciology*, 36(124):315–323, 1990. (Cited on page 9.)

Lazzara, L., I. Nardello, C. Ermanni, O. Mangoni, and V. Saggiomo. Light environment and seasonal dynamics of microalgae in the annual sea ice at Terra Nova Bay, Ross Sea, Antarctica. *Antarctic Science*, 19(01):83–92, 2007. http://dx.doi.org/10.1017/S0954102007000119. (Cited on pages 33, 34 and 35.)

Le Brocq, A. M., A. J. Payne, and A. Vieli. An improved Antarctic dataset for high resolution numerical ice sheet models (ALBMAP v1). *Earth System Science Data Discussions*, 3(1):195–230, 2010. http://dx.doi.org/10.5194/essd-2-247-2010. (Cited on page 21.)

Lefebvre, W. and H. Goosse. Influence of the Southern Annular Mode on the sea ice-ocean system: the role of the thermal and mechanical forcing. *Ocean Science*, 1(3):145–157, 2005. http://dx.doi.org/10.5194/os-1-145-2005. (Cited on page 16.)

Lefebvre, W. and H. Goosse. An analysis of the atmospheric processes driving the large-scale winter sea ice variability in the Southern Ocean. *Journal of Geophysical Research: Oceans*, 113(C2), 2008. http://dx.doi.org/10.1029/2006JC004032. (Cited on page 16.)

Lei, R., Z. Li, B. Cheng, Z. Zhang, and P. Heil. Annual cycle of landfast sea ice in Prydz Bay, east Antarctica. *Journal of Geophysical Research: Oceans*, 115(C2):C02006, 2010. http://dx.doi.org/10.1029/2008JC005223. (Cited on page 38.)

Lenaerts, J. T. M., E. van Meijgaard, M. R. van den Broeke, S. R. M. Ligtenberg, M. Horwath, and E. Isaksson. Recent snowfall anomalies in Dronning Maud Land, East Antarctica, in a historical and future climate perspective. *Geophysical Research Letters*, 40(11):2684–2688, 2013. http://dx.doi.org/10.1002/grl.50559. (Cited on page 20.)

Leonard, G. H., C. R. Purdie, P. J. Langhorne, T. G. Haskell, M. J. M. Williams, and R. D. Frew. Observations of platelet ice growth and oceanographic conditions during the winter of 2003 in McMurdo Sound, Antarctica. *Journal of Geophysical Research: Oceans*, 111(C4), 2006. http://dx.doi.org/10.1029/2005JC002952. (Cited on pages 33 and 38.)

Leonard, G. H., P. J. Langhorne, M. J. M. Williams, R. Vennell, C. R. Purdie, D. E. Dempsey, T. G. Haskell, and R. D. Frew. Evolution of supercooling under coastal Antarctic sea ice during winter. *Antarctic Science*, 23(4):399–409, 2011. http://dx.doi.org/10.1017/S0954102011000265. (Cited on page 38.)

Lewis, E. L. and R. G. Perkin. Ice pumps and their rates. *Journal of Geophysical Research: Oceans*, 91 (C10):11756–11762, 1986. http://dx.doi.org/10.1029/JC091iC10p11756. (Cited on page 28.)

Lieser, J. L., M. R. A., A. D. Fraser, M. G. Haward, P. Heil, K. L. Lannuzel, D. Meiners, J. Melbourne-Thomas, A. J. Press, and G. D. Williams. *Position Analysis: Antarctic sea ice and climate change 2014*. Antarctic Climate & Ecosystems Cooperative Research Centre, Hobart, Tasmania, Australia, 2013. (Cited on pages 16 and 17.)

Lines, L. R. and S. Treitel. Tutorial: A review of least-squares inversion and its application to geophysical problems. *Geophysical prospecting*, 32(2):159–186, 1984. http://dx.doi.org/10.1111/j.1365-2478.1984.tb00726.x. (Cited on page 106.)

Littlepage, J. L. Oceanographic investigations in McMurdo Sound, Antarctica. In *Biology of the Antarctic Seas II*, volume 5 of *Antarct. Res. Ser.*, pages 1–37. AGU, Washington, DC, 1965. http://dx.doi.org/10.1029/AR005p0001. (Cited on page 33.)

Liu, J., J. A. Curry, and D. G. Martinson. Interpretation of recent Antarctic sea ice variability. *Geophysical Research Letters*, 31(2):L02205, 2004. http://dx.doi.org/10.1029/2003GL018732. (Cited on page 16.)

Liu, J. P. and J. A. Curry. Accelerated warming of the Southern Ocean and its impacts on the hydrological cycle and sea ice. *Proceedings of the National Academy of Sciences of the United States of America*, 107(34):14987–14992, 2010. http://dx.doi.org/10.1073/pnas.1003336107. (Cited on page 16.)

Lizotte, M. P. and C. W. Sullivan. Photosynthesis-irradiance relationships in microalgae associated with Antarctic pack ice - evidence for in situ activity. *Marine Ecology Progress Series*, 71(2):175–184, 1991. (Cited on page 34.)

Mackintosh, N. A. Sea ice limits. *Discovery Rep.*, 36:13 pp, 1972. (Cited on page 12.)

Mackintosh, N. A. and H. F. P. Herdman. Distribution of the pack-ice in the Southern Ocean. *Discovery Rep.*, 19:285–296, 1940. (Cited on page 12.)

Mager, S. M., I. J. Smith, E. W. Kempema, B. J. Thomson, and G. H. Leonard. Anchor ice in polar oceans. *Progress in Physical Geography*, 37(4):468–483, 2013. http://dx.doi.org/10.1177/0309133313479815. (Cited on pages 24, 26, 27, 35 and 36.)

Mahoney, A. R., A. J. Gough, P. J. Langhorne, N. J. Robinson, C. L. Stevens, M. M. J. Williams, and T. G. Haskell. The seasonal appearance of ice shelf water in coastal Antarctica and its effect on sea ice growth. *Journal of Geophysical Research: Oceans*, 116, 2011. http://dx.doi.org/10.1029/2011JC007060. (Cited on page 33.)

Mahoney, A., H. Eicken, and L. Shapiro. How fast is landfast sea ice? A study of the attachment and detachment of nearshore ice at Barrow, Alaska. *Cold Regions Science and Technology*, 47(3):233–255, 2007. http://dx.doi.org/10.1016/j.coldregions.2006.09.005. (Cited on pages 18 and 19.)

Mahoney, A., H. Eicken, A. G. Gaylord, and L. Shapiro. Alaska landfast sea ice: Links with bathymetry and atmospheric circulation. *Journal of Geophysical Research: Oceans*, 112(C2):C02001, 2007a. http://dx.doi.org/10.1029/2006JC003559. (Cited on page 19.)

Maksym, T., S. E. Stammerjohn, S. Ackley, and R. Massom. Antarctic Sea Ice-A Polar Opposite? *Oceanography*, 25(3):140–151, 2012. http://dx.doi.org/10.5670/oceanog.2012.88. (Cited on pages 15 and 16.)

Malmgren, F. On the properties of sea ice. In *Scientific Results of the Norwegian North Pole Expedition With the Maud 1919-1925*, volume 1a, pages 1–67. John Griegs, Bergen, Norway, 1927. (Cited on page 8.)

Mangoni, O., M. Saggiomo, M. Modigh, G. Catalano, A. Zingone, and V. Saggiomo. The role of platelet ice microalgae in seeding phytoplankton blooms in Terra Nova Bay (Ross Sea, Antarctica): a mesocosm experiment. *Polar Biology*, 32(3):311–323, 2009. http://dx.doi.org/10.1007/s00300-008-0507-z. (Cited on pages 33 and 34.)

Markus, T. and D. J. Cavalieri. Interannual and regional variability of Southern Ocean snow on sea ice. *Annals of Glaciology*, 44:53–57, 2006. http://dx.doi.org/10.3189/172756406781811475. (Cited on page 110.)

Markus, T., R. Massom, A. Worby, V. Lytle, N. Kurtz, and T. Maksym. Freeboard, snow depth and sea-ice roughness in East Antarctica from in situ and multiple satellite data. *Annals of Glaciology*, 52:242–248, 2011. http://dx.doi.org/10.3189/172756411795931570. (Cited on page 15.)

Marschall, H.-P. The overwintering strategy of Antarctic krill under the pack-ice of the Weddell Sea. *Polar Biology*, 9(2):129–135, 1988. http://dx.doi.org/10.1007/BF00442041. (Cited on page 35.)

Marshall, G. J., P. A. Stott, J. Turner, W. M. Connolley, J. C. King, and T. A. Lachlan-Cope. Causes of exceptional atmospheric circulation changes in the Southern Hemisphere. *Geophysical Research Letters*, 31(14), 2004. http://dx.doi.org/10.1029/2004GL019952. (Cited on page 17.)

Martin, S. Ice stalactites: comparison of a laminar flow theory with experiment. *Journal of Fluid Mechanics*, 63:51–79, 1974. http://dx.doi.org/10.1017/S0022112074001017. (Cited on page 27.)

Martin, S. Frazil ice in rivers and oceans. *Annual Review of Fluid Mechanics*, 13:379–397, 1981. http://dx.doi.org/10.1146/annurev.fl.13.010181.002115. (Cited on page 27.)

Martinson, D. G. Antarctic circumpolar current's role in the Antarctic ice system: An overview. *Palaeogeography Palaeoclimatology Palaeoecology*, 335:71–74, 2012. http://dx.doi.org/10.1016/j.palaeo.2011.04.007. (Cited on pages 13 and 16.)

Massom, R. A., H. Eicken, C. Haas, M. O. Jeffries, M. R. Drinkwater, M. Sturm, A. P. Worby, X. Wu, V. I. Lytle, S. Ushio, K. Morris, P. A. Reid, S. G. Warren, and I. Allison. Snow on Antarctic sea ice. *Reviews of Geophysics*, 39(3):413–445, 2001a. http://dx.doi.org/10.1029/2000RG000085. (Cited on pages 9 and 10.)

Massom, R. A., K. L. Hill, V. I. Lytle, A. P. Worby, M. Paget, and I. Allison. Effects of regional fast-ice and iceberg distributions on the behaviour of the Mertz Glacier polynya, East Antarctica. *Annals of Glaciology*, 33:391–398, 2001b. http://dx.doi.org/10.3189/172756401781818518. (Cited on pages 18 and 19.)

Massom, R. A., K. Jacka, M. J. Pook, C. Fowler, N. Adams, and N. Bindoff. An anomalous late-season change in the regional sea ice regime in the vicinity of the Mertz Glacier Polynya, East Antarctica. *Journal of Geophysical Research: Oceans*, 108(C7):3212, 2003. http://dx.doi.org/10.1029/2002JC001354. (Cited on page 19.)

Massom, R. A., K. Hill, C. Barbraud, N. Adams, A. Ancel, L. Emmerson, and M. J. Pook. Fast ice distribution in Adélie Land, East Antarctica: interannual variability and implications for emperor penguins Aptenodytes forsteri. *Marine Ecology Progress Series*, 374:243–257, 2009. http://dx.doi.org/10.3354/meps07734. (Cited on page 19.)

Massom, R. A., A. B. Giles, H. A. Fricker, R. C. Warner, B. Legrésy, G. Hyland, N. Young, and A. Fraser. Examining the interaction between multi-year landfast sea ice and the Mertz Glacier Tongue, East Antarctica: Another factor in ice sheet stability? *Journal of Geophysical Research: Oceans*, 115(C12): C12027, 2010. http://dx.doi.org/10.1029/2009JC006083. (Cited on page 19.)

Massom, R. A. and S. E. Stammerjohn. Antarctic sea ice change and variability - Physical and ecological implications. *Polar Science*, 4(2):149–186, 2010. http://dx.doi.org/10.1016/j.polar.2010.05.001. (Cited on page 15.)

McGrath Grossi, S., S. T. Kottmeier, R. L. Moe, G. T. Taylor, and C. W. Sullivan. Sea ice microbial communities - VI - Growth and primary production in bottom ice under graded snow cover. *Marine Ecology - Progress Series*, 35:153–164, 1987. (Cited on pages 33, 34 and 35.)

McGuinness, M. J., M. J. M. Williams, P. J. Langhorne, C. Purdie, and J. Crook. Frazil deposition under growing sea ice. *Journal of Geophysical Research: Oceans*, 114, 2009. http://dx.doi.org/10.1029/2007JC004414. (Cited on pages 30, 33 and 38.)

McMillan, M., A. Shepherd, A. Sundal, K. Briggs, A. Muir, A. Ridout, A. Hogg, and D. Wingham. Increased ice losses from Antarctica detected by CryoSat-2. *Geophysical Research Letters*, 41(11): 2014GL060111, 2014. http://dx.doi.org/10.1002/2014GL060111. (Cited on page 15.)

McMinn, A., C. Ashworth, and K. G. Ryan. In situ net primary productivity of an Antarctic fast ice bottom algal community. *Aquatic Microbial Ecology*, 21(2):177–185, 2000. http://dx.doi.org/10.3354/ame021177. (Cited on page 19.)

Meredith, M. P. and J. C. King. Rapid climate change in the ocean west of the Antarctic Peninsula during the second half of the 20th century. *Geophysical Research Letters*, 32(19), 2005. (Cited on pages 15 and 16.)

Morassutti, M. P. Climate model sensitivity to sea ice albedo parameterization. *Theoretical and Applied Climatology*, 44(1):25–36, 1991. http://dx.doi.org/10.1007/BF00865548. (Cited on page 10.)

Moretskii, V. N. Underwater sea ice (in russian). *Probl. Arkt. Antarkt.*, 19:32–38, 1965. (Cited on pages 26, 30 and 33.)

Morgan, V. I. Oxygen isotope evidence for bottom freezing on the Amery Ice Shelf. *Nature*, 238(5364): 393–394, 1972. http://dx.doi.org/10.1038/238393a0. (Cited on page 36.)

Murphy, E. J., A. Clarke, C. Symon, and J. Priddle. Temporal variation in Antarctic sea ice - analysis of a long-term fast-ice record from the South-Orkney Islands. *Deep-Sea Research Part I-Oceanographic Research Papers*, 42(7):1045–1062, 1995. http://dx.doi.org/10.1016/0967-0637(95)00057-D. (Cited on pages 12 and 19.)

Nagler, T. and H. Rott. Snow classification algorithm for Envisat ASAR. In *Proc. of the 2004 ENVISAT & ERS Symposium, Salzburg, Austria*, pages 6–10, 2004. (Cited on page 110.)

Neckel, N., R. Drews, W. Rack, and D. Steinhage. Basal melting at the Ekström Ice Shelf, Antarctica, estimated from mass flux divergence. *Annals of Glaciology*, 53(60):294–302, 2012. http://dx.doi.org/10.3189/2012AoG60A167. (Cited on page 40.)

Nicol, S., A. Worby, and R. Leaper. Changes in the Antarctic sea ice ecosystem: potential effects on krill and baleen whales. *Marine and Freshwater Research*, 59(5):361–382, 2008. http://dx.doi.org/10.1071/MF07161. (Cited on page 12.)

Nicolaus, M. *Observation and modelling of snow melt and superimposed ice formation on Arctic and Antarctic sea ice (in German)*, volume 535. Alfred-Wegener-Institute Helmholtz-Center for Polar and Marine Research, 2006. http://dx.doi.org/hdl:10013/epic.10540. (Cited on page 9.)

Nicolaus, M. and K. Grosfeld. Ice-Ocean interactions underneath the Antarctic Ice Shelf Ekströmisen. *Polarforschung*, 72(1):17–29, 2004. http://dx.doi.org/10013/epic.21552.d001. (Cited on page 40.)

Nicolaus, M., C. Haas, J. Bareiss, and S. Willmes. A model study of differences of snow thinning on Arctic and Antarctic first-year sea ice during spring and summer. *Annals of Glaciology*, 44:147–153, 2006. http://dx.doi.org/hdl:10013/epic.24393.d001. (Cited on page 12.)

Nicolaus, M., S. R. Hudson, S. Gerland, and K. Munderloh. A modern concept for autonomous and continuous measurements of spectral albedo and transmittance of sea ice. *Cold Regions Science and Technology*, 62(1):14–28, 2010a. http://dx.doi.org/10.1016/j.coldregions.2010.03.001. (Cited on page 52.)

Niedrauer, T. M. and S. Martin. An experimental study of brine drainage and convection in Young Sea ice. *Journal of Geophysical Research: Oceans*, 84(C3):1176–1186, 1979. http://dx.doi.org/10.1029/JC084iC03p01176. (Cited on page 8.)

Oerter, H., J. Kipfstuhl, J. Determann, H. Miller, D. Wagenbach, A. Minikin, and W. Graft. Evidence for basal marine ice in the Filchner- Ronne Ice Shelf. *Nature*, 358(6385):399–401, 1992. http://dx.doi.org/10.1038/358399a0. (Cited on page 37.)

Osterkamp, J. P. and T. E. Gosink. Observations and analysis of sediment laden sea ice. In Barnes, P., D. Schell, and E. Reimnitz, editors, *The Alaska Beaufort Sea: Ecosystem and Environment*, pages 73–94. Academic Press, San Francisco, CA, 1984. (Cited on page 35.)

Ozsoy-Cicek, B., S. Kern, S. F. Ackley, H. Xie, and A. E. Tekeli. Intercomparisons of Antarctic sea ice types from visual ship, RADARSAT-1 SAR, Envisat ASAR, QuikSCAT, and AMSR-E satellite observations in the Bellingshausen Sea. *Deep Sea Research Part II: Topical Studies in Oceanography*, 58(9-10):1092–1111, 2011. http://www.sciencedirect.com/science/article/pii/S0967064510003164. (Cited on pages 14 and 110.)

Ozsoy-Cicek, B., S. Ackley, H. Xie, D. Yi, and J. Zwally. Sea ice thickness retrieval algorithms based on in situ surface elevation and thickness values for application to altimetry. *Journal of Geophysical Research: Oceans*, 118(8):3807–3822, 2013. http://dx.doi.org/10.1002/jgrc.20252. (Cited on pages 14 and 15.)

Paige, R. A. *Crystallographic studies of sea ice in McMurdo Sound, Antarctica*. Naval Facilities Engineering Command, U.S. Naval Civil Engineering Laboratory, Port Hueneme, Calif., 1966. http://dx.doi.org/10.5962/bhl.title.47716. (Cited on page 33.)

Palmisano, A. C. and C. W. Sullivan. Physiological response of micro-algae in the ice-platelet layer to low-light conditions. In Siegfried, W. R., P. R. Condy, and R. M. Laws, editors, *Antarctic Nutrient Cycles and Food Webs*, chapter 12, pages 84–88. Springer Berlin Heidelberg, 1985. http://dx.doi.org/10.1007/978-3-642-82275-9_12. (Cited on page 34.)

Palmisano, A. C., J. Beeler SooHoo, and C. W. Sullivan. Effects of four environmental variables on photosynthesis-irradiance relationships in Antarctic sea-ice microalgae. *Marine Biology*, 94(2):299–306, 1987. http://dx.doi.org/10.1007/BF00392944. (Cited on page 34.)

Palmisano, A. C., J. B. SooHoo, and C. W. Sullivan. Photosynthesis-irradiance relationships in sea ice microalgae from McMurdo Sound, Antarctica. *Journal of Phycology*, 21(3):341–346, 1985. http://dx.doi.org/10.1111/j.0022-3646.1985.00341.x. (Cited on page 34.)

Parkinson, C. L. and D. J. Cavalieri. Antarctic sea ice variability and trends, 1979-2010. *The Cryosphere*, 6(4):871–880, 2012. http://dx.doi.org/10.5194/tc-6-871-2012. (Cited on pages 13, 14 and 15.)

Parkinson, C. L. Search for the little ice age in Southern Ocean sea ice records. *Annals of Glaciology*, 14: 221–225, 1990. (Cited on page 12.)

Paul, S., S. Willmes, M. Hoppmann, P. A. Hunkeler, G. Heinemann, M. Nicolaus, and R. Timmermann. The impact of early summer snow properties on land-fast sea-ice X-band backscatter. *Annals of Glaciology*, 56(69), 2015. http://dx.doi.org/10.3189/2015AoG69A715. (Cited on pages 109 and 198.)

Penrose, J. D., M. Conde, and T. J. Pauly. Acoustic detection of ice crystals in Antarctic waters. *Journal of Geophysical Research: Oceans*, 99(C6):12573–12580, 1994. http://dx.doi.org/10.1029/93JC03507. (Cited on pages 33 and 34.)

Perovich, D. K. *The optical properties of sea ice*. Monogr. 96-1. Cold Reg. Res. and Eng. Lab, Hanover, N. H., 1996. (Cited on pages 8 and 9.)

Perovich, D. K. The Changing Arctic Sea Ice Cover. *Oceanography*, 24(3):162–173, 2011. http://dx.doi.org/10.5670/oceanog.2011.68. (Cited on page 12.)

Perovich, D. K., B. C. Elder, K. J. Claffey, S. Stammerjohn, R. Smith, S. F. Ackley, H. R. Krouse, and A. J. Gow. Winter sea-ice properties in Marguerite Bay, Antarctica. *Deep Sea Research Part II: Topical Studies in Oceanography*, 51(17-19):2023–2039, 2004. http://dx.doi.org/10.1016/j.dsr2.2004.07.024. (Cited on page 14.)

Perovich, D. K., J. A. Richter-Menge, K. F. Jones, and B. Light. Sunlight, water, and ice: Extreme Arctic sea ice melt during the summer of 2007. *Geophysical Research Letters*, 35(11):L11501, 2008. http://dx.doi.org/10.1029/2008GL034007. (Cited on page 15.)

Petrich, C. and H. Eicken. Growth, Structure and Properties of Sea Ice. In *Sea Ice*, pages 23–77. Wiley-Blackwell, 2010. http://dx.doi.org/10.1002/9781444317145.ch2. (Cited on page 10.)

Pezza, A. B., H. A. Rashid, and I. Simmonds. Climate links and recent extremes in Antarctic sea ice, high-latitude cyclones, Southern Annular Mode and ENSO. *Climate Dynamics*, 38(1-2):57–73, 2012. http://dx.doi.org/10.1007/s00382-011-1044-y. (Cited on page 16.)

Pfaffhuber, A. A., S. Hendricks, and Y. A. Kvistedal. Progressing from 1D to 2D and 3D near-surface airborne electromagnetic mapping with a multisensor, airborne sea-ice explorer. *Geophysics*, 77 (4):WB109–WB117, 2012. http://dx.doi.org/10.1190/geo2011-0375.1. (Cited on page 108.)

Price, D., W. Rack, P. J. Langhorne, C. Haas, G. Leonard, and K. Barnsdale. The sub-ice platelet layer and its influence on freeboard to thickness conversion of Antarctic sea ice. *The Cryosphere*, 8(3): 1031–1039, 2014. http://dx.doi.org/10.5194/tc-8-1031-2014. (Cited on page 33.)

Pringle, D. J., H. J. Trodahl, and T. G. Haskell. Direct measurement of sea ice thermal conductivity: No surface reduction. *Journal of Geophysical Research: Oceans*, 111(C5):C05020, 2006. http://dx.doi.org/10.1029/2005JC002990. (Cited on page 38.)

Pringle, D. J., H. Eicken, H. J. Trodahl, and L. G. E. Backstrom. Thermal conductivity of landfast Antarctic and Arctic sea ice. *Journal of Geophysical Research*, 112(C4), 2007. http://dx.doi.org/10.1029/2006JC003641. (Cited on page 8.)

Pritchard, H. D., S. R. M. Ligtenberg, H. A. Fricker, D. G. Vaughan, M. R. van den Broeke, and L. Padman. Antarctic ice-sheet loss driven by basal melting of ice shelves. *Nature*, 484(7395):502–505, 2012. http://dx.doi.org/10.1038/nature10968. (Cited on pages 21, 22 and 118.)

Purdie, C., P. Langhorne, G. Leonard, and T. Haskell. Growth of first-year landfast Antarctic sea ice determined from winter temperature measurements. *Ann. Glaciol.*, 44:172, 2006. http://dx.doi.org/10.3189/172756406781811853. (Cited on pages 29 and 33.)

Quetin, L. B., R. M. Ross, T. K. Frazer, and K. L. Haberman. Factors affecting distribution and abundance of zooplankton, with an emphasis on Antarctic krill, Euphausia Superba. In *Foundations for Ecological Research West of the Antarctic Peninsula*, pages 357–371. American Geophysical Union, 2013. http://dx.doi.org/10.1029/AR070p0357. (Cited on page 35.)

Rack, W., C. Haas, and P. J. Langhorne. Airborne thickness and freeboard measurements over the McMurdo Ice Shelf, Antarctica, and implications for ice density. *Journal of Geophysical Research: Oceans*, 118(11):5899–5907, 2013. http://dx.doi.org/10.1002/2013JC009084. (Cited on page 103.)

Rakusa-Suszczewski, S. The biology of *Paramoera walkeri Stebbing* (Amphipoda) and the Antarctica sub-fast ice community. *Polish Archives Hydrobiology*, 19:11–36, 1972. (Cited on page 35.)

Raphael, M. N. and W. Hobbs. The influence of the large-scale atmospheric circulation on Antarctic sea ice during ice advance and retreat seasons. *Geophysical Research Letters*, 41(14):5037–5045, 2014. http://dx.doi.org/10.1002/2014GL060365. (Cited on pages 16 and 17.)

Regoli, F., M. Nigro, M. Benedetti, D. Fattorini, and S. Gorbi. Antioxidant efficiency in early life stages of the Antarctic silverfish, *Pleuragramma Antarcticum*: responsiveness to pro-oxidant conditions of platelet ice and chemical exposure. *Aquatic Toxicology*, 75(1):43–52, 2005. http://dx.doi.org/10.1016/j.aquatox.2005.07.003. (Cited on pages 33 and 35.)

Reid, J. E., A. P. Worby, J. Vrbancich, and A. I. S. Munro. Shipborne electromagnetic measurements of antarctic sea-ice thickness. *Geophysics*, 68(5):1537–1546, 2003. http://dx.doi.org/10.1190/1.1620627. (Cited on page 103.)

Reid, P., S. Stammerjohn, R. Massom, T. Scambos, , and J. Lieser. The record 2013 Southern Hemisphere sea-ice extent maximum. *Annals of Glaciology*, 56(69), 2014. http://dx.doi.org/10.3189/2015AoG69A892. (Cited on pages 14 and 17.)

Reijnders, P. J. H., J. Plötz, J. Zegers, and M. Gräfe. Breeding biology of weddell seals (*Leptonychotes weddellii*) at Drescher Inlet, Riiser-Larsen Ice Shelf, Antarctica. *Polar Biology*, 10(4):301–306, 1990. http://dx.doi.org/10.1007/BF00238429. (Cited on page 19.)

Renwick, J. A. Southern Hemisphere circulation and relations with sea ice and sea surface temperature. *Journal of Climate*, 15(21):3058–3068, 2002. http://dx.doi.org/10.1175/1520-0442(2002)015<3058:SHCARW>2.0.CO;2. (Cited on page 16.)

Ricker, R., S. Hendricks, V. Helm, H. Skourup, and M. Davidson. Sensitivity of CryoSat-2 Arctic sea-ice volume trends on radar-waveform interpretation. *The Cryosphere Discuss.*, 8(2):1831–1871, 2014. http://dx.doi.org/10.5194/tcd-8-1831-2014. (Cited on pages 10 and 103.)

Rignot, E., I. Velicogna, M. R. van den Broeke, A. Monaghan, and J. T. M. Lenaerts. Acceleration of the contribution of the Greenland and Antarctic ice sheets to sea level rise. *Geophysical Research Letters*, 38(5):L05503, 2011. http://dx.doi.org/10.1029/2011GL046583. (Cited on page 21.)

Rignot, E., S. Jacobs, J. Mouginot, and B. Scheuchl. Ice-shelf melting around Antarctica. *Science*, 341(6143):266–270, 2013. http://dx.doi.org/10.1126/science.1235798. (Cited on pages 21, 22 and 32.)

Rignot, E., J. Mouginot, M. Morlighem, H. Seroussi, and B. Scheuchl. Widespread, rapid grounding line retreat of Pine Island, Thwaites, Smith, and Kohler glaciers, West Antarctica, from 1992 to 2011. *Geophysical Research Letters*, 41(10):3502–3509, 2014. http://dx.doi.org/10.1002/2014GL060140. (Cited on page 22.)

Rimbu, N., G. Lohmann, G. König-Langlo, C. Necula, and M. Ionita. Daily to intraseasonal oscillations at Antarctic research station Neumayer. *Antarctic Science*, 26(02):193–204, 2014. http://dx.doi.org/10.1017/S0954102013000540. (Cited on page 42.)

Rintoul, S. R. On the origin and influence of Adélie Land bottom water. In *Ocean, Ice, and Atmosphere: Interactions at the Antarctic Continental Margin*, pages 151–171. American Geophysical Union, 1985. http://dx.doi.org/10.1029/AR075p0151. (Cited on page 19.)

Robin, G. d. Q. Formation, flow, and desintegration of ice shelves. *Journal of Glaciology*, 24(90):259–271, 1979. (Cited on pages 21, 28 and 37.)

Robinson, N. J., M. J. M. Williams, C. L. Stevens, P. J. Langhorne, and T. G. Haskell. Evolution of a supercooled Ice Shelf Water plume with an actively growing sub-ice platelet matrix. *Journal of Geophysical Research: Oceans*, 119:3425–3446, 2014. http://dx.doi.org/10.1002/2013JC009399. (Cited on page 29.)

Sandhäger, H. and N. Blindow. Surface elevation, ice thickness, and subglacial-bedrock topography of Ekström Ice Shelf (Antarctica) and its catchment area. *Annals of Glaciology*, 30(1):61–68, 2000. http://dx.doi.org/10.3189/172756400781820723. (Cited on page 40.)

Scambos, T., C. Hulbe, and M. Fahnestock. Climate-induced ice shelf disintegration in the Antarctic Peninsula. In *Antarctic Peninsula Climate Variability: Historical and Paleoenvironmental Perspectives*, volume 79 of *Antarct. Res. Ser.*, pages 79–92. AGU, Washington, D.C., 2003. http://dx.doi.org/10.1029/AR079p0079. (Cited on pages 12 and 22.)

Schlosser, E. Effects of seasonal variability of accumulation on yearly mean δ^{18}O values in Antarctic snow. *Journal of Glaciology*, 45(151):463–468, 1999. (Cited on page 42.)

Schnack-Schiel, S. B., D. B. Thomas, H.-U. B. Dahms, C. B. Hass, and E. B. Mizdalski. Copepods in Antarctic Sea Ice. In *Antarctic Sea Ice: Biological Processes, Interactions and Variability*, pages 173–182. American Geophysical Union, 2013. http://dx.doi.org/10.1029/AR073p0173. (Cited on page 35.)

Serikov, M. I. Struktura morskogo antarkticheskogo l'da (Structure of Antarctic sea ice). *Sov. Antarctic Exped. Inform. Bull.*, 39:13–14, 1963. (Cited on page 33.)

Shepherd, A., E. R. Ivins, A. Geruo, V. R. Barletta, M. J. Bentley, S. Bettadpur, K. H. Briggs, D. H. Bromwich, R. Forsberg, N. Galin, M. Horwath, S. Jacobs, I. Joughin, M. A. King, J. T. M. Lenaerts, J. L. Li, S. R. M. Ligtenberg, A. Luckman, S. B. Luthcke, M. McMillan, R. Meister, G. Milne, J. Mouginot, A. Muir, J. P. Nicolas, J. Paden, A. J. Payne, H. Pritchard, E. Rignot, H. Rott, L. S. Sorensen, T. A. Scambos, B. Scheuchl, E. J. O. Schrama, B. Smith, A. V. Sundal, J. H. van Angelen, W. J. van de Berg, M. R. van den Broeke, D. G. Vaughan, I. Velicogna, J. Wahr, P. L. Whitehouse, D. J. Wingham, D. H. Yi, D. Young, and H. J. Zwally. A reconciled estimate of ice-sheet mass balance. *Science*, 338(6111): 1183–1189, 2012. http://dx.doi.org/10.1126/science.1228102. (Cited on page 17.)

Sigmond, M. and J. C. Fyfe. Has the ozone hole contributed to increased Antarctic sea ice extent? *Geophysical Research Letters*, 37(18):L18502, 2010. http://dx.doi.org/10.1029/2010GL044301. (Cited on page 17.)

Simmonds, I. Modes of atmospheric variability over the Southern Ocean. *Journal of Geophysical Research: Oceans*, 108(C4), 2003. http://dx.doi.org/10.1029/2000JC000542. (Cited on page 16.)

Simmonds, I. and I. Rudeva. The great Arctic cyclone of August 2012. *Geophysical Research Letters*, 39 (23):L23709, 2012. http://dx.doi.org/10.1029/2012GL054259. (Cited on page 12.)

Simpkins, G. R., L. M. Ciasto, D. W. J. Thompson, and M. H. England. Seasonal relationships between large-scale climate variability and Antarctic sea ice concentration. *Journal of Climate*, 25(16):5451–5469, 2012. http://dx.doi.org/10.1175/JCLI-D-11-00367.1. (Cited on page 16.)

Simpkins, G. R., L. M. Ciasto, and M. H. England. Observed variations in multidecadal Antarctic sea ice trends during 1979-2012. *Geophysical Research Letters*, 40(14):3643–3648, 2013. doi:http://dx.doi.org/10.1002/grl.50715. (Cited on pages 15 and 16.)

Siripunvaraporn, W. and G. Egbert. An efficient data-subspace inversion method for 2-d magnetotelluric data. *Geophysics*, 65(3):791–803, 2000. doi:http://dx.doi.org/10.1190/1.1444778. (Cited on page 107.)

Smedsrud, L. H. and A. Jenkins. Frazil ice formation in an ice shelf water plume. *Journal of Geophysical Research: Oceans*, 109(C03025), 2004. http://dx.doi.org/10.1029/2003JC001851. (Cited on pages 29 and 37.)

Smetacek, V., R. Scharek, L. I. Gordon, H. Eicken, E. Fahrbach, G. Rohardt, and S. Moore. Early spring phytoplankton blooms in ice platelet layers of the southern Weddell Sea, Antarctica. *Deep Sea Research Part A. Oceanographic Research Papers*, 39(2):153–168, 1992. http://dx.doi.org/10.1016/0198-0149(92)90102-Y. (Cited on pages 33, 34 and 35.)

Smith, I. J., P. J. Langhorne, H. J. Trodahl, T. G. Haskell, and D. M. Cole. Platelet ice - The McMurdo sound debate . In Shen, H. T., editor, *Ice in Surface Waters*, pages 829–834. Balkema, 1999. (Cited on page 24.)

Smith, I. J., P. J. Langhorne, T. G. Haskell, H. J. Trodahl, R. Frew, and M. R. Vennell. Platelet ice and the land-fast sea ice of McMurdo Sound, Antarctica. *Annals of Glaciology, Vol 33*, 33:21–27, 2001. http://dx.doi.org/10.3189/172756401781818365. (Cited on pages 24, 30, 33 and 38.)

Smith, I. J., P. J. Langhorne, R. D. Frew, R. Vennell, and T. G. Haskell. Sea ice growth rates near ice shelves. *Cold Regions Science and Technology*, 83-84(0):57–70, 2012. http://dx.doi.org/10.1016/j.coldregions.2012.06.005. (Cited on page 33.)

Souchez, R., M. Meneghel, J. L. Tison, R. Lorrain, D. Ronveaux, C. Baroni, A. Lozej, I. Tabacco, and J. Jouzel. Ice composition evidence of marine ice transfer along the bottom of a small Antarctic ice shelf. *Geophysical Research Letters*, 18(5):849–852, 1991. http://dx.doi.org/10.1029/91GL01077. (Cited on page 26.)

Squire, V. A. The marginal ice zone. In Lepparanta, M., editor, *The Physics of Ice Covered Seas*, pages 381 – 446. Univ. of Helsinki, Helsinki, 1998. (Cited on page 12.)

Stammerjohn, S., R. Massom, D. Rind, and D. Martinson. Regions of rapid sea ice change: An inter-hemispheric seasonal comparison. *Geophysical Research Letters*, 39, 2012. http://dx.doi.org/10.1029/2012GL050874. (Cited on pages 15 and 16.)

Stroeve, J. C., M. C. Serreze, M. M. Holland, J. E. Kay, J. Malanik, and A. P. Barrett. The Arctic's rapidly shrinking sea ice cover: a research synthesis. *Climatic Change*, 110(3-4):1005–1027, 2012. http://dx.doi.org/10.1007/s10584-011-0101-1. (Cited on page 12.)

Sullivan, S. T. K., S. M. Grossi, and C. W. Sea ice microbial communities. VIII. Bacterial production in annual sea ice of McMurdo Sound, Antarctica. *Marine Ecology - Progress Series*, 35:175–186, 1987. (Cited on pages 33 and 35.)

Swart, N. C. and J. C. Fyfe. The influence of recent Antarctic ice sheet retreat on simulated sea ice area trends. *Geophysical Research Letters*, pages 4328–4332, 2013. http://dx.doi.org/doi:10.1002/grl.50820. (Cited on page 17.)

Swithinbank, C. W. *Satellite Image Atlas of Glaciers of then World: Antarctica*. USGS Prof. Paper 1386-B. U.S. Geological Survey, 1988. (Cited on page 21.)

Tamura, T., K. I. Ohshima, and S. Nihashi. Mapping of sea ice production for Antarctic coastal polynyas. *Geophysical Research Letters*, 35(7), 2008. http://dx.doi.org/10.1029/2007GL032903. (Cited on page 19.)

Tamura, T., G. D. Williams, A. D. Fraser, and K. I. Ohshima. Potential regime shift in decreased sea ice production after the Mertz Glacier calving. *Nature Communications*, 3, 2012. http://dx.doi.org/10.1038/ncomms1820. (Cited on page 19.)

Tang, S. L., D. H. Qin, J. W. Ren, J. C. Kang, and Z. J. Li. Structure, salinity and isotopic composition of multi-year landfast sea ice in Nella Fjord, Antarctica. *Cold Regions Science and Technology*, 49(2):170–177, 2007. http://dx.doi.org/10.1016/j.coldregions.2007.03.005. (Cited on page 38.)

Thomas, D. N. and G. S. Dieckmann. Antarctic sea ice - a habitat for extremophiles. *Science*, 295(5555): 641–644, 2002. http://dx.doi.org/hdl:10013/epic.26120. (Cited on page 8.)

Thompson, D. W. J., S. Solomon, P. J. Kushner, M. H. England, K. M. Grise, and D. J. Karoly. Signatures of the Antarctic ozone hole in Southern Hemisphere surface climate change. *Nature Geoscience*, 4(11): 741–749, 2011. 10.1038/ngeo1296. (Cited on page 16.)

Tison, J.-L. Ice-ocean interactions in Antarctica: the marine-ice perspective, 2002. (Cited on page 36.)

Tison, J.-L., D. Ronveaux, and R. D. Lorrain. Low salinity frazil ice generation at the base of a small Antarctic ice shelf. *Antarctic Science*, 5(03):309–322, 1993. http://dx.doi.org/10.1017/S0954102093000409. (Cited on page 26.)

Tison, J.-L., R. D. Lorrain, A. Bouzette, M. Dini, A. Bondesan, and M. StiéVenard. Linking Landfast Sea Ice Variability to Marine Ice Accretion at Hells Gate Ice Shelf, Ross Sea. In *Antarctic Sea Ice: Physical Processes, Interactions and Variability*, pages 375–407. American Geophysical Union, 1998. http://dx.doi.org/10.1029/AR074p0375. (Cited on pages 18, 30, 36 and 37.)

Toggweiler, J. R. and B. Samuels. Effect of sea ice on the salinity of Antarctic bottom waters. *Journal of Physical Oceanography*, 25(9):1980–1997, 1995. http://dx.doi.org/10.1175/1520-0485(1995)025<1980:EOSIOT>2.0.CO;2. (Cited on page 8.)

Trodahl, H. J., M. J. McGuinness, P. J. Langhorne, K. Collins, A. E. Pantoja, I. J. Smith, and T. G. Haskell. Heat transport in McMurdo Sound first-year fast ice. *Journal of Geophysical Research: Oceans*, 105(C5):11347–11358, 2000. http://dx.doi.org/10.1029/1999JC000003. (Cited on page 38.)

Turner, J., J. C. Comiso, G. J. Marshall, T. A. Lachlan-Cope, T. Bracegirdle, T. Maksym, M. P. Meredith, Z. M. Wang, and A. Orr. Non-annular atmospheric circulation change induced by stratospheric ozone depletion and its role in the recent increase of Antarctic sea ice extent. *Geophysical Research Letters*, 36, 2009. http://dx.doi.org/10.1029/2009GL037524. (Cited on pages 13 and 16.)

Turner, J., T. J. Bracegirdle, T. Phillips, G. J. Marshall, and J. S. Hosking. An initial assessment of Antarctic sea ice extent in the CMIP5 models. *Journal of Climate*, 26(5):1473–1484, 2013a. http://dx.doi.org/10.1175/JCLI-D-12-00068.1. (Cited on page 17.)

Turner, J. G. J. M. *Climate Change in the Polar Regions*. Cambridge University Press, Cambridge, UK, 2011. (Cited on page 16.)

Turner, J. and J. Overland. Contrasting climate change in the two polar regions. *Polar Research*, 28(2): 146–164, 2009. http://dx.doi.org/10.1111/j.1751-8369.2009.00128.x. (Cited on page 20.)

Turner, J., J. S. Hosking, T. Phillips, and G. J. Marshall. Temporal and spatial evolution of the Antarctic sea ice prior to the September 2012 record maximum extent. *Geophysical Research Letters*, 40(22): 2013GL058371, 2013b. http://dx.doi.org/10.1002/2013GL058371. (Cited on page 14.)

Turner, J., T. Phillips, J. S. Hosking, G. J. Marshall, and A. Orr. The Amundsen Sea low. *International Journal of Climatology*, 33(7):1818–1829, 2013c. 10.1002/joc.3558. (Cited on page 17.)

Turner, J., N. E. Barrand, T. J. Bracegirdle, P. Convey, D. A. Hodgson, M. Jarvis, A. Jenkins, G. Marshall, M. P. Meredith, H. Roscoe, J. Shanklin, J. French, H. Goosse, M. Guglielmin, J. Gutt, S. Jacobs, M. C. I. Kennicutt, V. Masson-Delmotte, P. Mayewski, F. Navarro, S. Robinson, T. Scambos,

M. Sparrow, C. Summerhayes, K. Speer, and A. Klepikov. Antarctic climate change and the environment: an update. *Polar Record*, 50(03):237–259, 2014. http://dx.doi.org/10.1017/S0032247413000296. (Cited on page 17.)

Uto, S., H. Shimoda, and S. Ushio. Characteristics of sea-ice thickness and snow-depth distributions of the summer landfast ice in Lützow-Holm Bay, East Antarctica. *Annals of Glaciology*, 44(1), 2006. http://dx.doi.org/10.3189/172756406781811240. (Cited on page 38.)

Vacchi, M., M. La Mesa, M. Dalu, and J. Macdonald. Early life stages in the life cycle of Antarctic silverfish, *Pleuragramma Antarcticum* in Terra Nova Bay, Ross Sea. *Antarctic Science*, 16(3):299–305, 2004. http://dx.doi.org/10.1017/S0954102004002135. (Cited on pages 33 and 35.)

Vancoppenolle, M., H. Goosse, A. de Montety, T. Fichefet, B. Tremblay, and J. L. Tison. Modeling brine and nutrient dynamics in Antarctic sea ice: The case of dissolved silica. *Journal of Geophysical Research: Oceans*, 115, 2010. http://dx.doi.org/10.1029/2009JC005369. (Cited on page 8.)

Wadhams, P., M. A. Lange, and S. F. Ackley. The ice thickness distribution across the Atlantic sector of the Antarctic Ocean in midwinter. *Journal of Geophysical Research: Oceans*, 92(C13):14535–14552, 1987. http://dx.doi.org/10.1029/JC092iC13p14535. (Cited on pages 10 and 14.)

Walker, T. D. and H. J. Marchant. The seasonal occurrence of chroococcoid cyanobacteria at an Antarctic coastal site. *Polar Biology*, 9(3):193–196, 1989. http://dx.doi.org/10.1007/BF00297175. (Cited on page 34.)

Wang, X., H. Xie, Y. Ke, S. F. Ackley, and L. Liu. A method to automatically determine sea level for referencing snow freeboards and computing sea ice thicknesses from NASA IceBridge airborne LIDAR. *Remote Sensing of Environment*, 131:160–172, 2013. http://dx.doi.org/10.1016/j.rse.2012.12.022. (Cited on page 14.)

Warren, S. G., C. S. Roesler, V. I. Morgan, R. E. Brandt, I. D. Goodwin, and I. Allison. Green icebergs formed by freezing of organic-rich seawater to the base of Antarctic ice shelves. *Journal of Geophysical Research: Oceans*, 98(C4):6921–6928, 1993. http://dx.doi.org/10.1029/92JC02751. (Cited on pages 34 and 37.)

Weeks, W. F. Growth conditions and the structure and properties of sea ice. In Leppäranta, M., editor, *Physics of ice covered seas*, volume 1, pages 25–104. Helsinki University Press, 1998. (Cited on page 12.)

Weeks, W. F. On sea ice. In *On sea ice*. University of Alaska Press, Fairbanks, AK, 2010. http://dx.doi.org/10.1002/gj.1285. (Cited on pages 8, 10 and 26.)

Willatt, R. C., K. A. Giles, S. W. Laxon, L. Stone-Drake, and A. P. Worby. Field investigations of Ku-band radar penetration into snow cover on Antarctic sea ice. *IEEE Transactions on Geoscience and Remote Sensing*, 48(1):365–372, 2010. http://dx.doi.org/10.1109/TGRS.2009.2028237. (Cited on page 15.)

Williams, G. D., N. L. Bindoff, S. J. Marsland, and S. R. Rintoul. Formation and export of dense shelf water from the Adélie Depression, East Antarctica. *Journal of Geophysical Research: Oceans*, 113 (C4):C04039, 2008. http://dx.doi.org/10.1029/2007JC004346. (Cited on page 19.)

Williams, M. J. M., A. Jenkins, and J. Determann. Physical controls on ocean circulation beneath ice shelves revealed by numerical models. *Ocean, Ice, and Atmosphere : Interactions At the Antarctic Continental Margin*, 75:285–299, 1998. http://dx.doi.org/10.1029/AR075p0285. (Cited on page 29.)

Willmes, S., T. Krumpen, S. Adams, L. Rabenstein, C. Haas, J. Hoelemann, S. Hendricks, and G. Heinemann. Cross-validation of polynya monitoring methods from multisensor satellite and airborne data: a case study for the Laptev Sea. *Canadian Journal of Remote Sensing*, 36:S196–S210, 2010. http://dx.doi.org/10.5589/m10-012. (Cited on page 110.)

Willmes, S., C. Haas, and M. Nicolaus. High radar-backscatter regions on Antarctic sea-ice and their relation to sea-ice and snow properties and meteorological conditions. *International Journal of Remote Sensing*, 32(14):3967–3984, 2011. http://dx.doi.org/10.1080/01431161003801344. (Cited on page 110.)

Willmes, S., J. Bareiss, C. Haas, and M. Nicolaus. The importance of diurnal processes for the seasonal cycle of sea-ice microwave brightness temperatures during early summer in the Weddell Sea, Antarctica. *Annals of Glaciology*, 44:297–302, 2006. http://dx.doi.org/10.3189/172756406781811817. (Cited on pages 12 and 110.)

WMO. WMO sea-ice nomenclature, codes, and illustrated glossary, 1970. http://www.aari.nw.ru/gdsidb/XML/wmo_259.php. (Cited on pages 10, 18 and 26.)

Woehler, E. J. *The Distribution and Abundance of Antarctic and Subantarctic Penguins*. Scientific Committee on Antarctic Research, Cambridge, 1993. (Cited on page 43.)

Wongpan, P., P. J. Langhorne, D. E. Dempsey, L. Hahn-Woernle, and Z. Sun. Simulation of the crystal growth of platelet sea ice with diffusive heat and mass transfer. *56*, 69, 2015. (Cited on page 33.)

Worby, A. P. and J. C. Comiso. Studies of the Antarctic sea ice edge and ice extent from satellite and ship observations. *Remote Sensing of Environment*, 92(1):98–111, 2004. (Cited on page 13.)

Worby, A. P., R. A. Massom, I. Allison, V. I. Lytle, and R. Heil. East Antarctic sea ice: A review of its structure, properties and drift. In Jeffries, M. O., editor, *Antarctic Sea ice: Physical processes, interactions and variability*, volume 74, pages 41–67. American Geophysical Union, 1998. http://dx.doi.org/10.1029/AR074p0041. (Cited on page 10.)

Worby, A. P., C. A. Geiger, M. J. Paget, M. L. Van Woert, S. F. Ackley, and T. L. DeLiberty. Thickness distribution of Antarctic sea ice. *Journal of Geophysical Research: Oceans*, 113(C5), 2008a. http://dx.doi.org/10.1029/2007JC004254. (Cited on pages 14 and 15.)

Worby, A. P., T. Markus, A. D. Steer, V. I. Lytle, and R. A. Massom. Evaluation of AMSR-E snow depth product over East Antarctic sea ice using in situ measurements and aerial photography. *Journal of Geophysical Research: Oceans*, 113(C5):C05S94, 2008b. http://dx.doi.org/10.1029/2007JC004181. (Cited on page 110.)

Wright, C. and R. Priestley. *Glaciology - British (Terra Nova) Antarctic Expedition 1910-1913*. Harrison and Sons, London, UK, 1922. (Cited on pages 24, 26 and 33.)

Yackel, J. J., D. G. Barber, T. N. Papakyriakou, and C. Breneman. First-year sea ice spring melt transitions in the Canadian Arctic Archipelago from time-series synthetic aperture radar data, 1992-2002. *Hydrol. Process.*, 21(2):253–265, 2007. http://dx.doi.org/10.1002/hyp.6240. (Cited on page 110.)

Yackel, J. and D. Barber. Observations of snow water equivalent change on landfast first-year sea ice in winter using synthetic aperture radar data. *IEEE Transactions on Geoscience and Remote Sensing*, 45 (4):1005–1015, 2007. (Cited on pages 10 and 110.)

Yi, D. H., H. J. Zwally, and J. W. Robbins. ICESat observations of seasonal and interannual variations of sea-ice freeboard and estimated thickness in the Weddell Sea, Antarctica (2003-2009). *Annals of Glaciology*, 52(57):43–51, 2011. http://dx.doi.org/10.3189/172756411795931480. (Cited on page 15.)

Yuan, X. and C. Li. Climate modes in southern high latitudes and their impacts on Antarctic sea ice. *Journal of Geophysical Research: Oceans*, 113(C6):C06S91, 2008. http://dx.doi.org/10.1029/2006JC004067. (Cited on page 16.)

Zahnen, N., F. Jung-Rothenhäusler, H. Oerter, F. Wilhelms, and H. Miller. Correlation between Antarctic dry snow properties and backscattering characteristics in RADARSAT SAR imagery. In *Proceedings of EARSeL-LISSIG-Workshop Observing our Cryosphere from Space*, volume 141, 2002. (Cited on page 110.)

Zhang, J. L. Increasing Antarctic sea ice under warming atmospheric and oceanic conditions. *Journal of Climate*, 20(11):2515–2529, 2007. http://dx.doi.org/10.1175/JCLI4136.1. (Cited on page 16.)

Zitterbart, D. P., S. Richter, G. Spiekermann, L. K. Behrens, J. Regnery, R. P. Fontes, T. Hänssler, G. König-Langlo, R. Weller, and B. Fabry. Are environmental factors responsible for changed breeding behaviour in emperor penguins? *Antarctic Science*, 26(05):563–564, 2014. http://dx.doi.org/10.1017/S0954102014000285. (Cited on page 44.)

Zotikov, I., V. Zagardnov, and J. Raikovsky. Core Drilling Through the Ross Ice Shelf (Antarctica) Confirmed Basal Freezing. *Science*, 207(4438):1463–1465, 1980. http://dx.doi.org/10.1126/science.207.4438.1463. (Cited on pages 36 and 37.)

Zwally, H. J., C. L. Parkinson, and J. C. Comiso. Variability of Antarctic sea ice and changes in carbon-dioxide. *Science*, 220(4601):1005–1012, 1983. http://dx.doi.org/10.1126/science.220.4601.1005. (Cited on page 12.)

Zwally, H. J., J. C. Comiso, C. L. Parkinson, D. J. Cavalieri, and P. Gloersen. Variability of Antarctic sea ice 1979-1998. *Journal of Geophysical Research: Oceans*, 107(C5), 2002. http://dx.doi.org/10.1029/2000JC000733. (Cited on page 110.)

Zwally, H. J., D. H. Yi, R. Kwok, and Y. H. Zhao. ICESat measurements of sea ice freeboard and estimates of sea ice thickness in the Weddell Sea. *Journal of Geophysical Research: Oceans*, 113(C2), 2008. http://dx.doi.org/10.1029/2007JC004284. (Cited on page 15.)

List of Figures

List of Tables

List of Acronyms

ACoC .. Antarctic Coastal Current
AFIN .. Antarctic Fast Ice Network
APIS ... Antarctic Peninsula Ice Sheet
ASL ... Amundsen Sea Low
ASPeCt . Antarctic Sea Ice Processes and Climate
AVHRR Advanced Very High Resolution Radiometer
AWS ... Automatic Weather Station
CTD ... Conductivity-Temperature-Depth
DLR ... German Aerospace Center
EAIS ... East Antarctic Ice Sheet
EC ..... Eddy Covariance
EIS .... Ekström Ice Shelf
EM .... Electromagnetic
EMILIA Electro-Magnetic Inversion with Least Intricate Algorithms
ENSO .. El Niño-Southern Oscillation
ESA .... European Space Agency
EWIS .. Eastern Weddell Ice Shelves
HSSW .. High Salinity Shelf Water
IBCSO . International Bathymetric Chart of the Southern Ocean
ICESat . Ice, Cloud, and Land Elevation Satellite
IMB ... Ice Mass Balance Buoy
ISW .... Ice Shelf Water
IVF .... Ice Volume Fraction
LCI .... Lateral Constraint Inversion
LIA .... Local Incidence Angle
MODIS Moderate Resolution Imaging Spectroradiometer
MSA ... Methane Sulphonic Acid
NASA .. National Aeronautics and Space Administration
NBSX .. Norwegian-British-Swedish Antarctic Expedition
NOAA . National Oceanic and Atmospheric Administration
PALAOA Perennial Acoustic Observatory in the Antarctic Ocean
SAM ... Southern Annular Mode
SAMS .. Scottish Association for Marine Science
SAR ... Synthetic Aperture Radar
SC ..... ScanSAR
SM ..... StripMap
SVD ... Singular Value Decomposition
TC ..... Thermistor Chain
TSX ... TerraSAR-X
WAIS .. West Antarctic Ice Sheet
WMO .. World Meteorological Organization

Acknowledgements

First and foremost, this dissertation would not have been possible without the inspiring support of my main supervisor and friend, Marcel Nicolaus. You have not only entrusted me with the responsibility to work on such a meaningful subject, I could also always rely on your advice and constructive feedback. You are a great supervisor.

I further deeply acknowledge the guidance and continuous encouragement of my committee members, Rüdiger Gerdes, Vikram Unnithan, Ralph Timmermann and Stefan Hendricks.

Since motivation, or more specifically the lack thereof, is by definition always an issue during a PhD, I deeply appreciate the constant re-motivation by the many souls bearing me during the last three-and-a-half years, helping to escape out of the daily miseries of F-appendix along the way. This especially applies to my office mate Giulia and her bone-chewing companion, as well as the one-and-only Swiss soccer girl.

I am grateful to Gert König-Langlo for the fruitful discussions, overwhelming enthusiasm and unlimited support for the sea-ice project at Neumayer. I highly benefited from your experience and advice while I coordinated and supervised the overwinterers' work, which was always a great challenge.

Since our instrumentation at Neumayer was reliably unreliable, it was the friendly support of Bernd Loose, Daniel Zitterbart, Lars Kindermann and Alfons Eckstaller which regularly prevented a demise of our project through constant provision of spare parts.

Christine Wesche, Thomas Hollands and Wolfgang Dierking regularly helped to overcome the challenge to support our field crew with the all-seeing eyes of satellites. I further appreciate the discussions with Gerhard Dieckmann and Petra Heil, and the lab support of Sepp Kipfstuhl, Ilka Weikusat and Fernando Valero-Delgado.

Further afield, but still in Germany, I'd like to thank my project partners Günther Heinemann, Sascha Willmes, Uwe Baltes and Stephan Paul of the University of Trier for the interesting discussions during our project meetings.

The work in this project also led me into an interesting and diverse research community, where I found a precious network of ice-platelet and fast-ice enthusiasts, who share the same interests, and which I am grateful and proud to be part of.

I was lucky enough to spend quite some time in the field, where the friendly crew and participants of the expeditions ARK-26/3, ANT-Land 2012/13 and ANT-29/6 made these adventures the best time of my life. Naming everybody would probably be too much here, so I instead thank the cruise leaders, Ursula Schauer and Peter Lemke as representatives for all the kind people onboard. However, special thanks still go out to my NPBBs, for giving me the honor to share a melt pond with you at the North Pole. Maybe I

will design a T-Shirt about this event one day.

This dissertation would have been hopeless without the relentless efforts and sheer unlimited motivation and dedication of the Neumayer III overwintering teams ("Üwis"). My gratitude particularly goes to Holger Schmithüsen (Üwi 2010), Jölund Asseng (Üwi 2011), Thomas Schmidt, Meike Kühnel (Üwis 2012), Lisa-Katharina Behrens (Üwi 2013) and Elena Stautzebach (Üwi 2014), you kept the sea-ice monitoring at Atka Bay going despite all the technical and (environ)mental challenges. But of course also to all the other Üwis for your support of the project, thank you!

Last but not least, this thesis is dedicated to my beloved parents, my sisters and my girlfriend Lena, who supported me especially during times of deep desperation and hopelessness. Although I enjoyed these last years very much, I am glad that this adventure is now (nearly) over, and hope that I will have more time to spend with you in the future.

The following organizations are acknowledged for their support during candidature:

- The German Research Council (DFG) for kindly providing the funding of the project in the framework of the priority programme "Antarctic Research with comparative investigations in Arctic ice areas" by grants to SPP1158, NI 1092/2 and HE2740/12.
- The Alfred-Wegener-Institut Helmholtz-Zentrum für Polar und Meeresforschung for allowing me to partake in the RV Polarstern expeditions ARK-26/3 (Transarc, June to August 2011), and ANT-29/6 (AWECS, June to August 2013), as well as to join the ANT-Land campaign 2012/13 (November 2012 to January 2013) at Neumayer III; for providing all infrastructure, logistics, instrumentation, material, office space etc;
- The graduate school POLMAR for travel support to the summer school "Baltic Sea Winter Ecology" in Tvärminne, Finland, February 2012, to the IPY 2012 "From Knowledge to Action" Conference in Montréal, April 2012, and to the International Symposium on Sea Ice in a Changing Environment in Hobart, Tasmania, Australia, March 2014;
- The "Association of Polar Early Career Scientists " for travel support to the IPY 2012 "From Knowledge to Action" Conference in Montréal, April 2012;
- The "Climate and Cryosphere" project for travel support to the International Symposium on Sea Ice in a Changing Environment in Hobart, Tasmania, Australia, March 2014;

SIMBIS, forever![1]

[1] In case somebody is mistakenly not mentioned here, I hereby apologize and promise to buy you a beer.

Appendix I

Publication IV: ”Towards an estimation of sub sea-ice platelet-layer volume with multi-frequency electromagnetic induction sounding”

By Priska A. HUNKELER, Stefan HENDRICKS, **Mario HOPPMANN**,
Stephan PAUL and Rüdiger GERDES

This paper is reprinted from the Annals of Glaciology with permission of the International Glaciological Society (Hunkeler et al., 2015).

Annals of Glaciology 56(69) 2015 doi: 10.3189/2015AoG69A705 137

Towards an estimation of sub-sea-ice platelet-layer volume with multi-frequency electromagnetic induction sounding

Priska A. HUNKELER,[1] Stefan HENDRICKS,[1] Mario HOPPMANN,[1] Stephan PAUL,[2] Rüdiger GERDES[1]

[1]*Alfred-Wegener-Institut Helmholtz-Zentrum für Polar- und Meeresforschung, Bremerhaven, Germany*
E-mail: priska.hunkeler@awi.de
[2]*Environmental Meteorology, University of Trier, Trier, Germany*

ABSTRACT. Ice-platelet clusters modify the heat and mass balance of sea ice near Antarctic ice shelves and provide a unique habitat for ice-associated organisms. The amount and distribution of these ice crystals below the solid sea ice provide insight into melt rates and circulation regimes in the ice-shelf cavities, which are difficult to observe directly. However, little is known about the circum-Antarctic volume of the sub-sea-ice platelet layer, because observations have mostly been limited to point measurements. In this study, we present a new application of multi-frequency electromagnetic (EM) induction sounding to quantify platelet-layer properties. Combining in situ data with the theoretical response yields a bulk platelet-layer conductivity of $1154 \pm 271\,\mathrm{mS\,m^{-1}}$ and ice-volume fractions of 0.29–0.43. Calibration routines and uncertainties are discussed in detail to facilitate future studies. Our results suggest that multi-frequency EM induction sounding is a promising method to efficiently map platelet-layer volume on a larger scale than has previously been feasible.

KEYWORDS: basal melt, sea ice, sea-ice/ice-shelf interactions

INTRODUCTION

The Antarctic coastline is fringed by ice shelves, floating extensions of continental ice sheets (Le Brocq and others, 2010). Basal melt of ice shelves leads to the formation of water masses that are fresher and less dense than the surrounding ocean body (Mahoney and others, 2011). As the sea-water freezing point depends on pressure (Foldvik and Kvinge, 1974), the water becomes supercooled when the less dense plume rises. Ice platelets nucleate in the supercooled water, but the process of ice formation varies (Smith and others, 2001). Near the Ekström Ice Shelf in the eastern Weddell Sea, large amounts of ice platelets rise from the cavity below the ice shelf and accumulate underneath the sea ice (Eicken and Lange, 1989; Hoppmann and others, 2015). In McMurdo Sound, near the Ross Ice Shelf, platelet growth is often associated with in situ formation of ice platelets directly underneath the sea ice (Smith and others, 2001) or is interpreted as a combination of the two processes (Jeffries and others, 1993; Dempsey and others, 2010).

The resulting sub-sea-ice platelet layer, hereafter referred to as the platelet layer, may contribute significantly to the heat and mass balance of adjacent sea ice (Eicken and Lange, 1989) and represents a unique ice habitat (Arrigo and others, 1993). The additional buoyancy modifies the sea-ice freeboard, influencing satellite remote sensing near coastal areas in Antarctica (Rack and others, 2013; Price and others, 2014). Furthermore, the platelet layer is a direct indicator of ocean/ice-shelf interaction, and the amount of basal ice-shelf melt might be reflected in the volume of ice platelets found below landfast sea ice (Hoppmann and others, 2015), a region much more accessible than the cavities below ice shelves.

The total volume of ice platelets below the sea ice is a product of the layer thickness, the area and the ice-volume fraction. The platelet layer is up to several meters thick, usually determined with a thickness gauge, and the horizontal extent is given by point measurements. Previous investigations of ice-volume fractions in McMurdo Sound used estimates from core holes, ice-temperature profiles and horizontal thin sections. Results ranged from 0.2 to >0.5, while a recent study found an ice-volume fraction of 0.25 ± 0.06 using heat-flux calculations (Gough and others, 2012). At Atka Bay, Günther and Dieckmann (1999) calculated a value of 0.46, based on consideration of sea-ice isostasy. Kipfstuhl (1991) and Hoppmann and others (2015) compared their sea-ice thickness observations to a localized growth model and estimated ice-volume fractions of 0.2 and 0.25 ± 0.1, respectively.

One physical parameter which depends on the ice-volume fraction of the platelet layer is the electrical conductivity. Differences in conductivity are fundamental for sea-ice thickness retrieval with electromagnetic (EM) induction sounding, a common method typically applied with airborne (Haas and others, 2009) or ground-based devices (Kovacs and Morey, 1991; Haas and others, 1997; Haas, 1998; Reid and others, 2003). In general, a single frequency in the range 3000–10 000 Hz is used to estimate the distance of the sensor to the ice/water interface. The method is based on the assumption that sea ice can be described as a single level layer with negligible electrical conductivity ($<100\,\mathrm{mS\,m^{-1}}$; e.g. Reid and others, 2006) compared to sea water (e.g. $2690\,\mathrm{mS\,m^{-1}}$ in the winter Weddell Sea). This is a reasonable assumption for most offshore sea ice, but in the presence of a porous platelet layer it becomes invalid. In this case, a single-layer assumption will lead to either an overestimation of the solid sea-ice thickness (Rack and others, 2013) or an underestimation of total (solid ice + platelet layer) thickness with no possibility to resolve both layers. Single-frequency systems are sensitive to the thickness and the electrical bulk conductivity of the

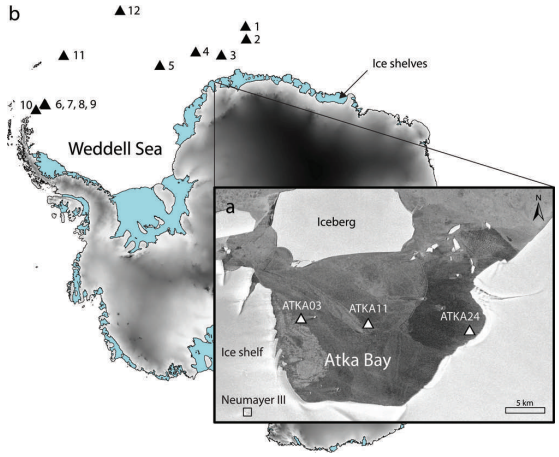

Fig. 1. Map of sea-ice study sites. (a) Enlarged map of Atka Bay, showing the survey sites with an underlying platelet layer (white triangles). Background: TerraSAR-X image from 15 November 2012, provided by the German Aerospace Center (DLR). (b) Calibration sites in the Weddell Sea without a platelet layer (black triangles). Blue areas indicate the locations of ice shelves (Fretwell and others, 2013; Bedmap2).

Fig. 2. Multi-frequency EM induction sounding data are recorded with the GEM-2 at different heights above sea ice. The signal directly depends on the distances to the conductive layers. Photograph by Sandra Schwegmann, 24 June 2013.

platelet layer, but do not provide enough observational constraints for an unambiguous resolution of layer thicknesses and conductivities. Therefore, those systems are not able to resolve multiple sea-ice layers with different electrical parameters. In exploration geophysics, it is therefore common to resolve a multilayered subsurface structure using either multiple frequencies, several transmitter/receiver configurations, or a combination of the two.

The aim of this study is to lay the foundations for rapid estimation of large-scale platelet-layer volumes, without the need for time-consuming sea-ice drilling experiments. We focus here on the analysis of multi-frequency EM induction sounding data at platelet-free calibration sites with known sea-ice thickness to assess calibration coefficients and data uncertainties for the individual instrumental frequencies. We apply calibration coefficients and uncertainties to a more complex situation with a platelet layer, to derive limitations for the parameterization of the platelet-layer conductivity and to investigate its relationship to ice-volume fraction.

METHOD

We used a commercial EM induction sensor (GEM-2, Geophex Ltd) for multi-frequency soundings on sea ice with an underlying platelet layer at several survey sites in Atka Bay. An estimation of instrumental uncertainties requires knowledge of the subsurface structure. At Atka Bay, these requirements were not fulfilled since the electrical bulk conductivity of the platelet layer is unknown and its estimation is a major goal of this study. Therefore, two additional datasets over simpler geophysical calibration targets were acquired to calculate the calibration coefficients and the uncertainties of the measurements. These calibrations were conducted over level sea ice in the central Weddell Sea (no platelet layer) and over the North Sea in Germany, where no sea ice was present (sea water only). Figure 1 shows the sea-ice survey and calibration sites.

Multi-frequency EM sounding

The GEM-2 instrument (Fig. 2) is a ground-based induction sensor with promising specifications for multilayer sea-ice thickness retrieval. It can be used either in horizontal or vertical coplanar mode with a transmitter/receiver coil spacing of 1.66 m. The coil spacing is a critical parameter, since, together with the chosen frequency, it limits the sounding depth. Although the coil spacing of the GEM-2 is small compared with the much used single-frequency Geonics EM-31 (3.67 m), it was considered to be sufficient for our purposes. The GEM-2 instrument can be operated simultaneously with up to five frequencies in a range 330–96 000 Hz. For calibration measurements in the Weddell and North Seas we used frequencies of 1530, 5310, 18 330, 63 030 and 93 090 Hz. At Atka Bay we used slightly different frequencies (450–93 030 Hz) at a sampling rate of 10 Hz.

During operation, a primary EM field is generated by the transmitter coil of the EM instrument. The primary field induces a secondary magnetic field in all nearby conductive layers. The receiver coil measures the superimposed signal of all resulting magnetic fields. The EM response is defined as the relative secondary field, which is the secondary field divided by the primary field. It can be expressed as a complex number with the in-phase, I (real part), and the quadrature, Q (imaginary part). In-phase and quadrature are dimensionless and are recorded in parts per million (ppm). An alternative representation is given by the amplitude, Amp, and phase, φ, where $\varphi = \arctan(Q/I)$ and $\mathrm{Amp} = \sqrt{I^2 + Q^2}$.

In practice, the primary field is often suppressed at the receiver coil to measure the minor secondary field at sufficient resolution. This is realized in the GEM-2 with a bucking coil, which is connected in series with the receiver coil, but has the opposite polarity (Won and others, 2003). The bucking coil has a defined area, number of turns and distance to the transmitter (1.035 m) to cancel the primary field at the receiver location with an equal current.

According to Frischknecht and others (1991), three types of systematic errors exist in in-phase and quadrature recordings, due to improper adjustment and calibration of

Table 1. Summary of GEM-2 datasets at Atka Bay. Date format is day/month. IT: measured sea-ice thickness (snow was removed); PLT: measured platelet-layer thickness; F: measured freeboard; T: air temperature measured at Neumayer III station; σ_i: estimated sea-ice conductivity; σ_{pl}: estimated platelet-layer conductivity

Site	Date (2012)	IT	PLT	F	T	σ_i	σ_{pl}	Frequencies
		m	m	m	°C	mS m^{-1}	mS m^{-1}	Hz
ATKA11	21/11	0.67	1.17	–0.03	−1.0	200	1225	475, 1525, 5325, 18 325, 63 025
ATKA11	26/11(1)	0.68	1.23	–0.01	−4.2	200	1125	5310, 18 330, 63 030, 93 090
ATKA24	26/11(2)	1.89	2.24	0.15	−4.6	40	1340	5310, 18 330, 63 030, 93 090
ATKA11	1/12(1)	0.70	1.43	0.01	−1.5	200	1017	450, 1530, 5310, 18 330, 63 030
ATKA11	1/12(2)	0.70	1.43	0.01	−1.5	200	1075	5310, 18 330, 63 030, 93 090
ATKA03	27/12(1)	2.69	4.21	0.33	−0.9	40	–	1530, 5310, 18 330, 63 030, 93 090
ATKA11	27/12(2)	0.79	1.11	0.07	−1.2	200	1143	1530, 5310, 18 330, 63 030, 93 090

the sensor: (1) zero-level offsets, I_c and Q_c, (2) scaling coefficients, A, and (3) phase-mixing coefficients, P_c, have to be applied to the measured in-phase and quadrature components, I_m and Q_m. The corrected in-phase, I, and quadrature, Q, are calculated as

$$I = A[(I_m + I_c)\cos(P_c) - (Q_m + Q_c)\sin(P_c)] \quad (1)$$

and

$$Q = A[(Q_m + Q_c)\cos(P_c) + (I_m + I_c)\sin(P_c)]. \quad (2)$$

A similar approach has been presented by Deszcz-Pan and others (1998), Reid and Bishop (2004), Brodie and Sambridge (2006) and Minsley and others (2012). Because of systematic errors in our instrument, we corrected our data according to Eqns (1) and (2) to get reliable results.

Bucking coil bias

We compared field data to numerical one-dimensional forward models (Anderson, 1979) to obtain the calibration coefficients at specific calibration sites. Model parameters were the EM frequency and the coil spacing and orientation, as well as the thickness and conductivity of multiple layers.

We found a significant bias between the actual GEM-2 response and the forward models at all sites and all frequencies. This deviation could not be explained with either realistic calibration coefficients, or with the layer conductivities at the calibration sites. We finally found that the bucking coil picked up, in addition to the primary field, a signal from the subsurface (secondary field), which could not be described with a constant factor, as described in the literature and performed during the internal instrumental processing. To account for the secondary field measured by the bucking coil, we implemented the bucking coil in our forward models as a second receiver and subtracted the result from the receiver response. By doing so, we achieved good agreement between data and forward models with realistic calibration coefficients.

Relation between electrical conductivity and porosity

Archie's law relates the bulk electrical conductivity, σ, of a porous layer to the porosity, Φ, the brine conductivity, σ_b, and the cementation factor, m (Archie, 1942):

$$\sigma = \sigma_b(\Phi)^m. \quad (3)$$

We used this law to convert (1) brine conductivity and brine volume of sea ice to bulk conductivity of the solid sea-ice layer and (2) bulk conductivity of the platelet layer to the actual ice-volume fraction. The empirical factor, m, depends, to a large extent, on the material grain shape and pore geometry (Salem and Chilingarian, 1999). Previous studies have often used a value of 1.75 for solid sea ice, and a range 1.55–2.2 is reported in the literature (Reid and others, 2006). Because of the different structure of the unconsolidated platelet layer, with higher connectivity and brine volume than solid sea ice, the cementation factor of solid sea ice might not be applicable to the platelet layer. We therefore tested a broad range of cementation factors from 1.5 to 2.5, values which are usually used for saturated sandstones (Glover and others, 1997). These structures are more likely to describe the connected pores of the platelet layer.

Field data

Atka Bay

We investigated properties of the platelet layer at Atka Bay at three sites between November 2012 and January 2013, operating from the German research station Neumayer III. The sites ATKA03, ATKA11 and ATKA24 (Fig. 1; Table 1) represent different fast-ice regimes. At ATKA11, where we repeated EM data acquisition five times, sea ice was ~4 months old, formed after a breakout in August 2012. Consequently, ATKA11 showed thinner sea ice than all the other sites. We found older first-year sea ice at ATKA24 and thicker rafted sea ice at ATKA03. A detailed description of the sea-ice conditions is given by Hoppmann and others (2015). At each site, we removed the snow and acquired multi-frequency EM data in 0.1 m steps in sensor altitude from the sea-ice surface to a maximum height of 2 m above the sea ice (Fig. 2).

After the EM sounding, we measured the freeboard, F, the sea-ice thickness, IT, and the platelet-layer thickness, PLT, with a modified thickness gauge through 0.05 m drillholes (Table 1). Individual ice platelets up to 0.1 m in diameter were observed. Manual sea-ice thickness measurements yielded an uncertainty of <0.1 m for solid sea ice. But we could only determine the platelet-layer thickness with an accuracy of ~0.3 m, as verified by an underwater camera (Hoppmann and others, 2015). The platelet layer often consisted of internal dense layers, and in the vicinity of sea water the platelet layer was generally looser than in the middle of the layer. Surprisingly, we often found a less dense layer next to the solid sea ice. For our further calculations, however, we assumed a homogeneous platelet layer.

To determine conductivities of the water column and the interstitial platelet-layer water, we used a conductivity–temperature–depth (CTD) probe (CTD75M, Sea & Sun Technology GmbH) to perform in total 22 down- and

Table 2. Summary of Weddell Sea and North Sea calibrations operated with frequencies 1530, 5310, 18 330, 63 030 and 93 090 Hz. Date format is day/month. IT: measured sea-ice thickness (snow was removed); F: measured freeboard; T: air temperature measured by *Polarstern*; σ_i: estimated sea-ice conductivity; σ_w: sea-water conductivity measured by *Polarstern* (daily average, Weddell Sea data) and by a handheld instrument (North Sea data). Note the low sea-water conductivity in the North Sea due to the inflow of fresh water (site 13)

Site	Date (2013)	IT	F	T	σ_i	σ_w
		m	m	°C	mS m^{-1}	mS m^{-1}
1	20/6	0.53	0.05	−21	80	2708
2	21/6	0.54	0.04	−19	80	2707
3	3/7	0.60	–0.20*	−28	80	2698
4	8/7	0.58	0.01	−13	50	2708
5	15/7	0.58	–	−3	10	2706
6	26/7	3.44	–	−20	5	2712
7	1/8(1)	2.75†	–0.01	−28	15	2715
8	1/8(2)	2.06	–0.01	−28	15	2715
9	1/8(3)	0.74	0.00	−28	100	2715
10	5/8	4.26‡	–	−6	2	2718
11	31/8	0.41	0.00	−14	0	2712
12	25/9	0.72	0.00	−11	300	2686
13	2/12	–	–	5	–	1200

*flooded calibration site.†0.69 m snow included, ‡>1 m snow included.

upward casts between 21 November 2012 and 7 January 2013. The instrument was operated through core holes 0.1 m in diameter, with a maximum depth range of 250 m. Small ice crystals regularly blocked the conductivity cell while the instrument was operating in the platelet layer, resulting in spuriously low conductivity values. We tried to minimize this risk by repeated up- and downward movements of the instrument. As the downward casts still contained spurious data, we determined from the undisturbed upward casts an average sea-water conductivity of 2690 mS m^{-1} below the platelet layer.

To compare the electrical conductivity of the solid sea-ice layer with results from the GEM-2, we retrieved several sea-ice cores and measured temperature and salinity profiles at 0.1 m intervals. Brine volume (porosity) was calculated according to Cox and Weeks (1983) and Leppäranta and Manninen (1988). Brine conductivity, σ_b, was determined after Stogryn and Desargant (1985) and Reid and others (2006). The bulk conductivity of the solid sea-ice layer, σ, was then calculated using Eqn (3) and a cementation factor, $m = 1.75$ (Reid and others, 2006).

Weddell Sea and North Sea

Electromagnetic calibration data from sites with no platelet layer were acquired in the central Weddell Sea at 12 sites during two winter expeditions with the German icebreaker RV *Polarstern* between June and September 2013 (Table 2). Sea-ice thickness was measured with a thickness gauge, and the conductivity of the sea water was obtained by the keel salinometer of RV *Polarstern* (IT and σ_w in Table 2).

On first-year sea ice the snow was removed, which made surface flooding visible at site 3 (Table 2). On multi-year sea ice, where it was not possible to remove the snow in the footprint area, we placed the GEM-2 on top of the snow and consequently included a second layer of 0 mS m^{-1} in the forward models (site 7). At site 10, we were not able to estimate the snow depth because of internal icy layers, and consequently used the same conductivity for the sea ice and the snow layer. The bulk conductivity, σ, of the solid sea ice was obtained in the same way as at Atka Bay.

An additional calibration dataset was acquired from the North Sea over mixed ocean and river inflow water at the mouth of the river Weser near Bremerhaven, Germany (last calibration in Table 2). The conductivity of the sea water was measured with a handheld conductivity meter (1200 mS m^{-1}). Without the presence of a sea-ice layer the EM response could be modelled as an ideal homogeneous half-space.

RESULTS

Calibration coefficients and uncertainties were calculated using the calibration data from the Weddell Sea and the North Sea. Coefficients were then applied to the Atka Bay data to estimate sea-ice and platelet-layer conductivities and the ice-volume fraction of the platelet layer.

GEM-2 uncertainties

Calibration coefficients and uncertainties were obtained by manually minimizing the difference between the GEM-2 data and theoretical forward models. Figure 3a and b show typical 63 030 Hz EM responses for different heights above sea water for the Weddell Sea calibrations. For the forward model (blue dashed line) the sea-ice layer was initially assumed to be non-conductive (0 mS m^{-1}) and a conductivity of 2700 mS m^{-1} was assigned to the sea water. The uncorrected datasets for in-phase and quadrature (Fig. 3a and b) differ significantly from each other and from the forward models. Reasons for this variability may originate from an incorrect calibration of the GEM-2 in general, the dependence of the EM response on environmental temperatures, the influence of sea-ice conductivity and variabilities of the drillhole sea-ice thickness estimations within the footprint of the instrument.

We therefore categorize the deviation from the forward models into two main parts: first, imprecise calibration of the individual frequencies as a mean offset to the forward models (systematic error); and second, the influence of environmental temperature, sea-ice conductivity and uncertainties of thickness estimations as the inter-variability between different calibrations. The first factor can be corrected by averaging the calibration coefficients for each frequency over all calibrations. The second factor describes the uncertainty of these mean calibration coefficients.

Zero-level offset coefficients, I_{c0} and Q_{c0} (Table 3), were measured by lifting the GEM-2 with RV *Polarstern*'s crane and acquiring data from several meters above ground. This free-air response was obtained for ~30 min once the instrument was in temperature equilibrium. To investigate the long-term drift and the temperature dependency, these measurements were carried out multiple times. Although the crane measurements were conducted at temperatures from −24 to –10°C, we did not observe a strong temperature dependence of the zero-level offsets for any frequency. Once the instrument was in temperature equilibrium, the instrumental noise (I_n and Q_n) was determined as the standard deviation of the time series. Mean scaling, A, and phase-mixing coefficients, P_c, were obtained at each site (Table 2) by manually minimizing the root-mean-square error (rmse) between in-phase and quadrature data and the forward models. It was

necessary to use different zero-level offset coefficients, I_c and Q_c, than those obtained from the free-air experiment to reach a satisfactory agreement with the forward models. These changes significantly increased the standard deviation and, thus, the uncertainty of zero-level offset coefficients of the individual frequencies. The average of all calibration coefficients, the standard deviations from individual calibration sites and the instrumental noise are summarized in Table 3. We did not use the data from thick sea ice (site 10, Table 2) to calculate these coefficients, because the signal values were low and calibration coefficients depended mainly on the estimated sea-ice conductivity.

The sea-ice conductivities, σ_i, for the forward models were determined with the local maximum of quadrature components of frequencies 63 030 and 93 090 Hz, which are assumed to be the most sensitive to sea-ice conductivity, due to their low penetration depth. This method was applied because it is almost independent of any zero-level offset, scaling and phase-mixing corrections. In Figure 3c this is shown for theoretical forward-model curves. One particular example, the calibration at flooded site 3 (Table 2), exhibits a conductivity of 1700 mS m^{-1} for the top 20 cm and the local maximum is shifted significantly to higher values (Fig. 3b, red). Small conductivity changes were also necessary to fit the local maximum for non-flooded calibration sites. Estimated sea-ice conductivities, σ_i, are summarized in Table 2.

Using Eqns (1) and (2), all calibration data were corrected with the mean coefficients, I_c, Q_c, A and P_c (Table 3). The total uncertainty for the in-phase component, ΔI, was calculated with the Gaussian law of error propagation according to

$$\Delta I^2 = \left(\frac{\delta I}{\delta I_c}\sigma_{I_c}\right)^2 + \left(\frac{\delta I}{\delta Q_c}\sigma_{Q_c}\right)^2 + \left(\frac{\delta I}{\delta A}\sigma_A\right)^2 + \left(\frac{\delta I}{\delta P_c}\sigma_{P_c}\right)^2 + \left(\frac{\delta I}{\delta I_m}\sigma_{I_n}\right)^2 + \left(\frac{\delta I}{\delta Q_m}\sigma_{Q_n}\right)^2, \quad (4)$$

under the assumption that the uncertainty of the measured in-phase and quadrature signal, I_m and Q_m, is described by the noise, I_n and Q_n, and the uncertainty of the remaining contributions is given by the standard deviations of the calibration coefficients. The calculation for ΔQ was performed accordingly. The corrected data (dots), the respective forward models (solid curves) and the estimated uncertainties (ellipses) for in-phase and quadrature are shown for one example dataset (site 1, Table 2) in Figure 4.

Using forward models as in Figure 4 and increasing the sea-ice thickness in 0.1 m steps (sea ice with 100 mS m^{-1}), over a depth of 10 m, the calculated uncertainties exceed in 3 m depth the difference of two consecutive responses. This means that it is possible to resolve solid sea ice up to 3 m thick at an accuracy of 0.1 m with GEM-2 specifications and given uncertainties.

Sea-ice conductivity

The conductivity of the solid sea ice was estimated for all calibration and survey sites by aligning the measured quadrature components of the two highest frequencies (63 030 and 93 090 Hz) to the modelled data. This procedure yielded sea-ice conductivities of 200 mS m^{-1} for thin sea ice (<1 m) at ATKA11 and conductivities of 40 mS m^{-1} for thicker sea ice at ATKA03 and ATKA24 (Table 1).

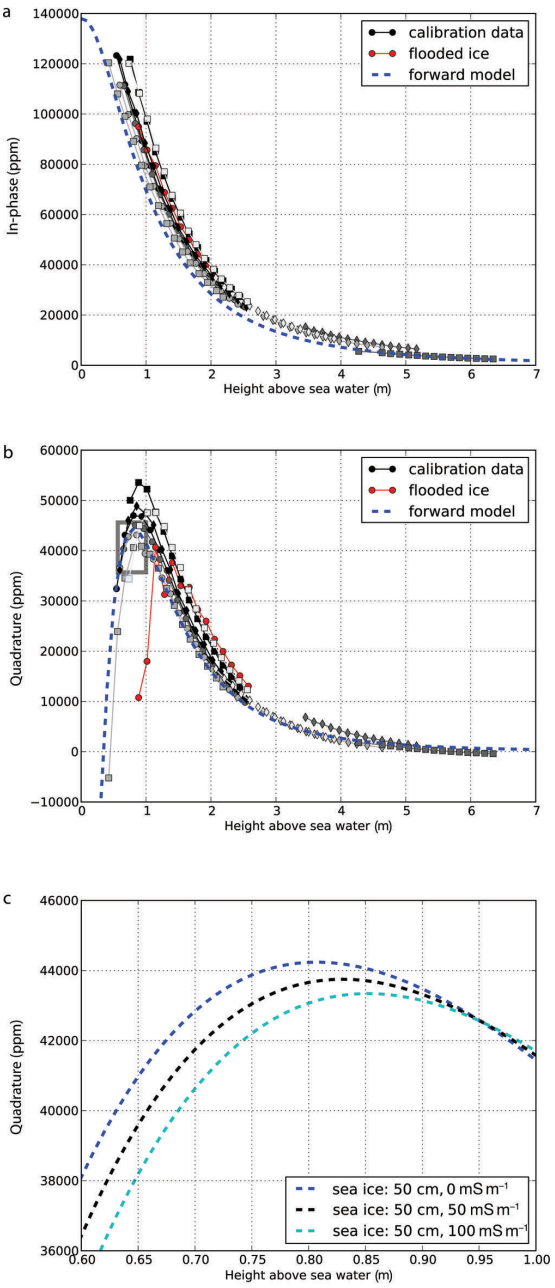

Fig. 3. Raw EM data (63 030 Hz) for all Weddell Sea datasets. (a) In-phase, (b) quadrature and (c) enlargement of box in (b). The forward models (blue dashed curves) were calculated by assuming a homogeneous half-space of 2700 mS m^{-1} and resistive sea ice (0 mS m^{-1}). Two additional forward models with increasing sea-ice conductivities (50 and 100 mS m^{-1}) are shown in (c).

Brine porosity and conductivity were used to calculate the reference bulk conductivity values (Eqn (3)). The conductivities of the three ATKA11 sea-ice cores were 139 ± 113, 141 ± 102 and 149 ± 77 mS m^{-1}. These high standard deviations were mostly due to high conductivities at the ice/water interface. If these were omitted, overall conductivities

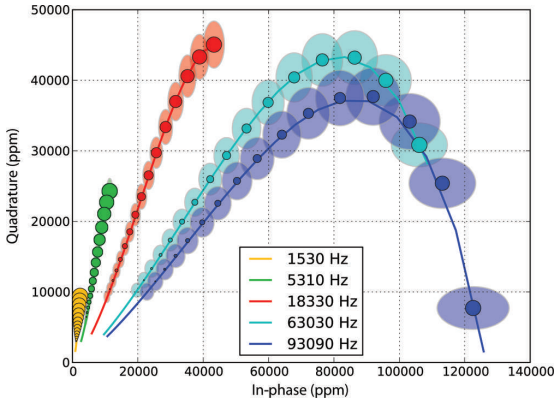

Fig. 4. Data from calibration site 1 (Table 2) with applied calibration coefficients. The instrument was lifted from zero (large dots) to 2 m (smaller dots) over 0.53 m thick sea ice with a conductivity of 80 mS m^{-1}. The semi-axes of the ellipses indicate the in-phase and quadrature uncertainties. The forward models (solid curves) for 0–3 m are shown for the different frequencies.

reduced to 100 ± 18, 114 ± 73 and 127 ± 47 mS m^{-1}. Sea-ice cores at ATKA03 and ATKA24 yielded a sea-ice conductivity of 56 ± 23 and 101 ± 35 mS m^{-1}, respectively.

In the Weddell Sea, nine sea-ice cores (<1 m) gave sea-ice conductivities between 35 and 72 mS m^{-1}, with an average of 56 ± 14 mS m^{-1}. The highest standard deviation in a single core was 55 mS m^{-1}. A thicker sea-ice core of 1.77 m yielded a bulk sea-ice conductivity of 17 ± 8 mS m^{-1}.

In contrast, sea-ice conductivities based on forward-model fitting at 63 030 and 93 090 Hz ranged from 0 to 100 mS m^{-1} (with one outlier of 300 mS m^{-1}) for thin sea ice (<1 m) and from 2 to 15 mS m^{-1} for thicker sea ice (>1 m; Table 2). A value of 300 mS m^{-1} is a rather high conductivity for first-year sea ice, and may be explained by the presence of surface flooding or internal layers. Excluding the outlier (300 mS m^{-1}), the conductivities from the sea-ice cores are in the same range as the conductivities from our results obtained by the GEM-2.

Bulk platelet-layer conductivity

The sea-ice conductivity at each site at Atka Bay was used as an input parameter for a series of forward models, together with the known thicknesses of solid sea ice and the platelet layer. We varied the electrical conductivity of the platelet layer using the full range of physically plausible conductivities, from a fully resistive layer (0 mS m^{-1}) to conductive sea water (2700 mS m^{-1}) in steps of 50 mS m^{-1}. From the series of forward models (e.g. ATKA11 at 18 330 Hz; Fig. 5) we calculated the best fit between the corrected GEM-2 data (applied calibration coefficients) and the forward models, based on the local minimum of the rmse (Fig. 6). This procedure was repeated at all sites at Atka Bay for both in-phase and quadrature components and for each frequency. We found that the best fit of in-phase and quadrature components did not always result in the same bulk platelet-layer conductivity. Assuming that both components should yield the same conductivity, we applied an additional phase correction at each site for every frequency. The new phase-mixing coefficients were averaged and included in the uncertainty estimation (P_{c2}, $\sigma_{P_{c2}}$; Table 3). The averaged coefficients were again applied to both components for all frequencies at all sites, except at ATKA03, where the signal was too insensitive to the bulk platelet-layer conductivity, due to generally low signal values on the thick sea ice. We repeated the estimation of bulk platelet-layer conductivity by finding the local minimum of the rmse and also considered the upper and lower limit of the in-phase (Fig. 6) and quadrature uncertainties.

We excluded the 450 Hz frequency and the in-phase component of the 1530 Hz channel from the analysis, due to a poor signal-to-noise ratio. We found that the quadrature component of the two highest frequencies only weakly depended on the bulk-conductivity variations of the platelet layer at most sites, and we thus excluded these from further analysis. Based on the small penetration depth of these frequencies and the typical thickness of the fast ice, this was not unexpected.

The local minima of the rmse of all processed frequencies and components were averaged by survey site (Fig. 7) and by individual frequencies (Fig. 8). For individual sites we found mean bulk platelet-layer conductivities in the range

Table 3. Calibration coefficients for all frequencies. Noise of in-phase, I_n, and quadrature, Q_n, components estimated by long time series; zero-level offset coefficients, I_{c0} and Q_{c0}, measured with a crane away from any conductive material. Zero-level offset coefficients, I_c and Q_c, scaling coefficients, A, and phase-mixing coefficients, P_c, obtained by minimizing the difference between field data and forward models. P_{c2} are the phase-mixing coefficients adjusted for the Atka Bay datasets. $\bar{x}$ is the arithmetic average and σ the 1σ standard deviation of the individual calibration coefficients

Frequency	$\bar{x}/\sigma$	I_n	Q_n	I_{c0}	I_c	Q_{c0}	Q_c	A	P_c	P_{c2}
Hz		ppm	ppm	ppm	ppm	ppm	ppm		°	°
1530	$\bar{x}$			−200	−45	−190	118	0.82	−0.07	−1.17
	σ	138	137	256	138	25	137	0.05	1.51	3.58
5310	$\bar{x}$			−799	−405	77	328	0.82	0.65	−1.10
	σ	128	127	249	269	12	365	0.06	0.66	0.61
18 330	$\bar{x}$			−183	417	487	671	0.83	0.87	−0.14
	σ	125	125	242	547	6	576	0.06	0.73	1.28
63 030	$\bar{x}$			−932	−757	1331	1081	0.87	0.92	1.79
	σ	146	135	284	695	133	498	0.07	0.98	2.98
93 090	$\bar{x}$			−3474	−3420	240	39	0.89	0.27	4.72
	σ	204	193	352	683	460	685	0.08	1.35	4.24

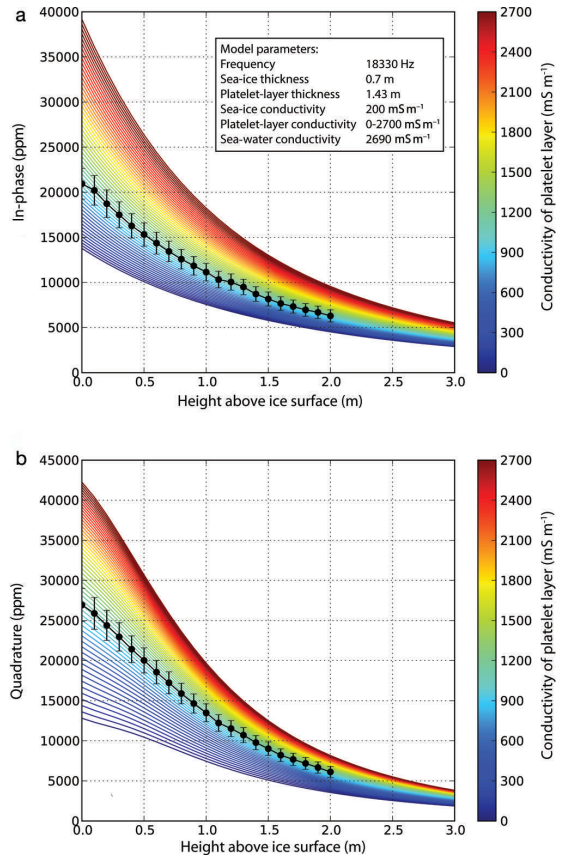

Fig. 5. Corrected dataset and corresponding uncertainties for the (a) in-phase and (b) quadrature 18 330 Hz component at ATKA11 (1 December 2012). The forward models were calculated assuming various platelet-layer conductivities (color bar).

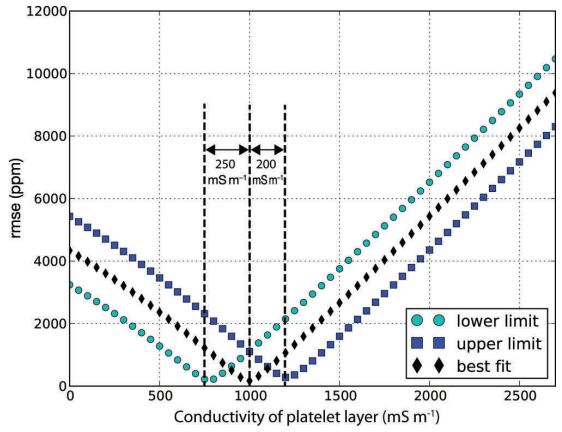

Fig. 6. Root-mean-square errors (rmse) were calculated for the in-phase component (Fig. 5a) to find the smallest difference between this dataset and individual forward models. This is shown for the best fit, for the lower limit of uncertainties and for the upper limit. The bulk platelet-layer conductivity is, in this example, 1000 mS m^{-1} with a difference of 250 mS m^{-1} to the lower and 200 mS m^{-1} to the upper limit.

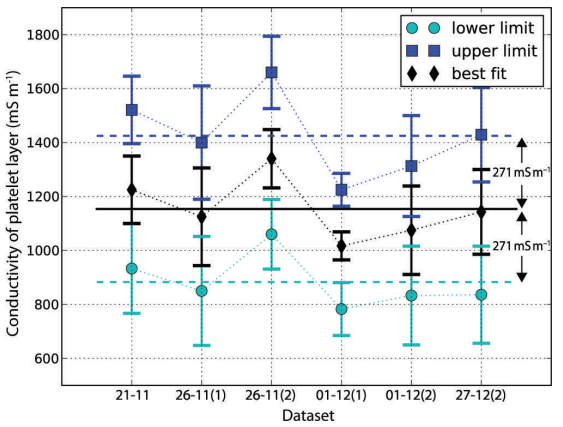

Fig. 7. Bulk platelet-layer conductivities. The results obtained using different frequencies are averaged and shown for the individual sites. The conductivities and the corresponding standard deviations are shown for the best fit, and the lower and upper limit of uncertainties. Dataset date format is day-month of 2012.

1017–1340 mS m^{-1} (Fig. 7, best fit). The mean of these values resulted in a bulk platelet-layer conductivity of 1154 mS m^{-1} (Fig. 7, solid black line). The mean value of the lower uncertainty limit was 883 mS m^{-1} and of the upper uncertainty limit 1425 mS m^{-1}, which resulted in an overall uncertainty of ±271 mS m^{-1}. We observed highest bulk platelet-layer conductivity at ATKA24, the site with a thicker sea ice and platelet layer (1.89 + 2.24 m) than at ATKA11. Here we assume that an internal conductive layer was located in the platelet layer.

We observed a frequency dependence of the bulk platelet-layer conductivity (Fig. 8), where higher frequencies tended to result in higher conductivities, even though upper layers may be, in general, more consolidated. Whether the reason for this relationship is a calibration error or insufficient description of the layering by the forward models is not known.

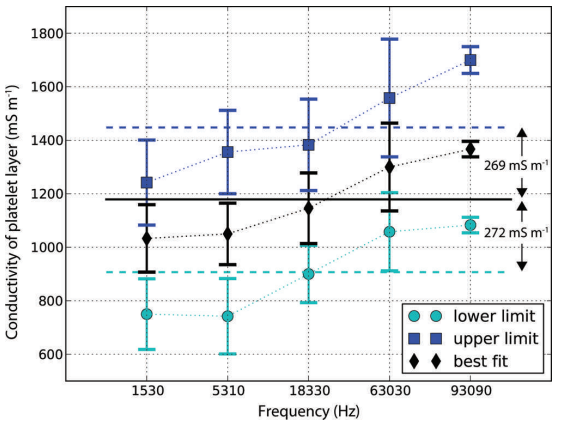

Fig. 8. Bulk platelet-layer conductivities. The results obtained at the different sites are averaged and shown for the individual frequencies. The conductivities and the corresponding standard deviations are shown for the best fit, and the lower and upper limit of uncertainties.

Ice-volume fraction of platelet layer

The next step was to convert the layer conductivity to porosity. We used Archie's law (Eqn (3)), where the brine conductivity, σ_b, is the conductivity of the liquid phase in the platelet layer. To a first-order approximation, σ_b can be described by the conductivity of the sea-water column below.

In eight down- and two upward CTD casts, the water in the platelet layer appeared to be much fresher than the sea water (1800 vs 2690 mS m^{-1}), but we interpret these low values as an interaction between ice platelets and the conductivity sensor. We assumed cementation factors, m, between 1.5 and 2.5. Applying these parameters to different brine conductivities, σ_b, and bulk platelet-layer conductivities, σ, with lower and upper limits of uncertainties, we found a range of ice-volume fractions ($1 - \Phi$, where Φ is porosity; Table 4).

The resulting ice-volume fractions were in the range 0.16–0.26 for sea-water conductivities σ_b = 1800 mS m^{-1}, which we considered to be spuriously low. For regular sea water of σ_b = 2690 mS m^{-1} the ice-volume fractions were in the range 0.29–0.43. Accounting for the lower and upper uncertainty limits, ice-volume fractions for spuriously low brine conductivity, σ_b, were 0.09–0.38, and for sea-water brine conductivity they were 0.22–0.52. The ice-volume fraction was equally influenced by the choice of cementation factor, m, and brine conductivity, σ_b.

Table 4. Ice-volume fractions of the platelet layer assuming different values for cementation factor, m, conductivities of interstitial water in the platelet layer, σ_b, and bulk platelet-layer conductivities, σ, of the lower uncertainty limit (883 mS m^{-1}), the best fit (1154 mS m^{-1}) and the upper uncertainty limit (1425 mS m^{-1})

σ_b (mS m^{-1}):	1800			2690		
σ (mS m^{-1}):	883	1154	1425	883	1154	1425
$m = 1.5$	0.38	0.26	0.14	0.52	0.43	0.35
$m = 2.0$	0.30	0.20	0.11	0.43	0.35	0.27
$m = 2.5$	0.25	0.16	0.09	0.36	0.29	0.22

DISCUSSION

We have shown that, for given thicknesses of solid sea ice and the platelet layer, it is possible to use multi-frequency EM induction soundings to resolve the bulk platelet-layer conductivity within an uncertainty range of 271 mS m^{-1}. The uncertainty is mainly governed by the inter-variability between calibrations, rather than by the instrumental noise of the GEM-2. Consequently, the uncertainties of the calibration coefficients can be reduced significantly with proper calibrations. As stated above, we are able to resolve with GEM-2 data a solid sea-ice layer of 3 m with an accuracy of 0.1 m, based on calculated uncertainties. Reducing the uncertainty by 50% will allow us to resolve solid sea ice of up to 4.20 m at an accuracy of 0.1 m. ATKA03 with its 2.69 m solid sea ice and 4.21 m platelet layer could not be resolved by the set-up used. Theoretical calculations, however, showed that it would be possible to resolve these layers with frequencies up to 18 330 Hz by further reducing the uncertainties.

During our first operations of the GEM-2 at Atka Bay fast ice, we tested different frequency configurations in order to evaluate its potential (Table 1). Frequencies of 1530, 5310, 18 330, 63 030 and 93 090 Hz showed promising results, as the various frequencies are sensitive to different depths, while a frequency as low as 450 Hz was too noisy. In general, lower frequencies are more sensitive to deeper structures, and higher frequencies to the shallower sea ice. With the two highest frequencies, we obtained sea-ice conductivities similar to those from independent results of sea-ice cores. This can be very useful for other studies, especially for a non-destructive determination of sea-ice properties (e.g. Haas and others, 2008). Although first-year sea ice is generally more electrically conductive than thick sea ice, the sea-ice conductivities from forward-model fitting at ATKA11 were with 200 mS m^{-1} unexpectedly high. At this site the freeboards were close to zero, and a slushy snow/ice interface was observed after the snow was removed, which probably influenced the GEM-2 recordings.

For further GEM-2 studies, where an absolute calibration is desired, we strongly suggest calculating calibration coefficients and uncertainties for all the individual frequencies. Nevertheless, the instrument can still be used in a traditional way for single-frequency sea-ice thickness retrievals, similar to an EM-31, where an exponential fit to calibration data at a single frequency is used to directly determine the sea-ice thickness (e.g. Haas and others, 1997). The advantages of the GEM-2 over the EM-31 are the different sounding depths, due to several frequencies, and recording of in-phase and quadrature. The two components provide independent measurements at a single frequency and thereby reduce the ambiguity of the recorded signal, which is important for the determination of the calibration coefficients. The in-phase component of the EM-31 is often at saturation, and the apparent conductivity is calculated with the quadrature component. In general, the in-phase component is more sensitive to deeper structures than the quadrature component.

Correcting the Atka Bay data with the calibration coefficients revealed that an additional phase shift had to be applied. This is possibly linked to the fundamentally different temperature regimes at the calibration sites, where the mean calibration coefficients were obtained. Slightly different frequency configurations had only a minor influence. This highlights the importance of careful calibration measurements for future field campaigns. We measured environmental temperatures during all our surveys, but could not see a strong temperature dependence of individual measurements, although the instrument was in temperature equilibrium with its surroundings.

While the uncertainty associated with the GEM-2 data mainly affects the estimation of platelet-layer conductivity, the subsequent conversion to ice-volume fraction strongly depends on physical assumptions of pore and ice-platelet shapes. For example, we assume that the pore-water is connected, which would generally indicate a low value for the cementation factor, m, in Archie's law (Glover, 2009). A lower value indicates spherical pores and grains (Salem and Chilingarian, 1999), but this is not the case for individual disk-shaped ice platelets within the platelet layer. Using thin sections for sea-ice cores from Atka Bay, Hoppmann and others (2015) found randomly oriented ice platelets (which agrees with recent findings of Gough and others, 2012). This factor might again result in a lower value of m, due to less

angularity. However, to date, no studies exist that describe the cementation factor, m, for the platelet layer using independent measurements. Instead, we calculated a brine platelet-layer conductivity with a range of values, 1.5–2.5, normally observed in sandstones (Glover and others, 1997). In general, we get better agreement with results from recent studies (Gough and others, 2012; Hoppmann and others, 2015) with higher cementation factors or lower brine conductivities.

The brine conductivity, σ_b, measured by CTD casts creates an additional uncertainty. Hoppmann and others (2015) showed that the platelet layer was already thinning when the GEM-2 surveys were conducted (November 2012–January 2013), due to the inflow of warm water masses. Hence, the brine conductivity may have decreased due to ice melt in late December. Nevertheless, these melt rates and the associated freshening do not explain the low conductivities ($\sim$1800 mS m^{-1}) recorded. Also, the bulk platelet-layer conductivity at ATKA11 on 27 December (Fig. 7) did not decrease compared with earlier calibrations.

Apart from the physical assumptions of the platelet layer and the conversion of conductivities to ice-volume fraction, we assumed the ideal case of two layers, which are level within the footprint of the sensor. We tried to compensate for this effect by measuring sea-ice thickness in the footprint range of the instrument through several drillholes. This assumption most likely does not hold for thicker sea ice and platelet layers, where sub-ice topographies or internal layers may be present more often.

With frequencies more sensitive to the solid sea-ice layer and the significant extension of the frequency range to lower values, we are confident that we can resolve both platelet-layer thickness and conductivity using a geophysical inversion scheme. The result of the inversion might be that a two-layer case is not sufficient; instead it may be necessary to have several platelet layers to explain the apparent relationship (Fig. 8) between bulk platelet-layer conductivity and frequency. However, data inversion is only possible when the bias of the bucking coil is included in inversion algorithms.

CONCLUSION

This study is a step towards sub-sea-ice platelet-layer volume estimation of Antarctic fast ice with EM induction sounding. We used the multi-frequency ground-based instrument GEM-2, operated at frequencies of 450–93 090 Hz. We compared measurements at sites of known sea-ice and platelet-layer thicknesses at Atka Bay with two-layered forward models, deriving a mean bulk platelet-layer conductivity of 1154 ± 271 mS m^{-1}. Assuming a range of cementation factors for the platelet layer, we obtained ice-volume fractions of 0.29–0.43, while values of 0.25 ± 0.06 and 0.25 ± 0.1 have recently been found by other methods (Gough and others, 2012; Hoppmann and others, 2015). Using the quadrature component of higher frequencies, 63 030 and 93 090 Hz, we were able to estimate conductivities of the solid sea-ice layer. Accurate calibrations are required to reduce the uncertainties of multi-frequency EM measurements to make them useful for the determination of the platelet-layer volume. Comparisons of calibration data and forward models revealed that it is crucial to include the signal response of the bucking coil in the theoretical calculations. In general, multi-frequency soundings are superior to single-frequency soundings and may also improve sea-ice thickness retrieval over deformed and porous sea ice that has similar macroscale properties to the platelet layer in Antarctica. Our results provide elemental physical constraints for the layer conductivities and ice-volume fractions. As we continue this work, we intend to conduct a joint analysis of all frequencies using a geophysical inversion to retrieve platelet-layer thickness and conductivities simultaneously. Multi-frequency EM induction sounding will enable us to survey ice-platelet volume below the Antarctic near-coastal sea ice on a much larger scale than by direct measurements through drillholes. Our method can also be applied to data from multi-frequency airborne sensors, which have recently been developed (Pfaffhuber and others, 2012).

ACKNOWLEDGEMENTS

We thank Thomas Schmidt, Meike Kühnel and Uwe Baltes for their fieldwork at Atka Bay. We thank the German Space Agency (DLR) for the TerraSAR-X image, and Christine Wesche for post-processing and calibrating the data. We are grateful to Robert Ricker, Thomas Krumpen and Martin Schiller for their fieldwork on board RV *Polarstern* (ANT-XXIX/6 and 7) and *Xenia II*. We thank Jean-Louis Tison for providing the sea-ice core data from the Weddell Sea campaign, and AWI logistics for their support. This work was partly supported by the German Research Council (DFG) in the framework of the priority program Antarctic Research, with comparative investigations in Arctic ice areas by grants SPP1158, NI1092/2 and HE2740/12, the graduate school POLMAR and the Alfred-Wegener-Institut Helmholtz-Zentrum für Polar- und Meeresforschung. We are also grateful to the reviewers whose comments and suggestions improved the clarity of the manuscript.

REFERENCES

Anderson WL (1979) Numerical integration of related Hankel transforms of orders 0 and 1 by adaptive digital filtering. *Geophysics*, **44**(7), 1287–1305 (doi: 10.1190/1.1441007)

Archie GE (1942) The electrical resistivity log as an aid in determining some reservoir characteristics. *Trans. AIME*, **146**(99), 54–62 (doi: 10.2118/942054-G)

Arrigo KR, Robinson DH and Sullivan CW (1993) A high resolution study of the platelet ice ecosystem in McMurdo Sound, Antarctica: photosynthetic and bio-optical characteristics of a dense microalgal bloom. *Mar. Ecol. Progr. Ser.*, **98**(1–2), 173–185

Brodie R and Sambridge M (2006) A holistic approach to inversion of frequency-domain airborne EM data. *Geophysics*, **71**(6), G301–G312 (doi: 10.1190/1.2356112)

Cox GFN and Weeks WF (1983) Equations for determining the gas and brine volumes in sea-ice samples. *J. Glaciol.*, **29**(102), 306–316

Dempsey DE, Langhorne PJ, Robinson NJ, Williams MJM, Haskell TG and Frew RD (2010) Observation and modeling of platelet ice fabric in McMurdo Sound, Antarctica. *J. Geophys. Res.*, **115**(C1), C01007 (doi: 10.1029/2008JC005264)

Deszcz-Pan M, Fitterman DV and Labson VF (1998) Reduction of inversion errors in helicopter EM data using auxiliary information. *Expl. Geophys.*, **29**(2), 142–146 (doi: 10.1071/EG998142)

Eicken H and Lange MA (1989) Development and properties of sea ice in the coastal regime of the southeastern Weddell Sea. *J. Geophys. Res.*, **94**(C6), 8193–8206 (doi: 10.1029/JC094iC06p08193)

Foldvik A and Kvinge T (1974) Conditional instability of sea water at the freezing point. *Deep-Sea Res.*, **21**(3), 169–174 (doi: 10.1016/0011-7471(74)90056-4)

Fretwell P and 59 others (2013) Bedmap2: improved ice bed, surface and thickness datasets for Antarctica. *Cryosphere*, **7**(1), 375–393 (doi: 10.5194/tc-7-375-2013)

Frischknecht FC, Labson VF, Spies BR and Anderson WL (1991) Profiling methods using small sources. In Nabighian MN ed. *Electromagnetic methods in applied geophysics, Vol. 2*. (Investigations in Geophysics 3) Society of Exploration Geophysicists, Tulsa, OK, 105–270

Glover P (2009) What is the cementation exponent? A new interpretation. *Lead. Edge*, **28**(1), 82–85 (doi: 10.1190/1.3064150)

Glover PWJ, Gómez JB, Meredith PG, Hayashi K, Sammonds PR and Murrell SAF (1997) Damage of saturated rocks undergoing triaxial deformation using complex electrical conductivity measurements: experimental results. *Phys. Chem. Earth*, **22**(1–2), 57–61 (doi: 10.1016/S0079-1946(97)00078-5)

Gough AJ, Mahoney AR, Langhorne PJ, Williams MJM, Robinson NJ and Haskell TG (2012) Signatures of supercooling: McMurdo Sound platelet ice. *J. Glaciol.*, **58**(207), 38–50 (doi: 10.3189/2012JoG10J218)

Günther S and Dieckmann G (1999) Seasonal development of high algal biomass in snow-covered fast ice and the underlying platelet layer in Atka Bay, Antarctica. *Antarct. Sci.*, **11**(3), 305–315 (doi: 10.1017/S0954102099000395)

Haas C (1998) Evaluation of ship-based electromagnetic inductive thickness measurements of summer sea-ice in the Bellingshausen and Amundsen Seas, Antarctica. *Cold Reg. Sci. Technol.*, **27**(1), 1–16 (doi: 10.1016/S0165-232X(97)00019-0)

Haas C, Gerland S, Eicken H and Miller H (1997) Comparison of sea-ice thickness measurements under summer and winter conditions in the Arctic using a small electromagnetic induction device. *Geophysics*, **62**(3), 749–757 (doi: 10.1190/1.1444184)

Haas C, Nicolaus M, Willmes S, Worby A and Flinspach D (2008) Sea ice and snow thickness and physical properties of an ice floe in the western Weddell Sea and their changes during spring warming. *Deep-Sea Res. II*, **55**(8–9), 963–974 (doi: 10.1016/j.dsr2.2007.12.020)

Haas C, Lobach J, Hendricks S, Rabenstein L and Pfaffling A (2009) Helicopter-borne measurements of sea ice thickness, using a small and lightweight, digital EM system. *J. Appl. Geophys.*, **67**(3), 234–241 (doi: 10.1016/j.jappgeo.2008.05.005)

Hoppmann M and 11 others (2015) Ice platelets below Weddell Sea landfast sea ice. *Ann. Glaciol.*, **56**(69) (see paper in this issue) (doi: 10.3189/2015AoG69A678)

Jeffries MO, Weeks WF, Shaw R and Morris K (1993) Structural characteristics of congelation and platelet ice and their role in the development of Antarctic land-fast sea ice. *J. Glaciol.*, **39**(132), 223–238

Kipfstuhl J (1991) Zur Entstehung von Unterwassereis und das Wachstum und die Energiebilanz des Meereises in der Atka Bucht, Antarktis. *Ber. Polarforsch/Rep. Pol. Res.* 85

Kovacs A and Morey RM (1991) Sounding sea ice thickness using a portable electromagnetic induction instrument. *Geophysics*, **56**(12), 1992–1998 (doi: 10.1190/1.1443011)

Le Brocq AM, Payne AJ and Vieli A (2010) An improved Antarctic dataset for high resolution numerical ice sheet models (ALBMAP v1). *Earth Syst. Sci. Data*, **2**(2), 247–260 (doi: 10.5194/essdd-3-195-2010)

Leppäranta M and Manninen T (1988) The brine and gas content of sea ice, with attention to low salinities and high temperatures. (Internal Rep. 88-2) Finnish Institute of Marine Research, Helsinki

Mahoney AR and 6 others (2011) The seasonal appearance of ice shelf water in coastal Antarctica and its effect on sea ice growth. *J. Geophys. Res.*, **116**(C11), C11032 (doi: 10.1029/2011JC007060)

Minsley BJ, Smith BD, Hammack R, Sams JI and Veloski G (2012) Calibration and filtering strategies for frequency domain electromagnetic data. *J. Appl. Geophys.*, **80**, 56–66 (doi: 10.1016/j.jappgeo.2012.01.008)

Pfaffhuber AA, Hendricks S, Hunkeler P and Kvistedal YA (2012) Introducing a new generation multi-sensor airborne system for mapping sea ice cover of polar oceans. *First Break*, **30**(8), 83–88

Price D, Rack W, Langhorne PJ, Haas C, Leonard G and Barnsdale K (2014) The sub-ice platelet layer and its influence on freeboard to thickness conversion of Antarctic sea ice. *Cryos. Discuss.*, **8**(1), 999–1022 (doi: 10.5194/tcd-8-999-2014)

Rack W, Haas C and Langhorne PJ (2013) Airborne thickness and freeboard measurements over the McMurdo Ice Shelf, Antarctica, and implications for ice density. *J. Geophys. Res.*, **118**(C11), 5899–5907 (doi: 10.1002/2013JC009084)

Reid JE and Bishop J (2004) Post-processing calibration of frequency-domain electromagnetic data for sea-ice thickness measurements. *Expl. Geophys.*, **35**(4), 283–287 (doi: 10.1071/EG04283)

Reid JE, Worby AP, Vrbancich J and Munro AIS (2003) Shipborne electromagnetic measurements of Antarctic sea-ice thickness. *Geophysics*, **68**(5), 1537–1546 (doi: 10.1190/1.1620627)

Reid JE, Pfaffling A, Worby AP and Bishop JR (2006) In situ measurements of the direct-current conductivity of Antarctic sea ice: implications for airborne electromagnetic sounding of sea-ice thickness. *Ann. Glaciol.*, **44**, 217–223 (doi: 10.3189/172756406781811772)

Salem HS and Chilingarian GV (1999) The cementation factor of Archie's equation for shaly sandstone reservoirs. *J. Petrol. Sci. Eng.*, **23**(2), 83–93 (doi: 10.1016/S0920-4105(99)00009-1)

Smith IJ, Langhorne PJ, Haskell TG, Trodahl HJ, Frew R and Vennell MR (2001) Platelet ice and the land-fast sea ice of McMurdo Sound, Antarctica. *Ann. Glaciol.*, **33**, 21–27 (doi: 10.3189/172756401781818365)

Stogryn A and Desargant GJ (1985) The dielectric properties of brine in sea ice at microwave frequencies. *IEEE Trans. Antennas Propag.*, **33**(5), 523–532 (doi: 10.1109/TAP.1985.1143610)

Won IJ, Oren A and Funak F (2003) GEM-2A: a programmable broadband helicopter-towed electromagnetic sensor. *Geophysics*, **68**(6), 1888–1895 (doi: 10.1190/1.1635041)

Appendix II

Publication V: ”Improved 1D inversions for sea ice thickness and conductivity from EM induction data: Inclusion of nonlinearities caused by passive bucking”

By Priska A. HUNKELER, Stefan HENDRICKS, **Mario HOPPMANN**, Colin G. FARQUHARSON, Thomas KALSCHEUER, Melchior GRAB, Manuela S. KAUFMANN, Lasse RABENSTEIN and Rüdiger GERDES

This manuscript was accepted by Geophysics in June 2015. It is supplied here as a pre-print version, and acknowledging SEG’s Policy on Open-access Publishing.

Improved 1D inversions for sea ice thickness and conductivity from EM induction data: Including nonlinearities caused by passive bucking

Priska A. Hunkeler*, Stefan Hendricks*, Mario Hoppmann*, Colin G. Farquharson†, Thomas Kalscheuer‡, Melchior Grab §, Manuela S. Kaufmann§, Lasse Rabenstein§, Rüdiger Gerdes*

ABSTRACT

The porosity of sea ice is a fundamental physical parameter that governs the mechanical strength of sea ice and the mobility of gases and nutrients for biological processes and biogeochemical cycles in the sea ice layer. Except from few coring sites little is known on the spatial distribution of the sea ice porosity and the variability of different sea ice types. But an efficient and non-destructive method to measure this property is currently missing. Sea ice porosity is however linked to the bulk electrical conductivity of sea ice, a parameter routinely used to discriminate between sea ice and seawater below by electromagnetic (EM) induction sensors. Here we evaluate the prospect of porosity retrieval of sea ice by means of bulk conductivity estimates using 1D multi-frequency EM inversion schemes. We focused on two inversion algorithms, a smoothness-constrained inversion and a Marquardt-Levenberg inversion, which we modified for the nonlinear signal bias caused by a passive bucking coil operated in such a highly conductive environment. Using synthetic modeling studies, 1D inversion algorithms and multiple frequencies, we show that we can resolve the sea ice conductivity within $\pm$ 0.01 S/m. Using standard assumptions for the conductivity-porosity relation of sea ice, we are able to estimate porosity with a uncertainty of $\pm$ 1.2 % which enables fast and non-destructive surveys of the internal state of the sea ice cover.

*Alfred-Wegener-Institut Helmholtz-Zentrum für Polar- und Meeresforschung, Bussestrasse 24, 27570 Bremerhaven, Germany
†Memorial University of Newfoundland, St. John's, NL A1B 3X5, Canada
‡Uppsala University, Department of Earth Sciences, Villavägen 16, SE-752 36 Uppsala, Sweden
§ETH Zurich, Institute of Geophysics, Sonnegstrasse 5, 8092 Zurich, Switzerland

INTRODUCTION

Along with the shrinking of the sea ice extent (Stroeve et al., 2012; Comiso and Hall, 2014) Arctic sea ice is thinning (Lindsay and Zhang, 2005; Haas et al., 2008; Kwok et al., 2009) and becoming younger (Maslanik et al., 2011). The change towards a younger sea ice cover leads

to changes in the average internal structure. For example, first-year sea ice shows higher absorption rates of shortwave radiation than does older sea ice, leading to a stronger internal warming and melting (Perovich et al., 2011; Nicolaus et al., 2012). This in turn, results in an increase of the connectivity of pores and brine channels, which governs the exchange of gases (Gosink et al., 1976) and nutrients (Krembs et al., 2011), as well as the mechanical strength (Kovacs, 1996). Here we develop and present a methodology to improve the use of electromagnetic (EM) induction sounding instruments to retrieve information related to the internal structure of different sea ice types, based on measurements of bulk electrical sea ice conductivity, hereinafter referred to as conductivity.

A physical parameter linked to the conductivity of the sea ice layer is its porosity (Archie, 1942). Pores of young sea ice are usually filled with highly saline brine left from the formation process, while in older, multi-year sea ice, this brine is usually replaced by fresher water due to meltwater flushing (Eicken et al., 2002; Vancoppenolle et al., 2007) or gravity drainage (Niedrauer and Martin, 1979; Notz and Worster, 2008). This also means that older, multi-year sea ice is electrically more resistive, while young, porous sea ice still has a high conductivity due to brine inclusions. Summer sea ice often shows macro-scale pores, as brine channels are widened and connected by melt processes. These pores then contain a mix of melt water and brine, which change the geochemistry of sea ice and the availability of nutrients for biological processes (Thomas and Dieckmann, 2009; Vancoppenolle et al., 2010). Mapping sea ice layer porosity by proxy measurements of sea ice conductivity would therefore enable improved process studies of sea ice mass balance and especially complex biogeochemical cycles at the atmosphere - sea ice - ocean interface. Information on the spatial variability, large-scale gradients and the annual cycle of internal sea ice properties is only sparsely available (e.g. Golden et al., 2007; Pringle et al., 2009). Current methods to obtain information on sea ice porosity are based on manual coring, whereas the high spatial variability in the sea ice cover calls for a rapid and non-destructive method.

The conductivity of sea ice, and in particular its large contrast with that of the ocean, is routinely utilized for sea ice thickness retrieval by frequency-domain electromagnetic induction sounders, which usually employ a single frequency in the range from 4 to 10 kHz. This method is deployed from helicopters (Kovacs and Holladay, 1990; Haas et al., 2009), aircraft (Haas et al., 2010), ship-mounted booms (Haas, 1998; Reid et al., 2003) or directly on the sea ice surface for high-resolution case studies (Eicken et al., 2001; Haas, 2004; Druckenmiller et al., 2009; Weissling et al., 2011). The retrieval algorithm assumes that sea ice and snow can be described by a single, flat 1D layer, which is usually the case for level sea ice, and that the effect of sea ice and snow conductivity on the EM response is negligible compared to the contribution from the underlying seawater. The EM response can be approximated with an exponential relation to the distance of the sea ice-water interface of either the in-phase or quadrature (out-of-phase) component, parameterized from calibration measurements or 1D forward models. The inverse of the exponential function then directly relates the EM response to the total thickness (snow and sea ice) for the given height of the sensor above the surface layer (Kovacs and Morey, 1991). We refer this method as EMPEX (empirical exponential), according to Pfaffling et al. (2007). This approach has proven to be a robust methodology for empirical sea ice thickness retrieval, but it inherently has to neglect any changes of the sea ice conductivity.

The assumption of a perfectly resistive, single layer of sea ice and snow is is justified in most cases, since the influence of the sea ice conductivity of dry cold level sea ice with typical thicknesses of 1-2 meters is small at the traditionally used frequency range (Pfaffling and Reid, 2009). However, there are cases, where the sea ice conductivity is a desired information for sea ice type classification and even becomes a dominant factor, e.g. for summer melt or the so-called sub-ice platelet layer. The latter is a layer of loose ice crystals (ice platelets) with a bulk conductivity between those of sea ice and ocean water (Rack et al., 2013; Hunkeler et al., 2015), may be located underneath coastal sea ice in Antarctica. Ice platelets originate from supercooled water in cavities below ice shelves and are a main contributor to the local sea ice mass balance. This special sea ice type is currently unmapped, except for sporadic manual measurements (e.g. Hoppmann et al., 2015). Also the sea ice thickness can vary on instrument subfootprint scales, and not all sea ice structures can be sufficiently described by a 1D geometry approximation within the footprint. The traditional 1D assumption leads to thickness biases for deformed sea ice, partly due to the geometric effect of sub-footprint scale thickness variability (Kovacs et al., 1995; Reid et al., 2003; Pfaffhuber et al., 2012) and partly due to the intrusion of saline seawater into the sea ice layer (Reid et al., 2006).

Operational needs for in-situ high-resolution sea ice surveys require a small sensor package that can be towed by foot or snow machine. It is a particular characteristic of such surveys that measurements are taken in a highly conductive environment given that the sensor is usually meters above seawater. The conductivities of sea ice layers we aim to resolve (0.01-0.2 S/m) can be 1 to 2 orders of magnitude smaller than the conductivity of the ocean (e.g. 2.7 S/m). Distances between the sensor and the saline ocean water can easily become smaller than the dimensions of the sensor itself. Previous EM sea ice studies have accounted for sea ice conductivities, such as Pfaffling and Reid (2009), who revealed that the lower frequency (3.68 kHz) of an airborne device is mostly sensitive to sea ice thickness, while higher frequencies (112 kHz) are needed to resolve sea ice conductivity. However, the difference in conductivity between first-year sea ice (0.05 S/m) and multi-year sea ice (< 0.01 S/m) could not be resolved for sea ice thinner than 2 m. In contrast, Hol-

laday et al. (1998) used airborne EM induction sounding to distinguish between first and multi-year sea ice by using 30 kHz and 90 kHz. Reid et al. (2003) concluded that it is necessary for sea ice thickness retrieval to account for conductive sea ice.

Since empirical analytic approaches for processing single-frequency EM data are insufficient to resolve thickness and conductivity of even a single layer, we assess the prospect of using 1D inversion algorithms on multi-frequency EM data, where (i) conductivity within fixed layers and (ii) conductivity and thickness of sea ice layers are adapted to minimize the difference between the signal response and forward models. In a previous study, Hunkeler et al. (2015) performed case studies with a ground-based device (GEM-2, Geophex Ltd.) at frequencies of 63.03 and 93.09 kHz and a coil spacing of 1.66 m, being able to resolve sea ice conductivities in agreement with estimates from sea ice cores. The assessment of sea ice conductivity in the present study is based on the same small-coil instrument, where 'small coil' refers to transmitter and receiver coils that have small diameters compared to the distance between them. Hence, the magnetic field generated by the transmitter is represented by a magnetic dipole and the measurements at the receiver coil are considered to be point measurements of the magnetic field (Farquharson, 2000). Processing routines of data from such small-coil instruments in highly conductive environments cannot be based on existing algorithms because of a nonlinear signal bias introduced by the passive bucking coil of the instrument. This coil is used to null the primary field at the receiver location and effectively acts as a second receiver. In low conductivity environments, the contribution of this second receiver can safely be approximated by a linear factor and the correction is often integrated in the sensor calibration. However, the contribution of the bucking coils significantly depends on the subsurface conductivity itself (Fitterman, 1998) and needs to be taken into account in the forward model and inversion scheme.

In this study, we use two modified geophysical inversion algorithms that specifically include the bucking coil. We use synthetic data and specific instrumental noise characteristics to run inversions for different thickness and conductivity scenarios as a proof-of-concept for the application to actual field data. We analyze the sensitivity of the inversion results and their success in resolving sea ice thickness and conductivity simultaneously. Finally, the porosity and its uncertainty is estimated from conductivity retrievals.

METHODS

We first describe principles behind multiple frequencies and passive EM bucking, then review two inversion algorithms with integrated contribution of the bucking coil correction for a small-coil EM instrument.

Multi-frequency measurements with small-coil systems

The quasi-static near-field zone (Spies and Frischknecht, 1991) is defined by the transmitter-receiver distance x_{Rx} being much smaller than the quasi-static plane-wave skin depth δ which is defined as

$$\delta = \sqrt{\frac{2}{\omega\mu\sigma}}, \tag{1}$$

where ω is the angular frequency ($\omega = 2\pi f$), μ is the magnetic permeability of free space ($\mu = 4\pi 10^{-7}$H/m) and σ is the conductivity. In the near-field zone using the same transmitter-receiver geometry, measurements at multiple frequencies do not add information over a single-frequency measurement, unless the conductivity shows frequency dependence. To increase the sounding depth, the transmitter-receiver distance has to be increased or the coil orientation has to be changed. The quasi-static transition zone corresponds to measurements with $x_{Rx} \sim \delta$. Compared to measurements in the near-field zone, the sounding depth increases additionally with decreasing frequency (Spies and Frischknecht, 1991). This results in additional information being retrieved using different frequencies.

The lower frequencies considered in our study, i.e. f_1=1.53 and f_2=5.31 kHz, represent measurements in the near-field zone. For instance, for measurements at frequency f_1, the skin depths in seawater (conductivity of 2.7 S/m) and sea ice of 0.2 S/m are δ = 7.8 m and δ = 28.8 m, respectively. Both skin depths are significantly larger than the transmitter-receiver separation of 1.66 m. However, measurements at higher frequencies, i.e. f_3=18.33, f_4=63.03 and f_5=93.09 kHz are effectively in the transition zone. For frequency f_5, δ = 1.0 m and δ = 3.6 m for seawater and sea ice with a conductivity of 0.2 S/m, respectively. This suggests that in highly conductive sea ice environments, soundings can be carried out by varying frequency even at transmitter-receiver separations as small as 1.66 m. Moreover, in our case of a moderately conductive layer being underlain by a highly conductive layer, resolution of layer parameters is generally much better than in the opposite case of a highly conductive layer being underlain by a moderately conductive layer (Spies and Frischknecht, 1991).

Passive EM bucking

Current EM induction instruments operate at single to multiple discrete frequencies. A typical EM instrument consists of three coils (Figure 1): transmitter coil (Tx), bucking coil (Bx) and receiver coil (Rx). The transmitter coil generates a primary magnetic field, inducing a secondary magnetic field in a conductive subsurface. The signal strength of this secondary field depends, amongst other things, on the distance from the instrument to a body and its conductivity. During a survey, the receiver coil records the superposition of the primary and secondary magnetic fields minus the bucking field.

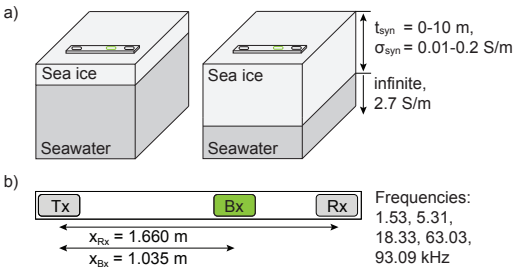

Figure 1: Diagrammatic sketch of multi-frequency EM device on level sea ice. In a) two exemplary stations with different sea ice thicknesses are shown. Synthetic data were calculated by assuming level sea ice thicknesses t_{syn} from 0-10 m in increments of 0.1 m and conductivities σ_{syn} of 0.01, 0.05, 0.10, 0.15 and 0.20 S/m. In b) the internal coil configuration and frequencies used for calculation of synthetic data are shown, x_{Rx} and x_{Bx} are the distances from the transmitter (Tx) to the receiver (Rx) and bucking coil (Bx), respectively. The bucking coil is used to null the primary field at the receiver location. Algorithms needed to be modified for a nonlinear bucking bias arising from measurements in highly conductive regimes.

The purpose of a bucking coil is to null the primary field at the receiver, which also avoids receiver saturation, and increases the dynamic range of the instrument (Won et al., 2003). It is connected in series and in opposite polarity to the receiver coil and technically acts as a second receiver. In free space the bucking coil measures the same absolute primary field signal as does the receiver coil when the following relation according to Won et al. (2003) is valid:

$$\frac{A_{Rx}n_{Rx}}{x_{Rx}^3} = \frac{A_{Bx}n_{Bx}}{x_{Bx}^3}, \quad (2)$$

where x_{Bx} is the distance between Tx and Bx, x_{Rx} is the distance between Tx and Rx and A and n are the area and number of turns of the respective coil. Typically x_{Bx} and x_{Rx} are in the order of 1-4 m, e.g., one particular commercial realization has $x_{Bx} = 1.035$ m and $x_{Rx} = 1.66$ m, and accommodates simultaneous operation of 0.3-96 kHz. The bucking coil, which is assumed to be linearly sensitive to the conductive subsurface, compensates internally for the primary field at the receiver location. However, in the seawater environment, the response of the bucking coil to the secondary field is nonlinear, leading to an overcorrection of the receiver signal depending on the conductivity structure of the subsurface (Fitterman, 1998). Hunkeler et al. (2015) accounted for this so-called bucking bias by modifying forward modeled data according to

$$\mathbf{d} = \mathbf{d}_{Rx} - \mathbf{d}_{Bx} = (\mathbf{I}_{Rx} + i\mathbf{Q}_{Rx}) - (\mathbf{I}_{Bx} + i\mathbf{Q}_{Bx}), \quad (3)$$

where $\mathbf{d}$ is the signal response at the receiver ($\mathbf{d}_{Rx}$) and bucking coil ($\mathbf{d}_{Bx}$) location. These signals can also be expressed as a complex number with real (in-phase I) and imaginary parts (quadrature Q), where I and Q are dimensionless and are measured in ppm (parts per million). An alternative representation of the signal is by its amplitude $A = \sqrt{I^2 + Q^2}$ and phase $\varphi = \arctan(Q/I)$. Hunkeler et al. (2015) achieved a satisfying agreement between field data and corrected forward modeled data by applying coefficients obtained from calibration experiments. In this study, we build upon these findings to implement the bucking coil directly into two different inversion algorithms.

Inverse modeling

The aim of an inversion algorithm is to find a plausible model (usually the simplest) which adequately fits the observed data within the data uncertainty (Farquharson et al., 2003). The process consists of two components: forward modeling and inversion. Forward modeling generates the data of a specific model; inversion automatically changes the model to reduce the misfit between measured and forward modeled data (Menke, 1989). We tested two inversion algorithms to resolve synthetic data of homogeneous sea ice for different thicknesses and conductivities. Forward modeling and inversion calculations were performed in 1D. We stitched the 1D inversion results of individual stations, which results in a 2D impression. With the first algorithm (EM1DFM, Farquharson (2000); Farquharson et al. (2003)), we only inverted for the conductivity within fixed layers of 0.1 m thickness, using vertical smoothing between layers. We call this inversion algorithm throughout the manuscript smoothness-constrained inversion. Since a vertical conductivity smoothing is not ideal in the case of a sharp sea ice/seawater interface, we applied a second algorithm, the Marquardt-Levenberg inversion (Jupp and Vozoff, 1975; Lines and Treitel, 1984). With only two distinct instead of many individual layers, and with sea ice thickness as an additional free parameter, this scheme may better reflect reality. In our study we used the Marquardt-Levenberg inversion algorithm from EMILIA (Electro Magnetic Inversion with Least Intricate Algorithms, Kalscheuer et al. (2010, 2012); Grab (2012)).

Smoothness-constrained inversion (EM1DFM)

The inversion problem is ill-posed and nonlinear. Therefore we derived at each iteration n a linearized approximation by searching for a change in the conductivity model which minimize the cost function

$$\Phi^n = \phi_d^n + \beta^n \phi_m^n, \quad (4)$$

where ϕ_d is the data misfit, β is the trade-off parameter and ϕ_m is the model-structure component (Farquharson et al., 2003). The data misfit ϕ_d is calculated according to Farquharson et al. (2003) by the l_2-norm

$$\phi_d^n = \|\mathbf{W}_d(\mathbf{d}^n - \mathbf{d}_{syn})\|^2, \quad (5)$$

where $\mathbf{d}_{syn}$ are the synthetic EM data. $\mathbf{d}^n$ are the forward-modeled data for the model $\mathbf{m}^n$ of the n^{th} iteration, where

$\mathbf{d}^n$ is defined as the non-linear forward operator $\mathbf{F}[\mathbf{m}^n]$. By accounting for the bucking bias, $\mathbf{d}_{syn}$ and $\mathbf{d}^n$ need to be modified according to Equation 3. $\mathbf{W}_d$ is a diagonal weighting matrix. For the bucking coil quantification (experiment 1, see below), $\mathbf{W}_d$ includes the reciprocal value of one percent of the synthetic data. For the synthetic modeling studies (experiments 2-4, see below), $\mathbf{W}_d$ includes the reciprocal standard deviations of the data, which were calculated from 30 minutes of free-air recordings of noise at each frequency for both in-phase and quadrature components (Hunkeler et al., 2015).

The model-structure component in Equation 4 is defined by

$$\phi_m^n = \alpha_s \|\mathbf{W}_s \mathbf{m}^n\|^2 + \alpha_z \|\mathbf{W}_z \mathbf{m}^n\|^2, \tag{6}$$

where $\mathbf{m}$ is the model vector of the logarithms of the layer conductivities and α_s (= 0.05) and α_z (= 1) are scaling coefficients. The diagonal matrix $\mathbf{W}_s$ contains elements which are equal to the square roots of the individual layer thicknesses (= 0.1 m). The matrix $\mathbf{W}_z$ is a first-order finite-difference operator. The rows are scaled by the reciprocals of the square roots of half the distance between the centers of two layers (Farquharson et al., 2003). The left term in Equation 6 quantifies the deviation from a reference model of 1 S/m and the right term the roughness of the model. Since α_s is significantly smaller than α_z, the right term dominates the model-structure component.

The trade-off parameter β (Equation 4) is a parameter which determines the balance between the data misfit and the model-structure component and is responsible to fit the observed data closely, whereas the constructed model should be as simple as possible (Farquharson et al., 2003). The noise is well known and therefore we adjusted β with a univariate search until the misfit ϕ_d matches a pre-defined target misfit in every iteration n. This is the maximum of the number of calculated responses N_d=10 (in-phase and quadrature for the five frequencies), or equal to $0.5\phi_d^{n-1}$, in order to allow only small changes in model structure at each iteration (discrepancy principle, Farquharson, 2000). In case the target misfit cannot be reached, the inversion algorithm searches for the smallest misfit.

The new model $\mathbf{m}^n$ is calculated from the previous model $\mathbf{m}^{n-1}$ by

$$\mathbf{m}^n = \mathbf{m}^{n-1} + \upsilon \delta \mathbf{m}^n, \tag{7}$$

where $\delta\mathbf{m}$ is the model update step and υ is the step length, which is halved when the cost function (Equation 4) does not immediately decrease. To find the model update step $\delta\mathbf{m}$, Equation 4 is differentiated with respect to $\delta\mathbf{m}$, set equal to zero and solved by a least-square approach for $\delta\mathbf{m}$ (Paige and Saunders, 1982; Farquharson et al., 2003). By doing so, the forward modeled data $\mathbf{d}^n$ in Equation 5 are approximated in the derivation of the inversion algorithm by

$$\mathbf{d}^n \approx \mathbf{d}^{n-1} + \mathbf{J}^{n-1} \delta \mathbf{m}^n, \tag{8}$$

where $\mathbf{J}$ is the Jacobian matrix of sensitivities (Farquharson and Oldenburg, 1996). $\mathbf{J}$ consists of the partial derivatives of the data with respect to the model parameters (logarithms of conductivities, σ) for the j^{th} layer and i^{th} station:

$$J_{ij}^n = \frac{\partial d_{Rx,i}}{\partial \log \sigma_j^n} - \frac{\partial d_{Bx,i}}{\partial \log \sigma_j^n}, \tag{9}$$

where d is the signal response at the receiver coil (d_{Rx}) and bucking coil (d_{Bx}) locations. These sensitivities quantify how the forward modeled data are affected by changing the conductivity of each layer (Farquharson and Oldenburg, 1993). The second term in Equation 9 is not required if the bucking coil modification is to be ignored.

To evaluate the compatibility of the new model $\mathbf{m}^n$ with the field data, the full forward response $\mathbf{d}^n = \mathbf{F}[\mathbf{m}^n]$ is then used to calculate ϕ_d (not approximation in Equation 8). The convergence of the inversion algorithm is determined using two convergence criteria according to Gill et al. (1981) and Farquharson (2000).

To assess how well synthetic data for a constructed model fit the measured data, we calculated the root-mean square error (RMSE)

$$\text{RMSE} = \sqrt{\frac{1}{N_d}\phi_d}. \tag{10}$$

An inversion with RMSE close to 1 is considered reliable without fitting too much to noise (Kalscheuer et al., 2013).

Marquardt-Levenberg inversion (EMILIA)

The Marquardt-Levenberg algorithm of EMILIA was recently modified to account for the bucking-coil bias by implementation of Equations 3 and 9 (Kaufmann, 2014). The cost function Φ is similar to Equation 4. The quantity ϕ_d is defined in a similar manner to Equation 5 (more below). The quantity β governs the magnitude of the damping and specifies the confidence in the previous model (damping factor). The quantity ϕ_m is now defined as

$$\phi_m^n = \|(\mathbf{m}^n - \mathbf{m}^{n-1})\|^2 \tag{11}$$

for the nth iteration. Since the difference between the new model $\mathbf{m}^n$ and the previous model $\mathbf{m}^{n-1}$ is limited, the inversion result is influenced by the starting model. The starting model is the first assumed subsurface model with defined thicknesses and conductivities of sea ice and underlying seawater, which is adapted during the inversion process. The RMSE is calculated according to Equation 10, where for RMSE > 1 a line search is performed for β and the model is adapted accordingly (Kalscheuer et al., 2013). In order to improve sea ice thickness results from the Marquardt-Levenberg inversion, we weighted the data misfit ϕ_{dw} according to Kalscheuer et al. (2013):

$$\phi_{dw}^n = \| \frac{\mathbf{W}_d(\mathbf{d}^n - \mathbf{d}_{syn})}{w} \|^2, \tag{12}$$

where the weight factor w, obtained from normalized synthetic data of one frequency and one component, decreases

exponentially for different stations, but is kept constant as the iterations proceed. Small values of w were assigned to stations of thick sea ice to increase their weights. The misfit ϕ_{dw} is normalized by the sum of the squared weight factor w^2 to achieve the intended weighted RMSE (RMSE_w) of 1

$$\mathrm{RMSE}_w = \sqrt{\frac{w^2}{N_d}\phi_{dw}}, \tag{13}$$

where ϕ_{dw} is the weighted data misfit and N_d the number of calculated responses.

Most-squares inversion

For sensitivity calculations, we applied to some of our 2-layer Marquardt-Levenberg inversions a model error and resolution analysis. This method is based on the truncated singular value decomposition (TSVD) of the sensitivity matrix (Kalscheuer and Pedersen, 2007). Since the effective number of model parameters is two (conductivity σ and thickness t of sea ice), the truncation level of the TSVD was set to two in the analyses of these models. Due to the very limited number of model parameters, both layer parameters are perfectly resolved. Hence, in assessing how well the layer parameters are constrained, only the model parameter uncertainties need to be further considered.

To partly account for the non-linearity of the inversion problem, we computed error estimates for the final inversion models using most-squares inversion (Jackson, 1976; Meju and Hutton, 1992; Meju, 1994). A most-squares inversion is an iterative method that determines, starting from the least-squares inversion results, bounding model values which are representative of the variability of the model parameters. The goal is to assess the stability of model parameters (Meju and Hutton, 1992). Owing to the logarithmic transformation of model parameters during inversion, the most-squares errors $1/f^-_{MSQ}$ and f^+_{MSQ} correspond to parameter ranges $\sigma/f^-_{MSQ},\ldots,f^+_{MSQ}\cdot\sigma$ and $t/f^-_{MSQ},\ldots,f^+_{MSQ}\cdot t$ of layer conductivities and thicknesses, respectively. Hence, a model parameter is well constrained with most-squares errors close to 1.

Synthetic data

To test the inversion algorithms, we used synthetic datasets for the in-phase and quadrature components, calculated by a 1D forward model using the implementation of Anderson (1979). We calculated two different types of synthetic datasets: (i) neglecting ($\mathbf{d}_{syn}$=$\mathbf{d}_{Rx}$); and (ii) accounting ($\mathbf{d}_{syn}$=$\mathbf{d}_{Rx}$-$\mathbf{d}_{Bx}$) for the bucking coil correction according to Equation 3. One dataset includes 101 stations, where the sea ice was increased from 0 to 10 m from one station to the next in increments of 0.1 m. These true thicknesses are hereinafter referred to as t_{syn}. Two exemplary stations are illustrated in Figure 1a, where a snow layer was neglected. We used typical conductivities σ_{syn} of different sea ice types between 0.01 and 0.2 S/m (Hunkeler et al., 2015) and a homogeneous half-space conductivity of 2.7 S/m, representing seawater. Inphase and quadrature responses were calculated at frequencies of 1.53, 5.31, 18.33, 63.03 and 93.09 kHz, a setup also used during surveys on sea ice (Hunkeler et al., 2015). For this proof-of-concept of the bucking coil implementation we did not account for any noise of the instrument (experiment 1). To simulate realistic data, we added Gaussian noise (corresponding to one standard deviation) to the in-phase and quadrature components, based on the free-air response for the respective frequencies (experiments 2-4). The assumed standard deviations between 125 and 204 ppm were calculated in an earlier study by Hunkeler et al. (2015), where higher frequencies showed higher instrumental noise. The synthetic data from the implementation of Anderson (1979) were compared to data forward modeled by the inversion algorithms considered here. The datasets computed by all three programs differed only by a few ppm, which is well within the noise level of the instrument.

RESULTS

We applied the two inversion algorithms to synthetic data. We first identify the impact of the bucking coil on the performance of the EM1DFM inversion (experiment 1). We then investigate whether multi-layered, Marquardt-Levenberg inversions are able to reliably reproduce t_{syn} and σ_{syn} (experiments 2-4).

Experiment 1: Influence of bucking coil

We used two synthetic datasets, with and without bucking bias, and two versions of EM1DFM, ignoring and considering the bucking bias. We tested the following three scenarios: (i) bucking bias neither in the data nor considered in EM1DFM, (ii) bucking bias in the data but not considered in EM1DFM, and (iii) bucking bias in the data and considered in EM1DFM. For all calculations we used σ_{syn} = 0.1 S/m, a seawater conductivity of 2.7 S/m, and t_{syn} of 0-10 m. For the starting model, we assigned to all stations 1 m thick sea ice with conductivities of 0.05 S/m and 2.7 S/m to the underlying sea water. We allowed a maximum of 40 iterations and set the uncertainties in $\mathbf{W}_d$ to one percent of the synthetic data.

For the first scenario, the RMSE (Equation 10) was, for most inversions, close to one and RMSE > 2 was found for only three stations (Figure 2a). Although the level of agreement between inversion results and the synthetic data was generally good, an accurate determination of sea ice thickness from these stations was difficult, because conductivities varied little between vertically adjacent layers, resulting in a smooth conductivity transition between sea ice and seawater. This transition zone from sea ice to seawater conductivities was small for thinner sea ice (t_{syn} < 4 m, white steps in Figures 2a-c), but widened towards thicker sea ice (3 m for t_{syn} = 10 m). Apart from this variable transition zone, σ_{syn} of 0.1 S/m (yellow in

Figure 2a) and seawater conductivity of 2.7 S/m (blue in Figure 2a) were reasonably reproduced.

We used for the second scenario the same setup as for the first scenario, and included the bucking bias in the synthetic data (Equation 3, Figure 2b), but not in the inversion algorithm. The algorithm completely failed to reproduce the data for $t_{syn} < 0.5$ m, where high RMSE values indicated that the target misfit was often not achieved. For t_{syn} between 0.5 and 1 m, the algorithm added an additional conductive layer close to the surface. Between 0.5 and 10 m, the transition zone was approximately 1 m too deep compared to t_{syn}. σ_{syn} of 0.1 S/m was only rarely reproduced, with sea ice conductivity in individual fixed layers being either too high (approximately 0.3 S/m, red in Figure 2b) or too low (close to 0 S/m, white in Figure 2b). For $t_{syn} > 5$ m, the algorithm added a conductive layer in the middle of the too resistive sea ice.

For the third scenario, we used the modified synthetic data from the second scenario together with the modified EM1DFM inversion algorithm (Equations 3 and 9). The results (Figure 2c) showed a substantial improvement over the second scenario (Figure 2b), where the RMSE and the resolved sea ice thickness and conductivity were comparable to those from the first scenario. For $t_{syn} < 0.5$ m, conductivities similar to the underlying seawater indicate that σ_{syn} could not be resolved.

For all further experiments, we included the bucking coil in the synthetic data and inversions.

Experiment 2: Smoothness-constrained inversion

In a second experiment, we used synthetic data with added Gaussian noise and with σ_{syn} of 0.01, 0.05, 0.1 and 0.2 S/m. For each σ_{syn} we calculated the EM response for thicknesses t_{syn} of 0 to 10 m. The starting model contained for each station 3 m of 0.05 S/m (sea ice) and an underlying homogeneous half-space of 2.7 S/m (seawater). The data uncertainty was set to the standard deviation of the noise and a maximum of 40 iterations were allowed. At all stations, the algorithm stopped before 40 iterations, because convergence to the target misfit was reached, convergence to a minimum was reached, or no suitable model update step was found.

The results of the four scenarios generally showed a good agreement with the synthetic data (Figure 3). The number of stations for which the target misfit could not be achieved were 3, 19, 31 and 29 for σ_{syn} of 0.01, 0.05, 0.1 and 0.2 S/m, respectively. For all inversions, the first two stations with t_{syn} of 0 and 0.1 m showed high RMSE values (> 2). Nevertheless, for stations with RMSE < 2, sea ice thickness was reasonably resolved for all four scenarios, but the transition zone between sea ice and seawater conductivity became broader for higher σ_{syn}. At station 30 with 3 m thick sea ice for example, the zone was for $\sigma_{syn} = 0.01$ S/m only 0.5 m (Figure 3a), whereas for $\sigma_{syn} = 0.2$ S/m it was 1 m wide (Figure 3d). The resulting

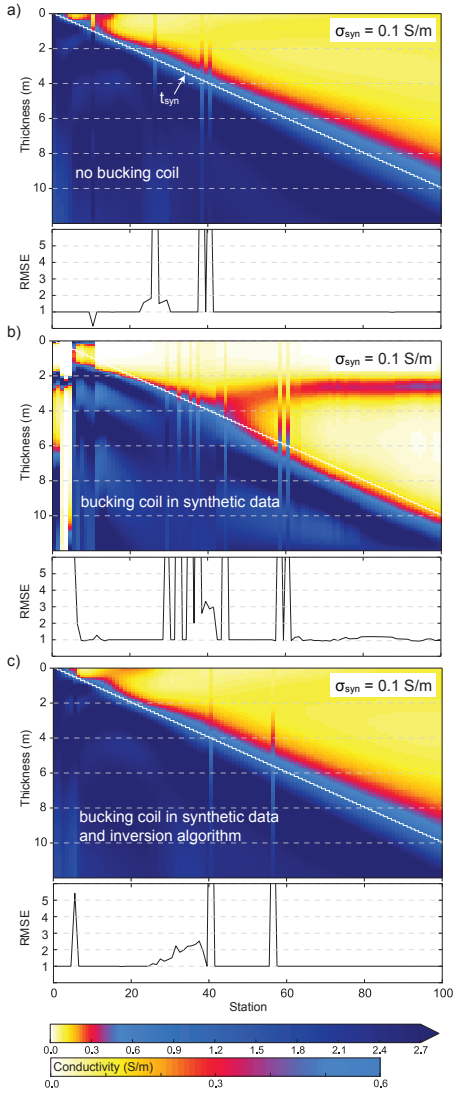

Figure 2: Influence of the bucking bias on sea ice thickness and conductivity retrieval (experiment 1). Each station represents a smoothness-constrained 1D inversion result (EM1DFM). The bucking-coil modification was applied to a) neither synthetic data nor inversion (scenario s1); b) only synthetic data (scenario s2); c) synthetic data and inversion (scenario s3). The colored regions show the resulting conductivities, from which we infer the sea ice thickness. σ_{syn} of 0.1 S/m, seawater conductivity of 2.7 S/m and t_{syn} (white steps) were reproduced best for scenarios s1 and s3. Below each scenario the RMSE is shown for all stations. The target misfit was reached when RMSE = 1.

sea ice conductivity was also more uniform for low σ_{syn} (Figure 3a), compared to the patchy conductivity results from higher σ_{syn} (Figure 3d). However, the sea ice conductivities were clearly distinguishable for the individual scenarios and can be resolved well within 0.05 S/m using EM1DFM.

For each of the four scenarios we obtained after the last iteration ten Jacobian matrices of sensitivities (Equation 9) from the five frequencies and both components (in-phase and quadrature). Each Jacobian matrix includes entries at every station in each layer for the respective scenario. In order to provide a quantified reliability estimate, we normalized all entries of the Jacobian matrices by the respective forward modeled data **d**, which were obtained after the last iteration. From the calculated normalized Jacobian matrices we selected for each layer the maximum of the ten entries. Here we show for each scenario the resulting 0.5%, 1% and 2% contour lines, along with the four resulting reliability areas (shaded areas in Figure 3). Small values of normalized Jacobian matrices indicate that a change in the conductivity barely affects the forward modeled data (Farquharson and Oldenburg, 1993), hence we trust regions with high sensitivities most.

Experiment 3: Marquardt-Levenberg inversion and most-squares inversion

We inverted the same synthetic data used in the second experiment (including Gaussian noise) by the Marquardt-Levenberg algorithm. The data uncertainty was again set to the standard deviation of the noise, and we used a starting model for each station of 0.05 S/m for the upper 3 m (sea ice) and 2.7 S/m for the homogeneous half-space below (seawater). The latter was fixed during this inversion since seawater conductivity is usually known and can be determined with tight bounds by sampling through boreholes. In the Eastern Weddell Sea, for example, the seawater conductivity ranged from 2.686 to 2.718 S/m over a time period of roughly three months (Hunkeler et al., 2015) and is usually assumed to be constant during a survey period. Tests showed that the Marquardt-Levenberg inversion performed considerably worse when allowing for a free seawater conductivity. Therefore only sea-ice thickness t and sea-ice conductivity σ were allowed to vary during a maximum of 300 iterations.

After the maximum of iterations was reached, t was for $t_{syn} < 5$ m well resolved for all four scenarios (Figure 4). The RMSE was generally higher for thicker sea ice compared to thinner sea ice in all scenarios. Most stations with a high RMSE were found for sea ice conductivity σ_{syn} of 0.2 S/m, where approximately half of the stations contained a RMSE > 1 (Figure 4d). The lowest values of RMSE and accurately recovered t (for $t_{syn} < 7$ m) were found for the inversions with $\sigma_{syn} = 0.05$ S/m, which is also the conductivity defined in the starting model (Figure 4b).

To quantify these findings, we compared the inversion results (plus results with $\sigma_{syn} = 0.15$ S/m) to t_{syn} (Figure 5a, scenarios s1-s5). The best resolved sea ice thickness t was found, as stated before, for $\sigma_{syn} = 0.05$ S/m (s2). However, t was generally reasonable reproduced for all scenarios $t_{syn} < 5$ m.

For comparison to resulting sea ice thickness t, we calculated thicknesses with the EMPEX approach. For the latter, we used the 5310 Hz in-phase forward responses, added Gaussian noise and fitted a single-exponential curve through the data (in-phase response vs. sea ice thickness). This curve fit represents the exponential function which is normally calculated from calibration measurements in the field. We used the in-phase component because it is more sensitive to deeper structures, and is monotonically decreasing with thickness in contrast to the quadrature component. The noise of the data was larger than the changes of the exponential function for thick sea ice with low signal responses. Hence, large sea ice thicknesses were poorly constrained. Because the exponential function was not approaching zero, a corresponding sea ice thickness could not always be found for low signal responses and sea ice > 8 m (Figure 5b).

In general, sea ice thickness t was underestimated with the Marquardt-Levenberg inversion, but overestimated with the calculated exponential function. With both methods reliable results were found for sea ice < 5 m. For thicker sea ice, the Marquardt-Levenberg inversion depends on σ_{syn}, on the starting model and the weighting of the data (more below). The sea ice thickness determination by the exponential approach did not depend on sea ice conductivity, because we calculated the exponential fit from the respective in-phase components.

The sea ice conductivity σ, however, could be resolved for scenarios s1-s5 (Figure 5a). Figure 5c shows distributions of σ, where individual histograms are clearly separated. For the scenario with the best resolved sea ice thickness t (s2), the narrowest conductivity distribution was found (0.05 S/m in Figure 5c). For scenarios s1-s5, the interquartile ranges of σ were within 0.01 S/m (Figure 5d).

In Table 1, we present the estimated model errors from most-squares inversion of the Marquardt-Levenberg inversion models for stations 11 and 31 (t_{syn} of 1 m and 3 m) for σ_{syn} of 0.05, 0.1 and 0.2 S/m (cf. Figures 4 and 5a). While the sea ice thicknesses t for station 11 were tightly constrained with $1/f^-_{MSQ} = 0.99$ and $f^+_{MSQ} = 1.01$ for all three cases, the sea ice conductivities σ showed more variability with $1/f^-_{MSQ}$ and f^+_{MSQ} varying from 0.92 to 0.99 and from 1.02 to 1.20, respectively. Similar results were found for thicker sea ice (station 31) with $1/f^-_{MSQ}$ between 0.97 and 0.99 and f^+_{MSQ} between 1.01 and 1.02 for t. σ showed again more variability with $1/f^-_{MSQ}$ between 0.95 and 0.97 and f^+_{MSQ} between 1.01 and 1.09. These results were not unexpected, because the thickness of a resistive layer is typically better constrained than its conductivity from inductive EM methods (e.g. Pfaffling and Reid, 2009). Similarly, the increase in error with in-

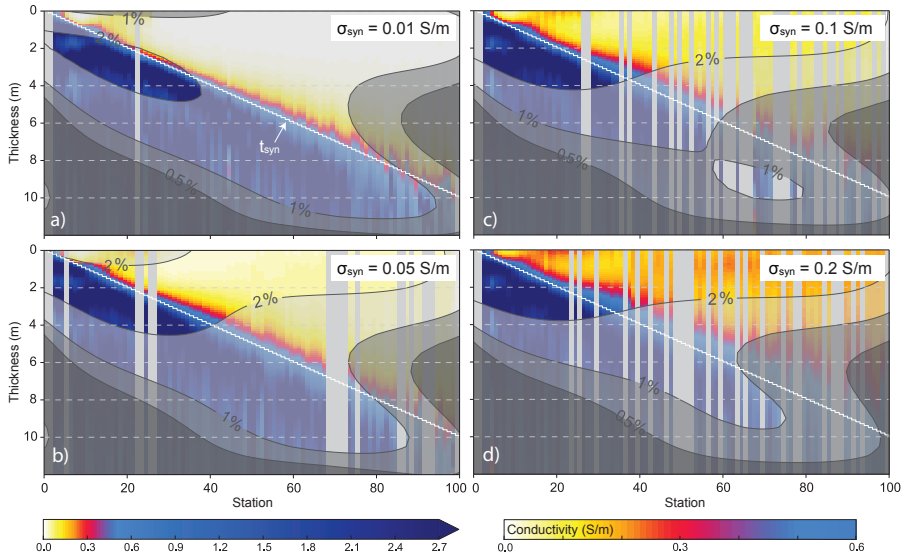

Figure 3: Results of smoothness-constrained inversions (EM1DFM, experiment 2). Each station represents a 1D inversion result. The colored regions show the resulting conductivities, from which we infer the sea ice thickness. σ_{syn} of a) 0.01, b) 0.05, c) 0.1, and d) 0.2 S/m, and seawater conductivity of 2.7 S/m were reproduced for all scenarios. Because of vertical smoothing, sea ice thickness can be approximated within a transition zone, which becomes broader for higher t_{syn} (white steps) and σ_{syn}. Four reliability areas from normalized Jacobian matrices are indicated with contour areas, below 0.5%, between 0.5 and 1%, between 1 and 2%, and above 2% which is considered to be a high sensitivity. Stations with high RMSE (> 2) were covered by a gray bar to highlight the reliable inversion results. Highest RMSE values were obtained for $\sigma_{syn} = 0.2$ S/m.

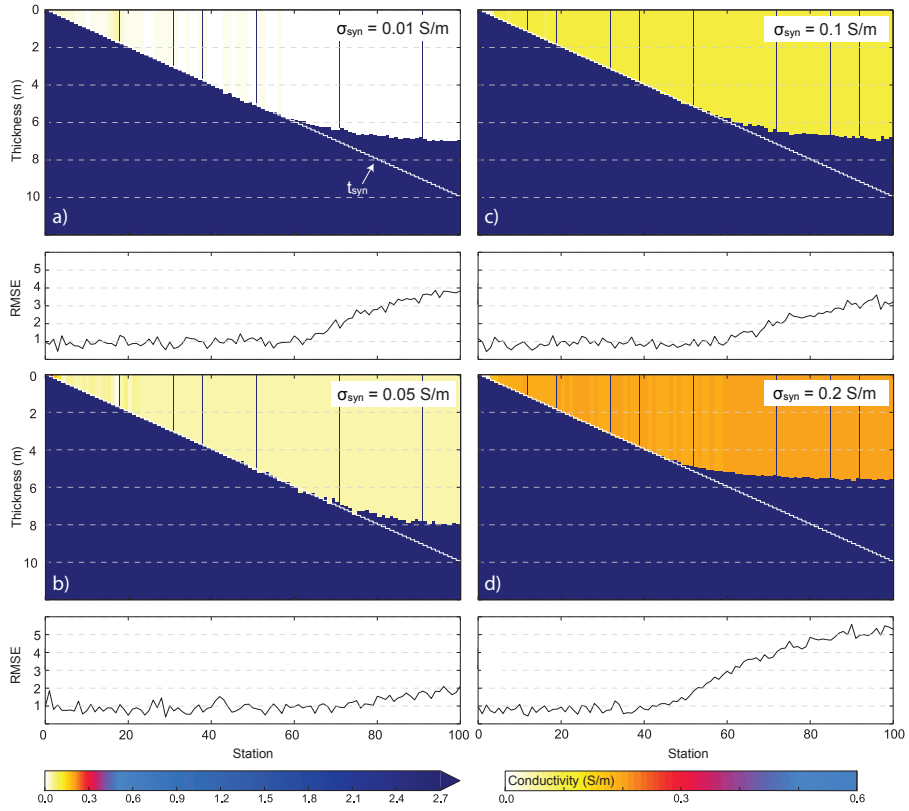

Figure 4: Results of sea ice thickness t and conductivity σ from Marquardt-Levenberg inversions (experiment 3). Each station represents a 1D inversion result. The colored regions show the resulting conductivities σ, from which we directly obtain the sea ice thickness t. σ_{syn} of a) 0.01, b) 0.05, c) 0.1, and d) 0.2 S/m were reproduced for all four scenarios. t_{syn} (white steps) were better reproduced for a), b) and c) compared to d). Below each scenario the RMSE is shown for individual stations, where the RMSE increases in all scenarios with higher t_{syn}, which causes smaller signal responses.

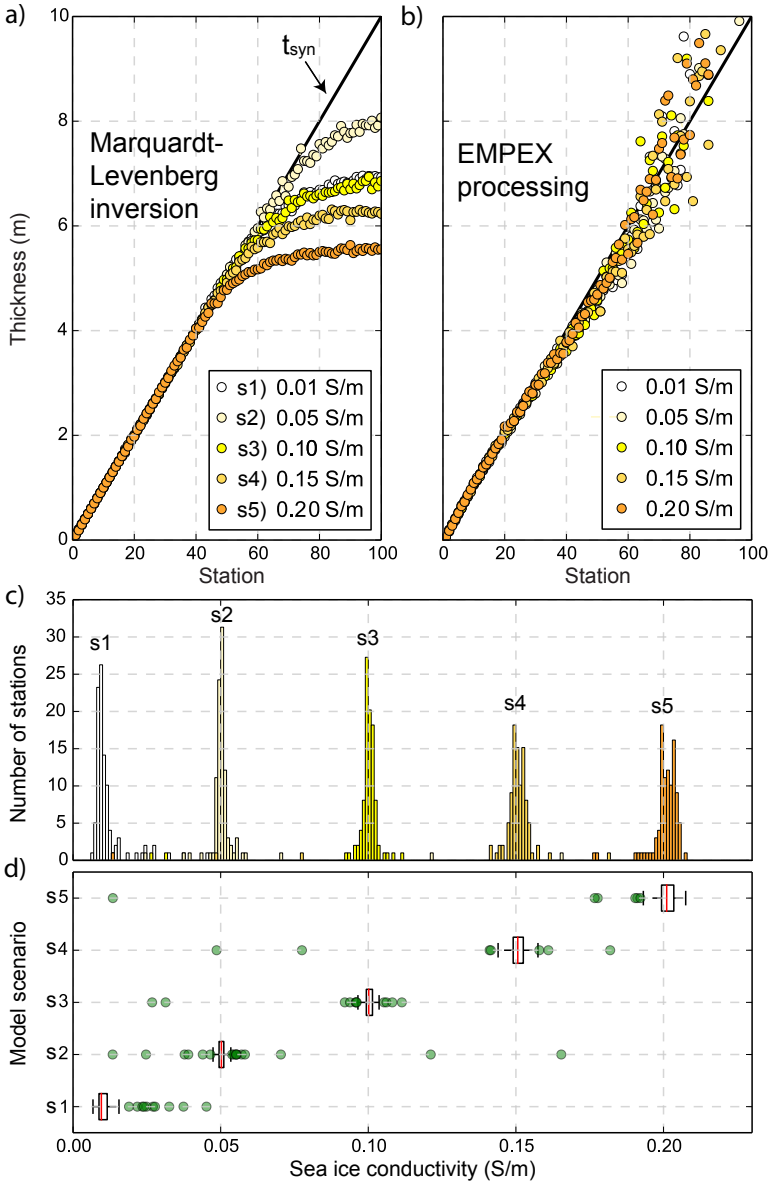

Figure 5: Validation of sea ice thickness t and conductivity σ from a) Marquardt-Levenberg inversions (experiment 3), and b) classical single-frequency processing (EMPEX) using the in-phase 5310 Hz component. In a) and b) t is compared to t_{syn} of 0-10 m. The Marquardt-Levenberg inversions underestimated t at stations of thick sea ice ($t_{syn} > 5$ m) for all scenarios with σ_{syn} of 0.01 (s1), 0.05 (s2), 0.10 (s3), 0.15 (s4), and 0.20 (s5) S/m. σ_{syn} is compared to σ obtained from the scenarios s1-s5, illustrated with histograms in c) and box plots in d). Excluding the outliers, σ can be resolved within $\pm$ 0.01 S/m, independent from t.

creasing thickness is consistent. σ is better constrained for higher σ_{syn}, whereas the most-squares errors of σ are larger for thinner sea ice. Generally, all errors are very low and all parameters are well constrained, because only two model parameters are considered.

Experiment 4: Marquardt-Levenberg inversion

In order to quantify the effect of a priori information, we inverted synthetic data (σ_{syn} of 0.1 S/m and t_{syn} = 0-10 m) with different starting models and data weighting.

In a first step, the dataset was inverted in a similar manner to experiments 2 and 3. We varied the starting model (Figure 6a), by using for each station 3 m thick sea ice, σ_{syn} of 0.05 (s1), 0.1 (s2) and 0.2 S/m (s3) and a homogeneous half-space of 2.7 S/m. The starting model did not have a strong influence on sea ice thickness t, where $t_{syn} < 6$ m was reliably reproduced from all conductivities in the starting model (Figure 6a). But even after 300 iterations, the RMSE did not reach 1 (scenarios s1-s3 in Table 2 with RMSE values of 1.74-1.87).

In a second step, we used the same starting model as in scenarios s1-s3, but weighted the data misfit according to Equation 12. We calculated the weight factors w by using the normalized synthetic data of the 5310 Hz in-phase component with added Gaussian noise. Sea ice thickness t (for $t_{syn} > 6$ m) was better resolved compared to the results without weighting (Figure 6b), which was also supported by the reduced RMSE values of 0.99-1.16 (scenarios s4-s6 in Table 2). For the starting models with sea ice conductivities of 0.05 S/m and 0.1 S/m, convergence was reached after 104 and 58 iterations, respectively, which was faster than for the other scenarios.

In a third step, we did not weight the data, but used the sea ice thickness results from the 0.1 S/m exponential fit from Figure 5b in the starting model. In the cases for which it was not possible during EMPEX processing to find for low in-phase values a corresponding sea ice thickness, we used the thickness from the previous station. This is still apparent in the results, where layered structures are recognizable for sea ice > 9 m (Figure 6c). But sea ice thickness t again improved for $t_{syn} > 6$ m compared to the case in Figure 6a. RMSE values of 1.04-1.10 for scenarios s7-s9 were smaller than for scenarios s1-s3 (Table 2). Sea ice thicknesses t from scenarios s7-s9 were similar and therefore did not depend much on sea ice conductivities of the starting model (Figure 6c).

In general, sea ice thickness t was reasonably resolved by the Marquardt-Levenberg algorithm for $t_{syn} < 6$ m, regardless of weights and starting model. With weight factors and results from single-frequency thickness estimates, t improved for $t_{syn} > 6$ m. Although it was not always possible to resolve t up to 10 m, the sea ice conductivities σ were resolved within $\pm$ 0.01 S/m for all scenarios (Figure 6d). Outliers of σ rather contained a too low than a too high conductivity value.

Porosity estimation

We reformulated Archie's Law (Archie, 1942) to calculate the sea ice porosity Φ

$$\Phi = \left(\frac{\sigma}{\sigma_b}\right)^{\frac{1}{m}}, \quad (14)$$

where σ is the bulk electrical conductivity, σ_b is the brine conductivity, and m is an empirical cementation factor. Our previous results showed that the uncertainty of σ is 0.01 S/m.

The cementation factor m depends on the connectivity of the pores and the pore shapes which is related to the structure of sea ice and the c-axis orientation of individual crystals (Reid et al., 2006). The mobility of ions and the permeability are therefore closely linked to this parameter. With respect to sea ice, the literature suggests m between 1.55 and 2.2 (Thyssen et al., 1974; Morey et al., 1984). Haas et al. (1997) and Worby et al. (1999) used a cementation factor of 1.75 for their calculations. Reid et al. (2006) used values of 1.75 and 2.2, stating that the horizontal conductivity of the sea ice is overestimated with a value of 1.75. Since this parameter is not better constrained for sea ice and also depends on sea ice types and seasonality we used a value of 1.75.

With temperature measurements of nine first-year sea ice cores from the winter Weddell Sea (Hunkeler et al., 2015), we calculated the mean brine conductivity of 4.69 $\pm$ 0.91 S/m according to Stogryn and Desargant (1985). At the same locations, Hunkeler et al. (2015) obtained from EM measurements at 63.03 and 93.09 kHz an average bulk conductivity of 0.06 S/m from seven experiments above thin sea ice (< 1 m). Assuming now $\sigma_b = 4.69 \pm 0.91$ S/m, m = 1.75, and σ = 0.06 $\pm$ 0.01 S/m, we obtain by applying Gaussian law of error propagation a porosity of Φ = 8.3 $\pm$ 1.2%. From the nine sea-ice cores, we calculated according to Cox and Weeks (1983) and Leppäranta and Manninen (1988) average brine volumes (porosities) of Φ = 9.5 $\pm$ 5.0%. The good agreement between porosities calculated from conductivities and direct measurements in sea-ice cores implies, that with the obtained uncertainty to determine the bulk conductivity from EM, a reasonable sea-ice porosity can be estimated.

DISCUSSION

We have shown that 1D inversions of EM data from passively bucked small coil systems must include the nonlinear contribution of the bucking coil when working close to a highly conductive environment. In our case of obtaining sea ice thickness and conductivity, the negligence of this contribution would lead to grossly wrong results for sea ice thinner than 2 m (Figure 2b), which is the typical level sea ice thickness in the Arctic and Antarctic. We calculated synthetic data based on a typical commercial instrument for sea ice research (Figure 1). The algorithm of including the bucking coil however will need to be made for all frequency-domain EM sensors that utilize

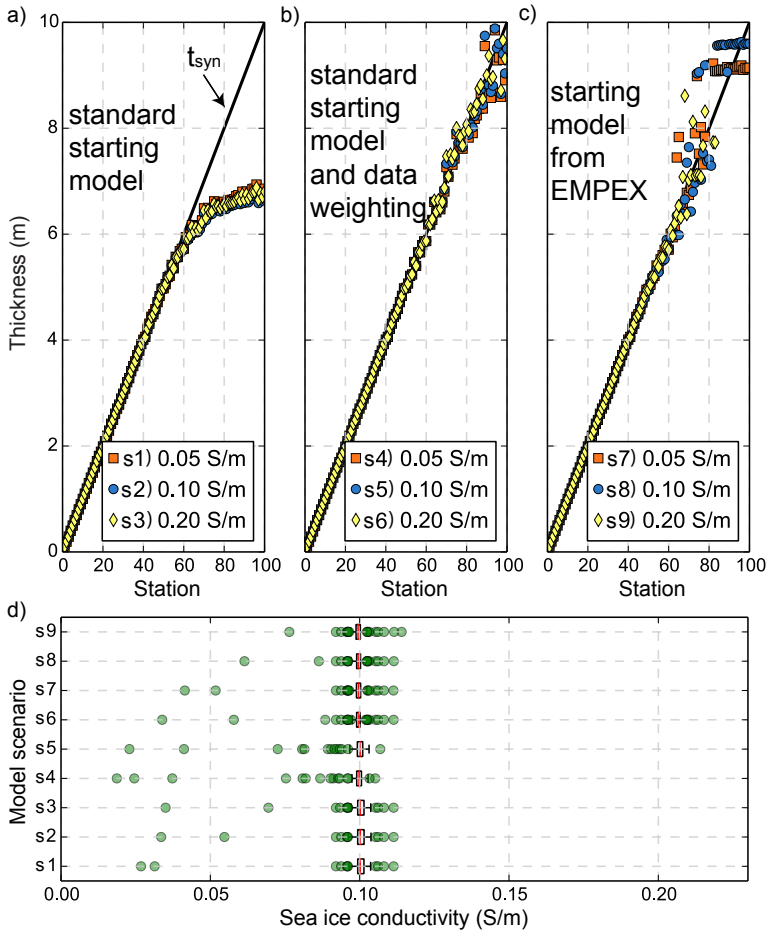

Figure 6: Influence of starting model and data weighting on sea ice thickness t and conductivity σ from Marquardt-Levenberg inversions (experiment 4). In comparison to the experiments before, we used here one σ_{syn} of 0.1 S/m, but several starting models which refer to scenarios s1-s9. In a), b) and c) t is compared to t_{syn} of 0-10 m. In a) the standard starting model was used with 3 m thick sea ice, but variable conductivities of 0.05 (s1), 0.1 (s2), 0.2 (s3) S/m, and an underlying fixed homogeneous half-space of 2.7 S/m. In b) the same starting model was used as in a), but the data were weighted (s4, s5, s6). In c) sea ice thickness results from EMPEX processing (0.1 S/m in Figure 5b) and sea ice conductivities of 0.05 (s7), 0.1 (s8), 0.2 (s9) S/m were used for the starting model. t improved with data weighting and a modified starting model obtained from EMPEX thicknesses. In d) σ_{syn} of 0.1 S/m is compared to the resulting sea ice conductivities σ from the individual scenarios, where σ was recovered for each scenario within $\pm$ 0.01 S/m.

Table 1: Error estimates for sea ice conductivities σ and thicknesses t of the 2-layer Marquardt-Levenberg models for stations 11 and 31 in Figures 4 and 5a. Error estimates $1/f^{-}_{MSQ}$ and f^{+}_{MSQ} were computed using most-squares inversions involving truncated singular value decomposition with a truncation level $p = 2$, the effective number of model parameters. A model parameter is well constrained with most-squares errors close to 1.

Parameter	$\sigma_{syn} = 0.05$ S/m		$\sigma_{syn} = 0.1$ S/m		$\sigma_{syn} = 0.2$ S/m	
	$1/f^{-}_{MSQ}$	f^{+}_{MSQ}	$1/f^{-}_{MSQ}$	f^{+}_{MSQ}	$1/f^{-}_{MSQ}$	f^{+}_{MSQ}
station 11						
σ	0.95	1.20	0.92	1.03	0.99	1.02
t	0.99	1.01	0.99	1.01	0.99	1.01
station 31						
σ	0.97	1.09	0.95	1.02	0.96	1.01
t	0.99	1.02	0.98	1.01	0.97	1.01

Table 2: Number of iterations and total RMSE of scenarios from Figure 6. The starting model contained sea ice conductivities σ_{start} of 0.05, 0.1 or 0.2 S/m. Scenarios s1-s3: starting model with 3 m thick sea ice and underlying homogeneous half-space of 2.7 S/m for all stations. Scenarios s4-s6: same starting model as for scenarios s1-s3, but weighted synthetic data. Scenarios s7-s9: starting model with sea ice thicknesses from single-frequency EMPEX processing.

	Scenarios s1-s3		Scenarios s4-s6		Scenarios s7-s9	
σ_{start}	RMSE	iterations	RMSE	iterations	RMSE	iterations
0.05 S/m	1.74	300	0.99	104	1.04	300
0.1 S/m	1.87	300	0.99	58	1.04	300
0.2 S/m	1.80	300	1.16	300	1.10	300

passive-bucking in high conductive environments (Fitterman, 1998). With the effect included, we were able to resolve conductivity and ultimately porosity with uncertainty values that motivate further studies and usage of the 1D inversions for field data. This and earlier case studies have shown that especially a high frequency range is required for the retrieval of sea ice conductivity.

Our aim was to jointly resolve sea ice thickness t and conductivity σ for a single layer with a thickness range of t_{syn} of 0-10 m and conductivities σ_{syn} of 0.01-0.2 S/m. We have tested two inversion methods, a smoothness-constrained (EM1DFM) and a Marquardt-Levenberg (EMILIA) inversion. In each scenario, we inverted synthetic data with constant conductivity σ_{syn} and the full range of physically feasible sea ice thicknesses t_{syn}, where the upper range includes extreme cases like decadal sea ice. During each iteration one β (trade-off parameter (EM1DFM) or damping factor (EMILIA)) is used for all stations simultaneously. The alternative would be separate inversions of all stations with individual β. This approach may lead to a faster convergence with fewer iterations. We however chose the single β approach, since we assume that stations are not independent and we want to reduce the potential for a wrong minimum of individual inversions.

EM1DFM inverts for the conductivity of multiple fixed layers; therefore the resolution of thickness depends on how the vertical conductivity gradient is evaluated (Figure 3). The conductivity transition zone between sea ice and seawater gets broader for thicker sea ice and also depends on σ_{syn}, thus, subsequently increasing the uncertainty of the thickness estimate. The Marquardt-Levenberg algorithm instead uses layer thickness as well as layer conductivity as free parameters, therefore removing the need for retrieving layer interfaces from conductivity gradients (Figure 4). While the description of sea ice as a layer of defined thickness with a conductivity discontinuity at the ice-water interface is a more realistic description of undeformed sea ice, internal structures such as from sea ice deformation or complex layering potentially can be better described by EM1DFM. However, the uncertainty of the interface location will be elevated by the process of vertical conductivity smoothing by EM1DFM. The choice of inversion scheme will therefore fall to the user and the specific application.

The best sea ice thickness results from the Marquardt-Levenberg inversions were found using data weights or tuning the starting model using single-frequency processing results (Figure 6). Higher weights for the weaker signals of thicker ice does increase the convergence rate and precision (Table 2). For real field data, we need to be careful when weighting low signal responses, since signal noise and instrument attitude errors may have an increased effect. In any case, with both inversion methods $t_{syn} < 5$ m were reasonably resolved. The conductivities of the starting model seemed to have little effect on the inversion results ($t_{syn} < 5$ m). The constant 3 m thick starting probably favored the better retrieval of thin sea ice.

Although the sea ice thickness is better constrained than the sea ice conductivity based on the most-square inversion (Table 1), it is determined by the Marquardt-Levenberg inversion with the five used frequencies within $\pm$ 0.01 S/m no matter how well the thickness was resolved, independent from the starting model, the weight factors and σ_{syn} (Figures 5d and 6d). Likewise sea ice conductiv-

ities can be reasonably well resolved for most of the fixed layers of EM1DFM inversions, provided that RMSE < 2 (Figure 3).

We have simplified sea ice as one homogeneous layer of prescribed thicknesses and conductivities, not accounting for any anisotropy due to higher conductivities in vertical brine channels (Reid et al., 2006). In nature, the simplification of level sea ice most likely applies to thermodynamically grown sea ice, which grows to a maximum of 2.5 meters (Thomas and Dieckmann, 2009) or to the Antarctic sub-ice platelet layer with multiple layers of different conductivities (Hunkeler et al., 2015). The sea ice-ocean interface or the interface between sea ice and the platelet layer are characterized by discontinuities in the vertical conductivity structure and by far smaller variability in the horizontal direction. To resolve such structures, lateral constraints between the models of adjacent stations (Auken et al., 2005) are assumed to be an appropriate modification of the Marquardt-Levenberg inversion resulting in a pseudo 2D inversion. But even pseudo 2D inversion cannot account for sea ice deformation features, where conductivities and sub-ice topographies vary additionally on sub-footprint scale. To account for complex topographies of deformed sea ice, we need to include the bucking bias in a full 2D inversion, where forward modeling responses and sensitivities are calculated in 2D.

The conversion of conductivity into porosity requires the knowledge of two parameters in Archie's Law (i) the cementation factor and (ii) the brine conductivity. First, we assume a cementation factor that is based on results from previous sea ice field experiments. Second, we used brine conductivities found in Antarctic winter sea ice cores. For sea ice throughout the freezing season this parameter is of second-order significance, since it is not assumed to vary much. In summer, the brine contains a mixture of saline brine and fresh water due to surface and internal melting, yielding a higher porosity than winter or spring sea ice (Vancoppenolle et al., 2007; Tison et al., 2008). In such cases, we can still make assumptions about the brine conductivity, but since we deal with higher uncertainties, the effect of porosity and brine conductivity on the bulk sea ice conductivity might not be fully separated in summer cases.

However, the uncertainty range of the sea ice conductivity in this idealized case is promising for retrieving porosity from actual field data. The improvement of 1D sea ice inversions presented in this study has therefore the potential to improve biogeochemical sea ice studies (e.g Arrigo et al., 1997) and estimations of sea ice density for satellite altimetry retrieval of sea ice thickness (Ricker et al., 2014) by large scale mapping of ice porosity.

CONCLUSION

Sea ice conductivity is a proxy parameter which can be used to derive porosity, albeit systematic measurements on scales larger than point measurements have been rare mostly due to a lack of suitable methodology. With the non-destructive method of multi-frequency EM sounding, this study aims to lay the foundation for a fast joint retrieval of sea ice thickness and porosity. We varied parameters of a synthetic dataset (thickness and conductivity) to assess the sensitivity of different parameter combinations in two geophysical inversion algorithms. Furthermore, we tested the influence of the starting model and data weighting. We calculated the synthetic data for a a small-coil system with frequencies relevant for sea ice research in the range of 1 to 100 kHz. The existing inversion algorithms were modified for a nonlinear correction of signal bias that is caused by passive bucking of the primary EM field close to highly conductive environments. Only with the integration of this sensor specific correction, were we able to resolve sea ice conductivity with a resolution of 0.01 S/m with 1D inversion methods. This resolution is sufficient to initiate field trials, to estimate sea ice porosity of different sea ice types, or the thickness and porosity in multi-year cases, such as flooded snow layers or sub-ice platelet layers near Antarctic ice shelves. Furthermore, detailed knowledge of porosity facilitates biogeochemical studies of sea ice, and sea ice densities estimated from porosities yield freeboard validations of satellites measurements. Though our approach improves sea ice surveying with EM induction sounding methods, it suffers the same limitations caused by the use of 1D forward models for essentially 3D targets with a significant sub-footprint scale variability. Since real world sea ice surveys are mostly conducted along transects, we suggest to modify 2D inversions methods to resolve thickness and internal conductivity changes at sub-footprint scales. Such a method would enable further studies of sea ice deformation, relevant for the improved estimation of sea ice volume.

ACKNOWLEDGMENT

Computing resources were provided by SNIC through the Uppsala Multidisciplinary Center for Advanced Computational Science (UPPMAX, Uppsala, Sweden) under project snic2014-1-243 and by Eidgenössische Technische Hochschule (ETH) in Zurich, Switzerland. Johan Hermansson at UPPMAX and Heinrich Horstmayer at ETH are acknowledged for assistance concerning technical and implementational aspects in making the code run. This work was partly funded by the POLMAR graduate school and the Alfred-Wegener-Institut Helmholtz-Zentrum für Polar- und Meeresforschung.

REFERENCES

Anderson, W. L., 1979, Numerical integration of related Hankel transforms of orders 0 and 1 by adaptive digital filtering: Geophysics, **44**, 1287–1305.

Archie, G. E., 1942, The electrical resistivity log as an aid in determining some reservoir characteristics: Trans. AIMe, **146**, 54–62.

Arrigo, K. R., D. L. Worthen, M. P. Lizotte, P. Dixon, and G. Dieckmann, 1997, Primary production in Antarctic sea ice: Science, **276**, 394–397.

Auken, E., A. V. Christiansen, B. H. Jacobsen, N. Foged, and K. I. Sørensen, 2005, Piecewise 1D laterally constrained inversion of resistivity data: Geophysical Prospecting, **53**, 497–506.

Comiso, J. C., and D. K. Hall, 2014, Climate trends in the Arctic as observed from space: Wiley Interdisciplinary Reviews: Climate Change, **5**, 389–409.

Cox, G. F. N., and W. F. Weeks, 1983, Equations for determining the gas and brine volumes in sea ice samples: US Army Corps of Engineers, Cold Regions Research & Engineering Laboratory, **29**.

Druckenmiller, M. L., H. Eicken, M. A. Johnson, D. J. Pringle, and C. C. Williams, 2009, Toward an integrated coastal sea-ice observatory: System components and a case study at Barrow, Alaska: Cold Regions Science and Technology, **56**, 61–72.

Eicken, H., H. R. Krouse, D. Kadko, and D. K. Perovich, 2002, Tracer studies of pathways and rates of meltwater transport through Arctic summer sea ice: Journal of Geophysical Research: Oceans, **107**, SHE–22.

Eicken, H., W. Tucker, and D. Perovich, 2001, Indirect measurements of the mass balance of summer Arctic sea ice with an electromagnetic induction technique: Annals of Glaciology, **33**, 194–200.

Farquharson, C., 2000, Background for Program EM1DFM. University of British Columbia.

Farquharson, C., and D. Oldenburg, 1993, Inversion of time-domain electromagnetic data for a horizontally layered Earth: Geophysical Journal International, **114**, 433–442.

———, 1996, Approximate sensitivities for the electromagnetic inverse problem: Geophysical Journal International, **126**, 235–252.

Farquharson, C. G., D. W. Oldenburg, and P. S. Routh, 2003, Simultaneous 1D inversion of loop-loop electromagnetic data for magnetic susceptibility and electrical conductivity: Geophysics, **68**, 1857–1869.

Fitterman, D. V., 1998, Sources of calibration errors in helicopter EM data: Exploration Geophysics, **29**, 65–70.

Gill, P. E., W. Murray, and M. H. Wright, 1981, Practical optimization: Academic Press, London.

Golden, K., H. Eicken, A. Heaton, J. Miner, D. Pringle, and J. Zhu, 2007, Thermal evolution of permeability and microstructure in sea ice: Geophysical research letters, **34**.

Gosink, T. A., J. G. Pearson, and J. J. Kelley, 1976, Gas movement through sea ice: Nature, **263**, 41–42.

Grab, M., 2012, Forward and inverse modelling of frequency-domain electromagnetic data from small coils: Master Thesis, IDEA League, ETH Zurich.

Haas, C., 1998, Evaluation of ship-based electromagnetic-inductive thickness measurements of summer sea-ice in the Bellingshausen and Amundsen Seas, Antarctica: Cold Regions Science and Technology, **27**, 1–16.

———, 2004, Late-summer sea ice thickness variability in the Arctic Transpolar Drift 1991–2001 derived from ground-based electromagnetic sounding: Geophysical research letters, **31**, L09402.

Haas, C., S. Gerland, H. Eicken, and H. Miller, 1997, Comparison of sea-ice thickness measurements under summer and winter conditions in the Arctic using a small electromagnetic induction device: Geophysics, **62**, 749–757.

Haas, C., S. Hendricks, H. Eicken, and A. Herber, 2010, Synoptic airborne thickness surveys reveal state of Arctic sea ice cover: Geophysical Research Letters, **37**, L09501.

Haas, C., J. Lobach, S. Hendricks, L. Rabenstein, and A. Pfaffling, 2009, Helicopter-borne measurements of sea ice thickness, using a small and lightweight, digital EM system: Journal of Applied Geophysics, **67**, 234–241.

Haas, C., A. Pfaffling, S. Hendricks, L. Rabenstein, J. Etienne, and I. Rigor, 2008, Reduced ice thickness in Arctic Transpolar Drift favors rapid ice retreat: Geophysical Research Letters, **35**, L17501.

Holladay, J. S., R. Z. Moucha, and S. J. Prinsenberg, 1998, Airborne Electromagnetic Sea Ice Sounding Measurements During SIMMS'95: Canadian Contractor Report of Hydrography and Ocean Sciences 50.

Hoppmann, M., M. Nicolaus, S. Paul, P. A. Hunkeler, G. Heinemann, S. Willmes, R. Timmermann, O. Boebel, T. Schmidt, M. Kühnel, G. König-Langlo, and R. Gerdes, 2015, Ice platelets below weddell sea landfast sea ice: Annals of Glaciology, **56**, 175–190.

Hunkeler, P. A., S. Hendricks, M. Hoppmann, S. Paul, and R. Gerdes, 2015, Towards an estimation of sub sea-ice platelet-layer volume with multi-frequency electromagnetic induction sounding: Annals of Glaciology, **56**, 137–146.

Jackson, D. D., 1976, Most squares inversion: Journal of Geophysical Research, **81**, 1027–1030.

Jupp, D., and K. Vozoff, 1975, Stable iterative methods for the inversion of geophysical data: Geophysical Journal International, **42**, 957–976.

Kalscheuer, T., M. Bastani, S. Donohue, L. Persson, A. Pfaffhuber, F. Reiser, and Z. Ren, 2013, Delineation of a quick clay zone at Smørgrav, Norway, with electromagnetic methods under geotechnical constraints: Journal of Applied Geophysics, **92**, 121–136.

Kalscheuer, T., J. Hübert, A. Kuvshinov, T. Lochbühler, and L. B. Pedersen, 2012, A hybrid regularization scheme for the inversion of magnetotelluric data from natural and controlled sources to layer and distortion

parameters: Geophysics, **77**, E301–E315.

Kalscheuer, T., M. D. l. Á. G. Juanatey, N. Meqbel, and L. B. Pedersen, 2010, Non-linear model error and resolution properties from two-dimensional single and joint inversions of direct current resistivity and radiomagnetotelluric data: Geophysical Journal International, **182**, 1174–1188.

Kalscheuer, T., and L. B. Pedersen, 2007, A non-linear truncated SVD variance and resolution analysis of two-dimensional magnetotelluric models: Geophysical Journal International, **169**, 435–447.

Kaufmann, M., 2014, Pseudo 2D inversion of multi-frequency coil-coil FDEM data: Master Thesis, IDEA League, ETH Zurich.

Kovacs, A., 1996, Sea ice: Part II. Estimating the full-scale tensile, flexural, and compressive strength of first-year ice: Technical report, DTIC Document.

Kovacs, A., and J. S. Holladay, 1990, Sea-ice thickness measurement using a small airborne electromagnetic sounding system: Geophysics, **55**, 1327–1337.

Kovacs, A., J. S. Holladay, and C. J. Bergeron Jr, 1995, The footprint/altitude ratio for helicopter electromagnetic sounding of sea-ice thickness: Comparison of theoretical and field estimates: Geophysics, **60**, 374–380.

Kovacs, A., and R. M. Morey, 1991, Sounding sea ice thickness using a portable electromagnetic induction instrument: Geophysics, **56**, 1992–1998.

Krembs, C., H. Eicken, and J. W. Deming, 2011, Exopolymer alteration of physical properties of sea ice and implications for ice habitability and biogeochemistry in a warmer Arctic: Proceedings of the National Academy of Sciences, **108**, 3653–3658.

Kwok, R., G. F. Cunningham, M. Wensnahan, I. Rigor, H. J. Zwally, and D. Yi, 2009, Thinning and volume loss of the Arctic Ocean sea ice cover: 2003-2008: Journal of Geophysical Research, **114**, C07005.

Leppäranta, M., and T. Manninen, 1988, The brine and gas content of sea ice with attention to low salinities and high temperatures: Internal Report 88-2, Helsinki.

Lindsay, R., and J. Zhang, 2005, The thinning of Arctic sea ice, 1988-2003: Have we passed a tipping point?: Journal of Climate, **18**, 4879–4894.

Lines, L., and S. Treitel, 1984, Tutorial: A review of least-squares inversion and its application to geophysical problems: Geophysical prospecting, **32**, 159–186.

Maslanik, J., J. Stroeve, C. Fowler, and W. Emery, 2011, Distribution and trends in Arctic sea ice age through spring 2011: Geophysical Research Letters, **38**, L13502.

Meju, M., and V. Hutton, 1992, Iterative most-squares inversion: application to magnetotelluric data: Geophysical journal international, **108**, 758–766.

Meju, M. A., 1994, Biased estimation: a simple framework for inversion and uncertainty analysis with prior information: Geophysical Journal International, **119**, 521–528.

Menke, W., 1989, Geophysical data analysis: Discrete inverse theory: International Geophysics Series, Academic Press, London, **45**.

Morey, R. M., A. Kovacs, and G. F. Cox, 1984, Electromagnetic properties of sea ice: Cold Regions Science and Technology, **9**, 53–75.

Nicolaus, M., C. Katlein, J. Maslanik, and S. Hendricks, 2012, Changes in Arctic sea ice result in increasing light transmittance and absorption: Geophysical Research Letters, **39**, L24501.

Niedrauer, T. M., and S. Martin, 1979, An experimental study of brine drainage and convection in young sea ice: Journal of Geophysical Research: Oceans, **84**, 1176–1186.

Notz, D., and M. G. Worster, 2008, In situ measurements of the evolution of young sea ice: Journal of Geophysical Research: Oceans, **113**, C03001.

Paige, C. C., and M. A. Saunders, 1982, LSQR: An algorithm for sparse linear equations and sparse least squares: ACM Transactions on Mathematical Software (TOMS), **8**, 43–71.

Perovich, D., K. Jones, B. Light, H. Eicken, T. Markus, J. Stroeve, and R. Lindsay, 2011, Solar partitioning in a changing Arctic sea-ice cover: Annals of Glaciology, **52**, 192–196.

Pfaffhuber, A. A., S. Hendricks, and Y. A. Kvistedal, 2012, Progressing from 1D to 2D and 3D near-surface airborne electromagnetic mapping with a multisensor, airborne sea-ice explorer: Geophysics, **77**, 109–117.

Pfaffling, A., C. Haas, and J. E. Reid, 2007, A direct helicopter EM sea ice thickness inversion, assessed with synthetic and field data: Geophysics, **72**, 127–137.

Pfaffling, A., and J. E. Reid, 2009, Sea ice as an evaluation target for HEM modelling and inversion: Journal of Applied Geophysics, **67**, 242–249.

Pringle, D., J. Miner, H. Eicken, and K. Golden, 2009, Pore space percolation in sea ice single crystals: Journal of Geophysical Research: Oceans (1978–2012), **114**.

Rack, W., C. Haas, and P. J. Langhorne, 2013, Airborne thickness and freeboard measurements over the McMurdo Ice Shelf, Antarctica, and implications for ice density: Journal of Geophysical Research: Oceans, **118**, 5899–5907.

Reid, J. E., A. Pfaffling, A. P. Worby, and J. R. Bishop, 2006, In situ measurements of the direct-current conductivity of Antarctic sea ice: implications for airborne electromagnetic sounding of sea-ice thickness: Annals of Glaciology, **44**, 217–223.

Reid, J. E., A. P. Worby, J. Vrbancich, and A. I. S. Munro, 2003, Shipborne electromagnetic measurements of Antarctic sea-ice thickness: Geophysics, **68**, 1537–1546.

Ricker, R., S. Hendricks, V. Helm, H. Skourup, and M. Davidson, 2014, Sensitivity of CryoSat-2 Arctic sea-ice freeboard and thickness on radar-waveform interpretation: The Cryosphere, **8**, 1607–1622.

Spies, B. R., and F. C. Frischknecht, 1991, Electromagnetic Sounding, *in* Electromagnetic Methods in Applied Geophysics: SEG, **2, Applications, Parts A and B**,

5, 285–425.

Stogryn, A., and G. Desargant, 1985, The dielectric properties of brine in sea ice at microwave frequencies: Antennas and Propagation, IEEE Transactions on, **33**, 523–532.

Stroeve, J. C., M. C. Serreze, M. M. Holland, J. E. Kay, J. Malanik, and A. P. Barrett, 2012, The Arctics rapidly shrinking sea ice cover: a research synthesis: Climatic Change, **110**, 1005–1027.

Thomas, D. N., and G. S. Dieckmann, 2009, Sea ice: John Wiley & Sons.

Thyssen, F., H. Kohnen, M. Cowan, and G. Timco, 1974, DC resistivity measurements on the sea ice near pond inlet, NWT (Baffin Island): Polarforschung, **44**, 117–126.

Tison, J.-L., A. Worby, B. Delille, F. Brabant, S. Papadimitriou, D. Thomas, J. De Jong, D. Lannuzel, and C. Haas, 2008, Temporal evolution of decaying summer first-year sea ice in the Western Weddell Sea, Antarctica: Deep Sea Research Part II: Topical Studies in Oceanography, **55**, 975–987.

Vancoppenolle, M., C. M. Bitz, and T. Fichefet, 2007, Summer landfast sea ice desalination at Point Barrow, Alaska: Modeling and observations: Journal of Geophysical Research: Oceans, **112**, C04022.

Vancoppenolle, M., H. Goosse, A. De Montety, T. Fichefet, B. Tremblay, and J.-L. Tison, 2010, Modeling brine and nutrient dynamics in Antarctic sea ice: The case of dissolved silica: Journal of Geophysical Research: Oceans, **115**, C02005.

Weissling, B., M. Lewis, and S. Ackley, 2011, Sea-ice thickness and mass at ice station Belgica, Bellingshausen Sea, Antarctica: Deep Sea Research Part II: Topical Studies in Oceanography, **58**, 1112–1124.

Won, I. J., A. Oren, and F. Funak, 2003, GEM-2A: A programmable broadband helicopter-towed electromagnetic sensor: Geophysics, **68**, 1888–1895.

Worby, A., P. Griffin, V. Lytle, and R. Massom, 1999, On the use of electromagnetic induction sounding to determine winter and spring sea ice thickness in the Antarctic: Cold Regions Science and Technology, **29**, 49–58.

Appendix III

Publication VI: ”A glimpse beneath Antarctic sea ice: platelet-layer volume from multi-frequency electromagnetic induction sounding”

By Priska A. HUNKELER, **Mario HOPPMANN**, Stefan HENDRICKS, Thomas KALSCHEUER and Rüdiger GERDES

This manuscript was submitted to Geophysical Research Letters in June 2015, and is currently under review. It is printed in this thesis acknowledging AGU’s Dual Publication policy.

GEOPHYSICAL RESEARCH LETTERS, VOL. ???, XXXX, DOI:10.1029/,

A glimpse beneath Antarctic sea ice: platelet-layer volume from multi-frequency electromagnetic induction sounding

P. A. Hunkeler[1], M. Hoppmann[1], S. Hendricks[1], T. Kalscheuer[2], R. Gerdes[1,3]

Ice shelves impact coastal Antarctic sea ice and the associated ecosystem through the formation of a sub-ice platelet layer. Despite its significance, the lack of suitable methodology impedes an Antarctic-wide quantification of this phenomenon. In this study, we inverted a unique multi-frequency electromagnetic (EM) induction sounding dataset obtained on an ice-shelf influenced fast-ice regime in the eastern Weddell Sea. In addition to consistent fast-ice thickness and -conductivities along > 100 km transects, we present the first extended, high resolution platelet-layer thickness and conductivity dataset recorded on sea ice. Ice-volume fractions calculated from conductivities suggest that a thicker platelet layer is more compacted than a loosely attached, young platelet layer. This study implies that multi-frequency EM is an effective approach in determining platelet-layer volume on a larger scale. When adapted to airborne multi-frequency EM, this method provides a crucial step towards an Antarctic-wide quantification of ocean/ice-shelf interaction.

1. Introduction

Around Antarctica, accumulations of individual ice crystals (platelets) are frequently observed below sea ice adjacent or attached to ice shelves. This phenomenon, hereinafter referred to as sub-ice platelet layer, reflects basal melt processes in nearby ice-shelf cavities and is a result of a current pattern referred to as "ice pump" [*Lewis and Perkin*, 1986]. This special sea-ice type not only modifies the properties, mass- and energy balance of an overlying solid sea-ice cover [*Eicken and Lange*, 1989; *Gough et al.*, 2012; *Hoppmann et al.*, 2015b], it also acts as a habitat for a substantial seasonal bloom of micro algae [*Arrigo et al.*, 1993; *Günther and Dieckmann*, 1999, 2001], provides a protective environment for coastal fish species [*Vacchi et al.*, 2000], and might also allow conclusions about processes in the ice-shelf cavity, which are otherwise difficult to investigate. The additional buoyancy provided by the underlying platelets modifies the sea-ice freeboard, influencing satellite remote sensing near coastal areas in Antarctica [*Rack et al.*, 2013; *Price et al.*, 2014].

The total volume of ice platelets below a sea-ice cover is the product of the platelet-layer thickness, area and ice-volume fraction. The platelet-layer thickness is usually determined with a weighted measuring tape [*Crocker*, 1988], an approach which is time-consuming and only allows for a very limited spatial coverage. The temporal evolution of platelet-layer thickness is obtained by repeated drill-hole measurements, or by autonomous instrumentation at a fixed site [*Hoppmann et al.*, 2015a]. Although progress has been made in estimating the ice-volume fraction using a variety of methods [e.g. *Gough et al.*, 2012; *Hunkeler et al.*, 2015; *Hoppmann et al.*, 2015b, a], the large-scale determination of platelet-layer properties remains a challenge due to the lack of a suitable methodology.

A promising approach to detect platelet-layer properties by a non-destructive method has recently been identified. *Hunkeler et al.* [2015] used the response of a ground-based, multi-frequency electromagnetic (EM) induction sounding instrument to determine the electrical conductivity (hereinafter referred to as conductivity) of the platelet layer. They found an average conductivity of 1.154 Sm^{-1}, and calculated ice-volume fractions of 0.29 - 0.43 using Archie's Law [*Archie*, 1942] with varying cementation factors.

In the present study, we build up on these investigations and present the first comprehensive, high resolution platelet-layer thickness and -conductivity dataset recorded on Antarctic sea ice. We applied a laterally-constrained Marquardt-Levenberg inversion to a unique multi-frequency EM induction sounding dataset obtained on immobile sea ice (fast ice) attached to an ice shelf in the eastern Weddell Sea. We tested the performance of the inversion using synthetic EM data and validated the final inversion results with drill-hole measurements.

2. Methods

2.1. Field measurements

The area under investigation is the seasonal fast ice of Atka Bay, a sheltered embayment in the front of the Ekström Ice Shelf in the eastern Weddell Sea, Antarctica (Figure 1a,b). The fast ice at Atka Bay exhibits a several meter thick platelet layer, which has been the subject of several investigations [*Kipfstuhl*, 1991; *Günther and Dieckmann*, 1999; *Hunkeler et al.*, 2015; *Hoppmann et al.*, 2015b, a]. This region is one of the rare locations around coastal Antarctica where year-round studies of sea ice are possible, due to the presence of the German wintering station Neumayer III.

Sea ice at Atka Bay is characterized by a distinct seasonal cycle: a closed sea-ice cover typically establishes between March and May, destabilizing and breaking up between December and February [*Hoppmann et al.*, 2015b]. Between break-up and new formation, nearly the entire bay is free of sea ice. The sea-ice conditions in 2012, the year this study took place, were slightly different: during August, approximately one third of the 440 km^2 fast ice area broke up during a storm (Figure 1b, *Hoppmann et al.*, 2015b). A continuous sea-ice cover was re-established in the breakup area after a large iceberg grounded in front of Atka Bay in September. Otherwise, the sea-ice conditions were comparable to other years: sea ice in the western part showed ridging and rafting due to predominantly easterly winds, while the eastern

[1]Alfred-Wegener-Institut Helmholtz-Zentrum für Polar- und Meeresforschung, Bussestrasse 24, 27570 Bremerhaven, Germany
[2]Uppsala University, Department of Earth Sciences, Villavgen 16, SE-752 36 Uppsala, Sweden
[3]Jacobs University Bremen gGmbH, Campus Ring 1, 28759 Bremen, Germany

0094-8276/15/$5.00

part exhibited mainly thermodynamically grown sea ice. As a result, sea ice in the east was generally thinner than the deformed sea ice of the western part. Thickest and oldest sea ice was observed in the southwestern part of Atka Bay. Drill-hole measurements at several sites between June 2012 and February 2013 indicated that the platelet layer reached its average maximum of around 4-5 m in December [*Hoppmann et al.*, 2015b].

We operated a commercially available multi-frequency EM induction instrument (GEM-2, Geophex Ltd.) on the fast ice on four occasions between November and December 2012. The instrument was configured to simultaneously record GPS position and EM soundings at frequencies of 1530, 5310, 18330, 63030 and 93090 Hz with a sampling rate of 10 Hz. The instrument was mounted in a kayak and pulled over the sea ice a few meters behind a snowmobile. In total, we acquired approximately 118 km of multi-frequency EM data across Atka Bay (Figure 1b, Table 1). We assume no significant new platelet accumulation during the study period and consequently regard all transects as a synoptic measurement. However, Transect 1 from 26 November was excluded from all further calculations since the frequency setup was different (no 1530 Hz), and the same track was repeated later in December.

Sea-ice thickness, snow depth and freeboard were measured with regular thickness tapes. Platelet-layer thickness was determined using the metal-bar method [*Crocker*, 1988], with a potential underestimation of up to 0.3 m as apparent from simultaneous real-time video. The data were already presented in *Hoppmann et al.* [2015b], and are used here for validation.

Table 1. Summary of multi-frequency EM data across Atka Bay. T corresponds to the transects as indicated in Figure 1b, the date refers to the year 2012; n is the total number of individual stations for the respective transect; sub-T refers to the number of sub-transects used for an inversion; rmse is the root-mean-square-error threshold for the respective sub-transect, above which an inversion result was omitted from further analysis; dist is the straight-line distance, and dist true is the true distance between first and last station.

T	Date	n	sub-T	rmse	dist (km)	dist true (km)
1	26-Nov	6442	3	10, 10, 10	24.6	25.8
2	16-Dec	6339	2	10, 10	24.6	25.4
3	20-Dec	3464	2	10, 20	13.4	13.9
4	20-Dec	4588	2	20, 20	17.7	18.4
5	20-Dec	3365	2	25, 20	12.9	13.5
6	21-Dec	2322	1	25	9.2	9.3
7	21-Dec	2887	1	20	10.6	11.5

2.2. Geophysical inversion

A geophysical inversion is an algorithm which calculates and iteratively adjusts a model of the subsurface, until the modeled signal response fit the measured response within its uncertainty. Sea ice in Atka Bay represents a simple, almost 1D target for geophysical inversions with three separate layers, mainly characterized by their different conductivities: sea ice plus snow, the platelet layer and seawater [*Hunkeler et al.*, 2015]. This leads to distinct conductivity interfaces in the vertical and a smooth horizontal conductivity gradient.

To reflect these characteristics, we used a 1D Marquardt-Levenberg (ML) inversion [*Lines and Treitel*, 1984] implemented in EMILIA [Electro-Magnetic Inversion with Least Intricate Algorithms, *Kalscheuer et al.*, 2010, 2012; *Grab*, 2012; *Kalscheuer*, 2014]. To test the performance of the ML inversion, we inverted synthetic data. similarly to *Hunkeler et al.* [accepted]. To determine which model parameters are constrained well by our data, we performed a most-squares inversion [*Jackson*, 1976]. Finally, we used a laterally-constrained ML inversion [*Auken et al.*, 2005] for field data processing, resulting in a pseudo-2D model.

Since the differences between the iterations are limited by the algorithm, a well-chosen starting model is crucial. In all inversions, the following starting model was used: 1) a layer with a thickness (conductivity) of 1 m (0.05 Sm^{-1}), representing sea ice plus snow; 2) a layer with a thickness (conductivity) of 2 m (1.15 Sm^{-1}), representing the platelet layer; 3) a homogeneous half space with a conductivity of 2.7 Sm^{-1} [*Hunkeler et al.*, 2015], representing the seawater. All inversions were performed using these three layers, allowing for four free parameters: 1) sea-ice thickness and 2) -conductivity, 3) platelet-layer thicknesses and 4) -conductivity. Since the seawater conductivity is assumed constant during the study period, this parameter was fixed for all inversions. For each inversion, we calculated the root-mean-square error (rmse) between modeled and measured signal response with values close to 1 being very good, indicating that a minimum was found without fitting too much to noise [*Kalscheuer et al.*, 2013].

2.2.1. Synthetic data and ML inversion,

To test the performance of the ML algorithm, we inverted a set of synthetic data based on the conditions encountered in the field. We calculated a series of 1D forward models for our standard frequency setup from the implementation of *Anderson* [1979], using all combinations of sea-ice thicknesses between 0.5 - 4 m, and platelet-layer thicknesses between 0.5 - 10 m, in increments of 0.5 m. We assigned conductivities of sea ice, platelet layer and seawater to 0.05, 1.15 and 2.7 Sm^{-1}, respectively. In order to better represent real data, we added Gaussian noise corresponding to one standard deviation from a series of EM recordings in free air [*Hunkeler et al.*, 2015].

In a series of experiments, we inverted a synthetic dataset comprising of one defined sea-ice thickness (e.g. 0.5 m) in combination with increasing platelet-layers thicknesses between 0.5 and 10 m, in steps of 0.5 m. Each combination of sea ice + platelet layer represents one 1D inversion. This procedure was repeated for the range of sea-ice thicknesses indicated earlier, resulting in a total of eight experiments.

2.2.2. Most-squares inversion

For the assessment of how well our free model parameters are resolved and constrained by the data, we performed 1) a model error and resolution analysis and 2) most-squares inversions.

We have applied first the model error and resolution analysis to ML models from synthetic data with sea-ice thicknesses of 1 m, 2.5 m and 4 m and platelet-layer thicknesses of 1 to 9 m, based on the truncated singular value decomposition (TSVD) of the sensitivity matrix [*Kalscheuer and Pedersen*, 2007]. Since the effective number of model parameters is four (conductivities and thicknesses of the upper two layers, i.e. of the sea ice and platelet layers), a truncation level of four was used in the analyses of these models.

To proof the linearized error estimates from the TSVD, we computed error estimates for the final inversion models using most-squares inversion [e.g. *Jackson*, 1976; *Meju and Hutton*, 1992; *Meju*, 1994], partly accounting for the nonlinearity of the inversion problem. Owing to the logarithmic transformation of model parameters during inversion, the most-squares uncertainties $1/f^{-}_{MSQ}$ and f^{+}_{MSQ} correspond to parameter ranges $\sigma/f^{-}_{MSQ}, \ldots, f^{+}_{MSQ} \cdot \sigma$ and $t/f^{-}_{MSQ}, \ldots, f^{+}_{MSQ} \cdot t$ of layer conductivities and thicknesses, respectively.

2.2.3. Transects and laterally-constrained ML inversion

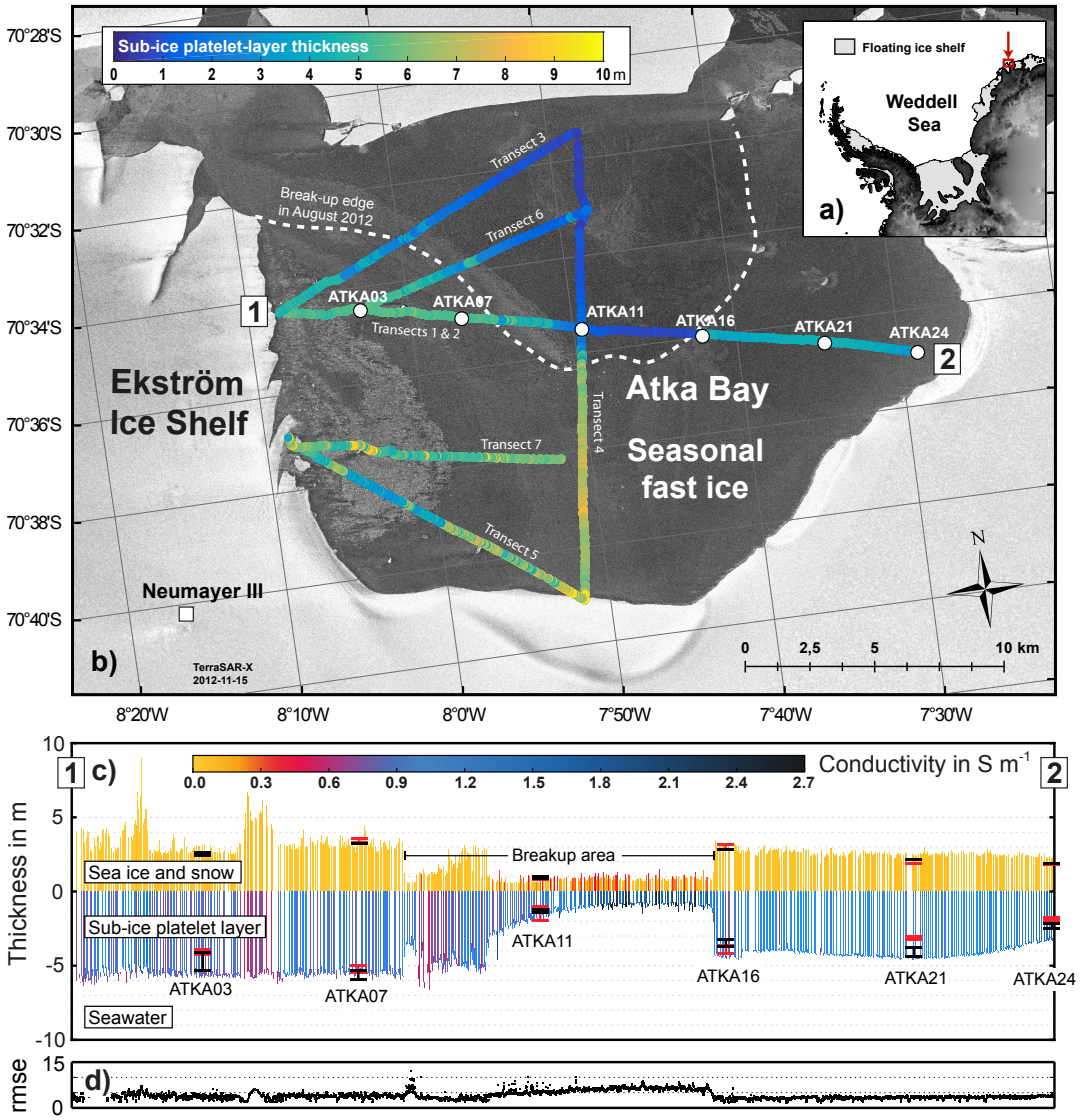

Figure 1. Platelet-layer thickness and conductivity below Atka Bay landfast sea ice. a) Location of Atka Bay in the eastern Weddell Sea. b) Enlargement of red box in a), indicating the August 2012 break-up edge (dashed line), sites of drillings (circles) and the platelet-layer thickness obtained from laterally-constrained Marquardt-Levenberg inversion of multi-frequency EM data (colors). Background: TerraSAR-X image from 15 November 2012, provided by the German Aerospace Agency (DLR). c) Exemplary results for sea-ice and platelet-layer thickness and -conductivity from inversions of Transect 2 (between "1" and "2" indicated in b), along with the range of simultaneous drill-hole measurements obtained in November (red bars) and December 2012 (black bars). d) Corresponding root-mean-square errors (rmse) of individual stations.

The transect data were filtered to obtain a spacing of 4 m between measurements, in order to reduce the computing time. All data were corrected using instrument-specific calibration coefficients, as calculated by *Hunkeler et al.* [2015]. Since we assumed correct calibrations, the uncertainties for in-phase and quadrature recordings at all frequencies reduced to noise measurements in free air [*Hunkeler et al.*, 2015].

In *Hunkeler et al.* [accepted] individual 1D models were stitched together to get a 2D impression of the inversion results along a transect. To build a laterally smooth 2D model, horizontal smoothing of layer conductivities and thicknesses

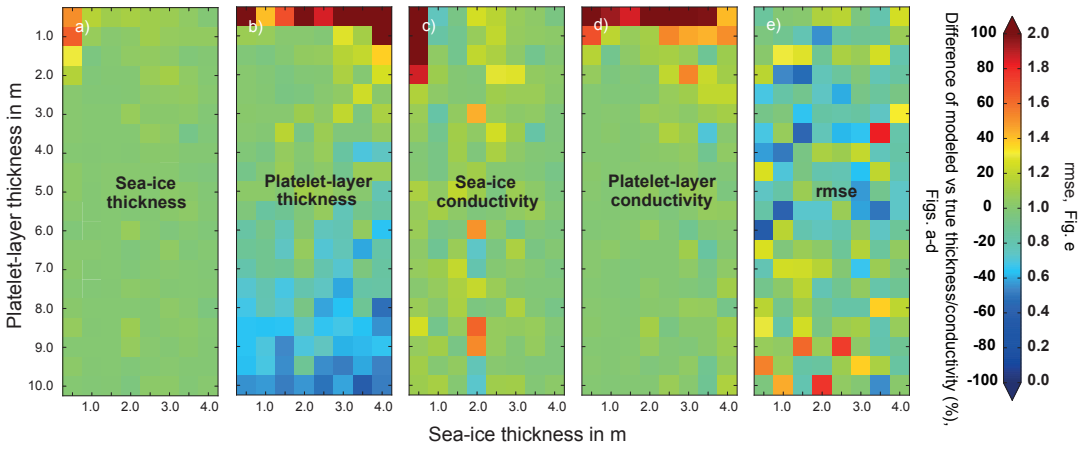

Figure 2. Normalized differences between synthetic data and Marquardt-Levenberg inversion results for various combinations of sea-ice (0.5-4 m) and platelet-layer (0.5-10 m) thicknesses. Results for a) sea-ice thickness, b) platelet-layer thickness, c) sea-ice conductivity, d) platelet-layer conductivity, and e) rmse. Synthetic data were calculated with sea-ice and platelet-layer conductivities of 0.05 Sm^{-1} and 1.15 Sm^{-1}, respectively and seawater conductivity of 2.7 Sm^{-1}. Red (blue) colors indicate overestimations (underestimations) of the inversion results compared to synthetic data.

was implemented in [*Kaufmann*, 2014] by minimizing the differences between layer parameters of adjacent stations. The smoothness constraints were implemented as first-order differences of the layer parameters. The resulting pseudo 2D model contains distinct layers, but smooth lateral variations of conductivity and thickness within each layer. Since we expect the thicknesses of adjacent stations to vary more than their conductivities, we weighted the penalty on conductivity variation four times that of thickness variation. We allowed for a maximum of 100 iterations.

After the inversion, we applied a filter to the results. We defined upper and lower conductivity thresholds at 2.7 and 0.5 Sm^{-1}, between which the data was considered plausible. For platelet-layer conductivities < 0.5 Sm^{-1}, the algorithm often found a wrong minimum with too small platelet-layer conductivities in combination with too thin sea ice + snow. Platelet-layer conductivities above those of seawater (> 2.7 Sm^{-1}) are not possible, and were not considered further. In addition, we excluded stations with a high rmse, ignoring results which exceeded a certain threshold (Table 1). This threshold was estimated by visual inspection, and varied between sub-transects due to the different sea-ice/platelet layer conditions or noise in the data.

3. Results

3.1. Inversion performance

3.1.1. Synthetic data

The differences between the inversion results and the synthetic data are shown in Figure 2, normalized to the true values. The columns correspond to the eight experiments outlined above. For most of the inversions, the rmse was close to 1 (Figure 2e, green), but increased for thicker platelet layers. Calculated sea-ice thicknesses and conductivities (Figures 2 a and c) generally agreed well with the true values, with thin sea ice (0.5 m) and thin platelet layers (0.5 and 1 m) being the exceptions. In these cases, the conductivity and thickness of the sea ice were overestimated. The platelet-layer conductivity (Figure 2d) was also well recovered (± 10 %), except for thin platelet-layer thickness (0.5 and 1 m), where the conductivity was overestimated. The platelet-layer thickness (Figure 2b) was overestimated for a thin platelet layer (0.5 m), and underestimated for a thick platelet layer (> 7 m). But in-between the platelet-layer thickness was resolved within ± 10 %. Since we seldom observed sea-ice thicknesses < 0.5 m and platelet-layer thicknesses > 7 m in the field, we consider the performance of the inversion algorithm to be very reliable. We needed between 3 (3, 3.5, 4 m sea ice) and 54 (0.5 m sea ice) iterations to match the desired rmse of 1.

3.1.2. Most-squares inversion

Error and resolution analyses suggest that due to the limited number of model parameters, all four layer parameters are perfectly resolved. Hence, in assessing how well the layer parameters are constrained, only the model parameter uncertainties need to be further considered by using most-squares inversion.

In Table 2, we present the model uncertainties of six of the 3-layer ML inversion models (cf. Figure 2). In accordance with our expectation that the thickness of a resistive layer is typically better constrained by inductive EM methods than its conductivity [e.g. *Pfaffling and Reid*, 2009], the thicknesses t_s of the sea-ice layer are more tightly constrained than the sea-ice conductivities σ_s ($1/f^-_{MSQ} \geq 0.97$ and $f^+_{MSQ} \leq 1.04$ for t_s compared to $1/f^-_{MSQ} \geq 0.86$ and $f^+_{MSQ} \leq 1.21$ for σ_s). For the sea-ice thicknesses considered here, the uncertainty of the thickness t_p of the platelet layer increases systematically with increasing combined thickness of the sea ice and platelet layers ($1/f^-_{MSQ} = 0.94$ and $f^+_{MSQ} = 1.19$ for $t_s + t_p = 2$ m compared to $1/f^-_{MSQ} = 0.83$ and $f^+_{MSQ} = 1.58$ for $t_s + t_p = 11.5$ m). This suggests that, for the larger combined thicknesses, the constraints provided by the GEM-2 data for the deeper part of the platelet layer are limited. The uncertainty of the conductivity σ_p of the platelet layer varies with the thickness of the overlying sea-ice ($1/f^-_{MSQ} \geq 0.91$ and $f^+_{MSQ} \leq 1.06$, $1/f^-_{MSQ} \geq 0.95$ and $f^+_{MSQ} \leq 1.06$ and $1/f^-_{MSQ} = 0.90$ and $f^+_{MSQ} = 1.12$ for $t_s = 1$m, 2.5 m and 4 m, respectively). That σ_p appears to be more tightly constrained for $t_s = 2.5$m may result from, that $t_s = 2.5$m matches more favorably to the depth of investigation range of the instrument than the other values of t_s analyzed.

Table 2. Error estimates for conductivities σ and thicknesses t of the sea ice (subscript s) and platelet (subscript p) layers of some of the 3-layer Marquardt-Levenberg models in Figure 2. Error estimates $1/f^{-}_{MSQ}$ and f^{+}_{MSQ} are computed using most-squares inversions involving truncated singular value decomposition with a truncation level $p = 4$, the effective number of model parameters. Error estimates were calculated for often observed sea-ice and platelet-layer thicknesses, marked in Figure 3d.

Parameter	$1/f^{-}_{MSQ}$	f^{+}_{MSQ}	$1/f^{-}_{MSQ}$	f^{+}_{MSQ}
	1 m sea ice + 1 m platelet layer		1 m sea ice + 3 m platelet layer	
σ_s	0.92	1.04	0.91	1.02
σ_p	0.91	1.06	0.99	1.01
t_s	0.97	1.04	0.99	1.01
t_p	0.94	1.19	0.96	1.09
	2.5 m sea ice + 4.5 m platelet layer		2.5 m sea ice + 5.5 m platelet layer	
σ_s	0.88	1.17	0.86	1.21
σ_p	0.95	1.06	0.95	1.05
t_s	0.97	1.03	0.97	1.03
t_p	0.89	1.16	0.84	1.32
	2.5 m sea ice + 9 m platelet layer		4 m sea ice + 5.5 m platelet layer	
σ_s	0.86	1.21	0.96	1.05
σ_p	0.95	1.05	0.90	1.12
t_s	0.97	1.03	0.97	1.03
t_p	0.83	1.58	0.80	1.31

3.1.3. Transects

Generally, the rmse of the field data inversions were higher compared to the inversions of synthetic data. Highest rmse were found for the first section of transect 5, where the platelet layer was especially thick and a rmse threshold of 25 was used (Table 1). The lowest rmse was for each transect found for iteration 100, the defined maximum value. Higher rmse from field data inversion compared to synthetic data inversion may originate from the higher number of stations. But also systematic errors, as an incorrect calibration or the drift of the instrument, or vibrations and jerks of the EM instrument in the kayak behind the snowmobile may play a role.

For transect 2, the rmse of individual stations is shown in Figure 1d. In total, 291 of 6442 stations from transect 2 exceeded the defined thresholds of rmse (> 10) and of the platelet-layer conductivity (< 0.5 and > 2.7 Sm^{-1}). Generally, our models compare favorably to drill-hole measurements, which confirmed our confidence in the inversion results (more below).

3.2. Sea ice and platelet-layer spatial variability

All the transects were inverted for sea-ice and platelet layer thickness and conductivity. Figure 1b presents the resulting platelet-layer thicknesses (t_p), overlaid on a TerraSAR-X image from 15 November 2012, obtained shortly before the GEM-2 transects. t_p ranged between 0 and 10 m, with the lowest values (< 2 m) lying within the August break-up area (dashed line) and the highest (7-10 m) in the central south as well as close to the southern ice-shelf edge. t_p generally increased towards the ice-shelf edges bordering the bay in the west and south, but decreased towards the eastern margin.

Figure 1c gives a detailed view on the inversion results of Transect 2, which followed a regular route between the northern sea-ice ramp (labeled "1") and the westernmost point, ATKA24 (labeled "2"). The combined sea-ice plus snow thickness, t_s, is plotted in positive y-direction and ranged between 0.56 and 9.15 m. A thin sea-ice + snow layer was found in the break-up area, whereas the largest layer thickness was found in dynamically deformed area at the beginning of the transect. Thick snow + sea ice between ATKA03 and ATKA07 is the result of snow accumulation behind an iceberg. t_s was generally more homogeneous in the thermodynamically grown eastern part of the bay compared to the deformed western part. The overall snow and sea-ice distribution in the Atka Bay has been discussed in detail in an earlier study [*Hoppmann et al.*, 2015b]. The bulk conductivity of sea-ice plus snow, σ_s, varied between 0.013 and 0.538 Sm^{-1}. Highest conductivities were found in the break-up area, where flooding was observed.

The platelet-layer thickness t_p is plotted in negative y-direction and ranged between 0.63 and 6.63 m. The platelet-layer conductivity σ_p ranged from 0.50 to 2.68 Sm^{-1}. The thinnest and most conductive platelet layer was found in the break-up area, whereas the lowest conductivities of the platelet layer were observed in deformed areas (western part of break-up area) and at the location of the thickest sea-ice and snow load. The latter finding has to be regarded with care as it is unlikely that low conductivities exist only where the load is high. In the western part of the bay the platelet-layer thickness was around 1 m thicker than in the eastern part. There was a sharp cut in platelet-layer thickness at the eastern break-up edge nearby ATKA16, whereas platelet-layer thickness gradually increased in the deformed western edge nearby ATKA11.

The EM-derived thickness results are in very good agreement with manual measurements obtained from drillings at regular sites in November (range indicated by red bars in Figure 1c) and December (black bars). The bars show the total range, where at each site up to 5 measurements were taken. The level of agreement between t_p and the drillings is remarkable, especially when taking into account that the manual measurements by the metal-bar method likely underestimated the true thickness [*Hoppmann et al.*, 2015b].

3.3. Thickness and conductivity distributions

We calculated histograms from inversion results of sea-ice and platelet layer conductivity and thickness, combining data of all transects. t_s and t_p both exhibited a broad distribution with several modes (Figures 3a and b), with peaks at 0.8 and 2.6 m for t_s, and 0.7, 4.3 and 5.5 m for t_p. The corresponding 2D histogram shows a bimodal distribution (Figure 3d). The mode with thinner thicknesses corresponded to the sea ice and platelet layer in the break-up area. The broader mode corresponded to thicker fast ice and platelet layer, which may represent the thermodynamically grown sea ice overlying a platelet layer of undisturbed accumulation. A thicker platelet layer may correspond do rather deformed areas in the southwestern/western part of the bay.

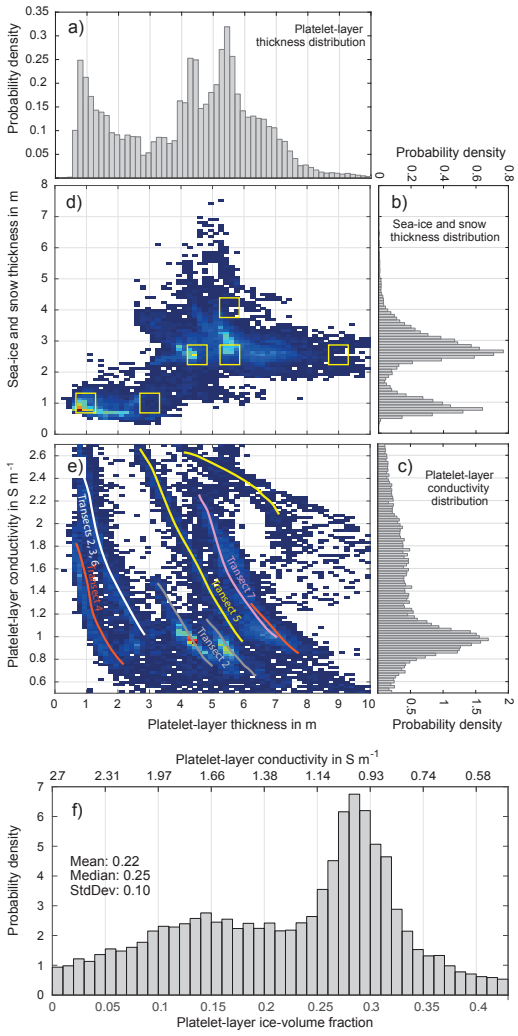

Figure 3. Probability density distributions of transects 2-7 of a) platelet-layer thickness, b) sea-ice + snow thickness, and c) platelet-layer conductivity. 2D histograms of d) platelet-layer vs. sea-ice + snow thickness and e) platelet-layer thickness vs. platelet-layer conductivity. Yellow squares in d) indicating the thicknesses used for most-squares inversions of synthetic data (Table 2). Colored lines in e) show roughly which transects the data belong to. f) Distribution of platelet-layer ice-volume fractions calculated from Archie's Law assuming a cementation factor m = 3. A distinct peak of the distribution is observed at a platelet-layer ice-volume fraction of 0.27.

σ_p exhibited a very broad distribution with a peak at around 1 Sm^{-1} (Figure 3c). The 2D histogram of σ_p and t_p reveals an inversely proportional dependency of t_p and σ_p (Figure 3e). This is plausible since a thicker platelet layer is likely more compressed because of increased buoyancy of underlying platelets and compaction due to ocean currents, leading to lower conductivity. These relationship was found for all individual transects (Figure 3e).

3.4. Platelet-layer ice-volume fraction

As demonstrated in an earlier study [*Hunkeler et al.*, 2015], we converted the conductivity of the platelet layer (σ_p) to its ice-volume fraction (β) using Archie's law

$$\beta = 1 - \sqrt[m]{\frac{\sigma_p}{\sigma_b}}, \qquad (1)$$

where σ_b is the brine conductivity (seawater conductivity of 2.7 Sm^{-1}), m is the cementation factor, and β is 1 minus the porosity Φ [*Archie*, 1942].

The distribution of ice-volume fractions β (in Figure 3f shown for m = 3) is generally similar to the distribution of σ_p. For m = 3, the mean, median and standard deviation are 0.22, 0.25 and 0.10, respectively. Depending on the choice of m, the distribution of β shifts to the left (m > 3) or right (m < 3). For m = 2, the mean, median and standard deviation are 0.31, 0.35 and 0.13, respectively. For m = 4, the mean, median and standard deviation are 0.17, 0.19 and 0.08, respectively.

4. Discussion

Owing to its pronounced increase in conductivity with depth, the 3-layer case of sea ice, platelet layer and seawater is an ideal target for inversions of electromagnetic induction sounding data [*Spies and Frischknecht*, 1991]. We deal with clearly distinct layers and a well-defined underlying homogeneous half space (seawater). Since the conductivity exhibits abrupt changes in vertical direction, we decided to use a Marquardt-Levenberg inversion for layer conductivities and thicknesses. The additionally employed lateral constraints between the layer parameters of abutting stations are well suited to mimic the smooth changes of layer conductivities in lateral direction. Moreover, giving more weight to lateral smoothing of conductivities than to thickness, accounts for the possibility of abrupt changes of layer thicknesses between abutting stations. Hence, by using laterally-constrained Marquardt-Levenberg inversion we have a reasonable tool to process the EM induction sounding data collected across Atka Bay.

We assumed here for three distinct, perfectly homogeneous layers, but by measuring sea-ice or platelet layer thickness in the field, we often experienced inhomogeneities in sea ice and platelet layer, especially in the western deformed area of Atka Bay. Interior melt of fast ice in summer [*Hoppmann et al.*, 2015a] for example leads to an increased permeability. Once a certain permeability is reached, it may lead to surface flooding given that the snow load on top is high enough to suppress the ice surface below the water level. Through this process, a highly conductive layer of slush is formed at the surface. In the break-up area this was observed in the field [*Paul et al.*, 2015], but also in the inversion results (purple sea ice in Figure 1c). Since it is in principle possible to determine the presence of surface flooding from EM data [*Hunkeler et al.*, 2015], we included an additional free layer to invert for an additional conductive layer above sea ice. But we were not successful to resolve for this additional layer, maybe the sea ice was already too porous and contained also higher conductivities.

Generally, Marquardt-Levenberg inversion results of synthetic data support the sensitivity of the employed EM instrument to both sea-ice and platelet-layer conductivity and thickness for platelet layer > 0.5 m and < 7 m (Figure 2b).

The most-squares inversions of synthetic data were calculated for the modes in Figure 3d. The results indicate that the platelet-layer thickness is poorly constrained for relatively thick sea ice + platelet layer (Table 2). Anyhow, the results from transects 2 fit perfectly to drill-hole measurements of sea-ice and platelet-layer thickness.

With the breakup event in August we had a special sea-ice situation in the Atka Bay. This was a lucky circumstance for studying the evolution of sea ice and the underlying platelet layer with its different formation dates and thus ages. In general, conductivity is higher for a thinner and younger platelet layer, which implies that an older thick platelet layer is more compacted and denser than a young thin platelet layer (Figure 3e). The conversion of platelet-layer conductivity with Archie's law [*Archie*, 1942] to ice-volume fraction reveals a broad distribution depending on the thickness and age of the platelet layer. *Hunkeler et al.* [2015] used mainly calibration measurements at ATKA11 over thin sea ice and platelet layer to calculate platelet-layer conductivities of 1154 ± 271 Sm^{-1} and from that ice-volume fractions of 0.29 (m = 2.5) to 0.43 (m = 1.5). The assumption of cementation factor $m \approx 2$ might be a reason why *Hunkeler et al.* [2015] retrieved higher ice-volume fraction than recent studies, which found ice-volume fractions of 0.25 ± 0.06 [*Gough et al.*, 2012] and 0.18 ± 0.09 [*Hoppmann et al.*, 2015a]. By using different compaction factors m, the ice-volume fraction distribution in Figure 3f is shifted horizontally. To obtain the best agreement with the ice-volume fractions suggested by *Gough et al.* [2012] and *Hoppmann et al.* [2015a], cementation factors m = 3 or even higher may need to be considered. *Jackson et al.* [1978] found a cementation factor of 1.9 for platy shell fragments with a sphericity of 0.5. Loose platelets may be even less spherical which would lead to a higher cementation factor.

Besides buoyancy, the compaction of the platelet layer may depend on ocean currents and their transport and redistribution below sea ice. The spatial homogeneity of the platelet layer over relatively large distances is an indication of the tendency of loose crystals to redistribute over kilometer scale under the influence of currents. The thickest platelet-layer is found in the southwestern area of the bay (Figure 1b), where individual ice platelets may be released from the ice-shelf cavity. However, easterly currents probably lead to an increasing platelet-layer thickness in the western part of the break-up area, whereas the break-up edge at the eastern side is perfectly sharp. Therefore, a smaller amount of ice platelets is released from some cavities in the eastern part of the bay.

Hoppmann et al. [2015b] found for 2012 an average annual platelet-layer thickness of 4 m. Neglecting thin sea ice in the break-up area, the obtained platelet-layer thicknesses from EM data with modes between 4-6 m (Figure 3a) suggest, that the platelet-layer in 2012 was even thicker. Therefore, also the contribution of ocean/ice-shelf interaction to ice volume in this region might be even higher than previously thought.

Our next steps involve adaption of EM induction measurements for platelet-layer retrieval to airborne devices, since potentially a platelet layer can be found in Antarctic coastal areas underneath fast ice [*Fraser et al.*, 2012] or mobile sea ice close to ice shelves.

5. Conclusion

In this study, we obtained a substantial multi-frequency EM induction sounding dataset on an Antarctic fast-ice regime with an underlying platelet layer. We calculated fast-ice and platelet-layer thickness and conductivity using this unique dataset as an input for a laterally-constrained Marquardt-Levenberg inversion scheme. Our results provide evidence that platelet-layer thickness retrieval is possible using a non-destructive method, significantly facilitating its volume estimation. When applied regularly on more sites in coastal Antarctica, this approach could be an important and step towards a better understanding of ocean/ice-shelf/sea-ice interaction, without the need for extensive logistics. The current limitation to spatial scales of up to 100 km due to operation by snowmobiles could be overcome by an adaptation of this methodology to airborne multi-frequency EM measurements.

Acknowledgments.

This work would not have been possible without the Neumayer III infrastructure and the help of the wintering crew 2012. The authors are grateful to Stephan Paul and Uwe Baltes for their assistance in the field, and to the AWI logistics for their support. The computations were performed on resources provided by SNIC through Uppsala Multidisciplinary Center for Advanced Computational Science (UPPMAX) under Project snic2014-1-243. Johan Hermansson at UPPMAX is acknowledged for assistance concerning technical and implementational aspects in making the code run on the UPPMAX resources. This work was funded by the POLMAR graduate school and the German Research Council (DFG) in the framework of its priority program "Antarctic Research with comparative investigations in Arctic ice areas" by grants to SPP1158, NI 1092/2 and HE2740/12. The data used here are publicly available at http://doi.pangaea.de/10.1594/PANGAEA.845535.

References

Anderson, W. L., Numerical integration of related Hankel transforms of orders 0 and 1 by adaptive digital filtering, *Geophysics*, *44*(7), 1287–1305, 1979.

Archie, G. E., The Electrical Resistivity Log as an Aid in Determining Some Reservoir Characteristics, *Transactions of the AIME*, *146*, doi:10.2118/942054-G, 1942.

Arrigo, K. R., D. H. Robinson, and C. W. Sullivan, A high-resolution study of the platelet ice ecosystem in McMurdo Sound, Antarctica: Photosynthetic and bio-optical characteristics of a dense microalgal bloom, *Marine Ecology Progress Series*, *98*(1-2), 173–185, doi:10.3354/meps098173, 1993.

Auken, E., A. V. Christiansen, B. H. Jacobsen, N. Foged, and K. I. Sørensen, Piecewise 1D laterally constrained inversion of resistivity data, *Geophysical Prospecting*, *53*(4), 497–506, doi:10.1111/j.1365-2478.2005.00486.x, 2005.

Crocker, G., Physical processes in Antarctic landfast sea ice, Ph.D. thesis, University of Cambridge, 1988.

Eicken, H., and M. A. Lange, Development and properties of sea ice in the coastal regime of the southeastern Weddell Sea, *Journal of Geophysical Research: Oceans*, *94*(C6), 8193–8206, doi:10.1029/JC094iC06p08193, 1989.

Fraser, A. D., R. A. Massom, K. J. Michael, B. K. Galton-Fenzi, and J. L. Lieser, East Antarctic landfast sea ice distribution and variability, 2000-08, *Journal of Climate*, *25*(4), 1137–1156, doi:10.1175/JCLI-D-10-05032.1, 2012.

Gough, A. J., A. R. Mahoney, P. J. Langhorne, M. J. M. Williams, N. J. Robinson, and T. G. Haskell, Signatures of supercooling: McMurdo Sound platelet ice, *Journal of Glaciology*, *58*(207), 38–50, doi:10.3189/2012JoG10J218, 2012.

Grab, M., Forward and inverse modelling of frequency-domain electromagnetic data from small coils, *Master Thesis, IDEA League, ETH Zurich*, 2012.

Günther, S., and G. S. Dieckmann, Seasonal development of algal biomass in snow-covered fast ice and the underlying platelet layer in the Weddell Sea, Antarctica, *Antarctic Science*, *11*(3), 305–315, doi:10.1017/S0954102099000395, 1999.

Günther, S., and G. S. Dieckmann, Vertical zonation and community transition of sea-ice diatoms in fast ice and platelet layer, Weddell Sea, Antarctica, *Annals of Glaciology*, *33*(1), 287–296, doi:10.3189/172756401781818590, 2001.

Hoppmann, M., M. Nicolaus, S. Paul, P. A. Hunkeler, P. Heil, L.-K. Behrens, G. König-Langlo, and R. Gerdes, Seasonal evolution of an ice-shelf influenced fast-ice regime, derived from an autonomous thermistor chain, *Journal of Geophysical Research: Oceans*, *120*, 17031724, doi:10.1002/2014JC010327, 2015a.

Hoppmann, M., M. Nicolaus, S. Paul, P. A. Hunkeler, G. Heinemann, S. Willmes, R. Timmermann, and O. Boebel, Ice platelets below Weddell Sea land-fast sea ice, *Annals of Glaciology*, *56*(69), 175–190, doi:10.3189/2015AoG69A678, 2015b.

Hunkeler, P. A., S. Hendricks, M. Hoppmann, S. Paul, and R. Gerdes, Towards an estimation of sub-sea-ice platelet-layer volume with multi-frequency electromagnetic induction sounding, *Annals of Glaciology*, *56*(69), 137–146, doi: 10.3189/2015AoG69A705, 2015.

Hunkeler, P. A., S. Hendricks, M. Hoppmann, C. G. Farquharson, T. Kalscheuer, M. Grab, M. S. Kaufmann, L. Rabenstein, and R. Gerdes, Improved 1D inversions of sea ice thickness and conductivity from EM induction data: Algorithms to account for nonlinearities caused by passive bucking, *Geophysics*, accepted.

Jackson, D. D., Most squares inversion, *Journal of Geophysical Research*, *81*(5), 1027–1030, 1976.

Jackson, P., D. T. Smith, and P. Stanford, Resistivity-porosity-particle shape relationships for marine sands, *Geophysics*, *43*(6), 1250–1268, doi:10.1190/1.1440891, 1978.

Kalscheuer, T., EMILIA - ElectroMagnetic Inversion with Least Intricate Algorithms User manual, *Tech. rep.*, Uppsala University, Department of Earth Sciences, 2014.

Kalscheuer, T., and L. B. Pedersen, A non-linear truncated SVD variance and resolution analysis of two-dimensional magnetotelluric models, *Geophysical Journal International*, *169*(2), 435–447, doi:10.1111/j.1365-246X.2006.03320.x, 2007.

Kalscheuer, T., M. D. l. Á. G. Juanatey, N. Meqbel, and L. B. Pedersen, Non-linear model error and resolution properties from two-dimensional single and joint inversions of direct current resistivity and radiomagnetotelluric data, *Geophysical Journal International*, *182*(3), 1174–1188, doi:10.1111/j.1365-246X.2010.04686.x, 2010.

Kalscheuer, T., J. Hübert, A. Kuvshinov, T. Lochbühler, and L. B. Pedersen, A hybrid regularization scheme for the inversion of magnetotelluric data from natural and controlled sources to layer and distortion parameters, *Geophysics*, *77*(4), E301–E315, doi:10.1190/geo2012-0018.1, 2012.

Kalscheuer, T., M. Bastani, S. Donohue, L. Persson, A. Pfaffhuber, F. Reiser, and Z. Ren, Delineation of a quick clay zone at Smørgrav, Norway, with electromagnetic methods under geotechnical constraints, *Journal of Applied Geophysics*, *92*, 121–136, 2013.

Kaufmann, M. S., Pseudo 2D inversion of multi-frequency coil-coil FDEM data, Master's thesis, Master Thesis, IDEA League, ETH Zurich, 2014.

Kipfstuhl, J., On the formation of underwater ice and the growth and energy budget of the sea ice in Atka Bay, Antarctica (Zur Entstehung von Unterwassereis und das Wachstum und die Energiebilanz des Meereises in der Atka Bucht, Antarktis, mostly in German), *Reports on Polar and Marine Research (Berichte zur Polarforschung)*, *85*, 88p, doi:hdl:10013/epic.10085.d001, 1991.

Lewis, E. L., and R. G. Perkin, Ice pumps and their rates, *Journal of Geophysical Research: Oceans*, *91*(C10), 11,756–11,762, doi:10.1029/JC091iC10p11756, 1986.

Lines, L. R., and S. Treitel, Tutorial: A review of least-squares inversion and its application to geophysical problems, *Geophysical prospecting*, *32*(2), 159–186, 1984.

Meju, M., and V. Hutton, Iterative most-squares inversion: application to magnetotelluric data, *Geophysical journal international*, *108*(3), 758–766, doi:10.1111/j.1365-246X.1992.tb03467.x, 1992.

Meju, M. A., Biased estimation: a simple framework for inversion and uncertainty analysis with prior information, *Geophysical Journal International*, *119*(2), 521–528, doi:10.1111/j.1365-246X.1994.tb00139.x, 1994.

Paul, S., S. Willmes, M. Hoppmann, P. A. Hunkeler, G. Heinemann, M. Nicolaus, and R. Timmermann, The impact of early summer snow properties on land-fast sea-ice X-band backscatter, *Annals of Glaciology*, *56*(69), 263–273, doi: 10.3189/2015AoG69A715, 2015.

Pfaffling, A., and J. E. Reid, Sea ice as an evaluation target for HEM modelling and inversion, *Journal of Applied Geophysics*, *67*(3), 242–249, doi:10.1016/j.jappgeo.2008.05.010, 2009.

Price, D., W. Rack, P. J. Langhorne, C. Haas, G. Leonard, and K. Barnsdale, The sub-ice platelet layer and its influence on freeboard to thickness conversion of Antarctic sea ice, *The Cryosphere*, *8*(3), 1031–1039, doi:10.5194/tc-8-1031-2014, 2014.

Rack, W., C. Haas, and P. J. Langhorne, Airborne thickness and freeboard measurements over the McMurdo Ice Shelf, Antarctica, and implications for ice density, *Journal of Geophysical Research: Oceans*, *118*(11), 5899–5907, doi: 10.1002/2013JC009084, 2013.

Spies, B. R., and F. C. Frischknecht, Electromagnetic sounding, pp. 285–426, Oklahoma City, OK: Society of Exploration Geophysicists, 1991.

Vacchi, M., M. Mesa, and S. Greco, The coastal fish fauna of Terra Nova Bay, Ross Sea, Antarctica, in *Ross Sea Ecology (ed F. M. Faranda and L. Guglielmo and A. Ianora)*, chap. 32, pp. 457–468, Springer Berlin Heidelberg, doi:10.1007/978-3-642-59607-0_32, 2000.

P. A. Hunkeler, Alfred-Wegener-Institut Helmholtz-Zentrum für Polar- und Meeresforschung, Bussestr. 24, 27570 Bremerhaven, Germany. (Priska.Hunkeler@awi.de)

Appendix IV

Publication VII: ”TSX-data for studies of snow on ice sheets and sea ice - preliminary results”

By Wolfgang DIERKING, Stefanie LIENOW, Christine WESCHE, Wolfgang RACK, **Mario HOPPMANN** and Sascha WILLMES

This paper is published in Proceedings of the 5. TerraSAR-X / 4. Tandem-X Science Team Meeting.

TSX-DATA FOR STUDIES OF SNOW ON ICE SHEETS AND SEA ICE – PRELIMINARY RESULTS

Wolfgang Dierking[1], Stefanie Linow[1], Christine Wesche[1], Wolfgang Rack[2], Mario Hoppmann[1], Sascha Willmes[3]

[1]The Alfred Wegener Institute, Helmholtz Centre for Polar and Marine Research, Bussestr. 24, 27570 Bremerhaven, Germany, Wolfgang.Dierking@awi.de
[2]Gateway Antarctica, Center for Antarctic Studies and Research, University of Canterbury, Private Bag 4800, 8140 Christchurch, New Zealand, Wolfgang.Rack@canterbury.ac.nz
[3]Environmental Meteorology, University of Trier, Behringstraße 21, D-54286 Trier, Germany, willmes@uni-trier.de

ABSTRACT

The balances between mass gain and loss of the ice sheets and of the polar sea ice have received increased attention because of their influence on changes of Earth's environment. In this context, investigations of snow accumulation on ice sheets and snow load on sea ice are important topics of recent research. This short note motivates the need for such investigations. First results addressing snow accumulation rates over Dronning Maud Land (Antarctica) and snow deposition on sea ice in Atka Bay (Dronning Maud Land) obtained from TSX images are presented.

1 Introduction

Considering the influence of climate change on the environmental conditions in the Polar Regions (and vice versa the effect of environmental changes in the Polar Regions on regional and global climate), the mass balances of ice sheets and sea ice need to be continuously monitored. The mass balances of the ice sheets, i. e. the difference between mass gain by snow accumulation and mass loss by melting processes and iceberg calving, affect, e. g., sea level variations and the freshwater flux into the ocean [1]. The mass balance of sea ice is reflected by variations of its extent, concentration (areal fraction of ice per unit area), drift, deformation, and thickness and has an impact on parameters related to climate, such as the albedo [2]. However, monitoring strategies are complex and require elaborate measurements including the use of different satellite sensors. Here, we discuss the role of the TSX mission in retrieving information about snow accumulation on ice sheets and snow load on sea ice. The former is of importance to estimate the gain of mass of the Antarctic and Greenland ice sheets as function of time and space, the latter plays an important role in the retrieval of sea ice thickness using laser or radar altimetry.

Over the ice sheets, the accumulation needs to be known over large areas. Ground measurements serve as calibration and validation points [3]. Satellite data from sensors with large spatial coverage and high temporal sampling rate (such as passive microwave radiometers) are used to interpolate between these points [4]. SAR data have been applied on regional and local scales [5]. The radar backscattering intensity depends on the snow/firn grain size and the thickness of the annual firn layers, besides firn density and temperature. (Firn is a transition stage between snow and glacial ice with densities of 400-830 kg/m^3.) Since large grain sizes and thin annual layers are characteristic for low accumulation, and small grains deposited in thicker layers are typical for high accumulation, radar can be used to indirectly measure accumulation rates. It is important to emphasize that the measured rates are averages down to depths determined by the penetration of the radar waves into the firn. For a detailed discussion of accumulation retrieval by means of SAR see Dierking et al. [5].

For measurements of sea ice thickness using Cryosat-2 (radar altimeter data), individual radar echoes reflected from the ground are separated into groups separating first-year and multi-year ice from open water and thin ice. The ice freeboard (i. e. the vertical distance between the ice surface and the water surface) is obtained by subtracting travel times over ice from travel times over water. The conversion of freeboard into ice thickness is carried

out assuming hydrostatic equilibrium. Hereto, the average ice and water densities are needed as well as the snow mass per unit area on the ice [6].

2 Data

In the studies presented here we concentrate on Dronning Maud Land in Antarctica (western boundary 20°W, eastern boundary 44°38'E). The Atka Bay, which is a test site for studying snow on sea ice, is located at 70°35'S 7°51'W.

The objective of our investigations on accumulation rates on the ice sheets is to analyse whether multi-frequency and multi-polarization SAR data improve the retrieval of accumulation rates and provide additional insight into the interaction between radar waves and firn. Besides the ASAR images mentioned in [5], we used six RS-2 (Radarsat-2) images from January 2012 (quad-pol., five from ascending orbit, one descending, incidence angles 30.4°-32°, pixel size 25 m) and 18 TSX images acquired from February to April 2013 (stripmap HH- and VV-polarization, ten from ascending orbit, eight descending, incidence angles 27.5°-33.4°, pixel size 10 m). The images were acquired over the Kottas Traverse in Dronning Maud Land, for which in-situ measured accumulation data are available (see **Figure 1**).

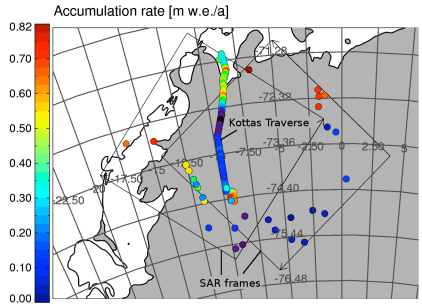

Figure 1 Accumulation rates along the Kottas Traverse and adjacent test sites. Also shown are the positions of two ASAR WSM-frames (ascending and descending orbit) used for the analysis.

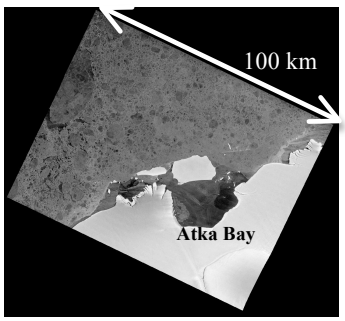

Figure 2 Fast sea ice in Atka Bay. The larger iceberg grounded at the northern border of the Bay is B15G. The elongated iceberg west of it is drifting.

For the study dealing with snow on sea ice we analysed four TSX-ScanSAR images (HH-polarization, incidence angles at image centre between 34.3° and 42.0°, pixel size 25 m) and eight scenes in stripmap-mode (4 HH+VV-pol., 2 HH+HV-pol., 2 HH single-polarization, incidence angles between 20.8° and 44.6°, pixel size 6 m). A TSX-ScanSAR scene from Atka Bay is shown in **Figure 2**.

3 Results

3.1 Kottas Traverse – Land Ice

The radar backscattering characteristics of firn depend on size, shape, orientation, volume fraction, and absorption loss of the scattering elements, and on the absorption loss of the background medium. In low-density firn closer to the surface of the ice sheets, scattering originates from snow grains, and the background medium is air. At larger depths, isolated air bubbles scatter the penetrating radar waves, whereas ice is the host medium. The volume

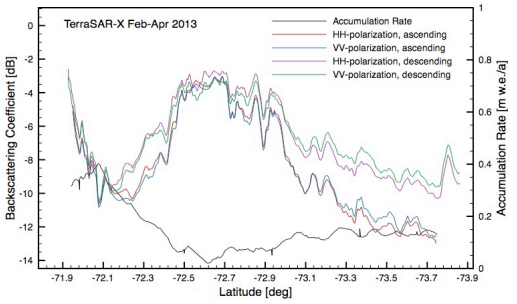

Figure 3 Radar backscattering coefficients measured at X-band (HH- and VV-polarization) along the Kottas Traverse from ascending (headings 321-326°) and descending orbit (214-219°) Also shown is the accumulation rate measured in-situ.

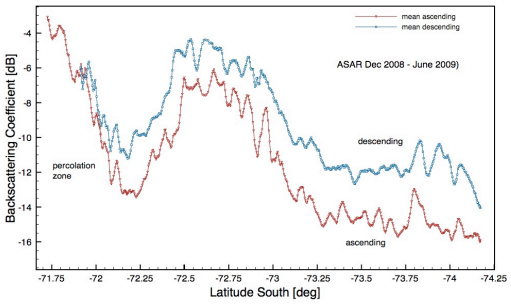

Figure 4 Radar backscattering coefficients measured at C-band (ASAR WSM, HH-polarization) over the Kottas Traverse from ascending (heading 344°) and descending (195°) orbit.

scattering contribution is usually calculated assuming that the scattering particles are of spherical shape [5]. Over the ice sheets, it is observed that the radar backscattering coefficient depends on look direction [7]. This azimuthal anisotropy is related to wave-like undulations of the ice surface on scales of decimetres to tens of metres (sastrugi). Since the surface scattering contribution of dry snow and firn is very low, it is assumed that also the surfaces from former years, which are buried under the most recent snow layers, contribute to the radar scattering.

In **Figure 3**, the backscattering coefficients obtained from TSX images along the Kottas-Traverse are depicted. They reveal a small difference between HH- and VV-polarization (0-0.5 dB) and a varying difference (0-3 dB) between ascending and descending orbit, with small values at low accumulation rates. For comparison, the results found at C-band HH-polarization (data source: ASAR WSM imagery) are shown in **Figure 4** . At low accumulation rates, the difference between ascending and descending orbit is between 0.5 and 3 dB, for higher rates, it varies between 3 and 5 dB. North of about 72.1°S along the Kottas traverse, the firn regime changes from dry snow to the percolation zone. In this regime, radar backscattering characteristics are more complex due to varying moisture content and the formation of ice lenses, pipes and channels in the firn volume.

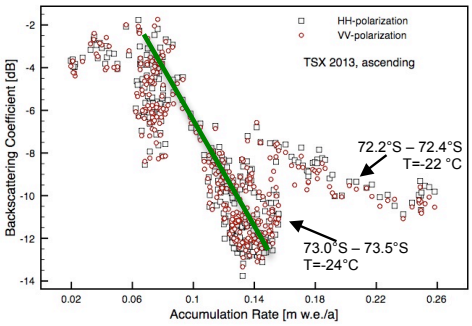

Figure 5 TSX-backscattering coefficients as a function of accumulation rate, measured along the Kottas-Traverse (ascending orbit).

One goal of our study is to find a relationship between measured radar parameters and the accumulation rate. In this context, we discuss the results presented in Figs. 5-7. In **Figure 5**, the X-band backscattering coefficients σ^0 at VV- and HH-polarization observed along the Kottas-Traverse are plotted as functions of the accumulation rate. For low accumulation rates (<0.05 m w.e./a) there is no recognizable sensitivity. At mid range (accumulation rates from 0.05 to 0.15 m w.e./a), σ^0reveals a strong gradient, indicated by the green line. However, in this case the data from the profile segment 72.2-72.4°S are excluded. They indicate a much weaker gradient. Since in dual-polarization stripmap mode of TSX, both channels are acquired coherently, we can also investigate the phase difference between the HH- and VV-polarized radar sinal. Over the Kottas Traverse, the phases are only weakly sensitive to the accumulation (for data from the ascending orbit even less than for descending orbit, see **Figure 6**). For comparison we show the corresponding result from RS-2 for which the phase sensitivity is much stronger.

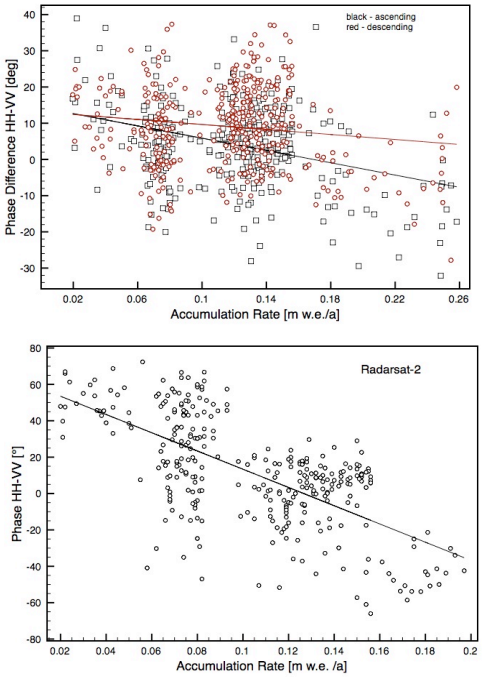

Figure 6 Phase difference between the HH- and the VV-polarized channel as a function of accumulation rate, measured along the Kottas Traverse. Top: from TSX-data (ascending and descending orbit). Bottom: from RS-2 (ascending orbit).

3.2 Atka Bay – Sea Ice

On the fast sea ice in Atka Bay, field measurements were carried out from November 2012 until January 2013. The data include snow thickness, depth profiles of snow temperature, density, and grain size, and ice properties at a number of test sites distributed over the frozen bay area. Snow thickness was highly variable (0-0.8 m). During a strong storm event, the snow was redistributed. Melt onset started in mid December.

The goal of this study is to assess whether properties of a snow layer on sea ice can be retrieved from radar data, and - if this is the case – under which conditions. In this initial phase of our study we focus on analysing radar signatures acquired for dif-

ferent surface and ice characteristics (sea ice type , surface roughness, snow properties). In **Figure 7**, cases are shown where the effect of snow, e. g. on the downwind side of an iceberg, can be recognized in TSX-images. It is interesting to note that the varying snow and ice properties are not only reflected in the radar intensity but also in the phase difference between the HH- and VV-polarized channel and the corresponding correlation (see **Figure 8**).

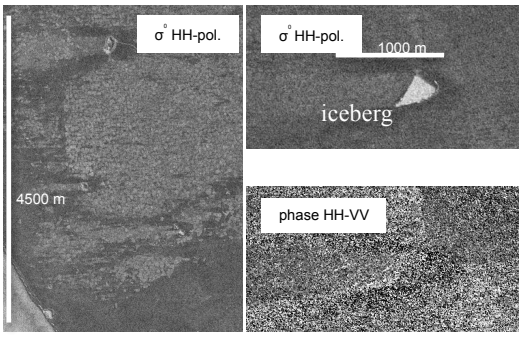

Figure 7 X-band backscattering coefficient at HH-polarization and phase difference HH-VV observed on fast sea ice in Atka Bay (TSX stripmap mode).

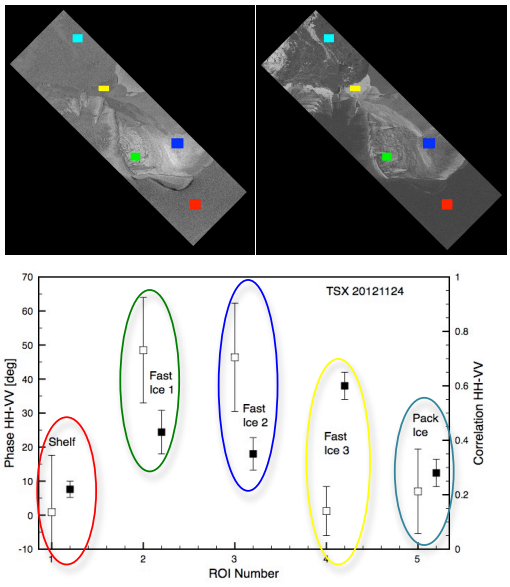

Figure 8 Phase difference and correlation between the HH- and VV-polarized TSX-signal over Atka Bay fast sea ice (test sites marked yellow, green and blue), pack ice (light blue) and the ice shelf (red). Black squares: correlation, white squares: phase.

4 Discussion

The TSX and RS-2 data acquired over the Kottas Traverse reveal a rather noisy pattern when plotted as a function of accumulation rate (Figs. 5 and 6), which poses a problem for developing a robust algorithm for retrieving average accumulation rates using SAR. Here further work is required for devising a method for pre-processing the SAR data. The sensitivities of the backscattering coefficient to accumulation rates at like-polarization are comparable at C- and X-band. At C-band the sensitivity at cross-polarization is larger than at like-polarization. The phase difference changes significantly as a function of accumulation rate at C-band but not at X-band. The reason for this sensitivity and the difference between C- and X-band needs to be analysed in detail. Also the differences of azimuthal anisotropy at C- and X-band will be studied further, taking into account the scene headings and radar penetration depths. For the Atka Bay, spatial and temporal variations of the TSX-backscattering signature have to be related to the snow and ice properties measured in the field. Our preliminary results indicate that phase difference and correlation between the HH- and VV-channel might give information about snow and ice conditions that is complementary to the radar intensity patterns.

Acknowledgement

Radar images were provided by projects TSX-OCE1592, TSX-MTH0123, and Radarsat-2 SOAR-EU 6766 which we gratefully acknowledge.

References

[1] Rignot, E., I. Velicogna, M. R. van den Broeke, A. Monaghan, and J. T. M. Lenaerts, *Acceleration of the contribution of the Greenland and Antarctic ice sheets to sea level rise*, Geophys. Res. Lett., 38, L05503, doi:10.1029/2011GL046583, 2011

[2] Serreze, M. C., M. M. Holland, and J. Stroeve, *Perspectives on the Arctic's shrinking sea ice cover*, Science, Vol. 315, 1533-1536, doi:10.1126/science.1139426, 2007

[3] Genthon, C., G. Krinner, and H. Castebrunet, *Antarctic precipitation and climate change predictions: horizontal resolution and margin vs plateau issues*, Annals of Glaciology Glaciology 50(50), 55-60, 2009

[4] Arthern, R. J., D. P. Winebrenner, and D. G. Vaughan, *Antarctic snow accumulation mapped using polarization of 4.3 cm wavelength microwave emission*, J. Geophys. Res., 111, D06107, doi:10.1029/2004JD005667., 2006

[5] Dierking, W., S. Linow, and W. Rack, *Towards a robust retrieval of snow accumulation over the Antarctic ice sheet using satellite radar*, J. Geophys. Res., 117, D09110, doi:10.1029/2011 JD017227, 2012

[6] Kwok, R., and C. F. Cunningham, *ICESAT over Arctic sea ice: Estimation of snow depth and ice thickness*, J. Geophys. Res., 116, C11018, doi:10.1029/2008JC005181, 2008

[7] Ashcraft, I. S., and D. G. Long, *Relating microwave backscatter azimuthal modulation to surface properties of the Greenland ice sheet*, J. Glaciol., 52(177), 257–266, doi:10.3189/172756506781828764, 2006

Appendix V

Publication VIII: ”The impact of early summer snow properties on land-fast sea-ice X-band backscatter”

By Stephan PAUL, Sascha WILLMES, **Mario HOPPMANN**,
Priska A. HUNKELER, Günther HEINEMANN, Marcel NICOLAUS
and Ralph TIMMERMANN

This paper is reprinted from the Annals of Glaciology with permission of the International Glaciological Society (Paul et al., 2015).

Annals of Glaciology 56(69) 2015 doi: 10.3189/2015AoG69A715 263

The impact of early-summer snow properties on Antarctic landfast sea-ice X-band backscatter

Stephan PAUL,[1] Sascha WILLMES,[1] Mario HOPPMANN,[2] Priska A. HUNKELER,[2] Christine WESCHE,[2] Marcel NICOLAUS,[2] Günther HEINEMANN,[1] Ralph TIMMERMANN[2]

[1]*Environmental Meteorology, University of Trier, Trier, Germany*
E-mail: paul@uni-trier.de
[2]*Alfred-Wegener-Institut Hemlholtz-Zentrum für Polar- und Meeresforschung, Bremerhaven, Germany*

ABSTRACT. Up to now, snow cover on Antarctic sea ice and its impact on radar backscatter, particularly after the onset of freeze/thaw processes, are not well understood. Here we present a combined analysis of in situ observations of snow properties from the landfast sea ice in Atka Bay, Antarctica, and high-resolution TerraSAR-X backscatter data, for the transition from austral spring (November 2012) to summer (January 2013). The physical changes in the seasonal snow cover during that time are reflected in the evolution of TerraSAR-X backscatter. We are able to explain 76–93% of the spatio-temporal variability of the TerraSAR-X backscatter signal with up to four snowpack parameters with a root-mean-squared error of 0.87–1.62 dB, using a simple multiple linear model. Over the complete study, and especially after the onset of early-melt processes and freeze/thaw cycles, the majority of variability in the backscatter is influenced by changes in snow/ice interface temperature, snow depth and top-layer grain size. This suggests it may be possible to retrieve snow physical properties over Antarctic sea ice from X-band SAR backscatter.

KEYWORDS: remote sensing, sea ice, snow, snow metamorphosis, snow physics

INTRODUCTION

Snow on sea ice is an important factor for the sea-ice mass and energy balance, due to its high albedo and low thermal conductivity (Yackel and Barber, 2007). Together with sea ice, snow plays a major role in modifying and influencing high-latitude atmospheric, oceanic and biogeophysical processes. Snow on sea ice accumulates and redistributes at different rates and shows a high spatio-temporal variability. However, the number of direct observations and measurements of snow is very limited for both polar regions (e.g. Barber and Thomas, 1998; Massom and others, 2001; Yackel and Barber, 2007). Understanding the relationship between snow properties (limited point measurements) and high-resolution spaceborne monitoring systems is desirable (Yackel and Barber, 2007).

As noted by Barber and Thomas (1998), interactions between the sea-ice snow cover and microwave radiation hold the potential for developing algorithms to estimate snow depth/snow-water equivalent, as well as snow physical properties over sea ice from satellite synthetic aperture radar (SAR) data. Snow affects the microwave interaction with sea ice through direct scattering based on the snow's physical properties (e.g. density, salinity, grain size and shape) and through thermodynamically controlled effects on the dielectric properties of the snow (e.g. its brine volume and wetness). Even a very shallow dry snow layer increases the backscatter from sea ice. However, additional dry snow does not further alter the received backscatter signal significantly (e.g. Kim and others, 1984; Barber and Thomas, 1998). This effect is linked to a higher ice-surface roughness and an increase in the dielectric contrast, which again is caused by brine wicking into the snow layer from the sea-ice surface (Kim and others, 1984).

The backscatter signal of sea ice in general is affected by two-way loss through the snow cover. If liquid water is present in the snowpack, both the real and the imaginary part of the dielectric constant increase, resulting in a higher signal loss. This makes the measured backscatter signal less sensitive to the underlying sea ice and boosts the surface- and volume-scattering contribution of the snowpack to the total signal (Kim and others, 1984; Barber and Thomas, 1998; Yackel and others, 2007).

Recent spaceborne SAR systems operate in different bands, at swath widths 30–500 km and at different spatial resolutions of 1–1000 m (Dierking, 2013). These systems are widely used for sea-ice monitoring and ice-type classification (e.g. Dierking, 2010, 2013; Eriksson and others, 2010), where the snow cover can generally be neglected in cold and dry conditions (e.g. Drinkwater and others, 1995; Dierking, 2013).

In the Arctic, several studies have investigated the relationship between snow physical properties and C-band SAR backscatter. Barber and Thomas (1998) investigated the general role of first-year sea-ice snow cover on microwave emission and scattering under laboratory conditions. Modelled and measured results suggest that, at 5 GHz, the volume-scattering contribution surpasses the surface-scattering contribution to the signal. This is reversed at 10 GHz, increasing the contribution of surface-scattering to the overall signal. The same study also found a strong influence of both snow-grain size and thermal effects on the microwave backscatter. Barber and Nghiem (1999) continued this work by further looking into the role of snow on the thermal dependence of sea-ice microwave backscatter. They highlighted the importance of the snow basal layer on the microwave backscatter and its controlling factors (e.g. snow/

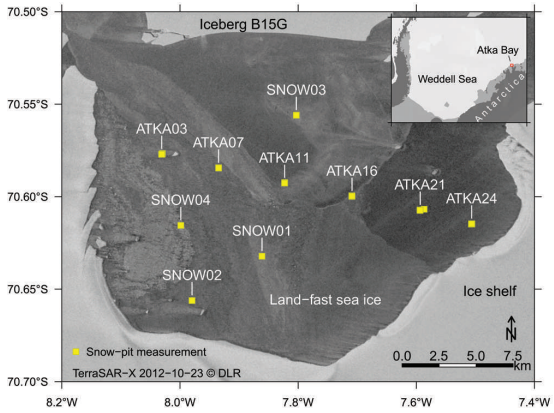

Fig. 1. Locations of all snow-pit measurements shown on a TerraSAR-X ScanSAR image of Atka Bay, Antarctica, 23 October 2012. Yellow squares mark the positions of all recorded snow pits. Both the main study sites (ATKA03–ATKA24) and additional snow pits (SNOW01–SNOW04) are shown. The inset shows the location of Atka Bay in the Weddell Sea region.

ice interface temperature, basal-layer grain size, ice-surface roughness and brine pockets within the sea-ice frazil layer).

The temporal evolution of European Remote-sensing Satellite (ERS) and RADARSAT C-band SAR backscatter time series was analysed by Barber (2005), in the context of sea-ice and snowpack evolution from freeze-up to melt. Yackel and others (2007) used RADARSAT data to detect changes in the snow water equivalent of the snow cover of first-year landfast ice. Yackel and Barber (2007) investigated the capabilities of C-band SAR to detect the onset of Arctic sea-ice melt in backscatter time series and the relationship between measured backscatter and snow albedo.

In the Antarctic, multiple studies have investigated the influence of snow cover on SAR backscatter, with a view to potentially retrieving snow properties over ice sheets (e.g. Kendra and others, 1998; Zahnen and others, 2003; Nagler and Rott, 2004; Dierking and others, 2012). However, few investigations concerned with the microwave signature of snow on sea ice have been conducted in the Antarctic, compared with the Arctic. Drinkwater and others (1995) investigated C-band backscatter of winter sea ice in the central Weddell Sea, where the dry snow cover can normally be neglected. Recent studies (e.g. Willmes and others, 2011) have examined the relation between Ku-band QuikSCAT scatterometer data and snow properties in high-backscatter pack-ice regions. Other studies investigated C-band SAR data and Ku-band scatterometer data for different regions in Antarctica (e.g. Worby and others, 2008; Kern and others, 2011; Ozsoy-Cicek and others, 2011). Nevertheless, further spatio-temporal high-resolution information about the snow on sea ice is required to validate satellite-derived data.

In this study, we present a combined analysis of in situ snow observations (physical/stratigraphic properties) and high-resolution TerraSAR-X (TSX) calibrated backscatter data (σ^0 (dB)), and their spatio-temporal evolution. Measurements originate from a field campaign on the landfast sea ice (fast ice) of Atka Bay, Antarctica, between November 2012 and January 2013. Atka Bay is a ~440 km^2 large embayment at the front of the Ekström Ice Shelf, Dronning Maud Land (Fig. 1) featuring a seasonal fast-ice cover. A more detailed description of the study area is given by Hoppmann and others (2015).

Compared to C-band SAR, X-band SAR is considered to be more sensitive to the snow cover, the upper subsurface ice layer and the onset of melt and freeze/thaw processes, due to its shorter wavelength (higher frequency) (e.g. Eriksson and others, 2010). We further present and discuss the interrelationship between TSX σ^0 data and coincident snow properties and evaluate the potential of X-band SAR backscatter to gather wider-scale information on physical and stratigraphic snow properties.

DATA AND METHODS

Field measurements

The meteorological data used here (Fig. 2) combine measurements recorded at the meteorological observatory of the German research station Neumayer III (50 m a.s.l.) and synoptic weather observations (König-Langlo, 2013a,b, c,d,e,f). While there are deficiencies due to local topography and elevation differences, the meteorological conditions at Atka Bay and Neumayer III are assumed to be comparable due to the general weather situation there. For example, Hoppmann and others (2015) found a general offset in 2 m air temperature of −1.05 K between the measurements at Neumayer III and Atka Bay.

In 2012, air temperatures increased to above the freezing point for the first time on 16 December (Fig. 2a). The onset of early melt is particularly important for our study because the existence of liquid water in the snowpack is expected to have a significant influence on the received radar signal (e.g. Yackel and Barber, 2007). The subsequent onset of freeze/thaw cycles leads to the formation of ice lenses and icy layers in the snowpack, as well as to the formation of superimposed (freshwater) ice, which is especially rich in air bubbles. These layers, in combination with the air bubbles, act as internal scatterers (Fierz and others, 2009; Willmes and others, 2011; Dierking, 2013).

Another important feature of our study is the occurrence of an 8 day storm event from 5 to 12 December 2012 (Fig. 2b). Sustained snowfall and redistribution occurred during this time, so no fieldwork was possible to monitor the snowpack changes. Other than the storm, we only recorded two single snowfall events during the entire study from 23 November 2012 to 7 January 2013. In general, easterly winds predominated (bringing higher wind speeds), which is in line with the long-term climatology for this region.

During the field campaign, we obtained snow physical property data from a total of 41 snow pits. Each comprised measurements of snowpack temperature and density gradients, 2 m air temperature and snow stratigraphy (i.e. grain-size distribution, snowpack layering and, mainly qualitative, estimates of snow liquid-water content, hardness and crystal type), following Fierz and others (2009). Our measurements focused on regular sampling sites along a ~25 km long west–east transect (ATKA03–ATKA24; Fig. 1), while additional snow-pit data were recorded sporadically at different locations on the Atka Bay fast ice (SNOW01–SNOW04; Fig. 1). The snow-pit locations were chosen to be representative of the surrounding area. Quantitative measurements of liquid-water content in the snowpack were possible only at the very end of our field campaign, due to the late arrival of the instrument.

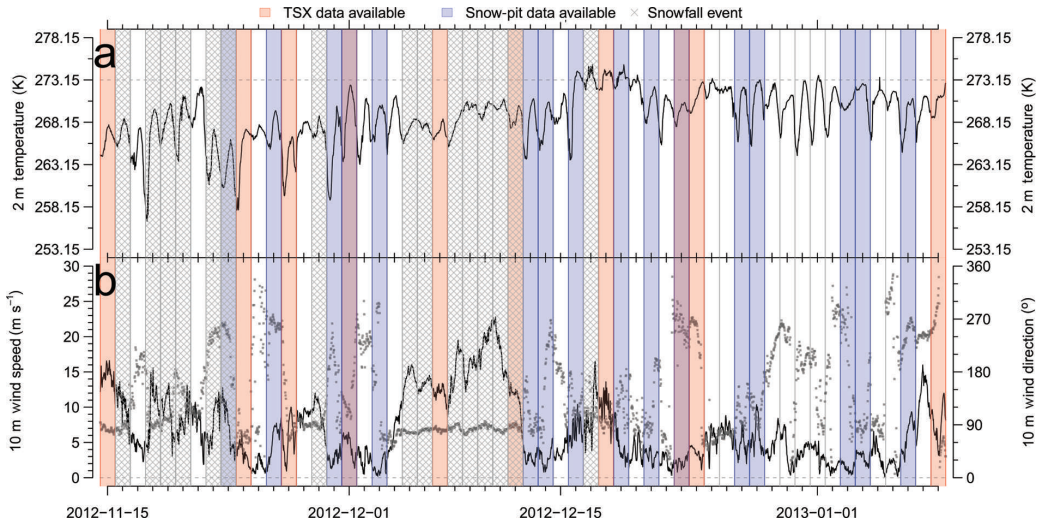

Fig. 2. Meteorological measurements of (a) 2 m air temperature and (b) 10 m wind speed (solid curve) and wind direction (dots). These datasets were recorded at Neumayer III station, ~8 km southwest of Atka Bay and are presented here as 30 min averages. Additionally, the red and blue bars indicate available TerraSAR-X swaths and snow-pit measurements acquired. Hatched areas mark days with snowfall events. Date format is yyyy-mm-dd.

We recorded snowpack temperature profiles using a penetration thermometer at a regular spacing. We also determined snow density of each layer by forcing a metal tube of known volume and weight into the snowpack, extracting it and measuring its weight in the field with a spring scale. Layers were distinguished by differences in grain size, crystal type, hardness and liquid-water content. Grain size and snow crystal type were determined visually using a magnifying glass, following Fierz and others (2009). Snow hardness was estimated by resistance to penetration (Fierz and others, 2009). Liquid-water content was categorized into 'dry' and 'not dry' by visual observation and manual probing, following Fierz and others (2009). Quantitative estimates of snow liquid-water content were recorded using a snow fork (Sihvola and Tiuri, 1986), but this was only possible at the very end of our field campaign, due to the late arrival of the instrument.

Snow conditions at Atka Bay in 2012 are briefly summarized here (they are discussed in more detail by Hoppmann and others, 2015). ATKA03 featured no consistent snow cover, due to its location ~2 km to the east of a grounded iceberg. The snow pits near ATKA03 therefore largely represent records from snow banks and larger snow patches. While icebergs shelter their leeward area from snow accumulation, ridges and icebergs increase the snow accumulation in their close windward proximity, leading to locally thicker snow and a more heterogeneous snowpack stratigraphy. This influenced the snow-pit records of ATKA07 and ATKA16. Additionally, ATKA16 was influenced by surface flooding by sea water. In a similar fashion to icebergs, the ice-shelf edge prevents large snow accumulations on its leeward side. This is considered to be the primary reason for the small snow depths but relative homogeneity in the snow cover at ATKA24. Due to the earlier breakout of sea ice at ATKA11 (Hoppmann and others, 2015), the ice as well as the snow cover was rather thin and influenced by flooding and refreezing over the course of the field campaign. ATKA21 exhibited a consistent but thicker snowpack than ATKA24.

The ice surface roughness is also a major factor influencing radar backscatter, depending on the horizontal roughness scale compared to the SAR wavelength. On sea ice with a surface roughness of comparable scale to the SAR wavelength, specular reflection leads to relatively low backscatter (Dierking, 2013). This circumstance was characteristic for the ice surface underlying the snow pits at ATKA11, ATKA16, ATKA21, ATKA24 and SNOW02. In the other pits, the ice surface was found to be rough compared to the X-band SAR wavelength.

The number of records in each snow pit varies with snow depth (i.e. more data points in deeper pits), existence of ice lenses/layers (e.g. it is difficult to measure the density in a layer of pure ice), number of layers, etc. Moreover, the snow-pit measurements comprise numerical (e.g. grain size, temperature profiles, snow depth, liquid-water content) and more qualitative values (e.g. hardness, liquid-water content, crystal type) of different nature. Consequently, difficulties arise when comparing measurements between snow pits and also when comparing them to the satellite observations. Hence, we derived several numerical snowpack parameters from our measurements (Fig. 3) in order to explain the variations in TSX σ^0. These parameters include the snow thickness, z_{snow} (m), the quantitative measurements of bulk liquid-water content in the snowpack from snow fork measurements, LWC (vol.%), the snowpack temperature gradient, $\partial T/\partial z$, not shown (K m^{-1}), 2 m air temperature, T_a, snow-surface temperature, T_s, and snow/ice interface temperature, T_i (K), the number of different layers, n_{lay}, the number of ice layers, n_{ice}, the number of layers containing liquid water, n_{lwc}, the grain size of the top/bottom layers, E_{top}/E_{bot} (m), the average snowpack grain size, $\overline{E}$, and the weighted-average snowpack grain size, $\overline{E}_w$ (m). The latter takes the different layer thicknesses into account. Due to the

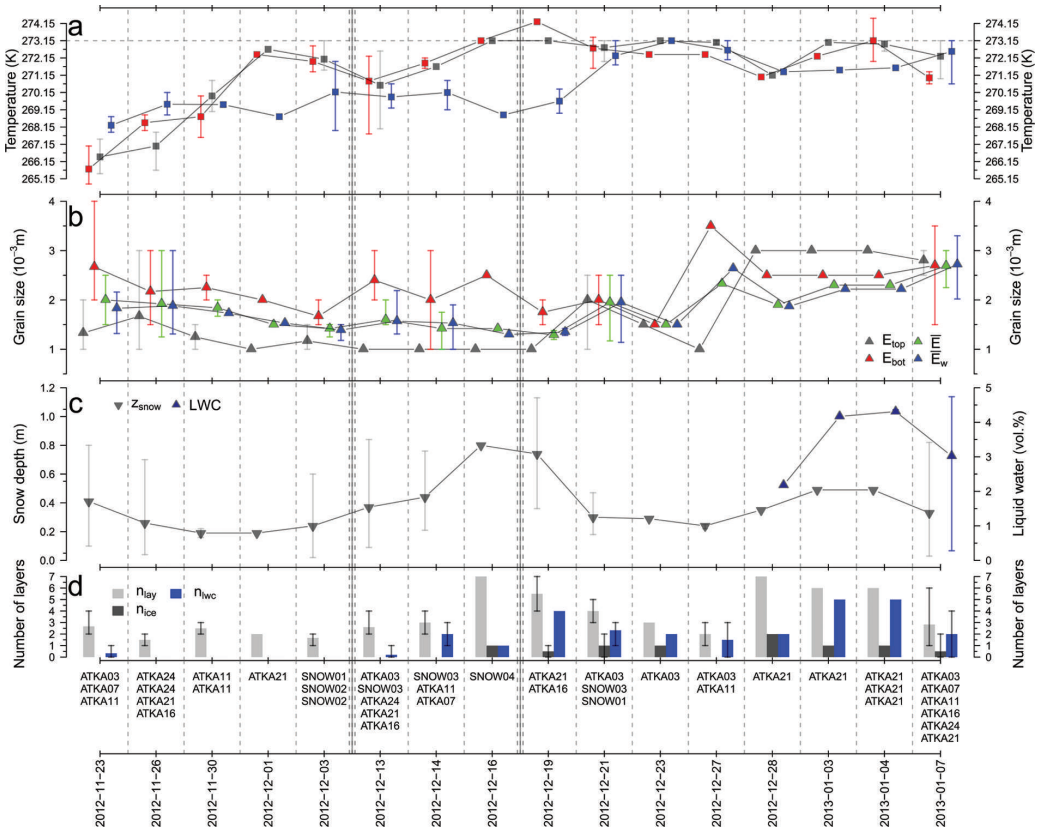

Fig. 3. Time series of daily averaged snowpack parameters. (a) 2 m air temperature measured at the snow-pit location (T_a, red squares), the snow-surface temperature (T_s, grey squares) and the snow/ice interface temperature (T_i, blue squares). (b) Top-/bottom-layer grain size (E_{top} and E_{bot}, grey/red triangles) and average/weighted-average snowpack grain size ($\overline{E}$ and $\overline{E}_w$, green/blue triangles). (c) Snow depth (z_{snow}, grey triangles) and the liquid-water content (LWC, blue triangles). (d) The numbers of layers in the snowpack (n_{lay}, light grey), ice layers (n_{ice}, dark grey) and layers containing liquid water (n_{lwc}, blue). Error bars indicate minimum/maximum values on days with several measurements. The corresponding measurement sites are shown under the bars (Fig. 1). The highlighted vertical double-dashed lines indicate large snowfall events between measurements. The *x*-axis spacing is not to scale, but distorted. Date format is yyyy-mm-dd.

frequent large wind-slab layers in the snowpacks, we felt the need to account for their very small grain sizes in an average snow grain-size parameter. However, the effects on σ^0 are small, as shown below.

For clarification, E_{bot} gives the grain size of the lowest layer in the snowpack that is still snow, i.e. E_{bot} potentially states values several cm above the snow/ice interface. This was necessary due to the frequent presence of ice layers in the bottommost part of the snowpack, which do not yield any grain-size information. This happened especially during the later stages of the field campaign. The density measurements (not shown) were used to calculate the bulk snow-water equivalent (SWE, not shown) for each snow pit, but were otherwise omitted from all calculations, due to the limited number of measurements per pit and their low vertical resolution. The course of SWE is naturally very similar to that of z_{snow} and is therefore not shown.

Due to logistical constraints, we were not able to collect snow samples to estimate snowpack salinity for all snow-pit measurements. Salinity is, however, a crucial parameter in determining σ^0, due to its influence on the dielectric properties of snow and sea ice and its impact on the penetration depth. This shortcoming represents an obstacle for the interpretation of temporal backscatter changes. Dierking (2013) states a typical penetration depth of 0.03–0.15 m for X-band SAR on first-year sea ice under dry snow conditions. Barber and others (1995) showed that the snow/ice interface temperature influences the brine volume fraction. This rise in brine volume fraction leads to an increase in the dielectric constant in the sea-ice surface, which again increases σ^0. However, the snow basal layer is also likely to have high salinity values (Massom and others, 2001), which might mask out underlying changes in the sea ice, especially after the onset of freeze/thaw cycles and in the presence of liquid water (Yackel and others, 2007).

Similar to the records of 2 m air temperature (Fig. 2a), the averaged snowpack temperature values (Fig. 3a) of all snow-pit measurements acquired on a given day increased towards the freezing point, and T_a as well as T_s reached this as early as 16 December 2012. Because of this, we considered all measurements after 16 December 2012 as being after the onset of early freeze/thaw processes.

Satellite measurements

TerraSAR-X is a spaceborne side-looking X-band SAR instrument run by the German Aerospace Center (DLR).

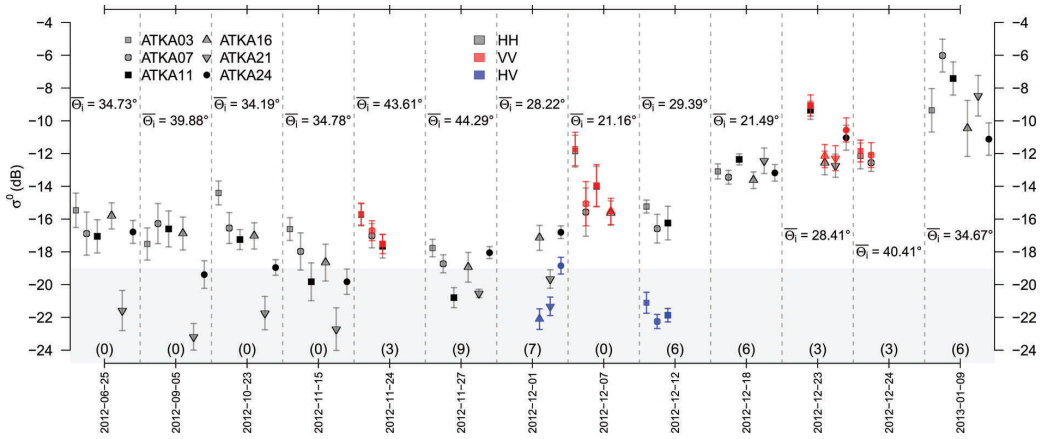

Fig. 4. Temporal evolution of the TSX backscatter (σ^0) for all available TSX swaths and polarizations (HH = black, VV = red, HV = blue). Shown is the average σ^0 for a 5 pixel × 5 pixel raster of each main study site (different symbols). Error bars indicate two standard deviations. Due to the smaller spatial coverage of the TSX StripMap mode, not all ATKA03–ATKA24 sites are covered by each swath. Additionally, the mean local incidence angle, $\overline{\Theta_i}$, is shown and the number of matched snow-pit measurements is given in parentheses (including match-ups with system-noise-influenced σ^0 values). Values influenced by the system noise, i.e. the noise-equivalent sigma zero (NESZ), are highlighted by the grey area at the bottom. Date format is yyyy-mm-dd.

The satellite has been operational since June 2007 in a polar orbit at 514 km altitude and can operate in four different imaging modes. Relevant to this study are the ScanSAR mode (SC) in single polarization and StripMap mode (SM) in single and dual polarization, due to their capability to sufficiently cover Atka Bay. The swath width changes with mode and polarization. In ScanSAR mode, a swath covers a ground area of $150 \times 100\,km^2$. In StripMap mode, the coverage changes to $50 \times 30\,km^2$ ($50 \times 15\,km^2$) in single (dual) polarization mode (Fritz and Eineder, 2008).

A total of 13 TerraSAR-X swaths were obtained before and during the field campaign (Table 1). Five scenes were recorded in single HH-polarization SC mode, while four scenes were acquired in dual-polarization SM mode in HH/VV configuration and two in HH/HV. Additionally, two scenes were acquired in single HH-polarization SM mode. All TSX scenes were radiometrically calibrated using a commercial software package (SARscape) and georeferenced on a common pixel size of 25 m. Due to increasing pixel size by multi-looking, the effect of speckle was reduced. The equivalent number of looks (ENL) increased by the grade of multi-looking, which depends on the initial pixel size (e.g. SC: 18.5 m; SM dual: 6.6 m; and SM single: 3.3 m (Table 1)). It is important to note that the noise-equivalent sigma zero (NESZ) level is −19 dB. All pixel values below the NESZ are influenced by system noise and were excluded from further investigation as a precaution (Fig. 4).

Due to logistical constraints, the number of snow-pit measurements directly matching a coincident TSX swath is very low (Fig. 2). Unfortunately, the two temporal matches between snow-pit measurements and TSX acquisitions could not be incorporated into our analysis. The respective

Table 1. Overview of TSX data, including initial acquisition resolution, swath coverage and minimum/maximum local incidence angles (LIA). SC/SM indicate the TerraSAR-X acquisition mode of ScanSAR/StripMap. HH/VV/HV indicate the polarization as a combination of transmitted and received signal. Start and end time give the time of acquisition in UTC of each TSX swath. Also shown are the number of snow-pit measurements assigned to each TSX swath

Date	Mode	Polarization	Initial resolution	Coverage	Minimum LIA	Maximum LIA	Start time	End time	Snow pits
dd/mm/yy			m	km^2	°	°			
25/06/2012	SC	HH	18.5	150 × 100	33.18	36.55	04:23:44	04:24:06	0
05/09/2012	SC	HH	18.5	150 × 100	38.47	41.56	04:15:10	04:15:32	0
23/10/2012	SC	HH	18.5	150 × 100	31.84	35.60	20:38:12	20:38:34	0
15/11/2012	SC	HH	18.5	150 × 100	33.23	36.60	04:23:46	04:23:58	0
24/11/2012	SC	HH	18.5	150 × 100	33.20	36.26	04:23:41	04:24:00	3
27/11/2012	SM	HH/VV	6.6	50 × 15	42.63	45.03	20:55:20	20:55:28	9
01/12/2012	SM	HH	3.3	50 × 30	43.42	45.94	04:06:47	04:06:55	7
07/12/2012	SM	HH/HV	6.6	50 × 15	27.42	29.51	04:32:20	04:32:28	0
12/12/2012	SM	HH/VV	6.6	50 × 15	19.85	21.95	20:21:14	20:21:22	6
18/12/2012	SM	HH/HV	6.6	50 × 15	28.43	30.85	04:32:19	04:32:27	6
23/12/2012	SM	HH	3.3	50 × 30	19.84	23.13	20:21:13	20:21:21	3
24/12/2012	SM	HH/VV	6.6	50 × 15	27.43	29.55	04:32:18	04:32:26	3
09/01/2013	SM	HH/VV	6.6	50 × 15	39.62	41.58	04:15:17	04:15:25	6

TSX σ^0 value of the first coincident match was influenced by system noise, while the second snow pit fell outside the TSX StripMap image. We chose to extract the average TSX backscatter values, σ^0, of a 5 pixel $\times$ 5 pixel raster (i.e. $125 \times 125\,m^2$), along with its standard deviation at the position of each snow-pit measurement. To link as many snow-pit measurements as possible to the TSX backscatter extracts, we used the TSX data from all available swaths in a ± 5 day range of each snow-pit measurement. By doing so, we were able to match at least one TSX σ^0 record with one of our snow-pit measurements, despite differences in spatial coverage of each TSX swath.

While this approach is not ideal given the synoptic-scale atmospheric changes that can influence the snowpack during a 5 day window, we tried to reduce the influence of known meteorological events. Following the lack of observational snow data during the storm, we excluded the TSX swath of 7 December 2012 from our analysis. Also we did not match snow-pit measurements recorded before the second snowfall event on 17 December 2012 with TSX swaths acquired after that snowfall event (Figs 2 and 3). This left us with 35 match-ups, excluding those with system-noise-influenced σ^0 values. The majority of these data pairs (22) show a maximum temporal difference of 2 days. Five cases each have a time lag of 3 or 4 days, and three cases a time lag of 5 days.

In the following, we explore information regarding resolution, coverage, acquisition time and local incidence angle of the TSX data (Table 1). In order to account for the wide range of local incidence angles (LIAs) covered by the TSX swaths (Table 1), we divided our dataset into three different LIA classes (LIA1: LIA $> 36°$; LIA2: $36° \geq$ LIA $> 27°$; and LIA3: LIA $< 27°$), so as to review similar TSX swaths together. We chose this approach in order to examine the potential influences on the TSX σ^0 signal of different snowpack parameters on different LIAs. Due to the bipolar temporal distribution of the TSX swaths by means of acquisition time (early morning/late evening), no further steps were taken to account for diurnal variations in the signal.

Correlation coefficients were calculated to analyse relationships between individual snowpack parameters and corresponding TSX σ^0 values. In addition, simple linear regression models were fitted to the σ^0 values and snowpack parameter groups to investigate the power and significance of the correlation, as well as the significance of the explained σ^0 variance. Finally, we fitted a simple multiple linear regression model to our different datasets, to investigate its potential for maximizing the explained σ^0 variance with a minimum of snowpack parameters per LIA class. Due to the limited number of matched snow-pit and TSX-swath measurements, the focus lies on the extracted HH-like polarization TSX backscatter data, hereafter named σ^0_{HH}.

RESULTS AND DISCUSSION

Spatio-temporal snowpack changes

Because of the irregular temporal coverage of measurements at the different study sites and the different initial snowpack situation at each study site, further investigation of the various datasets (Fig. 3) is required. The observations taken on 23 and 26 November 2012 represent the late-winter setting of a still relatively cold environment (Figs 2a and 3a). At this stage, at all main study sites (ATKA03–ATKA24) measurements were taken once, with ATKA07/16 at the upper end of the spectrum with regard to snow depth, number of layers and bottom-layer grain sizes and ATKA11/24 at the lower end.

Proceeding in time, a general increase in surface temperature, T_s, and air temperature, T_a, was noticeable. However, the snow/ice interface temperature, T_i, remained fairly constant, only varying with snow depth (Fig. 3a and c). On 16 December 2012, temperature measurements of T_a above the freezing point and T_s at the freezing point were recorded, followed by an increase in T_i. This led to near-isothermal snow conditions.

Between the initial conditions on 23/26 November 2012 and the end conditions on 7 January 2013, when coincident sampling at all main study sites took place again, an average increase and vertical equalization of the grain-size parameters occurred (Fig. 3b). This was driven by the equi-temperature metamorphism processes in the snowpack (Fierz and others, 2009). Furthermore, our few direct measurements of liquid-water content covered the whole spectrum between 1 and 5 vol.% on 7 January 2013. Such a range is expected to significantly affect the received backscatter signal (e.g. Yackel and Barber, 2007). In general, liquid water was found throughout the snow column (Fig. 3d), with the exceptions of 23 November 2012 and 13 December 2012, when flooded slush layers occurred at the snowpack base (ATKA11 and ATKA16).

Following the onset of freeze/thaw cycles and early melt, the degree of snowpack stratification increased, with an increase in the number of layers in general and in ice layers (Fig. 3d). Note that average values are shown, which might lead to the false impression that the degree of stratification falls off again at the end of the field campaign.

Spatio-temporal backscatter variations

Analysing the spatio-temporal variations of the TSX backscatter (σ^0; Fig. 4), one needs to consider that not all study sites were covered in each swath (Table 1). We consider the HH-polarization data (Fig. 4, black) in SC and SM modes as well as the VV-polarization data (red) and the HV cross-polarization data (blue) in SM mode. Observed differences between the measurements at both HH and VV polarization are fairly small, while cross-polarization yields generally lower backscatter values. However, variations between the study sites can be large.

In the extracted TSX backscatter values of the first four swaths, there was an increasing spread in σ^0 between the different study sites, in addition to a steady overall decrease in σ^0. In particular, ATKA21 peaks compared with the other study sites, despite differences in σ^0 due to different average LIA, $\overline{\Theta_i}$. It should be added that the very low values of σ^0 for the first few swaths are very close to or below the noise floor of TSX, which starts influencing the received signal below a threshold of -19 dB (worst case)/-22 dB (normal) as stated by Fritz and Eineder (2008). However, the TSX data used in the later analyses were generally well above this noise floor and are unlikely to have been affected by it.

The X-band SAR microwave radiation did not significantly interact with the present dry snowpack in the early TSX swaths; this is consistent with the observations of Dierking (2013) and Drinkwater and others (1995). The spatial differences (Fig. 4) for the first four swaths are primarily linked to localized growth conditions during sea-ice formation and differing sea-ice compositions (salinity, proportion

of incorporated frazil ice, columnar ice and platelet ice) which each affect the X-band SAR microwave radiation in a different way (e.g. Dierking, 2013). The small decrease in σ^0 over time (on average ~2 dB) is probably due to a decrease in brine volume fraction in the snow-basal layer, as well as the ice-surface layer, due to low winter temperatures and still increasing ice thickness, which decreases the dielectric constant. This was noted for C-band SAR time series (e.g. Yackel and Barber, 2007) and also seems applicable for X-band SAR data. However, our data are not sufficient to assess this quantitatively. The comparably high σ^0 values on 24 November 2012, despite the large local incidence angle, might be correlated to the increase in temperature around 20/21 November 2012 and the subsequent drop in temperature by ~10 K (Fig. 2a). Unfortunately, there are no in situ temperature observations to verify this.

Hoppmann and others (2015) discuss the different types of sea ice at Atka Bay and their structures. Their description of the primary ice-formation processes can be linked to the σ^0 signals (Figs 1 and 4) before the onset of melt and freeze/thaw cycles. In areas where dynamical-growth processes dominated, σ^0 is generally higher (e.g. the area around ATKA03/07). This results from the presence of pressure ridges that increase the surface scattering of the X-band radiation (Eriksson and others, 2010). The highest signal is returned from the area of second-year sea ice close to the western ice-shelf edge. Here volume scattering is increased by air bubble inclusions, as well as surface scattering by the overall deformed structure of the ice. This adds up to a higher overall signal. An area of thermodynamic growth (ATKA21/24) generally has level ice with lower backscatter values (e.g. Dierking, 2013).

Across all incidence angles, there is an increase in σ^0 over the field study. For LIA of 34–35°, there is an average increase of 10–12 dB in σ^0 for all ATKA stations between 15 November 2012 and 9 January 2013. A similar, but smaller, increase was found for swaths with an average LIA of ~29°. However, considerable spatial variability was evident, with ATKA11 exhibiting the highest variability.

The high σ^0 values in the 9 January 2013 swath very likely originate from several freeze/thaw cycles, especially between 31 December 2012 and 5 January 2013 (Fig. 2a). These potentially increased the amount of volume scattering, through the formation of ice layers and an increase in grain sizes (Willmes and others, 2011). A steady increase in snow surface and snow/ice interface temperature and grain enlargement is seen in our measurements (Fig. 3a and b). Also, more stratification and an increased number of ice layers occur after the onset of freeze/thaw processes. All this potentially raises the returned backscatter. Nothing can be said about LIA3, due to the limited number of swaths and measurements taken in this LIA class.

The general increase in σ^0 can be attributed to significant volume scattering by the snow basal-layer grains at ~1–3 vol.% of liquid water. With increasing liquid-water content, surface scattering further contributes to the overall signal (Barber and others, 1994; Barber, 2005).

Relationship between backscatter and snowpack characteristics

Here we correlate σ^0_{HH} and the previously discussed snowpack parameters (Table 2; only significant correlations are shown). The statistical parameters include the correlation coefficient, R, the stability index, R^2, stating the explained variance, the p-value of the calculated f-test, p, stating the level of significance of the regression, and the sample size, n, as well as the statistical power. Power gives the probability that the H_0 hypothesis is rejected (i.e. there is no correlation), where H_0 is truly false (Cohen, 1988).

Table 2. Summary of statistical parameters explaining the relationship between TSX backscatter σ^0_{HH} and snowpack parameters (only parameters with significant correlations are shown, $\alpha = 0.95$). Presented are the correlation coefficient, R, the stability index, R^2, the p-value of the calculated f-test, p, the sample size, n, and the statistical power. The results are shown per LIA class and data subset, where ALL equals all measurements per LIA class, SDS indicates a snow data subset of sites with $z_{snow} < 0.6$ m and EMO corresponds to measurements after the onset of early melt

		Subset	R	R^2	p	n	Power
LIA1							
σ^0_{HH}	T_a	ALL	0.843	0.711	0.002	10	0.906
σ^0_{HH}	T_s	ALL	0.895	0.801	<0.001	10	0.971
σ^0_{HH}	T_i	ALL	0.859	0.738	0.001	10	0.930
σ^0_{HH}	T_a	SDS	0.831	0.691	0.011	8	0.763
σ^0_{HH}	T_s	SDS	0.890	0.792	0.003	8	0.892
σ^0_{HH}	T_i	SDS	0.845	0.714	0.008	8	0.794
σ^0_{HH}	SWE	SDS	0.716	0.513	0.046	8	0.517
σ^0_{HH}	n_{lay}	SDS	0.889	0.790	0.003	8	0.890
LIA2							
σ^0_{HH}	T_s	ALL	0.506	0.256	0.023	20	0.632
σ^0_{HH}	T_i	ALL	0.771	0.594	<0.001	20	0.989
σ^0_{HH}	E_{top}	ALL	0.677	0.458	0.001	20	0.927
σ^0_{HH}	$\overline{E}$	ALL	0.504	0.254	0.023	20	0.628
σ^0_{HH}	$\overline{E}_w$	ALL	0.493	0.243	0.027	20	0.605
σ^0_{HH}	T_i	EMO	0.760	0.577	0.011	10	0.753
σ^0_{HH}	E_{top}	EMO	0.847	0.717	0.002	10	0.913
σ^0_{HH}	$\overline{E}$	EMO	0.772	0.596	0.009	10	0.777
σ^0_{HH}	T_s	SDS	0.620	0.385	0.014	15	0.711
σ^0_{HH}	T_i	SDS	0.881	0.776	<0.001	15	0.998
σ^0_{HH}	E_{top}	SDS	0.665	0.442	0.007	15	0.796

The results of Table 2 indicate a rather moderate dependency of observed σ^0_{HH} on the chosen snowpack parameters. However, there is a recurring set of snowpack parameters showing significant correlations to different degrees for all LIA classes and most data subsets. However, the rather low-to-moderate correlation coefficients and stability indices, as well as the low power values, have to be considered and are constrained by the small sample size. For LIA3, there were not enough samples to conduct meaningful calculations.

After visual screening and simple linear model iterations to find the best fit, we found that subsetting the dataset to measurements taken on snowpacks with a maximum depth of 0.60 m reveals a significantly higher correlation between z_{snow} and σ^0_{HH} for all LIA classes (Fig. 5). While 0.60 m of snow is rather thick for Antarctic sea ice, 8 out of 35 of our snow-pit measurements featured a snow depth exceeding this threshold, while still being representative for their general area. However, these correlations are not necessarily significant (Table 2), given a level of significance (α) of 0.95, but exclusion of our very deep snow-pit measurements is likely to influence the correlations of other snowpack parameters to σ^0_{HH} (e.g. the snow/ice-surface temperature due to the X-band signal penetration depth (Table 2)).

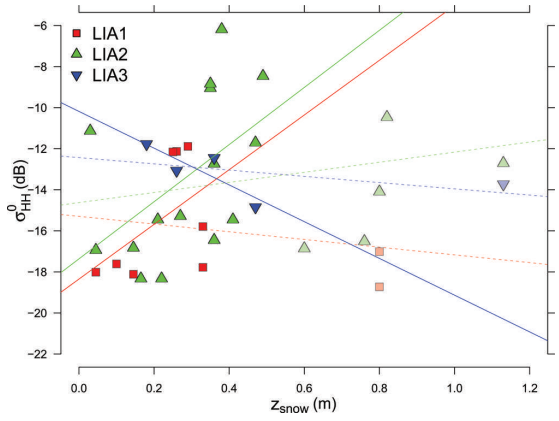

Fig. 5. Scatter plot of snow depth (z_{snow}) against TSX HH backscatter (σ^0_{HH}). Shown are the snow depths and their corresponding local incidence angle (LIA) class-based σ^0_{HH} values. Value pairs above/below the 0.6 m threshold are plotted transparent/solid. The corresponding regression lines are shown, where solid lines correspond to the value pairs with $z_{snow} < 0.6$ m and dashed lines are for the complete dataset.

Neglecting the scatter loss, we calculated the theoretical penetration depths from the bulk dielectric constant for a range of bulk snow liquid-water content and bulk snow densities from our measurements, by solely considering the absorption loss. This was done using the governing equations for wet snow provided by Hallikainen and Winebrenner (1992). A liquid-water content of 0.35–0.5 vol.%, for example, led to a penetration depth at TSX X-band of 0.4–0.75 m. This might explain the increase in correlation between σ^0_{HH} and, especially, T_i. At a snow liquid-water content of 1–3 vol.%, the theoretical penetration depth decreases to 0.05–0.20 m. However, given the temperature records (Fig. 2a), the high values of liquid water within the snow are likely to be snapshots of a constantly changing snowpack, due to thaw/refreeze cycling.

The overall most reliable results were found for the LIA2 class (Table 2), i.e. LIA 36–27°, where sufficient sample size corresponds to the high statistical power of the significant correlations. Snow/ice interface temperature, T_i, and top-layer grain size, E_{top}, showed significant correlation coefficients ($p < 0.01$) with high power values close to 1. This implies (with high confidence) that the results are not based on random noise. These numbers change slightly, depending on the subset used. Limiting ourselves to measurements with snow depths of <0.6 m (SDS), the correlation coefficient and stability index for the snow/ice interface temperature, T_i, increase, probably due to their capturing the penetration depth of X-band radar. For greater snow depths, the ice/snow interface becomes invisible, due to the limited penetration depth of X-band radar (Yackel and Barber, 2007).

We chose an approach to evaluate the amount of variance in our TSX σ^0_{HH} that can be explained by the snowpack parameters, by using a simple multiple linear model. Each model estimate started with all the snowpack parameters as input. Using stepwise regression modelling, the parameter with the highest p-value (i.e. the least significant contribution to the overall explained variance, R^2, was removed from the model at each iteration. After several iterations, a significant model fit was achieved in most cases. The iteration stopped when, in a subsequent step, the overall explained variance dropped significantly and the model significance decreased. However, no significant model fits could be found for some LIA classes and data subsets, due to the limited sample size (especially for the LIA3 class).

Table 3. Different model fits to the TSX backscatter σ^0_{HH} data. Presented are the sample size, n, the p-value of the calculated f-test, p, the adjusted stability index, R^2_{adj}, that shows the explained variance adjusted for the different amount of predictors, and the predictors of σ^0. Also shown is the root-mean-squared error of the cross validation (dB; RMSE). Model fits are identified by tags based on the LIA and data limitations, where SDS stands for snow-depth subset and EMO means early-melt onset

Model fit	n	p	R^2_{adj}	Predictors	RMSE
LIA1	10	0.002	0.7595	z_{snow}, SWE	1.50
LIA2	20	<0.001	0.8421	z_{snow}, T_i, E_{top}	1.56
LIA3	5		no model fit found		
LIA1SDS	8	0.007	0.9158	T_i, SWE	1.00
LIA2SDS	15	<0.001	0.8584	z_{snow}, T_i, E_{top}	1.62
LIA3SDS	4		no model fit found		
LIA1EMO	3		no model fit found		
LIA2EMO	10	<0.001	0.9323	T_s, T_i, E_{top}, $\overline{E}$	0.87
LIA3EMO	5		no model fit found		

The model name tags (Table 3) correspond to the underlying data subsets (e.g. limited to measurement sites with $z_{snow} < 0.6$ m (SDS) or after the onset of early-melt processes on 16 December 2012 (EMO)). Table 3 also shows the sample size, n, the p-value of the calculated f-test, p, and the stability index, R^2_{adj}. The latter is corrected (adjusted) for the different amount of predictors which can lead to an increased general stability index, R^2. All model fits are significant and explain 76–93% (R^2_{adj}) of their representative observed σ^0_{HH} variance.

To evaluate the quality of our model fits we chose a cross-validation approach, due to the limited sample size. Here the model was set up with the significant predictors calculated from the complete sample size, n, but based on a sample size of $n - 1$. Iteratively, each member of the initial sample was excluded from the set-up, and was instead calculated by the model. The root-mean-squared error (RMSE) between the modelled and observed σ^0_{HH} values was then calculated. The results (Table 3) vary between 0.87 and 1.62 dB (LIA2EMO and LIA2SDS, respectively). These compare favourably with the absolute/relative radiometric accuracy of the TSX sensor (0.6/0.3 dB; Fritz and Eineder, 2008). However, the quite high stability indices of >90% were achieved on very small datasets with a comparably large number of predictors.

During the cross validation, it became clear that the σ^0_{HH} signatures of certain snow-pit measurements are more difficult to derive from the various model fits using different predictor set-ups, i.e. excluding those snow-pit measurements drastically decreased the RMSE, compared with the RMSE changes of the remaining iterations. An example is ATKA11. We attribute this to the recurrent surface flooding and refreezing that occurred during the course of our field campaign, which cannot be explained sufficiently with the snowpack parameters used here.

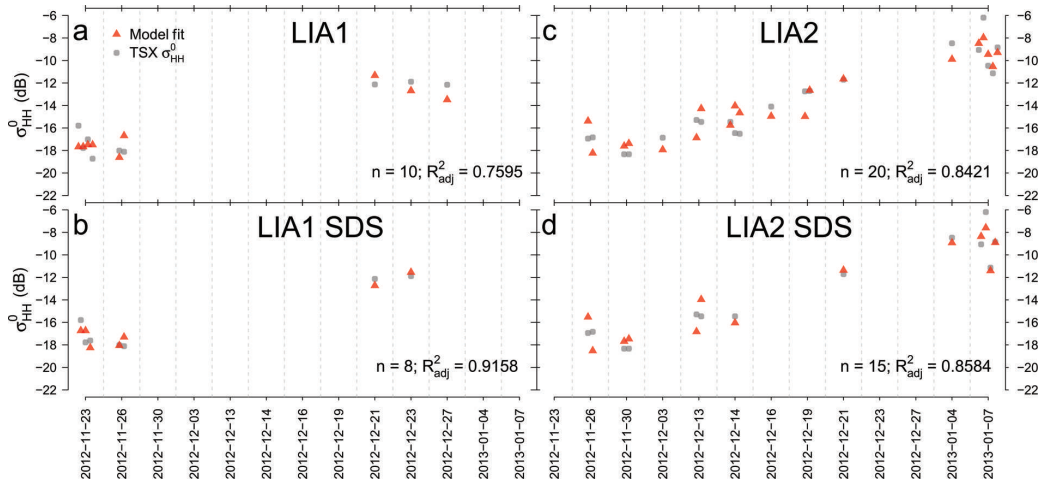

Fig. 6. Four different multiple linear model fits (a–d) (red triangles) to the extracted σ^0_{HH} values from all available snow-pit measurements in a ±5 day range (grey dots). (a) Based on all available snow-pit measurements for LIA1. (b) Limited to snow-pit measurements with $z_{snow} < 0.6$ m for LIA1. (c, d) the same set-ups as (a, b) for LIA2. All model fits are significant ($\alpha < 0.001$) and explain 76–91% (R^2_{adj}) of the total variance of σ^0_{HH}. Date format is yyyy-mm-dd.

The significant snow parameters (Table 2) also appear as model predictors in Table 3. Furthermore, the snow depth and snow water equivalent are significant contributors to the overall variance, despite showing non-significant correlations with σ^0_{HH} by themselves. While there are definitive internal correlations (e.g. between z_{snow} and SWE, or the temperature parameters), they are not interchangeable without a large drop in the stability indices.

Four representative model fits are discussed here (Fig. 6; grey dots indicate the measured TSX σ^0_{HH} values; red triangles correspond to the modelled backscatter). Model fit LIA1 (Fig. 6a) explains 76% (R^2_{adj}) of the σ^0_{HH} variance, spans a sample size of ten value pairs and is based on the predictors z_{snow} and SWE (Table 3). Model fit LIA2 (Fig. 6c) explains 84% (R^2_{adj}) of the σ^0_{HH} variance, spans a larger sample size of 20 value pairs and is based on the predictors z_{snow}, T_i and E_{top}. Furthermore, the overall temporal coverage of pre-melt-onset conditions as well as post-melt-onset conditions is better represented in the LIA2 than the LIA1 data. In combination with the larger sample size, this gives higher confidence in the general quality of the model fit to the LIA2 data. However, the dataset is too limited to further investigate differences between the different LIA classes.

The corresponding equations for the four model fits are:

$$\sigma^0_{LIA1} = -18.52 - 64.40 z_{snow} + 0.19\,SWE \quad (1)$$

$$\sigma^0_{LIA2} = -524.11 + 6.42 z_{snow} + 1.87 T_i + 1007.44 E_{top} \quad (2)$$

$$\sigma^0_{LIA1SDS} = -261.32 + 0.90 T_i + 0.03\,SWE \quad (3)$$

$$\sigma^0_{LIA2SDS} = -474.02 + 9.50 z_{snow} + 1.68 T_i + 1310.29 E_{top} \quad (4)$$

where σ^0 represents the modelled backscatter values, z_{snow} is the snow depth (m), SWE is the snow water equivalent (kg m^{-2}), T_i is the snow/ice interface temperature (K) and E_{top} is top-layer grain size (m).

All model fits are more sensitive to changes in grain size or temperature parameters (large slopes) than to snow depth or snow water equivalent (small slopes), based on Eqns (1–4). Even small changes in grain size and temperature predictors have a higher impact on the modelled backscatter. However, the snow depth shows a much higher spread in our dataset (Fig. 5) compared with the small spectrum of different top-layer grain sizes (Fig. 3b).

As stated by, for example, Yackel and Barber (2007) and Barber (2005), the snow/ice interface temperature as it affects the dielectric properties of the basal-snow layer (liquid-water content and brine volume fraction) is crucial for explaining the received radar backscatter. Although we did not measure snow salinity, the importance of snow/ice interface temperature is apparent in our results. Related as they are to the liquid-water content, snow grain size and volume are important determinants of volume scattering in the snowpack. Both are also reflected in our results, especially for the LIA2 class.

Because of the limited sample size, the additional potential of VV like-polarization and HV cross-polarization acquisitions could not be taken into account. It is expected that this capability will improve the retrieval of the physical properties of snow on Antarctic sea ice from X-band SAR backscatter data, but additional measurements and further investigation are necessary. This potential is underlined by the spatial and temporal differences between the like/like and like/cross-polarization TSX StripMap images (Fig. 4) for the different study sites. We were able to show that both the snow cover and the snow/ice interface have a strong influence on the TSX σ^0_{HH} signal. However, there are sources of error and uncertainties, due in large part to the lack of simultaneous daily measurements of snow physical properties and TSX swath coverage. Nonetheless, the onset of melt processes and freeze/thaw cycles is clearly recognizable in the X-band SAR backscatter time series.

SUMMARY AND CONCLUSION

In our study, we compared the spatio-temporal evolution of TerraSAR-X backscatter to in situ physical properties of snow on sea ice for a 2 month field campaign in Atka Bay from austral winter to early summer. Multiple linear models based

on different subsets of our data with respect to different local-incidence angles, were able to explain 76–93% of the observed TerraSAR-X HH-polarized backscatter, given a RMSE of 0.87–1.62 dB. The different quality of the model fits, i.e. their potential to explain a maximum percentage of the observed TerraSAR-X HH-polarized backscatter variance, results from the different subsets and limitations to the dataset, such as the exclusion of dry snow measurements. The correlation between the TerraSAR-X HH-polarized backscatter and the snow depth increases when the dataset is reduced to measurements in areas with a snow depth <0.6 m, which is still a rather large amount of snow for Antarctic sea ice. The potential to explain the variations in single-polarization HH X-band SAR backscatter with a few snow physical properties has not yet been presented in comparable detail under non-laboratory conditions. The possibility of fitting a simple multiple linear model to the measured TerraSAR-X HH-polarized backscatter based on up to four snowpack parameters also yields the potential to derive snow physical properties from X-band backscatter using an inverse approach. However, the data presented here cannot directly be used to retrieve snow physical parameters, particularly due to the limited sample size. Additional measurements are necessary (e.g. snow salinity and (quantitative) snow liquid-water content, which were very limited in our study). The addition of backscatter models, as well as snow/sea-ice models, might be informative in future studies and will further increase the potential of this dataset. Future snow-pit measurements and simultaneous TerraSAR-X acquisitions, especially in StripMap dual-polarization mode, are expected to further improve the potential for an inverse approach. Based on the relationships and links shown in this study, future work will necessarily focus on the development of an inverse approach to derive snow physical properties from X-band SAR backscatter.

ACKNOWLEDGEMENTS

This study was funded by the Deutsche Forschungsgemeinschaft in the framework of the priority programme SPP1158 'Antarctic Research with comparative investigations in Arctic ice areas' by grants HE2740/12 and NI1092/2. We thank the Neumayer III overwintering teams for their field support and also the Alfred Wegener Institute (AWI) logistics team for providing the infrastructure. We also thank the German Space Agency for the acquisition and provision of the TerraSAR-X data within the OCE1592 project and Gert König-Langlo for provision of the meteorological data. The help of Oliver Gutjahr with the statistical modelling is very much appreciated. We are also grateful to two anonymous reviewers, chief editor, Petra Heil, and scientific editor, Rob Massom, who helped to improve this study with their positive and constructive feedback.

REFERENCES

Barber DG (2005) Microwave remote sensing, sea ice and Arctic climate. *Phys. Can.*, **61**, 105–111

Barber DG and Nghiem SV (1999) The role of snow on the thermal dependence of microwave backscatter over sea ice. *J. Geophys. Res.*, **104**(C11), 25 789–25 803 (doi: 10.1029/1999JC900181)

Barber DG and Thomas A (1998) The influence of cloud cover on the radiation budget, physical properties, and microwave scattering coefficient (σ^0). *IEEE Trans. Geosci. Remote Sens.*, **36**(1), 38–50 (doi: 10.1109/36.655316)

Barber DG, Papakyriakou TN and LeDrew EF (1994) On the relationship between energy fluxes, dielectric properties, and microwave scattering over snow covered first-year sea ice during the spring transition period. *J. Geophys. Res.*, **99**(C11), 22 401–22 411 (doi: 10.1029/94JC02201)

Barber DG, Reddan SP and LeDrew EF (1995) Statistical characterization of the geophysical and electrical properties of snow on landfast first-year sea ice. *J. Geophys. Res.*, **100**(C2), 2673–2686 (doi: 10.1029/94JC02200)

Cohen J (1988) *Statistical power analysis for the behavioral sciences*, 2nd edn. Lawrence Erlbaum Associates, Hillsdale, NJ

Dierking W (2010) Mapping of different sea ice regimes using images from Sentinel-1 and ALOS synthetic aperture radar. *IEEE Trans. Geosci. Remote Sens.*, **48**(3), 1045–1058 (doi: 10.1109/TGRS.2009.2031806)

Dierking W (2013) Sea ice monitoring by synthetic aperture radar. *Oceanography*, **26**(2), 100–111 (doi: 10.5670/oceanog.2013.33)

Dierking W, Linow S and Rack W (2012) Toward a robust retrieval of snow accumulation over the Antarctic ice sheet using satellite radar. *J. Geophys. Res.*, **117**(D9), D09110 (doi: 10.1029/2011JD017227)

Drinkwater MR, Hosseinmostafa R and Gogineni P (1995) C-band backscatter measurements of winter sea-ice in the Weddell Sea, Antarctica. *Int. J. Remote Sens.*, **16**(17), 3365–3389 (doi: 10.1080/01431169508954635)

Eriksson LEB and 7 others (2010) Evaluation of new space-borne SAR sensors for sea-ice monitoring in the Baltic Sea. *Can. J. Remote Sens.*, **36**(S1), S56–S73 (doi: 10.5589/m10-020)

Fierz C and 8 others (2009) *The international classification for seasonal snow on the ground.* (IHP Technical Documents in Hydrology 83) UNESCO–International Hydrological Programme, Paris

Fritz T and Eineder M (2008) TerraSAR-X Ground Segment. *Basic Product Specification Document* TX-GS-DD-3302 Deutsches Zentrum für Luft- und Raumfahrt (DLR), Cologne

Hallikainen M and Winebrenner D (1992) The physical basis for sea ice remote sensing. In Carsey FD and 7 others eds. *Microwave remote sensing of sea ice*. American Geophysical Union, Washington, DC, 29–46

Hoppmann M and 11 others (2015) The role of ice platelets for Weddell Sea landfast sea ice. *Ann. Glaciol.*, **56**(69) (doi: 10.3189/2015AoG69A678) (see paper in this issue)

Kendra JR, Sarabandi K and Ulaby FT (1998) Radar measurements of snow: experiment and analysis. *IEEE Trans. Geosci. Remote Sens.*, **36**(3), 864–879 (doi: 10.1109/36.673679)

Kern S, Ozsoy-Cicek B, Willmes S, Nicolaus M, Haas C and Ackley S (2011) An intercomparison between AMSR-E snow-depth and satellite C- and Ku-band radar backscatter data for Antarctic sea ice. *Ann. Glaciol.*, **52**(57 Pt 2), 279–290 (doi: 10.3189/172756411795931750)

Kim YS, Onstott RG and Moore RK (1984) Effect of a snow cover on microwave backscatter from sea ice. *IEEE J. Ocean. Eng.*, **9**(5), 383–388 (doi: 10.1109/JOE.1984.1145649)

König-Langlo G (2013a) Continuous meteorological observations at Neumayer station (2012-11). *PANGAEA* (doi: 10.1594/PANGAEA.812150)

König-Langlo G (2013b) Continuous meteorological observations at Neumayer station (2012-12). *PANGAEA* (doi: 10.1594/PANGAEA.812151)

König-Langlo G (2013c) Continuous meteorological observations at Neumayer station (2013-01). *PANGAEA* (doi: 10.1594/PANGAEA.812152)

König-Langlo G (2013d) Meteorological synoptical observations at Neumayer station (2012-11). *PANGAEA* (doi: 10.1594/PANGAEA.811884)

König-Langlo G (2013e) Meteorological synoptical observations at Neumayer station (2012-12). *PANGAEA* (doi: 10.1594/PANGAEA.811889)

König-Langlo G (2013f) Meteorological synoptical observations at Neumayer station (2013-01). *PANGAEA* (doi: 10.1594/PANGAEA.811894)

Massom RA and 12 others (2001) Snow on Antarctic sea ice. *Rev. Geophys.*, **39**(3), 413–445 (doi: 10.1029/2000RG000085)

Nagler T and Rott H (2004) Snow classification algorithm for Envisat ASAR. In Lacoste H and Ouwehand L eds. *Proceedings of the 2004 Envisat and ERS Symposium, 6–10 September 2004, Salzburg, Austria*. (ESA SP-572) European Space Agency, Noordwijk

Ozsoy-Cicek B, Kern S, Ackley SF, Xie H and Tekeli AE (2011) Intercomparisons of Antarctic sea ice types from visual ship, RADARSAT-1SAR, Envisat ASAR, QuikSCAT, and AMSR-E satellite observations in the Bellingshausen Sea. *Deep-Sea Res. II*, **58**(9–10), 1092–1111 (doi: 10.1016/j.dsr2.2010.10.031)

Sihvola A and Tiuri M (1986) Snow fork for field determination of the density and wetness profiles of a snow pack. *IEEE Trans. Geosci. Remote Sens.*, **24**(5), 717–721 (doi: 10.1109/TGRS.1986.289619)

Willmes S, Haas C and Nicolaus M (2011) High radar-backscatter regions on Antarctic sea ice and their relation to sea-ice and snow properties and meteorological conditions. *Int. J. Remote Sens.*, **32**(14), 3967–3984 (doi: 10.1080/01431161003801344)

Worby AP, Markus T, Steel AD, Lytle VI and Massom RA (2008) Evaluation of AMSR-E snow depth product over East Antarctic sea ice using in situ measurements and aerial photography. *J. Geophys. Res.*, **113**(C5), C05S94 (doi: 10.1029/2007JC004181)

Yackel JJ and Barber DG (2007) Observations of snow water equivalent change on landfast first-year sea ice in winter using synthetic aperture radar data. *IEEE Trans. Geosci. Remote Sens.*, **45**(4), 1005–1015 (doi: 10.1109/TGRS.2006.890418)

Yackel JJ, Barber DG, Papakyriakou TN and Breneman C (2007) First-year sea ice spring melt transitions in the Canadian Arctic Archipelago from time-series synthetic aperture radar data, 1992–2002. *Hydrol. Process.*, **21**(2), 253–265 (doi: 10.1002/hyp.6240)

Zahnen N, Jung-Rothenhäusler F, Oerter H, Wilhelms F and Miller H (2003) Correlation between Antarctic dry snow properties and backscattering characteristics in RADARSAT SAR imagery. *EARSeL Proc.*, **2**(1) http://www.eproceedings.org/static/vol02_1/contents.html

Statutory Declaration

(on Authorship of a Dissertation)

I, Mario Hoppmann, hereby declare that I have written this PhD thesis independently, unless where clearly stated otherwise. I have used only the sources, the data and the support that I have clearly mentioned. This PhD thesis has not been submitted for conferral of degree elsewhere.

I confirm that no rights of third parties will be infringed by the publication of this thesis.

Bremen, 06 July 2015

Signature